Proceedings of the

XX INTERNATIONAL SCIENTIFIC CONFERENCE ELECTRONICS AND APPLIED PHYSICS

APHYS 2024

October, 22-25, 2024, Kyiv, Ukraine

Taras Shevchenko National University of Kyiv

Faculty of RadioPhysics, Electronics and Computer Systems

Organizing Committee

A. Netreba, Associate Professor – Chairman, Faculty of RadioPhysics, Electronics and Computer Systems, Taras Shevchenko National University of Kyiv
N. Bashmakova – Vice-Chairman, Faculty of RadioPhysics, Electronics and Computer Systems, Taras Shevchenko National University of Kyiv
V. Moiseienko, Laboratory Head – Secretary, Faculty of RadioPhysics, Electronics and Computer Systems, Taras Shevchenko National University of Kyiv
R. Bohdanov, Assistant, PhD. – Secretary, Faculty of RadioPhysics, Electronics and Computer Systems Taras Shevchenko National University of Kyiv
I. Anisimov, Professor, Faculty of RadioPhysics, Electronics and Computer Systems, Taras Shevchenko National University of Kyiv
Y. Boyko, Associate Professor, Faculty of RadioPhysics, Electronics and Computer Systems, Taras Shevchenko National University of Kyiv
A. Veklich, Professor, Faculty of RadioPhysics, Electronics and Computer Systems, Taras Shevchenko National University of Kyiv
V. Vysotskiy, Professor, Faculty of RadioPhysics, Electronics and Computer Systems, Taras Shevchenko National University of Kyiv
S. Radchenko, Associate Professor, Faculty of RadioPhysics, Electronics and Computer Systems, Taras Shevchenko National University of Kyiv
O. Nechyporuk, **Associate Professor**, Faculty of RadioPhysics, Electronics and Computer SystemsTaras Shevchenko National University of Kyiv
S. Savenkov, Professor, Faculty of RadioPhysics, Electronics and Computer Systems, Taras Shevchenko National University of Kyiv
V. Skryshevsky, Professor, Institute of High Technologies, Taras Shevchenko National University of Kyiv
A. Karlash, Associate Professor, Faculty of RadioPhysics, Electronics and Computer Systems, Taras Shevchenko National University of Kyiv
B. Hillebrands, Professor, Germany, Kaiserslautern University
M. Bartlova, Associate Professor Department of Physics, Faculty of Electrical Engineering and Communication, Brno University of Technology, Czech Republic.
O. Bondarchuk, Professor - International Iberian Nanotechnology Laboratory, Braga, Portugal
M. Strikha, Professor, Faculty of RadioPhysics, Electronics and Computer Systems, Taras Shevchenko National University of Kyiv
I.Fedirchuk, Assistant, Belgium, Antwerpen University
A. Goriachko, Associate Professor, Faculty of RadioPhysics, Electronics and Computer Systems, Taras Shevchenko National University of Kyiv
M. Kononov, Associate Professor, Faculty of RadioPhysics, Electronics and Computer Systems, Taras Shevchenko National University of Kyiv
I. Yastremsky, Associate Professor, Faculty of RadioPhysics, Electronics and Computer Systems, Taras Shevchenko National University of Kyiv
V. Ovechko, Professor, Faculty of RadioPhysics, Electronics and Computer Systems, Taras Shevchenko National University of Kyiv
A. Konovalov, Assistant, Faculty of RadioPhysics, Electronics and Computer Systems Taras Shevchenko National University of Kyiv
O. Ivanenko, Assistant, Faculty of RadioPhysics, Electronics and Computer Systems Taras Shevchenko National University of Kyiv
O. Mokhonko – PhD Student, Faculty of RadioPhysics, Electronics and Computer Systems, Taras Shevchenko National University of Kyiv
O. Murmantsev – PhD Student, Faculty of RadioPhysics, Electronics and Computer Systems, Taras Shevchenko National University of Kyiv
D. Sliusarenko – PhD Student, Faculty of RadioPhysics, Electronics and Computer Systems, Taras Shevchenko National University of Kyiv

General information

Date	October, 22-25, 2024
Location for mails	Taras Shevchenko National University of Kyiv Volodymyrska Str. 64/13, 01601 Kyiv – Ukraine
Physical location	Faculty of RadioPhysics, Electronics and Computer Systems, Taras Shevchenko National University of Kyiv, Prospect Glushkova, 4g, Kyiv 03022, Ukraine
Organization	Taras Shevchenko National University of Kyiv, Faculty of RadioPhysics, Electronics and Computer Systems

Scientific program

The Conference contributions are accepted from the following areas:
Laser Physics and Optoelectronics
Surface Physics, Nano- and Microelectronics
Physics of Semiconductors and Dielectrics, Semiconductor Devices
Physics of Magnetism
Computer Technologies
Mathematical Problems of Applied Physics
Medical Physics
Plasma Physics
Radio Engineering and Communications
Polarimetry: Theory and Applications

Conference site

All events associated with the XX INTERNATIONAL SCIENTIFIC CONFERENCE ELECTRONICS AND APPLIED PHYSICS will take place in on-line regime in 2024.

Time

Local time is one hour ahead of Middle European time – EEST (UTC+3).

Conference language

The language of the Conference Proceedings is English.

Presentation

The Conference program includes invited lectures and contributed papers. All reports will be lectured in oral presentation.
Invited talks: 40 minutes (including discussion)
Other talks: 20 minutes (including discussion)

Edited by D. Sliusarenko, O. Mokhonko.

E-mail: aphys@univ.kiev.ua
APHYS web-site: http://aphys.knu.ua/

PREFACE

The XX INTERNATIONAL SCIENTIFIC CONFERENCE ELECTRONICS AND APPLIED PHYSICS (APHYS'2024) will be held October, 22-25, 2024, in the capital of Ukraine Kyiv. The famous scientific and cultural center of Europe welcomes over 140 delegates from different Universities and Scientific Centers of European, American and Asian countries. This conference is dedicated to the memory of professor Naum Davydovych Morgulis (1904 - 1976), founder and head of the Kyiv Scientific School of Physical Electronics.

The goal of APHYS'2024 is to create a forum for discussing recent and relevant achievements in applied physics (radiophysics and electronics), bringing together scientists from various fields of physics, fostering collaboration, and encouraging international research in applied physics. Physics, development, manufacturing, and application of new physical ideas in relevant devices are particularly important for Ukraine as a member of the European community.

The APHYS'2024 is organized by Faculty of Radiophysics, Electronics and Computer Systems of Taras Shevchenko National University of Kyiv.

The Conference technical program is divided into ten sessions; three invited lectures and more than 120 oral contributions will be presented, discussed and argued.

We believe that APHYS'2024 will provide an opportunity for researchers, postgraduates and students to discuss their problems and provide and inspire the development of future research and success.

We hope the delegates will enjoy the meeting.

The next XXI INTERNATIONAL SCIENTIFIC CONFERENCE ELECTRONICS AND APPLIED PHYSICS (APHYS'2025) will be held in Kyiv, in October, 2025.

We will be glad to see you next year.

Sincerely yours,
Chairman of organizing committee of APHYS 2024 Dr. A. Netreba

INVITED LECTURES

A FAMOUS UKRAINIAN PHYSICIST NAUM DAVYDOVYCH MORGULIS

I.O. Anisimov

Taras Shevchenko National University of Kyiv,
Faculty of Radiophysics, Electronics and Computer Systems,
Glushkov Ave 4G, Kyiv, Ukraine, e-mail:anisimov1958igor@gmail.com

The report is devoted to the 120th anniversary of the birth of N. D. Morgulis - an outstanding Ukrainian physicist, corresponding member of the Academy of Sciences of Ukraine, professor, founder of the scientific school of physical electronics. The scientist's life path, his professional achievements and commemoration of his memory are highlighted. A list of the main publications of N.D. Morgulis is given.

N.D.Morgulis (1904-1976)

1. Biography

The prominent Ukrainian physicist Naum Davydovych Morgulis was born on May 14, 1904, in Letychiv, Podillia Gubernia (now Khmelnytsky Oblast), to a pharmacist. Soon they moved to Kyiv.

In 1926 N.D. Morgulis graduated from the physics department of the Kyiv Institute of Public Education (KIPE, the name of Kyiv University in that time) and worked for a year as a teacher at vocational schools. In 1927, he entered the postgraduate program at the Research Department of Physics of the All-Ukrainian Academy of Sciences (VUAN), which was later transformed into the Institute of Physics of the Ukrainian RSR. He worked at this institute until 1961 as a graduate student, researcher, group leader, head of the department (1936-1961), and vice-director (1937-1941).

At the same time, in 1927-1932, N.D. Morgulis was first a lecturer and then an associate professor at the Kyiv Polytechnic Institute. In 1932, he organized the specialization in electrophysics at KIPI. In 1934, after the reorganization of KINO into Kyiv State University (KSU), he became its professor. In 1937, on the basis of the specialization in electrophysics, he organized the department of the same name at the Faculty of Physics and Mathematics (since 1940 – at the Faculty of Physics) of KSU.

In 1937 he defended his doctoral dissertation, and in 1939 he was elected a corresponding member of the UkrRSR Academy of Sciences.

During the Second World War, while evacuated to Ufa, in 1941-43 he headed the department of the Ufa Medical Institute, and in 1943-1944 – the department of the Moscow Electrotechnical Institute of Transport

Engineers. At the same time, he worked in the defense industry – in the research and development department of one of the factories of the People's Commissariat of the Aviation Industry. After the end of World War II, he was a participant in the Soviet nuclear project.

In 1944, he returned to Kyiv, once again heading the Department of Electrophysics at the T.G.Shevchenko State University of Kyiv and a department at the Institute of Physics.

In 1952, the Faculty of Radiophysics was organized on the basis of the Department of Electrophysics of the KSU Faculty of Physics, and the department itself was renamed the Department of Electronics (later - Physical Electronics). N.D. Morgulis was its head almost until his death. He was the first professor at the Faculty of Radiophysics, developed its first curriculum, and his co-workers formed the backbone of the faculty. In the 1950s, he was the head of the closed research work "Cathode" – the first research work performed at the Faculty of Radiophysics. Its results were implemented at all enterprises in the then USSR that manufactured electronic tubes.

In 1961, N.D. Morgulis fully concentrated on his work at the T.G.Shevchenko Kyiv State University. In 1964, he organized a problematic laboratory of physical electronics on the basis of his department, which in its heyday included more than 100 employees.

N.D. Morgulis died on September 1, 1976 in Kyiv. He was buried at the Baikove cemetery.

2. Professional activity

N.D. Morgulis considered himself a successor of the Leningrad school of physical electronics of academician A.F. Ioffe (Leningrad was then a name of St. Petersburg). Throughout his life, he traveled to this city on business trips (usually on his birthday) and maintained scientific contacts with the Leningrad Institute of Physics and Technology.

N.D. Morgulis's scientific interests were concentrated in the field of physical electronics, to which plasma physics was later added. He was the author of both theoretical and experimental works, and published more than 200 scientific papers in total. His main scientific achievements include, in particular,

- creation of the ionization manometer theory (1930);
- substantiation of semiconductor properties of oxide cathodes (1946-1947);
- study of electronic and adsorption properties of metal film emitters;
- development of a plasma thermal emission converter of thermal energy into electrical energy (1941, 1949; in co-authorship);
- discovery of photoresonant plasma (1960-1971; co-authored).

He was one of the first in the former USSR to study the surface of solids in high vacuum.

A scientific school, the Kyiv School of Physical Electronics, was formed around N.D. Morgulis, whose staff worked at the Institute of Physics of the Ukrainian Academy of Sciences and at Taras Shevchenko National University of Kyiv. Kyiv became a significant scientific center in the field of physical electronics, which maintained scientific contacts with other similar centers.

For many years, N.D. Morgulis taught a course in physical electronics to students of his department. He was an excellent teacher, requiring students to work independently with scientific literature. Laboratory workshops at the department headed by him were created on the basis of real scientific installations.

Among the direct pupils of N.D. Morgulis are 3 academicians (Y.P. Korchovyi, A.G. Naumovets, M.G. Nakhodkin) and 4 corresponding members of the Academy of Sciences of Ukraine, 4 heads of departments at the Faculty of Radiophysics of the Kyiv National University (D.O. Gorodetskyi, S.M. Levytskyi, M.G. Nakhodkin, Y.I. Chutov), 7 doctors and more than 25 candidates of sciences, professors, laureates of the State Prizes of the USSR and Ukraine. Among the graduates of the Department of Electrophysics were Academician of the UkrSSR

Academy of Sciences S.I. Pekar (1938), Academician of the Kazakh Academy of Sciences V.M. Kelman (1939), and Lenin Prize winner in Science and Technology (the highest scientific award of the former USSR) E.I. Rashba.

N.D. Morgulis conducted extensive organizational work in the field of science.

He was a member of the editorial boards of periodicals, including the Ukrainian Physical Journal, the Journal of Radiophysics, "Bulletin of KSU. Physics", the periodical of the Academy of Sciences of the UkrSSR "Plasma Physics and Problems of Controlled Fusion".

He was an active participant and organizer of many All-Union scientific conferences, in particular, the permanent head of the All-Union Scientific Conferences on Low-Temperature Plasma Physics. He organized the Kyiv City Seminar on Plasma Physics and was its leader for many years.

Thanks to his ability to quickly make quantitative estimates, he always took an active part in the discussion of reports, often pointing out their mistakes to the authors.

He was a member of several scientific councils of the USSR Academy of Sciences and the Ukrainian Academy of Sciences (on physical electronics, plasma physics, energy conversion, and high-temperature thermal physics).

3. Honoring the memory

In 2004, on the occasion of the 100th anniversary of Morgulis' birth, a solemn meeting dedicated to his memory was held at the Faculty of Radiophysics of Taras Shevchenko National University of Kyiv. A special issue of the journal "KNU Bulletin. Radiophysics and Electronics", No. 6, 2004, which included scientific articles reflecting the current research directions of the scientific school founded by N.D. Morgilis. At the same time, a list of his scientific publications was published.

In 2007, the N.D. Morgulis Prize of the Presidium of the National Academy of Sciences of Ukraine was established, awarded for outstanding scientific works in the field of surface physics, physical and nanoelectronics.

In 2014, on the 110th anniversary of his birth, a memorial plaque was installed in the lobby of the Faculty of Radiophysics, Electronics and Computer Systems of the Kyiv National University (4G Glushkov Avenue). There is also a memorial plaque with his name on the main building of the Institute of Physics of the National Academy of Sciences of Ukraine (46 Nauky Avenue).

4. Main scientific publications

[1] Morgulis N.D. Thermoelectronic (plasma) energy converter. M., 1961.

[2] Morgulis N.D. Theory of the ionization manometer. Journal of Technical Physics. 1931. Vol.1, issue 1. C.57-62.

[3] N.D.Morgulis. Secondary-electron emission of metals at their bombardment by electrons. Uspekhi physicheskikh nauk. 1936. T.16, v.6. C.730-751.

[4] N.D.Morgulis. To the problem of the Schottky effect for complex semiconductor cathodes. Journal of Experimental and Theoretical Physics. 1946. Vol.16, issue 11. C.959-964.

[5] N.D.Morgulis, P.G.Borziak. Optical and photoelectric properties of silver-oxygen-zezium cathodes. Reports of the USSR Academy of Sciences. Physics. 1948. T.59, №4. C.625-628.

[6] N.D.Morgulis, D.A.Gorodetsky. Reflection of slow electrons from surfaces of pure and thin film-coated tungsten. Journal of Experimental and Theoretical Physics. 1956. Vol.30, issue 4. P.667-674.

[7] N.D.Morgulis. Conversion of thermal energy into electrical energy by means of thermoelectron emission. Uspekhi physicheskikh nauk. 1960. Vol.70, issue 4. P.679-692.

[8] N.D.Morgulis, A.M.Przhonsky. Nature of Ionization in Photoresonant Cesium Plasma. Journal of Experimental and Theoretical Physics. 1970. V.58, vol.6. C.1873-1878.

FEATURES OF PLASMA-SURFACE INTERACTION AT EXTREME OF PARTICLES AND ENERGY LOADS

V. A. Makhlai, S.S. Herashchenko, I. E. Garkusha, Yu.V. Petrov, N.V. Kulik , D.V. Yelisyeyev, Y.E. Volkova, P. B. Shevshuk, Yu. V. Siromolot, S.I. Lebedev

National Science Center "Kharkiv Institute of Physics and Technology", Institute of Plasma Physics, Kharkiv, Ukraine;
email:makhlay@kipt.kharkov.ua

The plasma energy transfer to plasma-facing materials, as well as the energy and particles exhaust, needs to be extensively studied for the implementation of the next-step fusion reactor project. Analysis of plasma-surface inter-action features has been performed using QSPA exposures of reference plasma-facing materials. The parameters of the plasma streams imitated conditions of transient events in a fusion reactor.

Introduction

High-power magnetically confined fusion devices produce very high heat and particle loads on the plasma-facing surfaces. Handling this heat is a major challenge in both present and future devices, e. g. DEMO [1]. The most dangerous transients in tokamaks are the disruptions and ELMs [1 - 4]. Unmitigated disruptions in DEMO will damage the divertor targets, leading to melting, melt splashing, and ionization [2, 3]. However, the target material vaporized from the target surface at the initial stage of the transient can create a secondary plasma shield of the vaporized material in front of the target, which effectively protects the target surface from the rest of the heat flux [1, 2, 4]. Injection of heavy noble gas in front of exposed surfaces might be one of the additional options for the mitigation of material damage in the course of severe transients and for efficient protection of divertor components in fusion devices.

Quasi-stationary plasma accelerators (QSPAs) have the capability to reproduce disruption and ELM impacts in terms of both heat load and particle flux to the surface which mimics the divertor conditions [2, 3]. The energy transfer from powerful plasma to tungsten surfaces during plasma-surface interactions (PSIs) has been investigated within the quasi-stationary plasma accelerators: QSPA Kh-50 and QSPA-M [5-8]. The studies of vapour shielding of liquid-metal tin capillary porous structures (CPSs) under plasma loads relevant to fusion reactor transient events have been also performed in simulation experiments using QSPA experimental facilities [6]. The influence of the additional injection of Ar cloud in front of the tungsten target on the shielding layer is also discussed [8]. The article presents a comparative study of the contribution of shielding layers in front of exposed surfaces to energy transfer from the powerful QSPA plasma streams to surfaces of different materials.

Experimental facilities, results and summary

The experiments were performed within two QSPAs devices: QSPA-M and QSPA Kh-50. The QSPA-M device can reproduce conditions of ITER ELM [5-8]. The plasma pulse duration of QSPA-M slightly exceeded 0.1 ms. The maximum value of the hydrogen plasma pressure measured with a piezo detector amounted to 0.3 MPa. The plasma stream diameter was around 5 cm in the presence of a B-field and increased to 15 cm when the external magnetic field was switched off. The value of energy density in the axis region of the plasma stream varied in a range of 0.1 to 1 MJ/m^2 [6,7]. The main parameters of the QSPA Kh-50 hydrogen plasma streams were as follows: an ion impact energy of about 0.4 keV, a maximum plasma pressure of 0.32 MPa, and a stream diameter of 18 cm. The plasma pulse shape was approximately triangular with a pulse duration of 0.25 ms. Energy density in the plasma stream achieved 3 MJ/m^2 [5-7].

The heat load absorbed by the tungsten (W) surface is approximately 60% of the impact plasma energy (> 1.2 MJ/m^2). Nevertheless, this heat load caused the melting onset on the exposed tungsten surfaces. The heat load to Sn surfaces reached a saturation point at 0.3 MJ/m^2 under the same impacting energy conditions. Thus, the

energy density delivered to the capillary porosity system wetted by tin is half as small as that of a tungsten surface. The lower evaporation threshold of Sn causes a large shielding effect. The thickness of the shielding layer increases with the growth of the magnetic field. Sn lines are detected at essentially longer distances of up to 3 cm from the exposed surface in the magnetic field of 0.8 T. When the magnetic field was switched off, the spectral lines of Sn were registered only in a very thin plasma layer near the exposed surface (<0.5 cm from the surface). Thus, a magnetic field promotes the plasma shield confinement in front of the surface. The combined tungsten-tin target can mitigate the influence of the plasma stream with larger energy compared to pure tungsten samples. Nevertheless, a large splashing of particles accompanied plasma-surface interaction with the target wetted by tin. Therefore, the evolution of CPS.

A special gas injector was designed for an additional pulsed injection of noble gas cloud (argon) along the exposed target surface into the zone of plasma-surface interaction. The injector is capable of generating a homogeneous gas flow with a maximum concentration over $n_{Ar} = 6 \times 10^{23}$ m^{-3} within a 0.5 ms pulse [8]. For pure hydrogen plasma exposures with an energy density of 0.8 MJ/m^2, some dynamical screening of the surface by the stopped head part of impacting hydrogen plasma occurs. The addition small amount of argon causes an increase in the thickness of the protective layer in front of the target in the presence of the magnetic field.

The experiments have shown that an increase in the argon gas density in front of the surface leads to a decrease (1.5 - 2 times) in the energy load delivered to the target surface. In the presence of a strong magnetic field (up to 1 T), both the thickness of the shielding layer and the fraction of the energy dissipated by the shield further increase. Even at rather moderate energy densities of the QSPA plasma streams in the experiments with Ar gas injection, less than 40% of the impacting plasma load is absorbed by the tungsten surface. The results demonstrate that this additional shielding attributed to the formation of a dense Ar-H plasma layer in front of the exposed surface should be favorable for the divertor armour performance, being important for decreasing the overall erosion of plasma-facing components and promoting suppression of W impurities transport to the core plasma in the course of transient events in a fusion reactor.

References

[1] G. Federici et al Fusion Eng. Des. vol. 136, p. 729, 2018.
[2] J.H. You et al. Fusion Engineering and Design. vol. 174, p. 112988, 2022.
[3] N. Mantel et. al. Nucl. Fusion vol. 62, p. 036017, 2022.
[4] S. Pestchanyi and F. Maviglia Fusion Sci. Technol. vol. 75, p.p. 647–53, 2019.
[5] S. S. Herashchenko et. al. Fusion Engineering and Design vol. 190, p. 113527, 2023.
[6] I.E. Garkusha et. al. Nucl. Fusion vol. 61, p. 116040, 2021.
[7] V. A. Makhlai et. al. Prob. of At. Sci. and Tech. #148 (6), p.p. 101-105, 2023.
[8] I. E. Garkusha et. al. Nucl. Fusion vol. 64, p. 056010, 2024.

X-ray PHOTOELECTRON SPECTROSCOPY: TOWARDS ASSESSING NANOINTERFACES

Oleksandr Bondarchuk*, **, ***

** International Iberian Nanotechnology Laboratory, Av. Mestre José Veiga, s/n, 4715-330, Braga, Portugal*
e-mail: alex.bondarchuk@inl.int
*** SPIN-Lab Centre for Microscopic Research on Matter, University of Silesia in Katowice, 75 Pułku Piechoty Str. 1A, Chorzów 41-500, Poland*
****Institute of Chemistry, University of Silesia in Katowice, 9 Szkolna Str., 40-006 Katowice, Poland*

X-ray photoelectron spectroscopy (XPS or ESCA) has a long history that can be traced back to the discovery of X-rays by Wilhelm Röntgen in 1895 and explanation of the photoelectron effect by Albert Einstein in 1905. Since 1950s the photoelectron effect has developed into one of powerful tools for studying the composition and electronic structure of matter, with Kai Sigbahn receiving the Nobel Prize in 1981 for the development of high-resolution XPS.

I will briefly present the basic concepts and observable effects in X-ray photoelectron spectroscopy (XPS) with focusing on the XPS spectra interpretation and analysis of some typical misinterpretations of the experimental data. I will then turn to some examples of applications of this technique. Some of the areas explored will be the use the XPS to assess structure and properties of solid-solid interfaces at nanoscale level using as examples supported nanoclusters and structure and properties of liquid- solid interfaces using the ionic liquid-graphite, ionic liquid-nano sized gold interfaces.

LASER PHYSICS

AND

OPTOELECTRONICS

DIELECTRIC LASER ACCELERATION OF NON-RELATIVISTIC ELECTRONS ON TRANSPARENT AND REFLECTIVE PERIODIC CHIP-STRUCTURES

Ihor Beznosenko*, Andrii Vasyliev, Gennadiy Sotnikov***, Serhii Kovalov****, Gennadiy Krivonosov*****, Roman Kniaziev******

** National Science Center "Kharkiv Institute of Physics and Technology", Kharkiv 61108, Ukraine*
e-mail: beznosenko1989@gmail.com
*** National Science Center "Kharkiv Institute of Physics and Technology", Kharkiv 61108, Ukraine*
e-mail: vasilyev.andrey90@gmail.com
**** National Science Center "Kharkiv Institute of Physics and Technology", Kharkiv 61108, Ukraine*
e-mail: sotnikov@kipt.kharkov.ua
***** National Science Center "Kharkiv Institute of Physics and Technology", Kharkiv 61108, Ukraine*
e-mail: covalov.sergiy@gmail.com
****** National Science Center "Kharkiv Institute of Physics and Technology", Kharkiv 61108, Ukraine*
e-mail: krivonosov40@gmail.com
******* National Science Center "Kharkiv Institute of Physics and Technology", Kharkiv 61108, Ukraine*
e-mail: rkniaziev@gmail.com

Dielectric laser electron accelerators have compact dimensions and high efficiency, which makes them attractive for many scientific and industrial applications [1]. Medical physics: to create high-energy electron beams used in radiotherapy for cancer treatment, as well as the analysis of biomolecules; Scientific research: in experiments to study fundamental particle interactions, for example in high-energy physics; Materials science: to analyze and modify the properties of materials using electron beams; Technology: in the production of microcircuits and semiconductor devices, where high-energy electrons are used for ion implantation.

Scheme of the experimental setup

The scheme of the setup for conducting experiments on laser acceleration of electrons on periodic chip-structures is presented in Fig. 1.

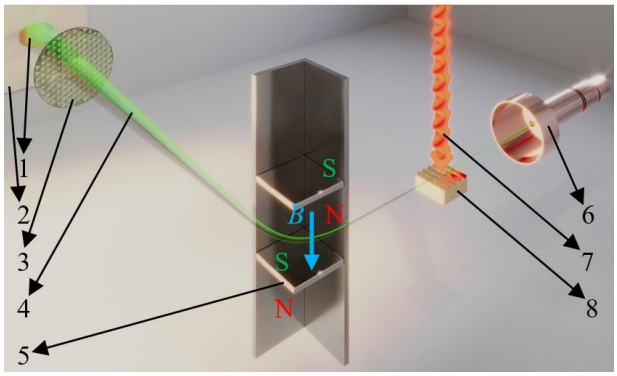

Fig. 1. 3D model of dielectric laser acceleration (DLA) experiment

An electron beam with a given initial energy is emitted using an electron gun (6). Next, electrons are injected into a modulated periodic electromagnetic field created by a laser pulse (7), which is reflected from a reflective periodic chip-structure (8) or passes through a transparent periodic structure [2] (then this structure will be above the electron beam in Fig. 1). The magnetic spectrometer (5) spatially separates electrons with different energies (the most accelerated electrons are shown in red, electrons with energies close to the initial ones are shown in green, and the most decelerated ones are shown in blue). These electrons (4) pass through the MCP (3) in order to increase the output signal from the electrons (1) on the phosphor screen (2).

Research on periodic chip-structures for DLA

The Particle in Cell (PIC) simulation method was used to investigate the acceleration rates of electrons with an initial energy of 33.9 keV and the quality of their beams during laser acceleration on single and double transparent periodic chip-structures of different configurations. The main dependences of electron acceleration rates on the geometry of transparent chip-structures are correlated with those described in [3]. It has been found that the highest acceleration rate (87 MeV/m) and the most collimated electron beam at the accelerator output can be obtained by double-sided irradiation of a double transparent periodic chip-structure with an asymmetric arrangement of pillars (the pillars of one half of the structure are opposite the grooves of the other half).

The acceleration rates of electrons with initial energy E_k = 33.9 keV and the quality of their beams during laser acceleration on single and double reflective periodic chip-structures of different configurations were also investigated. It has been found that the highest acceleration rate (202 MeV/m) and the most collimated electron beam at the accelerator output can be obtained by double-sided irradiation of a double reflective periodic chip-structure with a rectangular profile and a chirped period. However, the proposed for the first time scheme with tilting the phase front of laser radiation relative to the surface of the chips, which is presented in Fig. 2, can be the most practical DLA scheme with dephasing compensation.

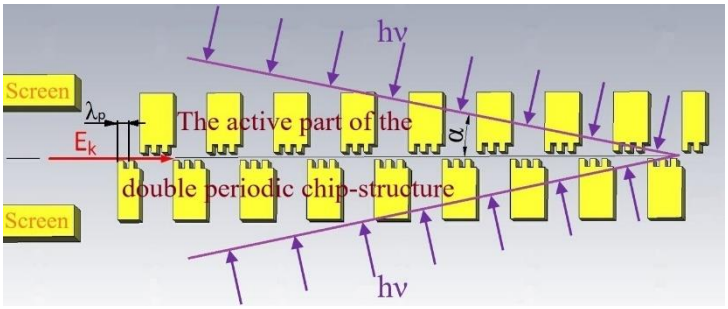

Fig. 2. Dephasing compensation during DLA on a double periodic chip-structure by tilting the phase front of laser radiation

$$\alpha = \arccos\left(1 - \frac{c \cdot \lambda_p}{\lambda \cdot (n-1)} \cdot \left(\frac{1}{\beta_1 \cdot c} - \frac{1}{\beta_n \cdot c}\right)\right),$$

where λ_p is length of the period of the chip-structure [3]; λ is central length of laser radiation; c is velocity of laser radiation in vacuum; β_1 is dimensionless velocity of the electron over the center of the first chosen pillar of the structure; β_n is dimensionless velocity of the electron over the center of the n-th pillar of the structure relative to the first chosen one: $\beta_n = \sqrt{1-(1+E_{kn}/E_0)^{-2}}$, $n = 2,3,4...N$, E_{kn} is kinetic energy of the electron over the center of the n-th pillar, E_0 = 511 keV is electron rest energy. β_1 and β_n are taken on the rectilinear section of acceleration. For our case of DLA, α angle calculated using the above formula was equal to 2 degrees and gave stable acceleration over the entire section of the periodic chip-structure onto which the laser radiation falls.

References

[1] R.J. England, U. Niedermayer, L. Schachter, T. Hughes, P. Musumeci, R.K. Li, W.D. Kimura. Considerations for a TeV collider based on dielectric laser accelerators // *JINST*. 2022, v. 17, p. 05012. http://doi.org/10.1088/1748-0221/17/05/P05012.

[2] J. Breuer. Dielectric laser acceleration of non-relativistic electrons at a photonic structure. Diss. Ludwig-Maximilians University. 2013, p. 10.

[3] Y. Wei. Investigations Into Dual-Grating Dielectric Laser-Driven Accelerators. Diss. the University of Liverpool, 2018, p. 41, p. 15, 46-52.

ENHANCED PRISM-COUPLED CHIRAL SENSING WITH PLASMONIC GRATINGS

O. Demianyk[*], S. Polevoy[**], V. Tuz[*], O. Yermakov[*]

**V.N. Karazin Kharkiv National University, 4 Svobody Square, Kharkiv 61022, Ukraine*
***O. Ya. Usikov Institute for Radiophysics and Electronics of the NASU, 12 Proskura st., Kharkiv 61085, Ukraine, e-mail: o.demianyk@gmail.com*

Chirality is an asymmetric property, so enantiomers show different responses under illumination with various polarization states. The angular shift of the resonant peak between the right- and left-handed circularly polarized light determines the sensitivity of the related chiroptical detector. The main idea is to apply a hyperbolic optical resonant metasurface supporting highly localized hyperbolic plasmon-polaritons of hybrid TE-TM polarization for sensing chiral molecules at their low concentrations. We expect the multifold enhancement of the real-time enantiomers detection using the developed nanostructures to outperform all the known techniques for chiroptical sensing.

Introduction

Chirality is used to describe an object that is not superposable on its mirror image. Despite having the same chemical structure, most chiral molecules show significant differences in biological activity, being the poison or the drug depending on the handedness. The main difficulty during the measurement of chiral substances is the need to detect extremely weak chiroptical signals from a small concentration of chiral molecules. The goal of our work is to develop a method that will allow us to separate a small concentration of chiral molecules with high accuracy in real-time measurements.

Methods

In this work, we first excite a surface plasmon-polariton via the prism coupling in the attenuated total internal reflection regime with a plane TM-polarized wave in Kretschmann configuration [1]. In this case, the small response in the TE-polarization emerges due to the mixing of electric and magnetic fields. As a result, there is an angular difference between the spectral resonances in right- and left-handed circular polarized waves due to the presence of chiral substance. To characterize the sensitivity of chiral substance detection we consider the amplitude and phase of the differential reflectance and the dependence of the angular shift on the chiral parameter.

Results

We aim to increase the angle of divergence between the reflection spectra peaks for the left- and right-handed circular polarization, and accordingly the efficiency of chiral sensing. It may be achieved via the enhancement of the response in TE polarization. Introducing the efficient 2D conducting layer instead of the metal film, we improve the efficiency of chiral sensing by about an order of magnitude. As a main result, we found the optimized design of gold thin nanogratings on the BK-7 glass achieving the improvement of the chiral sensitivity by about two orders of magnitude in comparison to the unstructured gold thin film. In this case the enhancement of the differential reflection coefficient resonance up to almost 100 times for the case of optimized nanograting. So, the simple measurement will allow us to define whether the chiral substance possesses D (+) or L (-) type of enantiomers.

Acknowledgments

The authors acknowledge the support from the EURIZON Fellowship Programme “Remote Research Grants EU#3003-EURIZON” (no. 871072).

References

[1] S. Droulias, L. Bougas, “Surface Plasmon Platform for Angle-Resolved Chiral Sensing”, ACS Photonics, vol. 6, pp. 1485-1492, May 2019.

MODELING AND OPTIMIZATION OF OPTOELECTRONIC SENSORS

Okhrimchuk O.B., Doctor of Technical Sciences, Professor Verbytskyi V.G.

National Technical University of Ukraine "Ihor Sikorsky Kyiv Polytechnic Institute",
e-mail: o.okhrimchuk-me26@lll.kpi.ua
National Technical University of Ukraine "Ihor Sikorsky Kyiv Polytechnic Institute",
e-mail: v.g.verbitskiy@gmail.com
Faculty of Electronics, Micro- and Nanosystem Engineering, National Technical University of Ukraine "Ihor Sikorsky Kyiv Polytechnic Institute", Kyiv 03056, Ukraine, e-mail: me@kpi.ua

The paper considers the optimal design of an optoelectronic sensor. It is characterised by the ability to measure displacement in the millimetre range with submicrometre resolution. The sensor consists of a triangular reflective grating and two fibre-optic probes. The measurement principle of the sensor is shown. The design of the triangular grating was mathematically optimised with respect to the grating pitch angle to increase the sensor resolution. The optimisation method revealed a global optimum at which the highest resolution is achieved.

Subtitle

Devices based on high-precision; low-power optoelectronic systems have been one of the main research topics in recent years. The development of optoelectronic sensors with high sensitivity, wide dynamic range and low power dissipation dominates the research field for various commercial applications, including transport, biomedicine, space, avionics and environmental monitoring. The use of mathematical models in combination with experimental research and technical development can significantly improve the efficiency and reliability of optoelectronic sensors, provide predictive capabilities for possible failures and plan their maintenance. This helps to prevent unforeseen situations and reduce system downtime.

Subtitle

High-resolution optical displacement sensors based on Fabry-Perot interferometers are widely used in optoelectronic devices due to their high displacement measurement accuracy and immunity to electromagnetic interference [1]. In a study by Chang-Ping Chang [2], the design of a conventional Fabry-Perot interferometer was modified to achieve 1/4 wavelength optical resolution. to achieve a measurement range of 100 mm. Another example is a wide-range sensor with three grating axes developed by Jie Lin [3]. This sensor can simultaneously measure translational motion in the X, Y, and Z axes. The grating encoder consists of a large area flat reflective grating with a period of 8 μm and an optical read head. To make the grating encoder more compact, a double emission grating element and two diffractive optical elements were introduced. Experimental results showed a resolution of 4 nm for movements in the Z-axis direction.

Akihide Kimura et al [4] described a three-axis surface encoder consisting of a planar array and an optical sensor head. It was designed and fabricated to measure sub-nanometer displacements in the X, Y, and Z axes. The dimensions of the optical sensor head were 50 mm (X) × 70 mm (Y) × 40 mm (Z), and the resolution of the sensor was better than 1 nm in all three axes.

There have also been several studies based on other optical methods for linear displacement measurement: a high-performance optical sensor was developed by A. Missoffe et al [5]. This compact measurement system consists of a laser diode module and an array of photodiodes. The system is characterized by its insensitivity to large mechanical defects. Experimental results show that the sensor can achieve nanometer resolution in the centimeter range.

The performance of the fiber optic displacement sensor is affected by geometric parameters such as fiber aperture, fiber core radius, distance between the transmitting and receiving fibers, angle between the two fibers, and reflector radius. It has been observed that the distance between the transmitting and receiving fibers should be kept as small as possible to increase the sensitivity.

Thus, to solve this problem, a multi-objective optimization method using natural metaheuristic algorithms is applied. This method is more complex than the optimization method applied to the sensor in this study: a Python programming environment is used to optimize the sensor, and an analytical model is used to determine the optimal geometric parameters of the cantilever for photoacoustic sensing by capacitive conduction. It can be said that the geometric parameters change the performance of the sensor, which is consistent with the optimization method used in this study.

A geometric model was developed to measure the geometric parameters of the arrays and simulate the behavior of the large-scale transducer. The model uses as inputs the geometric dimensions of each fiber and the distance between the gratings. At the output, the model outputs the characteristics of the corresponding sensor. These characteristics include sensor resolution and the overlap distance required to easily switch between two fiber sensors.

This model considers two conditions:

1. The distance between the probe and the grating step should be in the linear zone

2. The overlap distance required to switch between two successive fiber optic probe signals to avoid a break in the linear measurement during a step transition depends on the measured displacement rate. It is generally considered to be between 10 and 30 μm.

Optimization techniques have been proposed to improve sensor performance. The aim is to improve the highest sensor resolution (divergence resolution) by reducing the corresponding value. This can be achieved by using geometric parameters, in particular the angle ε.

The main goal of this development is to determine the optimal size of the planar sensor array that will improve the resolution. The physical model of the sensor has not yet been implemented, and the results are based on previously used programs in which the sensor principle was validated.

As a result, the geometric design of the optoelectronic sensor is improved in terms of sensitivity, resolution and measurement range. In this paper, a global optimum between the sensitivity and resolution of the sensor is obtained, which leads to an improvement in the overall performance of the sensor. This global optimum improves the sensitivity and resolution in the lateral direction even if the axial characteristics are unfavorable. Despite the increased measurement range, the sensitivity of the sensor increased to 4.28 mV/micron. However, higher sensitivity values could be achieved if the axial characteristics were better. On the other hand, the corresponding overlap criterion should be considered as a function of the sampling rate and sampling frequency of the measurement system. The geometrical parameters of the sensor in the optimum region will be considered during the fabrication of the grating in the future to experimentally confirm this global optimum. For the sensors mentioned in this study, in terms of resolution and measurement range, the worst-case resolution limit is at the nanometer scale.

References

[1] Kim, Y.-S.; Dagalakis, N.G.; Choi, Y.-M. Optical fiber Fabry-Pérot micro-displacement sensor for MEMS in-plane motion stage. Microelectron. Eng. 2020, 187–188, 6–13.

[2] Chang, C.P.; Tung, P.C.; Shyu, L.H.; Wang, Y.C.; Manske, E. Fabry–Perot displacement interferometer for the measuring range up to 100 mm. Measurement 2023, 46, 4094–4099.

[3] Lin, J.; Guan, J.; Wen, F.; Tan, J. High-resolution and wide range displacement measurement based on planar grating. Opt. Commun. 2021, 404, 132–138.

[4] Kimura, A.; Gao, W.; Kim, W.; Hosono, K.; Shimizu, Y.; Shi, L.; Zeng, L. A sub-nanometric three-axis surface encoder with short-period planar gratings for stage motion measuremen. Precis. Eng. 2022, 36, 576–585.

[5] Missoffe, A.; Chassagne, L.; Topçu, S.; Ruaux, P.; Cagneaux, B.; Alayli, Y. New simple optical sensor: From nanometer resolution to Centimeter displacement range. Sens. Actuators A 2018, 176, 46–52.

INVESTIGATION OF SELF-ACTION MANIFESTATION OF SUDAN 3 AND SUDAN 4 BASED PMMA COMPOSITES

Labunets A.R.[1], Ronkovych A.V.[2], Ilchenko S.G. [1], Komarenko D.O.[2], Ovdenko V.M.[1,2]

[1] Advanced Materials Nonlinear Optical Diagnostics Lab, Institute of Physics of the NAS of Ukraine. pr. Nauki, 46, Kyiv 03028, Ukraine, e-mail: andrew.ronkovich@gmail.com, komarenko.dmytro@gmail.com
[2] Department of Chemistry, Taras Shevchenko National University of Kyiv, Volodymyrska 64/13, 01601 Kyiv, Ukraine, e-mail: valeryovdenko@gmail.com, art.labunets@gmail.com

Azobenzenes are promising class of so-named A-π-D type organic molecules that showed possibilities of its application in wide range of technologies such as optics communications, sensing, nonlinear optics [1-2]. This is due to their trans→cis→trans photoisomerization. Nonlinear optical properties of numerous commercially available molecules such as Congo red, Disperse Red and Disperse Orange azo dyes was investigated in solutions and thin films using fundamental 532, 633 and 1064 nm laser excitation wavelength. However, until now, a large number of commercially available and promising azo-chromophores have not been sufficiently studied and compared in terms of their effectiveness with already known analogues. The simplest and fastest way to study the NLO properties of azo compounds is to incorporate them into polymer matrices in low concentrations in order to avoid both the solvation effect and possible aggregation of the substance, which can distort the obtained responses.

Substituent effect on self-action in Sudan-PMMA composites

Two commercially available azo-dyes ***Sudan 3*** and ***Sudan 4*** *(Figure 1)* were selected for NLO properties investigations. The scientific interest was to discover the influence of an additional azo fragment and two methyl substituents in the benzene ring on the magnitude of the refractive and absorptive NLO effects.

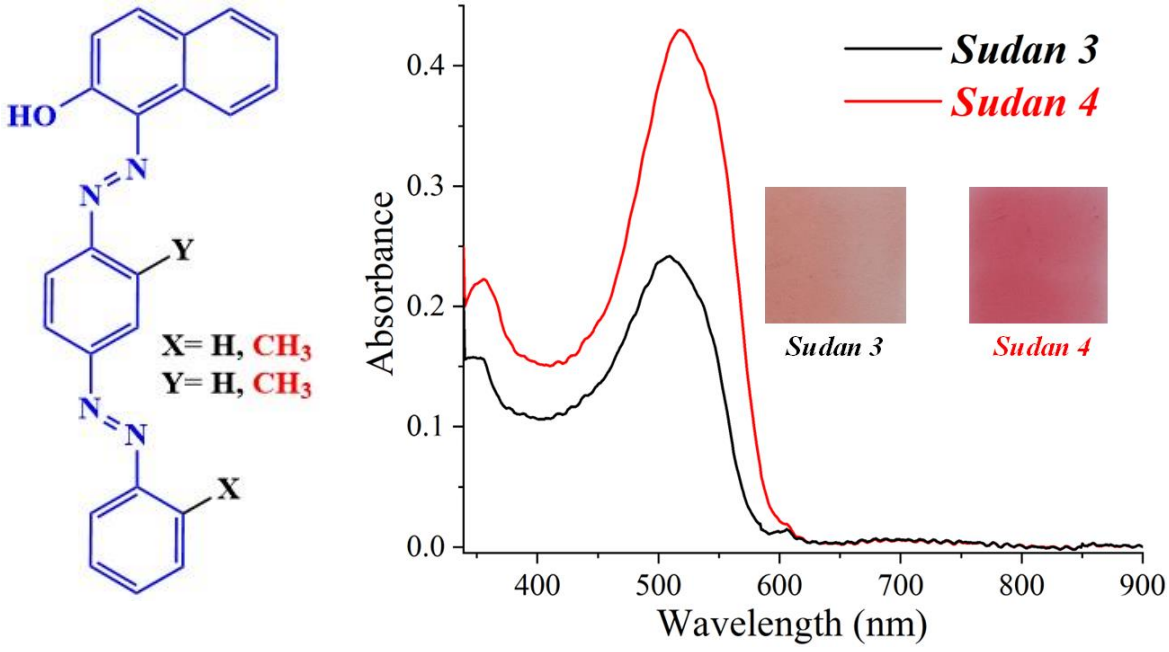

*Fig. 1. Azobenzenes **Sudan 3** and **Sudan 4** structures and UV-Vis spectra of thin PMMA films under investigation*

For this reason, molecules were incorporated into the optically transparent polymeric matrix. PMMA containing azo-chromophores (1 wt%) thin films with thickness about 5 μm were formed from DCE solution.

Experimental setup for nonlinear optical diagnostics *via* laser beam spatial profile distortions analysis in the far field included continuous wave DPSS laser excitation at 532 nm.

The films are colored in shades of red as shown in *Figure 1* and demonstrates absorption maxima at wavelengths of 508 (***Sudan 3***) nm and 518 (***Sudan 4***) nm, respectively, showing strong absorption at wavelengths of 532 nm. Thus, laser irradiation will promote resonant transitions in the molecules.

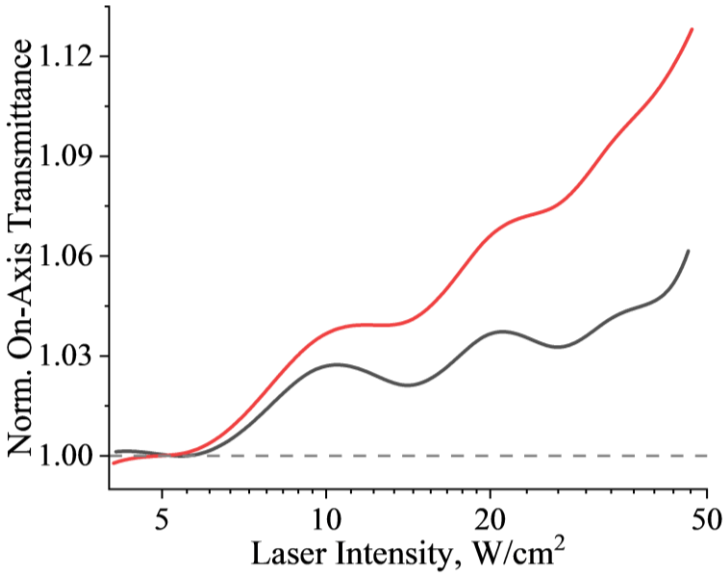

Fig. 2. Normalized on-axis transmittance in the far field of Sudan 3 (black line) and Sudan 4 (red line) azobenzenes in PMMA thin films under CW laser radiation at 532 nm.

Analysis of photoinduced variations of normalized on-axis transmittance are presented in semi-log scale on *Figure 2*. It is seen that refractive NLO response of ***Sudan 4*** ($Re(\chi^{(3)}) \sim 9.3\times10^{-3}$ esu for $I \sim 8$ *W/cm*^{2} and $Re(\chi^{(3)}) \sim 3.6\times10^{-3}$ esu for $I \sim 35$ *W/*cm^2) is generally higher than that of ***Sudan 3*** ($Re(\chi^{(3)}) \sim 6.7\times10^{-3}$ esu and $Re(\chi^{(3)}) \sim 1.4\times10^{-3}$ esu correspondingly). We believe that this could be explained by the electron-donor -CH_3 group incorporation to ***Sudan 4*** dye, which amplifies electron density transfer in a molecule compared to neutral -*H* group in ***Sudan 3***. However, optical quality factor FOM (figure of merit) values were ~ 0.8/0.9 for ***Sudan 3***/***Sudan 4*** at the initial part of the experiment ($I \sim 8$ *W/cm*^{2}), developing to 1.3/2.8, respectively, at moderate level of laser intensity. We, thus, can suggest that at the low level of irradiation fluence absorption is a dominant effect, while at higher intensities refractive NLO response becomes principal.

Conclusions. We have studied optical properties of thin PMMA films doped with two commercially available ***Sudan 3*** and ***Sudan 4*** azo dyes with two -N=N- moieties, which demonstrated efficient photoinduced variations of refractive index under CW laser radiation excitation at wavelength 532 nm. We have demonstrated an infulence of electron-donor -CH_3 group incorporation to the ***Sudan 4*** dye, where refractive NLO response was approximately 1.5 times higher than that for ***Sudan 3***. Though, at the initial stage of laser excitation a contribution of dyes' absorption is significant.

References

[1] V. M. Ovdenko, D. O. Komarenko et al. Optical Materials, 2023, 138, 113735.
[2] V. N. Ovdenko, V.V. Multian et al. J. Mater. Chem. C, 2020, 8(26), 9032-9045.

ENGINEERING OF PLASMONIC ANISOTROPIC NANOPATCH-BASED METASUrFACES

Hrinchenko A.*, Polevoy S., Demianyk O.*, Yermakov O.***

** V.N. Karazin National University, 4 Svobody square, Kharkiv, 61022, Ukraine, e-mail:artitus1509@gmail.com*
*** O. Ya. Usikov Institute for Radiophysics and Electronics NASU, 12 Akademika Proskura, Kharkiv, 61085, Ukraine*

Hyperbolic metasurfaces are known for their dispersion and polarization properties, such as negative refraction, hyperlensing, enhanced spontaneous emission, etc [1]. The surface waves localized at hyperbolic metasurfaces are called hyperbolic plasmon-polaritons and exhibit a lot of potential applications for planar technologies [2].

In this work, we analyze the dependencies of the spectral positions of the resonances and spectral bandwidth of hyperbolic regime for the metasurfaces based on square arrays of the nanodisks [3] and rectangular nanopatches. Namely, we study the resonant characteristics of metasurfaces by varying the size of the nanoparticles, the degree of stretching (anisotropy) and the period of the metasurface from the isotropic to extreme anisotropic cases. As a result, we defined the quadratic dependence of the spectral difference between the resonances for one of the resonances on the anisotropy degree, when the electric field is oriented along the stretching direction. Surface plasmons typically propagate radially (Fig.1a) in all directions, losing a significant portion of their energy during directional transmission. Typical values of the signal amplitude reaching the receiver usually do not exceed 0.1% of the signal amplitude at the source output, and this significantly limits the use of surface plasmons in practical applications. To solve this problem, we demonstrate the one special regime as plasmon canalization, which is characterized by a flat isofrequency contour (Fig.1b) and the self-collimated unidirectional propagation of surface wave. In this case, the signal transmission efficiency is close to the maximum, that is, the signal amplitude at the source output and at the receiver input are approximately the same, which makes it possible to ensure highly efficient signal transmission with minimal losses. The canalization takes place in the vicinity of one of the resonances highlighting the relevance of the metasurface engineering for the in-plane optical signal transferring.

A.H. acknowledges the support from IEEE Microwave Theory and Technology Society (IEEE MTT-S) within the Undergraduate/Pre-Graduate Scholarship.

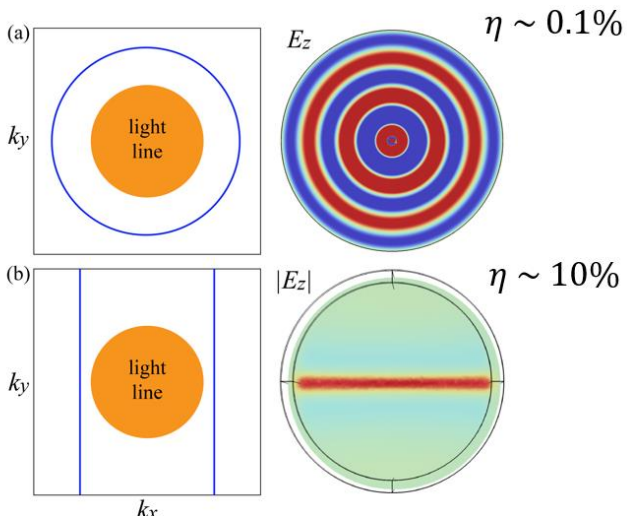

Fig. 1. Isofrequency contours and the spatial distributions of the normal components of electric field of surface waves in the (a) radially and (b) canalization regimes, respectively.

References

[1] O. Takayama, A.V. Lavrinenko, "Optics with hyperbolic materials," J. Opt. Soc. Am. B: Opt. Phys. vol. 36, pp. 38–48, Apr. 2019
[2] J. S. Gomez-Diaz, A. Alu, "Flatland optics with hyperbolic metasurfaces," ACS Photonics. vol. 3, pp. 2211-2224, Nov. 2016
[3] A. Hrinchenko, O. Yermakov, "Designing optical hyperbolic metasurfaces based on gold nanodisks," J. Phys. D: Appl. Phys. vol. 56. pp. 465105, Aug. 2023

ABSORPTION SPECTRA OF CHALCOGENIDE SEMICONDUCTORS DOPED WITH ERBIUM

O.V. Machulianskyi, V.V. Buteiets*****

** National Technical University of Ukraine "Igor Sikorsky Kyiv Polytechnic Institute"*
*Kyiv, Ukraine-, e-mail: ** machulansky@gmail.com, *** vira.byteets@gmail.com*

In this work, the optical absorption spectra of single crystals were investigated $(Ga_{70}La_{30})_2S_{300}$, $(Ga_{69,75}La_{29,75}Er_{0,5})_2S_{300}$ *in the range of 600-1050 nm.*

In modern materials science, which deals with semiconductor compounds, considerable attention is paid to the study of complex chalcogenide systems and crystal structures, in particular chalcogenide semiconductors doped with rare earth elements. These materials are characterized by high transparency in the visible and near-infrared spectral range, low phonon energy, and fairly high solubility of rare earth metals in both crystalline and amorphous forms.

The study of photoluminescence helps to understand the mechanisms of formation of energy states in ions of rare earth elements and to analyze transitions between excited states. These materials have prospects for use in photonic devices, lasers, optical amplifiers, light converters, and as electro-optical switches and memory elements.

Investigating the optical properties of single crystals $(Ga_{70}La_{30})_2S_{300}$, $(Ga_{69,75}La_{29,75}Er_{0,5})_2S_{300}$, is an important task that will enable the development of efficient materials for optoelectronics. Therefore, the aim of this work is to study the photoluminescence of single crystals $(Ga_{70}La_{30})_2S_{300}$, $(Ga_{69,75}La_{29,75}Er_{0,5})_2S_{300}$ *in the range of 600 - 1050 nm and depict them on graphs.*

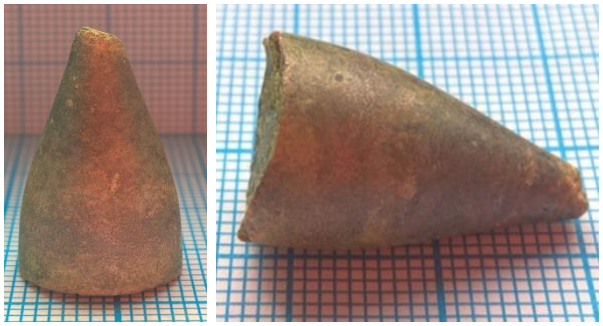

Single crystals $(Ga_{70}La_{30})_2S_{300}$, $(Ga_{69,75}La_{29,75}Er_{0,5})_2S_{300}$ were grown by the flux-melt method from their primary crystallization region. The synthesis of the starting alloys at a maximum temperature of 1200 K and crystal growth were carried out in the same evacuated quartz container with a conical bottom. The growth process was carried out in a vertical two-zone furnace. The maximum temperature was 1200 K, and the temperature gradient at the crystallization front was 20 K/cm. After melting the charge, the ampoule was lowered at the maximum rate until the bottom of the ampoule reached the undercooling temperature. After crystallization of 10 mm of the melt along the length of the ampoule, growth was stopped, and then 6.0-8.0 mm of the crystallized melt was melted back and annealed for 100 hours. Then, the single crystal was grown at a lowering rate of 5 mm/day. After the completion of the process, both furnaces were cooled to 820 K at a rate of 50-70 K/day and the resulting single crystal was annealed for 100 hours.

The single crystals $(Ga_{70}La_{30})_2S_{300}$, $(Ga_{69,75}La_{29,75}Er_{0,5})_2S_{300}$ have a grayish color, a diameter of 15 mm, and a length of 24 mm. The middle part of these single crystals was chosen for the study of optical properties. For the studies, they were given the form of plane-parallel plates with a thickness of d2=0.6±0.02 mm. The samples were ground and polished with abrasive powders and diamond pastes.

Photoluminescence studies were carried out using an MDR-206 monochromator and a silicon photodetector. Excitation was provided by a diode laser with a power of 400 mW and an emission maximum of 800 nm. Both excitation and detection were performed from the same surface of the sample.

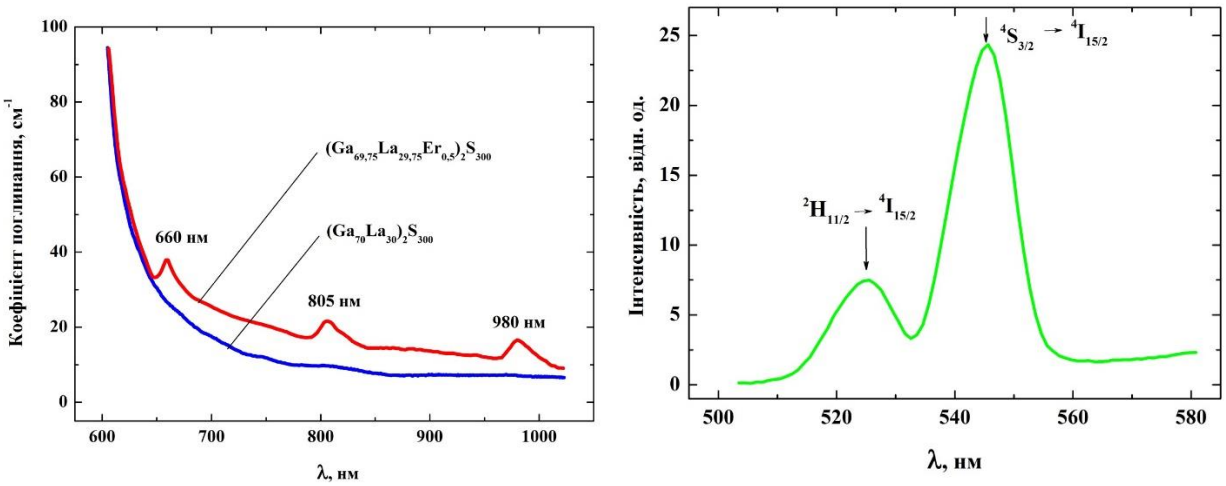

The optical absorption spectra of single crystals $(Ga_{70}La_{30})_2S_{300}$, $(Ga_{69,75}La_{29,75}Er_{0,5})_2S_{300}$ were studied in the spectral range of 600-1050 nm. At 50 cm^{-1}, their band gaps were estimated to be 1.99 eV and 1.98 eV for (Ga70La30)2S300 and $(Ga_{69,75}La_{29,75}Er_{0,5})_2S_{300}$, respectively. In the erbium-doped sample, narrow absorption bands with maxima of 660, 800, 980 nm corresponding to intra-center transitions in Er^{3+} ions were recorded.

Under excitation by a laser with a power of 400 mW and a wavelength of 800 nm, anti-Stokes photoluminescence was observed in the spectral range of 510–560 nm. The emission spectrum consists of two peaks at 525 and 545 nm.

It has been determined that doping with a rare-earth metal (Erbium) shifts the absorption edge of electromagnetic radiation in the optical range towards the infrared spectral range. $(Ga_{69,75}La_{29,75}Er_{0,5})_2S_{300}$ can be recommended as an infrared signal converter to the visible range, but this requires further research.

It has been determined that doping with a rare earth metal (Erbium) leads to a shift in the absorption edge of electromagnetic radiation in the optical range towards the infrared spectral range. $(Ga_{69,75}La_{29,75}Er_{0,5})_2S_{300}$ is particularly promising for the creation of upconverters, devices that convert light from the infrared to the visible range.

Links

[1] Fedotov V. V. Modern state of research on the optical properties of semiconductor materials [Text] / V. V. Fedotov // Technological audit and production reserves. - 2014. - No. 6/1. - P. 15-22;

[2] Prokopiv V.V. Materials of electronic equipment [Text]: education. manual / VV Prokopiv. – Ivano-Frankivsk: Prykarpattia National University named after Vasyl Stefanyk, 2009. – 288p.

[3] Frish S.E. Optical spectra of atoms [Text]: textbook / S.E. Frisch - St. Petersburg: "Lan" Publishing House, 2010. - 640 p.

IMPACT OF NITROGEN ATOM ON NLO SELF-ACTION EFFECT MANIFESTATION OF NAPHTHOL-CONTAINING AZOMETHINES INCORPORATED INTO PMMA MATRIX

Ronkovych A.V.[2], Labunets A.R.[1], Ilchenko S.G. [1], Komarenko D.O.[2], Ovdenko V.M.[1,2]

[1] *Advanced Materials Nonlinear Optical Diagnostics Lab, Institute of Physics of the NAS of Ukraine. pr. Nauki, 46, Kyiv 03028, Ukraine, e-mail: andrew.ronkovich@gmail.com, komarenko.dmytro@gmail.com*

[2] *Department of Chemistry, Taras Shevchenko National University of Kyiv, Volodymyrska 64/13, 01601 Kyiv, Ukraine, e-mail: valeryovdenko@gmail.com, art.labunets@gmail.com*

Organic polymeric materials with photoswitchable moieties able to photoinduced isomerization are promising candidates for applications in optical power limiting, all-optical switching, optical data storage and as non-linear optical (NLO) materials. Among them, several classes of compounds can be distinguished as those that contain two aromatic systems connected by a π-bridge. Azobenzenes are most often used for NLO applications. But azomethine (-CH=N-) linkages heterocyclic compounds have also gained much attention in last decades for their wide application in materials chemistry such as NLO, photonic and optical limiting materials. However, the ability to efficiently photoinduced charge/electron density transfer, as well as the efficient change in dipole moment during photodriven processes, have a significant impact on the efficiency of the nonlinear optical response. Thus, studying the influence of structural changes, such as the replacement of the benzene ring with 2- or 3-substituted pyridine, on the variation of the refractive and absorption NLO response is an important fundamental task.

Investigation of pyridine moiety effect on self-action manifestation of PMMA thin films doped with azomethine chromophores

In this work, three azomethine dyes (***Azm1***, ***Azm2*** and ***Azm3*** shown in *Figure 1*) were synthesized by the condensation reaction between 2-hydroxy-1-naphthaldehyde with different aromatic amines - aniline, 2-aminopyridine and 3-aminopyridine. It is worth noting that two of the azomethines are analogs of commercially available azo compounds (***Sudan 1*** dye [CAS# 842-07-9] and 1-(2-pyridyl azo)-2-naphthol (***PAN-2***) [CAS# 85-85-8]), which will further facilitate the comparison of azo and azomethine chromophores as materials for non-linear optical applications.

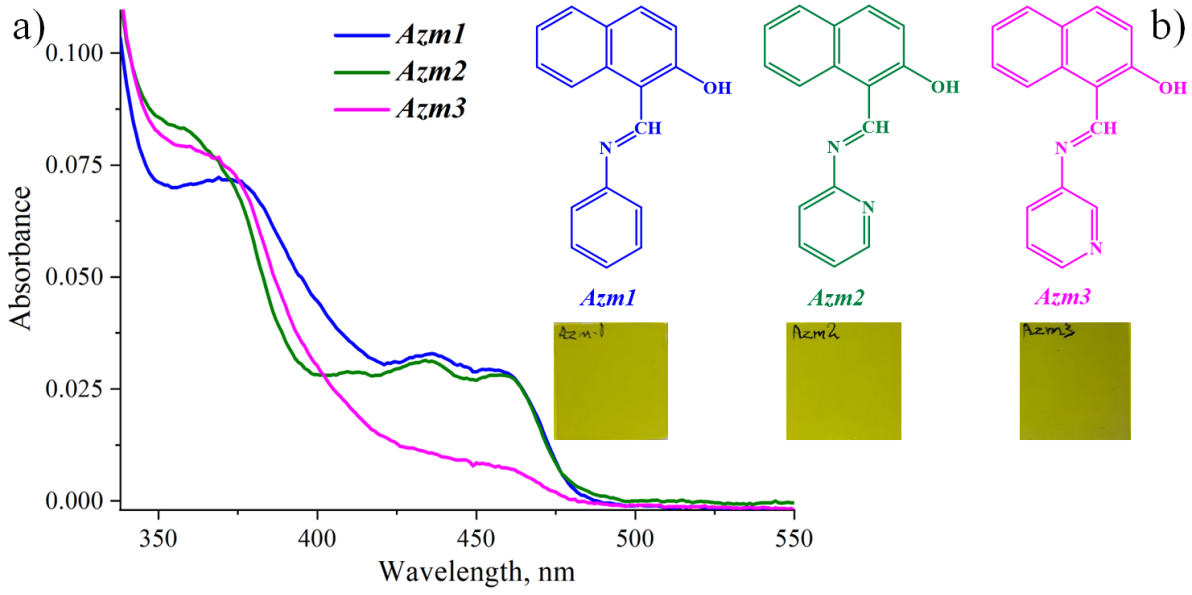

*Fig. 1. UV-Vis spectra (a) of thin PMMA films with 1% wt. of azomethines **Azm1**, **Azm2** and **Azm3** (b)*

The absorption spectra of ***Azm1*** and ***Azm2*** (*Figure 1*) show some similarities, while the spectrum of ***Azm3*** thin film has differences. None of the substances absorbs at the laser wavelength of 532 nm, being optically transparent in this region.

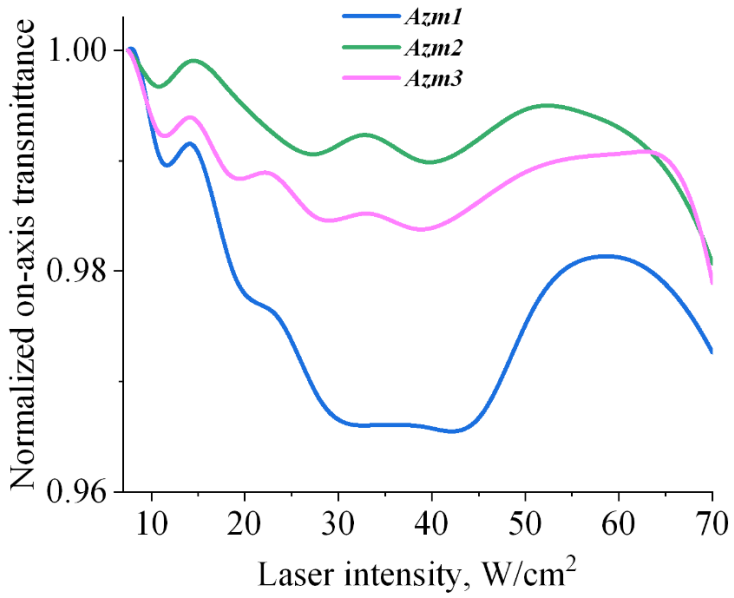

Fig. 2. Normalized on-axis transmittance of ***Azm1***, ***Azm2*** *and* ***Azm3*** *in PMMA thin films under CW laser radiation at 532 nm.*

A series of PMMA thin polymeric films with 1% wt. of incorporated synthesized azomethine dyes was studied under CW excitation of DPSS laser with wavelength $\lambda = 532$ nm. Since these samples are transparent in this region, absorptive analysis did not show surprising results at this range of intensities. Analysis of refractive NLO properties was based on photoinduced variations of on-axis transmittance, which are present on the *Figure 2*. All the dyes demonstrate self-defocusing effect with efficiencies in order ***Azm2*** < ***Azm3*** < ***Azm1*** with $|\mathrm{Re}(\chi^{(3)})| = 5.4\times10^{-2}$ esu $< 5.9\times10^{-2}$ esu $< 1.8\times10^{-2}$ esu respectively. Optical quality factor figure of merit (FOM) in this region showed that nitrogen carrying ***Azm2*** and ***Azm3*** dyes barely hit FOM = 1, while ***Azm1*** quality factor being 2.5 times higher. At laser excitation intensity $I \sim 30$ W/cm^2 NLO effect saturates similarly for all the samples, reaching 3% of self-defocusing for ***Azm1***, almost twice as effective as ***Azm3***. This separation could demonstrate an influence of nitrogen atom in ***Azm2*** and ***Azm3***, which *quenches* nonlinear process at this level of intensity. With a rise of intensity above 45 W/cm^2 there is an opposite self-focusing effect. ***Azm1*** again demonstrates the most effective response with $\mathrm{Re}(\chi^{(3)}) \sim 10^{-2}$ esu.

Conclusions. In this work, we have investigated a series of PMMA thin films doped with azomethine chromophores with variable type of aromatic ring (benzene, 2-pyridine, 3-pyridine). It was shown that in presence of nitrogen atom in the ring self-defocusing NLO effect got quenched in the range of small and moderate CW laser excitation intensities.

References

[1] V. N. Ovdenko, V.V. Multian et al. J. Mater. Chem. C, 2020, 8(26), 9032-9045.
[2] A.V.Uklein, E.V.Ouskova et al. Functional Materials, 2015, 22(1), 20-26.
[3] V.M. Ovdenko, D.O.Komarenko et al. Optical Materials, 2023, 138, 113735.

REACT IVE SINTERING OF TRANSPARENT YAG:Sm^{3+} CERAMICS: EFFECT OF STARTING ALUMINA NANOPOWDERS

Anton Balabanov, Ihor Vorona, Oksana Matvienko, Arsenii Tymoshenko, Serhii Parkhomenko

Olexander Budnikov, Olexander Tolmachev, Roman Yavetskiy

Institute for Single Crystals of NAS of Ukraine, Kharkiv 61072, Ukraine,
e-mail: balabanov@isc.kharkov.ua, balabanovanton964207@gmail.com

Introduction

Pulsed diode-pumped lasers based on $Y_3Al_5O_{12}:Nd^{3+}$ (YAG:Nd^{3+}) are used in medicine, scientific research, and for security and defense purposes. Parasitic oscillations and amplified spontaneous emission (ASE) effects significantly limit the efficiency of traditional high-power laser systems. Moreover, modern technology demands miniaturization and reduced energy consumption of lasers while maintaining high energy characteristics of the laser beam. The formation of complex laser elements that combine an active medium and layers capable of absorbing parasitic radiation is one of the most effective ways to suppress parasitic oscillations and ASE. In such media, consisting of YAG:Nd^{3+} active element surrounded by a layer that absorbs parasitic radiation, the latter can serve as an optical waveguide for pumping the active medium. The cladding material must be transparent at the pump wavelength of 808 nm and simultaneously have a high absorption coefficient at 1064 nm to suppress the parasitic emission of Nd^{3+} ions. The optical properties of YAG:Sm^{3+} make it an excellent candidate for suppressing parasitic oscillations in YAG:Nd^{3+} based lasers. To ensure maximum absorption of parasitic radiation, YAG:Sm^{3+} with a high doping concentration is required, which can be obtained by using YAG:Sm^{3+} optical ceramics. Previously, we investigated the influence of sintering temperature and dopant concentration on the physical properties of YAG:Sm^{3+} ceramics [1, 2]. The aim of this study was to investigate the effect of the structural and morphological properties of initial Al_2O_3 nanopowders on the densification, microstructure, and optical properties of YAG:Sm^{3+} ceramics.

Results

For the study, four batches of commercial Al_2O_3 nanopowders with different granulometric compositions were selected, with an average particle size ranging from 150 to 400 nm. These nanopowders exhibited high sintering activity and a low agglomeration degree. The influence of the structural parameters of the commercial nanopowders on the morphology of $5Al_2O_3+3Y_2O_3$ powder mixtures, obtained by high-energy milling in a planetary mill, was investigated. Most of the resulting powder mixtures had a bimodal particle size distribution. The larger particle fraction was primarily attributed to Y_2O_3 particles, while the smaller fraction consisted of Al_2O_3 particles. However, the powder mixture obtained using Sumitomo aluminum oxide was characterized by a unimodal particle size distribution and the absence of micron-sized agglomerates. It was demonstrated that the initial Sumitomo aluminum oxide powder ensures the production of $5Al_2O_3+3Y_2O_3$ mixtures with a uniform particle size distribution, which promotes efficient nanopowder densification.

Transparent YAG:Sm^{3+} ceramics were produced by reactive sintering in a vacuum using powder mixtures synthesized from different initial Al_2O_3 powders. The obtained samples were analyzed using spectroscopy and optical microscopy. The optical transmission of ceramics made from initial mixtures characterized by a bimodal particle size distribution ranged between 77-79% (at λ=808 nm). This was attributed to optical losses due to light scattering on pores. On the other hand, ceramics produced using Sumitomo powder exhibited a small number of residual pores, extremely low optical losses, and an optical transmission coefficient of 83%.

Conclusions

The influence of the characteristics of commercial Al_2O_3 nanopowders on the structural and morphological properties of $5Al_2O_3+3Y_2O_3$ powder mixtures, their sintering activity, as well as the morphology and optical

properties of transparent YAG:Sm^{3+} ceramics, was studied. The ceramics obtained using the mixture based on Sumitomo powder are characterized by an extremely low concentration of residual pores and an optical transmission coefficient exceeding 83%. This is attributed to the formation of a more homogeneous powder mixture, the absence of micron-sized aggregates, and the preservation of densification activity on the entire sintering trajectory.

Acknowledgements. This study was supported by the National Research Foundation of Ukraine, the Project No. 2023.04/0007 «Active elements of a complex design for advanced high-power laser systems».

References

[1] A.D. Timoshenko, A.G. Doroshenko, S.V. Parkhomenko, I.O. Vorona, O.S. Kryzhanovska, N.A. Safronova, O.O. Vovk, A.V. Tolmachev, V.N. Baumer, I. Matolínová, R.P. Yavetskiy, (INVITED) Effect of the sintering temperature on microstructure and optical properties of reactive sintered YAG:Sm^{3+} ceramics, Opt. Mater.: X 13 (2022) 100131

[2] A.D. Timoshenko, O.O. Matvienko, A.G. Doroshenko, S.V. Parkhomenko, I.O. Vorona, O.S. Kryzhanovska, N.A. Safronova, O.O. Vovk, A.V. Tolmachev, V.N. Baumer, I. Matolínová, S. Hau, C. Gheorghe, R.P. Yavetskiy, Highly-doped YAG:Sm^{3+} transparent ceramics: Effect of Sm^{3+} ions concentration, Ceram. Int. 49(5) (2023) 7524-7533

POLARIMETRY:
THEORY AND APPLICATIONS

MODERNIZATION OF RADAR SYSTEMS BASED ON METAMATERIALS

S. O. Remez, O. M. Ivanuta

Applied Physics Department, Faculty of Radiophysics, Electronics and Computer Systems,
Taras Shevchenko National University of Kyiv, Ukraine, Kyiv, Acad. Glushkova av., 4-g
Address, e-mail: archasmiel@gmail.com

Abstract

This study focuses on the application of metamaterials in modernizing radar systems, particularly in technologies that leverage these materials' unique electromagnetic properties. The research developed a simulation model using COMSOL Multiphysics software to analyze the performance enhancements achieved by integrating metamaterials into radar technology. The results demonstrate the potential of metamaterials to significantly improve radar performance, including resolution, detection capabilities, and overall system efficiency.

Introduction

Metamaterials, known for their exceptional electromagnetic properties, have garnered significant attention in recent years for their transformative potential in various scientific fields. These artificially engineered materials can manipulate electromagnetic waves in ways not possible with conventional materials, allowing for groundbreaking applications in radar technology. Their ability to exhibit a negative refractive index opens new possibilities for radar systems, including improved antenna design and enhanced signal processing capabilities.

In the context of radar modernization, metamaterials offer the potential to enhance the resolution and detection accuracy of radar systems significantly. This work aims to develop a simulation model that explores the integration of metamaterials into radar technology. By utilizing COMSOL Multiphysics software, the research will examine how these materials can be applied to improve radar performance and capabilities. The findings could have substantial implications for applications ranging from military surveillance to air traffic control and disaster management.

Theoretical Background

The underlying principles of metamaterials arise from their unique structural design, which allows them to interact with electromagnetic waves in unprecedented ways. One of the most notable properties of metamaterials is their ability to achieve a negative refractive index, resulting in phenomena such as reverse Snell's law, where electromagnetic waves bend in the opposite direction compared to natural materials. This property is crucial for modernizing radar systems, particularly in enhancing antenna designs and enabling advanced signal processing techniques.

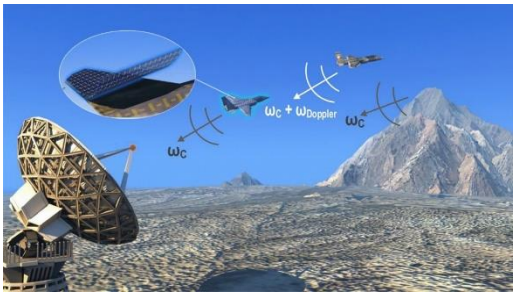

Fig. 1. The radar system actively detecting an aircraft

Figure 1. Shows a radar system actively detecting an aircraft. The radar's unique properties, enhanced by the integration of metamaterials, allow for improved range and target resolution. This figure emphasizes the enhanced detection capabilities and signal clarity resulting from the incorporation of metamaterials into radar systems, showcasing their potential to revolutionize aerial surveillance and tracking technologies.

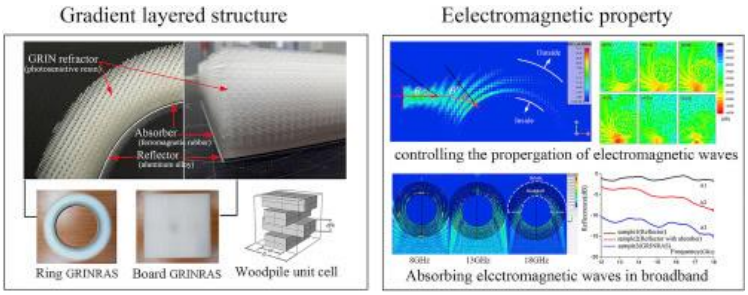

Fig. 2. The radar antenna performance

Figure 2. Illustrates the negative refraction effect achievable with metamaterials, which can be utilized to enhance radar antenna performance. This ability enables the development of high-resolution radar systems capable of detecting objects with greater accuracy.

References

[1] Shelby R. A., Smith D. R., Schultz S. Experimental confirmation of the negative refractive index // Nauka. 2001. Vol. 292, No. 5514. P. 77-79.

[2] Liu Y., Zhang S. Metamaterials: a new frontier of science and technology // Review of the Chemical Society. 2011. Vol. 40, No. 5. P. 2494-2507.

[3] Shelby R. A., Smith D. R., Nemeth-Nasser S. K., Schultz S. Microwave transmission through a two-dimensional isotropic left metamaterial // Applied Physics Letters. - 2001. - Vol. 78, No. 4. - pp. 489-491.

[4] Valentine J., Zhang S., Zentgraf T., Ulin-Avila E., Genov D. A., Bartal G., Zhang S. Three-dimensional optical metamaterial with a negative refractive index // Nature. 2008. Vol. 455, No. 7211. P. 376-379.

POLARIMETRIC CLEAR-SKY MEASUREMENTS WITH 555 NM IMAGING POLARIMETER

Syniavskyi I.*, Sosonkin M.*, Ivanov Yu.*, Danylevsky V.*, *,**

Milinevsky G.*, **, Osypenko R.*, Oberemok Ye.*, ***

** Main Astronomical Observatory of National Academy of Sciences of Ukraine, Kyiv 03680, Ukraine, e-mail: syniavskyi@gmail.com*

*** College of Physics, ICFS, Jilin University, Changchun, China*

****Faculty of RadioPhysics, Electronics and Computer Systems Taras Shevchenko National University of Kyiv, Kyiv 01601, Ukraine, email: oya@univ.kiev.ua*

The results of clear sky polarization measurements obtained by the imaging polarimetric module MSIP 555P are presented. The MSIP 555P is the narrowband 555 nm spectral channel of multispectral imaging polarimeter (MSIP). The behavior of obtained polarization pattern of scattered sunlight is qualitatively agreed with the pattern of Relay scattering for the given field of view (FOV) of the MSIP module. The discrepancy in absolute values is explained by the orientation error of the MSIP, the uncompensated distortion of the MSIP camera and the influence on the overall value of the degree of polarization of the component of solar radiation reflected by the earth's surface and then re-scattered by the atmosphere.

Multispectral imaging polarimeter

Multispectral multiple-viewing-angle measurements of both intensity and polarization of solar light scattered by aerosols and clouds from space allows a simultaneous retrieval of aerosol and surface properties with the aerosol parameters accuracy, which is sufficient for climate research. MultiSpectral Imaging Polarimeter (MSIP) a one of the Aerosol-UA space mission instruments for studying the global distribution and physical properties of aerosol particles and cloud formations in the Earth's atmosphere [1]. The MSIP consists of five optical channels with a field-of-view of 60°x60°. Three channels are polarizing that allows to perform polarimetric measurements of I, Q, U Stokes parameters at the central wavelengths of 410, 555, 865 nm with a spectral full width of half maximum 20 nm. Two channels of the MSIP provide photometric measurements in the eight spectral wavelengths with 410, 443, 470, 490, 555, 670, 865, and 910 nm with the FWHM of 20 to 40 nm. Polarimetric channels of MSIP all have the same construction and can be utilized separately as independent narrowband polarimeter. Therefore, identifying the features and shortcomings during testing of one MSIP channel, experience in accounting and eliminating them, developing and testing calibration procedures should significantly simplify the development and implementation of other MSIP channels. Today a most developed the 555 nm spectral polarimetric channel of MSIP (module MSIP 555P). Set of some calibration procedures are developed and tested successfully [2]. Now some reference and representative data is collected to partially provide an initial polarimeter's validation. In particular, the measurements of clear-sky scattering pattern is a really representative case since the polarization distribution of sunlight scattered by the clear Earth atmosphere well agrees with Relay scattering. Therefor we would like to present and discuss the results of clear sky polarization measurements obtained by the imaging polarimetric module MSIP 555P.

Experiment condition

Using a calibrated MSIP 555P module, polarimetric measurements of solar radiation scattered by the clear sky were carried out on 10/31/22 in the time interval from 12:00 to 16:30 on the territory of the Main Astronomical Observatory of the NASU (50°21'57.0"N 30°30'02.3"E). The photo of polarimetric modules 555P and 410P as the scheme of the experiment are shown in Fig. 1. Fig 1.b shows: θ - the Sun's altitude angle, ϕ - the azimuth of the Sun's position. Red balls indicate the conditional position of the Sun at the time of the measurements. The time of measurements and the angular positions of the Sun are shown in Figure 1 and also in Table 1.

Results and discussions

The results are shown a high maximum degree of polarization (up to 0.85) of solar radiation scattered by the celestial sphere at angles of 90° relative to the direction of the Sun. The high degree of polarization is explained by the low optical thickness, less than 0.04, of the layer of aerosols of fine and coarse fractions over the studied

area at the time of the experiment, as follows from the measurement results of the MAO photometer of the AERONET network. There is a qualitative coincidence of the experimental distributions of the degree of linear polarization in the field of view of the MSIP and the distributions modeled by Relay's formula. The discrepancy in absolute values is explained by the orientation error of the MSIP, the uncompensated distortion of the MSIP camera and the influence on the overall value of the degree of polarization of the component of solar radiation reflected by the earth's surface and then re-scattered by the atmosphere. The change in the azimuth of the maximum degree of polarization, which is determined by the MSIP, fully corresponds to the change in the azimuthal position of the Sun during the observations.

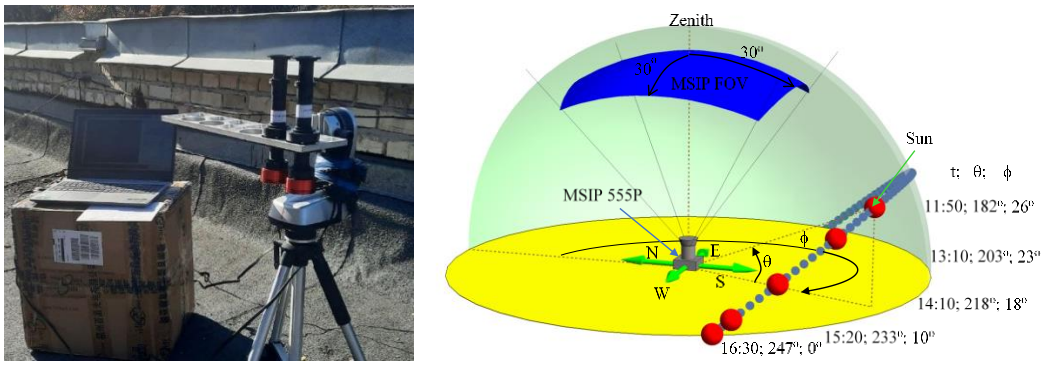

Fig. 1. a) polarimetric modules 555P and 410P: b) scheme of the clear sky measurements experiment

Table 1. Angular positions of the Sun at the measurements time, maximum degree of linear polarization (DoLP) and corresponding azimuth of polarization AoLP.

Time (t, h:m)	*Azimuth (ϕ,°)*	*Altitude (θ,°)*	*$DoLP_{max}$*	*AoLP, °*
11:50	182	26	0.78	44
13:10	203	23	0.82	23
14:10	218	18	0.83	8
15:20	233	10	0.85	-7
16:10	244	3	0.82	-19
16:30	247	0	0.82	-21

At figure 2 the experimental and modeled by Relay's formula distributions of DoLP in FOV of MSIP for measurement time (a) 11:50 and (b) 16:30 are shown.

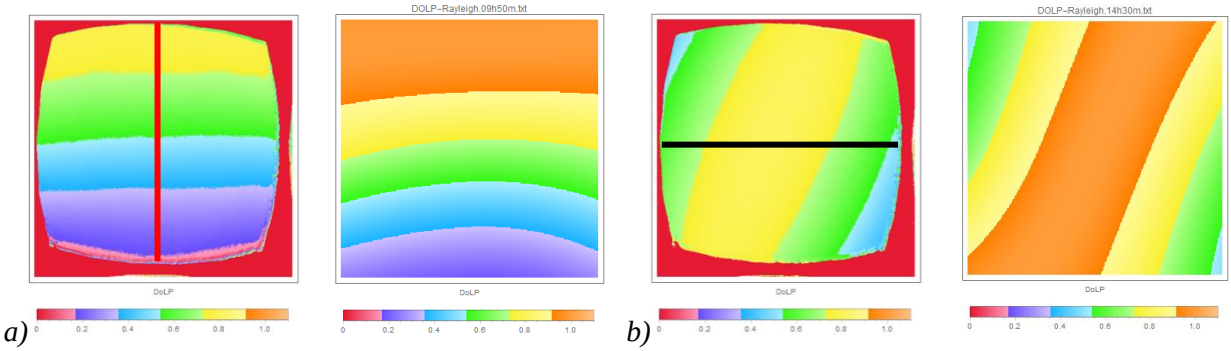

Fig. 2. Experimental and modeled by Relay's formula distributions of DoLP in FOV of MSIP

References

[1] Синявський І. І., Іванов Ю. С., Сосонкін М. Г., та ін. // КНІТ, 2018. Т.24(3), С. 23-32.

[2] Milinevsky G., Oberemok Y., Syniavskyi I., et al // JQSRT, 2019. Vol. 229. P. 92–105.

TUNABLE CONTROLLERS OF LIGHT POLARIZATION'S DEGREE

Kolomiets O.*, Savenkov S.*, Oberemok Ye.*, Kolomiets I.*, Syniavsky I., Ivanov Yu.****

**Taras Shevchenko National University of Kyiv, Kyiv 01601, Ukraine,*
e-mail: alextheseemanjones@gmail.com, sns@univ.kiev.ua, oya@univ.kiev.ua
***Main Astronomical Observatory of National Academy of Sciences of Ukraine, Kyiv 03680, Ukraine*
e-mail: syniavskyi@gmail.com

The report provides an overview of the schemes and principles of operation of existing devices producing the light with a certain degree of polarization. The modeling of these devises is carried out, that provides the assessment of its accuracy and dynamic range. The new possible scheme of light sources with a controlled degree of linear polarization is considered and analyzed.

Introduction

The problem of calibration and validation of the different polarimeters is on day. The sources with a linear and circular light polarization and unpolarized light are mainly used as a reference ones during polarimeters' calibration/validation process. These provides an accurate control the measurement of parameters of totally polarized light. At the same time the light under analysis may has partially polarization. Thus the reference sources with a controlled degree of polarization are also should be used for calibration and validation of polarimeters.

Brewster windows DoLP controller

Today, one of the common way to produce the light with a certain degree of linear polarization (DoLP) is the use of a sequence including a photometric sphere as a source of unpolarized light, a collimator and a stack of glass plates (a Brewster window, often made of K9 glass) with variable inclination [1-3]. In this case, to ensure the achromaticity of the system and to preserve the direction of light propagation, stacks of plates are placed in pairs with the opposite slope as in fig.1. In scheme fig.1 achievable values of DoLP of light at the output are in range of 0.0012 – 0.4, 0.6 with a theoretically estimated DoLP error of 0.0015 or even 0.0005. The main source of errors in such schemes is the error in set of tilt of the glass plates. Effective use of the scheme of fig.1 is possible with automated control of inclination of the plates. Analytical description of reflection/transmission/refraction in the system of fig.1 with many plates in a stack is complicated, if we take into account multiple reflections in each plate. Though the schemes with a single Brewster window are exist, these are demonstrating a strong dependence the DoLP of the output light on wave length. The alignment of the input and output beams was also not ensured. One of disadvantage of Brewster windows DoLP controllers they are used for calibration of polarimeters in a relatively small field of view 4° - 6°.

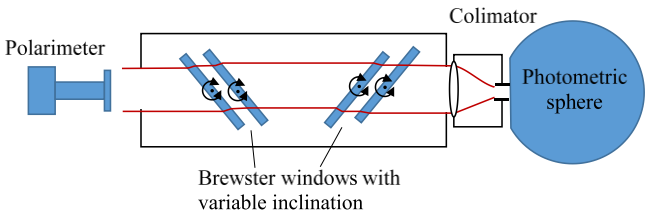

Fig. 1. Control value of Degree of Linear Polarization of light by the matched tilt of Brewster windows

LC depolarizers and tunable LC DoLP controllers

Other known controllers of polarization's degree are liquid crystal (LC) depolarizers [3,4]. These depolarizers are, in fact, a set of parallel wave plates with different birefringence or orientation of the fast axis. A polarized beam passing through such a depolarizer, in the cross-section of which are many different wave plates, undergoes

spatial polarization modulation so that the total polarization of the beam becomes uncertain (the beam is depolarized). The degree of uncertainty (depolarization) mainly depends on the density of the wave plates trough the beam's cross-section and type of wave plates (type of liquid crystals, dopants, alignment and phase of crystals and so on). Though LC depolarizers are pseudodepolarizers, and its depolarization factor depends on light wave length and they are not as effective as the crystal depolarizers or photometric sphere (achievable minimum of output light's degree of polarization is of 4%), but have the advantage of low cost and large size. Beside that the LC depolarizers may be electrically tuned depolarizers. For instance, in [3] proposed the wedge LC depolarizer that can be electrically switched ON and OFF.

We suppose that it is possible to use widespread types of LCD panels (TN, IPS or other types) as a tunable controller of DoLP. Since each pixel of the LC panel is a wave plate with an electrically tunable birefringence it is supposed to be used for accurate spatial polarization's modulation though the cross-section of input light beam. For instance, we expect, that in the case of using the panel of IPS type with input linear polarized but without of output linear polarizing cover, it is possible to form in beam's cross-section the two linearly polarized subset of micro beams, which mutual orientation of angles of linear polarization (AoLP) can be tuned by varying the voltages on pixels of LC panel cells (fig.2). When the average AoLP in subsets differs on 90°, the averaged DoLP of an entire beam will be near to zero. With the co-aligned AoLP in subsets the averaged DoLP of an entire beam will maximal (near to 1). Thereby accurately tuning mutually AoLP in beam's subsets by the voltage control of LC panel pixels we should accurately tuning average DoLP of entire output beam.

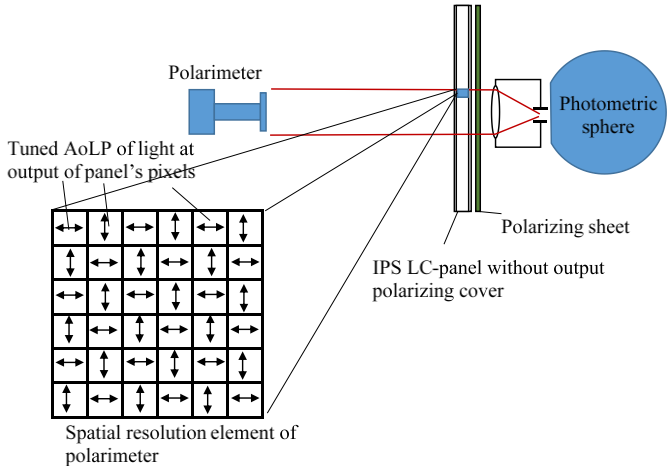

Fig. 2. Use a modified IPS LC-panel as a tunable DoLP light controller

References

[1] Zhengqiang Li, Kaitao Li, Li Li, Hua Xu, et al, "Calibration of the degree of linear polarization measurements of the polarized Sun-sky radiometer based on the POLBOX system," Appl. Opt. 57, 1011-1018 (2018)

[2] Chan Huang, Yuyang Chang, Guangfeng Xiang, Lin Han, Feinan Chen, et al, "Polarization measurement accuracy analysis and improvement methods for the directional polarimetric camera," Opt. Express 28, 38638-38666 (2020)

[3] Anna-Britt Mahler and Russell A. Chipman, "Polarization state generator: a polarimeter calibration standard," Appl. Opt. 50, 1726-1734 (2011)

[4] Nicholas J. Diorio, Jr., Michael R. Fisch, John L. West, Filled liquid crystal depolarizers, J. Appl. Phys. 90, 3675–3678 (2001)

[5] Bing-Yan Wei, Peng Chen, Shi-Jun Ge, et al, "Liquid crystal depolarizer based on photoalignment technology," Photon. Res. 4, 70-73 (2016)

COMPARISON OF POLARIMETRIC ANALYSIS METHODS OF ANISOTROPIC AND DEPOLARIZING PROPERTIES OF MEDIA

Andrii Fesenko*, Sergey N. Savenkov

**Faculty of RadioPhysics, Electronics and Computer Systems Taras Shevchenko National University of Kyiv, Kyiv 01601, Ukraine*
** email: fesenkoandrew@gmail.com*

This study proposes a simple technique for quantitative estimation of basic anisotropy types and depolarization properties present in complex anisotropic media based on the application of Frobenius matrix norm to measured Jones-Mueller matrix decomposition data, without the need to directly calculate appropriate polarization parameters of the studied media.

Introduction

Matrix methods used for characterization and analysis of anisotropic media have always been relatively computationally complex, requiring full calculation of polarization parameters characterizing the media even when only an initial estimate is necessary for the purposes of the research. This causes classification of complex anisotropic media according to the exhibited basic anisotropy types to be a needlessly time-consuming or computationally intensive task.

Multiplicative models of polarized light propagation in anisotropic media

The most well-known and conventionally used method to characterize anisotropic media is Mueller matrix decomposition [1] based on generalized Jones equivalence theorem [2], where any anisotropic media can be represented by a 4x4 Mueller matrix, which in turn can be represented with a product $\mathbf{M} = \mathbf{M}_d\mathbf{M}_0$, where $\mathbf{M}_d$ is a depolarization matrix, and $\mathbf{M}_0 = \mathbf{M}^{CP}(\varphi)\mathbf{M}^{LP}(\delta,\alpha)\mathbf{M}^{CA}(R)\mathbf{M}^{LA}(P,\theta)$ is a product of matrices representing basic anisotropy types present in the media. The multiplicative matrix approach allows to utilize standard matrix methods to manipulate matrix data to normalize it or extract qualitative conclusions.

One such method is used to filter the noise in experimentally measured data for non-depolarizing media [3], where the media is assumed to be non-depolarizing, and the measured matrix data is processed to remove the depolarization noise. The criterion for applicability of this method is expressed with an inequality $\left\|\mathbf{M} - \widetilde{\mathbf{M}}_J\right\|_F < \|\mathbf{S}\|_F$, where $\mathbf{M}$ is experimentally measured Mueller matrix, $\widetilde{\mathbf{M}}_J$ is the estimated Mueller-Jones matrix that actually characterizes non-depolarizing medium, $\mathbf{S}$ is experimental standard deviation matrix, and $\|\mathbf{X}\|_F$ denotes applying Frobenius matrix norm operation applied to matrix $\mathbf{X}$. Extending the application of this method to matrices of basic anisotropy allows to quantitatively estimate the impact of each specific type of basic anisotropy within a complex anisotropic media.

The following criterion was proposed to estimate the presence of basic anisotropy type within the studied media: $\ln\left(\frac{\|\Delta\mathbf{M}_i\|_F}{\|\mathbf{S}\|_F}\right) < 0,\ i = (CP, CA, LP, LA)|(D, D', R)$.

Criterion validation based on measured data

The applicability of the proposed method was validated by testing it on the experimentally measured Mueller matrices of various objects with anisotropic polarization properties, and further analysis of the obtained results allowed to perform the object classification according to the appropriate basic anisotropy types. The studied data in question [4] belonged to ferromagnetic fluid of varying purity in constant magnetic field, as well as an absorbing dielectric target submerged in water.

	M1	M2	M3
$\|\Delta\mathbf{M}_{CP}\|_F$	1.0991	0.7075	2.8284
$\|\Delta\mathbf{M}_{LP}\|_F$	0.0125	0.3633	2.8284
$\|\Delta\mathbf{M}_{LA}\|_F$	1.0991	0.7591	2.8286
$\|\Delta\mathbf{M}_{CA}\|_F$	2.5513	1.7215	4.4420
$\|\Delta\mathbf{M}_{R}\|_F$	0.0082	0.2311	0.0307
$\|\Delta\mathbf{M}_{D}\|_F$	1.0991	0.7210	2.8284
$\|\Delta\mathbf{M}_{0}\|_F$	0.0348	0.0472	0.1368

	M1	M2	M3
d	0.0067	-0.0018	0.0671
φ	-0.1902°	-5.7269°	6.2992°
α	-0.5856°	-5.0831°	-42.1663°
δ	-45.7333°	-27.5698°	-1.3727°
R	0.0014	0.0113	-0.0100
P	1.0101	0.7196	0.9831
θ	42.1126°	-24.3853°	-35.7416°

Tables 1, 2. Frobenius norms for studied media, and calculated polarization parameters for validation.

Direct parameter calculation verification matched the expected results estimated with the proposed criteria for estimating the influence of specific basic anisotropy types within complex anisotropic media. Obtained results indicate applicability of a wider class of generalized matrix operations and further research into similar techniques may lead to novel reevaluation of the specific matrix applications used for anisotropic media characterization while retaining physical meaning and allowing recontextualization of the available data.

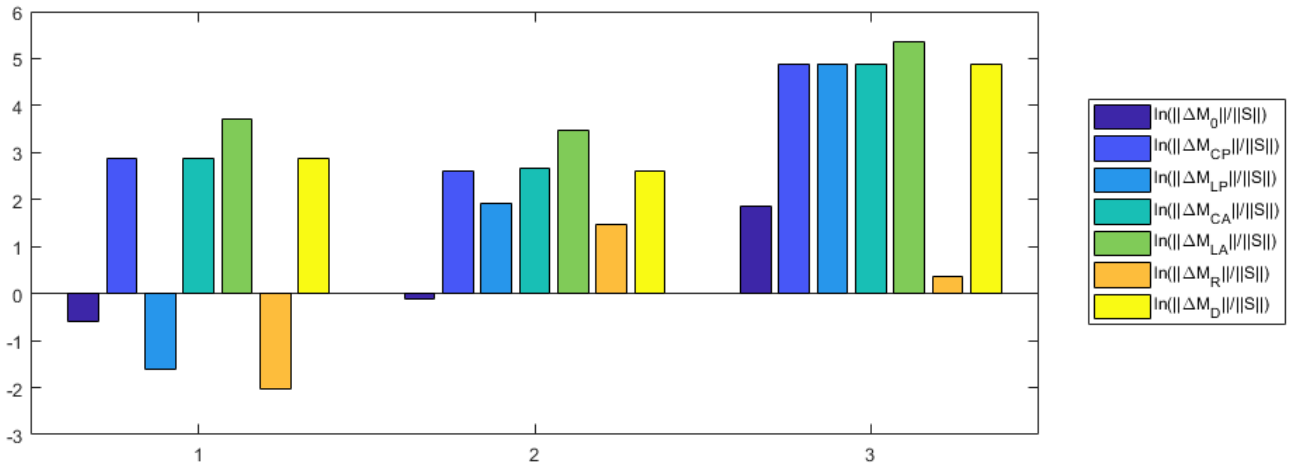

Fig.1. Proposed criterion derived value graph visualization for observed media.

References

[1] S.N. Savenkov, Ye. A. Oberemok. "Inverse problem of polarimetry for homogeneous anisotropy media on basis of Mueller matrix calculus," Proceedings of SPIE, vol.6536, p.65360E (8 pages), 2007.

[2] Ossikovski R. "Differential and product Mueller matrix decompositions: a formal comparison," Opt. Lett. vol. 37, pp. 220-222, 2012.

[3] Soe-Mie F. Nee. "Decomposition of Jones and Mueller matrices in terms of four basic polarization responses," J. Opt. Soc. Am. A. vol.31, pp.2518-2528, 2014.

[4] F. L. Roy-Brehonnet, B. Jeune et al. "Optical media and target characterization by Mueller matrix decomposition," Journal of Physics D: Appl. Phys. vol.29, pp. 34-38, 1996.

REDUCTION CONTROL OF FLUID STRUCTURE DISORDER DEGREE BY CRYOELECTRONICS METHODS

T. I. Biriukov, O. M. Ivanyuta

Applied Physics Department, Faculty of Radiophysics, Electronics and Computer Systems, Taras Shevchenko National University of Kyiv, Ukraine, Kyiv, Acad. Glushkova av., 4-g
e-mail: biriukov_t@knu.ua

Abstract

This study focuses on the research of the processes of self-organization of structures with dynamic inhomogeneities in order to develop physical foundations of the latest technologies and to devise a component base of active elements of devices with dynamic inhomogeneities control for polymer electronics. The research developed a simulation model using thermogenerator based on linear circuit of Peltier elements for experimental studies of the formation of a continuum environment inside of a slowed down thermodynamic process.

Introduction

Recent studies [1] shows that cryo-electron microscopy can be used to image frozen biological molecules without the use of markers that change the structure or the need to transform molecules into a crystalline form, providing an easier way to image molecules in their normal state. On the other hand, it was showed [2] that with the help of cryo-EM it is possible to improve the understanding of physico-chemical processes in solutions and to develop ordered structures. Supermolecules in complex structured and disordered environments can polymerize with given electrophysical parameters. In the vast majority, such environments are characterized by quasi-isotropic properties, which are beginning to be used for the development of the component base of passive elements of polymer (plastic) electronics. For the component base of active elements of electronics, anisotropic, continuous environments are necessary, that is, monomers with crystallization centers that can form structures with dynamic inhomogeneities. It can be assumed that the effective reduction of the degree of disorder of the liquid structure by cryoelectronics methods can become the basis for ideas for the construction of next-generation nanoreactors. The above-mentioned opportunities should be combined with successes in the field of polymer electronics [4] where it is shown that the methods of obtaining organic polymeric materials allow to have electrical conductivity which is comparable to the electrical conductivity of metals.

Physical properties of nanostructures, as well as prototypes of the component base of active elements of polymer electronics based on them, studied during the implementation of the project, can be used for the development of devices with control of dynamic inhomogeneities. Controlling the processes of reducing the degree of structural disorder on a microscopic and macroscopic scale is of great importance in such diverse fields as biology, nanoelectronics, nanoreactors, etc.

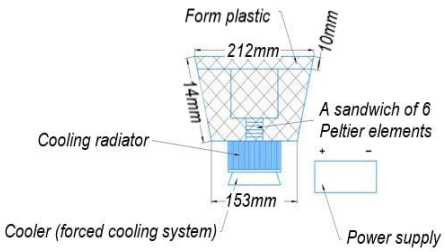

Figure 2. Schematic diagram of thermogenerator based on linear circuit of Peltier elements

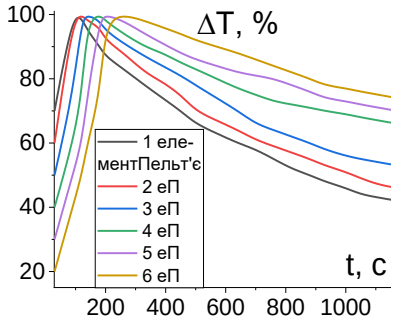

Figure 2. Temperature difference as a function of time

Theoretical Background

It has always been considered obvious that propagation of ordered signals is possible only in regular ordered environments. Strong scattering has always been considered as a source of information loss and distortion. However, recently it has become clear that amorphous materials can form stable structures. The transport of charges in a complex environment is accompanied by the destruction of the structure rather than by dissipative phenomena. Therefore, the application of solid-state electronics methods makes possible the drift of charges through a disordered environment and the restoration of the structure due to thermodynamic processes. Traditional and original research methods will be used to fulfill the purpose of the project. The study of patterns of self-organization mechanisms will be conducted with the help of computer modeling using synergy methods.

It is assumed that such modeling will allow constructing the electrophysical transmission characteristic of a disordered environment. This will allow solving the inverse problem of synthesis of an ordered environment to obtain a continuous environment with crystallization centers that can form structures with dynamic inhomogeneities with given characteristics.

Figure 1. shows developed model of thermogenerator based on linear circuit of Peltier elements for experimental studies of the formation of a continuum environment inside of a slowed down thermodynamic process.

Figure 2. illustrates the graph of dependence of the temperature difference as a function of time of thermogenerator based on linear circuit of Peltier elements. A non-linear function that has a tendency to fall after 150 seconds. Such behavior of the function is caused by the fact that the optimal oxidation occurs in 100 seconds, and when it increases further, the oxidation power falls exponentially, what is shown in the graphic.

References

[1] Dubochet J. et al. Cryo-electron microscopy of vitrified specimens // Quarterly Reviews of Biophysics – 1988 – 21 (2) – pp. 129-228.

[2] Dubochet J., A Reminiscence about Early Times of Vitreous Water in Electron Cryomicroscopy // Biophysical Journal – 2016 – 110 (4) – pp. 756-757.

[3] Sauvage J.-P., Topology and Molecular Machines: Two Interlinked Research Fields // Kharkiv Chemical Seminar NANU – 2022. https://www.nas.gov.ua/UA/Messages/news/Pages/View.aspx?MessageID=9426

[4] Shirakawa H., McDiarmid A., Heeger A., Twenty-five Years of Conducting Polymers // Chem. Commun. – 2003 - pp. 1-4.

PHYSICS OF MAGNETISM

FIRST-PRINCIPLES STUDY OF MAGNETIC GROUND STATES OF A COPPER-LEAD APATITE SERIES

I. V. Sukhenko*, V. L. Karbivskyy*, N. K. Kurgan*

**G. V. Kurdyumov Institute for Metal Physics of the NAS of Ukraine, 36 Academician Vernadsky Boulevard, UA-03142 Kyiv, Ukraine, e-mail: igor.suhenko@gmail.com*

We explore types of magnetic ordering in a family of copper-substituted lead apatite crystals by means of first-principle calculations. We show that by varying chemical composition it is possible to tune the ground state spin ordering through altering the degree of Cu-O hybridisation and the localisation of the magnetic moment, as well as bond lendths and unit cell geometry. Our results contribute to better understanding of the phase diagram of doped apatite systems and might prove valuable in studies of potential emergent superconductivity therein.

Introduction

Copper-substituted lead apatite systems have recently sparked attention due to reports of high-temperature superconductivity, while further studies revealed them hosting rich electronic structure featuring strongly correlated electrons, Fermi-level flat bands and competing magnetic orders. Here we explore family of compounds of the type $Pb_9Cu(XO_4)_6Y$, where X = P, V, As; Y = O, F_2. The choice of Y anion governs the geometry of the unit cell, shrinking and expanding the radius of the apatite c-axis column due to their differernt ionic radii; while the choice of X atom sets the geometry of Cu-O bonds and strongly affects the extent and nature of Cu-O hybridisation.

The calculations were executed using the Quantum ESPRESSO package [1-3] using Meta-GGA r^2SCAN (regularised-restored strongly constrained and appropriately normed functional [4]) combined with the application of norm-conserving pseudopitentials [5]. For antiferromagnetic configurations, 1x1x2 (Fig. 1) and 2x1x1 supercells were constructed.

Results and discussion

Total energies of model crystals' unit cells in ferromagnetic (FM), antiferromagnetic (AF, in-plane and out-of-plane) and non-magnetic (NM) configurations were calculated and compared. In all studied compounds, in-plane AFM and NM configurations turned out to have the highest energy, being several meV per atom higher than FM and out-of-plane AFM. FM and out-of-plane AFM, on the other hand, differed from each other only by tens of μeV/atom, with ferromagnetism prevaling in most cases except in $Pb_9Cu(VO_4)_6O$.

Table 1. Energy difference per atom $\Delta\varepsilon_{AFM\text{-}FM}$, μeV for different apatite compounds.

Y atom \ X atom	P	V	As
O	10	-48	35.8
F_2	17.9	5.4	11.02

The fact that all compounds favour a magnetically-ordered state is expected given the effective $3d^9$ configuration adopted by copper featuring an unpaired electron. The extent of Cu-O hybridisation has a larger impact on the competing orders than bare Cu-Cu distances, as the former shapes the real-space geometry of Cu 3*d*-associated wavefunctions. In fact, the shortest average nearest-neighbour Cu-O distances were observed in $Pb_9Cu(VO_4)_6O$, a compound with the strongest relative AFM coupling; furthermore, $\Delta\varepsilon$ increased monotonically with an increase in Cu-O distances throught the series of compounds under study.

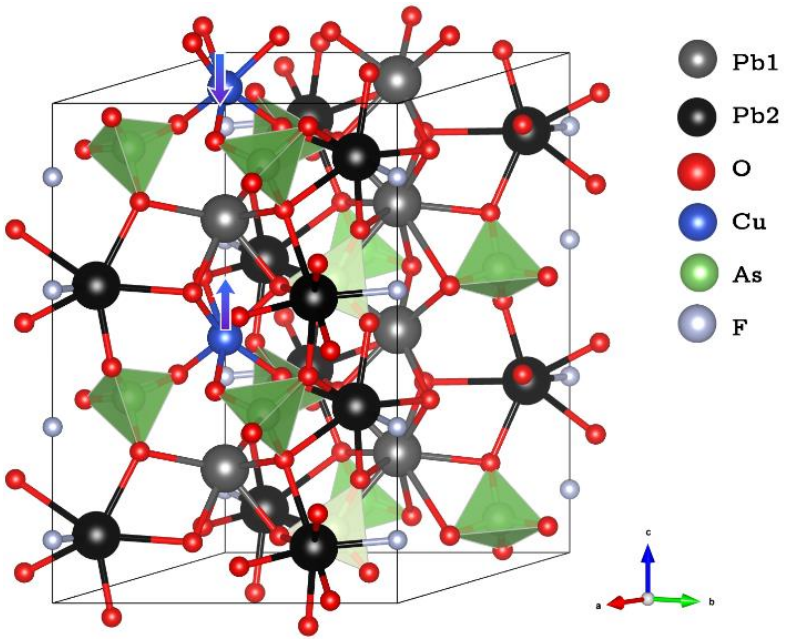

Fig. 1. Out-of-plane atniferromagnetic configuratoin of $Pb_9Cu(AsO_4)_6F_2$.

We also note that with such small energy differences, at orders of 10 μeV/atom it is likely that these materials would demonstrate paramagnetic response at room temperature. However, the results obtained provide an important strepping stone towards chemical contol of the magnetic phase diagram of doped apatite systems. Authors aknowledge the financial support of the National Research Foundation of Ukraine, Grant № 181/0242 (0124U003949).

References

[1] P. Giannozzi et al., J. Phys.:Condens. Matter 21 395502 (2009).
[2] P. Giannozzi et al., J. Phys.:Condens. Matter 29 465901 (2017).
[3] P. Giannozzi et al., J. Chem. Phys. 152 154105 (2020).
[4] J. W. Furness et al., J. Phys. Chem. Lett. 11(19):8208–8215 (2020).
[5] D. R. Hamann. Phys. Rev. B, 88(8) (2013).

BLOCH POINT SINGULARITY STRUCTURE

Ivan A. Yastremsky[1,2]

[1]Taras Shevchenko National University of Kiev, 03127 Kiev, Ukraine
[2]Helmholtz-Zentrum Dresden-Rossendorf e.V., Institute of Ion Beam Physics and Materials Research, Bautzner Landstrasse 400, 01328 Dresden, Germany

Abstract: *We demonstrate that typical radius of BP core within the widely used Landau model is substantially smaller that within more realistic mean-field model for low temperatures. We predict that the longitudinal nonlocal relaxation, calculated within the mean-field model, is lower compared to the contribution of nonlocal longitudinal relaxation, calculated within the Landau model.*

Recent advances in producing and characterizing nano and microstructures with a plethora of shapes and sizes as well as the first imaging of 3D magnetic configurations such as complex vortices, Bloch points and hopfions renewed the interest in describing the properties of three-dimensional (3D) magnetic profiles. Among the 3D magnetic profiles with topological protection, we can highlight the Bloch point (BP) [1, 2], which is a structure that presents a singular point at its center, where ferromagnetic order is destroyed.

Recent theoretical and experimental works showed that these magnetic singularities appear in magnetic nanodots with perpendicular magnetic anisotropy, in ferromagnets during the process of vortex core reversal, the reversal of skyrmions in confined helimagnetic structures, in a bilayer of nanodots of FeGe with different chiralities, in modulated nanowires with intrinsic Dzialoshinskii-Moriya interaction, and in cylindrical magnetic nanowires as the center of a vortex domain wall.

Recently it was identified that the contribution of the so far neglected longitudinal relaxation to the damping of domain walls (without strong structural suppression of the magnetization length) in ultrathin (2D) easy-axis magnetic films sufficiently far from the Curie temperature is comparable or even stronger than any other transversal mechanism discussed before, including spin-pumping [3]. This enhancement is associated with the Mermin-Wagner theorem and caused by a higher sensitivity of 2D ferromagnets to an effective field compared to their 3D counterparts.

In recent years, BPs are attracting more attention, particularly in nanomagnetic systems, since many theoretical works carried out in dynamic conditions have proposed that BPs bear critical roles in many dynamical phenomena of spin textures and influence their equilibrium states. For example, it was discussed that BPs work as key components to initiate the magnetization reversal process and domain wall (DW) motion in the magnetic cylinders. They are also known to mediate the switching of vortex and skyrmion cores. Injection and/or expulsion of BPs during the motion of magnetic DWs and switching of magnetic vortices or skyrmions were reported to change the topological numbers in spin textures. To properly use BPs in technological applications based on their stabilization and motion, it is crucial to analyze the fundamental properties of these structures. In particular, the BP mobility is strongly affected by the distribution of the magnetization length at the BP center [4].

The concept of point singularities in magnetism was introduced by Feldtkeller, who considered different magnetization distributions around the singularity and proposed the first estimations of the Bloch point shape. The defining property of a BP is that in a closed surface around its center, the direction of the magnetization field covers the whole solid angle an integer number of times. Later, Döring studied how magnetostatic energy governed the Bloch point structure by selecting the rotation angle inside the Bloch point. BP singularities were directly observed in yttrium iron garnet crystals.

The distribution of the magnetization length at the BP center at finite temperature is studied in Ref. [4, 5, 6]. For modelling of the free energy in these studies the Landau energy is adopted. Still in magnetism there is no region where the Landau expansion could be applied rigorously. The purpose of this study is to investigate the distribution of the magnetization length around the singularity of BP adopting more realistic free energy.

The model

We suppose that the magnetization of a ferromagnet **M** can change its length *M*. As we study the magnetization length distribution *M* around the singularity of BP, where the exchange energy dominates we restrict ourself to the case of isotropic ferromagnet. The conditions that determine the structure of a motionless soliton have a clear interpretation that the effective field (generalized forces) in the system equal to zero **H**=0 [3-6]. We calculate the radial distribution of *M* for the free energy in the frame of the mean-field approach for a spin *S*=1/2 and compare this result with those obtained in [4, 5, 6] for the energy in the Landau form. The preliminary results of these calculations are presented in Fig. 1 and Fig.2. The distance from the BP center *x* is measured in units, which is of the order of 1 nm for parameters of ultrathin films of Co [3].

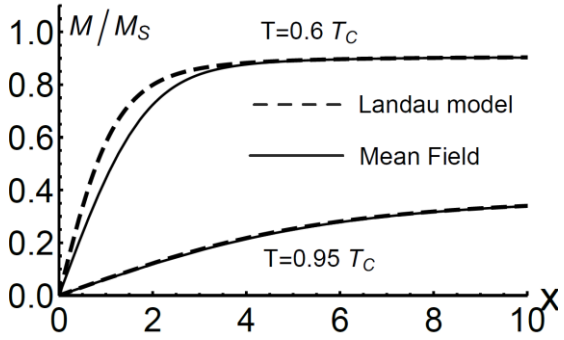

Fig. 1. The radial dependence of the normalized magnetization length for temperatures $T=0.6T_C$, $0.95\ T_C$ within the Landau and mean-field models.

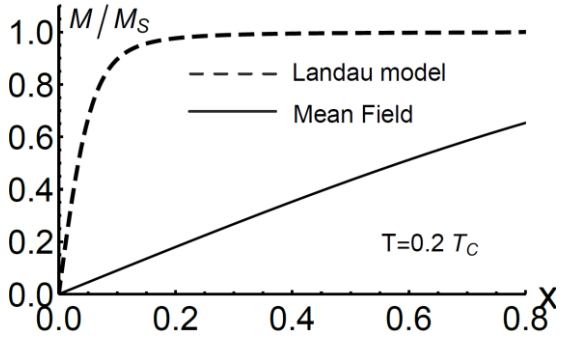

Fig. 2. The radial dependence of the normalized magnetization length for temperatures $T=0.2T_C$, within the Landau and mean-field models.

These figures demonstrate that the widely Landau model [4, 5, 6] is adequate only for temperatures sufficiently close to the Curie temperature. For low temperatures the Landau model gives substantially lower radius of BP core compared to the mean-field model. For example, for $T=0.2T_C$, the typical radius of BP within the Landau model is of the order of atomic unit and is about 15 times smaller than within more realistic mean-field model. Consequently, the long-wave approximation, exploited in [4, 5, 6], can hardly be justified for description of the variation of the magnetization length for low temperatures. We predict that the longitudinal nonlocal relaxation, calculated within the mean-field model, is lower compared to the contribution of nonlocal relaxation, calculated within the Landau model [4].

[1] Da Col, S. et al., Observation of Bloch-point domain walls in cylindrical magnetic nanowires. Phys. Rev. B 89, 180405 (2014).

[2] Im, M.-Y. et al., Dynamics of the Bloch point in an asymmetric permalloy disk. Nat. Commun. **10**, 593 (2019).

[3] I. A. Yastremsky, J. Fassbender, B. A. Ivanov, and D. Makarov, Enhanced Longitudinal Relaxation of Magnetic Solitons in Ultrathin Films, Phys. Rev. Appl. **17**, L061002 (2022).

[4] Galkina, E. G., Ivanov, B. A., Stephanovich, V. A., Phenomenological theory of Bloch point relaxation. J. Magn. Magn. Mater. **118**, 373 (1993).

[5] K. M. Lebecki, D. Hinzke, U. Nowak, and O. Chubykalo-Fesenko, Key role of temperature in ferromagnetic Bloch point simulations, Phys. Rev. B **86**, 094409 (2012).

[6] R. G. Elias and A. Verga, Magnetization structure of a Bloch point singularity, Eur. Phys. J. B **82**, 159 (2011).

TEMPERATURE CHANGES IN MAGNETIC PROPERTIES OF AL-SUBSTITUTED YTTRIUM IRON GARNETS

Vladyslav Borynskyi*, Dariia Popadiuk, Anatolii Kravets*, Yuliia Shlapa***, Serhii Solopan***, Vladislav Korenivski**, Anatolii Belous***, Alexandr Tovstolytkin***

**Institute of Magnetism of the NAS of Ukraine and MES of Ukraine,*
36-b, Akad. Vernadskogo blvd., Kyiv 03142, Ukraine, email: vladislav.borinskiy@gmail.com
***Nanostructure Physics, Royal Institute of Technology,*
12, Hannes Alfvénsväg, Stockholm 10691, Sweden, email: dashapopadiuk43@gmail.com
****V.I. Vernadsky Institute of General and Inorganic Chemistry of the NAS of Ukraine,*
32/34, Palladina ave., Kyiv 03142, Ukraine, email: yuliashlapa@ukr.net

Based on magnetostatic measurements of $Y_3AlFe_4O_{12}$, we study in detail the intrinsic magnetic parameters of such garnet crystals. Using the Law of Approach to Saturation we successfully determine otherwise indistinguishable contributions of effective magnetic anisotropy, structural and magnetic inhomogeneities. The temperature dependence of effective anisotropy constant is extracted from the experimental data and demonstrates strong exponential-like character. We show that despite Al substitution of Fe ions in YIG crystals leads to a significant drop in saturation magnetization, almost two-fold upturn in effective magnetic anisotropy is revealed. An estimation for temperature variation of spin-wave stiffness constant is also given, which should be useful for incorporation and further development of garnet materials in modern technologies.

Introduction

Since the middle of the 20th century yttrium iron garnets (YIG) have become the best choice material for many pioneering applications. Up until now YIG-based nanomaterials have been exploited in a number of technologies, *e.g*. telecommunication, microwave electronics, magneto-optics, spintronics and magnonics, owing to their outstanding physical characteristics [1]. Among such should be mentioned good dielectric properties, high Q-factor in the microwave range, small magnetic damping, significant optical activity, high chemical and structural stability. The complex crystal structure of a garnet, despite may seem as a disadvantage, grants a wide range of possibilities for material design with enhanced functional characteristics. The current state of the problem implies that, depending on a field of applications and an operating regime of a final device, additional technological demands are imposed on the involved magnetic material. Therefore, an increasing interest in substituted garnets with various dopants (Sm, In, Ca, Co, Ni, Mn, *etc*.) has been observed in last years. Al-doped yttrium iron garnets $Y_3AlFe_4O_{12}$ (YAIG) occupy a special spot among the class of substituted garnet materials. Several recent works postulate stricter material requirements compared to those a conventional YIG can meet – the need for increased permittivity ε and reduced coercive field ($H_c \lesssim 10$ Oe). While it was already shown, that YAIG is capable to fulfill the former demand, a systematic investigation on the latter, particularly, magnetic anisotropy of YAIG, is still lacking.

We prepared a series of YAIG ceramic samples in the form of flat parallelepipeds by sintering the $Y_3AlFe_4O_{12}$ nanopowder, obtained with our newly proposed efficient route for co-precipitation in aqueous solution, details on which are available in [2]. Magnetostatic measurements were carried out in the temperature range 3–370 K using PPMS DynaCool (Quantum Design Inc.) equipped with VSM magnetometer. Crystallographic properties and microstructure of the samples were also investigated using the XRD method and SEM, respectively.

Experiment & Results

Experimental hysteresis loops revealed soft coercive behavior, inherent to ferrimagnetic crystals with cubic symmetry. The coercive force reached its maximum value of 55 Oe at low temperature, however being higher than such for an undoped YIG (typically ~40 Oe). Due to the polycrystalline nature of YAIG ceramics, a number of

factors determine the resulting coercivity of a bulk sample. In addition to magnetocrystalline anisotropy, effects of domain wall motion, demagnetization, stochastic structural and magnetic inhomogeneities should also be carefully distinguished. In order to separate such terms and extract the intrinsic parameters in question, the Law of Approach to Saturation (LAS) was used, enabling us to fit the high-field part of the hysteresis loops. The determined effective anisotropy constant K_{eff} is shown in panel (a) and has a strong exponential-like temperature dependence. Its low-temperature absolute value is about twice lower than such of a pure YIG (24 kerg·cm^{-3}). A convenient way to assess the performance of the investigated garnet material is provided by the effective magnetic anisotropy field, recalculated using the retrieved K_{eff} values.

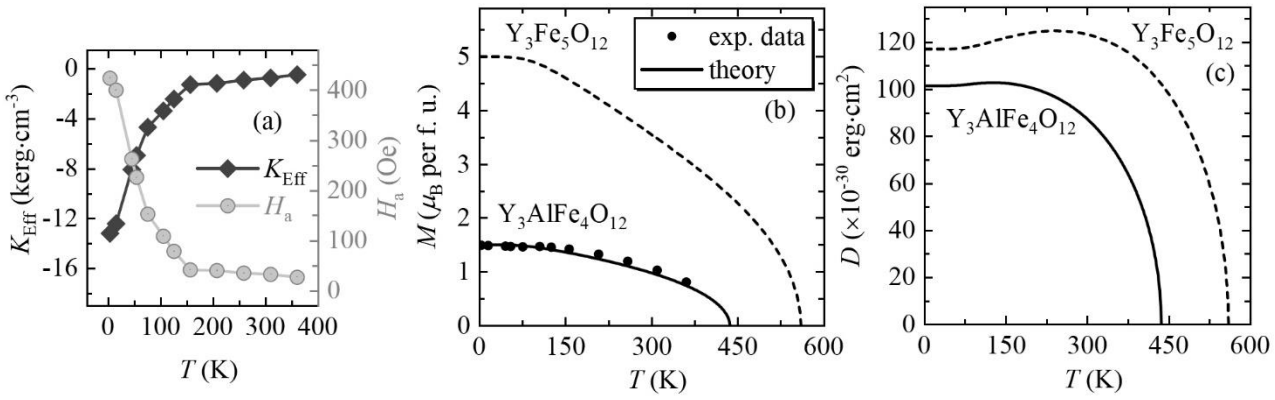

Fig. 1. (a) Dependencies of the effective magnetic anisotropy constant and the corresponding field versus temperature. (b) Comparison of the experimental and calculated thermomagnetization curves. (c) Temperature dependencies of the spin-wave stiffness for YIG and YAIG.

Another parameter that was determined by fitting the experimental data is the saturation magnetization of YAIG, depicted in panel (b). We utilized Brillouin-Weiss model, adapted specifically for substituted garnets [3], to independently calculate the temperature variation of YAIG and compare with the results from the LAS. An excellent agreement between the theory and the experiment was observed, well recreating both the significant drop of the saturation magnetization, caused by Al substitution of Fe ions, and its gradual fall with increasing temperature.

We used the values of M and K_{eff} to estimate the temperature dependence of the YAIG spin-wave stiffness constant, presented in panel (c). Our results provide valuable information on the key magnetic parameters of Al-substituted YIG, allowing to optimize the garnet material design to current technological demands. Furthermore, even though at low temperatures the effective magnetic anisotropy is notably larger in contrast to pure YIG, at room temperature it shows much lower values (50 Oe as opposed to 90 Oe), which might be useful for practical applications.

References

[1] V. Harris, Modern Ferrites: Emerging Technologies and Applications, Wiley, 2022.

[2] S. Solopan, A. Tovstolytkin, V. Zamorskyi, Y. Shlapa, V.-A. Maraloiu, O. Fedorchuk, and A. Belous, "Nanoscale $Y_3AlFe_4O_{12}$ Garnets: Looking into Subtle Features of Crystalline Structure and Properties Formation," J. Alloys Compd. vol. 968, pp. 172248, 2023.

[3] G. F. Dionne, "Molecular Field Coefficients of Substituted Yttrium Iron Garnets," J. Appl. Phys. vol. 41, pp. 4874, 1970.

DYNAMICS OF MAGNETIC FLUXONS IN A SUPERCONDUCTING MoRe FILM

Martynenko I.*, Kalenyuk O.A.* **, Kasatkin O. L. *

**G. V. Kurdyumov Institute for Metal Physics, 36 Academician Vernadsky Boulevard, UA-03142 Kyiv, Ukraine*
***Kyiv Academic University, 36 Academician Vernadsky Boulevard, UA-03142 Kyiv, Ukraine*
e-mail: i.martynenko@kau.edu.ua

The voltage-current characteristics of a thin superconducting film of MoRe alloy in a magnetic field were investigated. The influence of the magnetic field on the critical temperature was observed. Temperature dependencies of the critical current were obtained. In the magnetic field, a section characteristic of collective magnetic flux creep appears on the voltage-current characteristics. This section exhibits a kink, which may result from the fragmentation of a fluxon into fractional components in two-band superconductors under an applied current.

Introduction

Due to zero resistance and the rapid nature of processes, superconductors take the way for quantum electronics and quantum devices. Energy-independent quantized states are ideally suited for implementing classical Boolean logic. The magnetic fluxon (Abrikosov vortex) is the most compact magnetic object in superconductors and can be utilized to create high-density digital cryoelectronics [1]. In this study, the investigated superconducting material is the two-band $Mo_{0.6}Re_{0.4}$ alloy, which has a critical temperature of T_c=11K, with large and small energy gaps of Δl=2.3 meV and Δs=0.7 meV, respectively [2]. As a result of its two-band nature, the vortex splitting effect into fractional components occurs under the application of a direct current. These fractional components can increase the density of quantum states in logical fluxon elements. The vortex splitting effect was observed using scanning SQUID magnetometry [3]. The goal of this work was to identify signs of fractional vortex formation in the voltage-current characteristics of the two-band superconducting MoRe film.

Vortex Dynamics in the MoRe Superconductor Under the Influence of a Magnetic Field

The object of the study is a superconducting MoRe thin-film bridge with dimensions of 19x25 μm² and a thickness of 50 nm. The temperature dependence of the bridge's resistance shows a transition to the superconducting state (Fig. 1a) at a temperature of T_c=11.02 K without a magnetic field, and T_c=10.71 K at a magnetic field B=70 mT. The resistance of the bridge is R_n=200 Ω. The obtained temperature dependencies of the critical current (Fig. 1b) do not correspond to the approximation by the BCS theory, which describes the behavior for single-band superconductors. A decrease in the critical current under the influence of a small magnetic field was also observed. A series of voltage-current characteristic (V-I) measurements of the bridge at different temperatures were conducted in the range of ±10 mA with a current sweep rate of 0.01 mA/s, allowing the observation of thermal processes in the sample in a quasi-stationary regime. The I-V measurements without a magnetic field showed an instantaneous breakdown at the critical current due to thermal heating of the sample, with zero resistance before this transition. Hysteresis in the I-V curve was also observed, which is characteristic of thermal processes involving the formation of a hot spot. When measuring the I-V curve of the bridge in an external magnetic field of 70 mT, a transition to the resistive state was also observed. However, before this transition, a smooth voltage dependence up to ±1 mV was noted (Fig. 1a), indicating a resistive state with resistance on the order of 6 μ, much smaller than Rres. This resistive state is caused by vortex flow (flux-flow vortices) under the influence of the Lorentz force. In Fig. 1c, the collective vortex creep, which is described by equation (1) for single-band superconductors [2], is observed.

$$V(I) = V_0 * e^{(-(\frac{I_0}{I})^{\mu})} \quad (1)$$

$$\ln V\left(\frac{1}{I}\right) = V_{01} - I_{01} * (\frac{1}{I})^{\mu} \quad (2)$$

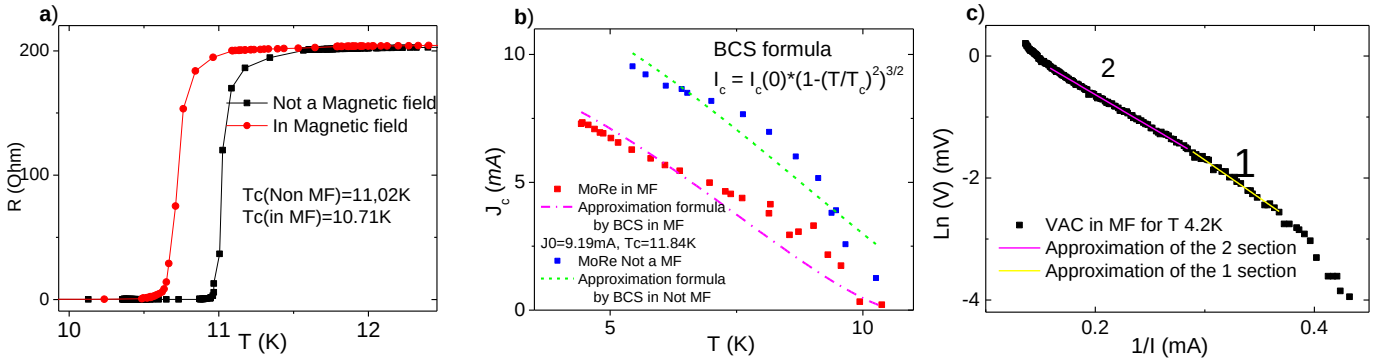

Fig. 1. a) Temperature dependence of the MoRe bridge with and without a magnetic field. b) Dependence of the critical current on temperature and its approximation according to BCS theory. c) V-I characteristics linearized according to equation (2).

By plotting the I-V characteristics according to the coordinates of equation (2), the effect of collective creep can be observed as a linear dependence. When approximating the linearized I-V curve, two linear sections are evident, which may indicate the fragmentation of vortices into fractional components due to the applied current [3]. The separate approximation of these sections yields an atypical value of the exponent $\mu=2$ in the low-current region (for single-band superconductors, $\mu<1$), which could be evidence of vortex fractionalization.

This research was carried out within the framework of the project 2023.04/0157 funded by the National Research Foundation of Ukraine

References

[1] Golod, T., Iovan, A., & Krasnov, V. M. (2015). Single Abrikosov vortices as quantized information bits. Nature Communications, 6(1). doi:10.1038/ncomms9628

[2] I. Martynenko, O. Kalenyuk, A. Shapovalov, H. Kondakova, V. Shamaev, O. Boliasova, and O. Zhitlukhina, Proximity Effect between a Two-Band Superconductor and a Ferromagnet, Metallofiz. Noveishie Tekhnol., 45, No. 10: 1141—1150 (2023)

[3] Experimental observation of fractional vortices by use of scanning SQUID magnetometry: Y. Iguchi, R. Shi, K. Kihou, C.-H. Lee, V. Grinenko, E. Babaev, and K. A. Moler, Science 380, 1244 (2023)

[4] Dissociation Transition of a Composite Lattice of Magnetic Vortices in the Flux-Flow Regime of Two-Band Superconductors Shi-Zeng Lin* and Lev N. Bulaevskii DOI: 10.1103/PhysRevLett.110.087003

[5] Vortex dynamics in YBCO single crystals at high temperaturesm. A. OBOLENSKII, A. V. Bondarenko, A. A. Prodan, R. V. Vovk, M. G. Revyakina, M. Pissas, G. Kallias, D. Niarchos, AND T. R. Arouri DOI:10.1142/9789812793676_0057

MATHEMATICAL PROBLEMS OF APPLIED PHYSICS

MONO-FRACTAL ANALYSYS WITH THE HURST DIMENSION USAGE IN APPLIED PHYSICS

Leonid F. Chernogor*, Oleg V. Lazorenko, Andriy A. Onishchenko*****

** School of Radiophysics, Biomedical Electronics and Computer Systems,*
V. N. Karazin Kharkiv National University, Kharkiv 61022, Ukraine e-mail: Leonid.F.Chernogor@gmail.com
*** School of Physics, V. N. Karazin Kharkiv National University, Kharkiv 61022, Ukraine,*
e-mail: Oleg.V.Lazorenko@karazin.ua
**** Faculty of Automatics and Computerized Technologies, Kharkiv National University of Radioelectronics,*
Kharkiv 61166, Ukraine, email: Andrey.Onishchenko@nure.ua

Basing on the mono-fractal analysis results obtained for the sunspot numbers time series, the effectiveness of the Hurst fractal dimension calculated with rescaled range method application was shown. A good example of the second order fractal existence in practice was considered.

Introduction

In this work, to describe the mono-fractal properties of a fractal process, we use only the Hurst dimension D calculated with application of the rescaled range analysis (RRA) method (see, for example, [1]). The RRA method accuracy was improved with the Corrective Function Method usage [2]. To show the pecularities of the mono-fractal analysis used in such way for the applied physics, the sunspot numbers time series as a well-known fractal natural process was chosen.

Previous Studies of Fractal Properties of the Sunspot Numbers Time Series

The time series of sunspot numbers, which characterizes solar activity and is associated with the counting of sunspots, is unique in the sense that observations have been conducted since 1610, although complete and reliable data have only been available since 1849 (see, for example, [3]). It is well known that it has a pronounced 11-year cycle, superimposed perhaps on another slower component with a period of about a hundred years (see, for example, [4]). However, this information was obtained in the “pre-fractal” era. First fractal analysis of the time series of Wolf numbers was carried out by B. Mandelbrot and J. Wallis in 1969 in the work [5]. Been translated into current terminology, it turned out that in the ranges of periods from 3 to 30 months and from 30 to 100 years, the fractal dimension is $D \approx 1.1$. These results were obtained using the R/S method [5]. In a number of later works quite similar results were obtained using other methods of fractal analysis, in particular, $D \approx 1.2$ in [6], $D \approx 1.0-1.2$ in [7] and $D \approx 1.2-1.3$ in [8]. Thus, it has been established that the time series of sunspot numbers is a fractal process, well described by the model of generalized Brownian motion. The fractal dimension D of this process is in the range $D \approx 1.1-1.3$. Consequently, the series of sunspot numbers has the property of persistence. Since 2006, regular studies of the multifractal properties of the Wolf number series have been conducted. It has been established that the sinusoidal trend has a significant negative impact on the estimates obtained. After its removal, it turned out that the fractal dimension of the series as a whole is $D \approx 1.88 \pm 0.01$ [9]. And this value differs significantly from that given by mono-fractal analysis methods. The explanation for this is simple: it is necessary to compare either the results obtained without a trend or with a trend. And this, unfortunately, was not done in [9]. Moreover, in 2009, in the work [10], a different mechanism for removing the sinusoidal trend was proposed, and the value for the fractal dimension turned out to be different: $D \approx 1.26$, which is quite consistent with the results presented above.

Fractal Analysys of the Sunspot Numbers Time Series

For present analysis, the daily total sunspot numbers from 1/1/1818 till 31/07/2024 were chosen [11]. Of course, as well as all useful information about fractal structure of a signal is consisted in high-frequency part of Fourier spectrum, any averaging is not preferable. But the low-frequency part impact on the Hurst dimension estimations can be successfully reduced by differentiation operation usage. Namely this approach is used in our investigations. As it had been found by B. Mandelbrot [5], the sunspot time series in whole is not mono-fractal. However, there are some ranges of periods, where mono-fractal properties can be discovered. From the fig. 1,

where the dependence of $\log(R/S)$ vs $\log n$ is shown, such ranges and corresponding values of Hurst fractal dimension D are defined. It was found that in the ranges of periods from 7 to 70 days ($\log n = 1.95 - 4.25$) $D \approx 1.66 \pm 0.01$, from 3 to 30 months ($\log n = 4.50 - 6.80$) $D \approx 1.91 \pm 0.01$, from 30 to 90 months ($\log n = 6.80 - 7.90$) and from 30 to 200 years ($\log n = 9.29 - 11.20$) $D \approx 1.58 \pm 0.01$. In other ranges, where given dependence cannot be successfully approximated by a straight line, the sunspot time series is appeared to be not fractal. If for straight line approximation building, one uses all points shown at the fig. 1, some averaged Hurst fractal dimension D value, which is able to describe the whole signal. This value is found to be $D \approx 1.78 \pm 0.01$.

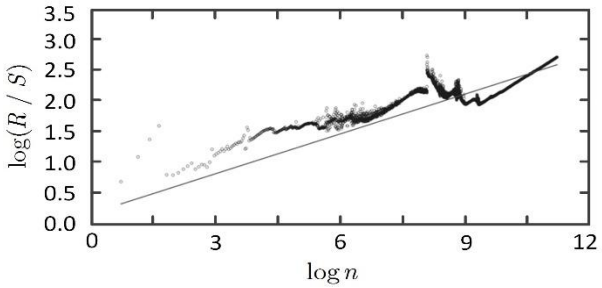

Fig. 1. The dependence of $\log(R/S)$ *vs* $\log n$.

In 2023 in the paper [12], the concept of the so-called 'second-order fractals' has been introduced. By the definition, second-order fractal is a fractal, fractal dimension of which is appeared to be a fractal function of time or space variable. A fractal signal with such property is called as second-order fractal signal. If the function $D(t)$ is considered without any, it was found to be namely second-order fractal signals. In such case, its Hurst fractal dimension is appeared to be $D = 1.68 \pm 0.01$.

References

[1] O. V. Lazorenko, L. F. Chernogor, "Fractal radio physics. 2. Fractal and multifractal analyses of signals and processes" Radio Phys. Radio Astron., vol. 28, no. 1, pp. 5 – 70, 2023 (in Ukrainian).

[2] O. V. Lazorenko, A. A. Onishchenko, L. F. Chernogor, "Corrective function method for the fractal analysis", Radiotekhnika: All-Ukr. Sci. Inter- dep. Mag., no. 210, pp. 177 – 187, 2022 (in Ukrainian).

[3] Yu. I. Vitinskii, "Solar activity forecasting", NASA TTF-289 TT65-50115, 1965.

[4] M.Frame, A. Urry, *Fractal Worlds: Grown, Built, and Imagined, New Haven*. London: Yale University Press, 2016.

[5] B. Mandelbrot, J. R. Wallis, "Computer experiments with fractional Gaussian noises", Water Resources Res., vol. 5. no. 1, pp. 228-241, 1969.

[6] A. Ruzmaikin, J. Feynman, P. Robinson, "Long-term persistence of solar activity", Solar Physics, vol. 152, no. 1, pp. 313, 1994.

[7] M. G. Ogurtsov, "New evidence for long-ierm persistence in the Sun's activity", Solar Physics, vol. 220, no. 1, pp. 93–105, 2004.

[8] M. Rypdal, K. Rypdal, "Is there long-range memory in solar activity on timescales shorter than the sunspot period?", Journal of Geophysical Research: Space Physics., vol. 117, no. A4., 2012.

[9] M. S. Movahed, G. R. Jafari, F. Ghasemi, S. Rahvar, M. R. R. Tabar, "Multifractal detrended fluctuation analysis of sunspot time series", Journal of Statistical Mechanics: Theory and Experiment, vol. 02, P02003–P02003, 2006.

[10] J. Hu, J. Gao, X. Wang, "Multifractal analysis of sunspot time series: the effects of the 11-year cycle and Fourier truncation", Journal of Statistical Mechanics: Theory and Experiment, vol. 02, P02066, 2009.

[11] https://www.sidc.be/SILSO/datafiles

[12] L. F. Chernogor, O. V. Lazorenko, A. A. Onishchenko, "Fractal analysis for low temperature physics", Low Temperature Physics, vol. 49, no. 4, pp. 459 – 465, 2023.

RESEARCH OF EXPERT ASSESSMENTS OF INVESTMENT PROJECTS USING FUZZY SET THEORY METHODS

M.V. Maksyuta, D.T. Nidzelsky, V.V. Obukhovsky

Faculty of Radio Physics, Electronics and Computer Systems Taras Shevchenko Kyiv National University of Kyiv, Glushkova ave., 4g, e-mail: anonimnay005@gmail.com

This study employs fuzzy set theory methods to assess three nearly equivalent investment projects evaluated by a corresponding number of experts. The evaluation is based on a set of predefined factors reflecting the project's goal, methods of implementation, timelines, and uniqueness. Using these factors, fuzzy subsets with corresponding membership functions were created. Calculations of the effectiveness indicators for the investment projects were performed using alpha-level generalization principles ("0.25, 0.5, 0.75-level principles of generalization"). The study also examines the consistency of expert opinions using linear and quadratic fuzziness indices, probabilistic, and non-probabilistic entropy functions. Moreover, the minimum number of experts required to mitigate the influence of corruption in project assessments was determined.

Let there be three investment projects (denoted by **A**, **B**, **C**) from various industries such as manufacturing, construction, and agriculture. An analysis based on a general set $\mathbf{E} = \{x_1,...,x_n\}$ (we take $n=10$ and such as, for example, in work [1]) is performed by k experts, with k = 5,10,15. Each project is assigned an index to identify the specific expert working on it, for instance, $\mathbf{A}_k$ refers to the k-th expert working on project **A**. The assessments from [1], given on a 100-point scale, are converted into membership functions $0 \le \mu^{(i)}_{\underset{\sim}{\mathbf{A}}_j}, \mu^{(i)}_{\underset{\sim}{\mathbf{B}}_j}, \mu^{(i)}_{\underset{\sim}{\mathbf{C}}_j} \le 1$, $(i=1,...,n;\ j=1,...,k)$, forming fuzzy subsets [2, 3]:

$$\underset{\sim}{\mathbf{A}}_j = \left\{ \begin{pmatrix} x_1 \\ \mu^{(1)}_{\underset{\sim}{\mathrm{A}}_j} \end{pmatrix}, \begin{pmatrix} x_2 \\ \mu^{(2)}_{\underset{\sim}{\mathrm{A}}_j} \end{pmatrix}, \begin{pmatrix} x_3 \\ \mu^{(3)}_{\underset{\sim}{\mathrm{A}}_j} \end{pmatrix}, \begin{pmatrix} x_4 \\ \mu^{(4)}_{\underset{\sim}{\mathrm{A}}_j} \end{pmatrix}, \begin{pmatrix} x_5 \\ \mu^{(5)}_{\underset{\sim}{\mathrm{A}}_j} \end{pmatrix}, \begin{pmatrix} x_6 \\ \mu^{(6)}_{\underset{\sim}{\mathrm{A}}_j} \end{pmatrix}, \begin{pmatrix} x_7 \\ \mu^{(7)}_{\underset{\sim}{\mathrm{A}}_j} \end{pmatrix}, \begin{pmatrix} x_8 \\ \mu^{(8)}_{\underset{\sim}{\mathrm{A}}_j} \end{pmatrix}, \begin{pmatrix} x_9 \\ \mu^{(9)}_{\underset{\sim}{\mathrm{A}}_j} \end{pmatrix}, \begin{pmatrix} x_{10} \\ \mu^{(10)}_{\underset{\sim}{\mathrm{A}}_j} \end{pmatrix} \right\},$$

$$\underset{\sim}{\mathbf{B}}_j = \left\{ \begin{pmatrix} x_1 \\ \mu^{(1)}_{\underset{\sim}{\mathrm{B}}_j} \end{pmatrix}, \begin{pmatrix} x_2 \\ \mu^{(2)}_{\underset{\sim}{\mathrm{B}}_j} \end{pmatrix}, \begin{pmatrix} x_3 \\ \mu^{(3)}_{\underset{\sim}{\mathrm{B}}_j} \end{pmatrix}, \begin{pmatrix} x_4 \\ \mu^{(4)}_{\underset{\sim}{\mathrm{B}}_j} \end{pmatrix}, \begin{pmatrix} x_5 \\ \mu^{(5)}_{\underset{\sim}{\mathrm{B}}_j} \end{pmatrix}, \begin{pmatrix} x_6 \\ \mu^{(6)}_{\underset{\sim}{\mathrm{B}}_j} \end{pmatrix}, \begin{pmatrix} x_7 \\ \mu^{(7)}_{\underset{\sim}{\mathrm{B}}_j} \end{pmatrix}, \begin{pmatrix} x_8 \\ \mu^{(8)}_{\underset{\sim}{\mathrm{B}}_j} \end{pmatrix}, \begin{pmatrix} x_9 \\ \mu^{(9)}_{\underset{\sim}{\mathrm{B}}_j} \end{pmatrix}, \begin{pmatrix} x_{10} \\ \mu^{(10)}_{\underset{\sim}{\mathrm{B}}_j} \end{pmatrix} \right\},$$

$$\underset{\sim}{\mathbf{C}}_j = \left\{ \begin{pmatrix} x_1 \\ \mu^{(1)}_{\underset{\sim}{\mathrm{C}}_j} \end{pmatrix}, \begin{pmatrix} x_2 \\ \mu^{(2)}_{\underset{\sim}{\mathrm{C}}_j} \end{pmatrix}, \begin{pmatrix} x_3 \\ \mu^{(3)}_{\underset{\sim}{\mathrm{C}}_j} \end{pmatrix}, \begin{pmatrix} x_4 \\ \mu^{(4)}_{\underset{\sim}{\mathrm{C}}_j} \end{pmatrix}, \begin{pmatrix} x_5 \\ \mu^{(5)}_{\underset{\sim}{\mathrm{C}}_j} \end{pmatrix}, \begin{pmatrix} x_6 \\ \mu^{(6)}_{\underset{\sim}{\mathrm{C}}_j} \end{pmatrix}, \begin{pmatrix} x_7 \\ \mu^{(7)}_{\underset{\sim}{\mathrm{C}}_j} \end{pmatrix}, \begin{pmatrix} x_8 \\ \mu^{(8)}_{\underset{\sim}{\mathrm{C}}_j} \end{pmatrix}, \begin{pmatrix} x_9 \\ \mu^{(9)}_{\underset{\sim}{\mathrm{C}}_j} \end{pmatrix}, \begin{pmatrix} x_{10} \\ \mu^{(10)}_{\underset{\sim}{\mathrm{C}}_j} \end{pmatrix} \right\}.$$

As proposed in [4], selecting the most attractive project can be performed based on α-level generalization principles. To do this, first, for fuzzy subsets $\underset{\sim}{\mathbf{A}}_j$, $\underset{\sim}{\mathbf{B}}_j$, $\underset{\sim}{\mathbf{C}}_j$ we build ordinary subsets $\underline{\underset{\sim}{\mathbf{A}}}_{j\alpha}$, $\underline{\underset{\sim}{\mathbf{B}}}_{j\alpha}$, $\underline{\underset{\sim}{\mathbf{C}}}_{j\alpha}$ α-levels, in which the characteristic functions of the membership of their elements are written in the following form [3]:

$$\mu_{\underline{\underset{\sim}{\mathbf{A}}}_{j\alpha,i},\underline{\underset{\sim}{\mathbf{B}}}_{j\alpha,i},\underline{\underset{\sim}{\mathbf{C}}}_{j\alpha,i}} = \theta\left[\mu_{\underset{\sim}{\mathbf{A}}_j,\underset{\sim}{\mathbf{B}}_j,\underset{\sim}{\mathbf{C}}_j}(x_i) - \alpha \right],$$

where $\theta(x)$ – Heaviside function. After which, for clarity, we will use histograms and calculate the indicators of effectiveness in percentage for the skin of the prescribed IP for "0.25, 0.5, 0.75 – according to the same principles of registration" for the type with this formula:

$$\Pi_{(\mathbf{A},\mathbf{B},\mathbf{C})} = \frac{1}{nk}\sum_{i=1}^{n}\sum_{j=1}^{k}\left(\mu_{\mathbf{A}_{j,(0.25,0.5,0.75);i}},\mu_{\mathbf{B}_{j,(0.25,0.5,0.75);i}},\mu_{\mathbf{C}_{j,(0.25,0.5,0.75);i}}\right)100\% .$$

In order to achieve a more objective choice of one of the investment projects, efficiency indicators were calculated even with a smaller number of factors (the most important ones were chosen). The influence of the corruption component was investigated separately, as a result of which it was established that for its almost complete leveling, the number of qualified experts should exceed the number of corrupt experts by approximately five times.

Calculations of the information measure of the coincidence of experts' opinions during their examination of investment projects were suggested in the paper to be performed using linear and quadratic indices of ambiguity [3], as well as using probabilistic and non-probabilistic entropy functions [3, 5]. It is shown that the linear index of vagueness and the non-probability entropy of the type

$$d\left(\underset{\sim}{\mu}_{\mathbf{A}_j,\mathbf{B}_j,\mathbf{C}_j}\right) = \frac{1}{n}\sum_{i=1}^{n} S\left[\underset{\sim}{\mu}_{\mathbf{A}_j,\mathbf{B}_j,\mathbf{C}_j}(x_i)\right]$$

are the best correlate. Here $S(x) = -x\ln x - (1-x)\ln(1-x)$ is the so-called Shannon function (see, for example, [5]).

As was demonstrated in work [6], such relatively simple mathematical calculations make it possible to fairly objectively conduct monitoring (in this case, on a number of experts), confirming or denying their professional qualifications, identifying corruption components, etc.

References

[1] M.V. Dobryanska, Investment support for technological renewal of machine-building enterprises (dissertation for obtaining the scientific degree of Candidate of Economic Sciences). – Lviv: Lviv Polytechnic Publishing House, 2016. – 216 p.

[2] L.A. Zadeh, Fuzzy Sets. Inform. and Control. Vol. 8, pp. 338-353.

[3] A. Kofman, Introduction to the theory of fuzzy sets. – M: "Radio and communication", 1982. - 432 p.

[4] R.A. Fayziev, U.T. Khaitmatov, O.Kh. Azamatov, Sh.R. Jumaniyazov, H.Kh. Khasanova, Using the theory of fuzzy sets in the economic analysis of investment projects / International Journal of Innovative Technologies in Economy, 2018, V.2, 5(17), pp. 44 – 48. https://doi.org/10.31435/rsglobal_ijite/0162018/5672

[5] A. De Luca, S.A. Termini, Definition of a Non-probabilistic Entropy in the Setting of Fuzzy Sets Theory. Inform. and Control, 1972, Vol. 20, pp. 301 – 312.

[6] S.I. Kolesnyk, M.V. Maksyuta, V.V. Obukhovsky, Comparative analysis of some anti-missile defense/air defense systems using the theory of fuzzy sets / Bulletin of Taras Shevchenko National University of Kyiv, series of physical and mathematical sciences, No. 1, 2023. – C. 111 – 117.

SOLVING TOMOGRAPHY PROBLEMS IN THE INFORMATION SPACE OF POSSIBLE SOLUTIONS

Sergiy I. Melnyk*, Sergiy M. Labazov, Serhii S. Melnyk*****

** Department of statistical radiophysics O. Ya. Usikov Institute for Radiophysics and Electronics Kharkiv, Ukraine, Address, e-mail: melnyksergiy72@gmail.com*
*** Department of statistical radiophysics O. Ya. Usikov Institute for Radiophysics and Electronics Kharkiv, Ukraine, Address, e-mail: labazov@ire.kharkov.ua*
**** Department of theoretical physics O. Ya. Usikov Institute for Radiophysics and Electronics Kharkiv, Ukraine, email: melnik.teor@gmail.com*

A comparative analysis of classical tomography methods and a method for minimizing the complexity of describing measurement results relative to a priori information about a possible solution to the problem was carried out. A new method is proposed for solving tomography problems in the information space of possible solutions, built on the basis of a measure (distance), calculated as the relative complexity of describing any pair of them .Using the example of the problem of tomography of current distribution using SQUID microscopy, it is shown that the new approach has significant advantages.

Keywords – tomography, information space, theory of complexity, SQUID-microscopy, inverse problem

1. The method of minimizing the length of the description as a tomography problem in the information space of states

A comparative analysis of classical methods for solving ill-posed inverse problems associated with the tomography problem and a relatively new method for minimizing the description length shows that the second has advantages. This is due to the fact that it can take into account arbitrary patterns of the set of results obtained, and not just simple and a priori expected ones. However, the practical application of the new method encounters computational and algorithmic difficulties. In the paper [1] we proposed a methodology for constructing an information space in which the relative complexity of two information objects (IOs) can be used to determine the measure between them. This set of IOs can be partially ordered according to the criterion of whether one IO belongs to another.

For the relative complexity of any three information objects, the "triangle inequality" $S_{\Omega_k}(A/B) + S_{\Omega_k}(B/C) \geq S_{\Omega_k}(A/C)$ has been proven, which allows us to consider the solution to the problem of finding the shortest (and therefore most plausible) description of measurement results as a continuous "trajectory" of minimum length in the information space of possible models of the observed object. However, in most cases, the description of each of the possible models (A, B, C ...) requires specifying a large number of parameters, and the corresponding space turns out to be multidimensional. As a result, the problem of determining the "distance" for each pair of its points and the subsequent search for a trajectory of minimum length is a task that cannot be realized in practice. Nevertheless, an appropriate choice of the "description language" of Ω_k models allows us to reduce the dimensionality of the information space and construct a converging algorithm for finding the shortest trajectory between the given points [2]. The language we use to describe the model of an object as a finite set of point individual inhomogeneities allows us to reduce the set of parameters for their description to a set of 3 coordinates, and the commutativity property $S_{\Omega_k}(A/B) + S_{\Omega_k}(B) = S_{\Omega_k}(B/A) + S_{\Omega_k}(A) = S_{\Omega_k}(B + A)$ ensures the stability and convergence of the algorithm for finding the minimum complexity of describing the measurement results. The last of the algorithms is a development of linear programming methods. They can be interpreted as difference schemes for modeling a diffusion (Born approximation) or wave process. The performance of the developed algorithms is illustrated by the results of developing a tomography algorithm for the SQUID microscopy [3]. It improve the resolution by SQUID microscopy an order of magnitude.

2. Implementation of the method in the problem of developing the SQUID microscopy method

As part of our joint work with LG (ROK), we developed a numerical model of the operation of a SQUID microscope. The essence of the model was to calculate the magnetic flux through the sensor generated by the subsurface current paths of printed circuit boards in order to reconstruct the currents flowing through them. To reconstruct the current distribution from the noisy distribution of the magnetic flux recorded by a sensor located at a given height, the following algorithm was used:

- search for the coordinate of an additional unit current (specified as a δ function) for which the relative complexity of describing the obtained scanning result is minimal;
- repeating this procedure until the addition of the next unit current reduces the complexity of describing the scanning results (when finding the corresponding coordinate);
- the reducing the complexity of the description by combining unit currents into rectangular distributions of finite width (which corresponds to a priori information about a uniform distribution of current density across the width of the current paths).

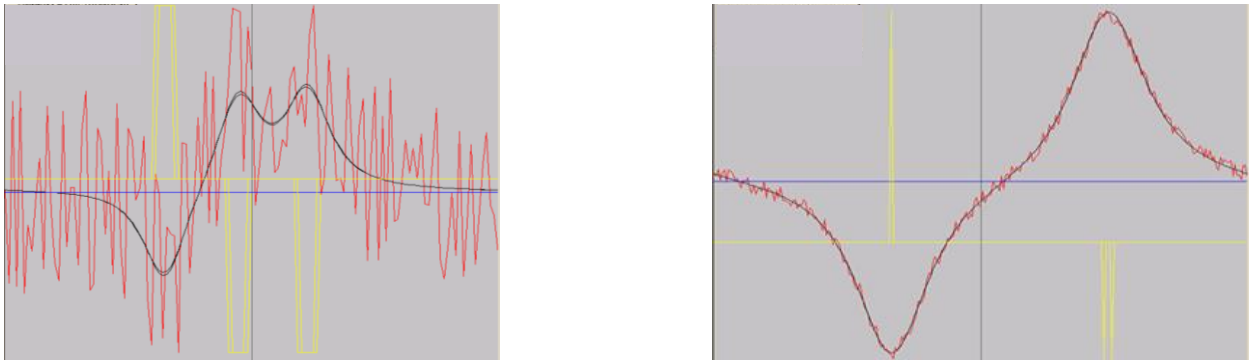

Fig. 1. The results of computer simulation of the SQUID tomography procedure

In the numerical experiment, three current paths of the same width were specified with the opposite direction of the current in one of them (shown in the figure 1 by yellow lines). Numerical calculations were used to obtain the dependence of the magnetic flux through the SQUID loop, which scans the distribution of currents at a given height - one of the black lines in the figure. In addition to this, the magnetic flux was noisy with noise with a Gaussian distribution with dispersion equal to 50% of the maximum value of the magnetic flux - the red line in the figure.A simplified algorithm for searching for the simplest description of the measurement results made it possible to identify 58 out of 66 bits of information about the current distribution parameters. As a result, the current value in the current tracks and their locations were determined accurately (taking into account the a priori specified discreteness of these values), and the width of the tracks was determined with an error of 1 step of a discrete set of values. The resolution of the SQUID microscope was increased by 4 times (figure on the right, noise level 5%).

References

[1] Melnyk S.I., Tuluzov I.G. “The possibility of constructing a relativistic space of information states based on the theory of complexity and analogies with physical space-time,” arXiv preprint arXiv:1703.08069. – 2017.

[2] Melnyk S.I. “Uncertainty and accuracy of measurements as parameters of optimal description their results,” Sistemi obrobki Informácie. 2010. 4(76). — pp. 56-62

[3] Melnyk S. I. and Slipchenko N. I., “Information method of resolution increasing in SQUID-microscopy,” 24th International Crimean Conference Microwave & Telecommunication Technology, Sevastopol, 2014. – P. 767-768

STUDY OF SPONTANEOUS RADIATION DURING CHANNELING OF LOW-RELATIVISTIC ELECTRONS IN THE MAIN PLANES OF A FLUORITE CRYSTAL

M.V. Maksyuta, A.O. Stakhova, V.I. Vysotskii, S.V. Efimenko

Faculty of Radio Physics, Electronics and Computer Systems Taras Shevchenko Kyiv National University of Kyiv, Glushkova ave., 4g, e-mail: anonimnay005@gmail.com

In the work, using the Barrett, Firsov and Moliere approximations, the interaction potentials of negatively charged particles at T = 300 K with the main planes (100), (110) and (111) in the fluorite CaF_2 crystal are calculated. For weakly relativistic electrons with the Lorentz-factor $\gamma = 30$, the energy levels and the corresponding wave functions are found as a result of the numerical solution of the Schrödinger equation. Using these data for electron beams moving at zero angles with respect to the channeling planes with different angular dispersions, the spectra of spontaneous short-wave radiation are calculated in the dipole approximation. As a result, it was shown that for a certain optimal angular dispersion, the intensity of spontaneous radiation manifests itself in a fairly wide spectral range. The work also investigates the effect of the temperature factor on the interaction potential in the (111) planes and, accordingly, on the spectral distribution of spontaneous radiation.

The interaction potentials of electrons with the main planes (100), (110) and (111) were calculated in the CaF_2 fluorite crystal at T = 300 K in relative units $\xi = x/d$ using the Barrett, Firsov and Moliere approximations (see, for example, [1]). Here d, respectively, are equal to $a/2$, $a/\sqrt{2}$ and $a/2\sqrt{2}$, a is the crystal lattice constant. The structure of the unit cell of this complex crystal, which belongs to the halides (see [2]), is shown in Fig. 1a. In the (111) plane, an additional calculation was also carried out at T = 1500 K. The corresponding interaction potentials are shown in Fig. 1b, c.

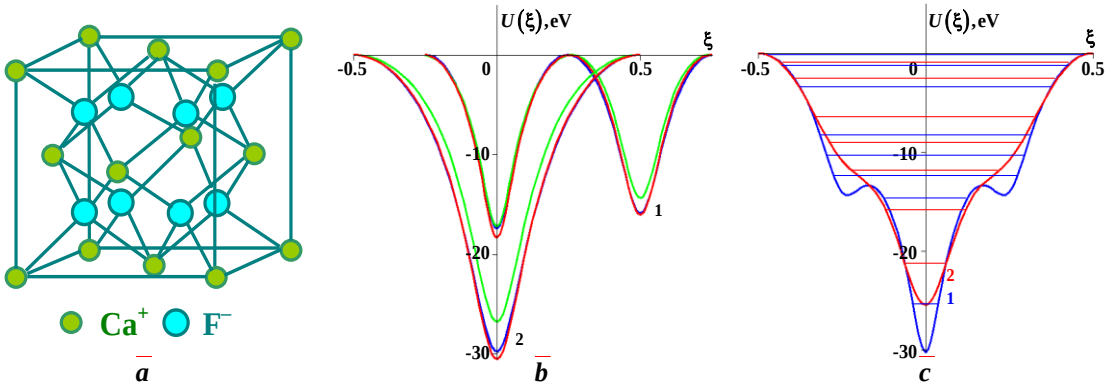

Fig. 1. *(a) –The structure of the unit cell of the fluorite crystal; electron interaction potentials: (b) – with planes (100) (curves 1) and (110) (curves 2) (the Barrett, Firsov and Moliere approximations correspond to blue, green and red curves), (c) – with planes (111) (curve 1 is calculated at T = 300 K, and curve 2, respectively, at T = 1500 K)*

As can be seen from Fig. 1b, the potential wells depths in the (100) and (110) planes for the Barrett and Moliere approximations almost coincide. For the (111) planes, the potential wells depths for the Barrett approximation take intermediate values between the depths of the wells for the Firsov and Moliere approximations. Further analysis was carried out using the Barrett approximation. At the Lorentz-factor $\gamma = 30$, the transverse energy levels and the corresponding wave functions in all potential wells are numerically found.

The level systems shown in Fig. 1c demonstrate that in such potential wells the equidistance increases with rise crystal temperature, which affects the spontaneous radiation spectrum (compare the spectra in Fig. 2c, d). Spectral distributions $G(\nu)$ of spontaneous radiation (see, for example, [1]) are shown in Fig. 2a, b, c, d.

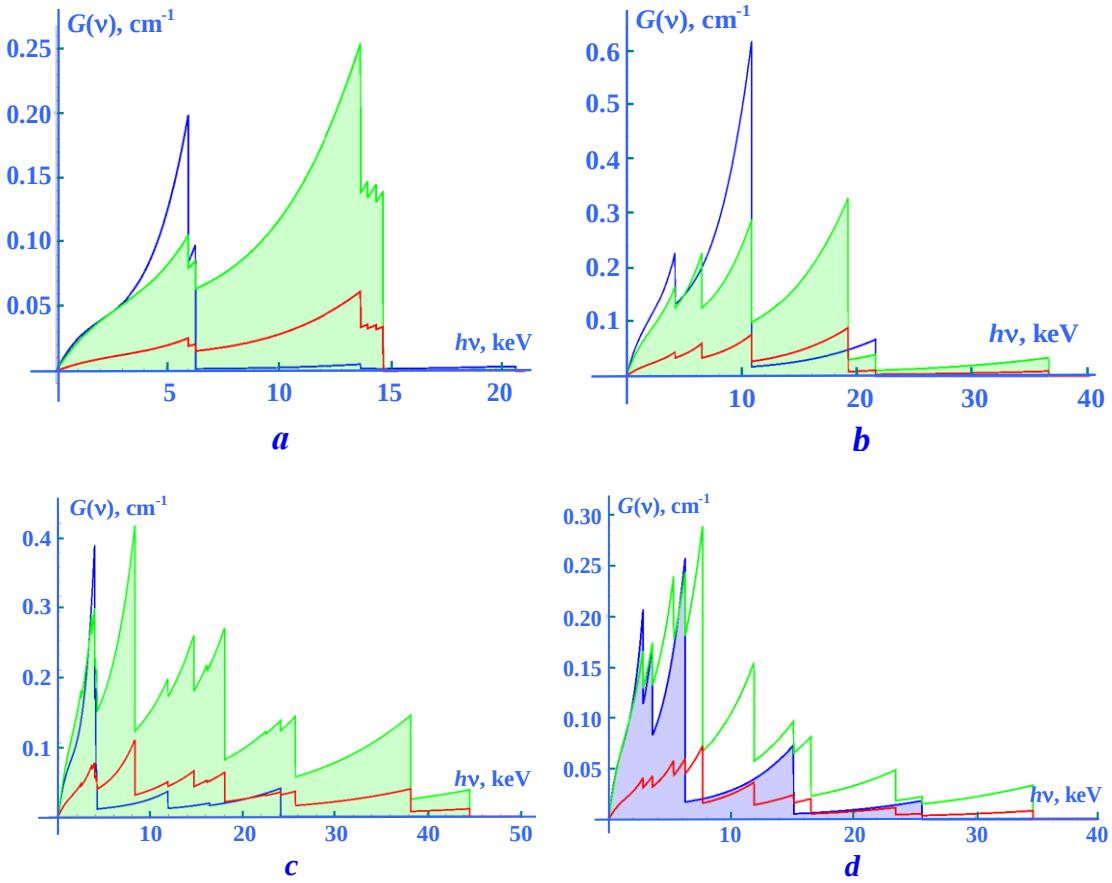

Fig. 2. *Spectral distributions of spontaneous radiation during motion per unit path of an electron beam with a Lorentz-factor $\gamma = 30$ and with angular dispersions $\theta_0 = 0,0.5,1$ mrad (blue, green and red curves, respectively) in a fluorite crystal in the planes (100) – (a), (110) – (b), (111) at T = 300 K – (c) and at T = 1500 K – (d)*

From the calculation results presented in Fig. 2, it is evident that the spontaneous radiation intensities in all main planes with optimal angular dispersion $\theta_0 = 0.5$ mrad reach higher values compared to the experimental intensities observed in lithium halide crystals under similar channeling conditions (see [1]).

References

[1] N.V. Maksyuta, V.I. Vysotskii, S.V. Efimenko, Quasicharacteristic radiation of relativistic electrons at orientation motion in lithium halides crystals along charged planes and axe, J. Phys.: Conf. Series. 732 (2016) 012023.

[2] B.F. Ormont, Structures of inorganic substances, M. – L.: GITTL, 1950.

FEATURES OF CHANNELING POSITIVELY CHARGED PARTICLES ALONG PYRAMIDAL DIRECTIONS IN HEXAGONAL CRYSTALS

M.V. Maksyuta, V.I. Vysotskii, D.M. Maksyuta, S.V. Efimenko

Faculty of Radio Physics, Electronics and Computer Systems Taras Shevchenko Kyiv National University of Kyiv, Glushkova ave., 4g, e-mail: maksyuta.dima@outlook.com

In this work, using the Barrett approximation, the interaction potentials of positively charged particles with axes lying in the pyramidal planes of hexagonal crystals of Be, Mg, Sc, Ti, Co, Zn, Se, Y, Zr, Tc, Ru, Cd, Te and La are calculated. It is shown that in the crystals of Co, Zn, Tc and Ru there are sufficiently deep potential wells in these directions, where it is possible to carry out channeled motion of positively charged particles (protons, ions, positrons) in order to obtain shorter-wave spontaneous radiation compared to channeling along the c-axes.

In work [1], the interaction potentials of positively charged particles with c-axes in hexagonal crystals of Be, Mg, Sc, Ti, Co, Zn, Se, Y, Zr, Tc, Ru, Cd, Te and La were calculated. It was shown that for many of these crystals sufficiently deep potential wells arise allowing effective channeling of weakly relativistic positrons is possible to achieve sufficiently intense spontaneous short-wave radiation. In this work, the interaction potentials in the so-called pyramidal directions [3] (see Fig. 1a) are calculated in the same crystals using the Barrett approximation (see [2]). Fig. 1b, c show the projections of these axes onto planes orthogonal to them. As shown in these figures, the 24 nearest axes are used to determine the potential profiles in the regions

$$D_1(\xi,\eta)=\left[|\xi|\le 1/2,|\eta|\le c\left(1-|\xi|\right)/d_1\right],\ D_2(\xi,\eta)=\left[|\xi|\le\left(1-d_2|\eta|/c\right)/\sqrt{3},|\eta|\le c/2d_2\right],$$

where $\xi=x/a$ and $\eta=y/a$ are relative coordinates, $d_1=\left(c^2+3a^2\right)^{1/2}$ and $d_2=\left(c^2+4a^2\right)^{1/2}$ are the distances between atoms of the hexagonal crystal, respectively, along pyramidal directions 1 and 2.

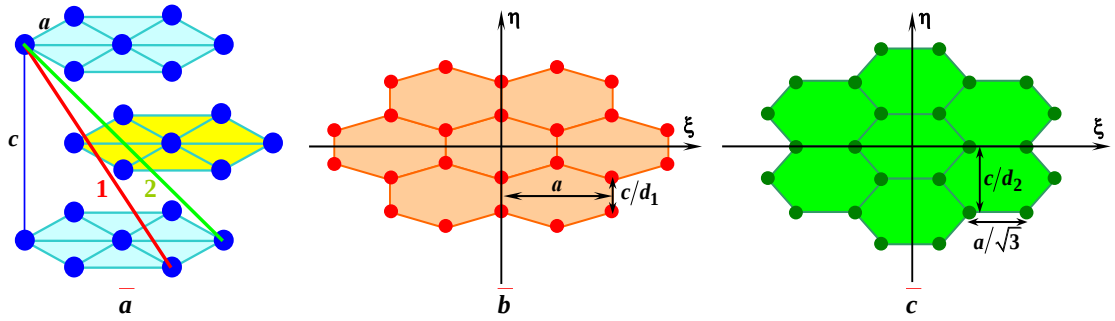

Fig. 1. *Crystal structure of a hexagonal crystal with pyramidal directions indicated (respectively, lines 1 and 2) – (a), projections of the pyramidal axes 1 – (b) and 2 – (c) onto planes orthogonal to these axes (in both cases we have networks of pyramidal axes located in the form of "honeycombs" deformed along the η axis)*

Figure 2a, b shows 3D-plots of the interaction potentials $U_{1,2}(\xi,\eta)$ plotted in regions $D_1(\xi,\eta)$, $D_2(\xi,\eta)$, and Figure 2c, d shows level lines for these potential wells plotted with a step of 1 eV for direction 1 and with a step of 0.5 eV for direction 2.

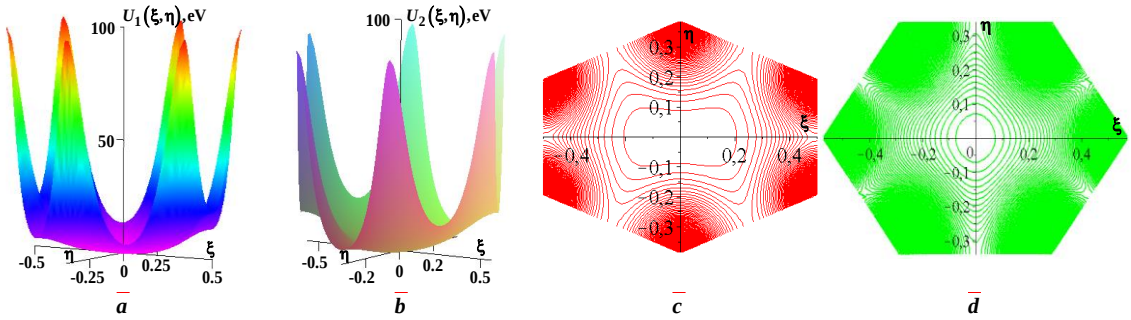

Fig. 2. *3D-plots of interaction potentials of positively charged particles with pyramidal axes in a Zn crystal, respectively, for directions 1 – (a) and 2 – (b); level lines plotted with a step of 1 eV, respectively, for 3D interaction potentials $U_1(\xi, \eta)$ – (c) and with a step of 0.5 eV for the interaction potential U2(ξ, η) – (d)*

Using these level lines, the depths of potential wells for all investigated hexagonal crystals were then estimated with sufficient accuracy for further analysis. The results of these calculations for both pyramidal directions are given in Table 1.

Table 1. *Values of potential well depths (in electron volts) in hexagonal crystals for positively charged particles moving along pyramidal directions 1 and 2*

Axis	Be	Mg	Sc	Ti	Co	Zn	Se	Y	Zr	Tc	Ru	Cd	Te	La
1	3	4	4	6	11	9	1	3	4	9	10	1	1	2
2	1.5	2.0	2.5	3.5	6.5	6.0	0.5	1.5	2.5	5.5	6.0	1.0	0.5	1.5

From the comparison of the numerical values of the potential wells depths in Table 1 with the numerical values given in Table 1 in the article [1], it is evident that the depths of potential wells, as expected, decrease approximately proportionally. However in the crystals of Co, Zn, Tc, Ru, the potential wells along the pyramidal axes remain the deepest. In the crystals of Be, Se, Y, Cd, Te, La, the potential well depths decrease sharply (especially in the direction 2).

In conclusion, it should be noted that, the transverse energy levels and their corresponding wave functions will be determined in the future by solving the Schrödinger equation numerically in these potential wells $U_{1,2}(\xi,\eta)$. Additionally the spectral distributions of spontaneous radiation will be calculated. Based on heuristic considerations, it should be expected that in such deformed potential reliefs, higher-frequency quanta of intense spontaneous radiation will be generated.

References

[1] N.V. Maksyuta, V.I. Vysotskii, D.N. Maksyuta, S.V. Efimenko, Study of spontaneous radiation during axial channeling of relativistic positrons in hexagonal crystals, Nuclear Instruments and Methods, **A, 1058** (2024) 168891.

[2] J.H. Barrett, Potential and stopping-power information from planar-channeling oscillations, Phys. Rev. **B 20(9)** (1979) 3535.

[3] Donald E. Sands, Introduction to Crystallography, New York: Dover Publication, Inc, 1993.

MATHEMATICAL SIMULATION OF CANTELEVER BENDING DURING INTERACTION WITH HYDROGEN

O.M. Liubymenko[1],

Donetsk National Technical University "Donetsk National Technical University", str. Potebni, 56, Lutsk, 43003, Ukraine, e.n.lyubimenko@gmail.com

The work considers the principle of operation of the hydrogen sensor, which is based on the interaction of hydrogen with a metal plate and the change of its characteristics under the influence of hydrogen. The sensor is used to determine and measure the concentration of hydrogen in the environment. The work investigated the kinetics of hydrogen adsorption and desorption on palladium cantilevers by measuring their bending during interaction with hydrogen, and also analyzed the obtained results. To analyze the behavior of palladium cantilevers in a hydrogen environment, a numerical method of solving the system of equations of hydrogen elasticity is used. The decision algorithm involves the step-by-step construction of elasticity matrices and stress tensors, with their further calculation. The obtained simulation results show changes in hydrogen concentration, stresses, displacements and deformations in the metal plate at different moments of time. These data are important for analyzing the dynamics of metal-hydrogen interaction processes, understanding the mechanisms of hydrogen destruction and changes in the plasticity of metal materials.

A hydrogen sensor is a device designed to detect and control the concentration of hydrogen in various environments. It is a thin metal plate that changes its dimensions under the influence of hydrogen: it is saturated with hydrogen, as a result of which the length and thickness of the plate change, which leads to the closing of an electrical contact and the generation of a hydrogen leakage signal. In order to better understand the processes of hydrogen diffusion and the influence of this process on the change in the shape of the plate, the change in the concentration of hydrogen in the plate is mathematically modeled.

The kinetics of hydrogen adsorption and desorption on palladium plates were studied using thermoelastic measurements and physical models that explain the dissociation of hydrogen on the palladium surface and its subsequent desorption in molecular form. It is also important to take into account the stress in the material, the concentration of hydrogen, the displacement of the plate and the amount of its deformation during the hydrogen adsorption process.

Software modules for simulating the operation of sensors were developed to simplify the monitoring and analysis of data from such sensors. The main functionalities include simulation of sensor operation, processing and analysis of results, user-friendly interface, adaptability and integration with other systems.

The algorithm developed for solving the equations of hydrogen elasticity is based on numerical methods. It includes:

1. Setting the initial conditions.
2. Checking the stability of the method: the diffusion coefficient, time step and spatial step must meet certain conditions.
3. Initialization of arrays for hydrogen concentration, displacements and stresses.
4. Calculation of hydrogen concentration and displacements for each moment of time and each node of the plate.
5. Updating the values on the plate boundaries, calculating deformations and stresses.

After executing the algorithm, the obtained results can be used to evaluate the properties of elastic bodies and their response to external influences. Graphical results (Fig. 1) contain the following data:

1) hydrogen concentration along the plate at different time points,
2) hydrogen concentration in all nodes over time,
3) tension distribution along the plate at different moments of time,

4) tension in all nodes over time,
5) distribution of displacements along the plate at different moments of time,
6) displacement in all nodes over time,
7) distribution of deformations along the plate at different moments of time,
8) deformation in all nodes over time.

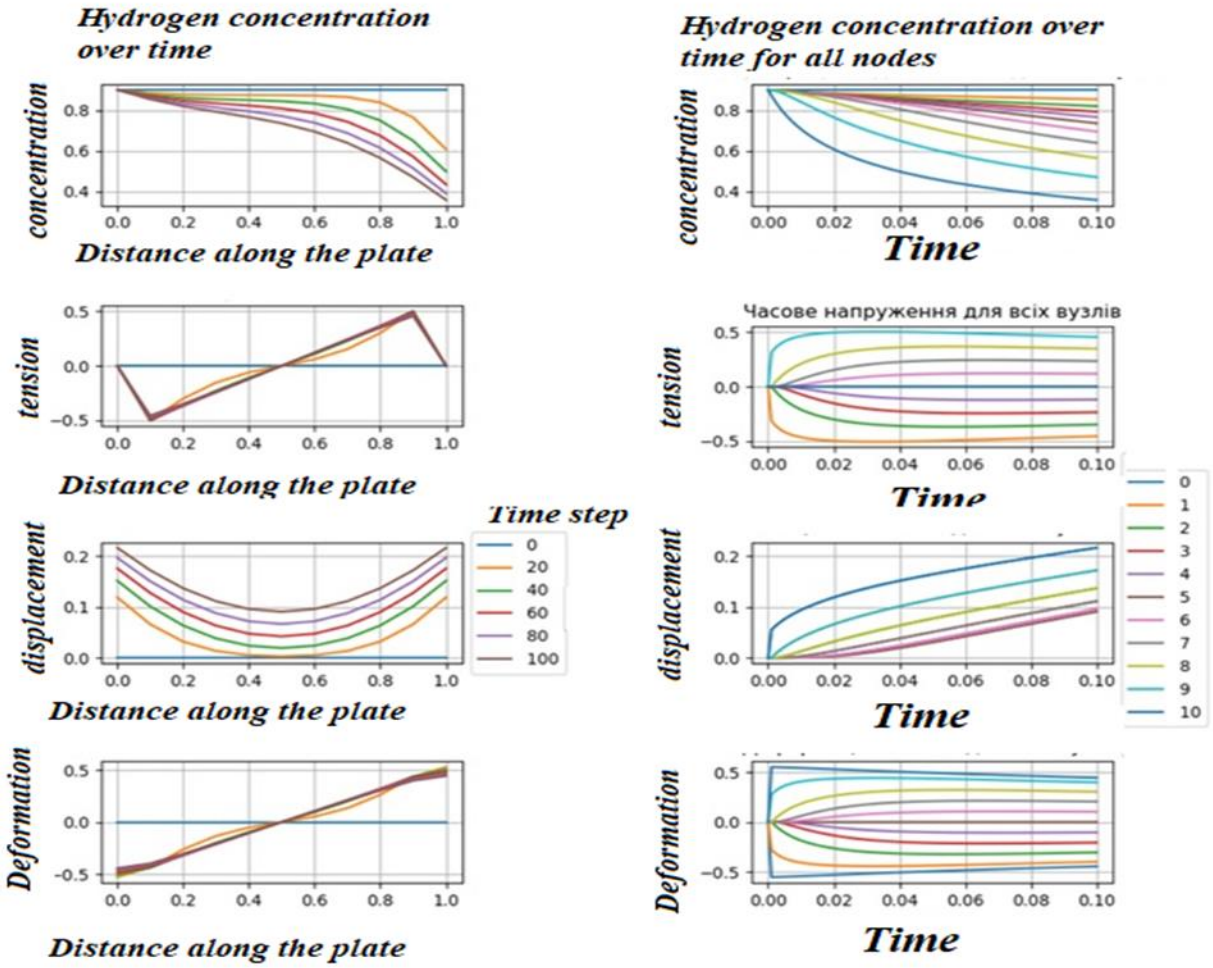

Fig. 1. Results of mathematical modeling of hydrogen detection in the sensor

These graphs are important for understanding the dynamic processes in metal, in particular with regard to the effect of hydrogen on the destruction of metal structures. The mathematical model allows you to analyze the change of key parameters and adapt them for further improvement of sensor systems. Mathematical modeling is an effective tool for solving the problems of hydrogen detection with the help of sensors, which provides reliable results and contributes to the further development of sensor technologies.

SURFACE PHYSICS,
NANO- AND MICROELECTRONICS

STUDY OF THE QUANTUM EFFICIENCY OF RADIATION AND PHYSICAL PROPERTIES OF HETEROLAYERS BASED ON CADMIUM TELLURIDE OBTAINED BY THE ISOVALENT SUBSTITUTION METHOD

Mazur T.M., Mateik G.D.

Department of Physical and Mathematical Sciences Ivano-Frankivsk National Technical University of Oil and Gas, 15 Karpatska St., Ivano-Frankivsk, 76019, Ukraine,
e-mail: tetiana.mazur@nung.edu.ua, galyna.mateik@gmail.com

The paper considers the method of isovalent substitution for obtaining heterolayers based on CdTe, which allows controlling the process of substitution of atoms with the same valence in the base material. The technique involves the use of isothermal annealing under vacuum conditions to achieve high quality of the crystal structure and small thickness of the layers, which minimizes self-absorption processes. The obtained heterolayers demonstrate high quantum efficiency of radiation ($\eta \approx$ 7-9%) in the near infrared range, which makes them promising for use in infrared optoelectronic devices.

One of the key materials for modern functional electronics is cadmium telluride (CdTe) [1]. This material is widely used to create various types of devices, the characteristics of which largely depend on the physical and technical parameters of CdTe. The direct band structure of cadmium telluride and its relatively wide band gap (E_g = 1.50 eV) make it promising for applications requiring high radiation efficiency in the near infrared range [1]. Highly efficient solar cells and optoelectronic detectors have been developed based on CdTe, which have found wide application in various systems. One of the key advantages of this material is the ability to regulate the conductivity type in II-VI compounds, which allows creating various devices. However, the quantum efficiency of emitting devices based on cadmium telluride remains low due to nonradiative recombination, which occurs at deep energy levels [2]. These levels are formed due to the presence of point defects, which are difficult to control during material synthesis.

In order to increase the radiation efficiency, it is important to develop methods for growing high-quality thin layers and heterostructures based on CdTe, as well as simultaneous doping of the material with appropriate impurities to control defects. This will significantly reduce nonradiative losses and increase the efficiency of devices based on cadmium telluride.

Heterolayers were obtained using the isothermal annealing method in pairs of isovalent elements [3]. This approach is based on the substitution of atoms with the same valence in the base material, which gave the method its name – isovalent substitution [4]. The method is especially effective in diffusion processes performed using the "closed tube" technology. Before the process, substrates of II-VI compound crystals underwent standard chemical-mechanical preparation. Then they were placed in quartz ampoules, which were evacuated to a pressure of no more than 10^{-4} Torr and sealed. In the ampoules, the base material substrate was located at one end, while the diffusant overhang was at the opposite end. Annealing was performed isothermally in a furnace under carefully selected temperature conditions. This technique allows for controlled substitution of atoms, which contributes to the formation of high-quality heterolayers with improved electrophysical properties.

An important characteristic of the obtained heterolayers is the high quantum efficiency of radiation in the edge region of the spectrum. In the near infrared range, this efficiency is approximately $\eta \approx$ 7–9 %. To estimate the radiation efficiency, a GaAs reference sample with a quantum efficiency of $\eta \approx$ 100 %. Such a relatively high quantum efficiency makes the obtained heterolayers promising for applications in infrared optoelectronic devices, especially where energy efficiency and reliability are critical.

The emission spectrum of heterolayers covers the photon energy range of 1.5–1.65 eV (corresponding to wavelengths $\Delta\lambda$ = 0.751–0.826 μm) with the main maximum at the photon energy $\hbar\omega_m$ = 1.55 eV (λ_m = 0.800 μm), which is shown in Fig. 1. In addition, a second, less intense maximum is observed at $\hbar\omega_m$ = 1.62 eV

(λ_m = 0.765 μm). The differential emission spectrum N'_ω, obtained using λ modulation, differs significantly in its shape from the classical photon distribution, which is also shown in Fig. 1. This spectrum demonstrates the presence of several features indicating the complex nature of the emission. It consists of several bands, each of which is due to different mechanisms of radiative recombination. Such a multi-band structure of the spectrum indicates that different defects, impurities or other factors affecting the energy distribution of radiation.

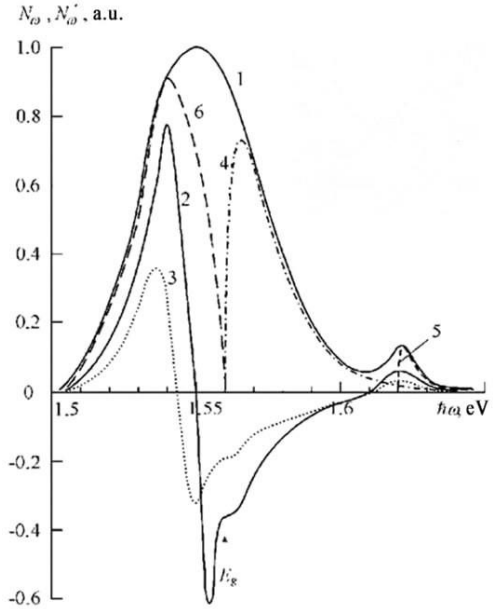

Fig. 1. Spectra of conventional (1) and modulated (2, 3) photoluminescence of α-CdTe/α-CdSe heterostructures of the hexagonal modification, as well as components of the emission bands due to interband radiative transitions of free charge carriers (4, 5) and annihilation of bound excitons (6). T = 300 K.

The minor contribution of self-absorption processes, as well as the possibility of observing it in the emission spectrum at the energy $\hbar\omega > E_g$, can be explained by the high quality of the crystal structure of the obtained layers, as well as their small thickness (d). This small thickness is the result of the modes used in obtaining the layers by the isovalent substitution method. These factors make it possible to observe the emission component in the energy range $\hbar\omega > E_g$, with a maximum at $\hbar\omega_m$ = 1.623 eV. This indicates the efficiency of radiative recombination processes in thin layers, reducing losses due to self-absorption and increasing the overall quantum efficiency of the emission.

References

[1] T.M. Mazur,V.V. Prokopiv, M.P. Mazur, U.M. Pysklynets, “Solar cells based on CdTe thin films,” Physics and chemistry of solid state. Vol. 22, N 4, pp. 817-827, 2021.

[2] V.V. Prokopiv, B.S. Dzundza, S.V. Sharyn, T.M. Mazur, L.V. Turovska, O.M. Matkivskyi, “Electrical Properties of Cadmium Telluride Thin Films Doped with Calcium and Lithium,” Physics and chemistry of solid state. Vol. 21, No. 2, pp. 232-237, 2020.

[3] V.P. Makhniy, M.M. Slyotov, O.M. Slyotov, Utility model patent No. 108145 “Method for manufacturing CdTe heterolayers of hexagonal modification”, State Service of Intellectual Property of Ukraine Bull. No. 13, 11.07.2016.

[4] V.I. Fistul, “Atoms of dopants in semiconductors (state and behavior),” M.: Fizmatlit, pp. 432, 2004.

PHOTON DRAG EFFECT AND ITS INFLUENCE ON THE OPTICAL, ELECTRICAL AND MAGNETIC CHARACTERISTICS OF NANOFILMS

Krupa M.M.

Institute of Magnetism of National Academy of Science and Ministry of Education and Science of Ukraine, 03143 Kiev, Vernadsky's bul.,36 Ukraine
krupa@imag.kiev.ua

This report presents the results of experimental studies of the influence of nanosecond and picosecond laser pulses on the structure, optical, electrical and magnetic characteristics of Bi-SiC, FeCo-SiC, $LaSrMn_3$ and NiFe nanofilms. The obtained results show that nanosecond and picosecond pulses of laser (excimer λ=248 nm, ruby λ=694,3 nm and neodymium λ=1,06 μ lasers) lead to the appearance of a potential difference between the input and output surfaces of multilayer nanofilms and the injection of electrons from the input nanolayer to the next nanolayer, which can lead to laser-stimulated diffusion of ionized atoms in the direction of action of laser radiation in composite nanofilms. In FeCo-SiC films, where the FeCo magnetic nanolayer has a high degree of spin polarization, a non-equilibrium magnetization occurs in the SiC nanolayer at the time of the laser pulse. The main physical mechanism that leads to such changes is the Photon drag effect, which describes the transfer of the momentum of photons to electrons as a result of absorption of laser radiation.

Irradiation with powerful laser pulses of finely dispersed NiFe nanofilms and amorphous $LaSrMn_3$ nanofilms leads to laser-stimulated recrystallization of the incoming nanolayer of the films. As a result, even after irradiation with a single laser pulse in NiFe films, the value of magnetic susceptibility increases and the value of coercive force decreases. In $LaSrMn_3$ films, a transition from an amorphous to a polycrystalline state is observed, the temperature dependence of their conductivity changes from semiconducting to metallic, and the film becomes magnetic, which may be related to its oxidation in the irradiation zone.

In absorbing films, under the action of powerful laser pulses close to the destruction threshold, the roughness of the input surface decreases, which may be related to the excitation of surface plasmons in the laser pulse's zone of action.

Research results show that using focused laser beams and a high-precision system for moving the film along two coordinates, it is possible to create a regular structure of nanoelements in composite nanofilms, the optical or magnetic characteristics of which differ from the similar characteristics of the matrix.

MICROWAVE PROPERTIES OF COMPOSITE BASED ON POLYURETHANE AND CARBON NANOTUBES

O.M. Gonchar*, V.A. Moiseienko, L.M. Grishchenko*****

** Institute of macromolecular Chemistry, NAS of Ukraine, Kharkivske highway, 48, 02160 Kyiv, Ukraine, e-mail: lexgon@ukr.net*

*** Independent Research & Development Laboratory "200k Electronics", Kyiv 01030, Ukraine, e-mail: vamrpd@gmail.com*

**** Department of Chemistry, Taras Shevchenko National University of Kyiv, Kyiv 01601, Ukraine, e-mail: liudmyla.grishchenko@ukr.net*

A polyurethane/carbon nanotube (CNT) nanocomposite was created by modifying CNTs with a cationic oligourethane that possesses functional amino groups, followed by the incorporation of these modified CNTs during the in situ synthesis process. The microwave properties of the resulting nanocomposites were examined within the X-band of microwave.

In recent decades, researchers have focused on developing protective measures against electromagnetic interference, including the creation of shielding materials utilizing carbon-based substances. Carbon materials (CMs) exhibit exceptional mechanical and physicochemical properties, largely determined by their surface chemistry, and can serve as fillers in innovative protective composites. These materials possess several advantageous characteristics, such as low density, natural availability, cost-effectiveness, high conductivity, and robust mechanical properties. Notably, CMs can undergo chemical modification, allowing the incorporation of functional groups or heteroatoms into their surface layers. Such modifications can significantly alter the chemical properties of CMs and influence their interactions with electromagnetic radiation. The purpose of this work was to obtain a composite material based on polyurethane (PU) as a polymer matrix and modified nanotubes as filler and to study the microwave properties of the obtained composites.

Modification of CNT

Carboxylated carbon nanotubes (CNTs) were employed to create modified CNTs. The modification process involved chemical adsorption through an ion exchange mechanism, executed in two stages. In the initial stage, the potasium form of carboxylated CNTs was synthesized by the reaction of carboxyl groups with an alkaline agent (potassium hydroxide):

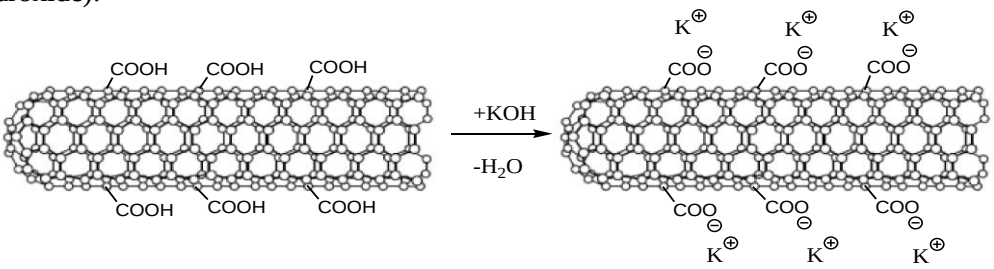

(1)

In the second stage, modified carbon nanotubes (CNTs) were modified by exchanging inorganic potassium cations for organic cations. This modification involved the addition of a cationic oligourethane (COU) solution to the potassium-exchanged CNT suspension. The quantity of the modifier was selected to match the exchange capacity of the CNTs. The COU used was a previously synthesized oligourethaneamine ammonium chloride, as detailed in reference [1].

Following the addition of the COU solution, the resulting suspension was diluted with distilled water to achieve a ratio of 1 g of CNT per 500 ml of water. The adsorption process was allowed to proceed for two days, after which the modified CNT precipitate was filtered, dried in an oven at 60 °C until a constant weight was attained, and subsequently ground into a fine powder.

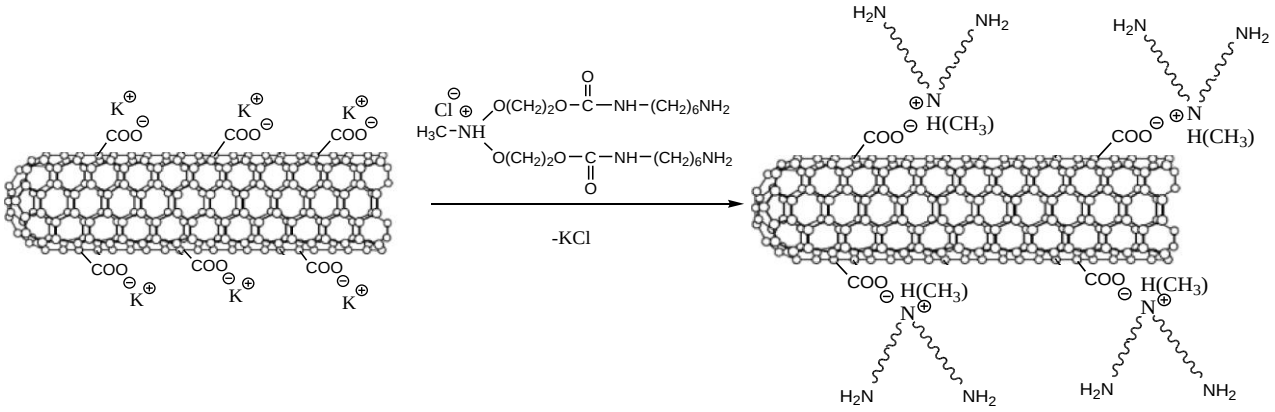

(2)

Production of polyurethane/CNT nanocomposite

To obtain a polyurethane/carbon nanotube (CNT) nanocomposite, modified CNTs were first dispersed in a dimethylformamide (DMF) medium using ultrasound. The resulting CNT dispersion in DMF was subsequently incorporated into a reaction mixture comprising polytetraoxymethylene glycol with a molecular weight of 1000 (POTMG-1000) and 4,4'-diphenylmethane diisocyanate (DFMDI). Following the formation of the prepolymer (macrodiisocyanate), diethylene glycol was introduced to lengthen the chain with the formation of linear polyurethane. Microwave reflection loss and microwave transmission loss of the prepared polyurethane/CNT nanocomposite were measured in the X-band of frequencies [2].

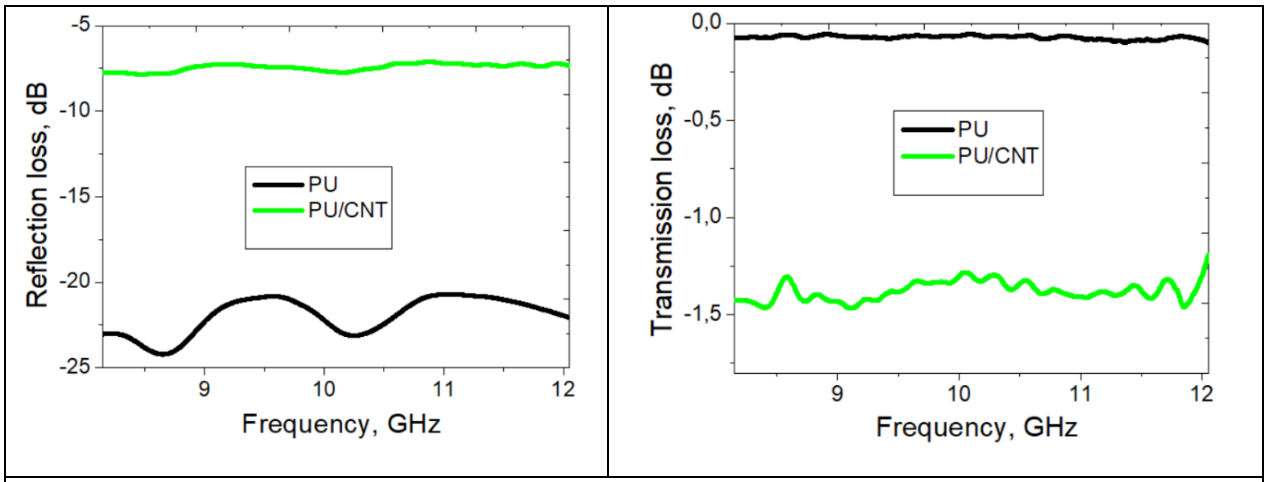

Fig.1. Reflection loss and transmission loss against frequency for X-band.

It was found that the addition of CNTs to polyurethane leads to a rapid increase in the reflection of microwave waves by the resulting composite material (-7.4 dB), which can be explained by the high conductivity of the filler compared to pure PU. At the same time, pure PU has very weak reflective properties, the average value of reflection loss in the X-band for pure PU is -22.0 dB. The study of the amount of transmission loss shows that samples of PU-based composites with CNT filler slightly weaken the signal (-1.4 dB, compared to pure PU - -0.1 dB). The obtained transmittance values allow us to speak about the relative radiolucency of the obtained composite material.

References

[1] O.M. Gonchar, "Modification of the montmorillonite surface with oligourethane containing functional amino groups", Chemistry, Physics and Technology of Surface, 2019, 10 (1), 87-93.

[2] L.M. Grishchenko, V.A. Moiseienko, A.M. Goriachko, A.V. Vakaliuk, I.P. Matushko, O.V. Mischanchuk, G.G. Tsapyuk, O.Yu. Boldyrieva, V.V. Lisnyak, "Preparation and electromagnetic microwave absorption performances of sulfurated and oxidized polyacrylonitrile carbon fibers", Molecular crystals and liquid crystals, 2023, 751(1), 1-9.

SIZE EFFECT ON ELECTROPHYSICAL PARAMETERS OF Fe/SiO_2 (MgO OR HfO_2) DISCONTINUOUS MULTILAYERS

Panchoshnyi O.*, Pazukha I., Vinnichenko Yu., Pylypenko O., Shkurdoda Yu.

Sumy State University, Sumy 40007, Ukraine
email: alexpanchoshniy@gmail.com*

In the category of nanoscale magnetic materials, ferromagnetic metal-insulator nanocomposites and layered structures of the $[FM/I]_n$ type occupy a special place. With appropriate ratios of volume fractions of components in nanocomposites and appropriate effective layer thicknesses in layered structures, they can consist of magnetic nanoparticles distributed in an insulator matrix. The scientific and practical importance of such materials is determined by the fact that their electrical and magnetic properties can be controlled by changing the concentration of components or the effective thickness of the layers, which in turn leads to a change in the size of magnetic nanoparticles and, as a consequence, changes in electrical conductivity, magnetic and magnetoresistive properties [1, 2]. This is especially evident in the dependence of the electrical resistance on the volume fraction of the components or the effective thickness of the layers. The critical behavior of this dependence is related to the difference in the conductivity mechanisms and the electrical resistance of the metallic and dielectric phases.

Based on the above, the purpose of this work was determined, which consisted of the experimental study of the study of electrical properties of layered structures $[Fe(d_{Fe})/I(3)]_{10}/Sub$ (I = SiO_2, HfO_2, MgO) as possible thermostable sensitive elements of applied structures.

The research results showed that the specific electrical resistance and temperature coefficient of resistance (TCR) of layered structures strongly depend on their composition and layer thickness. The resistivity of structures that were heat-stabilized at different temperatures, regardless of the type of insulator layers, decreases with an increase in the effective thickness of the metal layers. As-deposited structures at the maximum thickness of Fe layers typically reach a minimal value of ρ at about $(5\text{-}10)\cdot10^{-7}$ Ω·m. The resistivity reaches maximum values of 0.05-0.1 Ω·m for samples with d_{Fe} = 2 nm annealed at a temperature of 400 °C. Relatively large values f ρ for films annealed at a temperature of 400 °C can be primarily explained by the formation of oxide phases. For $[Fe(d_{Fe})/HfO_2(3)]_{10}/Sub$ samples an almost horizontal section is observed at d_{Fe} = 4-7 nm, which confirms the conclusions of the percolation theory model in the case of zero conductivity of dielectric regions.

It is noted that for the $Fe(d_{Fe})/SiO_2(3)]_{10}/Sub$ systems, the $\beta(d_{Fe})$ dependencies are monotonic and the TCR value increases with an increase in the effective thickness of the metal layers. At $d_{Fe} < 6$ nm, TCR takes on negative values for unannealed and annealed at different temperatures. For $d_{Fe} \geq 7$ nm samples annealed at a temperature of 300 °C a transition to positive TC values is observed. The only exception is the $[Fe(d_{Fe})/HfO_2(3)]_{10}$, systems, for which, regardless of heat treatment conditions, TCR values are negative, even at $d_{Fe} \geq 9$ nm.

References

[1] Fayyaz Muhammad, Hu Hong, Peng Zhang, Qaisar Abbas, “Measurement of magnetic field components using a single passive SAW magnetic sensor,” Sens. Actuat.: A. Phys., vol. 352, p. 114163, Apr. 2023.

[2] Anmol Mahendra, Prasanth Gupta, Simon Granville, John Kennedy, “Tailoring of magnetic anisotropy by ion irradiation for magnetic tunnel junction sensors,” J. Alloys Compd., vol. 910, p. 164902, Jul. 2022.

IMPORTANCE OF THE SURFACE FOR THE MANIFESTATION OF ELECTROMAGNETIC PROPERTIES OF NANOPOWDERS

Lina Sartinska [*], Vladimir Trachevsky [**], Igor Vorona [***]

** Department of Physics and Technology of Photoelectronic and Magnetoactive Materials, Frantsevich Institute for Problems of Materials Science, NASU, Omeliana Pritsaka str., 3, Kyiv 03142, Ukraine, email: l.sartinska@ipms.kyiv.ua*

*** Analytical Research Department, Laboratory for Synthesis and Diagnostics of Nanosystems and Nanomaterials, Technical Center of the NASU, Pokrovs'ka St., 13, Kyiv, 04070, Ukraine, email: Trachevsky.V.V@nas.gov.ua*

**** Optics and spectroscopy Department, V. Lashkaryov Institute of Semiconductor Physics, NASU, Nauky Ave., 41, Kyiv, 03028, Ukraine, email: vorona@isp.kiev.ua*

This work considers the interaction of ceramic nanopowders with an electromagnetic field. It is demonstrated that as received nanopowders can interact with a magnetic field in the same way as iron particles. EPR spectroscopy confirmed the presence of paramagnetic properties in nanopowders. Since paramagnetic properties are caused by the presence of atoms on the surface that have broken or unfilled bonds, saturation of the surface with oxygen results in the loss of magnetic properties due to compensation of these bonds.

Introduction

It is well known that exceptional physicochemical properties of powder can emerge when its size is reduced to the nanoscale. Among the various types of nanopowders, particular attention has been given to ceramic nanostructures, as they are highly stable, and their synthesis methods are well established and relatively inexpensive [1]. Surface effects influence the first few atomic layers beneath the surface, resulting in higher atomic density, lower activation energy for physicochemical reactions, changes in surface energy, and distinctive thermomechanical, electromagnetic, and optical properties. Since most chemical reactions occur on surfaces, nanopowders are significantly more reactive than their bulk counterparts.

Experimental

Si_3N_4, Si_3N_4-TiN, Al_2O_3, Si_3N_4-Al_2O_3, Si_3N_4-Y_2O_3, obtained by plasma chemical synthesis (Riga, Latvia), α-Al_2O_3 nanopowder of high purity, 99.9%, (Sumitomo AKP-50, Japan) and BN nanopowder obtained in a high flux optical furnace under effect of concentrated light radiation were used as initial.

Samples from plasma chemical nanopowders and nanopowders based on α-Al_2O_3 were obtained by hot pressing under the effect of induction heating [2], [3]. Hot pressing of plasma chemical powders was carried out at a temperature of 1820 °C. Discs from nanopowders based on α-Al_2O_3 were produced at different temperatures (1300-1720 ^{0}C). Wet erosion of discs based on α-Al_2O_3 was investigated using a modified high-speed mill. BN nanopowders were obtained by heating the surface of the initial boron powders in a high flux optical furnace furnace in a nitrogen flow. The composition and structure of the original powders and obtained samples were analyzed using SEM. Electron paramagnetic resonance (EPR) spectra were recorded by EPR ELEXIS 580 spectrometer at room temperature.

Results and Discussion

As received BN nanopowders and plasma chemical nanopowders were very active and can easily move under the influence of a magnetic field. Hot-pressed materials from nanopowders based on α-Al_2O_3 obtained by induction heating demonstrated the presence of a strengthened layer on the surface of the sample when heated at low temperatures, which was characterized by a fine structure and increased wear resistance (Fig. 1 a, b). At high temperatures hot-pressing this effect disappeared [3]. Hot-pressed samples obtained from plasma chemical powders at high temperatures did not have any peculiarities in the studied properties except for the difference in the color of the inner and outer surface of the sample (Fig. 1 c, d) [2].

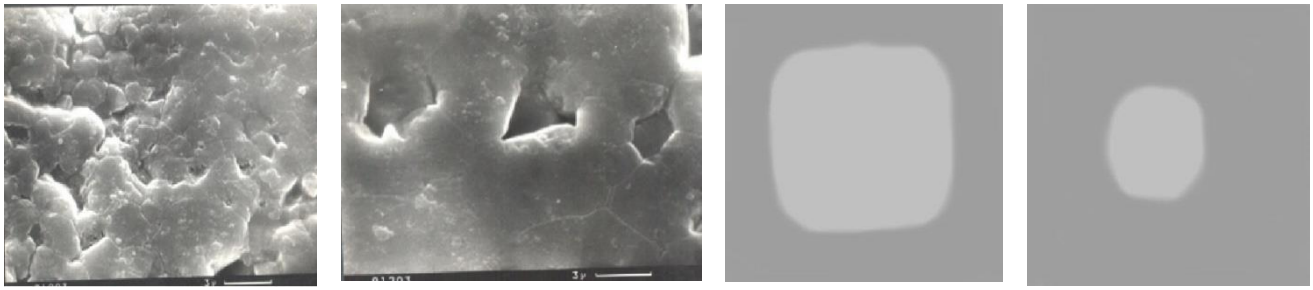

a *b* *c* *d*

Fig. 1. Effect of induction heating on materials from nanopowders based on α-Al_2O_3 prepared at low temperatures (a - surface of sample, b – inside sample) and from plasma chemical powders prepared at high temperatures (dwell time: c –1 min, d - 8 min).

BN nanopowders, which were obtained in a high flux furnace in a nitrogen flow, exhibited paramagnetic properties after synthesis (Fig. 2). The exposure of these nanopowders in an unprotected environment for a year led to their saturation with oxygen and the disappearance of paramagnetic properties. Increasing adsorbed oxygen from 2 wt. % up to 5 wt. % in plasma chemical nanopowders after exposure in an unprotected environment also results in the disappearance of interaction these powders with the magnetic field.

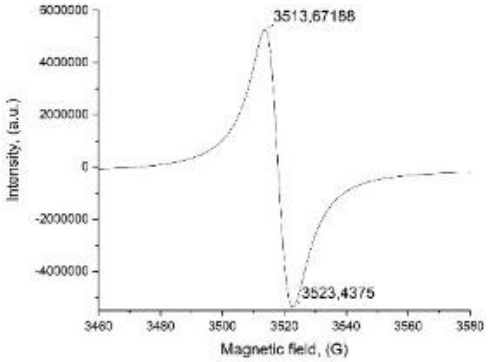

Fig. 2. EPR spectra of BN obtained from an equiaxed nanopowder of boron of a particle size ≤ 0.05 μm

Conclusion

Due to the developed surface of nanopowders and the formation of broken or unfilled bonds during synthesis, nanopowders can exhibit paramagnetic properties. Saturating the surface with oxygen and balancing the uncompensated bonds with oxygen leads to the loss of these properties.

References

[1] R. Wang, "The chemistry of nanomaterials - C. N. R. Rao, A. Müller, A. K. Cheetham (eds), WILEY-VCH Verlag GmbH & Co. KGaA, Weinheim 2004. ISBN 3-527-30686-2, 741 pages," *Colloid Polym. Sci.*, vol. 283, no. 2, p. 234, 2004, doi: 10.1007/s00396-004-1140-1.

[2] L. L. Sartinska, "Effect of Induction Heating on Surface Properties of Hot-Pressed Ceramics Based on Nanopowders Si3N4 and TiN," *Powders*, vol. 2, no. 4, pp. 697–708, Oct. 2023, doi: 10.3390/powders2040043.

[3] L. L. Sartinska, "Influence of grain boundaries on the properties of dense alumina ceramic," *Key Eng. Mater.*, vol. 206, pp. 1141–1144, 2001, doi: 10.4028/www.scientific.net/KEM.206-213.1141.

CALCULATION OF RADIO-OPTICAL PARAMETERS OF FE / GD_2O_3 FILM NANOSTRUCTURES IN THE DECIMETER RANGE

K.A. Korotkov, V, V. Netyaga

Institute for Problems of Materials Science, National Academy of Sciences of Ukraine,
3 Omelyana Pritsaka St., Kyiv-142, Ukraine
k.korotkov@ipms.kyiv.ua

The decimeter range of radar radiation is used by military systems for all armies of the world. Modern methods of protection of aircraft from detection are united in stealth technology, a set of methods to reduce the probability of detection of objects in the radar field. In this case, the main task is to suppress reflectivity. Solving this problem by changing the geometry and configuration of flying objects has led to a significant reduction in their aerodynamic characteristics. Currently, the idea of coating reflective surfaces with absorbing (paints and varnishes with special fillers) or scattering microporous materials (specially treated fabrics, etc.) is used.

Method of experiment

The structure of Fe / Gd_2O_3 nanofilms is considered as nanoporous [1], and therefore, having specific properties in the decimeter range. The latter is the subject of the study. To study the radio-optical properties, we used the method of impedance spectroscopy [2], which consists in analyzing the impedance Z(ω) and its components as a function of the AC frequency. The impedance frequency characteristics were measured on a Solarton 1250 FRA machine using the ZPlot computer program and analyzed using the ZView program.

Result & Discution

The measurement results are presented in the form of frequency dependence of complex quantities: impedance $Z = Z' + jZ''$; admittance $Y = Y' + jY''$ $\left(Y = \frac{1}{Z}\right)$; dielectric constant $\varepsilon = \frac{Y}{j\omega C_0} = \varepsilon' - j\varepsilon''$, where ε' and ε'' are real and imaginary parts, respectively; C_0 is the capacitance of a capacitor with the same geometric dimensions as the one measured, but filled with air.

Fig. 1 shows the calculated frequency dependence of the imaginary ε'' and real ε' parts of the dielectric constant components of the Fe/Gd_2O_3 sample based on the experimentally measured impedances according to the formulas [3]:

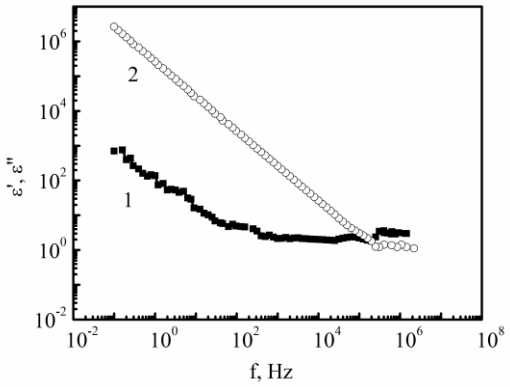

Fig. 1. Frequency dependence of the dielectric constant ε'-1, ε''-2 for the Fe/Gd_2O_3 nanostructure; the thickness of the Fe nanofilm is 11 nm.

From the experimentally obtained values of the real ε' and imaginary ε'' parts, we can calculate the total dielectric constant $\varepsilon = \sqrt{(\varepsilon')^2 + (\varepsilon'')^2}$.

According to the classical optical theory, the absorption coefficient $\alpha = \varepsilon - 1$ and the transmittance $T = 10^{-\alpha}$ can be calculated. From the absorption and transmittance coefficients, the reflection coefficient can be calculated: $R = 1 - (\alpha + T)$.

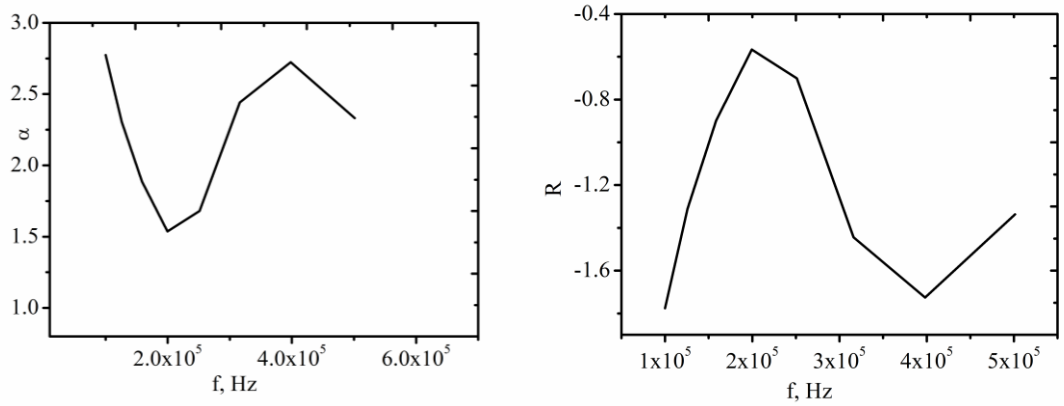

a) b)

Fig. 2 Frequency dependence of the absorption coefficients α(f)-a and reflection R(f)-b for Fe/Gd_2O_3 nanostructures with a thickness of 11 nm.

The calculated para-optical (*para* is Latin for similarity) values of the absorption coefficients α(f) and reflection R(f) for Fe/Gd_2O_3 nanostructures indicate the prospects of using such a structure in stealth technology.

The experimentally observed increase in the values of the absorption coefficients α(f) and reflection R(f) for Fe/Gd_2O_3 nanostructures compared to the Fe/SiO_2 structure is due to the influence of the d-f exchange interaction of the ferromagnetic oxide REM type [1].

References

[1] A.M. Kasumov; A.I. Dmitriev, K.A. Korotkov, et al, Influence of f-d exchange interaction on the properties of nanoscale structures based on Fe, Co, Ni metals and REM oxides. A review // Chemistry, Physics and Technology of Surface, 13 (4), 434-446 (2022)

[2] https://doi.org/10.15407/ hftp13.04.434

[3] Macdonald J. R. et al. Impedance spectroscopy: theory, experiment, and applications. – John Wiley & Sons P. 424-458, 2018.

[4] Bordi F., Cametti C., Colby R. H. Dielectric spectroscopy and conductivity of polyelectrolyte solutions //Journal of Physics: Condensed Matter.– V. 16 (49). R1423, 2004.

SIZE EFFECTS IN THE ELECTRICAL CONDUCTIVITY OF ISLAND AND DISCONTINUOUS MULTILAYER STRUCTURES BASED ON FeNi and SiOx

Dolhov-Hordiichuk S.*, Pazukha I., Horoviy R., Pylypenko O., Shkurdoda Yu.

Sumy State University, Sumy 40007, Ukraine
email: dolgov-gordijchuk.sergij@student.sumdu.edu.ua*

Properties of functional elements in nanoelectronics or spintronics, formed based on composite materials of ferromagnetic metal-insulator, significantly depend not only on the size and shape of the metal granules and their volume concentration but also on the nature of the granule distribution within the insulator matrix. At the same time, thin-film composite materials obtained by simultaneous condensation of ferromagnetic metal and insulator possess several structural features. Exhibit several unique structural characteristics. Firstly, a structure with a wide particle size distribution is formed. Secondly, the low mobility of oxide clusters leads to a slowdown in the processes of coalescence and recrystallization of the metal granules. As a result, composite materials are formed with an insulator amorphous matrix containing a relatively high concentration of ferromagnetic metal atoms. It is created featuring an insulator amorphous matrix that contains a relatively high concentration of ferromagnetic metal atoms. These structural features of composite materials significantly affect their physical properties. Thirdly, it is quite challenging to modify the size of magnetic granules in such films. The physical properties of layered films of the 'ferromagnetic metal/insulator' type significantly depend on the thickness of both metal and insulator layers. This is especially evident in the dependence of electrical resistance on the effective thickness of the layers.

In this study, discontinuous FeNi thin films were deposited on a glass-ceramic substrate by electron-beam sputtering using permalloy $Fe_{20}Ni_{80}$ sources at room temperature. The $[FeNi/SiO_x]_5$/Sub multilayer structure was also prepared under the same vacuum conditions as the discontinuous thin films at RT. The ferromagnetic (FeNi from 4 to 10 nm in thickness) and insulator (SiO_x from 4 to 10 nm in thickness) materials were deposited successively from two independent electron beam guns. It was shown that the resistivity of both as-deposited and annealed at 700 K $FeNi/SiO_x$ island films is several orders of magnitude higher than that of continuous films and decreases monotonically with an increase in the effective thickness of the FeNi layers. For $[FeNi/SiO_x]_5$ structures with a fixed insulator layer thickness (d_{SiO} = 5 nm), the resistivity of both as-deposited structures and those annealed at 500 K and 700 K decreases monotonically with the increase in the effective thickness of the metal layers. The maximum value is recorded for as-deposited structures with a minimum FeNi layer thickness (4 nm) and reaches $(1\text{-}1.7)\cdot 10^{-4}\ \Omega\cdot$m. At a metal layer thickness of 10 nm, the resistivity of structures annealed at 700 K reaches $(5\text{-}10)\cdot 10^{-7}\ \Omega\cdot$m. The relatively high resistivity values, even for films annealed at 700 K, can be explained by the fact that the metal layers in the layered structures are in a nanocrystalline state. It has been shown that for $FeNi/SiO_x$ island films with an effective thickness of 3-5 nm and layered structures $[Fe/SiO]_5$ with d_{Fe} < 4-5 nm and d_{SiO} = 5-7 nm, a tunneling mechanism of electrical resistance is observed. It is characterized by an increase in resistivity as the measurement temperature decreases. In the range of effective thicknesses of d_{Fe} = 7-8 nm and d_{FeNi} = 6-7 nm for single-layer structurally discontinuous films with d_{Fe} < 6-8 nm and d_{SiO} = 5-7 nm, a mixed conductivity mechanism is present. It is determined by conduction through the percolation cluster and tunneling between isolated metal clusters that are not part of the percolation cluster. Further increase of the effective metal thickness in both single-layer films and layered structures, metallic conductivity is observed. It is determined by conduction through a disordered metallic matrix.

ON THE CORRELATION BETWEEN ELECTRONIC AND MECHANICAL PROPERTIES OF PHOSPHORENE

A. G. Solomenko*, T. M. Radchenko, V. A. Tatarenko*****

Department of Metallic State Theory, G. V. Kurdyumov Institute for Metal Physics of the N.A.S. of Ukraine, 36 Academician Vernadsly Boulevard, Kyiv 03142, Ukraine
**sola@imp.kiev.ua, **tarad@imp.kiev.ua, ***tatar@imp.kiev.ua*

An object of our study is a single-layer black phosphorus, known as phosphorene, which is known as a promising material among the family of quasi-two-dimensional (2D) materials. Phosphorene, being a semiconductor with a direct band gap, possesses strong structural anisotropy and therefore interesting mechanical and electronic properties for applications in nanoelectronics and optoelectronics. The study concerns the contribution of the phosphorene's mechanical characteristics (through the Poisson's ratio) to the change of its electronic structure parameters.

Introduction

In contrast to atomically flat graphene, known as the forefather of phosphorene, the crystal structure of the latter (Fig. 1) is puckered (buckled, wrinkled), and therefore anisotropic, with single-layer of covalently bonded phosphorus atoms located in two different planes. Such a structural anisotropy is reflected in the anisotropic features, which deserved attention in many studies of the phosphorene's electronic, optical, thermal, transport, and mechanical properties (see [1, 2] and references therein).

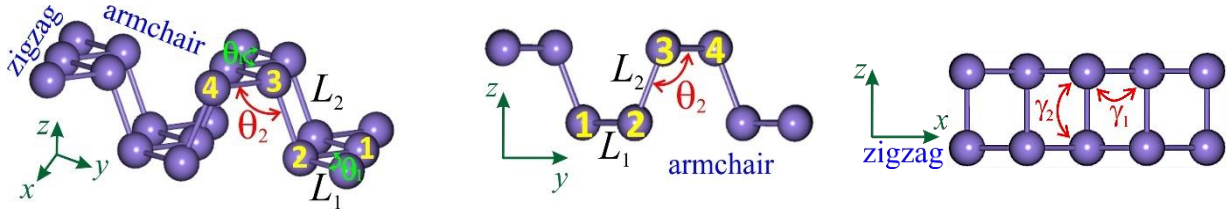

Fig. 1. Perspective (left) and side (centre and right) views of the black phosphorene crystal lattice, where L_1 and L_2 (θ_1 and θ_2) denote the intra- and inter-planar bond lengths (angles).

We consider two types of strains ε: uniaxial tensile and shear deformations. Both types can be directed along the zigzag (ε_{xx} and ε_{xy}) or armchair (ε_{yy} and ε_{yx}) edge. Independently on the strain type, the deformation induces the change of the bond lengths, and thus the changes of the hopping parameters between different atoms. Due to the extraordinary mechanical flexibility, phosphorene can sustain elastic deformations up to its failure limits of ≈27–30% at uniaxial strain depending on the stretching direction, and up to ≈10–13% at shear strains. In the literature, some authors claim even higher non-destructive limits: ≈48% of deformation along the armchair direction, ≈11% along the zigzag one, and up to 30–35% of shear strains.

Numerical calculations and results

To study the structural as well as electronic properties of phosphorene, we use the first principles calculations via the Quantum Espresso (QE) electronic-structure simulation package, which includes the DFT. As calculations for both strain types (stretching and shearing) show, monolayer phosphorene with applied strain along the zigzag (x) direction is more stable than that with applied strain along the armchair (y) direction. It means that phosphorene is more easily deformable along the zigzag direction as compared to the armchair one.

The intra-planar (L_1) and inter-planar (L_2) bond lengths as the functions of uniaxial tensile strain along zigzag and armchair directions exhibit approximately more or less linear behaviour. With all different directions of strain, the intra-planar bond length L_1 increases with increasing deformation: slightly at zigzag strain and strongly at

armchair one. In contrast to L_1, the inter-planar bond length L_2 increases with applied strain along the zigzag *x*-direction; however, decreases with increasing strain along the armchair *y*-direction. A similar situation is for shear strains (ε_{xy} and ε_{yx}). Firstly, all dependences of the bond lengths L_1 and L_2 manifest approximately linear dependences. Secondly, the intra-planar bond length L_1 increases with increasing deformation along both directions: slightly for the armchair shear and a little bit stronger for the zigzag one. However, the inter-planar bond length L_2 remains practically unchangeable with applied strain along both directions.

The intra- (θ_1) and inter-planar (θ_2) bond angles being dependent on the uniaxial tensile strain along zigzag and armchair directions show an opposite tendency under different directions of applied strain. With increasing the strain ε_{xx} along the zigzag direction, the intra-planar bond angle θ_1 weakly decreases, whereas the inter-planar bond angle θ_2 increases. However, with increasing the strain ε_{yy} along the armchair direction, the intra-planar bond angle θ_1 significantly increases, while the inter-planar bond angle θ_2 weakly decreases. Another situation occurs for shear strains (ε_{xy}, ε_{yx}). While the intra-planar bond angle θ_1 greatly decreases for both directions, the inter-planar bond angle θ_2 remains practically unchangeable as it is for the inter-planar bond length L_2.

Calculated bond lengths and angles allow us to calculate Poisson's ratios and compare them with those available in the literature. These ratios act as input parameters in the tight-binding model used to calculate the density of states and thereby extract the band gap value in the phosphorene electronic structure. We described this model in our recent papers [1, 2]. As known, Poisson's ratios relate to elastic moduli and depend on the direction of strain, that is characterize the structural and mechanical anisotropy of phosphorene. Therefore, to examine the correlation between the mechanical and electronic properties of phosphorene, we calculate how the band gap varies depending on strain for different Poisson ratios. Performing such a procedure, we introduced the parameter, which describes how the band gap changes with a change in strain. Actually, this parameter acts as an analogue of the thermal expansion coefficient or compressibility coefficient. As estimations show, if the strain increases by 1%, the band gap varies by 0.1 eV for a higher ratio of in-plane Poisson's ratios along two directions, and two times less for a lower ratio. Thus, the stronger anisotropy makes it possible to manipulate and control the band gap in a wider range.

Conclusions

High structural anisotropy of monolayer phosphorene manifests in its mechanical properties, particularly in its response to applied uniaxial tensile and shear strains. Phosphorene is more stable being strained along the zigzag direction as compared with the armchair direction for both deformation types: tensile and shear. Al calculated structural parameters — the intra- and inter-planar bond lengths and angles — manifest approximately linear behaviour under the tensile and shear strains along both considered directions. The intra-planar bond lengths behave similarly with all types and directions of deformations: increase slightly or strongly. However, the inter-planar bond lengths can increase, decrease, or remain practically unchangeable depending on the strain type and direction. In contrast to the bond lengths, the bond angles show an opposite tendency (decrease or increase) under different directions of tensile strain; however, behave similarly (decrease or practically do not change) for shear strain. The stronger structural and mechanical anisotropy makes it possible to manipulate and control the electronic band gap of phosphorene in a wider range, which can be used to design its potential application in electronics and straintronics.

References

[1] A. G. Solomenko, I. Y. Sahalianov, T. M. Radchenko, and V. A. Tatarenko, "Straintronics in phosphorene via tensile vs shear strains and their combinations for manipulating the band gap", Scientific Reports, vol. 13, pp. 13444-1–12, 2023. https://doi.org/10.1038/s41598-023-40541-7

[2] A. G. Solomenko, I. Y. Sahalianov, T. M. Radchenko, and V. A. Tatarenko, "Deformation-induced band gap variation in phosphorene: tight-binding model vs. first-principles simulations", Molecular Crystals and Liquid Crystals, vol. 768, No. 9, pp. 238–250, 2024. https://doi.org/10.1080/15421406.2024.2348204

SPR EFFECT IN THIN FILMS OF HIGH-CONDUCTIVE METALS

A.I. Biletskiy O.L. Kukla, O.N. Fedchenko

V. Lashkaryov Institute of Semiconductor Physics, National Academy of Sciences of Ukraine, Kyiv, 03028, Ukraine email: belanton11@gmail.com

This work evaluates the use of various high-conductivity metals for implementing the spectral surface plasmon resonance (SPR) effect in the visible spectrum range. The metals considered are thin films of gold, silver, copper, aluminum, and a bimetallic silver-gold coating on a glass substrate. The detailed spectral characteristics of reflection were calculated in the Kretschmann configuration, including the formation of a thin dielectric film on the metal surface that imitates a layer of biomolecules. The width of the region of implementation of the full-fledged SPR effect in the visible range of the spectrum was determined and sensitivity to the influence of an external dielectric layer for each metal was assessed.

The SPR method is widely applied for detecting biomolecule interactions on metal surfaces. Gold is commonly used due to its stability and the well-established surface chemistry methods, but its SPR effect occurs in the red and infrared regions, limiting design flexibility. Silver, copper, and aluminum offer SPR at shorter wavelengths, which may be useful in chromatic mode detection. The work analyzes these metals' suitability for chromatic SPR biosensors that could enable multichannel analysis using RGB camera systems.

The spectral range of occurrence of the SPR effect in thin metal films is determined by the optical parameters of the metal and the dielectric. Thus, the condition for the existence of plasmon-polariton resonance at the metal-dielectric interface is the fulfillment of the relation $\varepsilon_m < -\varepsilon_d$, where ε_m is the real part of the permittivity of the metal (it is negative), ε_d is the permittivity of the dielectric. The optical constants of the metal n, k are related to the complex permittivity $\varepsilon' + i\varepsilon''$ as follows: $(n+ik)^2 = \varepsilon' + i\varepsilon''$. Spectral dependences of optical parameters n, k for thin films of gold, silver, copper and aluminum were obtained from an available reference site [1]. We calculated the spectral and angular dependences of the reflection coefficient R upon excitation of SPR in the Kretschmann geometry for a semi-cylindrical glass prism with a refractive index of 1.61 in films of all the specified types of metals in order to determine the width of the region of implementation of the full-fledged SPR effect in the range of visible wavelengths. We also estimate the effect of the external thin dielectric layer (a 5-10 nm thick film with a refractive index of 1.48, close to that of the oligonucleotide layers) deposited on the metal surface. The calculations were performed using the freely available WinSpall 3.02 program for modeling SPR curves [2]. For consistency, the following film thicknesses were used in the calculations of the reflectance spectra: 50 nm for gold, 40 nm for silver, 35 nm for copper and 20 nm for aluminum. Fig. 1 shows a family of model SPR reflectance curves $R(\theta)$ for 40 nm thick silver films in contact with water for the visible wavelength range.

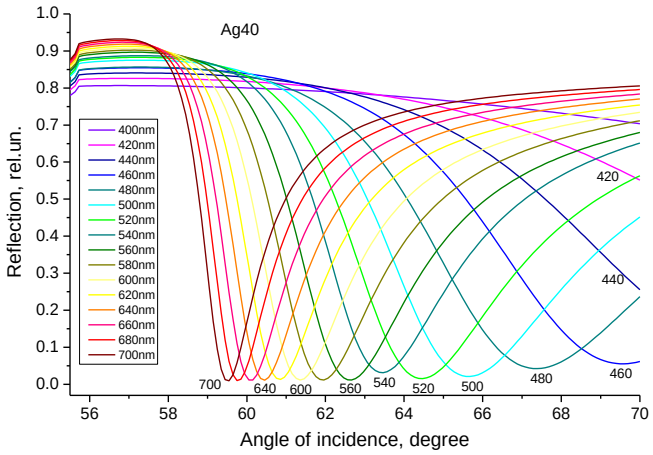

Fig.1. Spectral dependences of the reflectance coefficient on the excitation of SPR in a 40 nm thick silver film in contact with water; the initial wavelength of 700 nm is shortened stepwise by 20 nm up to 400 nm.

As one can see a full minimum of SPR reflection is observed here throughout the entire visible range of waves from 700 nm up to 400 nm, allowing the use of this entire range for RGB registration. The spectral reflection curves calculated in the wavelength scale $R(\lambda)$ at fixed angles of incidence of light in the case of pure silver are shown in Fig. 2. It is evident that these curves have a U-shaped form with a deep minimum of reflection for all angles in the range of 59-70°.

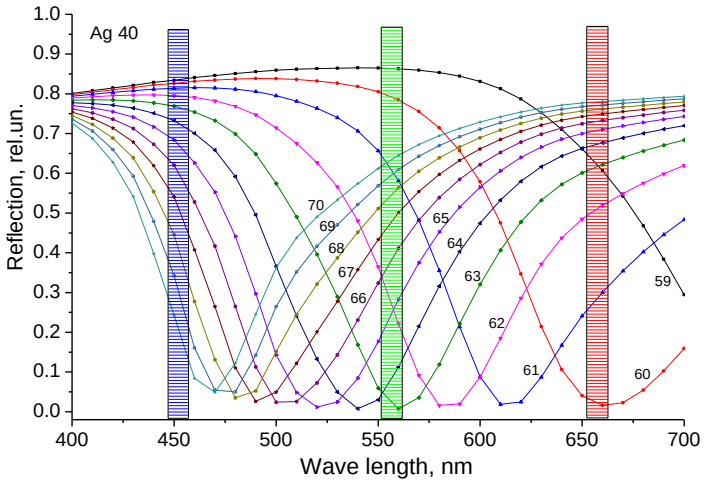

Fig.2. Spectral dependences of internal reflection for a 40 nm thick silver film at different angles of light incidence. The colored bars indicate the positions of the spectral components R, G, B.

Similar dependency graphs were obtained for all other considered metal options. As a result, the following outcomes were obtained. Gold films exhibit SPR only in the red and infrared regions (>500 nm). This limits their applicability in chromatic detection using RGB components but offers well-established surface chemistry benefits for biosensing. Silver shows the highest sensitivity and supports a full SPR effect across the entire visible spectrum (400-700 nm). This makes it the best option for RGB-based chromatic SPR sensors. However, silver's chemical reactivity requires a protective layer, which can be a thin gold film or a polymer. Bimetallic structure with a 40 nm silver layer with a 5 nm gold overlayer shifts the SPR effect into the green region while maintaining good sensitivity. Though it slightly reduces the SPR spectrum's breadth, it adds chemical stability. Copper operates well in the red region but is not suitable for green or blue components. Aluminum, on the other hand, supports SPR primarily in the blue region. Both metals are thus limited in their chromatic range.

Conclusion

This study concludes that silver offers the broadest and most sensitive SPR detection across the visible spectrum. Bimetallic silver-gold structures provide a good balance of sensitivity and chemical stability, while gold is effective in the red and infrared ranges. Copper and aluminum are less effective for full chromatic detection, being confined to specific spectral regions. Calculations also showed that silver is the best metal in terms of sensitivity to the appearance of an external dielectric layer (simulating the adsorption layer of biomolecules) both by changing the value of the reflection coefficient at a fixed angle of incidence of the beam, and by shifting the angle of the SPR minimum at a fixed wavelength.

Reference

[1] https://refractiveindex.info/ (accessed 05.08.2024)
[2] *Resonant Technologies GmbH*. http://www.res-tec.de (accessed 30.07.2024)

LASER DESORPTION/IONIZATION MASS SPECTROMETRIC STUDY OF COMPOSITES BASED ON TRANSITION METAL DICHALCOGENIDES AND ORGANIC COMPOUNDS

Kosevich M.V.[*,], Boryak O.A.[*], Shelkovsky V.S.[*], Zobnina V.G.[*], Kuzema P.O.[***], Karachevtsev V.A.[*]**

**B. Verkin Institute for Low Temperature Physics and Engineering of the National Academy of Sciences of Ukraine, 47 Nauky Avenue, Kharkiv, 61103, Ukraine, mvkosevich@gmail.com*
*** School of RadioPhysics, Biomedical Electronics and Computer Systems, V.N. Karazin Kharkiv National University, 4 Svobody Square, Kharkiv, 61022, Ukraine*
****Chuiko Institute of Surface Chemistry of the National Academy of Sciences of Ukraine, 17 General Naumov Str., Kyiv, 03164, Ukraine, coralchance@gmail.com*

Mutual influence of the components of nanocomposites of transition metal dichalcogenides (TMD) MoS_2, $MoSe_2$, or WS_2 with organic compounds methylene blue (MB) or polyethylene glycol (PEG-600) are studied by means of laser desorption/ionization mass spectrometry.

Background

The background of the present work is formed by a number of inter-disciplinary statements:

- object: nanomaterials based on transition metal dichalcogenides (TMD) are currently tested for numerous useful applications, including electronics, spintronic, nanophotonics, biosensing, cancer therapy, drug delivery;
- method: possibilities of the present-day mass spectrometry go beyond just analytical applications and permit modeling of various physical processes in the systems under study;
- idea: mass spectrometric probing of nanomaterials and nanocomposites by means of desorption/ionization techniques can provide useful information on intermolecular interactions and mutual effect of the components of nanocomposites.

The aim of the present work was to characterize model nanosystems composed of TMD MoS_2, $MoSe_2$, WS_2 and organic molecules of different nature – organic salt methylene blue (MB) dye and organic polymer polyethylene glycol (PEG-600). Such combinations unite components exhibiting various mechanisms of biological activity promising, in particular, in cancer therapy: TMD are tested in photothermal therapy, MB is applied in photodynamic therapy, and PEGs improve bioavailability of nanoparticles.

Experimental

2D nanoflakes of TMD MoS_2, $MoSe_2$, WS_2 were prepared by sonication of their crystalline powders in aqueous medium without any additives or with addition of MB or PEG-600 either as exfoliating agents or components of the nanocomposites. The resulting nanomaterials were studied by laser desorption/ionization (LDI) mass spectrometry using a MALDI-TOF instrument Autoflex II (Bruker, Germany) and applying experimental parameters described elsewhere.

Results and discussion

LDI mass spectra of TMD-based nanomaterials have a number of distinctive features. Electronegativity of chalcogens provides stabilization of negative ions sputtered from the TMD by laser irradiation, while many organic compounds generate positively charged ions. This effect permits to obtain LDI mass spectra of inorganic and organic components of the nanocomposites separately in the negative and positive ion modes. Polyisotopic nature of all chemical elements in the composition of the TMD is responsible for the correspondence of peak groups with appropriate isotopic distribution to any cluster ion sputtered from the TMD.

In Fig. 1 LDI mass spectra of (MoS_2-MB) system depicting general features of TMD-MB nanocomposites are presented. In the positive ion mode (Fig. 1a) only one ion corresponding to the intact cation of the MB^+ organic

dye is recorded for its composites with all three studied TMD. In the negative ion mode sets of $Mo_xS_yO_z^-$ clusters are recorded. The cluster pattern of the LDI mass spectrum of pure MoS_2 nanoflakes (Fig. 1c) is distorted in the presence of MB, which evidences mutual effect of the nanocomposite components.

It is suggested that MB cations are adsorbed on the partially negatively charged surface of MoS_2, and the existence of the "preformed" cations provides their easy desorption by laser irradiation under LDI conditions.

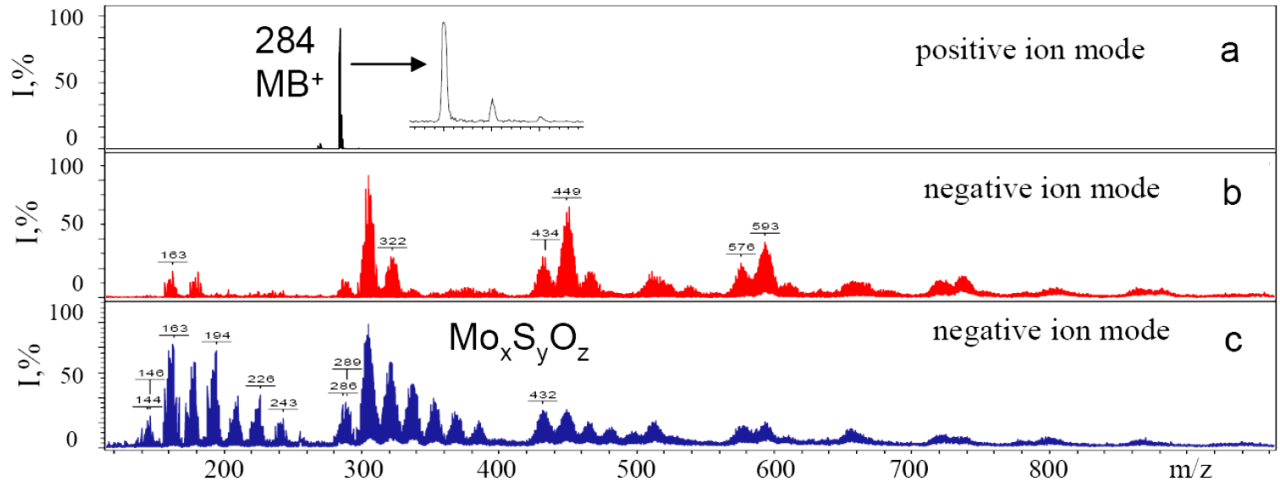

Fig. 1. LDI mass spectra of the (MoS_2-MB) nanocomposite: a – positive ion mode, MB^+ cation, m/z 284 is present; b – negative ion mode, sets of $Mo_xS_yO_z^-$ clusters are present; c – negative ion mode spectrum for pure MoS_2 nanoflakes is presented for comparison.

In Fig 2 LDI mass spectra of (WS_2-PEG-600) nanocomposite are presented. Two bell-shaped sets of cationized oligomers: $[HO-(CH_2-CH_2-O)_n-H]\bullet K^+$, $[H-(CH_2-CH_2-O)_n-H]\bullet K^+$ characteristic of polyethylene glycols are recorded in the positive ion mode (Fig. 2a). In the negative ion mode sets of clusters $W_xS_yO_z^-$ are recorded, Again, cluster pattern of the nanocomposite (Fig. 2b) differs from that for pure WS_2 (Fig. 2c).

Similar features are observed for all other combinations of TMD with MB or PEG-600.

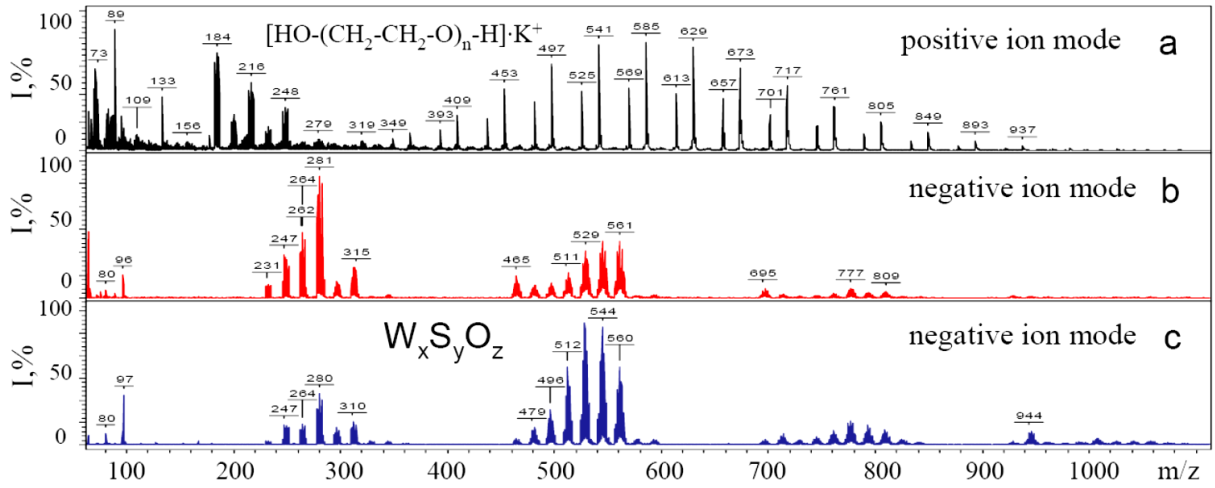

Fig. 2. LDI mass spectra of the (WS_2-PEG-600) nanocomposite: a – positive ion mode, sets of oligomers $[HO-(CH_2-CH_2-O)_n-H]\cdot K^+$, $[H-(CH_2-CH_2-O)_n-H]\cdot K^+$ characteristic of PEG-600 are recorded; b – negative ion mode, sets of $W_xS_yO_z^-$ clusters are present; c – negative ion spectrum for pure WS_2 nanoflakes.

It may be concluded that LDI mass spectrometric data point to mutual effect of inorganic and organic components in the TMD MoS_2, $MoSe_2$, WS_2 nanocomposites with MB or PEG-600.

ASPECTS OF ELECTRONIC STRUCTURE OF HYDROXYPYROMORPHITE SURFACE - $Pb_{10}(PO_4)_6(OH)_2$

S. S. Smolyak*, N. A. Kurgan*, I. V. Sukhenko*, V. L. Karbivskyy*

**G. V. Kurdyumov Institute for Metal Physics, 36 Academician Vernadsky Boulevard, UA-03142 Kyiv, Ukraine, e-mail: sssmolyak@gmail.com*

The electronic structure of hydroxypyromorphite - $Pb_{10}(PO_4)_6(OH)_2$. has been studied by experimental and theoretical methods: X-ray photoelectron spectroscopy (XPS) and the density functional theory (DFT). The role of the of the oxygen tetrahedra sublattice and valence states of lead in the formation of the structure and features of the total density of states of the occupied part of the valence band is demonstrated.

The publication of Korean scientists in 2023 [1] on the detection of superconductivity in copper-doped lead oxopyromorphite prompted the world community to study this type of compound. We have conducted an experimental and theoretical study of the electronic structure of lead hydroxyapatite - $Pb_{10}(PO_4)_6(OH)_2$.

Comparison of the binding energies of the internal levels (Table 1) shows an increase in the binding energy of the core 4*f*-electrons of lead, thereby indicating a decrease in the electron density on lead atoms while transitioning from the metallic state to the compound $Pb_{10}(PO_4)_6(OH)_2$. The decrease in the binding energies of the oxygen 1*s* level and the phosphorus 2*p* level within the transition from calcium apatite to hydroxypyromorphite indicates an increase in the electron density on these elements. The established increase in the negative charge on oxygen, together with the increase in the electron density on phosphorus, indicates an increase in the ionic component of the chemical bond involving lead.

Table 1. Binding energies of core levels of atoms in studied compounds.

Compound	O *1s*	Pb $4f_{7/2}$	P *2p*
$Pb_{10}(PO_4)_6(OH)_2$	530.7	138.4	132.9
$Ca_{10}(PO_4)_6(OH)_2$	531.2	-	133.3
Pb metal	-	136.8	-

According to the calculations performed for the hydroxypyromorphite compound, 6*p* orbitals of lead make a slightly lower relative contribution to the upper part of the valence band compared to the 3*d*-4*s* orbitals of calcium, which may indicate a higher degree of ionicity of the chemical bond between lead and the surrounding oxygen. One of the features of the electronic structure of hydroxopyromorphite is the participation of an lone 6*s* electron pair with low binding energy in the chemical bonding. A decrease in the electron density of 6*p* electrons leads to an even greater decrease in the binding energy, and thus the 6*s* states of lead are located in the upper part of the valence band of hydroxopyromorphite.

The partial density of states of lead obtained by quantum mechanical calculations shows *6s-p* hybridization for lead atoms in the first crystallographic position, while for lead atoms in the second crystallographic position, this hybridization is significantly less pronounced, which leads to the fact that for $Pb_{(2)}$ atoms the covalent component of chemical bonding with oxygen atoms is somewhat smaller than for $Pb_{(2)}$ atoms (Fig.1). Thus, the decrease in the ionic component of the chemical bond in the overall balance of charge compensation in lead apatites relative to calcium apatites is mainly due to lead atoms in the first crystallographic position with a more pronounced covalent component of the chemical bond.

The presence of a pronounced s-density for $Pb_{(1)}$ atoms near the top of the valence band, together with the presence of an electron density at the corresponding energy level of the oxygen atom $O_{(1)}$, which belongs to the

PO_4 tetrahedron, indicates the possibility of metal-metal interaction, which, given that direct interaction between lead atoms in the apatite structure is impossible due to the atomic structure, is carried out with a certain degree of mediation through Pb-O-Pb oxygen atoms. This feature corresponds to the peak E (Fig. 1) on the PDOS curve. Thus, it can be concluded that the interaction in the metal sublattice exists mainly between atoms in the $Pb_{(1)}$ positions with the participation of oxygen atoms from PO_4 tetrahedra, whose states form the top of the valence band.

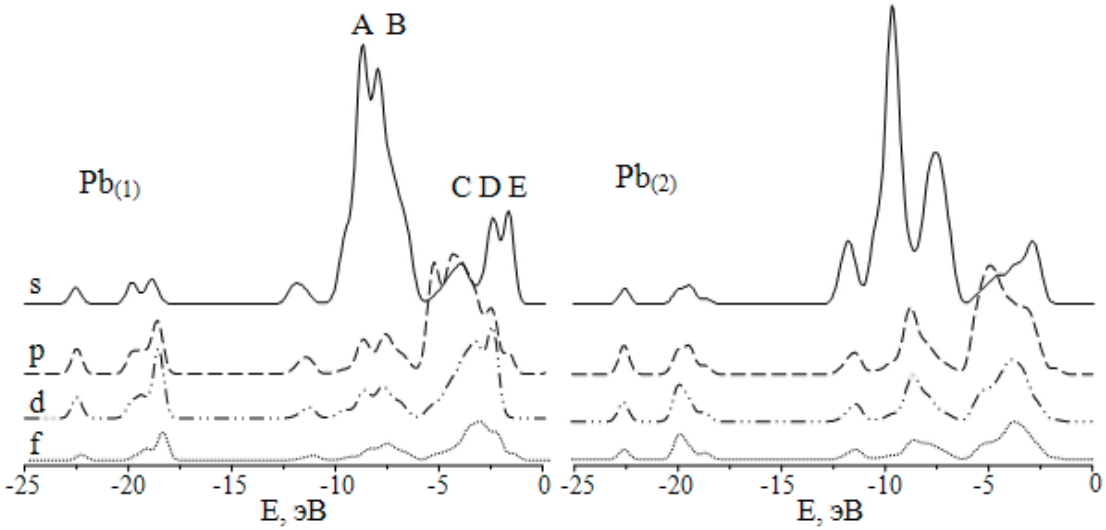

Fig. 1. Comparative contribution of lead orbitals to the density of states of the compound $Pb_{10}(PO_4)_6(OH)_2$.

Conclusions.

The structure of the occupied part of the valence band of lead apatite, as in the case of calcium apatite, has a pronounced band character with different widths of individual subbands. Two structural regions separated by energy are observed: the upper and lower parts of the valence band. The sublattice of oxygen tetrahedra is crucial in shaping the shape and main features of the total density of electronic states.

In the metal sublattice, indirect metal-metal interaction is observed, which is carried out mainly between atoms in $Me_{(2)}$ positions with the participation of oxygen atoms of the hydroxyl group, while $Me_{(2)}$-$O_{(3)}$-$Me_{(1)}$ channel of interaction through oxygen atoms form tetrahedra is less pronounced.

A peculiarity of the electronic structure of hydroxypyromorphite is an increase in the ionic component of the chemical bond between lead and oxygen compared to calcium apatite. For lead atoms, the initially inactive $6s^2$ electron pair participates in the chemical bond due to *6s-p* hybridization and the formation of a "stereochemically active" lone pair that actively interacts with the valence electrons of oxygen.

For lead atoms in two different crystallographic positions, there are significant differences in the formation chemical bonds, with lead in the first position having a larger covalent component, which leads to a decrease in the ionic component in the overall charge balance compared to calcium apatite.

The authors acknowledge the financial support of the National Research Foundation of Ukraine, Grant No. 181/0242 (0124U003949).

References

[1] Sukbae Lee et al, 2023. arXiv: 2307.12008.

$IN_{2-Y}SN_YO_3$ AS TRANSPARENT SUPERCONDUCTOR: ELECTROCHEMICAL REDUCTION METOD

Menesenko D.*,, Feia O.*,**,***, Makivska V.**, Shapovalov A.*,****

**Kyiv Academic University, 36 Academician Vernadsky Boulevard, UA-03142 Kyiv, Ukraine*
***G. V. Kurdyumov Institute for Metal Physics, 36 Academician Vernadsky Boulevard, UA-03142 Kyiv, Ukraine*
****Institut für Festkörperforschung, Leibniz IFW Dresden, Dresden 01069, Germany*
e-mail: d.menesenko@kau.edu.ua

In the present study we propose an explanation of the electrochemical reduction process leading to superconducting characteristics in transparent $In_{2-y}Sn_yO_3$ thin films. Experimental studies of the samples and the density functional theory (DFT) simulation with ab initio modelling of phase transition pathways calculations allowed us to create a suitable model that explains the electrochemical reduction process responsible for the observed superconductivity in such samples.

Introduction

Today, much of the attention is focused on quantum electronics and quantum devices. Developed countries and leading companies in the world are investing a lot of money and effort to create powerful quantum technologies for computing and data transmission. Transparent superconductivity, a fairly young narrow field, the prospect for superconducting photonics and detection of certain ranges of electromagnetic waves can open up new opportunities for quantum technology and possibly fundamentally new devices. ($In_{2-y}Sn_yO_{3-\delta}$ referred here as ITO) is an n-type semiconductor with a high electron density on the order of 10^{21} cm^{-3} and low resistivity, ~10^{-4} Ω·cm. At 9-10% of tin contents (y), the film exhibits a high optical transmittance (~90%) and few Ohm surface resistance which attracted a variety of optoelectronic applications [1]. Previous studies showed that the electrochemically reduced commercial ITO films could exhibit superconducting properties, with a critical temperature around ~5K [2] accompanied by the appearance of a yellowish color. The origin of superconductivity in ITO using electrochemical reduction was explored. DFT calculations helped shed light on the behavior of individual particles in ITO samples. The obtained results suggest that electrochemical reduction of ITO leading to strong oxygen deficiency at a thin surface layer on the top of polycrystalline ITO film with grain-size of 20-50 nm followed by the emergence of SC state.

Superconductivity in electrochemicaly reduced ITO films

In previous works we found that ITO films grown in an oxygen deficient environment show SC onset, i.e. decline from normal state semiconducting behavior, at T close to 10 K [3]. In another our work [4] using measurement of transport characteristics by the van der Pauw method we showed heterogeneity of superconducting characteristics, and electromagnetic studies indicate two-dimensional superconducting characteristics on the surface of the sample, the SEM results showed that the surface structure of the investigated ITO films changes significantly with increasing reduction time. We performed ab initio modelling of phase transition pathways to estimate that H^+ and Mg^{2+} cations migrate inside ITO bulk. Our modelling supports the hypothesis about a predominantly at-surface mechanism of interaction between cations and ITO. An example of the H^+ pathway inside the ITO bulk is shown in Fig.1a, with the corresponding energy barrier depicted in Fig.1b. The first and last points after relaxation have the same energy because they are symmetrically equivalent. However, the migration of H^+ is challenging. It forms hydrogen bonds with oxygen atoms (shown as peaks at approximately 0.25 and 0.85 on the reaction coordinate in Fig.1b), and then creates a covalent bond with an oxygen atom at the center of the path. The reaction barrier for this path is 2.83 eV, indicating that H^+ atoms will not migrate deeply from the surfaces in the process shown. H^+ moves more easily through an O_V vacancy between the first and last points (orange curve in Fig. 1b). In this case, the starting and end points are not equivalent, with a barrier of 1.11 eV in one direction and 1.76 eV in the reverse direction. Such barrier values are still unfavorable for H migration

in ITO. Mg^{2+} migration (green curve in Fig.1b) is also unlikely, with a barrier comparable to H^+. During migration, Mg^{2+} creates bonds with O and In/Sn. To model vacancy diffusion, for the starting and end points we used ITO structures with neighboring O_V cites. The energy barrier for such migration is 1.77 eV (red curve in Fig.1b), which is comparable to H^+ movement through an O_V vacancy and significantly lower than the barriers for H^+ and Mg^{2+} migrations. This may indicate that O atoms move more easily from the bulk to the surface and then either escape or react with surface cations.

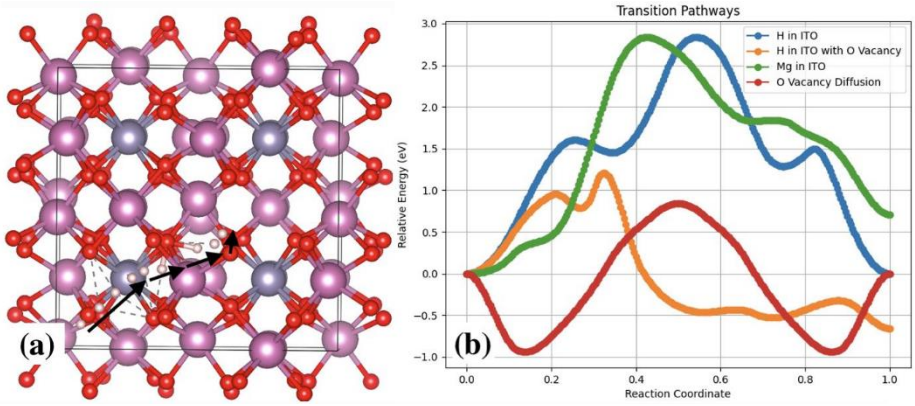

Fig. 1. *Path of H cation in bulk ITO between two relaxed 16c positions* ***(a)*** *and energy barriers for transition pathways for 4 cases: H in ITO (showed on picture (a), H in ITO with O vacancy between start and last points, Mg in ITO, migration of O vacancy* ***(b)***

We propose a possible explanation for the electrochemical reaction that occurs at the electrolyte/ITO interface during electrochemical reduction. The process can bring strong reduction of the ITO surface. Due to limited access of H^+ and Mg^{2+} cations into ITO structure, these cations form a dense layer at the electrolyte/ITO interface. The H^+ and Mg^{2+} cations attract to the surface of ITO free electrons injected from the working electrode under applied negative potential to the ITO film. These electrons reduce In^{3+} and Sn^{4+} cations and decrease the bonding energy with oxygen. Strong potential of the dense layer can locally extract the oxygen anions which have substantially decreased bonding energy with neighbouring indium and tin cations. The extracted oxygen anions chemically react with H^+ and Mg^{2+} to give water or precipitated MgO at the bottom of the vial (pale grey precipitate appears on the bottom of vial after 5-6 intercalation cycles). The part of reduced cations (In^+ and Sn^+) neutralized to metallic state eventually create small clusters in the ITO film and on the surface of the film.

This research of transparent superconductors is supported by the NATO Science for Peace and Security Programme, project SPS G6082. This work was also partially supported by the Ministry of Education and Science of Ukraine under contract No. M/83-2024

References

[1] C. Zhang, C. Ji, Y.-B. Park, and L. J. Guo, “Thin-metal-film-based transparent conductors: material preparation, optical design, and device applications,” *Adv. Optical Mater.* vol. 9, no. 3, Nov. 2020, Art. no. 2001298.

[2] A. E. Aliev, K. Xiong, K. Cho, and M. B. Salamon, “Reversible superconductivity in electrochromic indium-tin oxide films,” *Appl. Phys. Lett.*, vol. 101, no. 25, Dec. 2012, Art. no. 252603.

[3] D. Menesenko, O. Feia, A. Shapovalov, V. Tarenkov, I. Gavrysh, E. Zhitlukhina, M. Belogolovskii, A. Parra, and A. Aliev, “Two-phase/two-gap scenario in heavily reduced superconducting ITO films revealed by point-contact spectroscopy,” *Low Temp. Phys.*, vol. 50, no. 8, August 2024, pp. 688-692.

[4] A. Shapovalov, D. Menesenko, E. Zhitlukhina, A. Parra, A. Aliev, V. Shamaev, M. Gregor, and T. Plecenik, “Inhomogeneous resistivity of transparent superconductor films revealed by the van der Pauw technique,” *Metallofiz. Noveishie Tekhnol.*, vol. 46, no. 6, pp. 517–529, June 2024.

LEED APPLICATIONS IN COMPLEX AND NON-IDEAL SURFACE STRUCTURES

A.G. Fedorus*, A.M. Goriachko, D.V. Rumiantsev***

** Institute of Physics of the National Academy of Sciences of Ukraine, Nauky av., 46, Kyiv, 03028, Ukraine, e-mail: rumiantsevdmytro@gmail.com*

*** Taras Shevchenko National University of Kyiv, Kyiv 01601, Ukraine*

Since its invention in the 1930s by Davisson and Germer [1], Low-Energy Electron Diffraction (LEED) has evolved into a widely used technique for studying surface structures, with modern commercially available LEED systems being introduced in the 1970s [2]. This method has proven essential for characterizing the surface symmetry, atomic arrangement, and condition of surface for materials with long-range order [3].

In our study of ultra-thin metal film adsorption of beryllium and cerium on Mo(112) and their interaction with oxygen, we obtained and analyzed LEED patterns corresponding to distinct surface structures, including epitaxial monolayers (fig. 1 a), superstructures (fig. 1 b), mesoscopic domains (fig. 1 c), nanoribbons (fig. 1 d), and overlayer that are besides the integer-order (fig. 1 e). We present a detailed discussion of the LEED pattern interpretation process, the advanced analytical techniques employed, and the limitations of the method in characterizing complex surface systems.

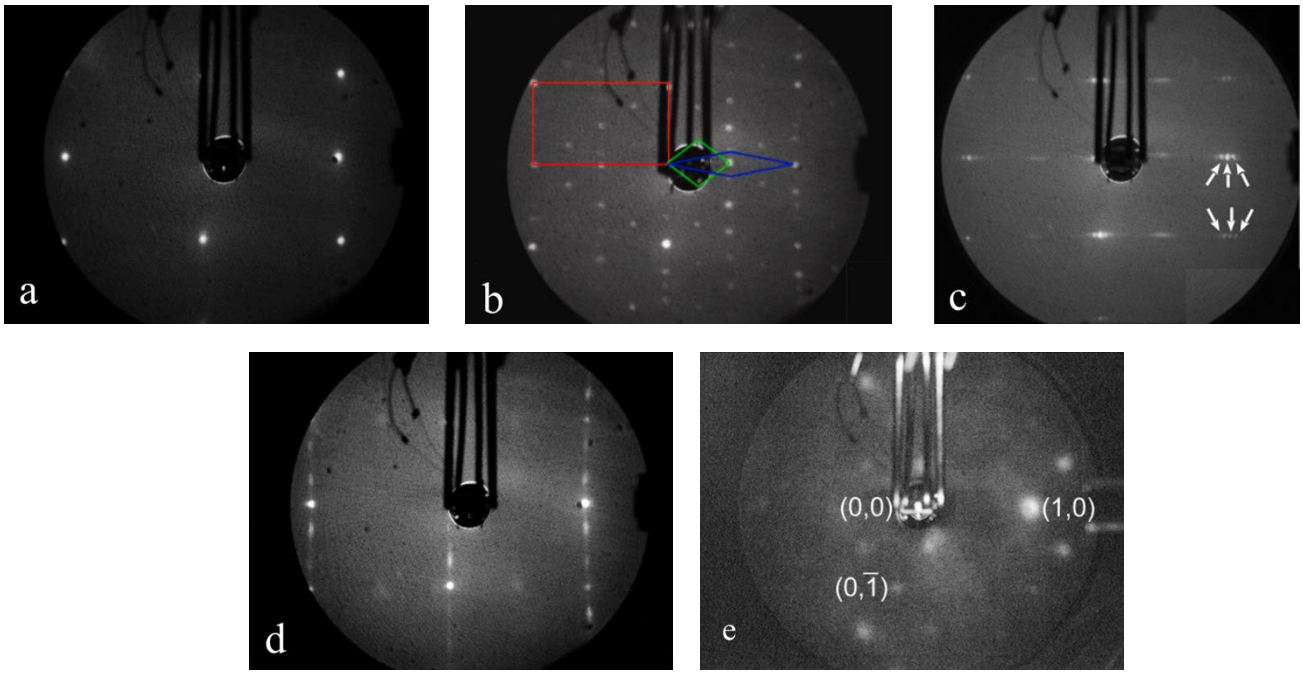

Fig. 1. LEED patterns

References

[1] Davisson, C., & Germer, L. H. (1927). The Scattering of Electrons by a Single Crystal of Nickel. Physical Review, 30(6), 705-740.

[2] Ertl, G., & Küppers, J. (1974). Low Energy Electrons and Surface Chemistry. Verlag Chemie.

[3] Van Hove, M. A., & Tong, S. Y. (1979). Surface Crystallography by LEED: Theory, Computation, and Structural Results. Springer-Verlag.

AUTOMATED TEMPERATURE CONTROL SYSTEM FOR HOT ISOSTATIC PRESSING EQUIPMENT

Yurii Skirta[1,2], Dmytro Velyhotskyi[1,2], Serhii Mamilov[1], Alexandr Tovstolytkin[1]

[1]Institute of Magnetism of the NAS of Ukraine, 36-b, Akad. Vernadskogo blvd., Kyiv 03142, Ukraine
[2]National Technical University of Ukraine "Igor Sikorsky Kyiv Polytechnic Institute", 37, Beresteisky Ave., Kyiv 03056, Ukraine, e-mail: skirtayuri@ukr.net, velyhotskyi@ukr.net

Hot isostatic pressing (HIP) is widely employed to enhance the physical and chemical characteristics of diverse materials, including alloys, steels, composites, powders, ceramics, semiconductors, and others. The precise control of heating parameters is critical during HIP operations, as deviating from prescribed parameters can result in sample deterioration or, at worst, the failure of HIP equipment. Consequently, to streamline the heating process, an automated temperature control system for the hot isostatic pressing equipment was conceptualized and developed. This innovation enables the real-time acquisition of the data on the temperature profiles during HIP equipment operations, facilitating the storage of this information in digital form.

Introduction

Hot isostatic pressing (HIP) represents a form of isostatic pressing wherein a liquid or gas functions as a pressure transfer medium, exerting uniform pressure across a workpiece to diminish porosity and enhance bulk density. The term "isostatic pressing" is derived from the equal pressure applied to every point on the workpiece's surface. Isostatic pressing can be categorized into three variants based on temperature conditions: cold isostatic pressing, warm isostatic pressing, and HIP. HIP operations typically involve temperatures ranging from hundreds to thousands of degrees Celsius. Moreover, HIP pressures can ascend to hundreds of MPa or even several GPa. The HIP process, depending on specific operational requirements, employs diverse gases as pressure media, including argon, helium, nitrogen, and oxygen [1, 2]. *The Institute of Magnetism of the National Academy of Sciences of Ukraine*, manages the scientific equipment known as the "*Laboratory Complex of Experimental Installations for Conducting Experiments in Conditions of High Gas and Hydrostatic Pressures and Temperatures*" [3], a facility that attained the status of national property in 2022. Facilitated by this HIP equipment, investigations into the impact of hot and cold isostatic pressing on material samples have been undertaken across a pressure range from 0 to 200 MPa and temperatures spanning 20 to 850°C. The admissible dimensions of samples for examination are between 6 and 12 mm in diameter and 150 mm in length. Notably, the HIP equipment accommodates six channels, allowing for the concurrent execution of six experiments. The current system for regulating the heating temperature of the working chambers in the HIP equipment relies on an outdated configuration, exhibiting noticeable limitations. A significant drawback lies in the utilization of outdated system components, compromising the reliability and precision of temperature control. Furthermore, the system encounters challenges in obtaining measurement data in digital form, relying on paper records through a chart recorder. To address these shortcomings, we propose an automated heating temperature control system for HIP equipment.

Proposed System

The system was developed utilizing commonly shared elements such as the ICP CON I-7019 ADC, Arduino Uno microcontroller, and K-type (chromel-alumel) thermocouples. This self-regulating system monitors the ongoing temperature in the working chambers and, when necessary, adjusts the temperature by controlling the power supply to the heating elements of the HIP equipment. All control for the developed system is executed through a PC employing the developed software, as illustrated in Fig. 1A. The PC facilitates data exchange and controls the ADC modules (ICP CON I-7019) and Arduino Uno through the RS-485 interface, employing a USB to RS-485 interface converter. Three K-type thermocouples (chromel-alumel) and a semiconductor temperature sensor LM35DZ are linked to the ports of the ADC module for temperature measurement. The thermocouples are

positioned on the body of each of the three heating elements of the HIP equipment. The semiconductor temperature sensor LM35DZ serves to measure the ambient temperature in the room, compensating for values obtained from the thermocouple. Relays, constructed based on the BTA41-600 triac and optocoupler with MOC3062 thyristor output, are utilized to activate and deactivate the heating elements through the digital outputs of the Arduino Uno module. Heating is achieved using resistive elements with a capacity of 1.5 kV, and the temperature is adjustable across a range from room temperature to 850 °C.

The primary interface of the software, as depicted in Fig. 1B, exhibits the current temperature values (T_1, T_2 and T_3) obtained from three thermocouples. The ambient room temperature is indicated in the T_0 field. In the field labeled as "*heating*", the numbers of the heating elements that were activated at that time to heat the working chambers are displayed. During this stage, pressure values are manually inputted into the designated fields – P_1, P_2, P_3. The obtained data is saved to a file, and its name is specified in the corresponding field.

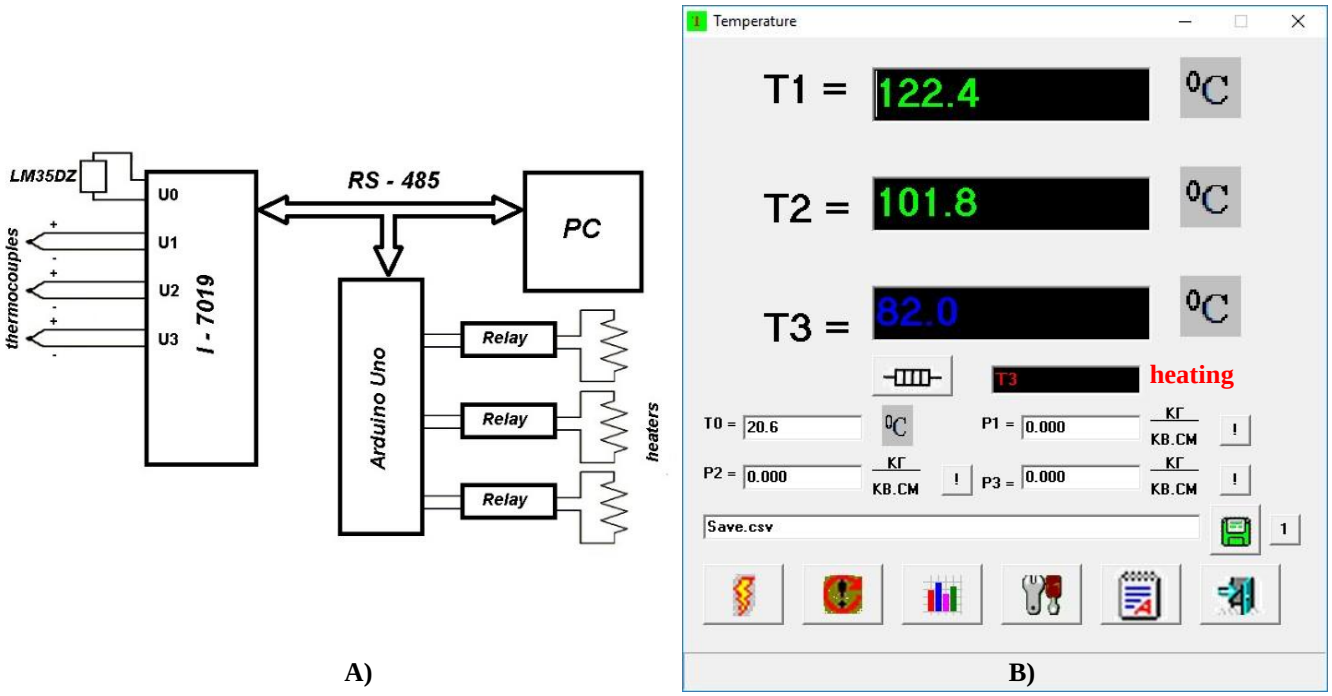

Fig. 1. A) Schematic diagram of the proposed system; B) The primary interface of the software

Conclusion

This article details the design and implementation of an automated heating temperature control system for HIP equipment utilizing a personal computer, software, and a set of sensors. This system boasts advantages such as low cost, straightforward installation, minimal energy consumption, compact size, and user-friendly operation. The implementation of this system not only facilitates a reduction in electricity consumption but also enables the storage of temperature data acquired during HIP equipment experiments in digital format.

References

[1] Atkinson, H. V., & Davies, S. (2000). Fundamental aspects of hot isostatic pressing: an overview. *Metallurgical and materials transactions A*, 31, 2981-3000.

[2] Lei, Z., Yao, C., Guo, W., Wang, D., & Ma, Y. (2023). Progress on the Fabrication of Superconducting Wires and Tapes via Hot Isostatic Pressing. *Materials*, 16(5), 1786.

[3] See details here: https://sites.google.com/view/kyiv-hip/main.

OPTICAL ABSORPTION OF THE $KBI(MOO_4)_2$/PHOSPHATE-MOLYBDATE GLASS CERAMICS

A. Oliinyk, V. Borysiuk, Yu. Hizhnyi, S.G. Nedilko

Taras Shevchenko National University of Kyiv, 64/13 Volodymyrska st., 01601-Kyiv, Ukraine,
e-mail: andrik6603@gmail.com

Glass-ceramics of the $KBi(MoO_4)_2$ crystal/phosphate-molybdate glass type are technologically promising composite materials in which the crystal component is located in a glass matrix. In this work the properties of optical absorption by the luminescence centers in these glass ceramics - bismuth atoms and molybdate groups of MoO_4 - were theoretically modeled. Theoretical calculations of the optical absorption spectra of bismuth ions and molybdate groups located in the crystalline, glass, and their interphase layers were performed by means of the time-domain density functional theory (TD-DFT) method using the QM/MM approximation and the molecular cluster approach.

Glass-ceramics are composite materials in which the crystal component is embedded in a glass matrix. Great interest in the study of this kind of materials is associated with the wide possibilities of their application, in particular, in electronics [1], optical thermometry [2], biomedicine [3], and as sealing materials [4]. The properties of glass-ceramics are largely determined by processes in the "interphase layer", which has an atomic structure different from that of both the crystalline and glass components. At the same time, if the chemical composition of the crystal and the glass matrix are close, the transition between these phases should be smoother. This is especially important in the case of optical luminescent glass ceramics, where each inhomogeneity is a center of light scattering or absorption, i.e., affects the quality of the material.

The computational modeling of excited electronic states and optical spectra of bismuth ions in phosphate-molybdate glass ceramics was performed using the quantum chemical method in the molecular cluster approach. The molecular clusters of $KBi(MoO_4)_2$ crystal, phosphate-molybdate glass of a certain composition and their interface. The crystal structure cluster was formed from 2x4x4 unit cells of $KBi(MoO_4)_2$ crystal.

Calculations of the energies of excited electronic states and optical absorption spectra of bismuth ions were performed by the TD-DFT method in the basis of Gaussian atomic functions using the quantum chemical software package Gaussian 09 [5]. The influence of the neighbor environment on the calculated characteristics was taken into account using the ONIOM procedure, which is one of the variants of the QM/MM approach. In this approach, the system under consideration is divided into two parts - the domain of quantum mechanics (QM) and molecular mechanics (MM). For the atoms included in the QM domain, a quantum mechanical calculation of the electronic properties was performed, and all other atoms of the system included in the MM domain were approximated in the calculation by point charges or dipoles on the nuclei. Two bismuth ions located in the central part of the cluster were included in the QM region when calculating the spectra of bismuth in the $KBi(MoO_4)_2$ crystal, and all other atoms in the crystal cluster were included in the MM region. Similarly, the QM and MM regions of phosphate-molybdate glass clusters and the interphase were formed.

The LANL2DZ atomic basis set and the B3LYP functional were used to approximate the exchange-correlation potential in calculating the spectra.

As can be seen from Fig. 1, the calculated spectra of bismuth in the $KBi(MoO_4)_2$ crystal are characterized by a band in the 350 - 400 nm region, which generally coincides with the experimental data. The averaged spectra of bismuth atoms in the glass are characterized by bands at other sites, in particular at 300 nm and a low-intensity band in the 400 - 550 nm region. In the interphase, the calculated averaged spectra of bismuth atoms have distinct maxima at 270 and 430 nm. That is, our calculations suggest that the luminescence spectra of bismuth atoms in the crystal, glass, and interphase should differ significantly.

As can be seen from Fig. 2, the spectrum of the molybdate groups in the crystal is characterized by a long-wavelength band with a maximum at 470 nm. In the case of glass, the average spectrum of molybdate groups is

very broad and extends over the entire visible spectrum, up to the infrared spectral range, and the spectrum reaches a low-visible maximum in the region of 550 - 600 nm. In the case of the interphase, the spectrum similarly extends over the entire range under consideration and reaches a maximum near 550 nm.

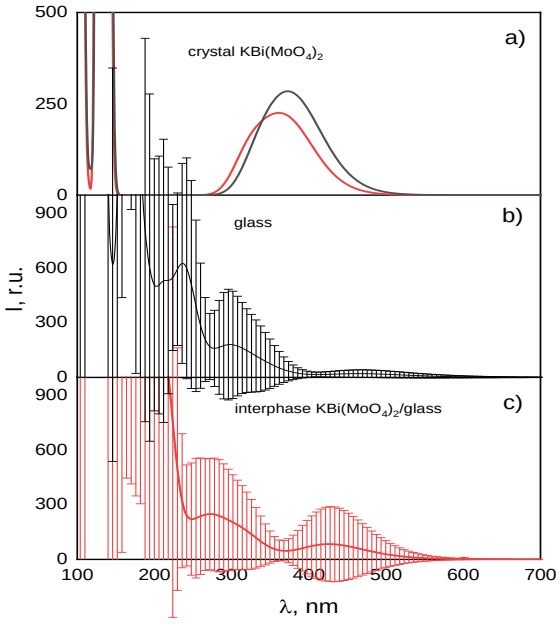

Fig. 1 Absorption spectra of bismuth atoms located in the different parts of the composite: crystal (a), glass (b), and interphase (c)

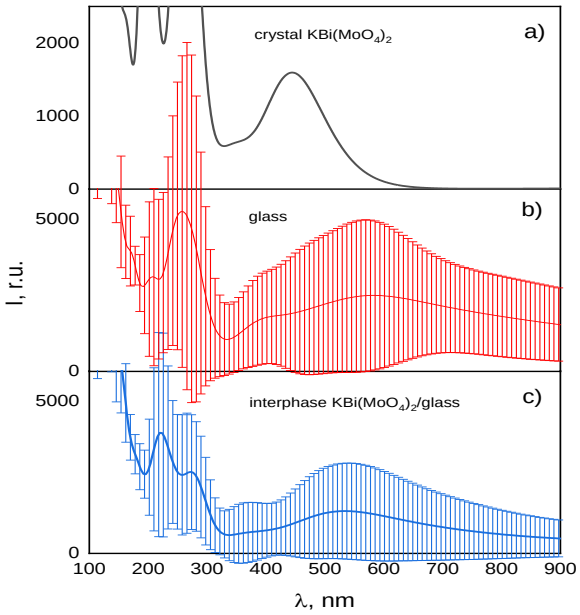

Fig. 2 Absorption spectra of molybdate groups located in the different parts of the composite: crystal (a), glass (b), and interphase (c)

According to the results of calculations, it was found that the optical absorption spectra of bismuth atoms and molybdate groups, which are possible luminescence centers of such glass ceramics, are significantly different in different regions of the composite material. In particular:

1) In the transition from glass to interphase, the average value of the spectral position of the maximum of the long-wavelength band of bismuth atoms shifts towards shorter wavelengths, from 374 nm (in the case of the glass) to 297 nm in the case of interphase.

2) In the transition from glass to the interphase, a shift in the average value of the maximum of the long-wave band of molybdate groups is also observed - towards short wavelengths, from 589 nm (in the case of the glass) to 377 nm in the case of the interphase.

3) The calculated spectra of bismuth in the KBi(MoO)4 crystal are characterized by a band in the region of 350 - 400 nm, which generally coincides with the experimental data.

4) The averaged spectra of bismuth atoms in the glass are characterized by a band at 300 nm and a low-intensity band in the region of 400 - 550 nm. Instead, in the interphase, the calculated averaged spectra of bismuth atoms have distinct maxima at 270 and 430 nm.

5) In the case of molybdate groups, a significant difference in the averaged spectra exists when comparing the cases of the crystal and the amorphous components (glass or interphase).

References

[1] Benyounoussy, S., Bih, L., Muñoz, F., Rubio-Marcos, F., & Bouari, A. E. (2021). Effect of the Na_2O–Nb_2O_5–P_2O_5 glass additive on the structure, dielectric and energy storage performances of sodium niobate ceramics. *Heliyon*, *7*(5), e07113.

[2] Zhang, R., Shang, F., & Chen, G. (2022). NaLaMo2O8: Yb3+, Er3+ transparent glass ceramics: Up-conversion luminescence. *Ceramics International*, *48*(11), 16099-16107.

[3] Mubina, M. K., Shailajha, S., Sankaranarayanan, R., & Smily, S. T. (2021). Enriched biological and mechanical properties of boron doped SiO2-CaO-Na2O-P2O5 BGC. *Journal of Non-Crystalline Solids*, *570*, 121007.

[4] Pascual, M. J. (2021). Glasses and Glass-Ceramics as Sealing Materials. *Journal: Encyclopedia of Materials: Technical Ceramics and Glasses*, 746-761.

[5] Frisch M. J., et al. Gaussian 09, Revision d. 01. Gaussian. Inc., Wallingford CT 201 (2009).

SCANNING TUNNELING MICROSCOPY OF METALLIC AND SEMICONDUCTING SURFACES WITH ATOMIC RESOLUTION

Vlad Rozhenko, Andrii Goriachko

Faculty of RadioPhysics, Electronics and Computer Systems, Taras Shevchenko National University of Kyiv, Kyiv 01601, Ukraine, email: vladrozhenko15@gmail.com

One of the most significant capabilities of scanning tunneling microscopy, as an analytical technique in the field of surface physics, is obtaining an image of the surface of conductive solids with atomic resolution. This enables direct visualization of the surface crystal lattice, direct measurement of interatomic distances and dimensions of the unit cell in the surface plane, and determination of its symmetry type. In this contribution we review the physical models describing imaging with atomic resolution and appropriate mathematical tools, as well as present some typical examples.

Tunneling Current

Scanning tunneling microscopy with atomic resolution is used to solve the following research problems: analytical confirmation of the fact that the surface of a solid body is in an atomically clean and atomically smooth state; measurement of the parameters of the crystalline structure of the surface of a solid (spatial period of translation, location of atoms within the unit cell, presence or absence of surface reconstruction); determination of the presence and comprehensive study of defects in the crystal structure of the solid surface (vacancies, internodal atoms, foreign atoms); studying at the atomic level the phenomenon of adsorption on the surface of foreign atoms, molecules or clusters (detailed localization of the spatial position and distribution of adsorbates, interaction between them); study of the atomic structure of surface nanostructures (study of dimensional effects - the influence of nanoscale spatial restrictions on the parameters of the crystal lattice). The elastic component of the tunneling current plays the main role in obtaining the STM image of the surface with atomic resolution, according to which we write the formula for the tunneling current in a simplified form (neglecting inelastic tunneling):

$$I = \frac{2\pi|q_e|}{\hbar}\int_{-\infty}^{\infty} g_s(E)\Phi_s(E)|M(E,E)|^2 g_f(E)\left[1-\Phi_f(E)\right]dE$$

Other things being equal, the matrix element M(E,E) has a decisive influence on the value of the tunneling current, which, in turn, is determined by the degree of overlap of the wave functions of both electrodes. This degree of overlap is determined by the region of space where the wave functions of both electrodes are simultaneously significantly different from zero. The specificity of the STM experiment is that one of the electrodes has the form of a high-aspect tip with one or several atoms on the top, so this region of space is limited to distances from the top of the tip of no more than tenths of a nanometer. Another important feature of STM is the change in the spatial position of the tip relative to the sample during the scanning process. At the same time, according to the spatial location of the atoms of the sample (obviously, the localization of the wave functions of the sample directly depends on this), the matrix element M(E,E) will change. If we consider the sample to be stationary and the orientation of the tip constant, then the relative location of the tip and the sample will be determined by the three coordinates (x,y,z) of a certain point of the tip. We will recall that we will traditionally use a coordinate system in which the X and Y axes lie in the nominal plane of the sample surface, and the Z axis is directed along the normal to it. In particular, if we consider the tip to be a cone with a rounded top, then as this point we can take the center of rounding, and if we consider the tip to be atomically sharp, then as this point we can take the location of the nucleus of the atom at the very top. In accordance with the above, the matrix element should also be considered as a function of the coordinates of the tip apex - M(E,E,x,y,z), while it depends on the electronic structure of both the sample and the tip.

The same can be said about the density of electronic states of the sample. If the polarity of the voltage applied between the sample and the tip is such that electrons tunnel from the sample to the tip, then the density of states

of the sample is $g_S(E)$. This density is a characteristic of the electronic states involved in tunneling. If, for example, we consider tunneling in a solid-state planar tunnel contact, the area of which is much larger than the area of the unit cell of the surface crystal structure, then $g_S(E)$ is the density of surface electronic states (SES) averaged in the surface plane of the sample - the density of states (DOS). If the opposite electrode is a tip of the STM, then only those electronic states of the sample that are localized on its surface in the vicinity of the tip with coordinates (x,y) will make a significant contribution to the tunneling current. In this situation, $g_S(E)$ is essentially the local density of electronic states (LDOS), which depends on the x and y coordinates - $g_S(E, x, y)$. At the same time, $g_S(E,x,y)$ is exclusively a characteristic of the sample and does not depend on the tip configuration. Assuming that the tip does not undergo changes during the scanning process, the local density of electronic states at its apex, $g_f(E)$, is the same at all spatial positions of the tip, that is, it does not depend on the coordinates. At this stage, it is advisable to rename the indices: instead of 'starting', which indicates the initial states in the tunneling process, we will use 'sample', which indicates the local density of states of the sample, i.e. $g_S(E,x,y)$ remains the same in the formulas; instead of 'final', which indicates the final states, we will use 'tip', which indicates the local density of tip states, that is, instead of $g_f(E)$, we will write $g_T(E)$.

Imaging in Constant Current Mode

In the constant current mode, the value of the tunnel current I(x,y,z) must remain constant, that is, $I(x,y,z) = I_0$. This is achieved by the fact that for each pair of coordinates (x,y), the tip position control system changes its z coordinate until the measured value of the tunnel current equals I_0. The fixed value of z is the solution of the equation

$$\frac{2\pi|q_e|}{\hbar}\int_{-\infty}^{\infty} g_s\,(E,x,y)\Phi_s(E)|M(E,E,x,y,z)|^2 g_T(E)[1-\Phi_T(E)]dE \;=\; I_0$$

in the case of a positive potential on the tip, and

$$\frac{2\pi|q_e|}{\hbar}\int_{-\infty}^{\infty} g_T\,(E)\Phi_T(E)|M(E,E,x,y,z)|^2 g_S(E,x,y)[1-\Phi_S(E)]dE \;=\; I_0$$

in the case of a positive potential on the sample.

These are complex integral equations that do not have analytical solutions, but one can qualitatively expect that for the points (x,y), which correspond to the location of the apex of the tip above the atom of the surface crystal lattice, we obtain smaller values of z than for positions of the apex of the tip above the internodal space. Experimentally measured values of z for each point (x,y) are used to graphically display the trajectory of the tip z(x,y). Considering that the trajectory of the tip reproduces the topography of the surface, we obtain a topographic map of the surface on which the brighter (that is, higher) areas will visualize the position of the surface atoms of the sample under study.

References

[1] O.S. Davydov, Quantum mechanics: a textbook. Kyiv: PH “Akademperiodyka”, 2012.

[2] A. Goriachko, P.V. Melnik, M.G. Nakhodkin, “New features of the Ge(111) surface with co-existing c(2 × 8) and 2 × 2 reconstructions investigated by scanning tunneling microscopy” Ukr. J. Phys., vol. 60, pp. 1132-1142, 2015.

[3] A. Goriachko, P.V. Melnik, M.G. Nakhodkin, “A suggestion of the graphene/Ge(111) structure based on ultra-high vacuum scanning tunneling microscopy investigation” Ukr. J. Phys., vol. 61, pp. 75-87, 2016.

PHYSICS OF SEMICONDUCTORS AND DIELECTRICS, SEMICONDUCTOR DEVICES

INVESTIGATION OF THE MECHANISM OF ELECTRICAL CONDUCTIVITY IN LEAD ZIRCONATE TITANATE FERROELECTRIC CERAMICS IN THE LOW FREQUENCY REGION

Lushchin S.P.

National University "Zaporizhzhia Polytechnic", 64, Zhukovskogo Street, Zaporizhzhia, 69063, Ukraine,
e-mail: luschin@zntu.edu.ua

The mechanism of electrical conductivity in lead zirconate titanate ferroelectric ceramics in the low frequency region of $0 < \nu < 100$ kHz has been investigated. The frequency relationship of the electrical conductivity of PZT ceramics in the frequency range of $0 < \nu < 100$ kHz has been analyzed. The change in electrical conductivity with frequency of the electric field in the PZT ceramics is explained by the jumping mechanism of charge transfer.

Introduction

Lead zirconate titanate ferroelectric PZT ceramics based on solid solution of lead zirconate titanate of composition $Pb(Zr,Ti)O_3$ is industrial basic material for the production of piezoelectric transducers nowadays. The study of the mechanism of electrical conductivity in polycrystalline PZT ceramics is of significant interest with regard to the practical use of such materials and the enhancement of the quality of piezoelectric transducers.

The purpose of the work

The purpose of this work was investigation of the mechanism of electrical conductivity in PZT-19 ceramics in the low frequency range of $0 < \nu < 100$ kHz. In this context, the task was to analyze the relationship between the electrical conductivity of PZT-19 ceramics and the frequency of alternating current and to determine the degree of disorder of the polycrystalline structure of PZT ceramics.

The analysis of researches and publications

PZT ceramics is a multi-phase polycrystalline system. In [1-3] possible mechanisms of changes in electrical conductivity of dielectrics are considered and it is noted that an increase in electrical conductivity is due to the delay of slow mechanisms of polarization. It was shown in the work of V.V. Prisedsky that in lead-containing perovskits the transfer of an electric charge is described by the theory of polarons of a small radius [4]. AC electrical conductivity of solid polycrystalline solutions of PZT is determined by the volume properties of crystallites and little sensitive to the state of intercrystalline boundaries [4].

Methodology of investigation

The experiments were performed on industrial samples of ferroelectric ceramics PZT-19. The measurement of electrical conductivity was performed on alternation current in the frequency range $0 < \nu < 100$ kHz at voltage $U = 5$ V. The alternative voltage was applied from a generator Г3-56/1 and controlled by oscilloscope С1-65. The current value, after rectification by a diode bridge, was measured with a microammeter М1200. Electrical conductivity was measured at atmospheric pressure and temperature $T = 300$ K. Samples of PZT-19 ceramics had nickel electrodes, which were applied by thermal vacuum spraying.

Results and discussion

Previously the frequency relationship of the electrical conductivity of PZT ceramics of the brand PZT-19 has been obtained [4]. The analysis of this relationship for PZT-19 ceramics has shown that conductivity increases with an increase in frequency. The equivalent electrical circuit of the multi-phase polycrystalline structure of the PZT ceramics can be represented by a combination of a large number of active resistances and capacitances. With increasing frequency of an alternating electric field, the electrical resistance should decrease and correspondingly the electrical conductivity increase.

The phenomenon of electrical conductivity dispersion in dielectrics is described using the universal power Jonscher law [1], which is represented by the following relationship:

$$\sigma \propto \nu^n,$$

where σ is the electrical conductivity; ν is the frequency of the alternating current; the powerful function indicator of the degree is $0.7 < n < 1$.

The analysis of the relationship between the electrical conductivity of the PZT-19 ceramics and the frequency of alternating current indicates, that in bilogarithmic coordinates $\ln \sigma = f(\ln \nu)$ the relationship is linear. The power function indicator in the frequency range of $0 < \nu < 20$ kHz is $n = 0.8$. At frequencies above 20 kHz, the value of the power function indicator decreases.

The rise in electrical conductivity observed in PZT ceramics can be attributed to the postponement of slow polarization processes [3]. This relationship is illustrative of the jumping conduction mechanism that occurs during the motion of ions and polarons in dielectrics under the influence of an electric field. Various charged particles do not have time to respond to a change in the electric field with increasing frequency and take localization positions. At the same time, they continuously move, following the change in the electric field and thereby contribute to an increase in electrical conductivity [3].

PZT ceramics is an ionic crystal with a tightly packed crystal lattice with the structure of perovskit. Therefore, such dielectric is dominated by jumping (polaron) electrical conductivity. Polarons move in a crystal by jumping from one lattice node to another under the influence of thermal fluctuations. The mobility of such carriers is extremely low, as evidenced by experimental studies [4]. The polaron conductivity mechanism is particularly characteristic of ionic crystals, in which the Coulomb interaction between electrons and ions of the crystal lattice is markedly high. The theory of small-radius polarons is used to describe the conductivity mechanism of the electrical conductivity of oxides with a perovskite structure, including PZT ceramics [4].

The jumping of charge to states near the Fermi level is accompanied by a characteristic dependence of electrical conductivity on the cyclic frequency of the measuring field, which is described by the Austin-Motta formula [2]. As established by the authors of the work [6], the basic patterns of dependence of electrical conductivity on the frequency of the electric field in a wide range of frequencies for disordered systems are caused by the occurrence of migration barriers for current carriers. They got an expression for the value of n through parameter α, which characterizes the degree of disordered of the system:

$$n = 1 - \frac{2(2+\alpha)}{(1+\alpha)\sqrt{1+\alpha}}.$$

Considering the value of the powerful function indicator for the PZT-19, the value of which is $n = 0.8$, from the above formula, we get the value of $\alpha = 95$. The obtained values of α indicate the significant disorder of PZT ceramics system, since for an unordered system $\alpha = 1$.

The analysis of the experimental results makes it possible to consider the transfer of electric charge in the polycrystalline structure of PZT ceramics as a jumping mechanism with the existence of a polaron electrical conductivity. The dependence of electrical conductivity of PZT ceramics on the frequency of electric field in the low frequency range is subject to the degree law of the Jonscher. The degree of disordered of the system for PZT-19 ceramics is indicative of a notable degree of disorder, which is a defining characteristic of polycrystalline materials.

References

[1] A.K. Jonscher, Universal relaxation law, London: Chelsea Dielectric Press, 1996.

[2] N. Mott, E. Devis, *Elektronnye processy v nekristallicheskih veshchestvah*. V.1. M: Mir, 1982.

[3] Ju.M Poplavko, *Fizika dijelektrikov: ucheb. posobie dlja vuzov*. Kiev: Vishha shkola, 1980.

[4] V.V. Prisedsky, *Nonstoichiometric ferroelectrics* $A^{II}B^{IV}O_3$. Donetsk: Knowledge, 2011.

[5] S.P. Lushchin, O.I. Zolotarevskiy, "Investigation of the frequency dependence of the electrical conductivity in PZT piezoceamics*",* Electrical Engineering and Power Engineering, No.1, pp. 8-15, 2020.

[6] V.N. Bondarev, P.V. Pikhitsa, "<Universal> frequency response of disordered conductors and related problems: a novel approach", Phys. Lett. A, 196, pp. 247-252, 1994.

A NEW POSSIBLE TYPE OF THE RESONANT-TUNNELING DIODE ON THE BASE OF 2D CHANNEL WITH A POTENTIAL WELL AND BARRIERS, CREATED BY DOPING WITH A POLARIZATION FIELD OF A MULTI-DOMAIN FERROELECTRIC

M.V. Strikha[1,2], A.M. Morozovska[3]

[1]*Taras Shevchenko National University of Kyiv, Faculty of Radiophysics, Electronics and Computer Systems, Hlushkov Ave., 4g, Kyiv, Ukraine;*
[2]*V.Lashkariov Institute of Semiconductor Physics, NAS Ukraine, Nauky Ave., 41, Kyiv, Ukraine,*
E-mail: maksym_strikha@hotmail.com
[3]*Institute of Physics, NAS Ukraine, Nauky Ave., 46, Kyiv, Ukraine,*
E-mail: anna.n.morozovska@gmail.com

Resonant-tunneling diodes (RTD), where tunneling occurs within sub-picoseconds time intervals and the I-V curve contains an interval with a negative slope in the range corresponding to the ultra-high frequencies, had played a principal role in the creation of modern THz emitters (see e.g. Ref.[1]). A traditional RTD, fabricated on the base of GaAs/AlAs, InGaAs/AlAs, and InAs/AlSb heterostructures, is characterized by the maximal current densities of 10^5 A/cm^{-2} order and demonstrates the intervals with the negative slope at room temperature (see e.g. Ref.[2]). However, in Ref.[3] the negative differential resistance (NDR) was achieved due to the resonance tunneling at room temperature in perovskite double-barrier heterostructures composed of a 10 unit-cell-thick $SrTiO_3$ quantum well sandwiched in two 10 unit-cell-thick $LaAlO_3$ barriers. When the paraelectric $SrTiO_3$ quantum well was replaced by a ferroelectric $BaTiO_3$, the onset of the NDR could be modulated by polarization switching in the ultrathin $BaTiO_3$. Recently the discovery of robust room-temperature ferroelectric-modulated resonant tunneling and NDR behaviors in all-perovskite-oxide $BaTiO_3/SrRuO_3/BaTiO_3$ QW structures was reported [4].

It was demonstrated in Refs.[5,6], that the existence of domain walls in a ferroelectric leads to the appearance of potential barriers in the closely deposited thin 2D conducting layer of graphene, MoS_2 etc. This opens a principal possibility of the RTD structure fabrication, presented in Fig.1: the regions with the p-type conductivity are realized near the heavily doped semiconductor terminals, and a quantum well with the n-type conductivity with an electron localized level inside it is between them.

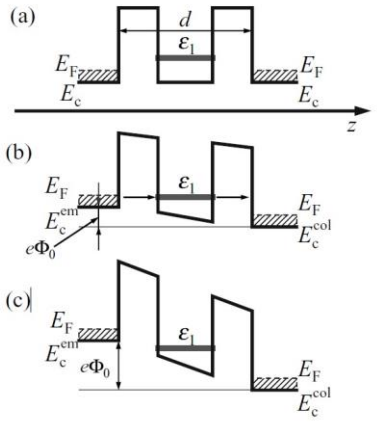

The principle of the RTD operation is: without the collector bias the current through the system (caused by the non-resonant tunneling or by the current over the barriers) is negligible small (Fig.1 a). When the collector bias shifts the level in the well into the range of the occupied states in the emitter conduction band, the resonant tunneling becomes possible and the current through the system increases (Fig. 1b). When the level becomes lower than the bottom of emitter conduction band, the current decreases and reaches its minimum (Fig.1c). This causes the NDR in the I-V curves.

Note, that Fig.1 presents an idealized picture, the real barriers and well are not rectangular [5,6]; therefore, the first localized energy level E_1 should be calculated numerically. However, in the simplest approximation of the rectangular infinitely deep well with the width L it is given by:

$$E_1 = E_w + \frac{\hbar^2 \pi^2}{2 m_c L^2} \tag{1}$$

Here E_w is the energy of the well bottom without the collector bias, m_c is an effective mass of electron in the well. When the collector bias Φ_o is applied (we assume that the half of this bias is applied to the left barrier and the other half to the right one) we get:

$$E_1(\Phi_o) = E_w + \frac{\hbar^2 \pi^2}{2 m_c L^2} - \frac{e\Phi_o}{2} \tag{2}$$

Following the procedure, presented in Ref.[2], we get the expression for the resonant current through the n-th level in the well:

$$I_n(\Phi_o) = \frac{e (m_c^{em})^{\frac{1}{2}}}{\sqrt{2}\pi^2 \hbar^2 L} (E_F^{em} - E_n(\Phi_o))(E_F^{em} - E_c^{em})^{\frac{1}{2}} \tag{3}$$

Here m_c^{em} is an effective mass of the electron in the emitter, other denotations are clear from Fig.1. Eq.(3) yields that the current increases with the approach of the level with the bias increase to the emitter conduction band bottom E_c^{em}. However, when the level becomes lover than E_c^{em}, the resonant tunnelling is no longer possible, and the current through the RTD is small. The maximal value of the current (3) can be modulated by the ferroelectric polarization P (which direction and magnitude contributes into the "overpotential" Φ) together with the width L (which is determined by the domain width/period).

References

[1] *Saeedkia, D.* Handbook of Terahertz Technology for Imaging, Sensing and Communications. Elsevier. p. 429 (2013).

[2] *Mitin V., Kochelap V., Stroscio M.* Introduction to Nanoelectronics: Science, Nanotechnology, Engineering, and Applications. Cambridge: Cambridge University Press. pp. 346 (2012).

[3] Ruifang Du, Xiangbiao Qiu, Aidong Li, Di Wu. Ferroelectric modulation on resonant tunneling through perovskite double-barriers. Applied Physics Letters 104(14):142907-142907 (2014).

[4] *Zhijun Ma et al*. A Room-Temperature Ferroelectric Resonant Tunneling Diode. Advanced Materials 34 (35): 2205359 (2022).

[5] *Anna N. Morozovska, Eugene A. Eliseev, and Maksym V. Strikha*. Ballistic conductivity of graphene channel with p-n junction at ferroelectric domain wall. Applied Physics Letters 108 (23): 232902 (2016).

[6] 6. *Maksym V. Strikha and Anna N. Morozovska*. Limits for the graphene on ferroelectric domain wall p-n-junction rectifier for different regimes of current. J. Appl. Phys. 120 (21) 214101 (2016).

EFFECT OF OXYGEN DOPING ON THE PHASE TRANSITION TEMPERATURE OF $CuInP_2S_6$ CRYSTALS

Alexander Molnar*, Dávid Gál **, Henrietta Bán*

** Uzhhorod National University, Department of the Physics of Semiconductors, Ukraine,*
e-mail: alexander.molnar@uzhnu.edu.ua
*** HUN-REN WIGNER Research Centre for Physics, Budapest 1121, Hungary,*
e-mail: galdavidagu7@gmail.com

The effect of oxygen enrichment of $CuInP_2S_6$ layered crystals is discussed. It is shown that the addition of oxygen during the growth of these single crystals allows the rise of the phase transition temperature by 20 degrees (up to 336K). Since the relatively low phase transition temperature of these materials is one of the limiting factors in their practical application, this solution (which is widely used in the semiconductor industry), allows to significantly improve the prospects for the use of $CuInP_2S_6$ as a gate dielectric for negative capacitance FET transistors (NC FET) and ferroelectric memory cells.

Recently, there has been an increased interest in two-dimensional layered crystals with multiferroic properties. Among them are $CuInP_2S_6$ crystals, in which ferroelectric properties are observed at room temperature, and they remain stable even when the active layer thickness is reduced below 4 nm [1]. This property makes it a promising candidate for use as a sub-gate dielectric layer (to create field-effect transistors with negative capacitance to improve subthreshold swing) and as an active material for creating small-sized ferroelectric memory cells.

One of the few disadvantages of $CuInP_2S_6$ crystals is the relatively low Curie temperature of 315K, which limits the temperature range of using devices based on it. To overcome this limitation, two solutions are currently known: using crystal compression, which leads to an increase in the phase transition temperature [2], or growing stoichiometrically deviated samples with an increased amount of indium [3], which leads to similar results.

We found another possibility to increase the phase transition temperature of $CuInP_2S_6$ crystals. When studying the temperature dependence of the dielectric permittivity of these crystals enriched with oxygen, we observed an increase in the Curie temperature by 20 degrees (336K). Since oxidation is a standard method in the semiconductor industry, the observed phenomenon can be utilized in designing future devices using $CuInP_2S_6$ layered ferroelectrics to increase their temperature range.

References

[1] F. Liu, L. You, K.L Seyler, X. Li, and others, “Room-temperature ferroelectricity in $CuInP_2S_6$ ultrathin flakes”, Nature Communications, N.7, p.12357, 2016.
[2] V.S. Shusta, I.P. Prits, P.P. Guranich, E.I. Gerzanich, A.G. Slivka, “Dielectric properties of $CuInP_2S_6$ crystals under high pressure”, Condensed Matter Physics, Vol. 10, pp. 91–94, 2007.
[3] M.A. Susner, M. Chyasnavichyus, A.A. Puretzky and others, “Cation−Eutectic Transition via Sublattice Melting in $CuInP_2S_6/In_{4/3}P_2S_6$ van der Waals Layered Crystals,” ACS Nano, Vol. 11, pp. 7060−7073, 2017.

X-RAY AND THERMOLUMINESCENCE OF GLASSY $LI_2B_4O_7$:GD AND LIB_3O_5:GD

V.M. Krasylynets, V.M. Holovey, I.I. Chychura

Institute of Electron Physics of the NAS of Ukraine, Uzhhorod, University str., 21, 88000, Ukraine, e-mail: kvn7@i.ua

A series of glassy $Li_2B_4O_7$:Gd (LTB:Gd) and LiB_3O_5:Gd (LBO:Gd) samples with a Gd_2O_3 content of 0.1–1.5 mol.% were synthesized. A study of their X-ray luminescence (XL) and thermoluminescence (TL) was carried out. A single peak with a maximum at 312 nm was found on the spectral dependences of the XL of all samples. The optimal content of Gd_2O_3 for x-ray phosphors based on them has been established. On the TL curves of glassy LTB:Gd and LBO:Gd in the entire range of activator concentrations, a single blurred low-intensity peak with a maximum at ~170-180°C was revealed.

Materials

The initial $Li_2B_4O_7$ (LTB) and LiB_3O_5 (LBO) were synthesized from high-purity boron oxide B_2O_3 and lithium carbonate Li_2CO_3. The glassy LTB:Gd and LBO:Gd samples with different contents of gadolinium oxide Gd_2O_3 were obtained by fusing calculated weights of previously obtained crystalline LTB or LBO with high-purity Gd_2O_3. For this purpose, their mixture was heated in platinum crucibles in the ambient atmosphere to 1020-1050°C and the resulting melt was kept at this temperature for ~15 h. Then, the crucible with the melt was rapidly cooled to 450°C. At these temperature it was additionally held for 3 hours to relieve stresses in the resulting ingot. After that, the crucible with the resulting product was cooled to room temperature (RT) in the furnace off mode. The glassy state of the obtained products and the absence of crystalline inclusions were confirmed by X-ray diffraction analysis using a DRON-4 X-ray diffractometer.

Further measurements of the spectral dependence X-ray luminescence (XL) were performed on samples made from LTB:Gd and LBO:Gd glassy slabs, which were in the form of plane-parallel plates of 5×5×1 mm with polished surfaces.

Experimental

Measurements of the spectral dependences of the XL and TL curves of glassy LTB:Gd and LBO:Gd samples were performed using the setups described in [1,2]. The samples were irradiated by radiation from an X-ray tube with a cobalt anticathode at a voltage of 35 keV and a current of 15 mA. The radiation dose rate was monitored using a ROBOTRON M2300 dosimeter. It was 7 Gy/min.

The irradiation dose of glassy LTB:Gd and LBO:Gd for studying their TL curves was 200 Gy and the heating rate was 0.5°C/s. TL curves were recorded no later than after 2 minutes. after the end of irradiation which made it possible to minimize the loss of intensity of low-temperature TL peaks due to fading.

Results

On the spectral dependences of glassy LTB:Gd and LBO:Gd a single peak with a maximum at 312 nm is observed, due to the optical transition $^6P_{7/2} \rightarrow {}^8S_{7/2}$ of the Gd^{3+} ion, in the entire concentration range of the activator. Its maximum intensity for LTB:Gd is observed at a Gd_2O_3 content of 1.0 mol. %. Then it decreases, which can be explained by the effect of concentration damping. For LBO:Gd the concentration dependence of the intensity of the above-mentioned peak is linear. According to the obtained data (table), the XL intensity of LBO:Gd glassy samples is much higher than that of LTB:Gd.

Table. Concentracion dependence of LTB:Gd and LBO:Gd glasses XL intensity.

Concentration Gd_2O_3, mol. %	LTB:Gd glass XL intensity, a.u. $x10^4$	LBO:Gd glass XL intensity, a.u. $x10^4$
0.1	0.45	0.72
0.5	1.83	3.48
1.0	3.45	7.24
1.5	2.86	11.95

The TL curves of glassy LTB:Gd and LBO:Gd have a single weak blurred peak with a maximum at ~170-180°C, the intensity of which decreases with increasing Gd_2O_3 content (Fig).

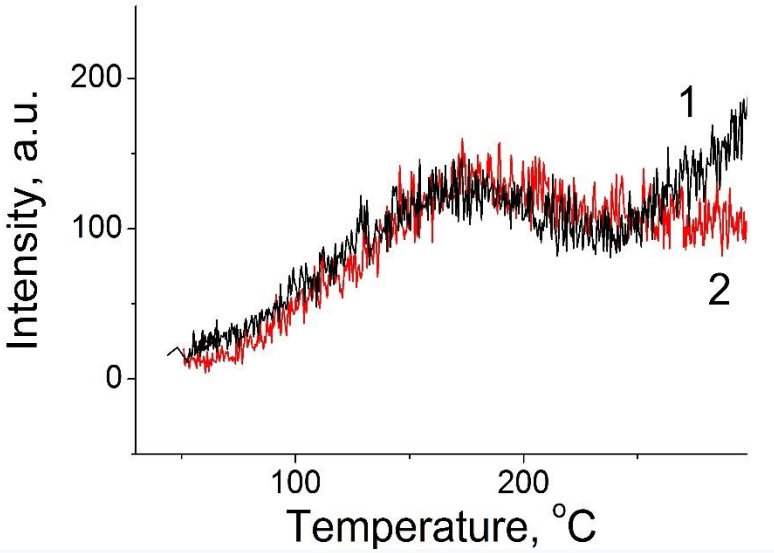

Fig. The TL curves of glassy LTB:Gd (1) and LBO:Gd (2)

The high XL intensity of glassy LTB:Gd and LBO:Gd samples compared to the insignificant intensity of their TL can be explained by the sharp predominance in their composition of charge carrier traps with low activation energy, the relaxation of which occurs already at RT. It is shown that glassy LTB:Gd and LBO:Gd are effective narrow-band phosphors for the UV range, thanks to which they can be used in photochemical and biological studies. Your Full Name

References

[1] B.M. Hunda et al., "Energy position of local adhesion levels and temperature dependence of X-ray luminescence of copper-doped single crystals of lithium tetraborate", Ukr. J. Phys., vol. 45, pp. 337-341, March 2000

[2] V.I. Lyamayev, "A low cost microcontroller-based measurement system for fractional glow technique", Meas. Sci. Technol., vol. 17, pp. 75-80, Dec. 2006, doi:10.1088/0957-0233/17/12/N01

FEATURES OF LOW-TEMPERATURE TRANSPORT PROPERTIES IN CO/AL_2O_3, CO/SIO_2 AND CO/TIO_2 GRANULAR NANOCOMPOSITES

O.E. Baibara[*], Y.A. Stelmakh[**], L.A. Krushinskaya[**], A.I. Ievtushenko[*]

[*]I.M. Frantsevych Institute for Problems of Material Science, National Academy of Sciences of Ukraine, 3 Omeljana Pritsaka str., Kyiv 03142, Ukraine, e-mail: o.baibara@ipms.kyiv.ua
[**]E.O. Paton Electric Welding Institute, National Academy of Sciences of Ukraine, 68 Antonowich str., Kyiv 03680, Ukraine

Granular nanocomposites (GN), consisting of magnetic nanoparticles randomly distributed in a dielectric matrix, occupy a special place in the class of granular materials. Due to the nanoscale of the nanoparticles (NPs), the existence of the core-shell structure in combination with the superparamagnetic nature of the fine NPs, GNs demonstrate new properties compared to the bulk samples, and can produce new physics that are absent in homogeneous materials. Despite the active research of GNs, a number of problems in understanding their properties remain open. These include the interpretation of the phenomenon of electrical conductivity and the explanation of the thermoelectric properties at concentrations below the metal-insulator transition [1,2].

Generally, the unique transport properties in granular nanocomposites are due to the existence of a percolation threshold, when at a certain concentration of metallic filler x it leads to the formation of an infinite conducting cluster due to the geometric contact of the filler. At concentrations below x, the system is in the dielectric regime and transport between the NPs occurs due to the transport of electrons or holes from charged to neutral NPs by hopping transport, which is the result of two combined mechanisms: thermal activation and tunnelling. While at relatively high temperatures, the usual activation mechanism is often observed for GNs, at lower temperatures and with a decrease in the NPs size, hopping transport can be effectively blocked by reducing the probability of tunneling of charge carriers from one nanoparticle to another. This results in the formation of the so-called Coulomb blockade, which leads to an increase in the low-temperature resistivity.

The resistivity of granular systems in the dielectric regime ($x < x_c$, where x_c is the percolation threshold) very often in a wide range of temperatures are described by the dependence: $\rho = \rho_0 \exp(T_0/T)^{1/2}$, where T_0 are sample dependent parameter, which holds the information on the dominating transport mechanism. It should be noted, that the such kind of $\rho(T)$ can be also observed in amorphous and doped crystalline semiconductors, for which the temperature dependence of the resistance is satisfactorily explained by the Efros-Shklovsky variable range hopping (VRH) processes.

However, how VRH concepts can be applied to granular systems remains open. One of the problems is that hopping processes in FMNC are associated with tunnelling through intermediate nanoparticles. While the tunnelling of electrons over long distances between distant centers of their localization is quite natural for doped semiconductors and arises from the exponential decay of the wave functions of the localized electrons, in GNs the metal occupies a finite volume of space, and hopping from one NP to another occurs through the nearest neighbor's grains with which they are connected by tunneling barriers. Therefore, debate arises in how to extend the VRH model of doped materials to granular metals. One of the primary concerns focuses on the value of characteristic temperature T_0 and the temperature range over which the law holds.

Granular nanocomposites with Co nanoparticles distributed in various dielectric amorphous matrixes Al_2O_3, SiO_2 and TiO_2 were grown by the EB-PVD method in the form of film with thickness from 0.8 to 10 μm on Al_2O_3 substrates (polycor). The Co concentration x varied in wide region from 10 to 70 at.% for all matrixes. Scanning electron microscopy studies have shown that for GNs with Co concentration in dielectric regime nanoparticles have dimensions near 5-10 nm and depends from the matrix. With increasing of Co concentration size of the NPs increases.

The temperature dependences of the resistance for GNs Co/Al_2O_3, Co/SiO_2 and Co/TiO_2 were investigated in the temperature range of 77 ÷ 290 K. Data were fitted by formula $\rho = \rho_0 \exp(T_0/T)^n$ where T_0 depends on the nature

of the material and n can assume values of 1/2 for granular materials. For GNs best fit corresponds to the value of n≈0.5 and discrepancy for different matrices are related to the peculiarities of the structure of these materials (Fig.1a). It has been shown that the value of the characteristic temperature T_0 depends from the concentration of Co and proportional s/d, where s is separations between NPs and d is the diameter of NPs.

We can also estimate a localization length (ξ) which is related through $T_0 = 2.8e^2/4\pi\varepsilon\varepsilon_0 k_B\xi$. Using the values for $\varepsilon(Al_2O_3) = 10.46$ and $T_0 = 8340$ K, we find $\xi \approx 6.7$ nm for sample with 13 at.% Co. The mean hopping distance and the average hopping energy between NPs are given by $r_o = \xi/4(T_0/T)^{1/2}$ and $W = k_BT/2(T_0/T)^{1/2}$ respectively. The corresponding values are calculated and plotted on Fig.1b.

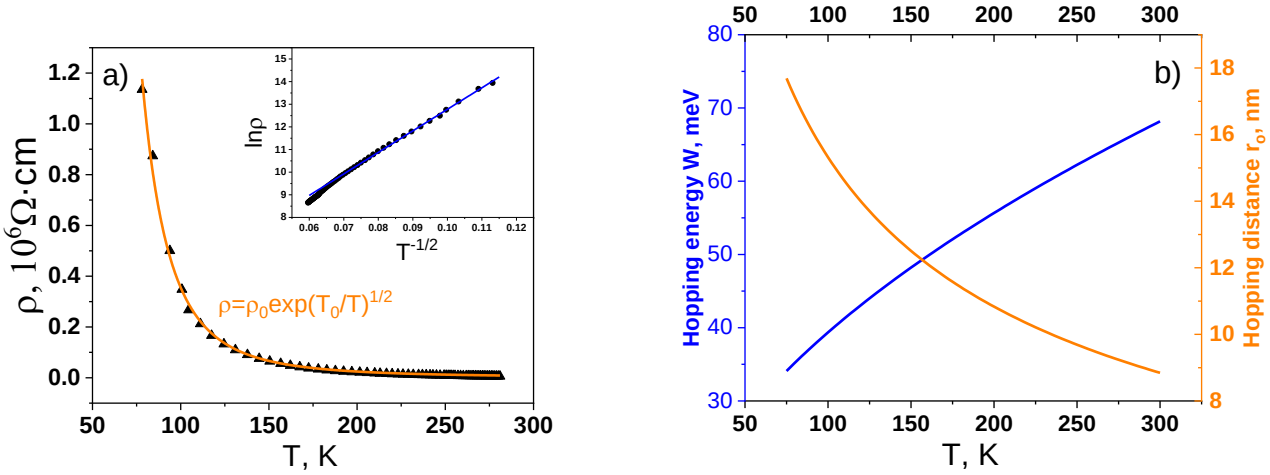

Fig. 1. Temperature dependence of the electric resistivity of Co/Al_2O_3 GN with 13 at.% Co (a); the average hopping energy and the mean hopping distance for Co/Al_2O_3 GN with 13 at.% Co (b)

Thermoelectric power (TEP) is another important physical quantity to investigate the transport properties of materials. The thermoelectric power (Seebeck coefficient) is defined as $S = \Delta V/\Delta T$ where ΔV is the electrical potential and ΔT is the temperature difference between the hot and cold ends of a sample. Thermoelectric properties were investigated in the temperature range of 77 ÷ 290 K and in magnetic fields up to 5 kOe. We observe negative value of thermoelectric power in the whole temperature range, which confirms that the charge carriers are the transferred electrons.

The significant increase in TEP (from the 10 μV/K at 280 K to near 3000 μV/K at 100 K) with decreasing temperature is observed for a GNs in the dielectric regime. It has been shown that the temperature dependence of the TEP is well described by an empirical formula $S(T)=A\exp(T_S/T)$ in temperature range 77-180 K. With a further increase in the concentration of the metallic phase, a quasi-metallic behavior of the TEP is observed with the appearance of a minimum, which is shifting towards lower temperatures. Theoretical justification requires further researches.

References

[1] G.V. Lashkarev, M.V. Radchenko, M.E. Bugaiova, O.E. Baibara, V. Knoff, T. Story, Y.A. Stelmakh, L.A. Krushinskaya, M. Foltyn and A.I. Dmitriev, "Giant Thermoelectric Power in Co/Al_2O_3 Ferromagnetic Nanocomposites Below Percolation Threshold", Phys. Stat. Sol. (b). vol. 254, pp. 153-158, 2017.

[2] G.V. Lashkarev, M. V. Radchenko, O. E. Baibara, M. E. Bugaiova, L.I. Petrosian, Y. Dumond, T. Story, W. Knoff, N. Nedelko, A. Ślawska-Waniewska, M. Foltyn, Y. A. Stelmakh, and L. A. Krushynskaya, "Nontrivial phenomena in magnetic nanocomposites Co/Al_2O_3 and Co/SiO_2", Low Temp. Phys. vol.45, pp. 228-231, 2019.

INFLUENCE OF THE PIEZOELECTRIC EFFECT ON THE Si-O-Gd CATHODE WORK FUNCTION

M.I. Fedorchenko*, O.I. Gudymenko, P.M. Lytvyn****

**Faculty of RadioPhysics, Electronics and Computer Systems Taras Shevchenko National University of Kyiv, 64/13 Volodymyrs'ka Str., 01601, Kyiv, Ukraine email: mifedorchenko@gmail.com*
***V. Lashkaryov Institute of Semiconductor Physics, National Academy of Sciences of Ukraine, 41 Nauka Ave., 03028, Kyiv, Ukraine email:gudymen@ukr.net*

Using the Auger electron and photoelectron spectroscopy, X-ray diffraction, atomic force, and Kelvin probe force microscopy techniques, the effect of a significant reduction in the work function of silicon surfaces upon adsorption of gadolinium and oxygen atoms on them was investigated. A model was proposed that explains the reduction of the effective work function of the Si-O-Gd surface to the value of 0.5-1.0 eV. This decrease is due to the layer of O-Gd dipoles on the cathode surface and the piezoelectric effect in the stressed crystallites of the textured phase in the volume of GdO_2 clusters.

We found that the oxidation of Gd atoms deposited on the Si surface leads to the creation of surfaces with a low work function of $\varphi \approx 0.5$-1 eV, which could become the basis for the creation of effective field emission cathodes [1-4]. The formed surfaces consist of protruding clusters with a diameter of 20–80 nm and a height of up to 20 nm. The heterogeneity of the surface relief correlates with the spatial distribution of the local work function. At the highest points of the relief, the smallest work function is observed. This behavior of the work function was explained by the formation of a layer of O-Gd dipoles near the surface. There was also an assumption about the possible influence on the output of the piezoelectric effect in the crystallites of the textured phase in the volume of protruding clusters, as it was established for the InGaN/GaN system [5]. But the textured phase type was not set. It was said that such a phase could be the Gd_2O_3, GdO_2 or $Gd_2Si_2O_7$ phase.

The purpose of this work was to conduct additional studies of the Si-O-Gd system using the Auger electron and photoelectron spectroscopy, scanning probe microscopy, and X-ray structural analysis to clarify our earlier experimental results and to propose an energy diagram of the Si-O-Gd cathode that would take into account all the results we obtained.

As a result of the research, it was established that the stressed textured phase is the GdO_2 phase.

Processing of the obtained data showed that due to the piezoelectric effect, an internal electric field with a strength of approximately 10^5 V/cm can arise in the volume of the strained crystallites of the textured GdO_2 phase.

The reduction of the effective work function of the Si-O-Gd cathode surface to 0.5-1.0 eV is due to the layer of O-Gd dipoles on the cathode surface and the piezoelectric effect in the stressed crystallites of the textured phase in the volume of GdO_2 clusters.

The energy diagram of the near-surface region of the Si-O-Gd cathode is presented.

Referenses

[1] M.G. Nakhodkin, M.I. Fedorchenko, Interaction of oxygen and gadolinium with Si(100)-2×1 surface. Formation of a system with 1-eV work function, Ukr. J. Phys., vol. 60, pp. 97-103, 2015.
[2] M.G. Nakhodkin, M.I. Fedorchenko, Photoelectron emission from Si–Gd–O cathode, Ukr. J. Phys., vol. 61, pp. 248-254, 2016.
[3] P.V. Melnik, M.G. Nakhodkin, M.I. Fedorchenko, Electronic and structural properties of Si-Gd-O electron emitter, Ukr. J. Phys., vol. 62, pp. 692-699, 2017.
[4] M.I. Fedorchenko, P.V. Melnik, M.G.Nakhodkin, O.I.Gudymenko, V.P.Kladko, P.M. Lytvyn Electronic and structural properties of Si-Gd-O electron emitter, Surf. Rev. and Lett., vol. 26, pp. 01-10, 2019.
[5] Robert D. Underwood, P. Kozodoy, S. Keller, S. P. DenBaars, and U. K. Mishra, Piezoelectric surface barrier lowering applied to InGaN/GaN field emitter arrays, Appl. Phys. Lett., vol. 73, pp.405-407, 1998.

THE INFLUENCE OF THE ULTRA-SMALL CONCENTRATINS OF FERROELECTRIC NANOPARTICLES ON THE IONIC TRANSPORT IN LIQUID CRYSTALS

Juliya M. Gudenko[1], Oleksandr S. Pylypchuk[1], Igor A. Gvozdovskyy[1], Serhii E. Ivanchenko[2], and Volodymir M. Poroshin[1]

[1]Institute of Physics, National Academy of Sciences of Ukraine, 46, pr. Nauky, 03028 Kyiv, Ukraine
[2]Frantsevich Institute for Problems in Materials Science, National Academy of Sciences of Ukraine, 3, str. Omeliana Pritsaka, 03142 Kyiv, Ukraine

The effect of the screening surface charge of $BaTiO_3$ nanoparticles on the ionic transport in a liquid crystal (LC 5CB) at low concentrations of the nanoparticles is shown. The current-voltage characteristics and the capacitance of the studied samples have significant changes already at concentrations of 0.5-1 wt.% of the nanoparticles. This is of interest because 1 wt. % of ferroelectric nanoparticles changes very little the effective permittivity, as well as the director orientation and elastic properties of the LC. The probable reason of the obtained results is the influence of ionic-electronic surface charges, which cover the ferroelectric nanoparticles and are polarized in an external field on the ionic transport in the LC.

Symmetric LC cells filled with pure 5CB nematic LC and a LC suspension with $BaTiO_3$ nanoparticles (NPs) of the average size 24 nm were studied. The studied cells were formed by two rubbed substrates (15×10 mm^2), oriented in the opposite direction of friction relative to each other, between which the studied suspensions were placed. The thickness of the cell is 21 ± 0.5 μm, the content of NPs is 0.5 wt.% and 1 wt.%. Current-voltage characteristics (I-V curves) of the LC cells measured in direct current mode, are shown in Fig. 1. It can be seen, the cell with pure LC has a lower electrical resistance than the cell with LC and NPs. Increasing the concentration of NPs from 0.5 wt.% to 1 wt.% leads to a further decrease in the resistance.

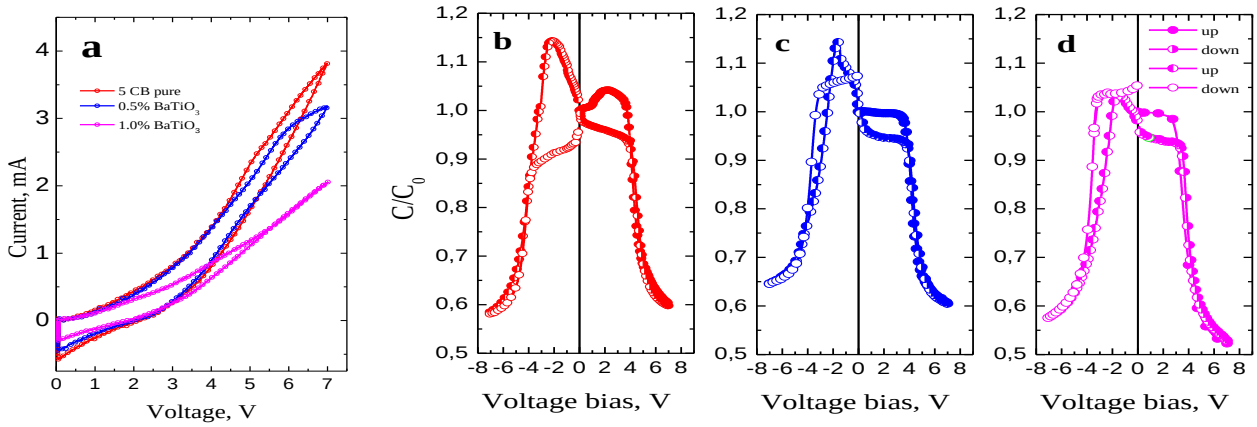

Figure 1. (a)*Current-voltage characteristics of the LC cells with different content of $BaTiO_3$ NPs measured at room temperature (300 K.* ***(b,c,d)*** *The dependence of the ratio C/C_0 (C is the capacitance, C_0 is a zero-bias capacitance) vs. the bias voltage of the LC cell with $BaTiO_3$ NPs measured at the T=300 K.* ***(b)*** *the cell with a pure LC 5CB (thickness 20 μm),* ***(c)*** *the LC cell with 0.5 wt.% $BaTiO_3$ NPs (thickness 20.7 μm),* ***(d)*** *the LC cell with 1.0 wt.% $BaTiO_3$ NPs (thickness 20.6 μm). The empty symbols correspond to increasing bias, filled symbols correspond to decreasing bias.*

A characteristic loop-like behavior is observed on the I-V curves, as well as on the volt-farad characteristics (C-V curves). The capacitance loop is the widest for a cell with pure LC, and becomes noticeably thinner in the presence of (0.5–1) wt.% of NPs (see Fig. 1). The reason for this may be the influence of ionic-electronic screening charges and the dielectrophoretic forces (which are very weak, but at the same time long-range) on the ionic

transport in the LC. If the I-V curves are more symmetrical with respect to the polarity change, the C-V curves are more asymmetric, which is explained, for example, by the removal of part of the space charge by a strong electric field.

The effective medium theoretical model is used for a calculating the effective capacitance of the 5CB LC and the 5CB colloidal with NPs. The effective medium approximation, also abbreviated as "EMA", was proposed by Carr et al. [1]. The calculated frequency dependences of the real part of the dielectric permittivity agree quantitatively with the experimentally measured curves (see Fig. 2).

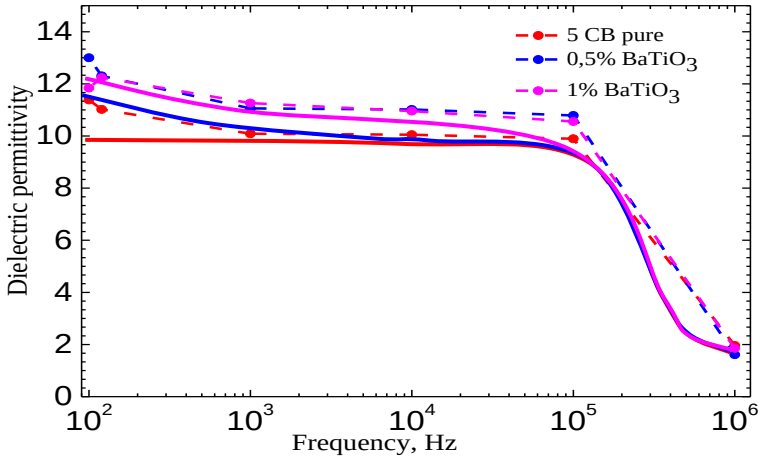

Figure 2. *Effective dielectric permittivity of the LC cells with $BaTiO_3$ NPs measured at 300 K (symbols joined by dashed lines). Solid curves are frequency dependences of the real part of the dielectric permittivity calculated in Ref.[4].*

Therefore, the visible influence of very small concentrations of $BaTiO_3$ NPs on the I-V and C-V curves of the LC 5CB has been revealed. The physical explanation of the observed effect is the influence of the surface screening charges of the NPs, which are polarized in the external field, on the slow ionic transport in the LC. To quantify the experimental results, we calculate the effective dielectric permittivity for an ensemble of NPs in a liquid dielectric medium in the effective medium approximation. Analytical calculations agree semi-quantitatively with experimental results. The obtained results can be used to adapt metamaterials for multiple practical applications.

Acknowledgement. The work of J.M.G. and O.S.P. are funded by the NRF of Ukraine: "Manyfold-degenerated metastable states of spontaneous polarization in nanoferroics: theory, experiment and perspectives for digital nanoelectronics", grant N 2023.03/0132. The work of V.M.P. is funded by the Target Program of the NAS of Ukraine, Project No. 4.8/23-p. The materials preparation characterization (S.E.I.) is sponsored by the NATO Science for Peace and Security Programme under grant SPS G5980 "FRAPCOM".

References

[1] G. L. Carr, S. Perkowitz, and D. B. Tanner. "Far-infrared properties of inhomogeneous materials."in: Infrared and millimeter waves. 13, ed. K.J. Button, Academic Press, Orlando. 171-263, 1985.

[2] O. S. Pylypchuk, S. E. Ivanchenko, M. Y. Yelisieiev et al." Anomalous Behavior of the Dielectric and Pyroelectric Responses of Ferroelectric Fine-Grained". Ceramics. https://doi.org/10.48550/arXiv.2407.01108.

[3] A. Bogi & S. Faetti. "Elastic, dielectric and optical constants of 4'-pentyl-4-cyanobiphenyl". Liquid Crystals. 28:5, 729-739,2001. http://dx.doi.org/10.1080/02678290010021589.

[4] J. M. Gudenko, O. S. Pylypchuk, V. V. Vainberg et al. "Ferroelectric Nanoparticles in Liquid Crystals: The Role of Ionic Transport at Small Concentrations of the Nanoparticles". Submitted to the Semiconductor Physics, Optoelectronics and Quantum Electronics, 2024.

PREPARATION OF POLYVINYL CHLORIDE/OXIDIZED ACTIVATED CARBON THIN-FILM COMPOSITES AND THEIR MICROWAVE ABSORPTION PRORERTIES

D.O. Zhytnyk*, I.P. Matushko, Yu.V. Noskov ***,**

V.A. Moiseienko**, O.V. Mischanchuk***** and L.M. Grishchenko***

**Faculty of RadioPhysics, Electronics and Computer Systems Taras Shevchenko National University of Kyiv, Kyiv 01601, Ukraine, email: radiodima2000@gmail.com*
***Faculty of Physics, Taras Shevchenko National University of Kyiv, Kyiv 03127, Ukraine, email: mipigor@gmail.com*
****Kukhar Institute of Bioorganic Chemistry and Petrochemistry, the National Academy of Science of Ukraine, Kyiv 02160, Ukraine, email: yuriy.noskov@gmail.com*
*****Independent Research & Development Laboratory "200k Electronics", Kyiv 01030, Ukraine, email: vamrpd@gmail.com*
******O.O. Chuiko Institute of Surface Chemistry of NAS of Ukraine, Kyiv 03164, Ukraine, e-mail: bigsnake@i.ua*

This study presents the preparation of thin composite films using polyvinylchloride as the base material and oxidized activated carbon samples as fillers, their study by the methods of SEM, TPD MS, TGA, FTIR. The microwave absorbing properties of the resulting films in the Ka-band were investigated.

Introduction

Carbon materials (CMs) have unique mechanical and physicochemical properties, which are determined by the surface chemistry and developed porous structure. They are widely used in many areas - they are used as catalysts, adsorbents, supercapacitors, and also as fillers in composite materials for electromagnetic shielding [1, 2]. One of the important advantages of CMs is their ability to chemical modification, which is important for the creation of materials with a set of predetermined properties, since the introduction of functional groups or heteroatoms into the surface layer of CMs can significantly affect not only the chemical properties of such materials, but also on the nature of the interaction of such material with electromagnetic radiation.

The purpose of this work was to obtain a composite material based on polyvinyl chloride as a polymer matrix and modified activated carbon and to study the microwave properties of the obtained composites.

Experimental

Activated carbon (AC) derived from apricot (*Prunus armeniaca* L.) pits was prepared by carbonization/steam activation technology. PVC was purchased from Sigma-Aldrich. Modification was carried out by oxidizing AC with a 15% solution of hydrogen peroxide (AC-H_2O_2), then washed with distilled water to a non-permanent pH of the washing water and dried in air at 120°C. Thin films of PVC/AC-H_2O_2 composites were prepared as follows. First, the AC-H_2O_2 powder was deashed by repeated washing with HCl solution (3 wt%). Then, the deashed AC-H_2O_2 powders were washed with distilled water until the pH of the washing water was 5.5–6.0, and then the deashed AC powders were filtered and air-dried at 110 °C. Then, a series of $(PVC)_{100-x}/(AC\text{-}H_2O_2)_x$ films were obtained by the method of hot pressing of powders of PVC and AC taken in different weight ratio x =0,2 -30 wt% of AC-H_2O_2. In the typical preparation, the deashed AC powder was first ground in an agate mortar. Then 0.2 g of PVC powder was mixed with the required amount of carbon. This mixture was reground in the same mortar to a relatively homogeneous state. It was then poured into a mold on a polyamide substrate and 70 mg of di-butyl phthalate (DBP) plasticizer for PVC was added. The $(PVC)_{100-x}/(AC\text{-}H_2O_2)_x$ films were prepared by pressing at 175 °C and 10 MPa pressure for 1 minute. The resulting $(PVC)_{100-x}/(AC\text{-}H_2O_2)_x$ composites and pure hot-pressed PVC samples prepared without AC-H_2O_2 were approximately 0.25 mm thick and 23 × 12 mm in size. These samples were used for further testing.

Results and discussion

The obtained material has the form of thin flexible films and contains a filler (AC-H_2O_2) that has a developed porous structure and a specific surface. It is shown that the oxidation of carbon with a hydrogen peroxide solution of the specified concentration is optimal for these samples of fillers, as they provide an optimal ratio of grafted functional groups/specific surface area. According to the SEM data, the oxygen concentration in oxidized carbon increases by more than 4 times compared to the initial AC sample. The concentration of all types of oxygen-containing functional groups of the filler was identified and quantified using the TPD IR method and titration according to the Böhm method. When studying the samples of composites by the FTIR method, it was found that the characteristic bands of PVC in the FTIR spectra of the films, regardless of the carbon content, are in most cases very slightly shifted compared to the pure polymer, or there is no shift at all. This indicates the absence of any chemical interaction between PVC and carbon in their mixture. However, physical interactions such as van der Waals bonds may be present. Some individual bands have a position in the mixture that is 5 cm^{-1} different from that in pure PVC, and this already indicates the presence of some chemical interaction between the components of the mixture, in particular, it is possible that such a shift is due to the formation of hydrogen bonds.

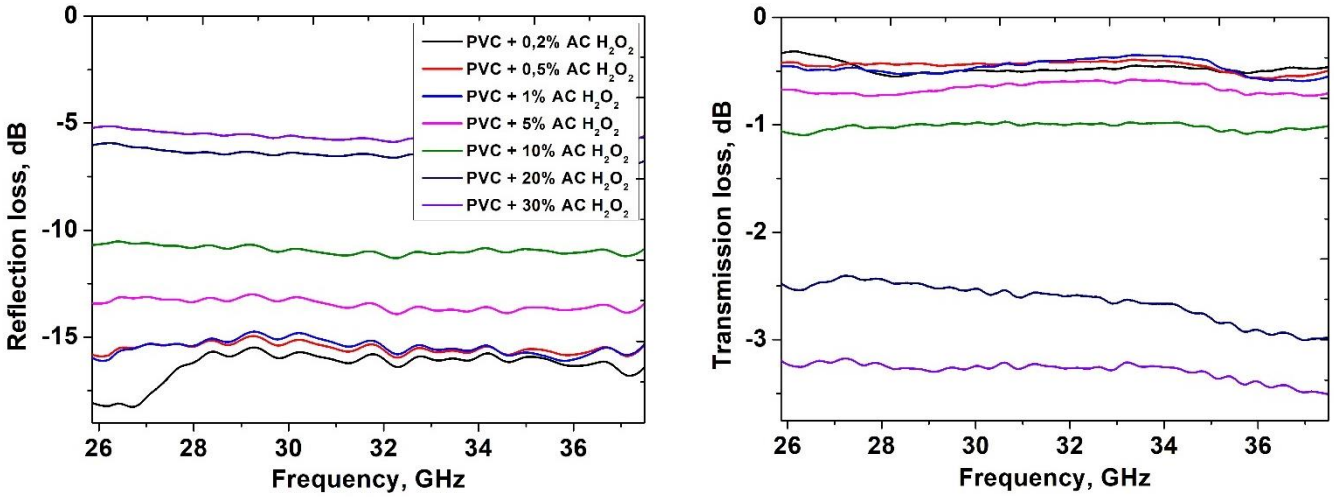

Fig.1. Frequency dependence of the reflection losses (a) and transmission losses (b) of the pure PVC and $(PVC)_{100-x}/(AC\text{-}H_2O_2)_x$ composite films in the Ka-band of microwaves

When studying the microwave properties of composite samples, it was established that the obtained material is radio-transparent in the Ka-band for low concentrations of AC-H_2O_2 (up to 10%), and by changing the concentration of the filler, the amount of reflection of microwave waves in the Ka-band can be programmed. A significant effect of filler concentration on the nature of interaction with EMF in the microwave band is shown. The tendency to increase the reflection loss value is observed over the entire investigated range of filler concentrations, the reflectance increases proportionally to the concentration of activated carbon in the composite, and reaches its maximum at a concentration of 30%. A significant decrease in transmittance is observed only for large filler concentrations (20%, 30%) in the composite, the average value of which is minimal for the sample with the maximum filler content.

References

[1] C. Li, D. Li, L. Zhang et al., "Boosted microwave absorption performance of transition metal doped TiN fibers at elevated temperature," *Nano Res.*, vol. 16, pp. 357-3579, Feb. 2023, doi: 10.1007/s12274-023-5398-3.

ELECTRONIC STRUCTURE OF THE NI:ZNSES SOLID SOLUTIONS

S.V. Syrotyuk, A.Y. Nakonechnyi, Y.V. Klysko

Lviv Polytechnic National University, Computerized Automation Systems Department
stepan.v.syrotiuk@lpnu.ua; adrian.y.nakonechnyi@lpnu.ua; yurii.v.klysko@lpnu.ua
Lviv 79013, 12 S. Bandera str, Ukraine

The spin-polarized electronic energy spectra of the Ni:ZnSeS solid solution were obtained based on calculations for the supercell, containing 64 atoms. At the first stage the structure parameters of the ZnSeS solid solution in the wurtzite structure have been optimized. Two steps were taken to achieve optimal structural parameters. First, the supercell parameters were optimized, and than, the internal coordinates of the atomsin a supercellhave been adjusted. Further, the structurally optimized supercells were used as a basis for obtaining the properties of the Ni:ZnSeS material, in which Ni replaces the Zn atom. The results of the calculations revealed significant differences in the parameters of the electronic energy spectrum of Ni:ZnSeS solid solutions related to the content of Se and S atoms.

Motivation

The ZnX compounds (X = S, Se, Te) with impurities of transition 3d elements are currently well studied experimentally. In particular, the characteristics of energy transmission in the mid-infrared range by ZnSe laser crystals doubly doped with Fe and Cr atoms were studied in works [1, 2]. The room-temperature kinetics of the Fe:Cr:ZnSe sample below the excitation of the chromium ion at 1560 nm shows that the energy transfer in the Fe-Cr- centers is characterized by a time of 290 ns.

However, solid solutions of T:ZnSeS (T = transition 3d element) are practically unexplored today. The lack of research results of the electronic structure of these materials makes the task of this problem urgent. That is why this work is devoted to the electronic theory of the mentioned materials using the example of Ni:ZnSeS, i.e. a solid solution of wurtzite ZnSeS with the Ni impurity, which replaces the Zn atom.

Results and discussions

The spin-polarized densities of 3d electronic states (DOS) for the solid solutions Ni:ZnSeS in the wurtzite structure are shown in Fig. 1. The energy is calculated relative to the Fermi level, i.e. E_F=0.

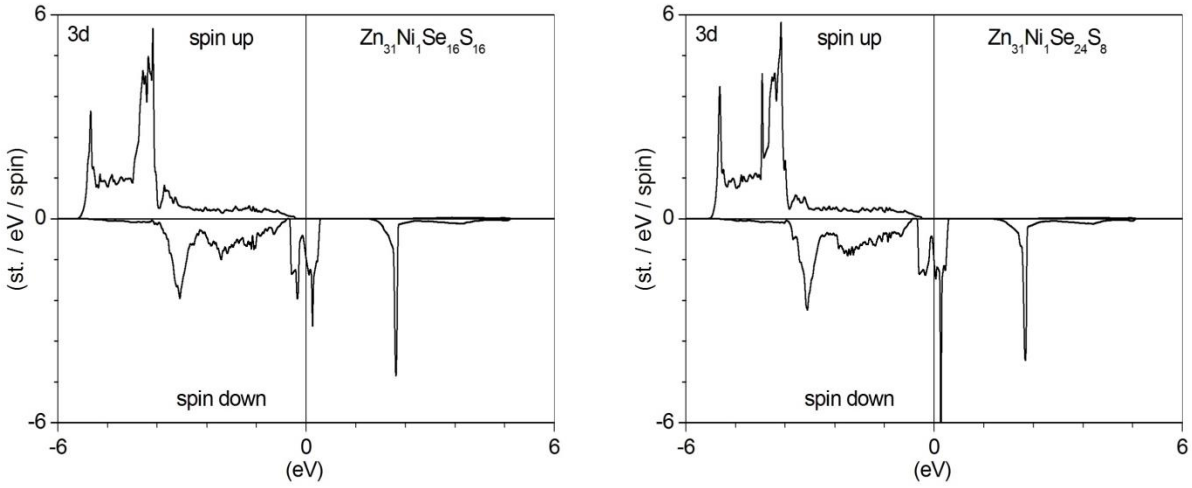

Fig. 1. The spin-polarized partial DOS of 3d electrons in Ni:ZnSeS solid solutions

For the material whose model is the supercell (Fig. 1) $Zn_{31}Ni_1Se_{16}S_{16}$, we obtained the following results. For the spin up the material is a direct band semiconductor with E_g = 1.58 eV. The spin down states show a metallic behaviour. The value of magnetic moment of a supercell equals to 2 μ_B

For the material represented by a supercell (Fig. 1) $Zn_{31}Ni_1Se_{24}S_8$ the obtained results are as follows. For the spin up the material is a direct band semiconductor with E_g = 1.55 eV. The spin down states show a metallic behaviour. The value of magnetic moment of a supercell equals to 2 μ_B.

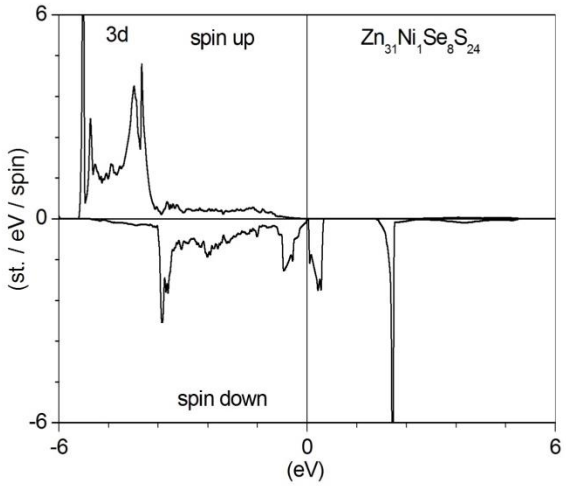

Fig. 2. The spin-polarized partial DOS of 3d electrons in Ni:ZnSeS solid solution

For the material represented by a supercell (Fig. 2) $Zn_{31}Ni_1Se_8S_{24}$ the obtained results are as follows. For the spin up states the material is a direct band semiconductor with E_g = 0.13 eV. For the spin down states the material also shows a semiconductor properties, with E_g = 1.83 eV. The value of magnetic moment of a supercell equals to 1.97 μ_B.

The electronic energy band structure of the hexagonal solid solutions ZnSeS with the Ni impurity has been evaluated by means of the ABINIT code [3]. It was established that the parameters of the electronic structure depend on the concentration of Se and S elements. In particular, materials represented by supercells $Zn_{31}Ni_1Se_{16}S_{16}$ and $Zn_{31}Ni_1Se_{24}S_8$ are semimetals. Therefore, it makes sense to study their application in spin electronics. However, this cannot be said about the material represented by the supercell $Zn_{31}Ni_1Se_8S_{24}$, since it exhibits semiconducting properties for both spin orientations.

References

[1] U. Demirbas, A. Sennaroglu, N. Vermeulen, H. Ottevaere, H. Thienpont, Continuous-wave fiber-pumped Cr2+:ZnSe laser. Proc. SPIE 6190, Solid State Lasers and Amplifiers II 61900A(10), 2006.

[2] V. Fedorov, T. Carlson, S. Mirov, Energy transfer in iron-chromium Co-doped ZnSe middle-infrared laser crystals. Opt. Mater. Exp. (9) 2340 – 2347, 2019.

[3] X. Gonze et al., *Recent developments in the ABINIT software package*, Comput. Phys. Comm. 205, 106 (2016).

OLED ON QUANTUM WELLS

Nataliia Kuzyk*, Pavlo Stakhira, Volodymyr Fitio*****

**Department of Electronic Engineering, Lviv Polytechnic National University, Lviv-79013, Ukraine, e-mail: nataliia.i.kuzyk@lpnu.ua*

***Department of Electronic Engineering, Lviv Polytechnic National University, Lviv-79013, Ukraine, e-mail: pavlo.y.stakhira@lpnu.ua*

**** Department of Electronic Engineering, Lviv Polytechnic National University, Lviv-79013, Ukraine, e-mail: volodymyr.m.fito@lpnu.ua*

An analysis of the emission of a typical OLED structure with three quantum wells has been conducted. The discrete energy levels of electrons and holes in the quantum wells were calculated by solving the stationary Schrödinger equation in the frequency domain. The evaluation demonstrated the localization of electrons and holes within the respective quantum wells. Considering the conducting evaluations of the bandgap of the organic semiconductor, the binding energy of the exciton, and the discrete energy levels of electrons and holes, an assessment of the emission spectrum of such an OLED was made.

Introduction

A distinctive constructive feature of quasi-two-dimensional organic heterostructures (OLEDs) based on quantum wells is the presence of a narrow-band emitting layer with a thickness comparable to the exciton Bohr radius (less than 10 nm) [1]. This emitting layer is formed between two wide-band organic layers with equable nanoscale thickness. Such a design of the organic light-emitting diode leads to an increase in the binding energy of Frenkel excitons localized in 2D quantum wells [2], which helps prevent the decrease in OLED efficiency with increasing brightness due to reduced triplet-triplet annihilation [3]. Typically, to more effectively mitigate this negative effect that arises at high current densities, the electroluminescent recombination zone is expanded by employing a cascade of quantum wells (Fig. 1) [4].

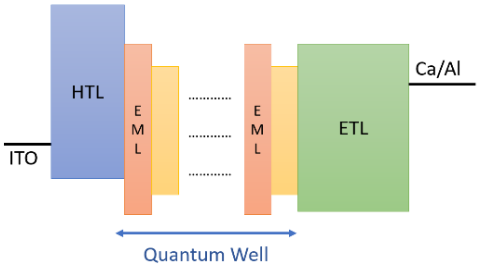

Fig. 1 A schematic diagram depicting the energy levels of OLEDs with MWQ structure [1]

In this study, a method of evaluating the discrete energy levels of electrons and holes in the respective quantum wells is presented through the solution of the stationary Schrödinger equation in the frequency domain, which is detailed in reference [5]. Additionally, by considering the binding energy of the electron and hole in the exciton and the bandgap width, the peak wavelength of electroluminescence can be determined.

The outcomes of the calculation of discrete levels of electrons and holes in quantum wells

The one-dimensional stationary Schrödinger equation is expressed as follows:

$$-\frac{\hbar^2}{2m}\frac{d^2\psi(x)}{dx^2} + U(x)\psi(x) = E\psi(x)\,. \tag{1}$$

In practice, a modified equation is applied, which is derived through a change of variables; the transformed equation (1) will be represented as follows:

$$-\frac{d^2\psi(x)}{dx^2} + U(x)\psi(x) = E\psi(x). \quad (2)$$

$\psi(x)$ functions, as a solution of the stationary Schrödinger equation corresponding to discrete energy levels, and their first derivatives approach zero in case if $x \to \pm\infty$. Therefore, for these functions, as well as their first and second derivatives, a Fourier transform exists, which is respectively equal [8]:

$$\psi(u) = \int_{-\infty}^{\infty} \psi(x)\, exp(-i2\pi ux)\, dx\,, \quad (3)$$

$$i2\pi u\psi(u) = \int_{-\infty}^{\infty} \frac{d\psi(x)}{dx} exp(-i2\pi ux)\, dx\,, \quad (4)$$

$$-(2\pi u)^2\psi(u) = \int_{-\infty}^{\infty} \frac{d^2\psi(x)}{dx^2} exp(-i2\pi ux)\, dx. \quad (5)$$

In case for both functions $g(x)$ and i $h(x)$, a Fourier transform exists, consequently $F\{g(x)\} = G(u)$, $F\{h(x)\} = H(u)$, the equation [8]

$$F\{g(x)h(x)\} = \int_{-\infty}^{\infty} G(u-v)H(v)dv\,, \quad (6)$$

$F\{...\}$ is a Fourier transformation. The content of the convolution theorem is described in expression (6)

A Fourier transformation was performed on both the right and left sides of equations (2), utilizing equations (3), (5), and (6). As a result, we obtain the following equation:

$$4\pi^2u^2\psi(u) + \int_{-\infty}^{\infty} U(u-v)\psi(v)dv = E\psi(u). \quad (7)$$

Thus, we have transitioned from the differential equation (2) concerning eigenfunctions (wave functions in the coordinate domain) and eigenvalues (corresponding to discrete energy levels) to the integral equation (7). In this equation, we can replace the integral with a summation and substitute continuous variables with discrete ones, resulting in:римаємо:

$$4\pi^2(s\Delta)^2\psi(s\Delta) + \sum_{p=-(N-1)/2}^{(N-1)/2} U(s\Delta - p\Delta)\psi(p\Delta)\,\Delta = E\psi(s\Delta), \quad (8)$$

де $\Delta = u_{max}\, u_s = s\Delta,\ v_p = p\Delta, -(N-1)/2 \le s, p \le (N-1)/2, s, p,$ – whole numbers.

$u_{\max}$ should be taken at such diapason, that on frequencies $|u| \ge u_{max}$ values of $\psi(u)$ were almost equal zero, at the same time N should have enough amount and preferably unpaired. It's evident that the sum in (10) should have N elements.

The last equation will be written for all discrete spatial frequencies причому міняється від до тоді сукупність цих рівнянь у кількості можна записати у вигляді матричного рівняння, причому є спільною для всіх :

$$(\boldsymbol{P} + \boldsymbol{U})\Psi = E\Psi, \quad (9)$$

where $\boldsymbol{P}$ – is a diagonal matrix with elements $4(\pi s\Delta)^2$, $\boldsymbol{U}$ – is a square symmetric matrix with elements $U(s\Delta - k\Delta)$, Ψ – is a vector-column with elements $\psi(s\Delta)$. and is the discret Fourier transform of the wave function, which corresponds to a discrete energy level E that stays in accordance with the postulates of quantum

mechanics and should be valid. Multiple eigenvalues and their corresponding eigenvectors may be obtained. By performing the inverse discrete Fourier transform of the eigenvector, the eigenfunction is derived $\psi(x)$.

To find the discrete energy levels of electrons and holes in quantum wells, the structure illustrated in Fig. 1 must be divided into three substructures: for electrons, the zero potential energy level will be situated at the top of the interlayer conduction band of the MQW; for holes, the zero potential energy level will be positioned at the valence band lowest energy value of the, with the width of the forbidden band defined as their difference.

Thus, in the quantum structure, changes in the energy constraints for the corresponding layers will be observed for electrons (from left to right)::-2.1→1.9,-2→2,-2.4→1.6,-4.0→0,-2.5→1.5,-4.0→0,-2.5→1.5,-4.0→0,-2.5→1.5,-2.7→1.3; the similar changes will be gained for holes:-5.2→0.7,-5.5→0.4,-6.0→-0.1,- 5.9→0,-6.8→-0.9,- 5.9→0,-6.8→-0.9,- 5.9→0,-6.8→-0.9,-6.0→-0.1.i.

Acknowledgment

This work was approved and financially supported by the Ministry of Education and Science of Ukraine under the grant program of the National Research Foundation number 0124U003833

References

[1] L. Cheng, T. Jiang, Y. Cao, C. Yi, N. Wang, W. Huang, & J. Wang, “Multiple-quantum-well perovskites for high-performance light-emitting diodes” Advanced Materials, vol. 32, Apr. 16, 2020.

[2] B. Yurke, R. Elliott & A. Sup, “Implementation of a Frenkel exciton-based controlled phase shifter” Implementation of a Frenkel exciton-based controlled phase shifter”

[3] I. Hladka, R. Lytvyn, D. Volyniuk, D. Gudeika, J. V. Ggrazulevicius, “W-shaped bipolar derivatives of carbazole and oxadiazole with high triplet energies for electro-luminescent devices”. Elsevier, Dyes Pigments vol. 149, pp. 812-821, Feb. 2018.

[4] Y Danyliv, D Volyniuk, O Bezvikonnyi, I Hladka, K Ivaniuk, I Helzhynskyy, P Stakhira, A Tomkeviciene, L Skhirtladze, J.V Grazulevicius, “Through-space charge transfer in luminophore based on phenyl-linked carbazole-and phthalimide moieties utilized in cyan-emitting OLEDs”, Elsevier, Dyes and Pigments, vol. 172, Jan. 2020.

[5] L. Yingkui, “Nondoped phosphorescent organic quantum well light-emitting device based on iridium complex: Synthesis, characterization, photophysical property, and electroluminescence performance”, Journal of Luminescence, vol. 131, pp. 1821–1826, Sep. 2011

[6] A. David, B. Miller, Optical physics of quantum wells, in Quantum Dynamics of Simple Systems, CRC Press, Boca Raton, 2020.

[7] V. Fitio, I. Yaremchuk, V. Romakh, & Y. Bobitski, “A Solution of One-Dimensional Stationary Schrödinger Equation by the Fourier Transform”, ACES JOURNAL, Vol. 30, No. 5, pp. 534-539, May 2015.

[8] J. W. Goodman, Introduction to Fourier Optics, McGraw-Hill Book Company, 1968.

APPLICATION OF CONCENTRATED SOLAR RADIATION FOR GROWING OF ZnO-Zn MICRO - AND NANOSTRUCTURES

Y.O. Kovalskyi[1], V. A. Karpyna[1], O.I. Olifan[1], S. P. Starik[2], D.S. Kamenskyh[2,3], A. I. Ievtushenko[1]

[1]I. Frantsevich Institute for Problems of Materials Science, NAS of Ukraine, 3 Omeljana Pritsaka str., Kyiv, 03142, Ukraine, y.kovalskyi@ipms.kyiv.ua
[2]V. Bakul Institute for Superhard Materials, NAS of Ukraine, 2 Avtozavodskaya str., 04074, Kyiv, Ukraine
[3]V. Kukhar Institute of Bioorganic Chemistry and Petrochemistry, NAS of Ukraine, 1 Academician Kukhar Str., Kyiv 02094, Ukraine

ZnO is a direct wide bandgap semiconductor with a high exciton binding energy (about 60 meV), exhibiting high UV emission and high transparency in the optical range, electron conductivity, making it promising for optoelectronic applications in the ultraviolet region of the spectrum. The properties of ZnO are closely dependent on the microstructure of the material, including crystal size, orientation, morphology and aspect ratio. In addition, ZnO is biologically safe and biocompatible, and can be used for biomedical applications without coating [1]. ZnO micro- and nanostructures have also been used as sensors with a high specific surface area, ultraviolet radiation sources, LEDs, and field-effect electronic display systems. Studies have shown that to create high-quality crystal structures, it is necessary to ensure a high growth rate, which can be achieved using the method of explosive evaporation (MEE) [2].

In different modification of CVD methods (for example, MOCVD, APMOCVD, PEMOCVD, etc) for evaporation of precursors one can used various electrical heaters or the last ones were placed in a furnace using quartz tubes as synthesis reactors that result in low-speed evaporation of precursors. The inertia of such heaters may lead to problems with the uniformity and stoichiometric ratio of ZnO nanostructures (NS) [3]. Therefore, the development of growth methods with high-speed precursor evaporation is interesting for the deposition of uniformly high-quality ZnO nanostructures. Hence, we propose a method of ZnO nanostructures growth that makes use of a solar concentrator. In a solar concentrator (Fig.1), the energy of the Sun is focused on the place where precursor boat is arranged.

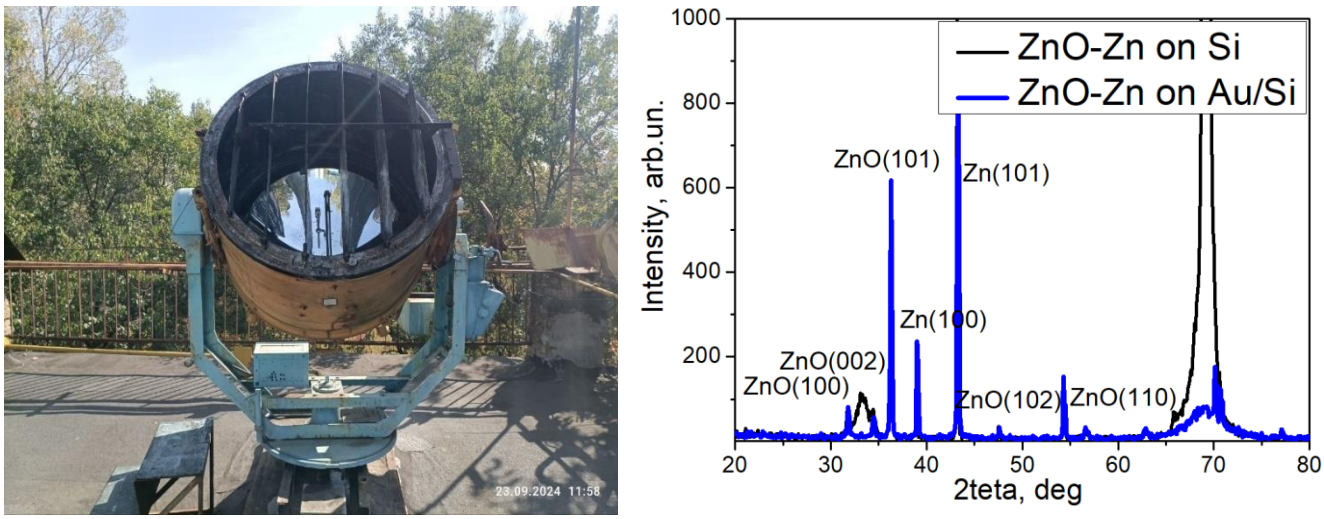

Fig 1. Solar concentrator of Geliocenter of I. Frantsevich Institute for Problems of Materials Science (Kyiv, Ukraine) (left) and XRD patterns of ZnO-Zn samples deposited on various substrates (right)

Therefore, the use of concentrated solar radiation allows the implementation of the condition for high-speed evaporation of the precursor. We called the proposed method of deposition as the method of explosive evaporation [2] because a precursor evaporated very quickly (resembling an explosion) due to the application of high power concentrated solar radiation.

The ZnO-Zn micro- and nanostructures were grown on unpolished Si substrates and polished Si substrates coated with gold (Au/Si) films, and the precursors (mixtures of ZnO-Carbon powders) were evaporated under the influence of intense solar radiation at the facilities of the Geliocenter of I. Frantsevich Institute for Problems of Materials Science, NAS of Ukraine (Kyiv, Ukraine).

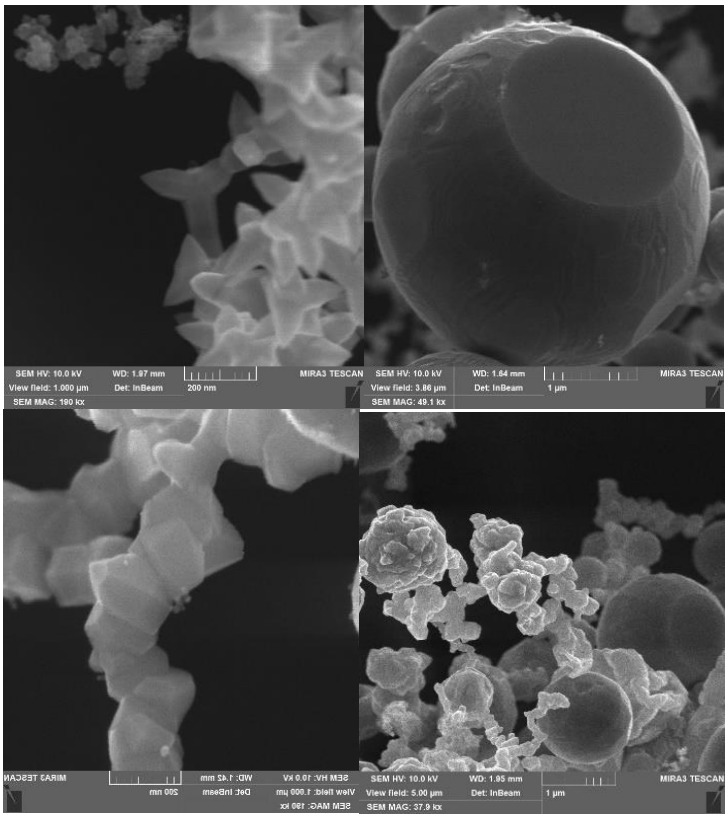

Fig. 2. SEM images of ZnO-Zn samples grown on Si and Au/Si substrates by the using concentrated solar irradiation

We carried out the XRD (Fig.1, right), SEM (Fig. 2) and elemental composition measurements that confirm the formation of ZnO-Zn micro- and nanostructures. The results will be discussed in detail.

References

[1] H. S. Jang, G. H. Jeong, H. J. Lee, H. S. Shin, Y. Hwa, S.-S. Chee, S. Y. Paek, J. M. Kim, B. Son, D. Kang, G. H. Ryu, "A general and facile approach to flower-like ZnO fabrication, Materials Today Advances," Materials Today Advances, vol. 20, pp. 100424, Dec. 2023.

[2] A. Ievtushenko, V. Tkach, V. Strelchuk, L. Petrosian, O. Kolomys, O. Kutsay, V. Garashchenko, O. Olifan, S. Korichev, G. Lashkarev and V. Khranovskyy, "Solar Explosive Evaporation Growth of ZnO Nanostructures," Applied Sciences,. vol.7, pp. 383, 12 Apr. 2017.

[3] V. Khranovskyy, I. Tsiaoussis, G.R. Yazdi, L. Hultman, R. Yakimova "Heteroepitaxial ZnO nanohexagons on p-type SiC. " Cryst. Growth, vol.312, pp.327–332, 09 May 2009.

JOSEPHSON JUNCTIONS WITH A METAL-DOPED SEMICONDUCTOR BARRIER

V.E.Shaternik*, V.L.Makivska*

** G.V.Kurdyumov Institute for Metal Physics,Vernadskii blvrd,36,Kyiv-03142,Ukraine,*
e-mail:Shaternikvolod@gmail.com

Josephson junctions with metal-doped semiconductor barriers are created and studied. The discussion is done within the framework of the multiple Andreev reflection model.

Superconducting Josephson junctions superconductor-barrier-superconductor have already found wide application in microelectronics, computer systems for recording and processing information, ultra-fast analog-to-digital converters, ultra-sensitive sensors of magnetic fields and microwave radiation, medicine, biology, geology, etc.

At the moment, Josephson junctions look like the most promising element base for creating a quantum Josephson computer and a cryogenic superconducting ultra-fast computer based on RSFQ (rapid single-flux logic), the development of which is being intensively carried out in developed countries of the world.

Technologically, Josephson junctions are manufactured either in the form of thin-film superconductor-insulator (or metal)-superconductor structures or in the form of point contacts of superconductors. The disadvantage of thin-film junctions is their relatively large capacity, which reduces the speed of these junctions and their operating frequencies. The point contacts junctions have an attractive negligible capacitance, but are mechanically unstable in operation.

The objective of the study was to develop and manufacture Josephson junctions that would be free from the above-mentioned drawbacks. Currently, nanostructured Josephson heterostructures are considered to be one of the most promising, in which charge transport occurs through energy states localized in their amorphous semiconductor barriers.

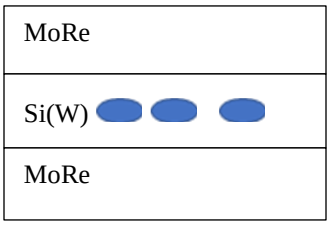

Fig.1.

Thin-film MoRe-Si(W)-MoRe junctions (Fig.1) were fabricated by magnetron sputtering of targets in an argon atmosphere, followed by deposition of thin films through metal masks on polycrystalline aluminum oxide (polycor) substrates or on sapphire substrates.

The film deposition was carried out at room temperature, so the films were formed amorphous. The Si(W) barrier films were formed by sputtering a complex target consisting of a single-crystal silicon Si plate, on the surface of which tungsten W wires of 0.3 mm thickness and about 10 mm length were laid in the amount of 20–30 pieces. The manufactured thin amorphous MoRe films had a critical superconducting transition temperature $T_C \approx 9.1$ K. The Si(W) barrier films had a thickness of several nanometers. It is impossible to study such a thickness of Si(W) films by transmission electron microscopy, since these films were burned through by the electron beam even at reduced voltages.

But the study of transmission electron microscopy of thicker Si(W) films produced under the same technological conditions showed that clusters of amorphous tungsten W are formed in amorphous silicon films Si.

A typical I–V characteristic of one of the MoRe-Si(W)-MoRe junctions is shown in Fig. 2

In order to study the distribution of transparencies in the formed Si(W) barrier,the model of multiple Andreev reflections was used, within the framework of which the quasiparticle I–V characteristics of the junctions were calculated and compared with the experimental ones [1].

An electron enters a quantum well between two superconductors and cannot leave it – Andreev reflections occur on the left and on the right (fig.3) the electron tunnels through the barrier and gains energy eV at each pass until attenuation. Current is transferred at each reflection, these contributions are summed up and the I–V characteristics are calculated (see Fig. 4) for barriers of different transparencies. It is also possible to calculate the

I–V characteristics for barriers with non-uniform transparency, when part of the junction area has low transparency, and the remaining area has high transparency (see Fig. 5). Based on the appearance of such quasiparticle I–V characteristics, it can be concluded (Fig. 2) that in the given case, the current in the junction is

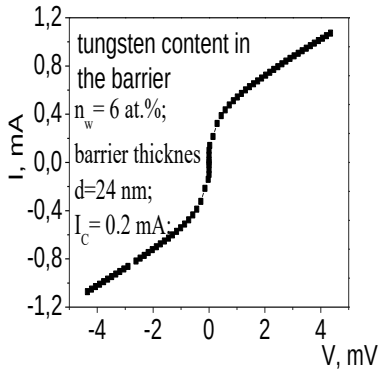

Fig.2.

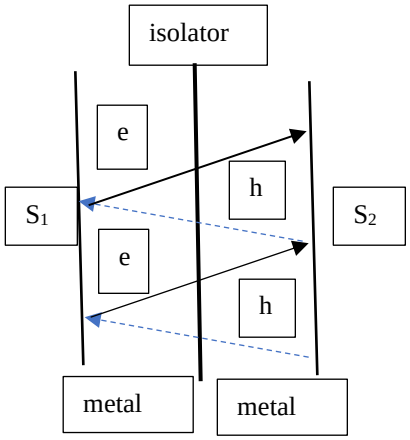

Fig.3.

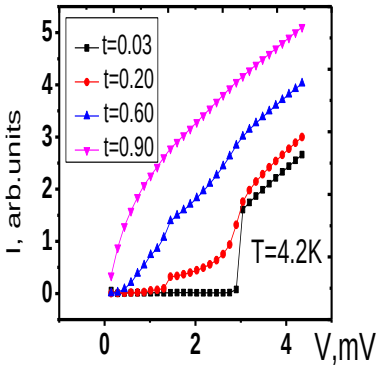

Fig.4.

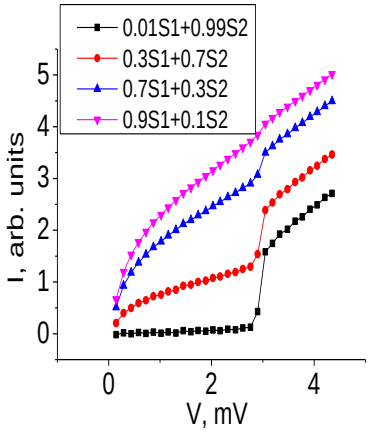

Fig. 5.

carried by barrier sections with high transparency close to unity, and the contribution of currents through sections with low transparency is negligibly small. That is, the junction functions as a set of point contacts connected in parallel.

New Josephson junctions MoRe-Si(W)-MoRe with barriers in the form of an amorphous semiconductor layer doped with metal clusters have been fabricated and studied.

The experimental I–V characteristics of the junctions are compared with those calculated within the framework of the multiple Andreev reflection model. It is shown that the junctions behave as a set of point contacts connected in parallel.

References

[1] M.Hurd Phys. Rev. B: Condens. Matter.-1997 II -vol.55, --N18 - P.R11993- R11999.

CONDUCTIVITY AND DEEP LEVELS IN GESN FILM

Kondratenko S.V. *, Datsenko O.I. *, Pocherpailo A.A. *, Kovanzhi P.O.*

**Faculty of Physics, Taras Shevchenko National University of Kyiv, Kyiv 01601, Ukraine, email: kondratenko@knu.ua*

A GeSn film gown on a Ge/Si virtual substrate was studied by impedance transient spectroscopy, and photoinduced current (PC) kinetics were analyzed within 89-290 K, It was found that relaxation time in the Sn-contained structures at temperatures below ~180 K is two orders shorter than that in the reference Ge/Si structure, where the conductivity is found to occur due to the carriers generated band-to-band in the Ge buffer. The complex PC kinetics and its peculiarities show that different layers of the structure dominate the photoresponse at different temperatures.

Introduction

GeSn is a novel material promising for the development of Ge-based optoelectronics. Unlike the basing indirect-gap material, GeSn acquires direct bandgap at Sn content above 6-10% [1,2], being more applicable for optoelectronics. A wider spectral range also characterizes the optoelectronic devices on this compound due to their narrowed bandgap. Understanding the conductivity and recombination mechanisms in GeSn films is necessary for its application in electronics. This work studies a GeSn film on Ge/Si substrate by impedance spectroscopy and photoinduced current (PC) kinetics at different temperatures. The activation energy of conductivity is estimated, and the levels of defects responsible for the carrier recombination are discussed.

Materials and Methods

A ~800 nm thick GeSn film with 12% Sn content was grown by CVD on a Si substrate above a 700 nm thick Ge buffer. A reference Ge/Si structure was also studied. Two ohmic lateral contacts of InGa eutectic were applied to 2×8 mm^2 samples. Impedance was investigated within a frequency range from 1 to 1000 kHz by an ST2829c LCR Meter by SourceTronic. The photocurrent was excited by 30 μs pulses of a 650 nm laser diode, and the electric signal amplified by a SR570 preamplifier by Stanford Research Instruments was detected by a Siglent SDS1072 oscilloscope. All the measurements were conducted at temperatures 80-293 K.

Results and Discussion

Spectra of real Z_1 and imaginary Z_2 parts of impedance were obtained for both the GeSn/Ge/Si and Ge/Si studied structures (Fig. 1a). The peak frequencies f_m of the Z_2 spectra allowed to obtain the carrier relaxation times as $\tau_{max} = (2\pi f_{max})^{-1}$, and their dependencies on temperature are given in Figure1b. The GeSn/Ge/Si structure at lower temperatures reveals relaxation two orders faster than the reference structure, although it manifests itself slower above ~ 220 K. As relaxation time depends on temperature as $\tau = \tau_0 \cdot \exp[E_a \cdot (k_B T)^{-1}]$ (E_a is the activation energy and k_B is Boltzmann constant) [3], the high-temperature slop of dependence of τ versus T^{-1} allows to obtain the activation energy of the conductivity ~360 meV for the reference sample. This value is close to half of the Ge bandgap of 0.74 eV at 0 K [4], thus we can conclude that the main conductivity is due to the carriers thermally generated band-to-band in the Ge buffer. At the highest used temperatures (above ~ 230 K) the reduction of the relaxation time slows, obviously due to the involvement of the Si substrate in the conductivity.

The kinetics of the PC under 650 nm excitation at different temperatures (Fig. 2) for both the studied structures was analyzed. The relaxation kinetics at the highest temperatures are well-fitted by a single exponent with a tens of (s) lifetime. When lowering the temperature below 200 K, another fast recombination channel with an order shorter lifetime start contrubute therefore the kinetics becomes faster. The shorter lifetime depends on temperature weakly, while the longer one reveals abnormal behavior, increasing with temperature.

When explaining the abnormal lifetime dependence on temperature, we should note that our structures are layered and have different conductivity channels. It is known [2] that the upper GeSn film contributes to the photoconductivity in the main at lower temperatures, while the impact of Si substrate becomes dominant at near-room ones. Thus, we refer to the abnormal lifetime behavior above 200 K to the bottom layers.

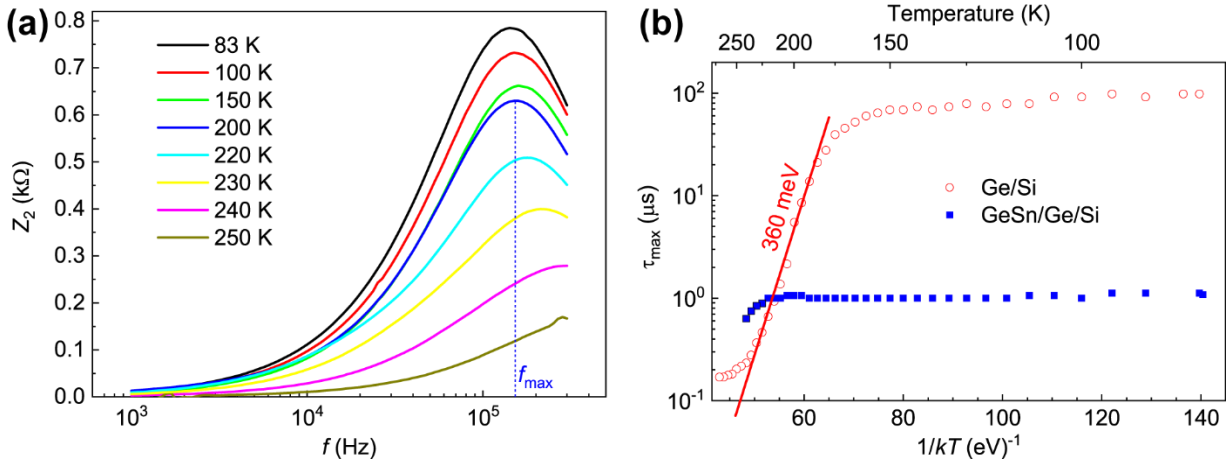

Fig. 1. Spectra of imaginary impedance for the GeSn/Ge/Si structure at different temperatures (a) and Arrhenius plot of the relaxation times with temperature in both the studied structures (b).

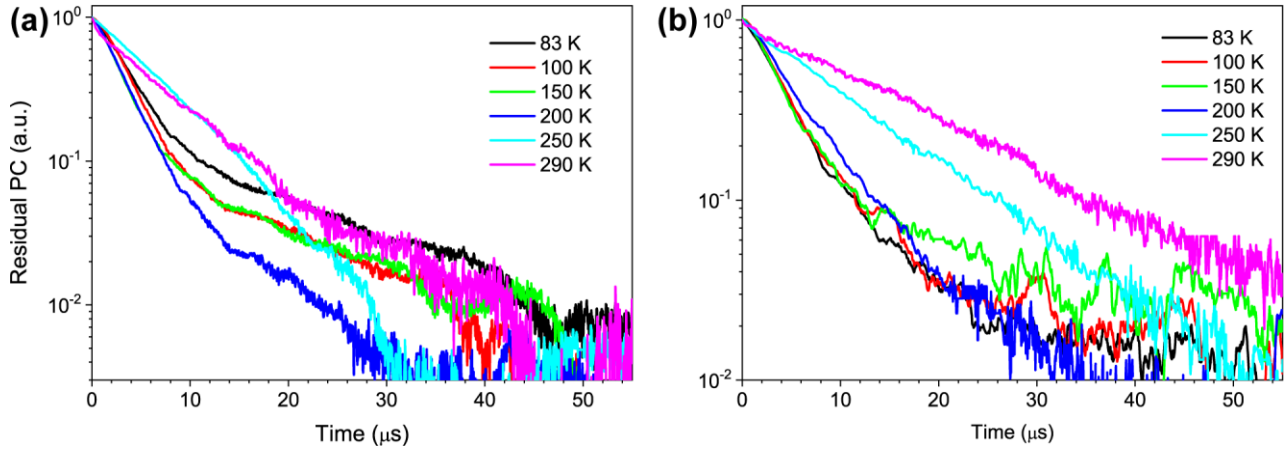

Fig. 2. Relaxation kinetics of PC for the Ge/Si (a) and GeSn/Ge/Si structures (b) at different temperatures.

Acknowledgments

The work is supported by the National Research Foundation of Ukraine (2023.03/0060).

References

[1] K. L. Low, Y. Yang, G. Han, W. Fan, and Y.-C. Yeo, Electronic band structure and effective mass parameters of $Ge_{1-x}Sn_x$ alloys, J. Appl. Phys. **112**, 103715 (2012).

[2] S. Kondratenko, O. Datsenko, A. V. Kuchuk, F. M. de Oliveira, D. Babich, P. M. Lytvyn, M. E. Ware, V. Lysenko, Sh.-Q. Yu, Y. I. Mazur, and G. J. Salamo, Photoconductivity of GeSn thin films with up to 15% Sn content, Phys. Rev. Mat. **7**(7), 074604 (2023).

[3] D. Das and S. Samanta, Complex dielectric characteristics, ac-conductivity, and impedance spectroscopy of B-doped nc-SiO_x:H thin films, ACS Appl. Electron. Mater. **3(**4), 1634–1647 (2021).

[4] C. Kittel, Introduction to Solid State Physics (6th Ed., New York: John Wiley, 1986), p. 185.

TRANSPORT OF CURRENT CARRIERS IN LEAD TELLURIDE FILMS

Mazur M.P.1, Mazur M.-Y. M.2

1 Ivano-Frankivsk National Technical University of Oil and Gas, 15 Karpatska St., Ivano-Frankivsk, 76019, Ukraine, e-mail: myroslav.mazur@nung.edu.ua,

2 Institute of Applied Systems Analysis, National Technical University of Ukraine «Igor Sikorsky Kyiv Polytechnic Institute», Ukraine, e-mail: mazur.markiian-yulian@lll.kpi.ua

The dependence of the mobility and conductivity of current carriers on thickness and temperature in thin p-PbTe films has been studied. The mechanisms of transport of current carriers to grain boundaries associated with thermionic emission have been established. The contribution of scattering at grain boundaries and the surface of thin films of lead tellurides has been identified.

Lorem ipsum dolor sit amet, consectetur adipisicing elit, sed do eiusmod tempor incididunt ut labore et dolore magna aliqua. Ut enim ad minim veniam, quis nostrud exercitation ullamco laboris nisi ut aliquip ex ea commodo consequat. Duis aute irure dolor in reprehenderit in voluptate velit esse cillum dolore eu fugiat nulla pariatur. Excepteur sint occaecat cupidatat non proident, sunt in culpa qui officia deserunt mollit anim id est laborum. Lead telluride films are a promising material for creating on their basis active elements of micro- and optoelectronics: sources of infrared radiation of the optical spectrum, X-ray and γ-ray detectors, thermoelectric energy converters.When studying transport phenomena in semiconductor films, the dependence of thickness properties is well known, since, along with bulk mechanisms of current carrier scattering, processes on the surface play an important role. In addition, in a number of polycrystalline films, the scattering of current carriers at grain boundaries predominates, since the total surface of crystallites can exceed the film surface by several orders of magnitude [1].

This paper presents a study confirming that in p-PbTe films the leading role in transport phenomena is played by processes at grain boundaries associated with the formation of potential barriers and thermionic emission of current carriers.

The films were fabricated using the hot wall method by deposition onto glass substrates as described in [2]. The film thickness was controlled by the deposition time. The structure of the films was analyzed using X-ray diffraction and electron microscopy techniques. Electrical conductivity measurements were carried out under direct current in the temperature range of 77–300 K. All films exhibited p-type (hole) conductivity, regardless of temperature or grain size.

The primary factors influencing grain size in polycrystalline films are the film thickness and substrate temperature [3]. By reducing the film thickness to 0.05 μm and lowering the substrate temperature to liquid nitrogen temperature, films with a grain size of approximately 2×10^{-7} cm can be achieved.

In the course of the work it was found that in p-PbTe films the dominant role in the transport phenomena is played by the processes at grain boundaries associated with the formation of potential barriers and thermionic emission of current carriers. The temperature dependences of the coefficients of transport phenomena for p-PbTe films were also studied and the energies of intergranular potential boundaries for p-PbTe films were determined, which are 0.06-0.1 eV. It was shown that the model of potential barriers with traps in the case of thermionic emission of current carriers through the boundaries explains well the experiment for thin p-PbTe films.

References

[1] V.V. Prokopiv, L.I. Nykyruy, O.M. Voznyak, B.S. Dzundza, I.V. Horichok, Ya.S. Yavorskyi, O.M. Matkivskyi, T.M. Mazur, “The Thermoelectric Solar Generator,” Physics and chemistry of solid state. Vol. 18, No 3, pp. 372-376, 2017.

[2] D.M. Freik, B. S. Dzundza, G. D. Mateik, Yu. V. Klanichka, “Charge Carrier Transport in Low-disperse Cadmium and Lead Tellurides Films,” Physics and chemistry of solid state. Vol. 7, No 2, pp. 245-248, 2006.

[3] Yu.A. Bratashevsky, V.D. Okunev, N.N. Pafomov, Z.A. Samoilenko, “Dimensional effects in polycrystalline PbTe films,” Solid state physics. 27(3), pp. 723-729, 1985.

WAYS TO INCREASE THE EFFICIENCY OF LOW-TEMPERATURE HEAT PIPES AS AUTONOMOUS HEAT SOURCES

Mazur T.M., Vashchyshak I.R.

Ivano-Frankivsk National Technical University of Oil and Gas, 15 Karpatska St., Ivano-Frankivsk, 76019, Ukraine, e-mail: tetiana.mazur@nung.edu.ua, iryna.vashchyshak@nung.edu.ua

Thermosyphons and wick heat pipes are highly efficient heat exchange devices that provide uniform temperature distribution and are used for rapid heating, cooling and heating. A promising direction is the use of tubes as autonomous heat sources for warming the body, especially in the event of a power outage. Various heating methods, including immersion in liquid, nichrome and ceramic heaters, have advantages and disadvantages. However, induction heating is the most effective, which allows achieving high thermal performance by heating the coolant inside the tube. The cylindrical induction method is especially promising, combining simplicity of design and reliability of operation at low frequencies.

Thermosyphons and wick heat pipes are highly efficient heat exchange devices that feature very high thermal conductivity coefficients and rapid surface heating [1,2]. Due to these properties, the temperature along the entire length of the tube remains virtually uniform, which allows them to be used for rapid heating of certain areas, temperature equalization, local heating, cooling, and also for space heating [3].

One of the promising areas of use of heat pipes is their use as low-temperature heat pipes for warming the human body. Most existing devices for this purpose, such as heating blankets or electric blankets, operate from a 220 V network. However, in the event of emergency power outages, which may occur due to damage to the energy infrastructure because of military operations, these devices become unusable. In such cases, people often use batteries or power banks as alternative energy sources to power low-temperature heat pipes, which allows them to operate even in the absence of a centralized power supply. Heat pipes powered by batteries or power banks can be an effective and autonomous source of heat in emergency situations, ensuring the safety and comfort of users.

The temperature and efficiency of a heat pipe directly depend on the type of energy source used to heat its lower end. There are several ways to heat this part of the tube: immersion in a hot liquid flow, use of a nichrome or ceramic heater, and induction.

High efficiency and heating speed are demonstrated by immersing the lower end of the tube in a collector with a flow of heated liquid. In this case, heat is transferred almost completely, which ensures maximum performance. However, this approach requires additional equipment, including pipelines, a liquid heating system, pumps, and an electronic control system, which complicates its use [1,4].

Heating with nichrome wire also showed good efficiency in the initial stages, but over time this method lost reliability due to overheating and oxidation of nichrome, which led to poor contact and a decrease in thermal performance [4].

The use of ceramic heaters has the advantage of ease of operation, since they only require a basic on/off system. However, this method somewhat reduces the overall efficiency due to the presence of a multi-layer structure, including thermal paste and aluminum dampers, which increases thermal resistance. The main disadvantages are the need for careful control of the power of each heater, the gradual degradation of dampers and thermal paste, which over time reduces the efficiency of heat transfer, and the low reliability of ceramic heaters [3,4].

In general, each of these methods has its own advantages and disadvantages, so the choice of a particular option depends on the specific requirements for the heating system and its operating conditions.

The described methods assume external heating of the heat pipe, in which part of the heat is lost due to dissipation into the environment. However, a more promising solution is to heat the coolant directly inside the tube using induction heating. This approach has several advantages.

Firstly, by precisely selecting parameters such as the length and diameter of the induction coil wire, the current, voltage and heat output can be adjusted to achieve the desired system characteristics. Secondly, because heating occurs inside the tube, the heating speed is significantly increased. Thirdly, the tube surface itself acts as a radiator for the induction coil, which prevents it from overheating and contributes to the stability of the system.

There are two main methods for inductively heating the bottom end of a heat pipe. The first is to install a flat spiral coil at the end of the tube, with a flat circular ferromagnetic core inside it, which is located opposite the coil. The second method involves using a cylindrical induction coil installed at the bottom of the tube, with a cylindrical magnetic core inside the tube.

The second option of induction heating is more attractive from a technical point of view. The production of a cylindrical coil and the corresponding core is simpler and less expensive. In addition, the system can operate at low operating frequencies, which does not lead to overheating of the control elements, simplifies the design and increases the reliability of the entire system. This approach also allows for a reduction in the size of the device and an improvement in heat transfer efficiency without significant energy losses.

References

[1] Vijayakumar P, M.E., Sajairaj S., Santhoshkumar R., “Review on conventional, modern heat pipes and its applications,” International Research Journal of Engineering and Technology (E-ISSN: 2395 -0056, P-ISSN: 2395-0072), vol. 03, Issue: 10, pp. 513-518, Oct. 2016.

[2] T.M. Mazur, M.M. Slyotov, V.V. Prokopiv, O.M. Slyotov, M.P. Mazur, “Light emitters based on II-VI chalcogenides with nanostructured surface,” Molecular Crystals and Liquid Crystals, 752(1), pp. 95–102, 2023.

[3] I.R. Vashchyshak, S.P. Vashchyshak, V.D. Mindyuk, “Energy-efficient heating system for the premises of technological gas transportation facilities using steam-droplet heaters,” Oil and Gas Energy 2017: Int. science and technology conf., pp. 285-288, May 15-19, Ivano-Frankivsk, 2017.

[4] I.R. Vashchyshak, S.P. Vashchyshak, O.V. Popovich, E.R. Dotsenko, “Improvement of steam-droplet heaters for heating systems of premises and buildings,” Methods and devices for quality control, 39(2), pp. 68-74, 2017.

MEDICAL PHYSICS

STAFFING CRISIS IN RADIATION ONCOLOGY OR WHERE TO GET MEDICAL PHYSICISTS?

Vashchyshyn V.

Oberig clinic, Zoolohichnz 3G, e-mail: v.vashchyshyn@oberig.ua

The concept of medical physics in Ukraine has evolved significantly over the past 20 years. These changes have primarily occurred in the employment structure of medical physicists. Until the 2010s and before the rapid development of radiation oncology in Ukraine, medical physicists were those who were engaged in basic research at the intersection of three sciences - physics, chemistry, and biology. Most of these areas could be attributed to biophysics to one degree or another. However, with the beginning of the modernization of radiation therapy and nuclear medicine, the number of medical physicists who associated themselves with clinical work was steadily increasing every year. At the moment, the demand for medical physicists significantly exceeds the supply in the labor market, which poses significant risks in the implementation of significant budget funds allocated for the development of modern radiation therapy departments.

Historical role of medical physicists in Ukraine and abroad

In Ukraine, historically, the paradigm has been that clinical work can be performed by graduates of medical universities, with some biologists in laboratory diagnostics and chemists in pharmacy. Physicists, given the previous historical experience in Ukraine, were engaged in fundamental research, the result of which could be implemented in clinical practice by medical specialists.

At the same time, already in the 60s of the 20th century, physicists with a specialization in medical physics in developed countries had already become an integral part of the radiation oncology team, i.e., they were directly involved in clinical work. According to the AAPM statistics for 2023, 76% of all medical physicists are primarily employed in radiation oncology. In developing countries, including Ukraine, this percentage is much higher and reaches 90-100% of all medical physicists.

This difference in the employment of medical physicists was the result not only of different views on the definition of “medical physics” but also of labor market conditions in different countries. In Ukraine, linear accelerators for radiation therapy began to appear only in the 2010s, requiring qualified physicists for their clinical use. Until then, Co60-based devices were used for radiation therapy, which were much easier to use and could be operated by physicians and accompanying technical staff, often called “radiologists.” That is, not so long ago, radiation oncology in the modern sense had just begun to take shape in Ukraine. That is why there was no need to train medical physicists involved in clinical work earlier.

Thus, medical physics is only in its infancy in Ukraine and needs not only academic reformatting to meet the modern requirements of radiation oncology, but also further regulation to control the necessary knowledge required to perform work duties.

The dynamics of demand for medical physicists

Between 2010 and 2020, the number of linear accelerators in Ukraine increased to 45 (Fig. 1), according to DIRAC statistics, which was the first significant impetus for medical physics to be paid attention to for reform. But unfortunately, there were no substantive academic improvements in the training of medical physicists, and almost all the necessary skills were acquired on the job.

	United States	Germany	France	Moldova	Georgia	Mongolia	China	India	Ukraine
2010	12.3	6.8	7.5	0.6	0.8	0.3	0.5	0.4	0.1
2020	12.1	8.2	7.5	0.7	0.9	0.5	1.2	0.8	1.1

Fig. 1: Number of linear accelerators per 1 million population.

However, the level of academic training was not the only challenging factor in the saturation of jobs at linear accelerators in radiation therapy departments. One of the main problems that arose was the total number of physics graduates. The tough demographic situation has reduced the total number of applicants, and social trends have further dampened the demand for admission to technical specialties, particularly physics. Thus, not only the total number of applicants to physics has dropped, but also the percentage of applicants to physics.

The general trend in Ukraine shows a gradual decline in the popularity of physical and natural sciences among applicants, in favor of humanities, management, and IT specialties. For example, in 2024, the most applications were submitted for Psychology, Management, and Philology.

To summarize, there is a negative situation where the number of physicists who want to become medical physicists is much smaller than the number of jobs, and this trend is only getting worse.

Current labor market situation

Over the past 2 years, 11 accelerators have been installed in private centers and 15 accelerators have been purchased for public centers, and a tender for an additional 5 accelerators will be announced in the coming months. The total number of physicists required for the normal operation of these accelerators is 60-90 [1], depending on the workload. Finding staff for this amount of equipment is an extremely difficult task, especially for public clinics with limited financial resources.

Such a rapid growth in the number of equipment may continue for the next 5-10 years if Ukraine continues the trend of modernizing radiation oncology. The plateau in the number of staff will occur when the number of accelerators will increase 3-4 times more and reach 4-6 accelerators per million population.

Ways to address the staff shortage

Due to the above-mentioned staffing problems, it is already possible to get a position as a medical physicist not only without work experience, but also without completing training programs in medical physics. In fact, due to the shortage, all physicists with any diploma that contains the word “physics” are now being invited to work in order to try to fill the gap.

Without popularization of technical specialties and an increase in the number of students enrolled in technical specialties, in the foreseeable future we may have a situation where some of the new radiation therapy departments will simply not work or will not work at full capacity due to the lack of medical physicists in the workplace.

The situation can be somewhat improved by increasing the level of theoretical and practical training of graduates, even if their number remains constant, increasing their professional efficiency. But this requires closer interaction between the academic and clinical environments.

References

[1] THE EUROPEAN FEDERATION OF ORGANISATIONS FOR MEDICAL PHYSICS, Criteria for the staffing levels in a Medical Physics Department, EFOMP Council September 1997

NON-INVASIVE BLOOD GLUCOSE MEASUREMENT USING MACHINE LEARNING

Serhiy Duha[1], Volodymyr Chuchkanov[2], Dmytro Velyhotskyi[1,3], Serhii Mamilov[3]

[1]National Technical University of Ukraine "Igor Sikorsky Kyiv Polytechnic Institute", 37, Beresteisky Ave., Kyiv 03056, Ukraine, e-mail: sergejduga02@gmail.com, velyhotskyi@ukr.net
[2]Taras Shevchenko National University of Kyiv, 63/13, Volodymyrska str., Kyiv 01601, Ukraine
[3]Institute of Magnetism of the NAS of Ukraine, 36-b, Akad. Vernadskogo blvd., Kyiv 03142, Ukraine

Diabetes is a leading cause of mortality worldwide, and individuals with the condition must frequently monitor their blood glucose levels using a glucometer, which requires painful finger pricks. Non-invasive glucose measurement offers a less intrusive alternative, potentially simplifying diagnosis and improving the quality of life for patients. This paper presents the outcomes of applying photoplethysmography signal processing combined with machine learning techniques for non-invasive blood glucose detection.

Research results

Photoplethysmography (PPG) signals were recorded at three wavelengths (568 nm, 660 nm, and 930 nm) with a sampling frequency of 357 Hz using a PPG system. Measurements were taken from the finger of a single volunteer in a resting state. Over the course of one day, 25 recordings were made, each lasting 3 minutes, before and after consuming a high-sugar meal. Segments of the PPG signals, 20 seconds in duration (7400 data points), were used to train the machine learning models. To eliminate signal artifacts that could significantly affect measurement accuracy, polynomial detrending of the 4th degree was applied. The wavelet decomposition method was then used to extract signal parameters, which were subsequently used to train machine learning models. Three models were selected for this study: XGBoost, Random Forest, and Gradient Boost [1]. Model accuracy was evaluated using cross-validation for the single volunteer. Figure 1 shows the glucose values predicted by one of the selected machine learning models compared to those measured using an invasive glucometer. The average root mean square error (RMSE) for each model was as follows: XGBoost – 0.51 mmol/L, Random Forest – 0.48 mmol/L, and Gradient Boost – 0.43 mmol/L.

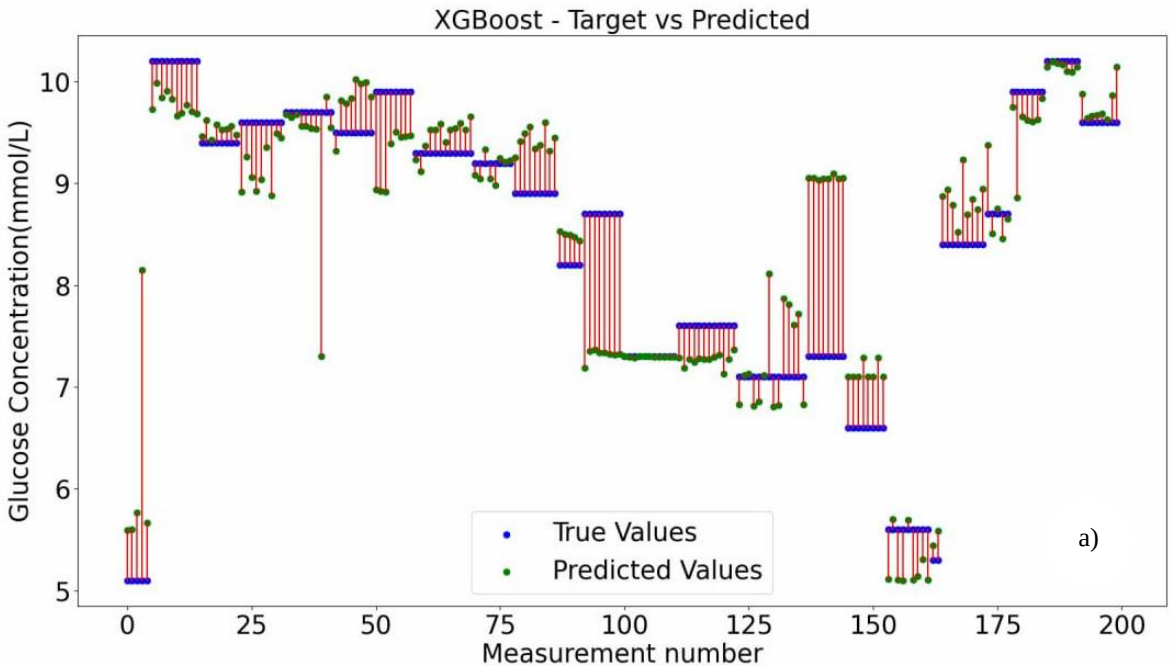

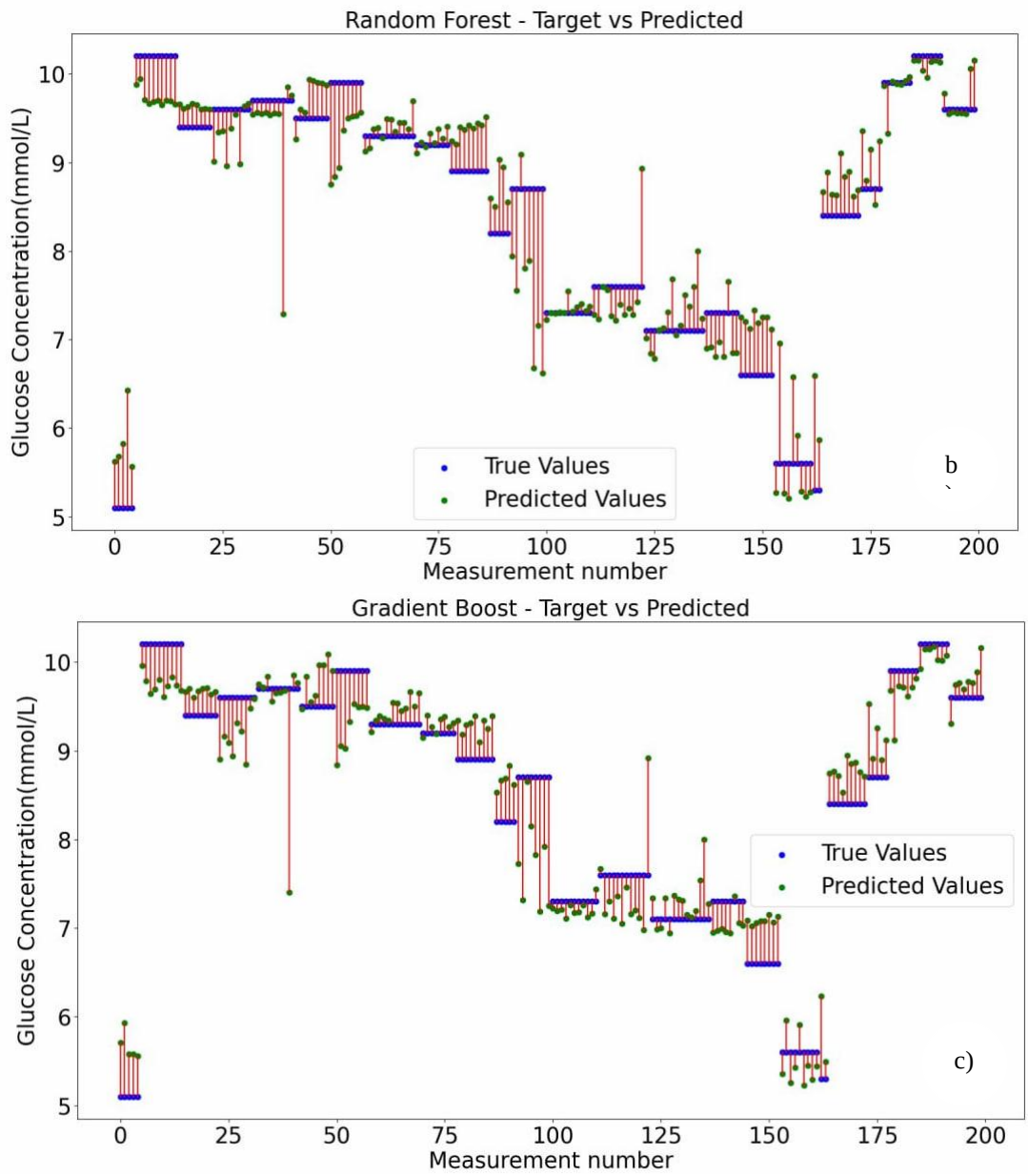

Fig. 1. Glucose values predicted by each of the three models compared to corresponding values measured using an invasive device: a) XGBoost, b) Random Forest, and c) Gradient Boost

Conclusion

Non-invasive blood glucose measurement remains a challenging task. It is still unclear which specific parameters of PPG signals yield the most accurate glucose level predictions. Additionally, external factors significantly influence measurement accuracy, complicating predictions and necessitating thorough, diverse data preparation. While the current system demonstrates satisfactory results, further research and optimization are required to improve its reliability and precision.

References

[1] Rachim, V. P., & Chung, W. Y. (2019). Wearable-band type visible-near infrared optical biosensor for non-invasive blood glucose monitoring. *Sensors and Actuators B: Chemical*, *286*, 173-180.

BIOLOGICAL TISSUE BOUNDARIES CONTRAST RESTORATION BY RELAXATION CHARACTERISTICS IN MRI

Komarov A. O.*, Netreba A. V.**

**, ** Faculty of Radiophysics, Electronics and Computer Systems Taras Shevchenko National University of Kyiv, Kyiv 01601, Ukraine,*
*e-mail: * aokomarov@knu.ua*

The method of increasing the contrast of biological tissue images obtained by the method of magnetic resonance imaging is considered. The voxel correlates with the pixel of the resulting image and contains information about the general feedback signal from the types of tissues in its composition. To increase the contrast of the image and to emphasize the boundaries between different types of tissues, their relaxation characteristics must be taken into account. Thus, it becomes possible to more clearly highlight the transition regions where there are several types of tissues within a single voxel.

This study investigates methods for enhancing image contrast and emphasizing the boundaries between areas of differing biological tissues in MRI. The relevance of this research lies in developing or improving techniques for processing tomographic data, particularly concerning the lack of diagnostic information from small anatomical structures and transitional areas between various tissue types. Image contrast enhancement is achieved by taking into account the relaxation characteristics of the tissues within each voxel and the histogram characteristics of the image fragments.

The spatial distribution characteristics of biological objects as constructed by MRI involve selective and controlled excitation of protons, based on the nuclear magnetic resonance phenomenon. The excitation coding technique and subsequent signal recording using pulse sequences provide spatial localization of the spin systems [1]. In a general form, the measured response signals can be expressed as:

$$S_n = \rho_n\left(1 - exp(-TR/T_{1n})\right) \cdot exp(-TE/T_{2n})$$

where symbol ρ denotes the proton density, respectively T_1 and T_2 denote spin-lattice and - spin-spin relaxation times. For biological tissues during the measurements, the values of the parameters TE and TR determine the type of weighting of the final proton distribution also spine-lattice time T_1 and spine-spine relaxation time T_2 are determined for each biological tissue type.

Before performing the transformation of the original image, it is necessary to determine the brightness limits of the pixels of the original image, which correspond to different types of biological tissues. Using the method of histogram analysis of MRI images [2] for fragments of diagnostic images. For the obtained pixel brightness limits corresponding to certain types of tissues and taking into account the mutual ratio of the density of the brightness distribution of images at the boundary of tissues with similar relaxation characteristics diagnostic images were recalculated.

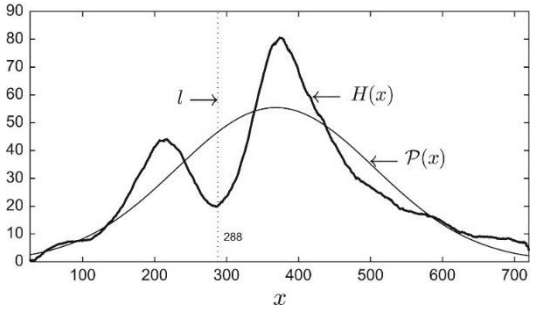

Fig. 1. Histogram analysis representation.

The histogram analysis method employed is an effective technique for the automatic segmentation of grey-level histograms. It aims to identify the concavity enclosed by the two most prominent peaks of the curve, which characterize the differences in signal values from various biological tissues obtained during tomographic research. In short, we seek the position of maximum divergence between the histogram and a single Gaussian fit. Fig. 2 illustrates how this concept is applied to separate a typical histogram with two noticeable peaks.

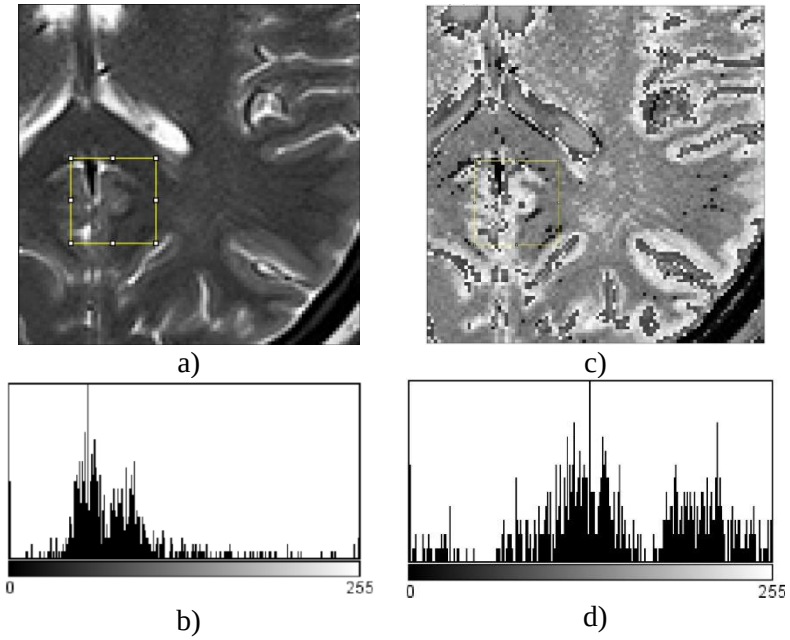

Fig. 2. MRI image fragment before (a) and after (c) reconstruction weighted by histogram analysis, along with the histogram of the recalculated image (d).

Images obtained through this method will exhibit sharper contrast along the boundaries between different tissue types. The overall structure of the tissues will remain unchanged due to their relaxation parameters, as shown in Fig. 2.

References

[1] A. V. Netreba, A. O. Komarov & Y. O. Kyiashko The multicomponent relaxation combination of proton magnetization in biological tissues magnetic resonance investigations // Molecular Crystals and Liquid Crystals, V.699:1, pp.71-81, DOI: 10.1080/15421406.2020.1732541

[2] Balan AG, Traina AJ, Ribeiro MX, Marques PM, Traina C Jr. Smart histogram analysis applied to the skull-stripping problem in T1-weighted MRI. Comput Biol Med. 2012 May;42(5):509-22. doi: 10.1016/j.compbiomed.2012.01.004. Epub 2012 Feb 13. PMID: 22336779.

QUANTUM-CHEMICAL AND SPECTRAL ANALYSIS OF ATP/AMP MOLECULES CONFORMERS IN WATER SURROUND

Yu.G. Terentieva[*], I.M. Dmitruk[*], K.O. Maiko[*], A.M. Rashevska[*], Ye.Yu. Stepanenko[**]

[*]Ukraine, Kyiv, Taras Shevchenko National University of Kyiv, Faculty of Physics, 60 Volodymirska Str., 03127

[**]Ukraine, Kyiv, Institute of Molecular Biology and Genetics of NASU, 150 Ac. Zabolotnogo St.

maiko_kate@ukr.net

The adenosine 5'-triphosphate (ATP) and its derivatives, ADP and AMP, play crucial role in many processes. For example, cAMP (adenosine 3′,5′-cyclic monophosphate), acts as a key second messenger in numerous signal transduction pathways and regulates various cellular functions [1].

So description of conformer properties and structural geometry of ATP/AMP is required for developing of medical approaches (such as preventing intracellular protein aggregation and influence on thermal stability of proteins[2],[3]), and allows to explain properly these biological macromolecules in the terms of biomolecular condensates (BCMs). Here we applied both theoretical and experimental methods to define possible conformers of ATP, which may be found in the aqueous solution, because most BCMs are located and act in aqueous media[4].

Spectral measurements of obtained aqueous solution included: absorption and fluorescence spectra at ambient temperature, the fluorescence excitation lifetimes. Theoretical part includes quantum-chemical calculations of molecular geometry of AMP/ATP in ground/excited states (non-empirical DFT/TD-DFT/6-311G+(d,p)/B3LYP level of theory) with different values of fixed torsion angle (with step of 5o) for analysis of possible conformer forms.

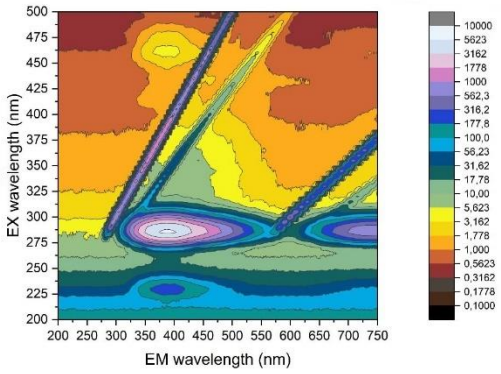

Fig. 1 5 EEM of ATP water solution (C=2·10-4 M, T=20°C)

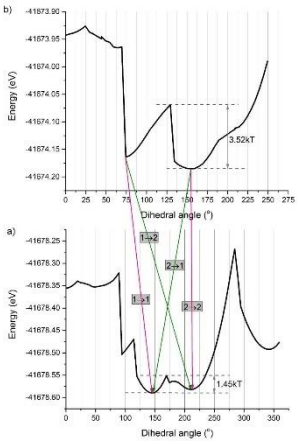

Fig. 2 The conformer profiles for AMP molecule in water for ground (a) and excited (b) states.

References

[1] The cyclic AMP signaling pathway: Exploring targets for successful drug discovery (Review) doi: 10.3892/mmr.2016.5005

[2] Jack V. Greiner, Thomas Glonek (2023) Adenosine Triphosphate (ATP) and Protein Aggregation in Age-Related Vision-Threatening Ocular Diseases, doi:10.3390/metabo13101100

[3] Xinwen Ou, Yichong Lao et al. (2021), JASC, ATP Can Efficiently Stabilize Protein through a Unique Mechanism, 1, 10, 1766-1777, https://doi.org/10.1021/jacsau.1c00316

[4] Condensed-matter chemistry: from materials to living organisms (2019), National Science Review 6(2):191-194, http://dx.doi.org/10.1093/nsr/nwy128

RECONSTRUCTION OF MAGNETIC RESONANCE IMAGES USING MULTIPLE PERIODOGRAM METHODS

Mamotenko S. P.*, Netreba A. V.**

** Faculty of Radiophysics, Electronics and Computer Systems, Taras Shevchenko National University of Kyiv. Volodymyrska Street, 64/13, Kyiv-01601, Ukraine.*
e-mail: serg9peter8@gmail.com
*** Faculty of Radiophysics, Electronics and Computer Systems, Taras Shevchenko National University of Kyiv. Volodymyrska Street, 64/13, Kyiv-01601, Ukraine.*
e-mail: avn@univ.kiev.ua

Magnetic Resonance Imaging (MRI) is one of the safest and widely used techniques for the visualization of different medical conditions. However, noise caused by patient movement during scanning or low magnetic field intensity makes it challenging to extract critical information from magnetic resonance images. Our research suggests a new approach for reconstructing MR images utilizing a Bartlett Periodogram during the initial noise reduction, which can be used without prior knowledge of specific noise characteristics. Additionally a comparison is drawn between this new approach and a Daniell periodogram method.

Methodology

Our methodology involves transforming the MR image corrupted by Gaussian noise from the spatial domain into the frequency domain using the two-dimensional Fourier transform (2DFT), which is a common method for reconstructing MR images [1]. The Bartlett Periodogram is applied as a spectral estimator to enhance the MR image by reducing noise variance. By dividing the frequency-domain data into multiple segments and averaging their periodograms, the Bartlett Periodogram provides a smoother estimate of the Power Spectral Density (PSD) [2]:

$$P_B(f) = \frac{1}{M}\sum_{i=1}^{M}\left|F_i(k_x, k_y)\right|^2$$

where $F_i(k_x, k_y)$ represents the discrete Fourier transform of the each segment of the input signal, and M is the number of segments used in averaging. The inverse Fourier transform is then performed to convert the frequency-domain data back into the spatial domain. To further enhance the contrast of the reconstructed image, adaptive histogram equalization is used.

The effectiveness of the method was evaluated by calculating the Pearson Correlation Coefficient (PCC) for the original, noisy and reconstructed images. Typically, PCC below 0.1 indicates a weak correlation, whereas a value above 0.9 indicates a strong correlation [3]:

$$r_{xy} = \frac{\sum_{i=1}^{n}\left(x_i - \underline{x}\right)\left(y_i - \underline{y}\right)}{\sqrt{\sum_{i=1}^{n}(x_i - \underline{x})^2}\sqrt{\sum_{i=1}^{n}\left(y_i - \underline{y}\right)^2}}$$

Compared to the Daniell Periodogram method, which was one the methods investigated in our previous research, the Bartlett Periodogram averages over multiple independent segments, leading to a more stable estimate of the PSD.

Results

Tests were conducted using a fragment of a brain MR image with dimensions of 255x255 pixels. Test run of the image reconstruction implemented using the Daniell Periodogram method will be demonstrated first:

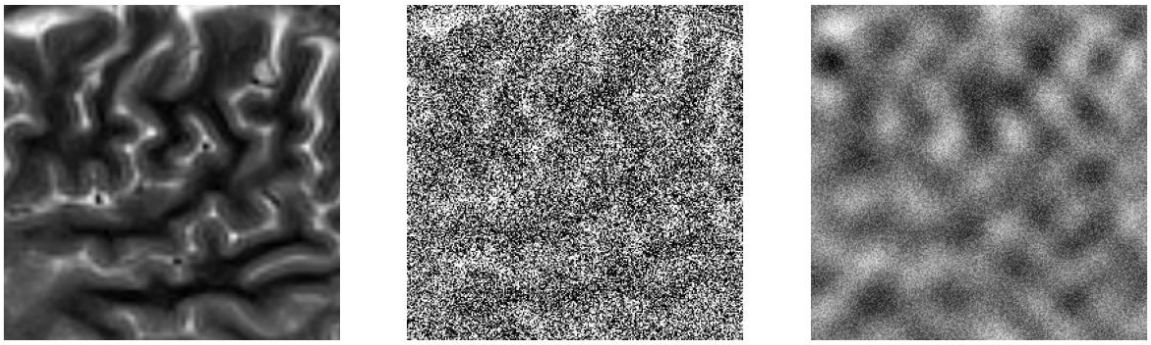

(a) (b) (c)

Fig. 1. Daniell Periodogram method. Original brain MR image (a), image with noise (b), reconstructed image (c).

The results show a visual improvement in image quality, however the reconstructed image visibly lacks the distinctive contours of the original. Additionally, some distortion arises as the result of PSD averaging due to the nature of the Daniell periodogram smoothing, which can possibly complicate the MRI interpretation process.

The test run conducted using the Bartlett Periodogram method:

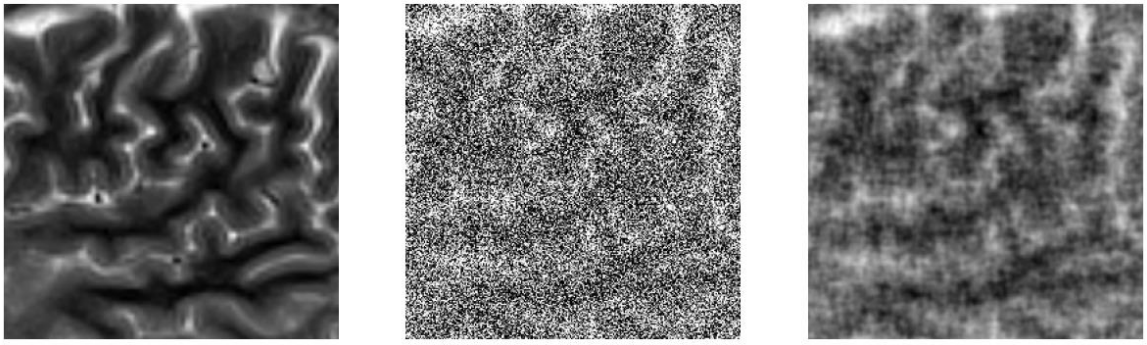

(a) (b) (c)

Fig. 2. Bartlett Periodogram method. Original brain MR image (a), image with noise (b), reconstructed image (c).

The reconstructed image visibly preserves the distinctive tissue structures visible on the original image, and significantly reduces the presence of the noise. The PCC of the reconstructed image shows a 4-fold increase compared to the PCC of the noisy one ($PCC^{reconstructed}$=0.84; PCC^{noisy}=0.21). Compared to the results obtained during the Daniell method tests, PCC of the image reconstructed by Bartlett method achieves a 57% increase in correlation. To surmise, the results of this study confirm the assumption that the Bartlett Periodogram method can be effective in enhancing MR image quality by reducing noise while retaining essential anatomical details.

References

[1] McVeigh, E. R., Henkelman, R. M., & Bronskill, M. J., "Noise and filtration in magnetic resonance imaging", *Medical physics*, vol. 12, pp. 586–591, 1985.

[2] S. Lawrence Marple, Jr., William M. Carey, "Digital Spectral Analysis with Applications", *J. Acoust. Soc. Am.*, vol. 86, (1986)

[3] Helmy Rahadian, Steven Bandong, Augie Widyotriatmo, Endra Joelianto, "Image encoding selection based on Pearson correlation coefficient for time series anomaly detection", *Alexandria Engineering Journal*, vol. 82, pp. 304-322, (2023).

MICROWAVE PROPERTIES OF COMPOSITE FILMS BASED ON POLYVINYL CHLORIDE AND BROMINATED ACTIVATED CARBON

Illia A. Metelskyi*, Dmytro O. Zhytnyk*, Igor P. Matushko, Yuriy V. Noskov***,**

Vladyslav A. Moiseienko**, Liudmyla M. Grishchenko***

**Faculty of RadioPhysics, Electronics and Computer Systems Taras Shevchenko National University of Kyiv, Kyiv 01601, Ukraine, email: metelskiy.illya@gmail.com*

***Faculty of Physics, Taras Shevchenko National University of Kyiv, Kyiv 03127, Ukraine, email: mipigor@gmail.com*

****Kukhar Institute of Bioorganic Chemistry and Petrochemistry, the National Academy of Science of Ukraine, Kyiv 02160, Ukraine, email: yuriy.noskov@gmail.com*

*****Independent Research & Development Laboratory "200k Electronics", Kyiv -01030, Ukraine, email: vamrpd@gmail.com*

This study presents the preparation of thin composite films using polyvinylchloride as the base material and brominated activated carbon samples as fillers, their study by the methods of SEM, TPD MS, TGA, FTIR. The microwave absorbing properties of the resulting films in the Ka-band were investigated.

Introduction

The rapid development of wireless communication, electronics, and medical device technologies has caused significant problems related to electromagnetic pollution [1]. They can harm human health, causing adverse effects such as impaired attention, memory, logic, and speech, as well as nervous and mental disorders, blood diseases, cancer, and Parkinson's and Alzheimer's diseases [2]. Extensive research is being conducted worldwide to develop optimal materials that absorb microwaves and convert electromagnetic energy into heat. Currently, there is an increasing demand for microwave-absorbing materials due to their use in military, commercial, and domestic applications. These materials are capable of absorbing incident electromagnetic radiation over a wide range of frequencies. Numerous microwave-absorbing materials have been developed, but it is critical to create materials with optimized properties.

The objective of the present study was to prepare polyvinyl chloride (PVC)-based composite films with activated carbon (AC) filler modified by bromination and to investigate the physicochemical properties of the brominated AC fillers (AC/Br_2) and the microwave properties of the respective composite films prepared with different AC/Br_2 filler contents.

Experimental

The composite films were created by blending PVC with activated carbon modified through liquid-phase bromination. Bromine was introduced into the carbon to alter its electromagnetic properties. The activated carbon was derived from apricot pits, which underwent carbonization and steam activation processes. The bromination added functional oxygen and bromine groups to the carbon, which influenced the material's conductivity and ability to absorb microwave radiation. The films were prepared using a hot-pressing technique, with different weight percentages of AC/Br_2 ranging from 0.2% to 30%.

Results and discussion

The bromination of activated carbon was found to significantly modify the carbon's surface by adding oxygen-containing functional groups such as phenolic and carboxyl groups. While the carbon's morphology was not drastically altered, a reduction in microporosity was observed due to the blocking of pores by chemisorbed bromine atoms.

Comparable thermal stability was demonstrated by both AC and AC/Br_2, though the presence of bromine caused the brominated carbon to exhibit slightly lower stability. Weight loss at temperatures below 520°C was attributed to the release of water and decomposition of oxygen-containing groups.

It was shown that as the AC/Br_2 content in the PVC films increased, their ability to reflect and absorb electromagnetic radiation in the Ka-band (25.9 to 37.5 GHz) also increased. Films containing 30% AC/Br_2 were found to significantly reduce microwave transmission by up to 40% and increase reflection losses, indicating their suitability for EMR shielding applications. However, films with lower AC/Br_2 content (0.2% to 10%) were observed to be more transparent to microwaves, showing potential for applications requiring minimal interference with EMR transmission. It was suggested that composite films with 0.2% to 5% AC/Br_2 content provide an optimal balance between transparency and protection, exhibiting minimal reflection loss of -18.8 dB (indicating only 2% power reflection) and effective performance over a broad frequency band. Films with 30% AC/Br_2 content were found to improve shielding properties by reducing transmitted wave power by up to 39%.

Table 1. Microwave parameters of PVC/AC/Br_2.

Sample[a]	S_{11} (dB)			S_{21} (dB)		
	Min.	Av.	Max.	Min.	Av.	Max.
PVC	-17.0	-15.7	-14.8	-0.7	-0.6	-0.3
0.2%	-18.8	-16.8	-15.2	-0.9	-0.6	-0.5
0.5%	-16.5	-14.7	-13.0	-1.2	-0.9	-0.5
1%	-15.7	-13.9	-12.4	-0.9	-0.8	-0.6
5%	-14.4	-13.7	-13.2	-0.8	-0.7	-0.5
10%	-12.9	-11.8	-10.7	-1.1	-0.9	-0.7
20%	-8.8	-8.6	-8.2	-2.4	-1.9	-1.6
30%	-6.3	-5.5	-4.4	-4.8	-4.1	-3.3

[a] Refers to the weight percentage of AC/Br_2 in PVC/AC/Br_2.

Conclusion

The study concludes that the microwave properties of PVC-based composite films can be finely tuned by adjusting the content of brominated activated carbon. At low filler content, the films are nearly transparent to microwaves, while higher concentrations provide effective EMR shielding. These findings suggest the potential of using such films in various applications, including military, commercial, and household products where electromagnetic interference or radiation protection is required. This research opens the door to further exploration of brominated porous carbon materials for their potential in creating advanced, lightweight EMR shielding materials. The tunability of the microwave absorption and reflection properties makes these composites highly versatile for different uses.

References

[1] Y. G. Dabholkar, A. G. Pusalkar, H. K. Velankar, “Effects of Cell Phone EMF Radiations on the Auditory System-A Review,” *Int. J. Health Sci. Res.*, vol. 6, pp. 506-515, Feb. 2016.

[2] H. Lim, J. Choi, H. Joo, M. Ha, “Exposures to radio-frequency electromagnetic fields and their impacts on children's health – What the science knows?” *Curr. Opin. Environ. Sci. Health*, vol. 32, Apr. 2023, Art. no. 100456, doi: 10.1016/j.coesh.2023.100456.

EFFECT OF MAGNETIC FIELD ON PHOTODISCITATION OF OXYHEMOGLOBIN UNDER THE INFLUENCE OF LASER RADIATION WITH A WAVELENGTH OF 605 NM

Oleksandra Ostapenko[1], Olga Salyuk[1,2], Dmytro Velyhotskyi[1,2], Serge Mamilov[1]

[1] Institute of Magnetism, NAS of Ukraine fnd MES of Ukraine, Kiev, Ukraine,
e-mail: alexandraost2001@gmail.com
[2] National Technical University of Ukraine"Igor Sikorsky Kyiv Polytechnic Institute", Kiev, Ukraine

The work is devoted to the study and evaluation of the combined effect of a magnetic field and laser irradiation on the process of photodissociation of oxyhemoglobin. Before the study, it was shown that the magnetic field does not affect the operation of the sensor. With the participation of volunteers, we took a photoplethysmogram, the values of which were averaged over time for calculation. The results showed that the magnetic field increases the efficiency of oxyhemoglobin photodissociation when exposed to external laser irradiation

Introduction

Today, low-intensity laser therapy takes its place among modern methods of treatment [1-3]. The main influencing factor is the photodissociation of oxyhemoglobin in arterial blood [4]. In recent years, bimolecular recombination of molecular oxygen with human hemoglobin under excitation in different spectral ranges has been actively studied, the mechanisms and dynamics of the photodissociation reaction and heme relaxation processes have been described. In work[5], based on the results of calculations of the charge distribution of oxygenated and deoxygenated heme, as well as on the basis of the theory of electronic excitations in acceptor molecules and hemoglobin absorption spectra, it was found that a low-intensity laser in the wavelength range of 800–1060 nm can promote the release of oxygen from oxyhemoglobin and improve the supply of oxygen from capillaries to the surrounding tissues. The study [6] examined the balance between oxygen use and delivery by assessing the concentration of local oxy- and deoxymyohemoglobin "in vivo". It has been found that low-intensity laser irradiation statistically increases the local oxygen concentration. However, the study of the simultaneous effects of laser irradiation and the magnetic field remains on the "sidelines" of research, despite some practical use [7,8]. The aim of our work is to study the combined effect of magnetic field and laser irradiation on the photodissociation of oxyhemoglobin in arterial blood

Materials and methods

In the experiment, photoplethysmogram signals were recorded at two wavelengths in the red (660 nm) and near-infrared IR (940 nm) range with a polling frequency of f = 348 Hz. The work uses a pulse oximetry sensor for the finger using light. The sensor contains a standard pair of LEDs with radiation wavelengths of 660 and 940 nm and a BPW34 photodiode (OSRAM). Control of the sensor operation, data collection and transmission were provided by a measuring unit connected to a personal computer, which processed information, displayed it on the monitor screen and stored the trend of signals on the hard disk.

The sensor was placed on the index finger of the right hand of the subjects, the external laser radiation of an LED with a wavelength of 605 nm was directed to the base of the first phalanx of the same finger. To investigate the effect of the magnetic field, a hand with a sensor was inserted into the gap of a permanent magnet. The studies involved 8 volunteers aged 25 to 54 years. The power level of the radiation used corresponded to that used in low-intensity laser therapy and is safe for humans, and the irradiation was carried out in a non-invasive way. For each subject, 15 to 20 recordings of signals were made according to the scheme: 30 seconds without radiation, 30 seconds with radiation turned on without a magnetic field, 30 seconds in a magnetic field, and 30 seconds without radiation. For each record, the mean values of local arterial blood SaO2 saturation at the non-irradiated and irradiated intervals and the change in SaO2 under the influence of irradiation were calculated, which was then averaged over the number of records. The errors were calculated using t-tables for probability p=0.95.

Results & Discussion

Before starting the main measurements, it was checked whether the magnetic field affected the operation of the sensor. To do this, a working sensor with a biotissue simulator in the middle was inserted into the gap of the magnet. No changes in the operation of the detector were recorded. The next step was to study the effect of a separate magnetic field on the value of arterial blood oxygen saturation. The measurement was carried out according to the same scheme as the main one, with the exception of irradiation. At a magnetic field of 10, 20 and 50 mT, the effect of the magnetic field on the value of arterial blood oxygen saturation was not recorded.

To study the simultaneous influence of the magnetic field and laser irradiation, irradiation with a power of 10 and 15 mW and a magnetic field of 10, 20 and 50 mT were used. We will estimate the photodissociation of oxyhemoglobin using the summary value of the change in arterial blood saturation (the ratio of the absolute change in arterial blood saturation to its initial value ΔSaO2/SaO2). At a magnetic field of 10 mT, no change in photolysis is recorded and ΔSaO2/SaO2 has a value of 4.65±0.52% for 10 mW and 5.79±0.48% for 15 mW. With an increase in the magnetic field to 20 mT with an irradiation power of 10 mW, we have 4.74±0.56% without a field and 5.02±0.51% in a magnetic field, and with an irradiation power of 15 mW - 5.72±0.46% without a field and 5.98±0.53% in a magnetic field. When the magnetic field reached 50 mT with an irradiation power of 10 mW, we have 4.77±0.55% without a field and 5.82±0.53% in a magnetic field, and with an irradiation power of 15 mW - 5.73±0.47% without a field and 6.46±0.54% in a magnetic field. Thus, the magnetic field increases the efficiency of oxyhemoglobin photodissociation when exposed to external laser irradiation.

This work was supported by the Ministry of Education and Science of Ukraine №ДР 0124U000326

References

[1] Rola, P.; Włodarczak, S.; Lesiak, M.; Doroszko, A.; Włodarczak, A. Changes in Cell Biology under the Influence of Low-Level Laser Therapy. Photonics 2022, 9, 502. https://doi.org/10.3390/photonics9070502.

[2] Madani, A., Ahrari, F., Fallahrastegar, A. et al. A randomized clinical trial comparing the efficacy of low-level laser therapy (LLLT) and laser acupuncture therapy (LAT) in patients with temporomandibular disorders. Lasers Med Sci 35, 181–192 (2020). https://doi.org/10.1007/s10103-019-02837-x.

[3] Farivar S, Malekshahabi T, Shiari R. Biological effects of low level laser therapy. J Lasers Med Sci. 2014 Spring;5(2):58-62. PMID: 25653800; PMCID: PMC4291815.

[4] S.O. Mamilov; S.S. Yesman; D.V. Velyhotsky. Investigation of the photodissociation quantum efficiency of hemoglobin derivatives. 2019 IEEE 39th International Conference on Electronics and Nanotechnology (ELNANO) Publication Year: 2019, Page(s): 466 – 470.

[5] Xu Y, Lin Y, Gao S, Shen J. Study on mechanism of release oxygen by photo-excited hemoglobin in low-level laser therapy. Lasers Med Sci. 2018 Jan;33(1):135-139. doi: 10.1007/s10103-017-2363-y.

[6] Linares SN, Beltrame T, Ferraresi C, Galdino GAM, Catai AM. Photobiomodulation effect on local hemoglobin concentration assessed by near-infrared spectroscopy in humans. Lasers Med Sci. 2020 Apr;35(3):641-649. doi: 10.1007/s10103-019-02861-x. Epub 2019 Aug 16. PMID: 31420794.

[7] Ruziyeva, K. A. ., & Burhonova, Z. K. K. . (2021). Complex Application Of Magnetic Laser Therapy And Propolis Tincture For The Prevention And Treatment Of Chronic Recurrent Aphthous Stomatitis. The American Journal of Medical Sciences and Pharmaceutical Research, 3(06), 127–130. https://doi.org/10.37547/TAJMSPR/Volume03Issue06-20

[8] Zdrodowska B, Leszczyńska-Filus M, Leszczyński R, Błaszczyk J. [Comparison of the effect of laser and magnetic therapy for pain level and the range of motion of the spine of people with osteoarthritis lower back]. Polski Merkuriusz Lekarski : Organ Polskiego Towarzystwa Lekarskiego. 2015 Jan;38(223):26-31. PMID: 25763584.

SPATIAL ATTENTION MODULE IN AUTOENCODER FOR DENOISING BIOMEDICAL VISUALIZATIONS

Sliusarenko Denys*, Netreba Andrii**

**Faculty of RadioPhysics, Electronics and Computer Systems Taras Shevchenko National University of Kyiv, Kyiv 01601, Ukraine, email: d.fulhem@gmail.com*
***Faculty of RadioPhysics, Electronics and Computer Systems Taras Shevchenko National University of Kyiv, Kyiv 01601, Ukraine, email: avn@univ.kiev.ua*

Method of integrating the spatial attention module into the autoencoder architecture to improve the quality of denoising biomedical visualizations is presented. The proposed approach is based on the additional introduction of the attention mechanism into the deep learning model. The attention module is implemented by combining information from average and maximum pooling followed by the application of a convolutional layer to generate a spatial attention map. Experimental results show that adding an attention module improves the quality of the obtained medical imaging images after denoising.

Introduction

With the development of deep learning, new approaches have appeared to solve the problem of the presence of noise and artifacts in medical images. Architectures based on autoencoders have shown significant potential in medical image processing tasks[1]. However, standard autoencoder architectures have limitations in their ability to preserve fine detail under denoising, especially in the context of biomedical imaging, where preserving high detail is critical[2]. We have already created networks that work qualitatively with noise reduction, but they also still require improvements for better application in clinical practice. This paper proposes an improvement of one of our autoencoder models.

Attention module

The model is a complex autoencoder architecture specifically designed to process images with different pixel ranges. This model is specially developed for the processing of MRI images, considering different ranges of pixel intensities. The use of separate encoders and decoders for each range allows the model to better learn the features of various structures in the image. A separately prescribed attention module was added to this model. The attention function in this model is implemented as a spatial attention mechanism.

Working principle: The average value for each spatial position over all channels is calculated. The maximum value for each spatial position on all channels is found. The statistics are concatenated to create a two-channel feature map. A 7x7 convolution with sigmoid activation is applied to create a single-channel attention map. The attention map multiplies the input data element by element, highlighting important areas. Figure 1 shows the general representation scheme of the attention module.

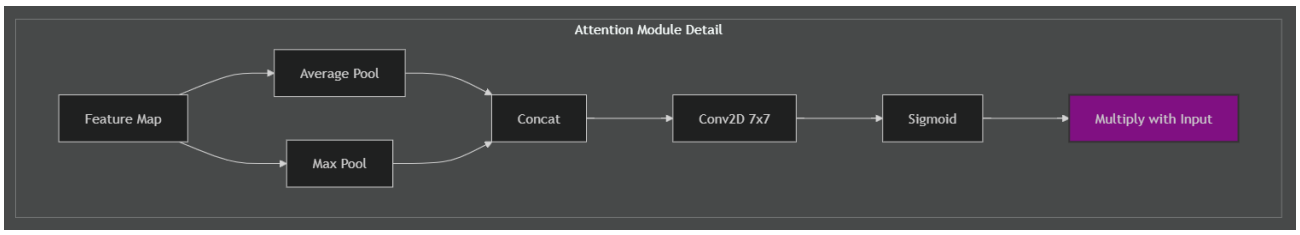

Figure 1. Attention module detail.

In terms of contributing to the denoising of medical images, the attention mechanism helps the model to focus on the most informative areas of the image. In medical images, these can be the borders of organs, pathological formations or specific anatomical structures[3]. The attention module can give less weight to areas of high noise, allowing the model to more effectively suppress noise in less important areas while preserving fine detail in critical areas.

By paying attention to the high-frequency components of the image, the module can help preserve and enhance fine details that are often lost with traditional denoising methods. Medical images often contain different tissue types with different noise characteristics to which such a model can adapt. In MRI images, there are often specific artifacts (for example, from movement). The attention mechanism can learn to identify these artifacts and reduce their impact on the final image. Comparing the results of the model before and after the implementation of the attention module, we noticed some visual and statistical improvement of the obtained denoised images, which indicates the appropriateness of using such a module in the selected model.

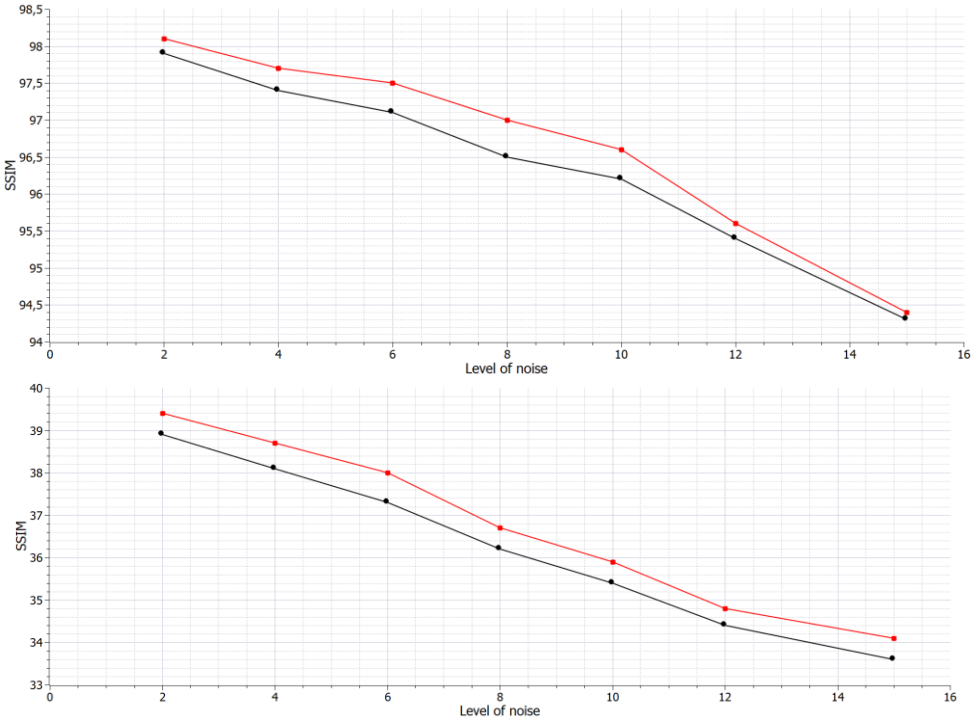

Graph 1. Comparison of PSNR and SSIM values of the model with and without the added attention module.

Graph 1 shows comparison of PSNR and SSIM values of the model with and without the added attention module. Red line – neural network with added attention module.

Conclusions

The integration of the attention module allows the model to apply the attention mechanism at different levels of abstraction, from low-level features to high-level structures. This approach improves the detail of the denoised images obtained, which in the future will lead to better clinical practices. Therefore, such a model shows particular efficiency in processing images with different noise levels and different types of tissues, which makes it a good tool for improving the quality of biomedical visualizations.

References

[1] D. Sliusarenko, A. Netreba, and S. Radchenko, 'MRI Denoising Neural Network Architecture Convolution', in *2023 IEEE 12th International Conference on Intelligent Data Acquisition and Advanced Computing Systems: Technology and Applications (IDAACS)*, Sep. 2023, pp. 968–971. doi: 10.1109/IDAACS58523.2023.10348629.

[2] S. V. Mohd Sagheer and S. N. George, 'A review on medical image denoising algorithms', *Biomed. Signal Process. Control*, vol. 61, p. 102036, Aug. 2020, doi: 10.1016/j.bspc.2020.102036.

[3] Y. Xie, B. Yang, Q. Guan, J. Zhang, Q. Wu, and Y. Xia, 'Attention Mechanisms in Medical Image Segmentation: A Survey', arXiv.org. Accessed: Oct. 04, 2024. [Online]. Available: https://arxiv.org/abs/2305.17937v1

PLASMA PHYSICS

NUMERICAL STUDY OF HEAT FLUX TO A SPHERICAL PARTICLE IN ATMOSPHERIC-PRESSURE ARGON PLASMA

D. V. Antoniv[1,2], A. I. Momot[1,2], I. V. Krivitsun[2]

Faculty of Physics, Taras Shevchenko National University of Kyiv, 64/13, Volodymyrs'ka St., Kyiv 01601, Ukraine; E.O. Paton Electric Welding Institute NAS of Ukraine, 11, Kazymyr Malevych St., Kyiv, 03150, Ukraine , e-mail: Adantoniv@gmail.com, momot.andriy@gmail.com

The heat flux to a metal particle in atmospheric-pressure argon plasma was studied numerically on the basis of the hydrodynamic (diffusion) equations for its components. The governing equations were formulated for plasma that is not in thermal and ionization equilibrium. The nonlinear problem was solved taking into account the temperature dependencies of transport and kinetic coefficients. The heat flux introduced by the plasma into the particle was compared with the results of a simple heat conduction model.

Model

Atmospheric-pressure plasma is widely used in various joining and material processing technologies, such as plasma welding, cutting, surfacing, plasma spraying, and the synthesis of metal nanopowders.

The mathematical model describing atmospheric pressure argon plasma includes the continuity equations, the equations of motion, and the energy equations for individual plasma components (atoms, ions, electrons) with the corresponding boundary conditions. A single stationary spherical particle of radius $a = 10^{-5} \div 10^{-4}$ m is placed into plasma. The characteristic time of plasma parameters establishing is much less than the temperature change of metal particle surface [1]. Thus, we consider the constant temperature of the particle surface $T_s = 1000$ K and study the stationary distribution of plasma characteristics near the particle. The portion of material evaporating from the particle, as well as electron emission, is negligible at T_s, and thus, these phenomena are not included in our model.

The plasma near the particle is in ionization non-equilibrium, and heavy plasma components (atoms and ions), have the same temperature, that differs from the electron temperature. This obliges us to use two-temperature model for plasma to adequately describe the physical processes. The thickness of the space charge layer formed near particle surface is of the order of the Debye radius r_D that is $r_D \sim 10^{-7}$m for the considered plasma parameters [1], which is much smaller than the particle radius ($r_D \ll a$). As such, the sheath can be considered as infinitely thin, and its outer boundary is assumed to coincide with the particle surface. To describe heat and mass dynamics, we used the approach proposed [2], and further developed in Refs. [3–5]. This approach neglects convective effects in plasma and assumes that the dominant mechanism of momentum and energy exchange between plasma components is collisions.

Results and discussion

Heat flux from plasma to particle consists of 5 parts. First two (q_{p1}, q_{p2}) are due to heat conductivity of electrons and heavy particles, third one (q_{p3}) is convective term, fourth (q_{p4}) corresponds to recombination of ions on the particle surface, fifth (q_{p5}) is inelastic collisions of ions with particle surface. The major contribution to the heat flux is provided by q_{p2}. The heat flux components are related as $q_{p2} > q_{p4} > q_{p5} > q_{p3} \approx q_{p1}$. The heat flux due to ion recombination on the particle surface q_{p4} becomes near the same as q_{p2} for unperturbed plasma temperature (far from particle) $T_0 \gtrsim 18000$ K.

Results from the simple heat transfer model ($q_p = \frac{\bar{\lambda}}{a}(T_0 - T_s)$, where $\bar{\lambda}$ is the mean total plasma thermal conductivity [1]) and our modeling a significant discrepancy in total heat flux near the particle surface – simple estimations differ drastically for small ($a < 10^{-5}$ m) particles and temperatures exceeding 18000 K. Comparing

obtained heat flux densities reveals that, in the simplified model q_p grows ever faster with temperature. In contrast, data, obtained from our modeling behaves quite differently: Firstly, it grows linearly ($T_0 < 7000$ K); when significant portion of atoms are ionized – it grows significantly faster ($T_0 = 7000 \div 16000$ K); after almost all atoms are ionized – the growth slows down, and a linear dependence established again ($T_0 > 16000$ K), but with a steeper slope than before. Thus, the simple formula gives quite accurate values of heat flux for $a = 5 \times 10^{-5} \div 10^{-4}$ and $T_0 \leq 14000$ K.

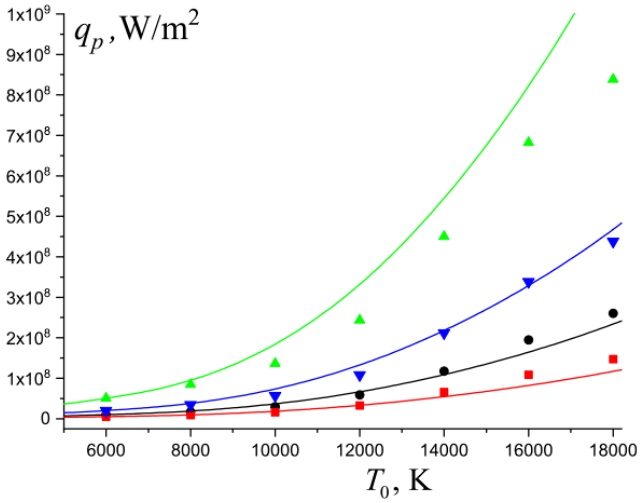

Fig. 1. Dependence of heat flux to the particle on unperturbed plasma temperature T_0 for $a = 10^{-5}$ m (green), 2.5×10^{-5} m (blue), 5×10^{-5} m (black), 10^{-4} m (red), and $T_s = 10^3$ K. Symbols are results of numerical calculations; lines represent simple model data.

References

[1] I V Krivtsun, A I Momot, D V Antoniv, and Binhao Qin. Characteristics of atmospheric pressure Ar-plasma around a spherical particle: Numerical study. Phys. Plasmas, 30(4):043513, 2023.

[2] N A Almeida, M S Benilov, and G V Naidis. Unified modelling of near-cathode plasma layers in high-pressure arc discharges. J. Phys. D: Appl. Phys., 41(24):245201, 2008.

[3] M Baeva, M S Benilov, N A Almeida, and D Uhrlandt. Novel non-equilibrium modelling of a dc electric arc in argon. J. Phys. D: Appl. Phys., 49(24):245205, 2016.

[4] I L Semenov, I V Krivtsun, and U Reisgen. Numerical study of the anode boundary layer in atmospheric pressure arc discharges. J. Phys. D: Appl. Phys., 49(10):105204, 201.

[5] D F N Santos, M Lisnyak, and M S Benilov. Account of diffusion in local thermodynamic equilibrium and two-temperature plasma models. J. Phys. D: Appl. Phys., 52(45):454003, 2019.

PLASMA DIAGNOSTICS OF MAGNETRON DISCHARGE WITH COPPER AND MOLYBDENUM VAPOURS ADMIXTURES

A. Murmantsev, A. Veklich, O. Kostyukevych, M. Papizh, A. Monastyrov

[1]*Taras Shevchenko National University of Kyiv, 63/13, Volodymyrska str., Kyiv 01601, Ukraine*
**murmantsev.aleksandr@gmail.com*

Magnetron discharge plasma with copper and molybdenum vapours admixtures are investigated by means of optical emission spectroscopy. A target, consisting of two semicircles made of copper and molybdenum, was vaporised using a magnetron sputtering system. The optical emission spectra were recorded in the spectral range of 440–910 nm. The plasma was produced in an argon atmosphere at pressures of 1.3, 6.7, 13.3, and 53.3 Pa with discharge currents ranging from 50 to 300 mA. Excitation temperatures were determined by Boltzmann plot technique based on emission intensities of Ar I, Cu I and Mo I spectral lines.

Introduction

As is known, magnetron discharge thin film deposition is widely used to meet the needs of the electronics industry [1]. In order to eliminate shortcomings of the traditional single-component thin films, so-called composite materials are used, in which the properties of different metals are additively combined. In particular, Cu-Mo composite materials are widely used in cooling and heat-sink elements in electronic device components such as microwave integrated circuits, insulated gate bipolar transistors, diode lasers or light emitting diodes [2]. Most of the works devoted to the deposition of Cu-Mo thin films is focused on the study of the films directly and do not consider the processes in the plasma of magnetron discharges, which are used for the generation of metal complexes and their deposition on the substrate. It is worth noting that the deposition of thin films after the formation of clusters in the magnetron discharge of several types of metals at once is promising. Thus, this work deals with on optical emission spectroscopy of magnetron discharge plasma with copper and molybdenum vapour admixtures.

Results and discussion

All studies were realized by magnetron sputtering deposition system described in detail in [3]. A 72 mm diameter disk made of copper was used as a target, on which a semicircle of the same diameter made of molybdenum was placed on top. The Solar LS SDH-IV spectrometer was used to register the emission spectra of the plasma in the spectral range of 440-910 nm. The entrance slit of the spectrometer was focused on the junction of different metals. Thus, it was possible to register the emission of magnetron discharge plasma with admixtures of both copper and molybdenum. The emission spectra were registered in argon at pressures of 1.3, 6.7, 13.3 and 53.3 Pa ($1\cdot10^{-2}$, $5\cdot10^{-2}$, $1\cdot10^{-1}$, $4\cdot10^{-1}$ Torr) in DC mode and at currents of 50, 100, 150, 200, 250 and 300 mA. The spectral lines of both metals and argon were clearly selected and used to determine the excitation temperatures by Boltzmann plot technique. The results of such determination are shown in Fig. 1 and 2, namely the current dependences of the excitation temperatures of copper, molybdenum and argon atoms.

One can see, that the temperatures, obtained from the spectral lines of metals and argon, tend to decrease with increasing current (Fig. 1). Moreover, the excitation temperature in copper and molybdenum atoms is lower than the excitation temperature in argon in all modes of discharge burning. Furthermore, a decrease in temperature with an increase in pressure is observed for all species (Fig. 2). It can also be seen from Fig. 1 that the difference between the excitation temperatures of atoms of both metals and argon atoms becomes smaller as the pressure of the surrounding gas increases.

It can be concluded, that the local thermodynamic equilibrium is not realised in such plasma. Indeed, the number densities of metal atoms in such discharge are substantially less than the number density of argon as a buffer gas. This results in a very small amount of metals in the plasma, which is insufficient for thermalization. In turn, argon gains more energy from the discharge compared to copper or molybdenum because it typically experiences more direct collisions with energetic electrons, resulting in a higher excitation temperature.

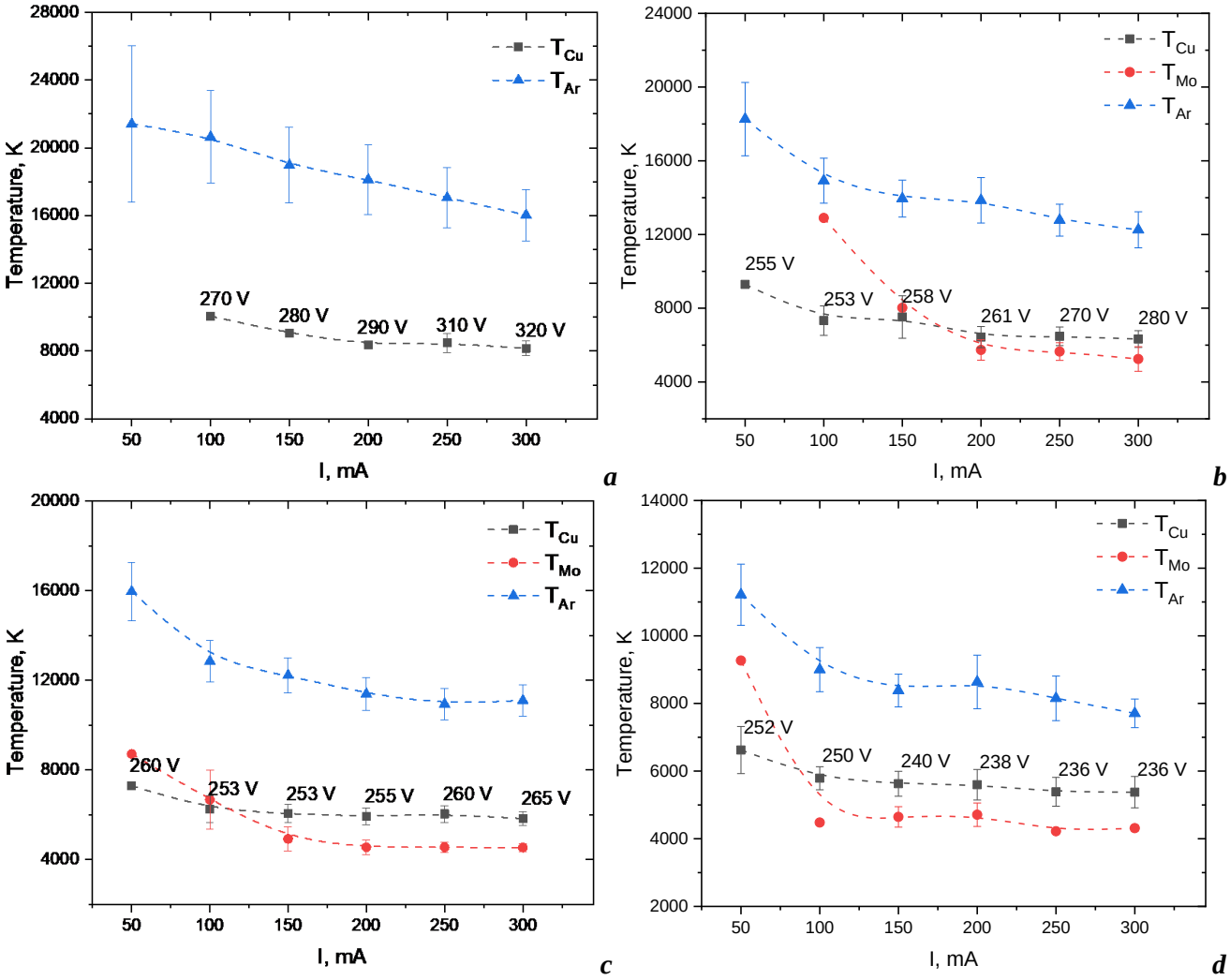

Fig. 1. Current dependences of the excitation temperatures of copper, molybdenum and argon atoms at pressure of (a) 0.01 Torr, (b) 0.05 Torr, (c) 0.1 Torr and (d) 0.4 Torr

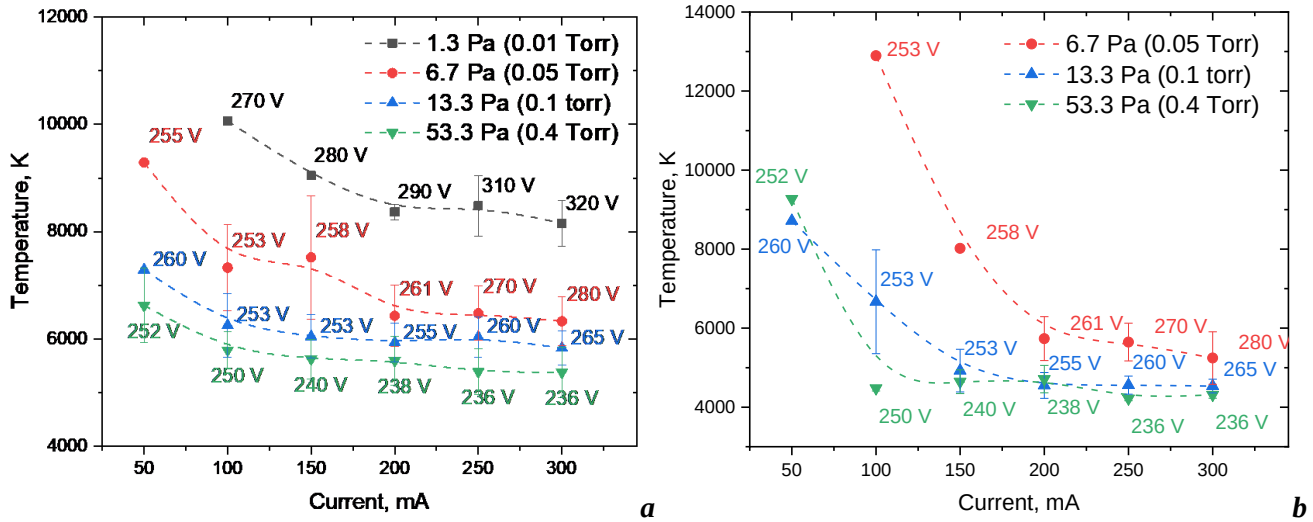

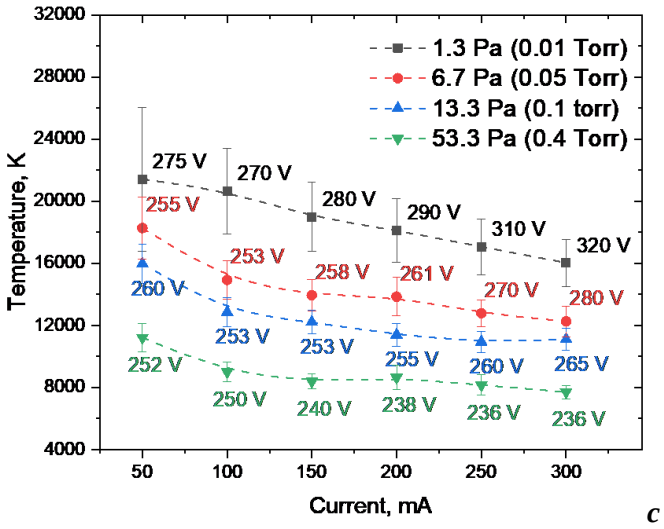

Fig. 2. Current dependences of the excitation temperatures of (a) copper, (b) molybdenum and (c) argon atoms at different pressures

As the pressure increased the collision (both elastic and inelastic) frequency between particles in the plasma increases. This leads to more energy redistribution through collisions, causing the energy to be spread across a larger number of particles, thereby lowering the excitation temperature.

Conclusions

The differences in excitation temperatures between argon, copper, and molybdenum suggest that local thermodynamic equilibrium is not realised in this plasma. The significantly lower number density of metal atoms in comparison to argon results in insufficient conditions for full thermalization, leading to different energy distributions for different species.

The observed decrease in excitation temperature with increasing current and pressure can be explained by the increased collision frequency and energy redistribution at higher pressures. It was found that as the pressure increases, the temperature difference between argon and metal atoms decreases. This can be explained due to the increased collisional interactions between particles at higher pressures, which promote energy redistribution across different species.

Acknowledgment

This work was supported by the National Research Foundation of Ukraine (Grant № 2023.03/0169).

References

[1] M. Vaidulych, J. Hanuš, J. Kousal, S. Kadlec, A. Marek, I. Khalakhan, A. Shelemin, P.Solař, A. Choukourov, O. Kylián, H. Biederman. Effect of magnetic field on the formation of Cu nanoparticles during magnetron sputtering in the gas aggregation cluster source // *Plasma Process and Polymers*. 2019. -e1900133. https://doi.org/10.1002/ppap.201900133

[2] L. Kai, M. Xiaojun, Q. Dan, Yu. Li, M. Yu, P. Yajuan, Ya. Bo, L. Yanhuai, H. Liucheng, F. Yanyan, S. Zhongxiao. Arc erosion resistance of CuCrMo films deposited via magnetron sputtering // *Mater. Res. Express*. 2021, V. 8, 066402. https://doi.org/10.1088/2053-1591/ac0179

[3] O.O. Murmantsev, A.M. Veklich, O.Yu. Kravchenko, O.M. Kostyukevych. Optical emission spectroscopy of magnetron discharge with metal vapours admixtures // *XVII International Scientific Conference «Electronics and Applied Physics» October, 19-23, 2021, Kyiv, Ukraine.* P. 69-72.

ELECTRON SOURCE BASED ON EMERGENCE OF SELF-INJECTED ELECTRON BUNCH AT PLASMA WAKEFIELD EXCITATION BY A TW LASER PULSE

D. S. Bondar*, V. I. Maslov, I. N. Onishchenko*****

**National Science Center "Kharkiv Institute of Physics and Technology", Akademichna street, b. 1, Kharkiv, Kharkiv region, Ukraine, e-mail: bondar.ds@yahoo.com*
*** National Science Center "Kharkiv Institute of Physics and Technology", Akademichna street, b. 1, Kharkiv, Kharkiv region, Ukraine*
Deutsches Elektronen-Synchrotron DESY, Notkestraße 85, Hamburg, Germany, e-mail: vimaslov1955@gmail.com
**** National Science Center "Kharkiv Institute of Physics and Technology", Akademichna street, b. 1, Kharkiv, Kharkiv region, Ukraine, e-mail: ipenma@ukr.net*

This paper presents simulations of wakefield excitation in plasma by a laser pulse with ten millijoule scale energy and 1, 2 TW power, aimed at generating self-injected relativistic electron bunches. Two plasma profiles, homogeneous and Gaussian, were considered. The study, based on the laser setup parameters of the NSC Kharkiv Institute of Physics and Technology, demonstrates the feasibility of producing high-energy electron bunches and highlights the benefits of plasma profiling for enhanced acceleration and self-injected bunches parameters.

Formation and parameters of self-injected bunches

Wakefield acceleration in high-density plasma effectively accelerates electrons to high energies, achieving GeV energies with high-intensity lasers [1]. Control of self-injected electron bunches through plasma density profiling has optimized bunch length, charge, and energy [2]. Longitudinal plasma profiling allows fine-tuning of electron energy and maintaining bunches in the acceleration phase [3]. These techniques are essential for developing compact, high-gradient accelerators, particularly using sub-TW and TW-class lasers [4]. During the study, two problems were successfully solved: firstly, for the given parameters of a real laser setup [5], the possibility of forming self-injected bunches with parameters that are relevant for modern accelerators was demonstrated. In addition, the advantage of using a Gaussian plasma profile has been demonstrated, which can be achieved experimentally [4] to increase the energy and situation time of a self-injected bunch in the accelerating phase of the wakefield. Simulation is completed using the commonly used for wakefield simulation 2.5-dimensional code OSIRIS [6].

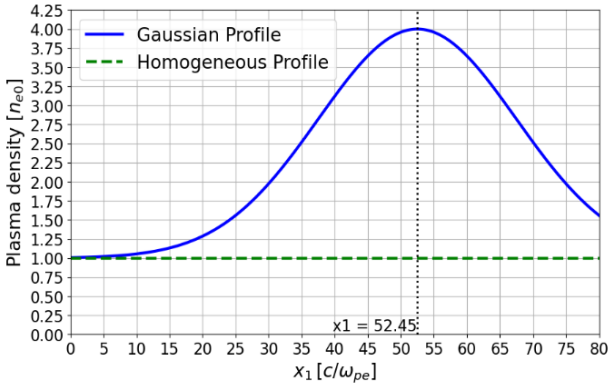

Fig. 1. Plasma electron density longitudinal profile $n_e(x)$. The position of the laser pulse is shown.

In the simulations, the laser parameters of the laser setup at the Institute of Plasma Electronics and New Acceleration Methods of the NSC KIPT were used. The laser had a wavelength of 800 nm, with a focal radius of 2.2 μm and operated at powers of 1 TW and 2 TW (homogeneoues plasma), and 2 TW (inhomogeneous plasma). The pulse duration was set to 20.4 fs, corresponding to pulse energies of 20.4 mJ and 40.8 mJ. The laser pulse

intensity profile of the laser was Gaussian, characterized by a standard deviation σ = 1.527 μm. A plasma density of $1.74*10^{19}$ cm^{-3} was chosen, corresponding to a commonly used value in similar research. In Fig. Figure 1 shows plasma density profiles. In Fig. Figure 2 shows the density, longitudinal momentum, and acceleration field in the region of the self-injected bunch. In homogeneous plasma (2 TW), a self-injected bunch was obtained with a length of 2.16 μm, a density of $2.7n_{e0}$, and a maximum energy of 6.74 MeV. In inhomogeneous plasma, the bunch parameters improved: the length increased to 1.66 μm, the density rose to $7.5n_{e0}$, and the maximum energy reached 11.17 MeV. The electron source capable of producing such high-quality bunches also proves its efficiency and suitability for various scientific and practical applications.

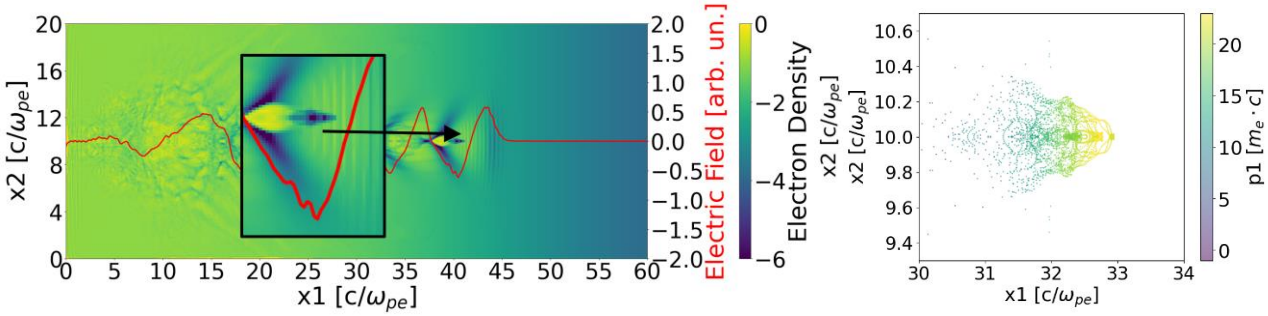

Fig. 2. (a) Density graph $n_e(x_1, x_2)$, longitudinal acceleration field $E_x(x_1)$; (b) longitudinal momentum of the bunch $p_1(x_1, x_2)$.

Numerical simulation showed that, under the given parameters, wakefield excitation in relatively high density plasma is accompanied by emergency of bunches with suitable characteristics for further research and obtaining high acceleration rates. The use of a inhomogeneous plasma profile enhances bunch energy and extends time of its stay in the acceleration phase.

Acknowledgements

The study is supported by the National Research Foundation of Ukraine under the program "Excellent Science in Ukraine" (project # 2023.03/0182).

References

[1] W. Leemans and E. Esarey, "Laser-driven plasma-wave electron accelerators," Phys. Today, vol. 62, no. 3, pp. 44–49, Mar. 2009, doi: 10.1063/1.3099645.

[2] D. S. Bondar, V. I. Maslov, and I. N. Onishchenko, "On Wakefield Acceleration in Inhomogeneous Plasma," Problems of Atomic Science and Technology, no. 3(151), 2024, doi: 10.46813/2024-151-055.

[3] C. Aniculaesei et al., "Electron energy increase in a laser wakefield accelerator using up-ramp plasma density profiles," Sci. Rep., vol. 9, p. 11249, 2019, doi: 10.1038/s41598-019-47677-5.

[4] Z.-H. He et al., "High repetition-rate wakefield electron source generated by few-millijoule, 30 fs laser pulses on a density downramp," New Journal of Physics, vol. 15, p. 053016, 2013, doi: 10.1088/1367-2630/15/5/053016.

[5] V. P. Leshchenko, A. V. Vasyliev, K. V. Galaydych, A. I. Povrozin, and G. V. Sotnikov, "Simultaneous Compensation of Second and Third Order Dispersion in CPA Laser Systems," Problems of Atomic Science and Technology, no. 4(146), 2023, doi: 10.46813/2023-146-041.

[6] R. Fonseca et al., "Exploiting multi-scale parallelism for large scale numerical modelling of laser wakefield accelerators," Plasma Phys. Control. Fusion, vol. 55, p. 124011, 2013, doi: 10.1088/0741-3335/55/12/124011.

STUDY OF THE IGNITION VOLTAGE OF A NEGATIVE PULSED CORONA DISCHARGE WITH COMBINED POWER SUPPLY

G. V. Taran, B.B. Kadolin, I.N. Onishchenko

NNC "Kharkiv Institute of Physics and Technology" NASU, Kharkiv, Ukraine
E-mail: tarang@kipt.kharkov.ua

The study investigates the ignition of a negative pulsed corona discharge in plasma-chemical reactors with a multi-pin segmented cathode. The dependence of the ignition voltage on the amplitude of the low-voltage DC applied in intervals between high-voltage pulses is presented. It is shown that under all investigated experimental conditions, the ignition voltage U_i decreases monotonically with the growth of U_{dc}/d. It is also demonstrated that electrode shielding leads to an increase in ignition voltage.

EXPERIMENTAL STUDIES

The plasma-chemical reactor consisted of a coaxial system with a cylindrical anode made of thin-walled stainless steel tubing with an internal insert of TMG-F/A1 graphite foil, 0.35 mm thick. The inner diameter of the anode was 38 mm, and the length was 500 mm. Along the anode axis, using a high-voltage insulator, a segmented cathode was placed, consisting of cathode sections mounted on a rod at a distance l from each other. Each cathode section was a 0.5 mm thick stainless steel disk with 25 radially arranged individual cathodes. Each individual cathode had a height of 3 mm and a rectangular cross-section of 0.5x0.5 mm. The allowable deviation of the segmented cathode axis from the cylindrical anode axis was no more than 50 μ. The inter-electrode gap d was 3.5, 4, 4.5, 5, and 5.5 mm. The distance between the cathode sections l was 4 mm, 6 mm, 8 mm, and 10 mm.

The power source was a high-voltage pulse generator with the following parameters: the amplitude of high-voltage pulses on a capacitive-resistive load was adjustable between 5-15 kV, the pulse duration at half-maximum was ~1 μs, and the pulse repetition frequency was 1-20 kHz, with a power of 150W. For the plasma-chemical reactors, a combined power supply was used, so along with тти he pulsed high-voltage power source, a low-voltage DC source with adjustable voltage in the range of 0 V to 1 kV was employed.

RESULTS OF THE STUDY

Consider the effect of low-voltage DC applied during the intervals between high-voltage pulses on the ignition voltage of a negative pulsed corona discharge in oxygen with varying geometric parameters of the electrode system. To this end, we introduce the average electric field strength across the gap during the intervals between high-voltage pulses U_{dc}/d, where U_{dc} is the DC voltage and d is the length of the discharge gap.

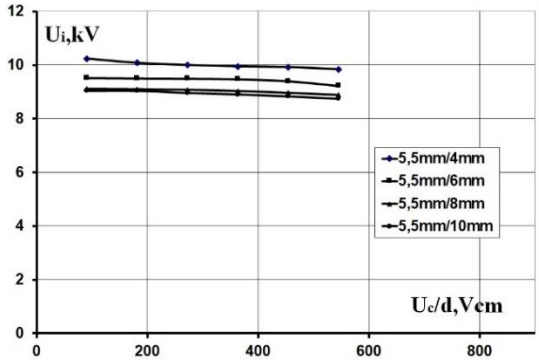

Fig. 1. The dependence of the ignition voltage U_i on U_{dc}/d in the electrode system with an inter-electrode gap d = 5.5 mm and cathode section distances l = 4 mm, 6 mm, 8mm, 10mm.

The given dependence (see Fig. 1) illustrates the relationship characteristic of all electrode system configurations between U_i and the distance between the cathode sections, *l*. The distance between the cathode sections, *l*, affects the degree of shielding of the cathodes from each other, which is manifested in the change in the distribution of the electric field strength in the immediate vicinity of the ionization region surrounding the cathode. The curves in Fig. 1 show that for electrode systems where the distance between the cathodes is less than or equal to the inter-electrode distance, $l \leq d$, the ignition voltage significantly exceeds the ignition voltage for electrode systems with $l > d$. Another feature is the monotonic decrease in the ignition voltage with increasing U_{dc}/d. The nature of the dependence is close to linear for the investigated range of $U_{dc}/d = 0 - 600$V/cm. It can be seen that for different distances *l* between the cathode sections, the curves run almost parallel, which means that the inhomogeneity of the electric field strength distribution at the cathode, determined by the geometric parameters of the electrode system, although it affects Ui, does not affect the magnitude of the change in ignition voltage U_i.

For a more detailed examination of the behavior of U_i depending on the average electric field strength across the discharge gap, we compare the ignition voltage in electrode systems with a similar distribution of the electric field strength at the cathode, i.e., with the same distance between cathode sections *l*, but for different inter-electrode gaps d.

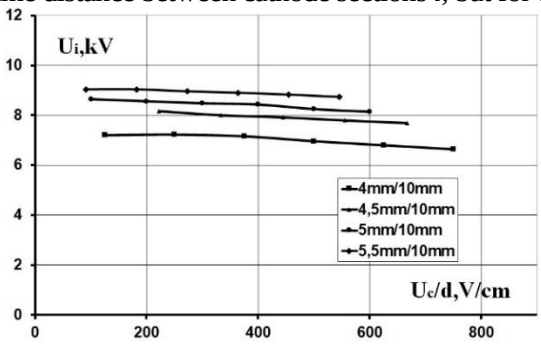

Fig. 2. Dependence of the ignition voltage U_i on U_{dc}/d in an electrode system with a distance between cathode sections of (l = 10) mm and an inter-electrode gap of (d = 4.0) mm, 4.5 mm, 5.0 mm, 5.5 mm.

The curves presented in Fig.2 show a strong dependence of U_i on the magnitude of the discharge gap. The shape of the curves in Fig. 2 is similar to that in Fig. 1. All experiments were conducted at the same high-voltage pulse repetition frequency of 12 kHz, which provides a time between high-voltage pulses of 83 μs. During the time between pulses, given a specific electric field strength, the distance can be estimated over which the bulk negative charge will drift in the electric field according to $v = \mu * E$, where μ is the mobility of negative ions, 2.2 $cm^2/V/s$, and E is the electric field strength in V/cm. In the considered range of electric field strength, during the time between pulses, 90.9 V/cm - 857 V/cm, the bulk charge will shift over a distance of 0.0167 cm - 0.157 cm, respectively.

The study is supported by the National Research Foundation of Ukraine under the Program “Science to Strengthen Defense Capabilities of Ukraine” (Project #2023.04/0092).

REFERENCES

[1] V. I. Golota, L. M. Zavada, B. B. Kadolin, I.A. Paschenko, S. G. Pugach, G.V.Taran and A.V. Yakoclev, “Pulsed discharge for ozone synthesis”, //*XV Int.Conf. on Gas Discharges and their Appl.*//, GD2004, Toulouse – France.5-10 September v.1, p.750-756,.

[2] Černák M., T. Hosokawa, S. Kobayashi, T. Kaneda "Streamer mechanism for negative corona current pulses *// J. Appl. Phys.*// 1998, v.83 p. 78-90.

[3] V. I. Golota, B.B. Kadolin, I.A. Paschenko Investigation of ozone synthesis in the negative pulsed corona discharge in oxygen at the combined supply voltage // *Problems of Atomic Science and Technology. Ser. «Plasma Physics»*// 2021, №1, p. 74-77

[4] G.V. Taran, B.B. Kadolin, V.M. Ostroushko, I.A. Paschenko Study of the dependence of the characteristics of the pulse negative corona on the parameters of the combined high voltage power supply // *Problems of Atomic Science and Technology, Ser. Plasma Electronics and New Methods of Acceleration*// 2023, №4, p. 160-163

PECULIARITIES OF NON-EQUILIBRIUM OF DYNAMIC PLASMA-CHEMICAL SYSTEMS

Valeriy Chernyak[1], Daniil Tretiakov[1], Vitalii Iukhymenko[1],Sergeiy Shulga[2], Volodymyr Trachevskiy[3], Oleksandr Kolomys[4], Victor Strelchuk[4], Volodymyr Kyslyi[4], Kostiantyn Iukhymenko[1], Olexander Tsymbaliuk[1], Sergeiy Nedovesov[1]

[1]Taras Shevchenko National University of Kyiv, Faculty of RECS, e-mail:chernyak_v@ukr.net
[2]Institute of Hydromechanics NAS of Ukraine, e-mail: sergey.v.shulga@gmail.com
[3]G. V. Kurdyumov Institute for Metal Physics of the NAS of Ukraine, e-mail: trachev@imp.kiev.ua
[4]V. Lashraryov Institute of semiconductor physics of the NAS of Ukraine, e-mail: olkolomys@gmail.com

It is always the most relevant for plasma chemistry, as a scientific direction for researching the possibilities of plasma activation of chemical transformations of substances, the solution of which problems using the methods of traditional chemistry is not possible or extremely difficult. Because plasma generation is associated with the use of an expensive type of energy (electricity) and the high temperature of heavy plasma components, which is not very compatible with such basic requirements for modern technological processes as energy efficiency and minimal harmful impact on the environment.

Many chemical technology processes take place at constant pressure and temperature, if they occur in open apparatuses, or at constant volume and temperature, if they occur in closed apparatuses, for example, in autoclaves. But it is fundamental for all chemical systems that the implementation of substance transformations takes place in quasi-equilibrium conditions [1]. This means that chemical thermodynamics determines the direction and limit of transformations of substances from the conditions in which these substances exist, and chemical kinetics determines the mechanism and regularities of the course of the chemical process over time.

The direction of the process and equilibrium in the system at constant pressure and temperature is determined by the Gibbs energy (Gibbs free energy or isobaric-isothermal potential) - G or at constant volume and temperature - the Helmholtz energy in physical chemistry [2]. Thus, the possibility of involuntary passage of chemical processes means in thermodynamic systems that only processes can occur arbitrarily in the system, that thermodynamic potentials will decrease under the condition of constancy of the corresponding natural variables. At the same time, it should be noted that the prophecies of chemical thermodynamics are most accurate in their "prohibitive" part. On the other hand, not all reactions for which $G < 0$ are "in a hurry" to take place in practice. [1].

The plasma activation of the process of synthesis of substances occurs when there is a significant energy-mass exchange with the environment or the presence of large values of the rate of the temperature change in the system, which leads to an unbalanced process in plasma-chemical systems. Accordingly, non-equilibrium chemical kinetics determines the regularities of the time course of substance transformation processes [3].

L. Polak formulated on the basis of the specifics of the theoretical description of the kinetics of chemical transformations [3] and the known results of experimental studies of reactions in non-equilibrium plasma at the beginning of the 80s of the 20th century. [4] the following statement [5]:

"The variety of phenomena that have already been found and can still be found in reacting physico-chemical systems is almost infinite. Usually, these systems are described by nonlinear differential equations in partial derivatives, and in a certain sense it can be said that "anything can happen...".

Non-equilibrium plasma chemistry revealed the many confirmations of this prophecy over the last 40 years of development. Namely, the progress in microelectronics during the transition from purely chemical to plasma-chemical technologies [6], the growth of diamond films at sub-atmospheric pressures [7], the synthesis of numerous forms of nano-sized materials [8], etc.

As you know, a universal chemical rule exists in organic chemistry:

"Always the synthesis of chiral compounds from achiral reagents leads to racemic modification". "Optically inactive reagents produce only optically inactive products" [9]. This rule is a consequence of the basic provisions of chemical thermodynamics and significantly limits the potential possibilities of organic, bio- and pharmaceutical chemistry.

This work is devoted to considering the results of our research on the possibility of violation of this rule in the plasma-liquid system, in which the nonequilibrium of the system is also caused by the lack of equiprobability in the directions of rotation of the reactant particles , which is ensured by the gas dynamics of the rotating gas flow in the system. A natural phenomenon that corresponds to the occurrence of this type of disequilibrium in the plasma-chemical system is the lightning in the Tornado gas stream and which was not noticed in the famous works of Stanley Miller [10].

The main results of these studies are:

1. For the first time, a number of plasma-chemical systems were developed for plasma activation of chemical transformations in non-equilibrium systems in the absence of equal probability in the directions of rotation of reactant molecules, which is ensured by the gas dynamics of the rotating gas flow in the system.

2. Secondary discharges supported by independent discharges were implemented for the first time. The principal feature of which is the ability to control the high-energy part of the plasma electron distribution function by energies within very wide limits.

3. Experimentally realized synthesis of an optically active medium activated by a plasma of a rotating 3-dimensional sliding discharge using only optically inactive reagents.

4. The change in the optical activity of aqueous solutions of polar chemically pure isomers during plasma activation is realized by tens of percent due to the significant influence on the change of OA direction of rotation of reactant molecules in the system.

5. A kinetic model of the synthesis of OA substances from optically inactive reagents in a dynamic plasma-chemical system has been developed, in which the gas-dynamics conditions not only the efficient energy-mass exchange of the system and the high rate of quenching of the synthesis products in the suspended layer, but also ensures the absence of equiprobability in the directions of rotational of the rotation excited reactant molecules.

References

[1] V.V. Zagorsky. Lectures on General and Inorganic Chemistry: http://www.chem.msu.ru

[2] A. G. Kaplaushenko, Yu. G. Samelyuk, Yu. S. Frolova, Chemical thermodynamics: a basic textbook for students of the specialty “Pharmacy, industrial pharmacy. Zaporizhzhya: ZDMFU, 2023.

[3] L. S. Polak. Nonequilibrium chemical kinetics and its application. Moscow: Nauka,1979.

[4] Polak L. S., Lebedev Yu. A., Levitsky I. A., et al. New problems of plasma-chemical kinetics: Prep. INHS USSR Academy of Sciences, 1981.

[5] Polak L.S., Mikhailov A.S. Self-organization in nonequilibrium physical and chemical systems. Moscow: Nauka, 1983.

[6] Plasma technology in the production of ULIS / Edit. N. Einspruck, D. Brown. Moscow: Mir, 1987.

[7] Maikl U. Geis, John C. Angus, “Semiconducting Diamond Films”, Scientifik American, pp.160-168, 1992.

[8] Rikizo Hatakeyama, “Nanocarbon materials fabricated using plasmas”, Rev. Mod. Plasma Phys. 1:7, pp.1-110. 2017.

[9] Morrison, R.T. and Boyd, R.N., Organic Chemistry, 5th ed. Allyn & Bacon Inc. 1987.

[10] [10 Stanley L. Miller, “A Production of Amino Acids Under Possible Primitive Earth Conditions”, Science, Vol. 117, P.528-529, 1953.

MODELLING OF ARGON-ACETYLENE PLASMA WITH DUST PARTICLES IN THE AFTERGLOW REGIME

I.B. Denysenko*, V.V. Vinnichenko*

**V.N. Karazin Kharkiv National University, 61022 Kharkiv, Ukraine,*
e-mails: igor.denysenko@karazin.ua, vladvinni@ukr.net

A theoretical model for argon-acetylene plasma afterglow with dust particles is presented. Using the model, plasma characteristics (electron and ion densities, electron temperature and densities of argon metastable atoms) as well as those of dust particles (mean dust charge and dust charge distribution function) are analysed. The studies are carried out for low and moderate initial electronegativities of plasma. Dust particles of different radii are considered. The calculated time dependences for the electron and metastable atom densities are found to be in agreement with the existing experimental data.

Theoretical description of model

A gas-discharge plasma of radius R = 15 cm and height L = 7 cm sustained in a mixture of argon and acetylene is considered. It is assumed that the plasma consists of electrons with density n_e and temperature T_e, eleven positive ions (Ar^+, ArH^+, C_2H^+, $C_2H_2^+$, $C_4H_2^+$, $C_6H_4^+$, $C_8H_6^+$, $C_{10}H_6^+$, $C_{12}H_6^+$, $C_{14}H_8^+$, $C_{16}H_8^+$), four nonradical neutrals (Ar, C_2H_2, H_2, C_4H_2) and two radicals (C_2H and H), as well as argon atoms in different excited states. The plasma also contains negative ions (C_2H^-, H_2CC^-, $C_4H_2^-$, $C_6H_2^-$, $C_8H_2^-$, $C_{10}H_2^-$ and $C_{12}H_2^-$) and dust particles with radius a_d. Here, we consider the case when the dust density is small (the absolute value of dust charge density is smaller than the electron density), and the dust particles do not affect much on gas-discharge characteristics. It is also assumed that the energy distributions for ions and electrons are Maxwellian, and that the positive ions and dust particles are at gas temperature T_g (400 K), while the temperature of negative ions T_- is assumed to be $3T_g$. The electron temperature T_e as a function of the afterglow time t is found using the power balance equation (Eq. (6) in [1]).

The density of a species X (electrons, H_2, C_4H_2, C_2H, H, argon atoms in excited states, as well as negative and positive ions, excepting $C_{16}H_8^+$, is found from the balance equation

$$\partial n^{(X)}/\partial t = \sum_i R_{G,i}^{(X)} - \sum_i R_{L,i}^{(X)}, \quad (1)$$

where $R_{G,i}^{(X)}$ and $R_{L,i}^{(X)}$ are, respectively, the rates for reactions describing generation and loss processes of the species X. The density of C_2H_2 is a parameter of this model. The density of $C_{16}H_8^+$ ions is obtained from the quasineutrality condition

$$\sum_\alpha n_\alpha^+ = n_e + \sum_\alpha n_\alpha^-, \quad (2)$$

where n_α^+ and n_α^- are, respectively, the densities of αth positive and negative ions.

Our model assumes that dust particles of the same radius a_d may have different charges $Z_d^k = ke$ (where k is an integer and e is the elementary charge) due to stochastic charge fluctuations connected with charge discreetness. The dust charge distribution function (DCDF) F_k (normalized by $\sum_k F_k = 1$) is calculated from the master equation describing dust charging as a one-step process [2]. We also calculated the mean dust charge Z_d assuming that dust particles of the same radius have the same charge. More details on our model can be found in [1].

Results of numerical calculations

The model presented in previous section has been used to study properties of plasma and dust charge as functions of time in an Ar/C_2H_2 plasma afterglow. The calculations have been carried out for the conditions close to the experiment in [3]. The calculated time dependences for the normalized electron and metastable atom

densities have been compared with the dependences measured in the experiment [3]. There is good quantitative agreement between the calculated and experimental time dependences (Fig. 1) if we take in the simulations n_{C2H2} = 4.0×10^{12} cm^{-3} and $n_e(t=0) = 4.0\times10^9$ cm^{-3}(corresponds to the experiment [3]).

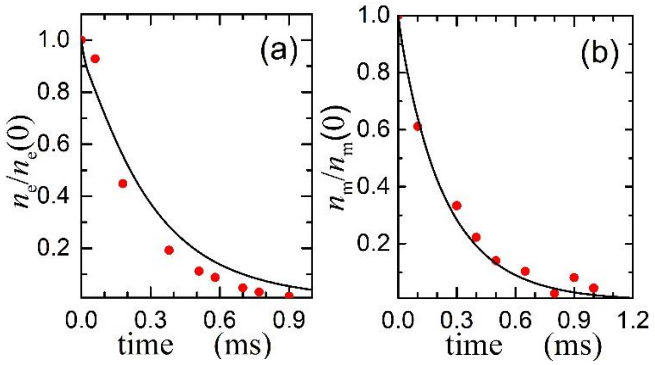

Fig. 1. The normalized electron (a) and metastable densities (b) as functions of time in argon-acetylene afterglow plasma. Solid lines — model; circles — experiment [3]. n_m is the density of metastable argon atoms.

However, the absolute value of the calculated initial metastable atoms' density is nearly 4 times larger than that measured in the experiment (the calculated and measured initial metastable densities are 10^{10} cm^{-3} and 2.7×10^9 cm^{-3}, respectively). This difference, in our opinion, is mainly due to some simplifications in our model, as well as due to the measurement method of n_m in the experiment [1, 3].

We also analyzed the time dependences for other plasma parameters (ion densities, electron temperature, densities of argon metastable atoms) and for dust charge characteristics for the conditions corresponding to Fig. 1 (the results are presented in [1]). Note that in the case corresponding to Fig. 1, the initial electronegativity of the bulk plasma α_b (t = 0) is very low (0.019). Due to the small α_b, the effect of negative ions on dust discharging in the afterglow plasma was found to be negligible [1]. Therefore, we considered the case when the initial electronegativity is not very small. In Fig. 2, plasma and dust charge parameters are shown for the case when n_{C2H2} = 5.0×10^{13} cm^{-3}, n_e (t = 0) = 10^9 cm^{-3} and α_b(t = 0) = 0.76.

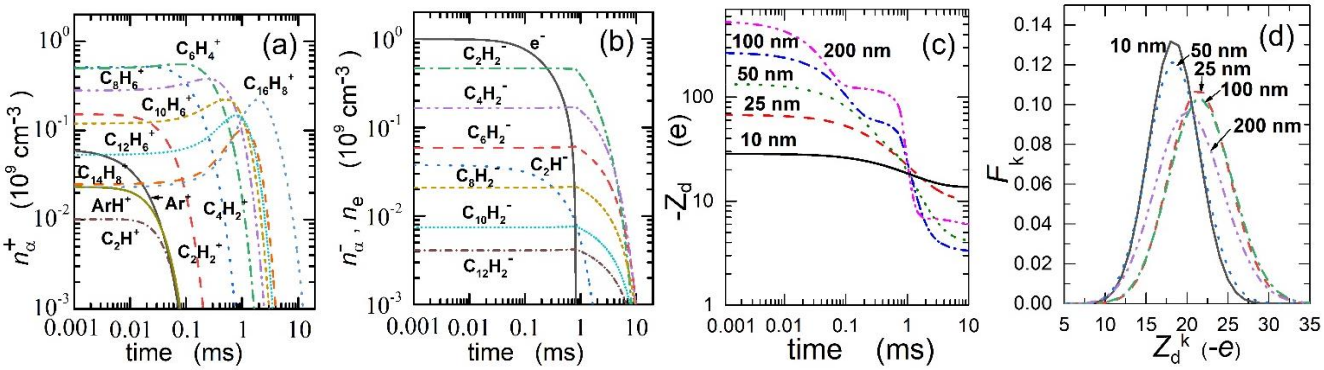

Fig. 2. The densities of positive ions (a), electron and negative ion densities (b), mean dust charge (c) and DCDF at t = 1 ms (c) for n_{C2H2} = 5.0×10^{13} cm^{-3}, n_e (t=0) = 10^9 cm^{-3} and different dust radii.

References

[1] I. B. Denysenko, M. Mikikian, N. A. Azarenkov, "Plasma properties and discharging of dust particles in an Ar/C2H2 plasma afterglow," J. Phys. D: Appl. Phys., vol. 57, 145202, 12 pp., 2024.

[2] T. Matsoukas, M. Russell, M. Smith, "Stochastic charge fluctuations in dusty plasmas," J. Vac. Sci. Technol. A, vol. 14, pp. 624-630, 1996.

[3] I. Stefanović, N. Sadeghi, J. Winter, B. Sikimić, "Influence of nanoparticle formation on the time and the space resolved metastable density in argon-acetylene plasmas", Plasma Sources Sci. Technol., vol. 26, 065014, 15 pp., 2017.

ANALYSIS OF THE IONIZATION REGION OF A MAGNETRON DISCHARGE IN ARGON WITH COPPER VAPOR USING A GLOBAL MODEL

I.B. Denysenko*, O.Y. Kravchenko, A.N. Veklich****

**V.N. Karazin Kharkiv National University, Kharkiv, Ukraine, e-mail: igor.denysenko@karazin.ua*
***Taras Shevchenko National University of Kyiv, Kyiv, Ukraine,*
e-mails: kay@univ.kiev.ua, veklich.an.n@knu.ua

A global model of the ionization region (IR) of a magnetron discharge in argon with copper target is presented. Using this model, the IR properties (the densities of ions and electrons, copper atoms and metastable argon atoms and the electron temperature) and the sheath properties (the sheath size and the ion energies with which they bombard the target) are analyzed under conditions corresponding to experiments (for neutral gas pressure in the range 0.01 Torr - 0.1 Torr). The model shows that the temperature of thermal electrons decreases with increasing the magnetron current and pressure, in agreement with experimental data.

Description of the simulation model

To analyse properties of a magnetron plasma in the ionization region (IR) near the target cathode, a global model is developed. The case where the gas discharge is operating in argon with copper target is considered. The global model assumes that the ionization region near the target can be described as a homogeneous half torus of mean radius $\bar{R}$ and of toroidal radius R_{tor} confined above the cathode racetrack [1]. The IR plasma volume is $V_{IR} = \pi^2 \bar{R} R_{tor}^2$, the area of its surface near the target is $S_{RT} = \pi[(\bar{R} + R_{tor})^2 - (\bar{R} - R_{tor})^2]$, while the area of half of torus surface is $S_{tor} = 2\pi^2 \bar{R} R_{tor}$. Here, it is assumed that $\bar{R}$ = 2.5 cm and R_{tor} = 0.75 cm. The dimensions of the IR correspond to the 7.2 cm cathode used in the experiment [2].

The dominant neutral species in the IR are argon atoms in the ground state (Ar_0) at density $n_{Ar} \approx \frac{P}{k_B T_g}$, where P is the gas pressure, k_B is the Boltzmann constant and $T_g (= 400\ K)$ is the neutral gas temperature. It is assumed that the discharge contains also copper atoms with density n_{Cu} which appear in the IR due to target sputtering by ion fluxes. We assume that there are thermal electrons (e^t) with density n_e and temperature T_e (in eV), singly ionized argon (Ar^+) and copper (Cu^+) ions with densities n_{Ar+} and n_{Cu+}, respectively, and hot electrons (e^H) (emitted secondary electrons at ion bombardment of the target) with density n_{eh} and temperature T_{eh} ($\gg T_e$). The magnetron discharge also contains metastable argon atoms (Ar_m) with density n_m, argon atoms in the resonance 4s states ($^3P_1$ and $^1P_1$) (Ar_r) with density n_r, as well as argon atoms in 4p states (Ar_{4p}) with density n_{4p}. It is assumed that the IR plasma is quasineutral ($n_{Ar+} + n_{Cu+} = n_e + n_{eh}$). The plasma is separated from the target by a high-voltage sheath which properties (the sheath size and the ion energies with which they bombard the target) are described using analytical equations presented in [3].

The global model includes the balance equations for Ar^+ and Cu^+ ions, Cu atoms, hot electrons, argon atoms in the metastable, resonance 4s states and 4p states and the power balance equation for thermal electrons. The detail information about the model equations and the processes taking into account by this model can be found in [1].

Here, we consider the intermediate pressure range [1.33 Pa (0.01 Torr) < P < 13.33 Pa (0.1 Torr)] corresponding to the experiment in [2]. Therefore, the model in [1], which was developed for P > 20 Pa, was slightly modified to take into account that the sheath near the target may be collisionless (In [1], the ion mean free paths are assumed to be smaller than the sheath size).

Results of numerical calculations

The model described in previous section was used to analyze properties of the IR and the sheath near the target of a magnetron discharge for the conditions of experiments in [2]. The model equations were solved for gas pressure (P), magnetron current (I_D) and voltage applied to the target (U_D) shown in table 1. In Fig. 1(a),

n_e , n_{Ar+}, n_{Cu+} , n_{eh} and n_{Cu} as functions of I_D are presented for P = 0.05 Torr. Fig. 1(a) shows that the densities of ions, electrons and copper atoms increase when the magnetron current becomes larger because of increasing the input power $I_D U_D$ (table 1) and due to intensification of the sputtering process.

Table 1. Parameters of magnetron discharge measured in [2].

P = 0.01 Torr		P = 0.05 Torr		P = 0.1 Torr	
I_D, mA	U_D, V	I_D, mA	U_D, V	I_D, mA	U_D, V
10	255	10	230	10	220
50	280	50	260	50	245
100	300	100	280	100	275
150	310	150	290	150	290
300	320	300	320	300	320

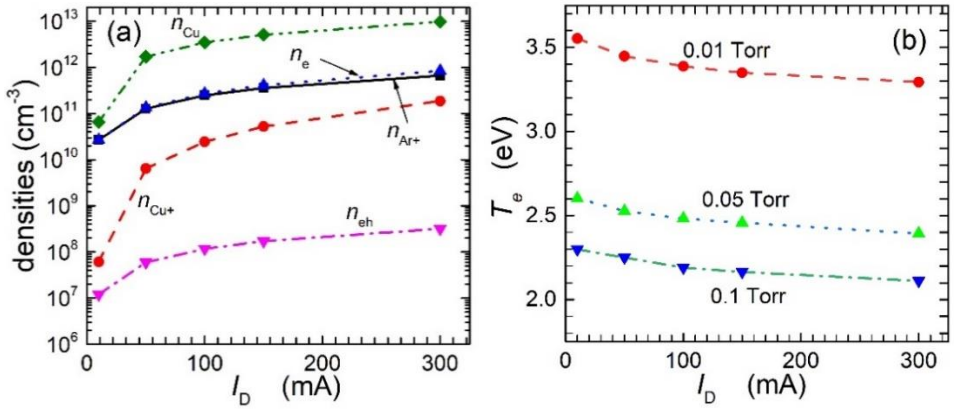

Fig. 1. The calculated electron and ion densities and Cu density for P =0.05 Torr (a) and the temperature of thermal electrons (b) as functions of the magnetron current for different pressures.

The temperature of thermal electrons decreases with increasing pressure and the magnetron current (Fig.1(b)), in agreement with the experimental results in [2]. In [2], the temperatures of energy level population of argon atoms were obtained by Boltzmann plot technique on the base of spectral lines of this element. In our opinion, the decrease of T_e at an increase of I_D is mainly because the density of Cu atoms becomes larger (the threshold energy for ionization of Cu atoms is smaller than that for ionization of Ar atoms) and due to increasing the density of hot electrons (Fig. 1(a)). More results of this study can be found elsewhere [4].

Acknowledgements

This work was supported by the National Research Foundation of Ukraine (Grant № 2023.03/0169).

References

[1] I.B. Denysenko, H. Kersten, A. Vahl, "Properties of the ionization region in a magnetron plasma at gas-aggregation-source-relevant pressure regime explored using a global model," J. Phys. D: Appl. Phys., vol. 57, 1335203, 12 pp., 2024.

[2] O.O. Murmantsev, A.M. Veklich, O.Yu. Kravchenko, O.M. Kostyukevych, "Optical emission spectroscopy of magnetron discharge with metal vapous admixtures", Proc. XVII International Scientific Conference "Electronics and Applied Physics", Kyiv, Ukraine, pp.69-72, October 2021.

[3] M.A. Lieberman, M.A. Lichtenberg, *Principle of Plasma Discharges and Material Processing*, 2nd ed. New Jersey: John Wiley & Sons Inc., 2005.

[4] I.B. Denysenko, O.Y. Kravchenko, A.N. Veklich, "Properties of the ionization region of a magnetron discharge in argon with copper vapor analyzed using a global model," Probl. At. Sci. Technol. 2024, *submitted.*

SPATIAL DISTRIBUTION OF ELECTRIC FIELD IN A TWO STAGE HALL TYPE PLASMA SOURCE

V.Yu. Bazhenov, A.M. Dobrovolskii, V.V. Tsiolko, V.M. Piun*

**Department of Gas Electronics, Institute of Physics NAS of Ukraine, Kyiv, Ukraine,*
e-mail: bazhenov@iop.kiev.ua, dobr@iop.kiev.ua, tsiolko@iop.kiev.ua

The two-stage plasma asymetric source of Hall type having common anode and two cathodes residing at locations with essentially different magnetic field configuration is experimentally studied. In particular, it was established that in the middle plane of the anode on the axis of the device, the value of the floating potential of the plasma is up to 95% of the anode voltage.

Introduction

Previously, we created the anode layer based source of a cylindrical plasma flow with enhanced efficiency of the discharge volume usage [1]. The source had the symmetric geometry of both stages. The proposed design used two cathodes in the form of several rods that were located inside the anode symmetrically relative to the middle plane of the anode. In this case, it is need to make the additional stage for resulted beam choice to make the thrust. The authors of the present work earlier studied the modified version of the previous device in which one half of the cathode system was replaced by a ring-shaped cathode located in a region with weak magnetic field, so that instead of being symmetrical the system becomes an asymmetric one [2]. At that, the working gas was injected along the axis of the system rather than through the anode. Such design looked a promising one from viewpoint of enhanced ion thrust due to optimizing the distribution of energy supplied by the power source between the stages of the device. Now we present the results of experimental studies of spatial distributions of the plasma floating potential inside the two stages of the proposed asymmetric discharge system with common anode and two cathodes residing at locations with essentially different magnetic field configuration.

Experimental setup and results

The investigated device (Fig. 1.) was placed inside a metal cylindrical vacuum chamber with a diameter of 500 mm, a length of 700 mm and a volume of 140 liters. Anode 3 of the device with an internal diameter of 59 mm and a length of 63 mm was located inside a quartz cylinder 4 with an internal diameter of 95 mm and a length of 150 mm. The "internal" cathode C1 consisted of 6 rods with a diameter of 3 mm and a length of 20 mm located in a circle at a certain distance from the inner surface of the anode. The role of the "external" cathode C2 was performed by a metal ring with an inner diameter of 65 mm and a height of 20 mm. Cathode C2 was mounted on the output flange 7 with a thickness of 10 mm flush with the inner plane of the flange. The distance from the anode to the inner plane of the output flange 7 was 45 mm.

When conducting experimental studies, the pulse-periodic mode of operation of the power source was used. The maximum amplitude of the impulse voltage at the anode Ua was 4.2 kV, and the maximum current through the cathodes C1, C2 was up to 0.5 A. When measuring the floating potential, two slightly different L-shaped Langmuir probes were used, both with the same lengths of the receiving part of 5 mm made of tungsten with a diameter of 0.19 mm. Probe 1 with a ceramic holder diameter of 3.2 mm and a length of 220 mm was used to measure the floating potential both inside and outside the anode. This probe could move in the radial direction in the range of R = ±24 mm and in the longitudinal direction L = 0 – 165 mm (the size of L was measured from the end of the anode closest to the cathode C1). Probe 2 with a diameter of a glass holder of 5 mm was used to measure U_f in the gap between the anode and the cathode C2 with a change in R within ± 48 mm. Fig. 2 shows the dependence of the values of $U_f^{max} – U_a^{max}$ on L and R. The same figure shows the placement of particular electrodes in the discharge gaps and the position of the magnetic field cusp.

The experimental studies of spatial distributions of the plasma floating potential inside the two-stage discharge system have shown a number of essential peculiarities inherent to the system under study. In the midle plane of

the anode with stronger magnetic field the radial distribution of the potential is practically uniform until about one half of the anode radius and is just about 100 V below the anode potential. Along the axis of the system, closer to the magnetic field cusp, essentially non-monotonous variation of the potential is observed. This region likely serves an efficient source of electrons which are supplied to the first stage along the magnetic field lines and flatten radial potential distribution in there. Such behavior promotes higher efficiency of the plasma generation in the studied two-stage discharge system. After proper subsequent optimization of the geometry and electric power supply such system can become an efficient large aperture source of high energy ions.

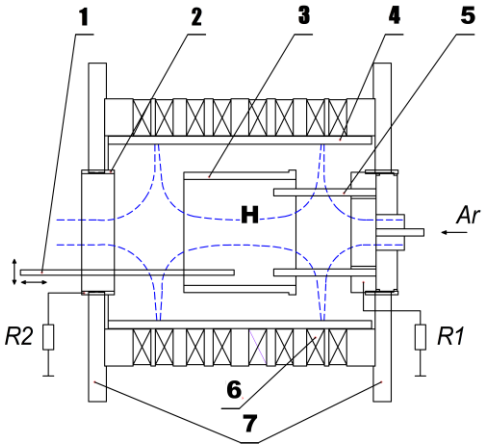

Fig. 1. 1 – Langmuir probes, 2 – cathode 2 C2, 3 – anode, 4 – quartz cylinder, 5 – cathode 1 C1, 6 – magnet system, 7 – dielectric flanges with a thickness of 10 mm, H – magnetic field lines.

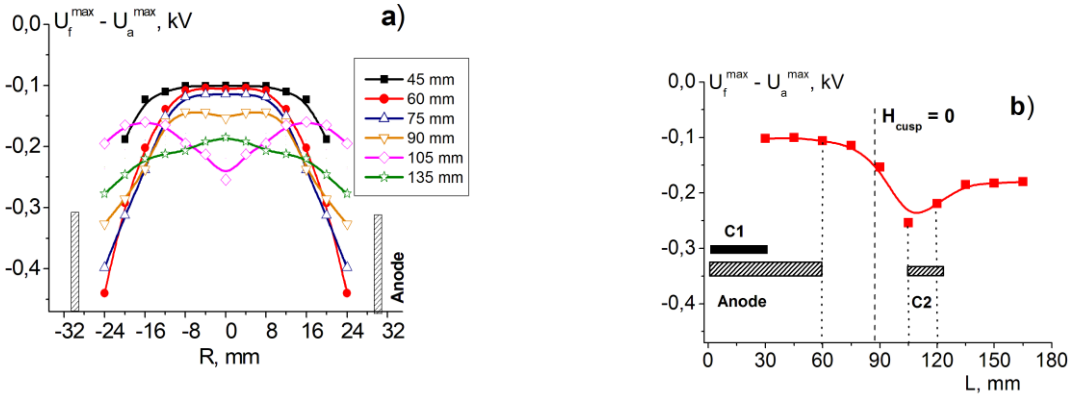

Fig. 2. a) – radial dependencies of $U_f^{max} – U_a^{max}$ at different distances L; b) Dependence of maximum values $U_f^{max} – U_a^{max}$ on distance L at the system axis (R = 0)

References

[1] I. Litovko, A. Goncharov, A. Dobrovolskyi, and I. Naiko. Plasma Science and Technology The Emerging Field Trends Erosion-Free Electric Hall Thrusters Systems/ Edited by Aamir Shahzad, InTechOpen, London, Chapter 11, p. 195-214. 2022.

[2] V.Yu. Bazhenov, A.M. Dobrovolskiy, V.V. Tsiolko, V.M. Piun. Two stage plasma source for large scale beam generation//PAST. Series “Plasma electronics and new methods of acceleration”. № 4. p. 121-124. 2023.

POWER DISTRIBUTION IN THE TWO STAGE HALL TYPE PLASMA SOURCE

V.Yu. Bazhenov, A.M. Dobrovolskii, V.V. Tsiolko, V.M. Piun*

**Department of Gas Electronics, Institute of Physics NAS of Ukraine, Kyiv, Ukraine,*
e-mail: bazhenov@iop.kiev.ua, dobr@iop.kiev.ua, tsiolko@iop.kiev.ua

The power distribution in two-stage plasma asymetric source of Hall type is experimentally studied. In particular, it was the system consumes maximum power in case of equal resistances on both cathodes. However, the power of the first stage is almost twice that of the second stage.

Introduction

Previously, we created the anode layer based source of a cylindrical plasma flow with enhanced efficiency of the discharge volume usage [1]. The source had the symmetric geometry of both stages. In this case, it is need to make the additional stage for resulted beam choice to make the thrust. In [2] we studied the modified version of the previous device in which one half of the cathode system was replaced by a ring-shaped cathode located in a region with weak magnetic field, so that instead of being symmetrical the system becomes an asymmetric one. The working gas was now injected along the axis of the system rather than through the anode. Such design looked a promising one from viewpoint of enhanced ion thrust due to optimizing the distribution of energy supplied by the power source between the stages of the device.

Experimental setup and results

The investigated device (Fig. 1.) was placed inside a metal cylindrical vacuum chamber with a diameter of 500 mm, a length of 700 mm and a volume of 140 liters. Anode 3 of the device with an internal diameter of 59 mm and a length of 63 mm was located inside a quartz cylinder 4 with an internal diameter of 95 mm and a length of 150 mm. The "internal" cathode C1 consisted of 6 rods with a diameter of 3 mm and a length of 20 mm located in a circle at a certain distance from the inner surface of the anode. The role of the "external" cathode C2 was performed by a metal ring with an inner diameter of 65 mm and a height of 20 mm. Cathode C2 was mounted on the output flange 7 with a thickness of 10 mm flush with the inner plane of the flange. The distance from the anode to the inner plane of the output flange 7 was 45 mm.

When studying the electro-physical characteristics of the discharge, measurements were made of voltages and currents of cathodes C_1, C_2 (U_{c1}, U_{c2}, I_{c1}, I_{c2}, respectively), anode voltage U_a, at different values of argon pressure and values of resistances R1, R2. pulsed voltage from the power source was applied to the discharge anode relative to the grounded chamber. Cathodes C1, C2 were connected to the grounded chamber through resistors R1, R2 of different values. This made it possible to raise the potentials of the cathodes during the discharge glow to simulate the operation of the device in free space.

The studies were performed using resistances of 10 kOhm and 820 Ohm in three options of their connection to the cathodes C1 and C2 (option I – R1 = 10 kOhm , R2 = 820 Ohm; option II – R1 = 820 Ohm R2 = 10 kOhm; option III R1= 820 Ohm, R2 = 820 Ohm). Fig. 2 a,b presents dynamic PVCs of the discharge stages in case of connecting the resistors by option I and II at argon pressure $0.9*10^{-4}$ Torr. One can see that for I the discharge at voltage U_{ign} □ 1.750 kV is initially ignited in low-current mode (milliampere range) and subsequently switches to high-current mode. The behaviors PVCs of the discharge stages differ significantly from each other. The main power is supplied in the external discharge stage between the anode and cathode C2 (W_{C2}^{max} □ 350 W). Comparison of Fig. 2a,b shows that when connecting resistors by option II, the redistribution of power between stages of the system changes. The value of the total maximum power in the discharge W_{sum}^{max} increases from 520 W to 700 W. This increase in power occurs mainly due to the increase in maximum discharge voltages and the major portion of the power (W_{C1}^{max} □ 500 W) is supplied in the internal stage between the anode and cathode C1. In the case for both stages are the same the maximum power W_{sum}^{max} □ 960 W is obtained, while a larger portion is supplied to the discharge through cathode C1 (W_{C1}^{max} □ 600 W), and is determined primarily by the difference in currents I_{C1}^{max}, I_{C2}^{max}.

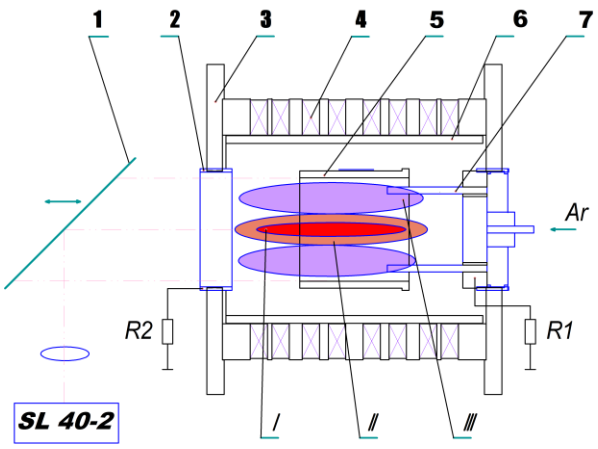

Fig. 1. Scheme of experimental device. 1 – movable mirror, 2 – external cathode C2, 3 – dielectric flanges, 4 – magnet system , 5 – anode, 6 – quartz cylinder, 7 – internal cathode C1, I, II, III – specific zones of the plasma glow.

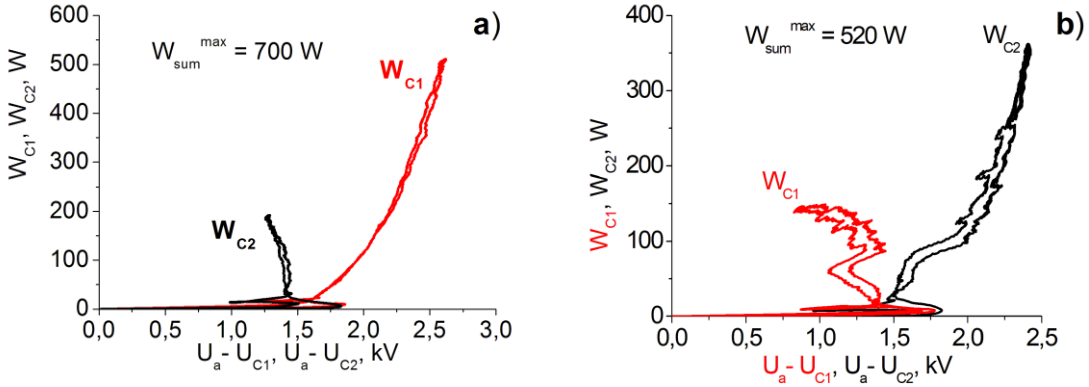

*Fig. 2. Dynamic PVCs of the discharge stages measured in C1 and C2 circuits. a) – R1 = 820 Ohm, R2 = 10 kOhm, P = 0.9*10-4 Torr. b) R1 = 10 kOhm, R2 = 820 Ohm, P = 0.9*10-4 Torr.*

The change in the argon pressure and the connection of various resistances to the cathodes C1, C2 in the three considered options significantly affects not only the total power consumed by the source, but also the power distribution between its discharge stages. It should be noted that equal resistances in different stages of the system do not equalize the distribution of energy between the stages. At the same time, the system consumes maximum power under the condition of equal resistances in the circuits of the cathodes. The power of the first stage in this regime is almost twice as high as the power of the second stage.

References

[1] I. Litovko, A. Goncharov, A. Dobrovolskyi, and I. Naiko. Plasma Science and Technology The Emerging Field Trends Erosion-Free Electric Hall Thrusters Systems/ Edited by Aamir Shahzad, InTechOpen, London, Chapter 11, p. 195-214. 2022.

[2] V.Yu. Bazhenov, A.M. Dobrovolskiy, V.V. Tsiolko, V.M. Piun. Two stage plasma source for large scale beam generation//PAST. Series “Plasma electronics and new methods of acceleration”. № 4. p. 121-124. 2023.

CHARACTERISTICS OF A SECONDARY DISCHARGES PLASMA SUPPORTED BY A GLIDING ROTATING DISCHARGES

V.Ya. Chernyak*, V.V. Iukhymenko*, O.O. Zavajenko*, S.S. Nedovesov*, D.D. Tretiakov*, K.V. Iukhymenko*, O.M. Tsymbaliuk*

** Faculty of RadioPhysics, Electronics and Computer Systems Taras Shevchenko National University of Kyiv, Kyiv 01601, Ukraine, e-mail: chernyak_v@ukr.net*

The paper presents systems with a secondary discharge of atmospheric pressure supported by a low-power (~ 100 W) rotating gliding discharge with solid and liquid electrodes in the air flow under conditions where the plasma length of the secondary discharge channel significantly exceeds the length of the self-discharge channel within 1÷100.

Introduction

For plasma chemistry, as a scientific direction for researching the possibilities of plasma activation of chemical transformations of substances, there always remain the most urgent problems, the solution of which is impossible or extremely complicated by the methods of traditional chemistry. Plasma generation involves the use of an expensive form of energy, namely electrical energy, and the high temperature of heavy plasma components, which is not very compatible with such basic requirements for modern technological applications.

Low-temperature plasma is used in various fields of science and technology [1-4]. There are many designs of plasma generators with different types of discharges. The physico-chemical activity of plasma has been known for over 100 years, however, systematic in-depth research of plasma chemistry began only in the mid-60s of the last century. Today there are many scientific works devoted to these studies. However, the problem of creating powerful industrial plasma-chemical atmospheric pressure systems with long-term operation, which could generate wide-aperture plasma streams, remains unsolved. The duration of operation of plasma generators is usually limited by electrode erosion. A promising source of atmospheric pressure plasma that meets the above requirements can be a secondary discharge supported by a rotating gliding discharge. Interest in such a system arose due to the fact that it makes it possible to obtain non-equilibrium atmospheric pressure plasma with a large cross-section (tens of cm^2) and volume [5].

Experimental set-up and methods

The experimental setup for the activation of chemical transformations of gaseous substances by a secondary discharge plasma sustained by a rotating gliding discharge is presented in Fig. 1 [6].

The distance between the self-sustained discharge electrodes was 1 mm. The diameters of the conical holes in the peripheral electrode (2) were 8 and 20 mm. The diameter of the mushroom-shaped rotating gliding discharge cathode was 24 mm. The ballast resistors in the power circuits of rotating gliding discharge and secondary discharge were 21.6 and 50 kΩ, respectively. The anode (peripheral electrode) is connected to the electrode and the cathode (ground) is connected to the peripheral flange (housing).

The current in the rotating gliding discharge power circuit was measured both by a milliammeter (Ipo) and by oscillograms of the voltage across the 50 Ohm measuring resistor (Ip). The voltage drop between the primary discharge electrodes of rotating gliding discharge was measured both by a kilovoltmeter with an input resistance of 10 MOhm (Upo) and by oscillograms from the output resistance of the 50 Ohm voltage divider (1:10.000) – Up.

The current in the secondary discharge power circuit was measured both by a milliammeter (Iso) and by oscillograms of the voltage across the 50 Ohm measuring resistor (Is). The voltage drop between the primary discharge electrodes of tornado discharge was measured both by a kilovoltmeter with an input resistance of 10 MOhm (Uso) and by oscillograms from the output resistance of the 50 Ohm voltage divider (1:10.000) – Us.

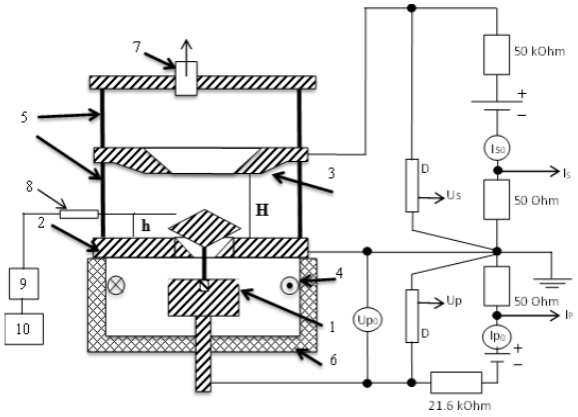

Fig. 1. Experimental setup for the activation of chemical transformations of gaseous substances by a secondary discharge plasma sustained by a rotating gliding discharge. 1 – high-voltage primary discharge electrode; 2 – grounding electrode; 3 – high-voltage secondary discharge electrode; 4 – gas inlet; 5 – quartz cylinder; 6 – dielectric; 7 – gas outlet; 8 – optical fiber; 9 – spectrometer; 10 – PC

Fig. 2 shows a typical photo of the secondary discharge – (b), sustained by a rotating gliding discharge – (a) at atmospheric pressure in an air stream.

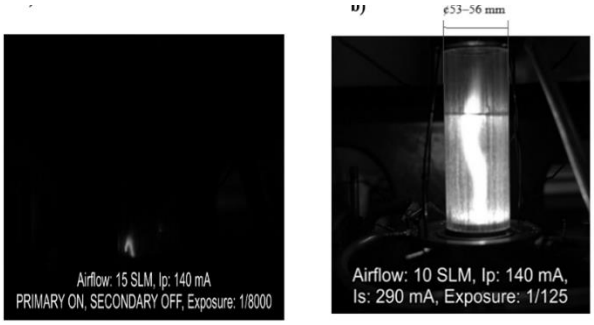

a *b*

Fig. 2. Typical photo of the rotating gliding discharge – (a) and the secondary discharge sustained by the rotating gliding discharge – (b) at atmospheric pressure in an air stream

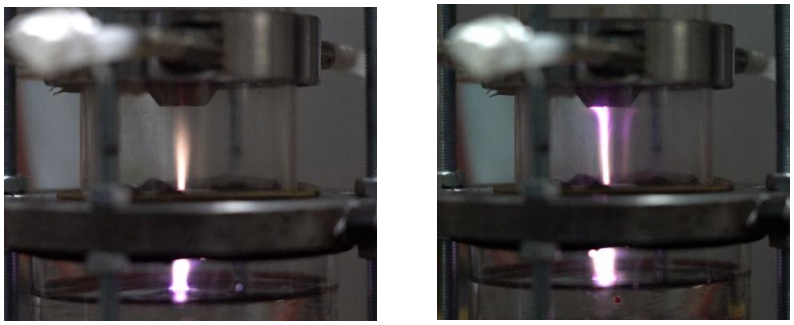

a) **b)**

Fig. 3. Photo of a rotating gliding discharge -a) and a secondary discharge supported by tornado discharge with a liquid electrode -b) at atmospheric pressure in an air stream

To increase the control parameters of plasma-chemical transformations in the system, a system with a secondary discharge supported by a tornado discharge with a liquid electrode for plasma chemical applications were created. Photos of the system are presented in Fig. 3.

Conclusions

It is shown that high-pressure plasma systems with a secondary discharge, which is supported by a rotating gliding discharge, can generate a non-equilibrium plasma of a much larger volume with a change in its parameters in a wider range of parameters than in systems with an independent discharge with the possibility of scaling the plasma chemical process.

Secondary discharges supported by independent discharges were implemented for the first time. The principal feature of which is the possibility of controlling the high-energy part by the plasma electron distribution function within very wide limits.

Reference

[1] A. Fridman *Plasma Chemistry*. USA: Cambridge University Press, 2008, P. 963.

[2] A. Fridman, G. Fridman *Plasma Medicine*. USA: John Wiley & Sons, Ltd, 2013, P. 545.

[3] C. Lazzaroni Study of various configurations of Micro Hollow Cathode Discharges in Ar/N2 used for boron nitride PECVD. Online low temperature plasma (OLTP) seminar, March 7, 2023, P. 2.

[4] M. Laroussi, S. Bekeschus, M. Keidar, A. Bogaerts, A. Fridman, X. Lu, K. Ostrikov, M. Hori, K. Stapelmann, V. Miller, S. Reuter, C. Laux, A. Mesbah, J. Walsh, C. Jiang, S. Mededovic, H. Tanaka, D. Liu, D. Yan, and M. Yusupov. IEEE TRANSACTIONS ON RADIATION AND PLASMA MEDICAL SCIENCES, VOL. 6, NO. 2, FEBRUARY 2022, PP. 127-157.

[5] Valeriy Ya. Chernyak, Vitalii V. Iukhymenko, Kostia V. Iukhymenko, Yevgen A. Oberemok, Daniil D. Tretiakov, Andriy M. Horiachko, Igor I. Fedirchyk and Olena V. Prysiazhna Plasmochemical synthesis of optically active substances // *IEEE Transactions on Plasma Science.* No. 3 (49), 1050-1054 (2021).

[6] V.Ya. Chernyak, V.V. Iukhymenko, K.V. Iukhymenko, D.D. Tretiakov, O.M. Tsymbaliuk, S.S. Nedovesov, Z.O. Prokofiieva Properties of a secondary discharge plasma supported by a rotating gliding discharge / Problems of Atomic Science and Technology. Series: Nuclear and physical research. – №6. – 2023. – P. 145-149.

ION FLUX SOURCE BASED ON A NON-SELF-SUSTAINED ARC DISCHARGE IN A LONGITUDINAL MAGNETIC FIELD

S. M. Gubarev*, V.O. Khomych, A.V. Ryabtsev*****

**Institute of Physics of NAS of Ukraine, 46, Nauky Av., Kyiv 03028, Ukraine, e-mail: gubarev@iop.kiev.ua*
*** Institute of Physics of NAS of Ukraine, 46, Nauky Av., Kyiv 03028, Ukraine, e-mail: khomich@iop.kiev.ua*
****Institute of Physics of NAS of Ukraine, 46, Nauky Av., Kyiv 03028, Ukraine, e-mail: ryabtsev@iop.kiev.ua*

This paper presents the results of experimental studies of an intense ion flux source based on a low-pressure non-self-sustained arc discharge in a longitudinal magnetic field. The obtained helium ion flux is characterized by a total current of up to 0.75 A, a current density of up to 10 A/cm², and a specific power at the collector of up to 6.4 kW/cm². The dependence of the ion flux on experimental parameters and conditions was investigated. The presented ion flux source can be used in ion-plasma technology processes.

Experimental setup

Intense ion fluxes are widely used in modern plasma technologies. Arc discharge plasma with a thermionic cathode in a strong longitudinal magnetic field is commonly used to generate ion fluxes. Particularly attractive is the arc discharge with electron oscillation in a magnetic field. This discharge provides almost complete gas ionization even at relatively low discharge currents. This work is a continuation of our previous studies on arc discharge plasma in a longitudinal magnetic field in both gases and metal vapors [1]. The goal of this study is to experimentally achieve conditions that allow the most efficient generation of an intense helium ion flux.

Fig.1 shows the general scheme of the experimental setup.

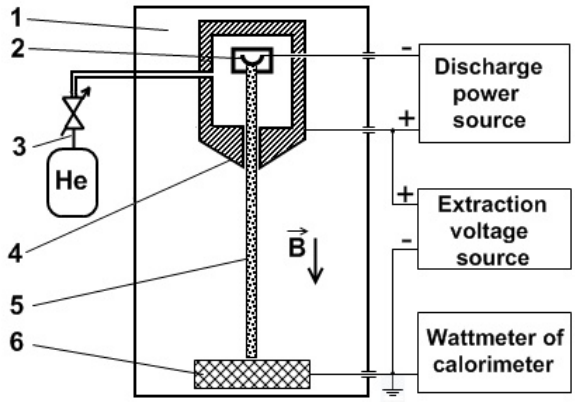

Fig. 1. Experimental setup: 1 – vacuum chamber, 2 – thermionic cathode, 3 – gas supply system, 4 – anode chamber, 5 – plasma column, 6 – collector

The residual pressure in the vacuum chamber was about 7×10^{-4} Pa. A copper water-cooled chamber 4 serves as the anode. Inside the anode chamber, there is a tungsten thermionic cathode 2 of direct heating, placed inside a molybdenum screen with an emission aperture. The anode chamber has a long opening of 3 mm diameter to transport the plasma flow to the collector 6. The plasma-forming gas is fed directly into the anode chamber, and its flow is regulated so that the pressure in the anode chamber ranges from 1 to 10 Pa. At the same time, the gas pressure in the vacuum chamber varies within the range of 7×10^{-3} to 7×10^{-2} Pa. Technically pure helium was used as the working gas. The vacuum chamber 1 is positioned between the poles of an electromagnet.

After ignition of the arc discharge between the anode chamber and the cathode, the discharge current could be continously varied from a minimum of 3 A to 16 A by adjusting the internal reactive resistance of the discharge power supply. The dense primary plasma generated in the anode chamber diffuses through the anode opening

along the magnetic field into the main volume of the vacuum chamber [1]. The effective diameter of the plasma column is practically equal to the size of the exit aperture of the anode chamber. By increasing the negative bias of the collector, an ion flux can be extracted from the plasma. The energy of the charged particle flux hitting on the collector is measured by a calorimetric method.

Experimental data and discussion

At a magnetic field induction of 0.34 T in the working area of the vacuum chamber and a discharge current I_d = 10 A, the maximum ion saturation current at the collector is reached at a pressure of 4×10^{-2} Pa in the vacuum chamber. In this case, the discharge voltage U_d is about 100 V.

Figure 2a shows the dependence of the experimentally measured current I_m on the collector as a function of the bias voltage U_{bias} for the specified parameters. Simultaneously, the power dissipated by the collector P_{cal} was recorded using a calorimetric wattmeter (Fig. 2b).

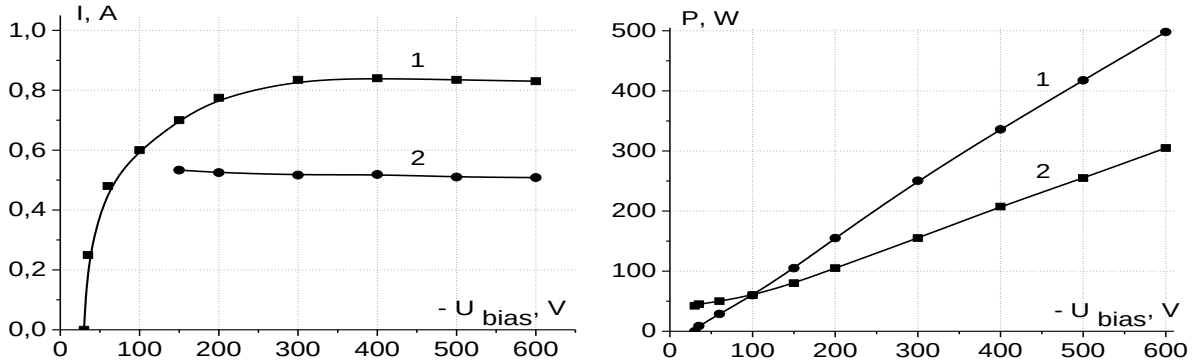

a) b)

Fig. 2. a) Currents to the collector as a function of the collector bias voltage. 1 - measured current I_m; 2 - calculated actual ion current I_i; b) Electrical and calorimetrically measured plasma flux power to the collector as a function of the collector bias voltage. 1 - electrical power P_{el}; 2 - calorimetrically measured power P_{cal}

Figure 2a also shows the actual ion current at the collector, which is determined as $I_i = P_{cal}/U_{bias}$ at values of U_{bias} (-150 V ÷ -600 V), when nearly all the electrons are reflected from the collector back into the plasma. The difference between I_m and I_i is due to the secondary ion-electron emission current from the collector. Figure 2b also shows the dependence of the electrical power of the plasma flow at the collector, calculated as $P_{el} = U_{bias}\times I_m$, on the bias voltage U_{bias}. Estimation of the electron temperature T_e [2], obtained by spectroscopic methods for conditions close to ours, gave a value of 5 eV. From Bohm's formula for the ion saturation current density $j_{i\,sat}$ on a negatively biased collector, considering the estimate of T_e and the measured value of $j_{i\,sat}$, the plasma concentration obtained in our experiment is $n_e \approx 10^{14}$ cm^{-3}. As the discharge current increases from 3 to 16 A, the actual ion current on the collector increases from 0.3 to 0.75 A. The total calorimetric power of the ion flow on the collector (at U_{bias} = -600 V, I_d = 16 A, $I_i \approx 0.75$ A) reaches 450 W, corresponding to a specific power density of 6.4 kW/cm².

Conclusions

The design and main characteristics of a source of intense helium ion flux based on a non-self-sustained low-pressure arc discharge with electrons oscillating in a magnetic field are presented. A helium ion flux to the collector with a total current of up to 0.75 A and a current density of up to ≈ 10 A/cm^2 and a specific power of up to 6.4 kW/cm^2 was obtained. This ion flux source can be used in the processes of ion-plasma technologies.

References

[1] M.D.Gabovych, V.A.Khomych, O.K.Nazarenko, “Elektronno-luchevaya svarka s legirovaniyem shva”, Avtomaticheskaya svarka, №10, pp.49-50, 1993.

[2] L.L.Pasechnik, O.V.Kozak, V.V.Yagola, “Uderzhaniye plotnoy plazmy s tokom v magnitnom pole”, Zhurnal tekhnicheskoy fiziki, vol.34, №5, pp.873-878, 1964.

DYNAMICS OF SPACE CHARGE WAVES IN THE AMPLIFICATION SECTION OF A SUPERHETERODYNE FEL WITH A QUASI-ELECTROSTATIC FIELD

Stanislav Ilin, Alexander Lysenko

Faculty of Electronics and Information Technology Sumy State University, Sumy 40007, Ukraine,
e-mail: sequell3@gmail.com

In the present work, we analyze the influence of an external quasi-electrostatic support field on the saturation level of the space charge wave. We found that this field with optimal parameters can increase the saturation level of the slow space charge wave up to 70%.

Introduction

Free electron lasers are the most powerful sources of electromagnetic waves in the terahertz frequency range [1]. Such lasers are used in spectroscopy, biomedical imaging, materials science [1], etc. In the present work we analyze the terahertz FELs namely superheterodyne free electron laser with an electrostatic undulator, which uses a longitudinal electrostatic undulator for further amplification of the electromagnetic signal wave. In our previous works [2,3] we studied how the undulator pump electrostatic field and the accompanying generated pump electrostatic field increase the growth increment of space charge waves (SCWs), due to which the saturation levels of the SCWs increase and at the same time the FEL amplifying section length decreases. However, another way to increase the level of the SCW is possible using an external quasi-electrostatic support field.

Model

The amplifying section of the parametric FEL consists of three main components (Fig. 1): 1 – modulated relativistic electron beam (REB); 2 – electrodes of the electrostatic undulator; 3 – lines of the periodic reverse longitudinal pump electric field. This system allows us to amplify the slow and fast SCWs [2]. In our new study we propose to introduce a quasi-electrostatic support field, which would help us to stabilize the constant component of the REB velocity in the saturation region. This field is created by the already existing electrodes 2.

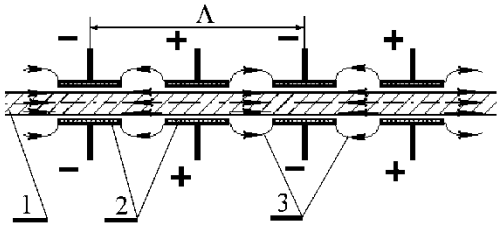

Fig.1. Scheme of the amplification section for the SCWs. Here 1 – relativistic electron beam (REB); 2 – electrostatic undulator; 3 – lines of the periodic reverse longitudinal pump electric field

Analysis

The saturation level of the SCWs is limited by the condition of three-wave parametric resonance between the waves of the slow and fast SCWs and the undulator pump electric field. This condition is violated mainly due to a significant change in the constant velocity of the REB in the region of the SCW large amplitudes. However, if we prevent the violation of the three-wave parametric resonance condition, the saturation level will increase significantly. Thus, we are looking for a quasi-electrostatic support field from the consideration of a minimal change in the constant component of the electron beam velocity.

After conducting a numerical study, we found a quasi-electrostatic field that keeps the REB velocity constant over a long distance of the amplification section. The quasi-electrostatic support field has the form of a dependence of the electric field strength E_0 on the z coordinate as shown on the Fig. 2 a, graph 1.

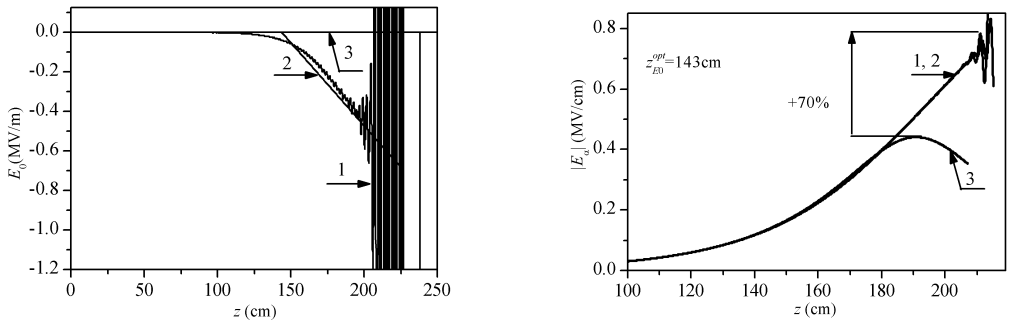

Fig. 2. a) – Dependences of the quasi-electrostatic support field strength E_0 on the z coordinate; b) – Dependences of the slow SCW electric strength amplitude modulus $|E_\alpha|$ on the longitudinal coordinate z at different values of the parameter τ_{E0}. Figures a and b show cases considering the influence of the: 1 – optimal quasi-electrostatic support field; 2 – linear quasi-electrostatic support field; 3 – without the quasi-electrostatic support field.

For the parametric description of this dependence, the graph 1 was fitted by several functions. The simplest and most convincing fit is achieved by a linear function (Fig. 2 a, graph 2), which has the form:

$$E_0(z) = \begin{cases} 0, z < z_{E_0} \\ \tau_{E_0}(z - z_{E_0}), z \geq z_{E_0} \end{cases}$$

In this dependence, the parameters z_{E0} and τ_{E0} can be interpreted as the coordinate of the beginning of the effective amplification of the SCW and the gradient of the quasi-electrostatic support field, respectively.

As we said earlier, the quasi-electrostatic support field should allow us to increase the saturation level of the slow SCW. Fig. 2 b shows the graphs of the dependence of the SCW strength modulus on the *z* coordinate when the SCW is affected by: 1 – the optimal quasi-electrostatic support field; 2 – the linear quasi-electrostatic support field; 3 – without the quasi-electrostatic support field.

In Fig. 2 b, we see that the optimal and linear quasi-electrostatic support fields increase the saturation level of the slow SCW by 70%. This result was achieved without any hardware complications of the superheterodyne FEL, but due to the electrostatic undulator as a generator of this field [2].

Conclusion

To find a suitable quasi-electrostatic support field, the criterion of minimizing the change in the constant velocity of the relativistic electron beam was chosen. This criterion allows us to maintain the condition of three-wave parametric resonance over a larger length of interaction of the pump electrostatic field with the slow SCW. As a result of the numerical research, the optimal form of the dependence of the strength modulus E_0 on the coordinate *z* was found (Fig. 2 a). Our studies have shown that due to the long-term action of three-wave parametric resonance, the saturation level of the slow SCW increases significantly (by 70%) (Fig. 2 b).

References

[1] Doria A. Terahertz free-electron laser / A. Doria, G. P. Gallerano, E. Giovenale // Advances in Terahertz Source Technologies. — Jenny Stanford Publishing, 2024.

[2] A.V. Lysenko, S.S. Ilin, “Multiharmonic Interactions of Longitudinal Waves in Amplification Section of Superheterodyne Free Electron Laser,” J. Nano- Electron. Phys., vol. 14, no. 5, pp. 05006-1–05006-6, 2022.

[3] A.V. Lysenko, O.I. Voroshylo, S.S. Ilin, “Influence of Generated Pump Electric Field on Multiharmonic Interaction of Waves in Amplification Section of Superheterodyne FEL”, Problems of atomic science and technology, no. 6, pp. 186–191, 2023.

INFLUENCE OF GAS PRESSURE ON THE GROwth OF CLUSTERS IN MAGNETRON DISCHARGE

Bibik A., Demeshko O., Kravchenko O.

Faculty of RadioPhysics, Electronics and Computer Systems Taras Shevchenko National University of Kyiv, Kyiv 01601, Ukraine, email: kay@univ.kiev.ua

On the basis of the hybrid model, the magnetron discharge was simulated in a cylindrical chamber filled with argon. The obtained results were used to study the effect of gas pressure on the sputtering of the copper cathode, the diffusion of copper atoms in the discharge chamber, and the process of cluster formation. It is shown that the number of copper atoms in the discharge chamber decreases with increasing gas pressure, and the dependence of the number of clusters on pressure is non-monotonic.

Introduction

Magnetron plasma sources are widely used for a variety of sputter-etching and thin-film deposition applications [1]. In addition, magnetron discharge is a convenient source of metal clusters [2]. The subsequent processes of cluster deposition onto a surface are of interest for nanotechnology applications. In particular, clusters can play a positive role in some material science applications such as electron field emitters [3] or in the catalytic and electromechanical industry due to their large surface to the volume ratio. However, the efficiency of cluster formation in a magnetron plasma depends on a number of parameters, such as gas pressure, energy of ions bombarding the cathode. In this work, using computer simulation, the effect of gas pressure on the sputtering of a copper cathode and the efficiency of cluster formation in a magnetron discharge chamber is investigated

Model and simulation method

In our model, the magnetron discharge chamber is a cylinder filled with argon under pressure p. A potential difference $V_0 = -300\,V$ is applied between the round copper cathode and anode of radius $R = 0.03\,m$. The distance between the cathode and the anode is $L = 0.03\,m$. A hybrid model is used to simulate the magnetron discharge [3], which assumes that plasma species are divided into two groups – high-energy and low energy. To the high-energy group belong electrons with total energy higher than excitation energy of argon atoms $\varepsilon^* = 11.55\,eV$. The low-energy group contains ions and electrons with energy less than ε^*. Particles could transfer from the high-energy group into the low-energy due to the energy loss on elementary interactions.

Low-energy particles treated by the fluid model [3]. To describe the potential of a self-consistent electric field, we used the Poisson equation. High-energy electrons arise as a result of secondary emission from the cathode when it is bombarded with ions. They are treated individually. For each electron the Newton equation of motion with a Lorentz force term is solved:

$$m\frac{d\vec{v}}{dt} = -eE - e\left[\vec{v}, \vec{B}\right],$$

where e is electron charge, $\vec{E}$ and $\vec{B}$ are electric and magnetic fields and $\vec{v}$ is the electron velocity. Input electric fields, for this equation, are take from the hydrodynamic part. Elementary processes, namely elastic collisions, excitation and ionization during collisions of high-energy electrons with argon atoms, are simulated by the Monte Carlo method The result of Monte Carlo calculus used in hydrodynamic part.

When bombarding the cathode with ions, copper atoms are emitted into the magnetron discharge chamber. The sputtering coefficient of the cathode depends on the energy of the ions and in our simulation was chosen according to experimental data. Further, the diffusion of copper atoms in the discharge chamber and the formation of clusters occurs, which are described according to the model presented in [4].

Results and discussion

We performed the plasma simulations under different gas pressure in order to investigate the influence of this parameter on electrode sputtering and cluster formation in the magnetron chamber. Spatial distributions of concentrations of ions and electrons, the potential of the self-consistent electric field in the discharge chamber, as well as the radial distributions of the flows of ions to the cathode and of copper atoms from the cathode were obtained.

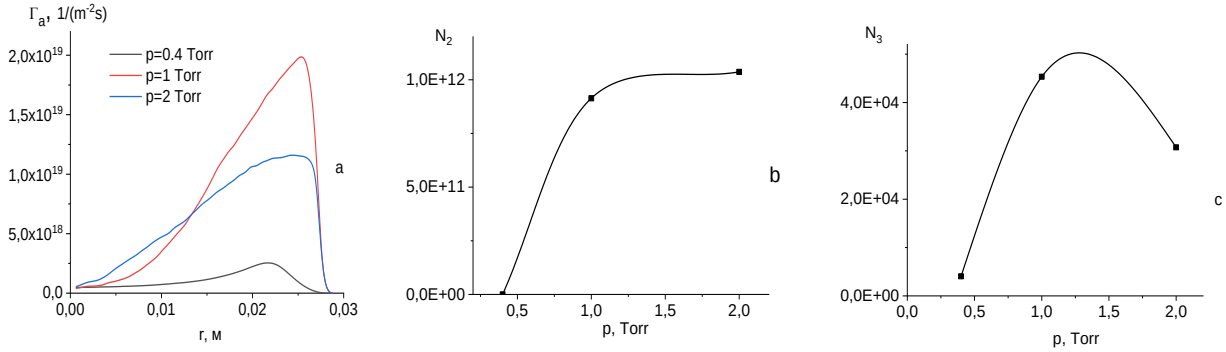

Fig. 1. Radial distributions copper atoms flows from the cathode for different pressures of gas (a), dependence of the total number of dimers (b) and clusters containing three atoms (c) in the chamber on gas pressure

Radial distributions of copper atom flows are very heterogeneous (Fig. 1a). The maxima of these flows are realized at the radial coordinate opposite to which the maximum concentration of ions occurs. The magnitude of the flow of atoms from the cathode depends on the pressure non-monotonically. This is explained by the fact that sputtering of the cathode depends not only on the flow of ions to the cathode, but also on the energy of the ions, which increases with decreasing gas pressure. However, the number of copper atoms in the discharge chamber decreases with an increase in gas pressure, which is due to a decrease in their diffusion. The simulation results also show that the total number of dimers in the chamber increases with increasing gas pressure (Fig. 1b), and the total number of clusters consisting of three copper atoms depends on the pressure non-monotonically (Fig.1c). In the pressure range of $0.4 \le p \le 2.0\,Torr$, their maximum number was reached at pressure $p = 1\,Torr$. At the pressure $p = 2\,Torr$ their number in the chamber decreases, which can be explained by a decrease in the concentration of copper atoms.

Acknowledgements

This work was supported by the National Research Foundation of Ukraine (Grant № 2023.03/0169).

References

[1] C. Christou , Z. H. Barber,"Ionization of sputtered material in a planar magnetron discharge", Journal of Vacuum Science and Technology, vol.18, 2020, pp. 2897–2907.

[2] Hippler R., B. M. Smirnov, I. Shyjumon, "Magnetron plasma and nanotechnology", Phys. Usp., vol. 50, 2007, pp. 455–488.

[3] A. Bogaerts, R. Gijbels, "Hybrid Monte Carlo model for a microsecond pulsed glow discharge", J. Anal. At. Spectrom., vol.15, 2000, pp. 895-905.

[4] O.Yu.Abakumenko, O.A. Demeshko, O.Yu. Kravchenko, "Growth and diffusion of clusters in the cylindrical magnetron chamber", XIX International Scientific Conference Electronics and Applied Physics, Oktober, 17-21, Kyiv, Ukraine, 2023.

INITIAL STAGE OF ELECTROMAGNETIC BEAM INTERACTION WITH DENSE PLASMA: CHARGE SEPARATION AND LANGMUIR WAVE DYNAMICS

B.R. Mykhailenko, I.O. Anisimov

Taras Shevchenko National University of Kyiv, Faculty of Radio Physics, Electronics and Computer Systems
E-mail: mihaylenko.bogdan12@gmail.com

Using computer simulation, the initial stage of low-power electromagnetic waves` beam nonlinear interaction with the overdense plasma layer was studied. It is shown that a quasi-stationary electric field forms on the plasma surface due to the ponderomotive force, resulting from charge separation and later reversing direction before disappearing. It is also demonstrated that the peripheral part of the beam excites a Langmuir wave at the second harmonic, which propagates deeper into the plasma.

The study of wave propagation through typically opaque plasma regions has been studied for decades [1], with applications in space communications, plasma diagnostics, and laser thermonuclear fusion. Our previous works [2-3] investigated plasma barrier transillumination during high-power electromagnetic beam interaction, which forms a reduced-density channel. This paper presents preliminary findings on quasi-stationary electric fields arising in plasma and nonlinear excitation of Langmuir waves by an incident electromagnetic wave.

The PIConGPU package [4], based on the particle-in-cell method, was used for 3D simulation. Using the ParaView package [5], analysis was conducted through three-dimensional visualizations of instantaneous values. Averaged values analysis was conducted in a custom program that reads raw values in OpenPMD format.

The following simulation parameters were used: fully ionized hydrogen plasma of a density $9 \cdot 10^{12} cm^{-3}$ (electron plasma frequency – 27 GHz); plasma temperature – 0.5 eV (isothermal plasma); the plasma layer thickness – 12.5 cm, radius – 21.5 cm; incident wave length – 3.33 cm (frequency – 9.9 GHz, i.e. plasma is opaque for this wave); pulse duration – 101 ns; pulse radius (at half maximum) – 4.9 cm; the maximum electric field amplitude is 0.964·MV/cm (4 times smaller than the amplitude of a moderate wave in [2-3]).

Fig. 1 a–c shows the axial component distribution of the averaged electric field in the plane containing the system axis at different times after the wave packet's leading edge impacts the plasma. At 0.56 ns, an outward-directed electric field forms on the plasma surface (Fig. 1a) due to the ponderomotive force from the non-uniform high-frequency field. Electrons move first, causing charge separation, which pulls ions. At 5.11 ns, the field reverses (Fig. 1b), and by 10.45 ns, it disappears. The field change occurs over ~5 ns, while the wave period is ~0.1 ns, making the field quasi-stationary. The longitudinal electric field seen on both sides of the barrier is likely unphysical, caused by electron absorption at the simulation boundaries, leading to a positive plasma charge.

Fig. 2a shows that deep within the plasma layer, where the wave beam hits, regions of periodic spatial changes in the longitudinal field emerge, interpreted as a Langmuir wave. Fig. 2b indicates this is accompanied by disturbances in electron velocity. When a transverse electromagnetic wave normally falls on plasma, electrons oscillate along the electric field and experience the magnetic field, resulting in a Lorentz force directed deeper into plasma. This force oscillates at twice the wave's frequency, which is believed to excite the Langmuir wave. The simulation confirms a Langmuir wave frequency of 19.8 GHz, double the 9.9 GHz of the incident wave.

The excitation mainly occurs at the wave beam's periphery, disappearing over time, likely due to plasma surface deformation. Previous studies explored nonlinear effects, such as second harmonic excitation and parametric excitation of Langmuir waves. However, nonlinear excitation of a Langmuir wave at double frequency, propagating into plasma, has not been discussed before.

Acknowledgment

This work has been carried out within the framework of the EUROfusion Consortium, funded by the European Union via the Euratom Research and Training Programme (Grant Agreement № 101052200 -EUROfusion). Views and opinions expressed are however those of the author(s) only and do not necessarily reflect those of the European Union or the European Commission. Neither the European Union nor the European Commission can be held responsible for them.

The work was partially supported within the framework of the research project 22 BF 052-02, carried out at Taras Shevchenko National University of Kyiv, funded by the Ministry of Education and Science of Ukraine.

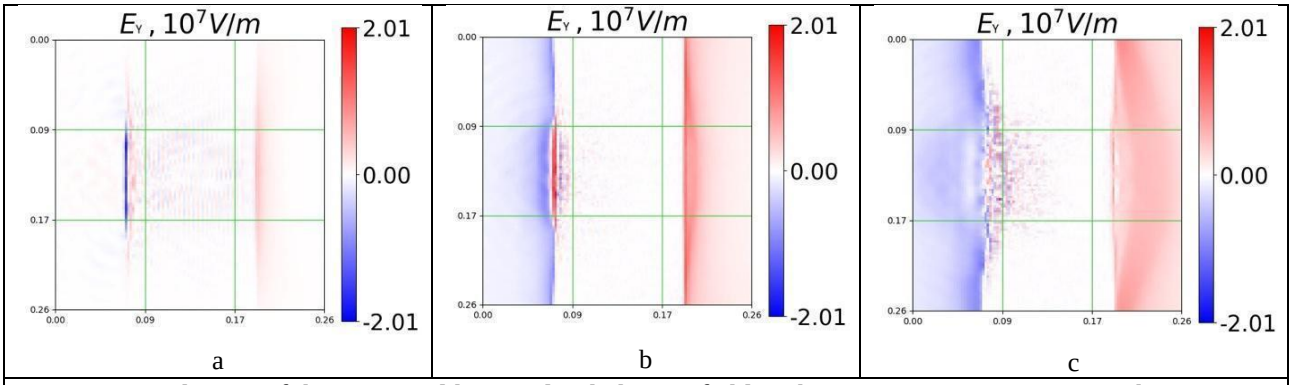

Fig. 1. Distribution of the averaged longitudinal electric field in the cross-section containing the system's axis at time points 0.56 ns (a), 5.11 ns (b), and 10.45 ns (c)

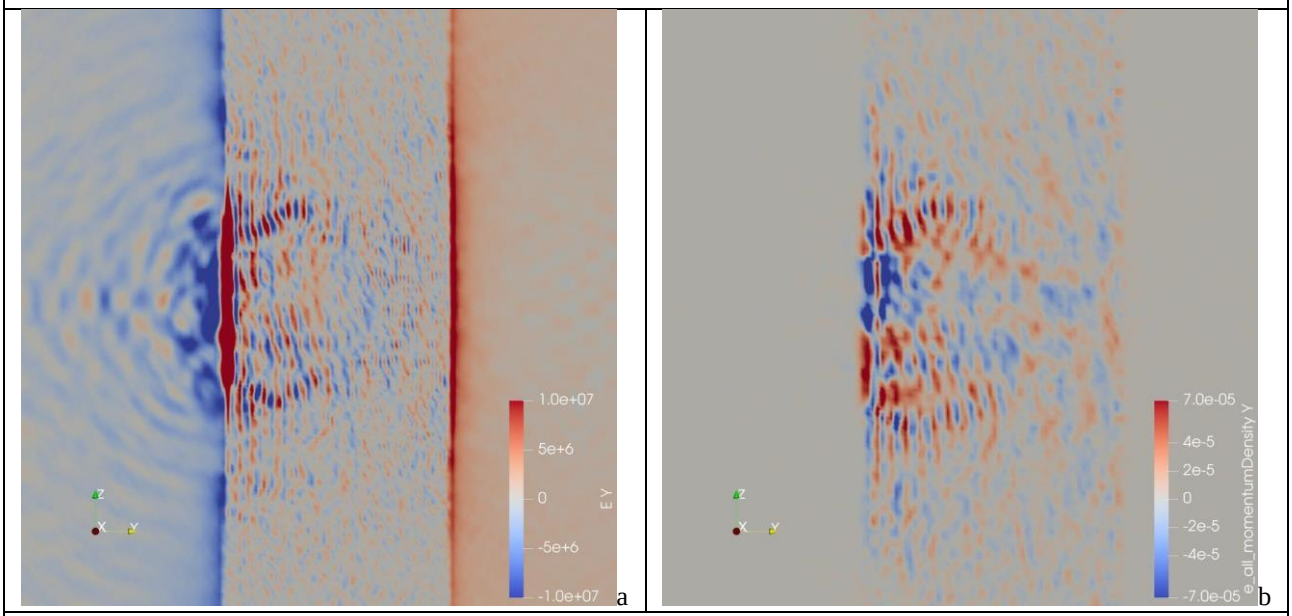

Fig. 2. Distribution of the instantaneous axial components of the electric field (a) and electron velocity (b) in the plane containing the system axis (t=4.5 ns)

References

[1] I.O.Anisimov, L.I.Romaniuk. // Ukr. Phys. Journ. Reviews. 6, 101 (2010). In Ukrainian.

[2] B.R. Mykhailenko, I.O. Anisimov. // Probl. of Atomic Sci. and Techn. №6 (130), 64 (2020).

[3] B.R. Mykhailenko, I.O. Anisimov. // Probl. of Atomic Sci. and Techn. 4 (134), 3 (2021).

[4] M Bussmann et al. // SC'13 Proc. Int. Conf. High Perform. Comp. Networking, Storage Anal. 60, 1 (2013).

[5] Ahrens, J. & Geveci, Berk & Law, Charles. (2005). ParaView: An End-User Tool for Large Data Visualization. Visualization Handbook.

TURBULENT ELECTRON MOTION AND DENSITY EVOLUTION IN ELECTROMAGNETIC BEAM-PLASMA INTERACTIONS

B.R. Mykhailenko, I.O. Anisimov

Taras Shevchenko National University of Kyiv, Faculty of Radio Physics, Electronics and Computer Systems
E-mail: mihaylenko.bogdan12@gmail.com

Using computer simulation, the initial stage of low-power electromagnetic waves` beam nonlinear interaction with the overdense plasma layer was studied. It is shown that a quasi-stationary electric field emerges in the plasma due to parametric instability, disrupting the initial axial symmetry of the system. This leads to azimuthal inhomogeneity, causing a redistribution of electron density. The ponderomotive force drives electrons deeper into the plasma, creating regions of increased electric fields and altered plasma permittivity. This process disturbs both longitudinal and transverse electron velocities, leading to a turbulent plasma motion.

The study of wave propagation through typically opaque plasma regions has been studied for decades [1], with applications in space communications, plasma diagnostics, and laser thermonuclear fusion. Our previous works [2-3] investigated plasma barrier transillumination during high-power electromagnetic beam interaction, which forms a reduced-density channel. This paper presents preliminary findings on axially asymmetric structures formation during electromagnetic beam nonlinear interaction with the dense plasma layer.

The PIConGPU package [4], based on the particle-in-cell method, was used for 3D simulation. Using the ParaView package [5], analysis was conducted through three-dimensional visualizations of instantaneous values. Averaged values analysis was conducted in a custom program that reads raw values in OpenPMD format.

The following simulation parameters were used: fully ionized hydrogen plasma of a density $9 \cdot 10^{12} cm^{-3}$ (electron plasma frequency – 27 GHz); plasma temperature – 0.5 eV (isothermal plasma); the plasma layer thickness – 12.5 cm, radius – 21.5 cm; incident wave length – 3.33 cm (frequency – 9.9 GHz, i.e. plasma is opaque for this wave); pulse duration – 101 ns; pulse radius (at half maximum) – 4.9 cm; the maximum electric field amplitude is 0.964·MV/cm (4 times smaller than the amplitude of a moderate wave in [2-3]).

The analyzed model is axially symmetric. However, in the near-axis region close to the plasma surface, the axial symmetry of the system is disrupted, and structures arise where coupled disturbances of the transverse and longitudinal components of the electric field, the longitudinal velocity of plasma electrons, and their density occur (see Figs. 1a-b). The emergence of these structures can be attributed to the development of a certain parametric instability of the plasma in the field of the incident wave, which breaks the axial symmetry of the model. Over time, these structures decay, which can also be associated with the nonlinear deformation of the plasma density's spatial distribution (see Fig. 2).

The initial stage of interaction between a low-power wave beam and the plasma ends with the formation of a deepening at the location of the axially asymmetric structure near the system's axis, with its surface resembling a truncated sphere.

Acknowledgment

This work has been carried out within the framework of the EUROfusion Consortium, funded by the European Union via the Euratom Research and Training Programme (Grant Agreement № 101052200 -EUROfusion). Views and opinions expressed are however those of the author(s) only and do not necessarily reflect those of the European Union or the European Commission. Neither the European Union nor the European Commission can be held responsible for them.

The work was partially supported within the framework of the research project 22 BF 052-02, carried out at Taras Shevchenko National University of Kyiv, funded by the Ministry of Education and Science of Ukraine.

References

[1] I.O.Anisimov, L.I.Romaniuk. // Ukr. Phys. Journ. Reviews. 6, 101 (2010). In Ukrainian.
[2] B.R. Mykhailenko, I.O. Anisimov. // Probl. of Atomic Sci. and Techn. №6 (130), 64 (2020).
[3] B.R. Mykhailenko, I.O. Anisimov. // Probl. of Atomic Sci. and Techn. 4 (134), 3 (2021).
[4] M Bussmann et al. // SC'13 Proc. Int. Conf. High Perform. Comp. Networking, Storage Anal. 60, 1 (2013).
[5] Ahrens, J. & Geveci, Berk & Law, Charles. (2005). ParaView: An End-User Tool for Large Data Visualization. Visualization Handbook.

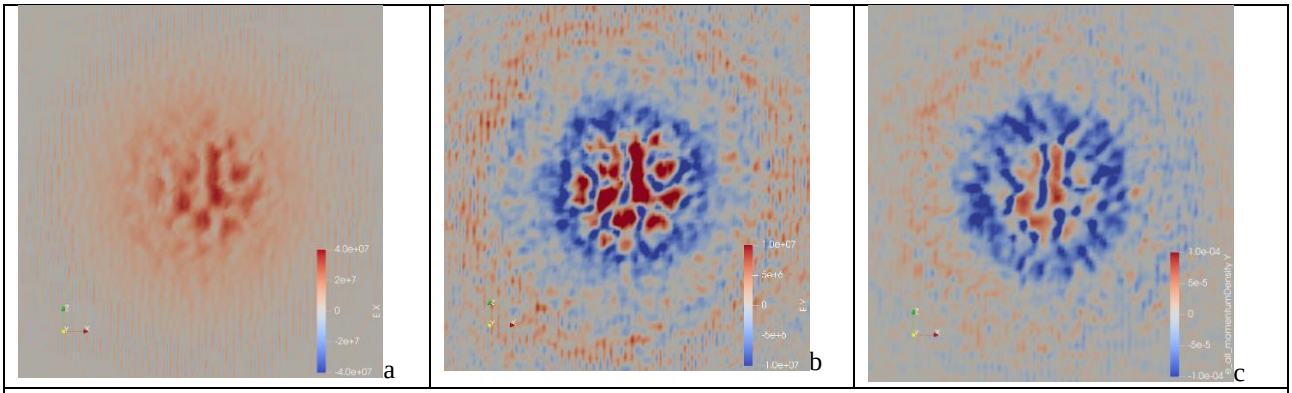

Fig. 1. Distributions of the instantaneous transverse (a) and longitudinal (b) electric fields, as well as the axial velocity of electrons (c) in the plane perpendicular to the axis of the system at a depth of 0.3 cm from the initial plasma boundary at the moment of time 4.5 ns

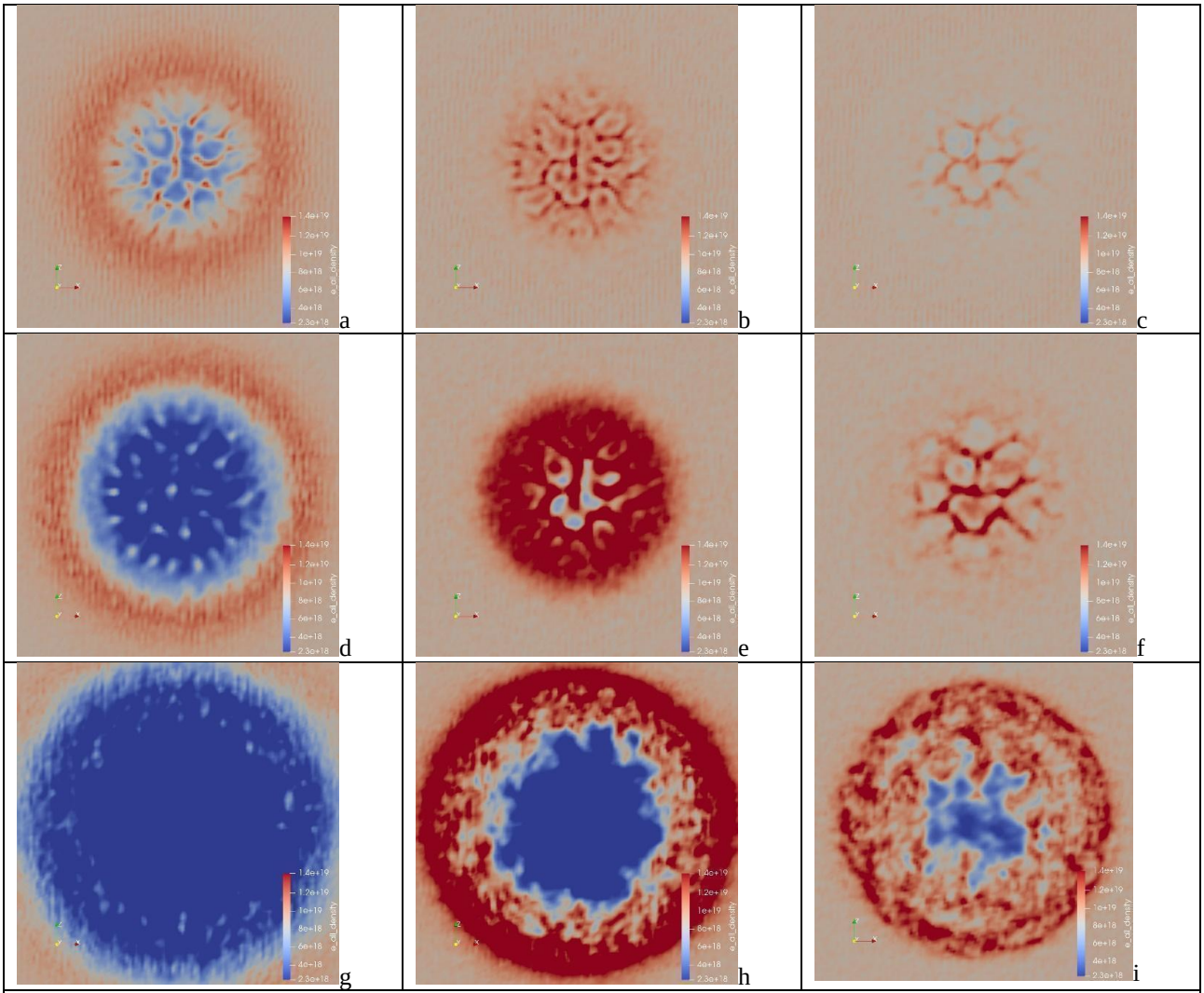

Fig. 2 Transverse distributions of instantaneous electron density at the time points 4.55 ns (a-c), 7.59 ns (d-f), and 19.73 ns (g-i) at depths of 0.3 cm (a, d, g), 0.8 cm (b, e, h), and 1.3 cm (c, f, i) from the initial boundary of the plasma layer

QUASI-MONOCHROMATIC WAVES EXCITED BY HIGH VOLTAGE UNIPOLAR PULSES IN A COAXIAL TRANSMISSION LINE WITH INSERTS LIKE FERRITE RINGS AND A METAL GRATING

A.B. Batrakov*, S.Yu. Karelin, O.M. Lebedenko, V.S. Mukhin, I.N. Onishchenko,

O.L. Rak, V.G. Sinitsin**, M.V. Volovenko

Institute for Plasma Electronics and New Methods of Acceleration,
National Science Center 'KIPT', Kharkiv 61000 ,Ukraine
**E-mail: a.batrakov67@gmail.com*
***E-mail: vgsin33@gmail.com*

Experimental data and results of numerical simulations are presented, concerning excitation of narrow band gigahertz-range wave trains in coaxial guiding structures that are partially filled with ferrimagnetic material and may also involve periodically arranged metal inserts.

Introduction

Novel methods of converting the energy of unidirectional pulses into high-frequency electromagnetic oscillations - with their subsequent radiation into free space - continue to attract attention of researchers. Possibilities are considered for generating pulsed oscillating waveforms of ultra-high frequency in vacuum-free structures, while never employing accelerated electron beams. The structures under discussion are coaxial transmission lines that are partially filled with a gyrotropic material with nonlinear electromagnetic response, specifically ferrite in a nearly saturated state [1-4].

Experimental

Shown in Fig1.below is the coaxial transmission line intended for generating high voltage, slowly attenuating electromagnetic oscillations. The source of primary pulses (denoted 1 in the Figure) is implemented as a dual pulse forming line (DPF, providing feed pulses of amplitudes up to 200 kV). Next goes the ferrite-containing pulse compressor 2 (provides for pulses' leading front lengths about 3 ns) and the section of principal importance for the case, namely the nonlinear tansmission line (NLTL) 3 which is the shaper and amplifier of the desired quasimonochromatic high power radiation. Section 4 is at the output, ending with an absorptive load. The high frequency component of the voltage between the line's electrodes is measured with the capacitive dividers S1, S2 and S3.

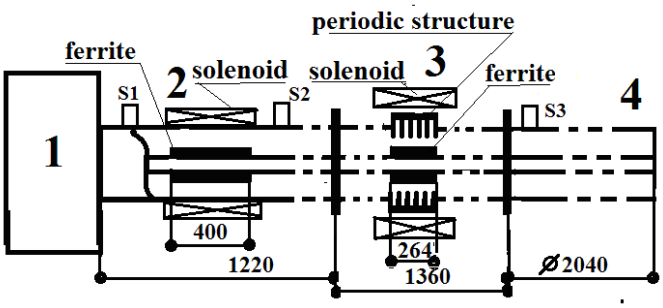

Fig. 1. Schematic of the high-voltage coaxial transmission line

Fig.2a and Fig.2b below demonstrate a typical signal form and the respective spectrum, as observed experimentally. These data permit evaluating parameters of the oscillations that are formed in the line, first of all the 32 kV amplitude. Next, recalling the wave impedance Z of the line to be close to 36 Ohm we can estimate the peak radiated power as W = 20 MW. The spectrum shown in Fig. 2 b suggests an estimate for the central frequency, specifically f_G=1.89 GHz, with the line width f/f_G=16per cent.

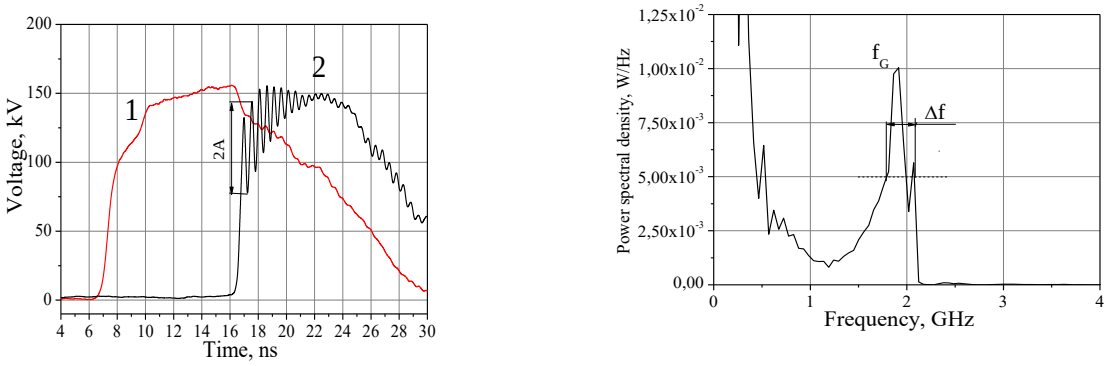

Fig. 2. Pulsed waveform and its spectrum as observed in experiments..

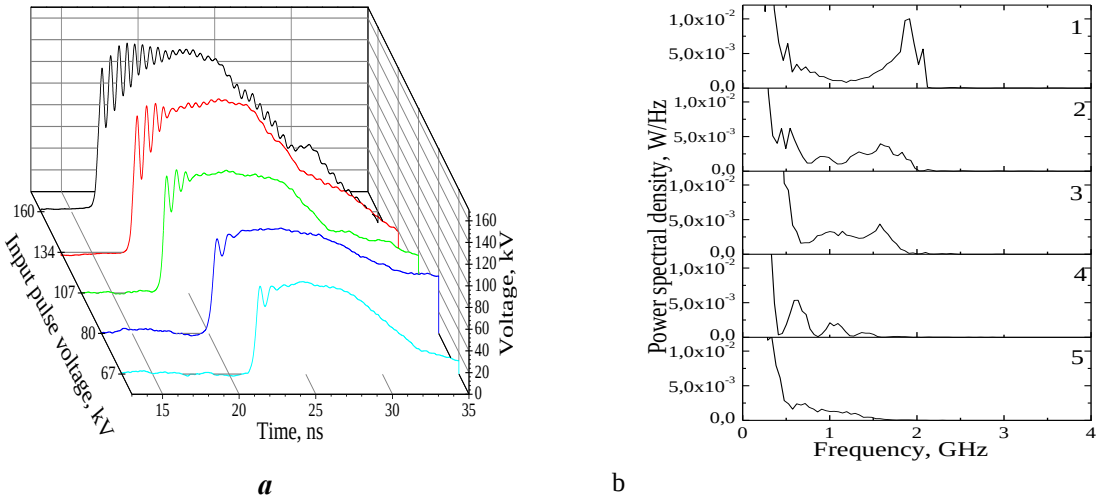

a b

*Fig.3. The pulsed voltage waveform (panel **a**) and its spectrum (panel **b**) as read by sensor S3 for a variety of incoming pulse voltages:1 – 160 kV; 2 – 134 kV; 3 – 107 kV; 4 – 80 kV;5 –67 kV.*

Conclusions

A coaxial transmission line involving a saturated ferrite core and a periodic structure made of metal, that has been fed with a unilateral, high voltage pulse of short duration demonstrated weakly decaying oscillations. The line of outer diameter 50.5 mm, filled with an isotropic dielectric (relative constant ε= 2.25) and a set of ferrite rings with ε =16 and μ about 4 or 5 in the saturated state, supported weakly decaying oscillations at central frequencies between 1.89 GHz and 2.2 GHz , with spectral band widths about 16 per cent. With magnitudes of the initial feeding pulse ranging from 160 kV to >300 kV an estimate for the instantaneous radiated power reached 20 MW.

References

[1] D.V. Reale. Coaxial Ferrimagnetic Based Gyromagnetic Nonlinear Transmission Lines as Compact High Power Microwave Sources. *A dissertation in electrical engineering*. Texas Tech University, December 2013.

[2] Coleman, P. D., Borchardt, J. J., Alexander, J. A., Williams, J. T., and Peters, T. F. Characterization of a synchronous wave in a nonlinear transmission line. In**:** *IEEE Pulsed Power Conference* , June 2011, pp. 173-177.

[3] S.Y. Karelin, V.G.Korenev, V.B. Krasovitsky, I.I. Magda, V.S. Mukhin, V.G. Sinitsin. Pulsed Power to Microwaves Conversion in Nonlinear Transmission Lines. *Radio physics and radio astronomy.* 2021, vol 26, No3, pp. 250-255. https://doi.org/10.15407/rpra26.03.250

[4] Karelin, S., Krasovitsky, V., Lebedenko, O., Magda, I., Mukhin, V., Korenev, V., and Volovenko, M. Cherenkov's Effect and Narrow-Line VHF Oscillations in a Ferrite-Filled Coaxial Line. In: 2022 IEEE 2nd Ukrainian Microwave Week (UkrMW). IEEE, 2022. p. 92-96.

STUDY OF ELECTRODYNAMICS' CHARACTERISTICS OF GAS DISCHARGE IN A NEEDLE-PLANE SYSTEM WITH ONE LIQUID ELECTRODE

I.N. Onishchenko., G.V. Taran, O.O. Zamuriev, P.O. Opaliev

NSC " Kharkiv Institute of Physics and Technology"
Akademichna street 1, Kharkiv, 61108, Ukraine email: onish@kipt.kharkov.ua

Researches were carried out on the electrodynamics' characteristics of gas discharge in a needle-plane electrode system with one liquid electrode at using high voltage of two types: unipolar negative pulsed and combined (sum of DC and high-frequency AC high voltage) ones. This is necessary in many applications, including the drinking water purification. Metal needle electrodes made of stainless steel were used, some of which were subjected to various treatments (polishing, coating with zinc nitride, titanium nitride or titanium oxide). It was shown that applying combined high voltage in the electrode system with a nitride coating results in a mean current 2 times smaller. When using a unipolar negative high-voltage pulse, the maximum mean discharge current was obtained with the untreated electrode system. This is due to the presence of a greater number of micro-protrusions on the needle electrodes, which leads to increased electric field intensity in the generation zone.

EXPERIMENTAL STUDIES

Experimental studies were conducted on the electrodynamics' characteristics of corona discharge with a liquid electrode under combined and pulsed high-voltage power with various coating of needle-like electrodes with nitrides and metal oxides. Combined high-voltage power is the sum of DC and high-frequency AC high voltage, with the DC voltage being lower than the ignition voltage of the discharge.

The research was carried out on a specially designed and manufactured experimental setup, in which the gas discharge is ignited directly above the surface of the water, i.e., the water serves as a liquid anode. Two high-voltage systems were used as the power supply. The first system generates a sinusoidal quasi-pulse high voltage. The second system produces a negative polarity pulse voltage with a duration of about 1 μs.

The discharge cell represents a needle-plane system, where the cathode is made in the shape of a "star" with a thickness of 0.1 mm, a diameter of 29 mm, and 31 "rays" made of stainless steel. The "rays" are bent at a 90-degree angle to the plane of the "star." The surface of stars were additionally polished and coated with zinc nitride spray, titanium nitride, or titanium oxide. The anode is a grounded metal container filled with tap water. The gap between the anode and cathode varies in the range of 4-6 mm.

RESULTS OF THE STUDY

Research on the electrodynamics' characteristics of a gas discharge in a needle-plane system with a single liquid electrode was conducted under the application of two types of high voltage to the discharge gap. The first cycle of experiments was carried out with the application of a combined voltage.

Fig. 1 shows the current-voltage characteristics of a gas discharge in a needle-plane system with one liquid electrode at an interelectrode gap of 4 mm and 6 mm.

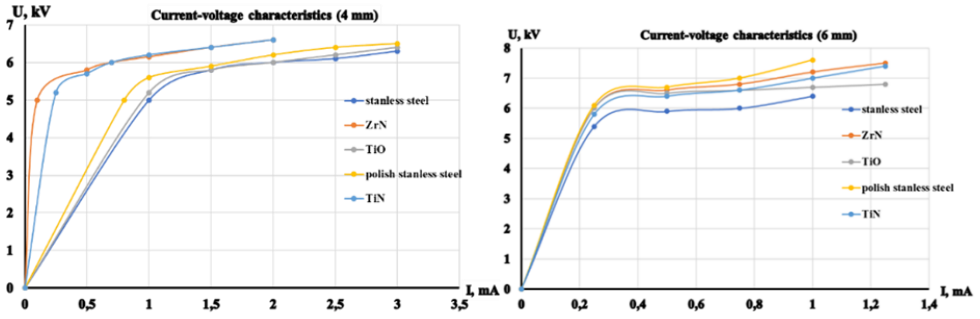

a b

Fig. 1. Volt-ampere characteristics of the discharge when using a supply of combined voltage with a gap of 4 mm (a)and 6 mm (b) between the cathode and anode.

The graphs of Fig. 1a show that to achieve the same average current, higher voltage needs to be applied to needle-like electrodes coated with metal nitrides, which leads to greater power being put in the discharge. This may be due to the increased resistance of the nitride layer and, consequently, to lower secondary ionization coefficient. However, in the electrode system with nitride-coated needle-like electrodes, a significantly lower (by a factor of 2) average current is achieved before the discharge transitions to the spark stage.

The graphs of Fig. 1b show that as the inter-electrode gap increases, the differences in the electrodynamics' characteristics of the discharge in electrode systems with different coatings on the needle-like electrodes become less significant. This is due to the increase in the drift zone of the discharge gap, which leads to a redistribution between displacement current and conduction current in the total current.

The second cycle of experiments was conducted using a pulsed high voltage power supply that generates unipolar negative pulses.

Fig. 2 shows the current-voltage characteristics of the gas discharge when applying high-voltage negative polarity pulses in the needle-plane electrode system with one liquid electrode. The gap size was 4 mm and 6 mm. The pulse repetition frequency was 5 kHz and 15 kHz.

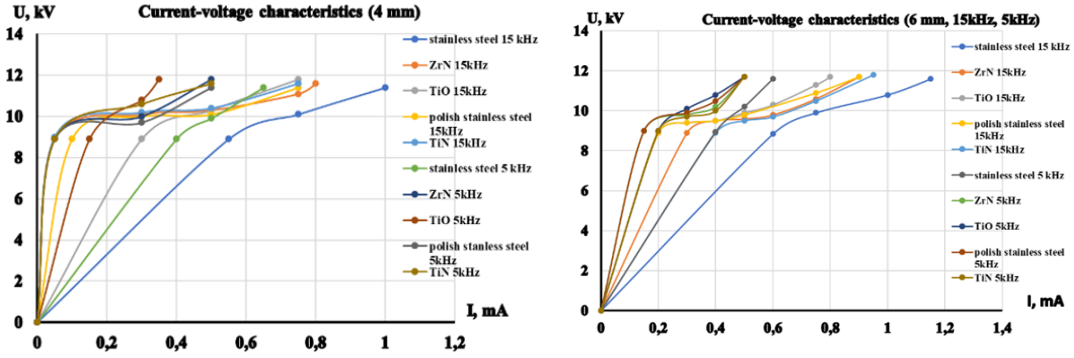

a b

Fig. 2. Volt-ampere characteristics of corona discharge using a pulse power source with a pulse repetition frequency of 5 and 15 kHz at a gap between the cathode and anode of 4 mm(a) and 6 mm (b).

From the graphs of Fig. 2, it can be concluded that the transition from the diffuse discharge stage to the spark stage, when a high-voltage pulse is applied to the discharge gap, occurs at the same applied voltage, regardless of the gap size and the type of coating on the needle electrodes. At the same time, the maximum average discharge current was obtained with untreated metallic electrodes. This may be due to the presence of more microprotrusions

on the needle electrodes, leading to a higher electric field intensity in the generation zone and, consequently, a higher pulse current in the discharge, regardless of the pulse repetition frequency.

The study is supported by the National Research Foundation of Ukraine under the Program “Science to Strengthen Defense Capabilities of Ukraine” (Project #2023.04/0092).

REFERANCES

[1] World Health Organization. Regional Office for Europe. Surveillance and response to water-related infectious diseases associated with water supplies. (https://iris.who.int/bitstream/handle/10665/330094/9789289054621.pdf)

[2] Muhammad Arif Malik, Abdul Ghaffar1 and Salman Akbar Malik Water purification by electrical discharges // *Plasma Sources Science and Technology*// 2001, v. 10, №1, p. 82-91.

[3] Petr Lukes, Martin Clupek1, Vaclav Babicky1, Vaclav Janda and Pavel Sunka Generation of ozone by pulsed corona discharge over water surface in hybrid gas–liquid electrical discharge reactor // *Journal of Physics D: Applied Physics* // 2005, №38, p. 409-416.

[4] M.A. Malik, A. Ghaffar, S.A. Malik. Water purification by electrical discharges // *Plasma Sources Sci. Technol.*// 2001, № 10, p. 82-91.

[5] Bolotov O.V., Golota V.I., Taran G.V .// Emission spectra and current characteristics of negative corona discharge in an electrode system with liquid anode//*Problems of Atomic Science and Technology, //* 2020, №6, p. 131–135

[6] Taran G.V., Kudin D.V., Zamuriev O.O., Opaliev P.O., Yaroshenko M.O., Korniykov O. M., Arefiev, V.L., Kalashnik, M.V. Studying the influence of plasma-chemical and ozone treatment on artificially implemented microflora in model aqueous solutions//*Problems of Atomic Science and Technology*, // 2021, №4, p. 177–182.

THE PHYSICAL MODEL OF THE SYNTHESIS OF OPTICALLY ACTIVE SUBSTANCES IN DYNAMIC PLASMA-CHEMICAL SYSTEMS

D.D. Tretiakov[1], V.Ya. Chernyak[1], V.V. Iukhymenko[1], K.V. Iukhymenko[1],

O.M. Tsymbaliuk[1] S.V. Shulga[2], S.S. Nedovesov[1]

[1]Taras Shevchenko National University of Kyiv, Faculty of RECS, Kyiv, Ukraine;
[2]Institute of Hydromechanics NAS of Ukraine Kyiv, Ukraine
E-mail: chernyak_v@ukr.net; yvitaliy@ukr.net; sergey.v.shulga@gmail.com

Prior research demonstrated a significant impact on optical activity of chiral isomers, particularly Glucose and Fructose. A plasma-liquid system with the activation of solution in organic solvents (ethanol, acetonitrile) with a rotating gliding discharge plasma was studied. Determination of plasma parameters was performed by plasma emission spectroscopy methods. It was shown that the plasma of both the rotating gliding discharge and the plasma of the secondary discharge supported by the gliding discharge are non-isothermal. Optical properties of treated substances were examined using UV absorption and polarimetry methods. It is shown that optical activity strongly depends on rotation direction in the system. A model describing possible kinetic process which lead to observed results is suggested

INTRODUCTION

The article's main focus is to suggest a possible physical model for experimentally discovered effects, namely an impact of rotation direction on optical activity of a treated substance. The effect and experimental methods were previously described in [1] and in [2]. A plasma-liquid system for processing solutions of high-molecular organic and inorganic compounds was used for our study [3].The system is based on a rotating gliding discharge directly immersed in the liquid [4].

THE MECHANISM OF ENANTIOMERIC RATIO DEVIATION

In organic chemistry, the rule states that "the synthesis of chiral compounds from achiral reagents always produces a racemic mixture" due to thermodynamic laws, which also define the equilibrium constant formula for reactions [5]. A deviation from this balance requires the system to be out of equilibrium, making a kinetic description essential [6]. Introducing directed rotational motion may affect isomer formation, as it impacts spatial orientation. Energy dissipation via the plasma-liquid boundary can stabilize energy-rich products, reducing the chance of reaction reversal. The system's unique features: non-thermal plasma, directed motion, and rapid energy dissipation - disrupt equilibrium, potentially leading to unequal isomer formation probabilities.

ROTATION OF MOLECULES IN A VORTEX

The rotation of molecules in a vortex is a key aspect of isomer formation mechanisms in the OKR reactor. Each infinitesimal volume rotates around its axis, characterized by vorticity, the curl of the velocity vector field [7]. Vorticity measures local fluid rotation, differing from solid body rotation, and is useful for describing deforming bodies.

Two extreme vortex cases are of interest: rotational (rigid-body-like) and irrotational. In rotational vortices, linear velocity is proportional to radius, and all elements rotate uniformly with no relative displacement. In irrotational vortices, linear velocity is inversely proportional to the distance from the vortex center, causing constant slippage between elements. In the studied system, a twisted gas flow induces fluid rotation, and since rigid-body conditions are not met, the fluid volumes rotate relative to their axes.

A complex vortex, as expected in the system, would have non-uniform vorticity vectors, indicating a gradient in angular velocity along the radius. This suggests that reagents traveling through the vortex experience changes in angular velocity and encounter rotating fluid volumes. A simulation in Solidworks, shown on figure 1, confirmed this, showing varying vorticity vectors and even a reversal in rotation direction across the plasma-liquid boundary. This difference in angular velocity implies relative rotation of infinitesimal elements relative to each other, affecting the system's behavior.

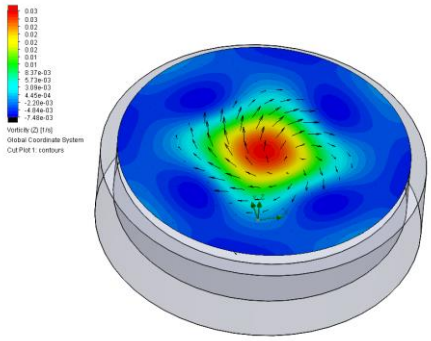

Figure 1 - Cross-sectional scheme of the plasma-liquid boundary. The vector field of vorticity is shown for a laminar flow, with the velocity reduced to 10 rad/sec to demonstrate the principle.

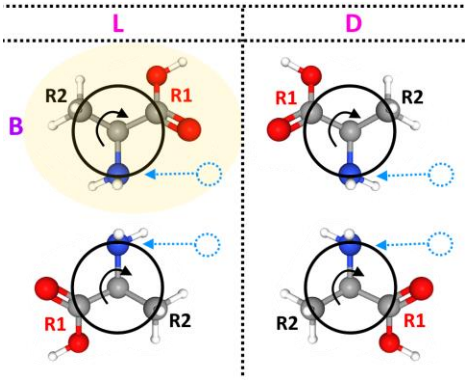

Figure 2 - Possible variants of the association process illustrated with an alanine molecule, flipped around the rotation plane. Letters L and D denote the left and right isomers of alanine, respectively. The yellow (B) marks the most probable formation process

ANALYSIS OF POSSIBLE MECHANISMS FOR CREATING A NON-RACEMIC MIXTURE USING A SIMPLIFIED MODEL

We focus on the synthesis features involving simple molecular particles, Ro, which are transported from the reactor's central zone (plasma) to the periphery, where they interact with complex asymmetric molecules, R1-R2, at the plasma-liquid boundary. Ro moves radially, while R1-R2, due to their complex structure, rotate in a fixed direction. Given the short-range interactions and inherent asymmetry of R1-R2, the spatial orientation during their association plays a crucial role, particularly in the polarization interaction between Ro and R1-R2.

This interaction depends on both the distance and spatial orientation of R1-R2 and the time Ro remains within the critical interaction radius. Considering the synthesis of mirror-symmetric isomers, the polarization interaction is maximal when Ro approaches from the R1 side and minimal when it approaches from the R2 side.

This can be understood as follows: the left-handed isomer differs from the right-handed one by the direction of radical attachment, either clockwise or counterclockwise relative to R1. When the radical's motion aligns with R1's rotation, the interaction time increases, making the radical more likely to attach behind R1. This leads to the predominant formation of one isomer over the other.

Figure 2 illustrates possible association processes using an alanine molecule, flipped around its rotation plane. Letters L and D denote left and right isomers, with the yellow-marked path (B) indicating the most probable isomer formation process.

ASSUMPTION ABOUT SPATIAL POSITIONING: MOMENT OF INERTIA

We assume that the mutual positioning of molecules is dictated by a plasma-liquid system with rotating gliding discharge, and that directed rotational motion is an important factor in this process. We will here explore the possible orientations of the rotating molecule and its axis of rotation.

In the case of classical chemical synthesis, molecular rotation is equally probable in all directions. As for the axis of rotation, according to classical mechanics, free rotation is possible around two axes: the largest and smallest axes of the inertia ellipsoid. The main axis of the inertia ellipsoid is more stable. Therefore, it is expected that, in the presence of directed motion in the system, the most pronounced molecular rotation will occur in the direction aligned with the rotational motion of the medium. The molecules or their radicals will align their principal axes of inertia parallel to the angular velocity of the medium.

CONCLUSIONS

1. The physical model makes it possible to describe the deviation of racemic ratio during synthesis in a dynamic plasma-chemical system.
2. The directional movement can lead to a deviation of the isomer ratio from the racemic one.
3. Molecules acquire a dominant plane of rotation due to the presence of vorticity in the system.
4. Each minimal volume of liquid in the studied systems rotates both relative to its radius vector and relative to neighboring volumes.

REFERENCES

[1] Valeriy Ya. Chernyak, Vitalii V. Iukhymenko, Kostia V. Iukhymenko, Yevgen A. Oberemok, Daniil D. Tretiakov, Andriy M. Horiachko, Igor I. Fedirchyk and Olena V. Prysiazhna: Plasmochemical synthesis of optically active substances // IEEE Transactions on Plasma Science. No. 3 (49), 1050-1054 (2021). DOI: 10.1109/TPS.2021.3064692

[2] V. Chernyak, S. Shulga, V. Trachevskiy, V. Iukhymenko, K. Iukhymenko, D.Tretiakov, V. Diamant, V. Voskobijnyk, O. Tsymbaliuk, S. Nedovesov, V. Kyslyi, O. Kolomys, Yu. Ponomarenko, Effects of non-equilibrium plasma processing on solutions of D-, L-isomers // XXIV International young scientists conference on applied physics ICAP2024, May 23-24, Kyiv, Ukraine, 2024, pp 117-118.

[3] V.V. Iukhymenko, V.Ya. Chernyak, D.K. Hamazin, D.S. Levko, V.A. Bortyshevsky, R.V. Korzh, Rotating gliding discharge submerged in liquid // Problems of Atomic Science and Technology. Series “Plasma Physics” (23). 2017, №1, p. 136-139.

[4] V. Chernyak. Gas discharge plasma in dynamics system as a noneqilibrium plasma sources // Proc. 3rd CzechRussian Seminar on Electrophysical and Thermophysical Processes in Low-temperature Plasma, Brno, 1999, Nov. 16-19, p. 94-99.

[5] Morrison, R.T. and Boyd, R.N., 1987. Organic Chemistry, 5th ed. Allyn & Bacon Inc. p. 150

[6] V.V. Zagorsky. Lectures on General and Inorganic Chemistry: http://www.chem.msu.ru

[7] Moffatt, H.K. (2015), "Fluid Dynamics", in Nicholas J. Higham; et al. (eds.), The Princeton Companion to Applied Mathematics, Princeton University Press, pp. 467–476

EVALUATION OF THE ELECTRON ENERGY DISTRIBUTION FUNCTION IN THE TWO STAGE HALL TYPE PLASMA SOURCE

V.Yu. Bazhenov, A.M. Dobrovolskii, V.V. Tsiolko, V.M. Piun*

**Department of Gas Electronics, Institute of Physics NAS of Ukraine, Kyiv, Ukraine,*
e-mail: bazhenov@iop.kiev.ua, dobr@iop.kiev.ua, tsiolko@iop.kiev.ua

The electron energy distribution function in two-stage asymetric plasma source of Hall type is experimentally studied. In particular, the existence of a group of electrons with energy of ≈ 35-50 eV was found in the axial zone of the plasma source.

Introduction

In [1] we studied the version of the two-stage asymetric plasma source of Hall type. The working gas injected along the axis of the system rather than through the anode in symmetric version. Such design looked a promising one from viewpoint of enhanced ion thrust due to optimizing the distribution of energy supplied by the power source between the stages of the device. An important issue for sources of the Hall type is the shape of the electron energy distribution function (EEDF). In this work, we investigated the EEDF for an asymmetric plasma source with an anode layer and two independent cathodes in different zones of the source magnetic field.

Experimental setup and results

Plasma emission spectra were studied using a CCD spectrometer SL40-2-2048 in the wavelength range of 400-900 nm with a resolution of about 0.5 nm. The design of the optical system provided spatial scanning of the emission detection zone along the radius of cylindrically symmetric plasma device (see Fig. 1) by longitudinal move of the mirror 1 reflecting radiation at an angle of 90^0, while other elements of the optical system remained stationary. The radiation entered the spectrometer through an optical waveguide with an effective input diameter of about 0.4 mm. The projection of the radiation reception zone onto the entrance of the waveguide was carried out using a lens with a focal length of 105 mm and a relative aperture that could vary from 1:4.5 to 1:16.

We have considered how the parameters of the operating modes of the source affect the emission behavior of the argon lines ArI, λ = 750.39 nm (transition $2p_1 \rightarrow 1s_2$, E_{th} = 13.48 eV), ArI, λ = 811.53 nm, (transition $2p_9 \rightarrow 1s_5$, E_{th} = 13.08 eV) and several emission lines of singly ionized Ar II.

At an argon pressure of < 10-3 Torr, the dominant mechanism in the population of the Ar ($2p_1$) level is excitation by an electron impact(14 eV) from the ground state, and the main part of the energy is emitted during the transition to the Ar($1s_2$) level (λ = 750.39 nm, E_{th} = 13.48 eV) [2]. Thus, intensity I_{750} is a certain measure of the plasma density and the content of electrons with energy greater than 14 eV. Unlike the case of the previous line, the main channel for the population of the Ar($2p_9$) state is excitation by an electron impact (in this case 2 eV) from the metastable $1s_5$ state, despite the fact that in the plasma metastable atoms make up only a small fraction ~ (10^{-5}–10^{-3}) of argon atoms [3].Knowing the intensity behavior of this line gives us information about the low-energy part of the EEDF. Emission of ionized argon line Ar II = 487.98 nm (transition 4s $^2P_{3/2}$ - 4p $^2D^0_{5/2}$, E_{th} = 35.44 eV) was chosen because its upper state is 20 eV above the ion state and 35 eV above the ground state of Ar. The maximum excitation crossing of these lines is reached at electron energy of 50 eV. That is, the radiation of this line is evidence of the existence in the plasma of a group of fast electrons with energy $\varepsilon \approx (35 – 50)$ eV.

The studies were performed using resistances of 10 kOhm and 820 Ohm in three options of their connection to the cathodes C1 and C2 (option I – R1 = 10 kOhm , R2 = 820 Ohm; option II – R1 = 820 Ohm R2 = 10 kOhm; option III R1= 820 Ohm, R2 = 820 Ohm). The argon pressure was varied from $0.9*10^{-4}$ Torr to $2.9*10^{-4}$ Torr. When considering the obtained radial dependences of line intensities, you have to keep that in mind that the obtained spectra are averaged not only over time, but also over the thickness of the discharge plasma L ≈ 100 mm. Therefore, on the basis of the obtained spectral data, only general conclusions can be drawn regarding the processes in the plasma.

As an example, Fig. 2 shows changes in the radial distribution of the intensities of the lines under consideration with changes in Ar pressure.

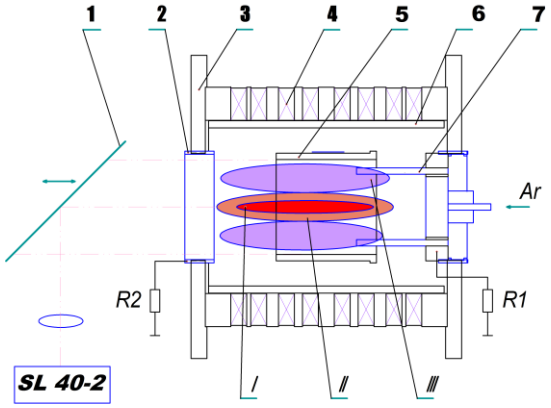

Fig. 1. Scheme of experimental device. 1 – movable mirror, 2 – external cathode C2, 3 – dielectric flanges, 4 – magnet system , 5 – anode, 6 – quartz cylinder, 7 – internal cathode C1, I, II, III – specific zones of the plasma glow.

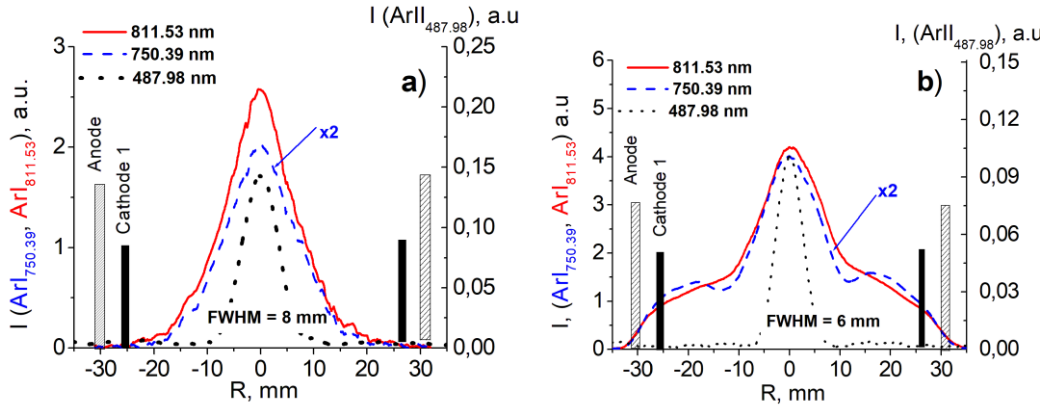

*Fig.2a,b.Averaged over time and observation line radial dependences of intensities of the emission lines for atomic argon ArI (750.39 nm), ArI (811.53 nm) and atomic argon ion ArII (487.98 nm). R1 = 10 kOhm, R2 = 820 Ohm. a) P = 0.9*10^{-4} Torr, b) P = 2.9*10^{-4} Torr*

The obtained results provide an understanding of the peculiarities of the change in EEDF shape of the source plasma depending on the modes of its operation. They show the formation in the near-axis volume of a significant number of "hot" electrons with energies from 14 eV to 50 eV. As the measurements show, the number of electrons capable of ionizing the working gas is very significant throughout the volume of the plasma source.

References

[1] V.Yu. Bazhenov, A.M. Dobrovolskiy, V.V. Tsiolko, V.M. Piun. Two stage plasma source for large scale beam generation//PAST. Series “Plasma electronics and new methods of acceleration”. № 4. p. 121-124. 2023.

[2] John B. Boffard, R.O. Jung, Chun C. Lin, A.E. Wendl. Optical emission measurements of electron energy distributions in low-pressure argon inductively coupled plasmas. Plasma Sources Sci. Technol. 19, (2010) 065001. DOI: 10.1088/0963-0252/19/6/065001.

[3] John B. Boffard, Garrett A. Piech, Mark F. Gehrke, L. W. Anderson, and Chun C. Lin. Measurement of electron-impact excitation cross section out of metastable levels of argon and comparison with ground state excitation. Phys. Rev. A 59, 2749 (1999). DOI: 10.1103/PhysRevA.59.2749.

PULSED ELECTRON BEAM PROCESSING OF MATERIAL SURFACES USING THE ACCELERATOR WITH A PLASMA OPENING SWITCH

D.V. Vinnikov[1,2], I.N. Onishchenko[1], V.B. Yuferov[1], O.M. Ozerov[1], V.V. Katrechko[1], V.I. Tkachov[1], A.B. Batrakov[1].

[1]National Science Center "Kharkiv and Institute of Physics and Technology", Kharkiv 61108, Ukraine,
[2]O.Ya. Usikov Institute for Radiophysics Electronics Kharkiv 61085, Ukraine
email: vinniden@gmail.com

This paper gives consideration to the possibility of using a small-sized electronic accelerator of a direct action equipped with the inductive energy storage device (IES) and a plasma opening switch (POS) to modify the surface properties of solid materials. Test specimens were exposed to the action of an electron beam with an energy of 200 keV, a current of up to 12 kA, and a duration of 100 to 200 ns, in a vacuum of $8 \cdot 10^{-5}$ Torr. Pure metals, their alloys, oxide coatings and composite polymers were subjected to such processing.

Electronic beam processing

Pulsed electron beam processing (EBP) is one of the most promising ways of modifying the structure of the near-surface layer of products made of various materials in order to improve their operational performances and impart new properties to the surfaces. Its essence lies in the effect of the energy flow of the electron beam on the surface of the processed material and also in the effect of the plasma formed during its passage to the target [1]. When the beam and plasma interact with the surface, their kinetic energy is spent on thermal effects. The outcome of the interaction of the beam and the plasma with the target depends on the energy of the beam, its shape and size, the interaction duration, the composition of the surrounding medium and the type of the processed specimen.

The studies of the effect on composite and carbon materials, as well as widely used structural metals, alloys and steel are of great interest.

Accelerator with a plasma opening switch

A distinctive feature of EBP based on an accelerator with IES and POS (see Fig. 1) in comparison with traditional EBP that uses beams of micro- and millisecond duration, is the duration of the beam, which does not exceed 200 ns [2.3,4].

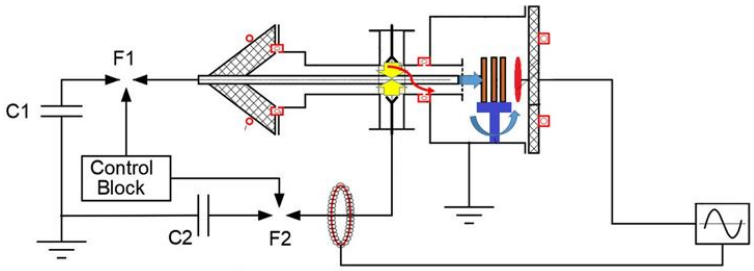

Fig.1. Diagram of the accelerator upgraded for processing materials

At the same time, the energy of the beam can attain up to 100 J/cm^2. The beam current in the geometry of a tubular copper cathode - mesh anode with a geometric transparency of 65% reaches 12 kA with an interelectrode gap of 6 mm. The beam diameter varies at about 30 mm. The charging voltage of the energy storage device of the pulse current generator reaches 45 kV. The charging voltage of plasma guns is up to 16 kV. The voltage is induced

due to the opening of the plasma switch and it results in the explosive emission of electrons from the end of the tubular cathode. A beam of electrons with energy of up to 200 keV is formed. This energy has sufficed for the change of the surface properties of a number of materials that are widely used for different technological purposes.

Experimental data

The effects of pulsed high-current electron-beam processing of nanosecond duration on targets made of metals, alloys, metals with oxide coatings, and composite polymers provided improvement and change of surface properties of materials made of stainless steel, coated with oxide coatings and composite carbon polymers CFRP. These types of materials are in demand due to their application in the engineering and space industries. The possibility of eliminating residual stresses on the surfaces in stainless steel specimens due to the reorientation of grains during the thermal effect of the beam has been proven. Annealing of stainless steel specimens is possible, and it results in the strengthening of the surfaces. The high level of wear resistance and heat resistance of the surfaces formed by the method of micro-plasma oxidation (MPO method) has been confirmed. Beams with energy of about 200 keV and a power of 10 J/cm^2 fail to change the previously acquired properties. The surfaces of the oxide films can be partially leveled due to the filling of the pores formed after the MPO process with the products of vacuum diode electrode erosion. Some competing processes can occur simultaneously on the surfaces, depending on the type of material. On the one hand, the surface is cleaned due to the effect of plasma flows and the spread of the electron beam in the presence of angular scattering. At the same time, these processes result in the thermal heating of the surface, its melting and leveling. This is typical for copper, aluminum, brass and stainless steel. On the other hand, the surface is saturated with erosion products of vacuum diode electrodes that settle in the form of a droplet phase with a size of up to 10 μm, which can increase the overall roughness of the surface. The CFRP composite polymer loses sulfur under the influence of the electron beam, and in addition, it increases the development of its surface by approximately 60% due to the kinetic and thermal effects of the electron beam. At the same time, the structure of carbon fibers is not disturbed, and the structure of the lower layers of the material is not destroyed (see Fig. 2).

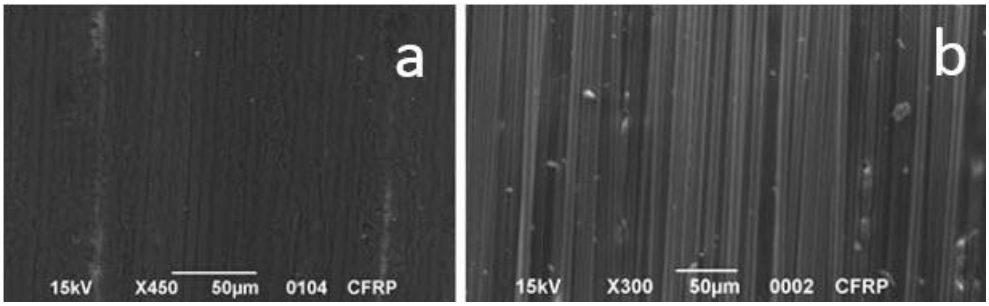

Fig.2- Original CFRP specimen, b- CFRP after the irradiation

Due to the effect of the electron beam on the surface of specimens made of stainless steel it was possible to improve the surface microhardness by 23% and remove surface stresses. The initial parameters of the discharge circuit of the accelerator and the amount of pulses that would ensure the acquired changes in the properties for each type of material have been determined.

To obtain appropriate data, a wide range of modern methods of non-destructive control of material surfaces were used, in particular diffractometry, raster electron microscopy, and terahertz ellipsometry. The use of an accelerator based on IES with POS for EBP of surfaces is appropriate for all considered types of materials.

This research was done within the budget program 6541030.

References

[1] D.V.Vinnikov, I.V.Buravilov, V.B.Yuferov, A.N.Ponomarev, V.I.Tkachev. Opportunitis for the use of the Small-size Accelerator VGIK-1// *Problems of Atomic Science and Technology.* 2019, № 6 p. 115-121.

[2] D.V. Vinnikov, V.V. Katrechko, V.B. Yuferov, V.I. Tkachev. Plasma Guns of an Erosion Type with the Pulse-Periodic Gas-Metal Injection// Problems of Atomic Science and Technology. 2022, №6(142). p. 60-65. https://doi.org/10.46813/2022-142-060

[3] D.V. Vinnikov, V.V. Katrechko, O.V. Manuilenko, O.M. Ozerov , I.N. Onishchenko V.I. Tkachev V.B. Yuferov, S.V. Marchenko. Improving the Functionality of the Small-dimension Accelerator DIN-2k with a Plasma Opening Switch // *Problems of Atomic Science and Technology.* 2024, № 3 (151) p. 60-66. https://doi.org/10.46813/2023-146-036

[4] D.V. Vinnikov, V.V. Katrechko, O.M. Ozerov, V.I. Tkachev, S.V. Marchenko V.B. Yuferov, O.V. Manuilenko. Influence of the Energy Parameters of the Primary Circuit on the Current Characteristics of the Din-2k Accelerator // *Problems of Atomic Science and Technology.* 2023, № 4 p. 36-40. https://doi.org/10.46813/2023-146-036

SOURCE OF POWERFUL X-RAY RADIATION BASED ON HIGH CURRENT PULSED ELECTRON ACCELERATOR "TEMP-B"

O.B. Batrakov, I.N. Onishchenko, S.I. Fedotov, E.G. Hlushko, A.O. Zinchenko

Institute for Plasma Electronics and New Acceleration Methods,
National Science Center 'KIPT', Str.Akademichna 1, Kharkiv, Ukraine, 61108
e-mail: a.batrakov67@gmail.com

In order to obtain a high power of bremsstrahlung X-ray radiation by a high-current relativistic electron beam of a direct-action pulsed accelerator, the necessary magnetic system, its control and power supply schemes have been developed. The source of powerful X-ray radiation is intended for the study of radiation resistance of materials of radioactive waste containers

The scheme has been developed for increasing the parameters of the bremsstrahlung X-ray source (BRS) with an exposure dose up to 9100 roentgens of the relativistic electron beam (REB) of the pulsed accelerator «TEMP-B» (energy of 0.35 <W <0.75 MeV, current J = 20 kA and pulse duration 1.5 μs) by means of the REB current increasing. The increase in the REP current is carried by using magnetic system with a higher magnetic field strength between REB transport chamber and BRS. The scheme of the magneto-isolated vacuum diode with correcting sections is shown in Fig. 1

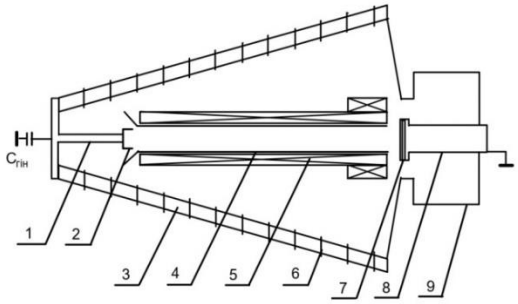

Fig. 1. Scheme of the magneto-isolated vacuum diode of the accelerator «TEMP-B» with correcting sections:
1 – cathode node; 2 – cathode; 3 – accelerator column insulator;
4 – anode insert with REB transport chamber; 5 – main and correcting magnetic field solenoids;
6 – gradient rings of the accelerator column; 7 – bremsstrahlung X-ray source BXS;
8 – X-ray input; 9 –camera for the interaction of the REB with X-ray converter

The high-current pulsed electron accelerator «TEMP-B» consists of the following main elements: pulsed voltage generator, magneto-insulated vacuum diode with a cathode node (1), cathode (2), anode insert with a REP transport chamber (4), camera for the interaction of the REB with X-ray converter (9), devices for registering the parameters of the accelerator. Placing the magnetic field solenoid (5) in such a way that its power lines close on the cathode node, which is connected to the high-voltage electrode of the accelerating column, we reduce the loss of electrons emitted from the cathode during the formation of the REB. If the force lines of the magnetic field are closed to the gradient rings (6) of the insulator of the accelerator column (3), then part of the electrons emitted from the cathode during the formation of REB may be deflected on them. The second place where the REP current is lost is the gap between the REB transport chamber and BRS converter. .In order to bring the REP without loss to BRS, it is necessary to increase the magnetic field strength on this gap, which can be done by using the correcting solenoids of the magnetic system. The parameters of the magnetic system with the main and correcting solenoids were calculated. Enameled copper wire Ø1.2 mm is used in the windings of the solenoids of the magnetic system. The length of the REB transport chamber, on which the solenoids are placed, is Lo = 750 mm, its outer diameter

is 76 mm. The total number of turns of the main and correcting sections of the solenoids is N = 2640. To reduce the current in the wire of the solenoid windings and reduce the total resistance of the solenoids, the main sections are connected in parallel. The correcting sections are connected in series with the main sections, respectively. By switching the main and correcting sections of the solenoids, as well as by changing the length of the correcting sections, it was possible to increase the magnetic field strength by two times, which makes it possible to improve the conditions for transporting the beam to the BRS.

To determine the heating of the magnetic system due to a current pulse, we use the heat balance equation

$$Q = tRI^2 = cmT \qquad (1)$$

where Q is the amount of released heat, I = 150 A is the current in the solenoid, R = 3.3 Ohm is the resistance of the solenoid winding, m = 3.4 kg is the mass of the solenoid wire, t = 50 10^{-3} sec is the duration of the switched-on magnetic fields, c – heat capacity of copper, T (ºC) is temperature:

$$T = \frac{I^2 Rt}{\text{cm}} \qquad (2)$$

During the current pulse solenoid winding is heated up by 2.9 ºC. For stable operation of the magnetic system forced cooling of the solenoids is required. Liquid nitrogen vapors from the adsorption pump are used to cool them. By connecting the radiator, located on the base of the solenoids of the magnetic system, to the place where the nitrogen vapor exits from the adsorption pump, we get the opportunity to cool the solenoids of the magnetic system without using additional equipment.

The strength of the magnetic field was calculated as a superposition of the strengths from all turns of the solenoids. The magnetic field strength in the center of the solenoid coil is determined by the formula:

$$H = \frac{0{,}4\pi \cdot I \cdot r_{cp}^2}{(r_{cp1}^2 + z^2)^{3/2}} \qquad (3)$$

where I = 150 A is the current in the solenoid, r_{avr} = 39 mm is the average radius of the main sections of the solenoid, and r_{cp1}^2 = 70 mm is the average radius of the corrective sections of the solenoid, z is the length from the center of the turn to the calculated point.

$$H_n = \sum H_i \qquad (4)$$

where H_n is the magnetic field strength at the n-th point, H_i is the magnetic field strength of each turn of the solenoid. The voltage at the point of interaction between the REP and the BRS converter is equal to H = 5.5 10^5 A/m

REFERENCES

[1] A.B. Batrakov, E.G. Glushko, A.M. Yegorov, A.A. Zinchenko, Yu.F. Lonin, A.G. Ponomaryov, A.V. Rybka, S.I. Fedotov, V.T. Uvarov Study of hard x-ray bremsstrahlung at the radiation-beam complex «TEMP» XXIV International Workshop on Charged Particle Accelerators, Kharkov, Ukraine, September 21-25, 2015, – p. 81.

[2] A.B. Batrakov, E.G. Glushko, A.A. Zinchenko Yu.F. Lonin, A.G. Ponomarev, S.I. Fedotov Pulsed magnetic system of the relativistic electron beam accelerator "Temp-B" Problems of Atomic Science and Technology. Series: Plasma electronics and new acceleration methods(8). – 2013. – № 4 (86) – p. 7 – 9.

[3] P.T. Chupikov, D.V. Medvedev, I.N. Onishchenko, B.D. Panasenko, Yu.V. Prokopenko, S.S. Pushkarev.

CHARACTERISTICS OF PULSED GAS DISCHARGE REACTOR FOR SYNTHESIS THIN FILMS OF TUNGSTEN AND ITS OXIDE

M.M. Feldiy*, O.K. Shuaibov*, O.Y. Minya*, R.V. Hrytsak*, A.O. Malinina*,

Y.Y. Bilak*, M.O. Margitych*, V.M. Krasylynets**

**Uzhhorod National University, Uzhhorod, Pidgirna str.54, 88000, Ukraine,*
e-mail: mike.feldiy@gmail.com
***Institute of Electron Physics of the NAS of Ukraine, Uzhhorod, University str., 21, 88000, Ukraine,*
e-mail: kvn7@i.ua

The characteristics of an atmospheric pressure plasma-chemical reactor for the synthesis of tungsten and tungsten oxide thin films, which operated using an overvoltage nanosecond discharge (OND) in mixtures of inert gases and air with tungsten vapor, are presented. The discharge was ignited between tungsten electrodes. The formation of tungsten clusters and its oxide in the plasma occurred in the process of introducing tungsten vapor into the discharge gap by the ectonic mechanism. This created the prerequisites for the synthesis of the corresponding thin films (W, WO_3), which were deposited on a glass substrate installed near the electrode system.

Introduction

Tungsten oxide (WO_3) is widely used to change the color of thin films during redox reactions if a small external voltage is applied to them (the phenomenon of electrochemistry) [1]. The synthesis of such films is carried out mainly by various chemical methods or by the method of explosion of thin wires [2], but the explosion method has limitations on the frequency of repetition pulses. The production of tungsten vapor during its thermal evaporation is limited by the high melting and vaporization temperature of tungsten (which exceeds 2000 K), so it is promising to use non-thermal (explosive) mechanisms of tungsten sputtering in plasma to synthesize tungsten-based films. Tungsten oxide films, when applied to tungsten, lead to an increase in its microhardness. The interest in the processes of sputtering pure tungsten in pulsed plasma is caused by the fact that the first wall of Tokamak-type fusion reactors is made of tungsten.

Currently, there are no studies of the conditions for the synthesis of thin films of tungsten and its oxide during deposition from a pulsed plasma in steam-gas mixtures of the "Ne, Ar, Kr, Air - W" type with the mechanism of ectonic erosion of electrodes.

The report presents the results of studying the characteristics of a plasma-chemical reactor based on the OND between tungsten electrodes in inert gases and atmospheric pressure air, which is promising for obtaining thin films of tungsten and tungsten oxide at discharge device temperatures less than 100 ^{0}C. The results of the study of tungsten oxide film obtained by micro-Raman laser scattering spectroscopy are presented.

Results and discussion

The study of the characteristics of OND in inert gases and air at atmospheric pressure was carried out using an experimental installation, the scheme of which is given in [3]. The distance between the tungsten electrodes was 2 mm. The electrodes were made in the form of rods with a diameter of 3 mm and a length of 50 mm with a radius of rounding of the working part of 1-2 mm. The electrodes were installed in a discharge dielectric chamber that could be pumped up to a residual pressure of 13 Pa.

High-voltage bipolar pulses lasting 100-150 ns and having an amplitude ranging from ±20 to ±40 kV were used to initiate the discharge on the electrodes. The frequency of the sequence of voltage pulses was in the range from 80 to 1000 Hz.

The OND created conditions that contributed to the formation of a beam of "runaway electrons" with high energy and X-ray radiation, as a result of which a uniform spherical discharge with a diameter of 2-3 mm was

formed between the electrodes at atmospheric pressures of the ignition gases, since the electron beam and accompanying X-ray radiation played a role system of automatic pre-ionization of the interelectrode gap.

The current and voltage waveforms showed time-decaying oscillations with a duration of approximately 80-100 ns, which arose due to a mismatch between the output resistance of the high-voltage modulator and the load resistance. The duration of the full voltage and discharge current oscillations was 450-500 ns.

For the OND, the amplitude of the positive polarity voltage at the electrodes reached about 30 kV at the initial stage of discharge, and the current was approximately 100 A. The maximum pulsed power of the OND reached 3 MW at a time of t = 30 ns, and the energy contribution to the plasma was 312.6 mJ. The pulsed discharge power reached 1.25 MW at t = 90 ns. The energy contribution to the plasma based on air at atmospheric pressure was equal to 176.9 mJ.

At the atmospheric pressure of krypton, the maximum pulsed power was 1.6 MW (at t_2 = 115 ns), and the energy contribution to the plasma was 263 mJ. For the OND in argon at atmospheric pressure, the amplitude of the first, second, and third voltage half-waves was in the range of 20-22 kV, respectively, at times: t_1 = 50, t_2 = 175, and t_3 = 300 ns, and the maximum current was about 110 A (t_1 = 60 ns). The maximum pulsed power of the OND reached 2.7 MW at t_1 = 35 ns, and the energy contribution to the plasma for one discharge pulse was about 239 mJ. The electrical characteristics of the OND in helium under the same discharge excitation conditions as in krypton and argon were similar in shape to the corresponding characteristics of the OND in krypton and argon, but the currents and voltages were lower, which led to a 2-3-fold reduction in the energy of the discharge pulse. Such a distribution of the electrical characteristics of the OND in different inert gases is due to the different plasma resistance and the different conditions for its coordination with the output resistance of the voltage modulator.

The spectral lines of emission of atoms and ions from the OND plasma in gas mixtures of air with tungsten vapor were observed against the background of continuous plasma radiation. The most pronounced continuum in the high voltage nanosecond discharge emission was observed in the spectral interval of 400-500 nm.

During operation of the reactor for 20-30 minutes and a frequency of 1000 Hz, on the substrate installed on at a distance of 1 cm from the center of the charge gap, thin films were deposited based on tungsten and buffer gas components (oxygen from air plasma). Synthesized thin films were analyzed using a Raman spectrometer Renishaw InVia confocal Raman microscope (UK).

Thus, it was found that at atmospheric pressure of inert gases and air, a spatially homogeneous OND is ignited between the tungsten electrodes, which is suitable for the synthesis of tungsten and tungsten oxide thin films at low temperatures of the reactor.

References

[1] Y. Shi, Y. Zang, “Designed growth of WO_3/PEDOT core/shell hybrid nanorod arrays with modulated electrochromic properties,” Chemical Engineering Journal, vol. 335, pp. 942951, Jan. 2019.

[2] Yu.O. Adamchuk, S.V. Chushchak, L.Z. Boguslavskii, A.V. Sinchuk, “The Regularities of Titanium and Tungsten Carbide Formation from Products of Electric Explosion Destruction of Conductors,” Surface Engineering and Applied Electrochemistry, vol. 3, pp.281-286, Jun. 2023.

[3] O.K. Shuaibov, A.O. Malinina, “Overstressed nanosecond Discharge in the Gases at Atmospheric Pressure and Its Application for the Synthesis of Nanostructures Based on Transition Metals,” Progress in Physics of Metals, vol. 22(3), pp. 382-439, 2021.

CALCULATION OF EQUILIBRIUM PLASMA COMPOSITION BASED ON OPTICAL EMISSION SPECTROSCOPY OF ELECTRIC DISCHARGE PLASMA

E. Sorokun*, I. Slisarenko, A. Murmantsev, V. Osidach, A. Veklich

Taras Shevchenko National University of Kyiv, 63/13, Volodymyrska str., Kyiv 01601, Ukraine
*sorokun.ernest@gmail.com

This work is devoted to study of the peculiarities of interaction of electrodes materials with the plasma of thermal electric arc discharge. The emission of electric arc discharges plasma between copper electrodes was studied by optical emission spectroscopy. The study was conducted at a discharge current of 3.5 and 30 A. The equilibrium plasma composition was calculated based on two different sets of input parameters. Namely, as the first set the radial distributions of excitation temperature and electron density were used, as the second one the radial distributions of excitation temperature and copper number density were used. The comparison of these results is carried out.

Introduction

Optical emission spectroscopy (OES) is a key technique for analyzing plasma processes that determine the behavior of materials under high-temperature conditions. It is widely used to characterize the emission spectra of excited atoms and ions, offering crucial information about the elemental composition and plasma parameters such as temperature and electron density. OES is invaluable for studying the erosion of electrodes material and evaluating energy dissipation channels of electric arc discharge.

This study focuses on using OES to analyze plasma generated by electric arc discharge between copper electrodes, a material commonly used in electrical components. The obtained data make it possible to elucidate the mechanisms of material erosion and its propagation in discharge gap. Additionally, this method allows investigating the erosion resistance of the electrodes depending on the arc conditions, such as duration and current intensity. By correlating spectroscopy data with erosion rates, this research aims to enhance the understanding of thermal erosion processes, contributing to the development of high-performance copper-based materials of contacts and/or electrodes [1].

Experimental methods

A free-burning arc was ignited in an air atmosphere between the flat surfaces of uncooled vertically oriented rod electrodes (diameter of 6 mm) made of copper. The discharge gap in all experimental studies was 8 mm, and the discharge current was kept at 3.5 A and 30 A. The plasma of each type of discharge was studied using optical emission spectroscopy [2]. The excitation temperature of copper atoms (which is equal to the plasma temperature under the assumption of local thermodynamic equilibrium) and the concentrations of copper atoms were determined using the Boltzmann plot technique based on the absolute intensities of Cu I spectral lines [3]. The radial distribution of electron density in the arc discharge plasma was determined based on the width of Cu I 515.3 nm spectral line. The equilibrium plasma composition was calculated based on two different sets of input parameters. Namely, the first set was the radial distributions of excitation temperature and electron density, and the second set was the radial distributions of excitation temperature and number density of copper.

Results and Discussion

When calculating the equilibrium plasma composition, a significant difference lies in how the parameters n_e, Cu, and Cu+ were obtained. In the first case (Fig. 1) n_e was determined from interferograms of Cu I spectral line. Then, based on the equilibrium composition calculation, the number density of Cu and Cu+ were obtained. In the second case (Fig. 2), the study was conducted using the method of absolute intensities, where the parameters of Cu were determined directly, and the radial distributions of n_e and Cu+ were subsequently derived from the equilibrium plasma composition calculation.

As seen in the figures for 3.5 A and 30 A, the radial distributions of n_e, Cu, and Cu+ coincide, which provides the possibility determining the erosion resistance of electrode materials in indirect way. This can be done by

following two approaches: in the first approach, using temperature and electron density as input parameters, and in the second, using temperature and the number density of metal atoms.

Thus, the agreement between the two methods demonstrates the feasibility of estimating the erosion resistance of electrode materials through indirect calculations, based on the equilibrium plasma composition in both approaches.

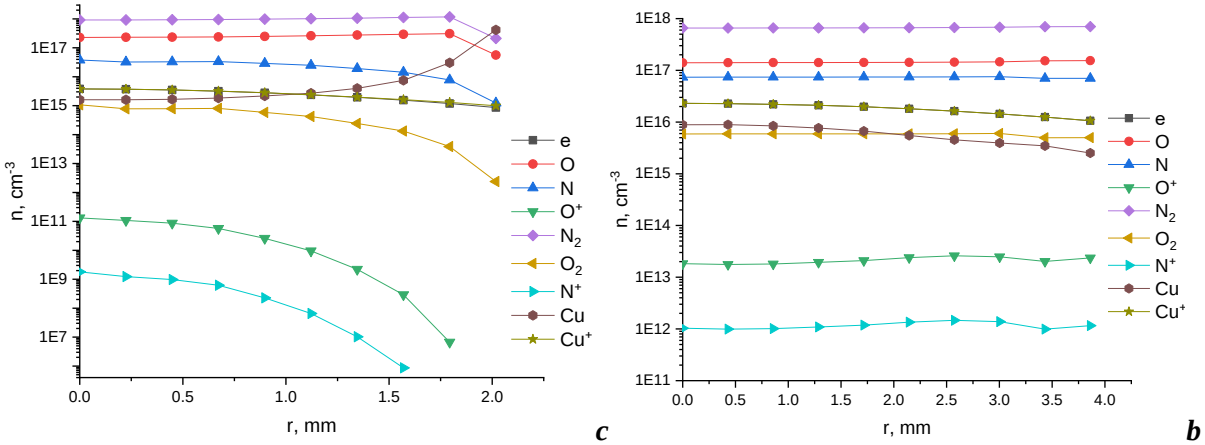

Fig. 1. Radial distribution of the equilibrium plasma composition calculated by the method of relative intensities for 3.5 A (a) and 30 A (b)

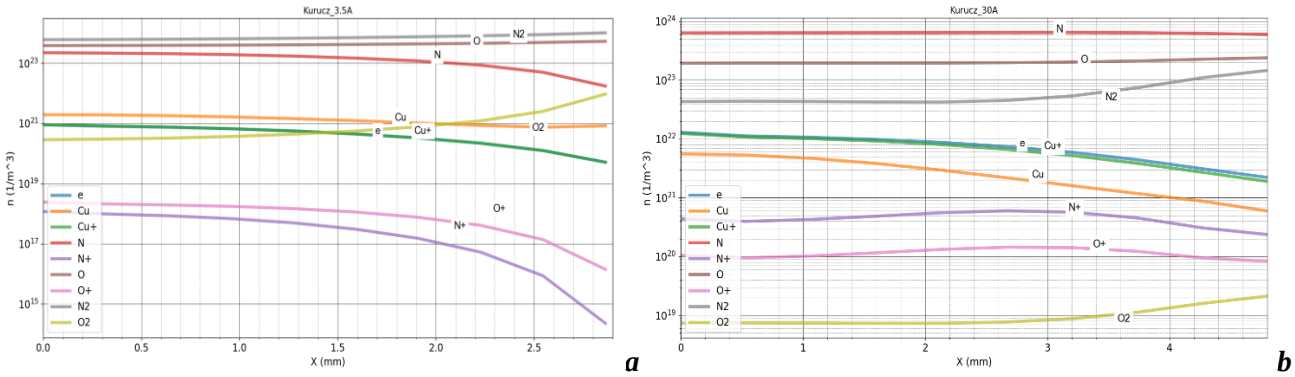

Fig. 2. Radial distribution of the equilibrium plasma composition calculated by the method of absolute intensities for 3.5 A (a) and 30 A (b)

References

[1] M. J. Kushner, "Modeling of the sputtering of copper electrodes in low-pressure arcs," J. Appl. Phys., vol. 95, no. 2, pp. 846–857, 2004.

[2] A. Murmantsev, A. Veklich, V. Boretskij, S. Fesenko, M. Kleshych, and O. Tolochyn, "Investigation of thermal plasma of arc discharge between novel composite Cu-W materials," Problems of Atomic Science and Technology, Series: Plasma Physics (29), vol. 143, no. 1, pp. 74–78, 2023.

[3] A. Murmantsev, "Investigation of Spatial Distribution of Metal Vapours Admixtures in the Plasma of an Electric Arc Discharge," Problems of Atomic Science and Technology, vol. 146, no. 4, pp. 139–146, 2023.

Acknowledgment

This work has been partially carried out within the framework of the EUROfusion Consortium, funded by the European Union via the Euratom Research and Training Programme (Grant Agreement No 101052200 — EUROfusion). Views and opinions expressed are however those of the author(s) only and do not necessarily reflect those of the European Union or the European Commission. Neither the European Union nor the European Commission can be held responsible for them.

COMPUTER TECHNOLOGIES

CAN ARTIFICIAL INTELLIGENCE REPLACE IT SPECIALISTS?

Pavlo Bachysh

Faculty of Electronics and Informational Technologies Sumy State University, Sumy, 40021,Ukraine, email: happytouni@gmail.com

Lorem ipsum dolor sit amet, consectetur adipisicing elit, sed do eiusmod tempor incididunt ut labore et dolore magna aliqua. Ut enim ad minim veniam, quis nostrud exercitation ullamco laboris nisi ut aliquip ex ea commodo consequat. Duis aute irure dolor in reprehenderit in voluptate velit esse cillum dolore eu fugiat nulla pariatur. Excepteur sint occaecat cupidatat non proident, sunt in culpa qui officia deserunt mollit anim id est laborum.

Introduction

Due to the rapid development of artificial intelligence in recent times, people began to worry that their workplace will be taken by this technology. Programmers, whose work was threatened, were no exception.

The purpose of this study is to explore the possibilities of AI now and in the near future. Will artificial intelligence replace programmers?

Main Part

Today, AI is really capable of generating code at a user's request. For example, I wrote a very short ChatGPT query “Generate HTML code for the school website using CSS” and this is what I got as a result.

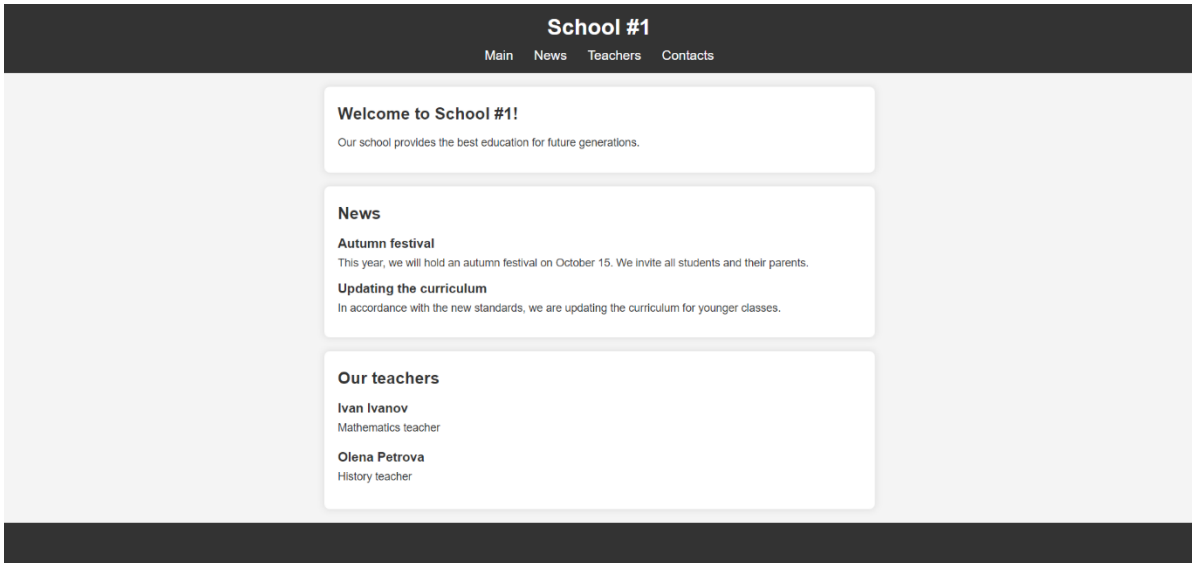

Picture 1. Result

Despite the inaccuracy and non-specificity of the request, AI created an eye-pleasing site layout. But this does not mean that Frontend programmers are no longer needed. It will be difficult for the customer to describe the site in detail to an intelligent machine. But the programmer will need less time to write the foundation code of the site, and will be able to devote more time to finishing. Using this example, I demonstrated that AI is a good tool in the hands of a specialist, and not a replacement for him. Head of EPAM in Ukraine Stepan Mitish said: "Artificial intelligence will not replace programmers in the coming years, but its use will definitely change the market." He meant that those who will use AI will replace those who do not. This statement is based on the fact that AI will

help to perform a simple job in a few minutes that takes a long time for an ordinary person. Such tasks are: generation of simple code, search for information about various libraries and frameworks, can prepare a report, form a checklist for colleagues, help in making simple decisions.

Although AI has a lot of functionality, there is also something that, unlike a person, it does not have - Soft Skills. Analysis of client requirements, solving problems that require critical thinking, people-management, interaction with the team and emotional intelligence are all advantages of human intelligence. Also, so far, humans are better at solving complex problems with many different contexts, developing complex architectural systems, testing and quality assurance, and of course inventing something completely new.

So, for today, artificial intelligence is not a real threat to programmers, but on the contrary, it is a great tool that must be mastered to optimize the workflow.

References

[1] https://careers.easternpeak.com/blog/will-ai-replace-software-engineers/
[2] https://dev.ua/news/chy-pravda-shcho-shi-zaminyt-prohramistiv-1699007397
[3] https://dou.ua/forums/topic/41558/
[4] Online workshop within the Open IT project: "Career and opportunities in IT: will AI replace IT specialists"

MONITORING THE FUNCTIONAL AND PSYCHO-EMOTIONAL STATE OF MILITARY PERSONNEL IN COMBAT CONDITIONS: AN INNOVATIVE APPROACH TO ECG ANALYSIS

Mykhailo Bocharov*, Illya Chaikovsky**

**National Defense University of Ukraine, Kyiv, Ukraine, email: mboch75@gmail.com*
***Glushkov Institute of Cybernetics of National Academy of Science, Kyiv, Ukraine, email: illya.chaikovsky@gmail.com*

The procedure for monitoring the readiness of servicemen in combat conditions is conditioned by such interrelated goals of armed struggle as maximum realization of combat potential and minimization of personnel losses. The aim of the work is to improve the procedures for monitoring the functional and psycho-emotional state of military personnel in combat conditions.

A review of the hostilities in Russia's war against Ukraine shows a systemic change in the following factors: Increase in the number of troops; Increased intensity and density of fire; Increased sanitary and psychogenic losses of military personnel; decrease in the professional and physical qualities of the mobilization resource; decrease in the adequacy of methods for studying the quality of military personnel.

The conditions of the russian-ukrainian war are gradually changing. The increase in losses among ur troops increases the importance of monitoring the functional and psycho-emotional state of Ukrainian defenders in combat conditions.

Of course, over time, in difficult conditions, the functional state of a person deteriorates, and his or her reserve of adaptive capabilities decreases. Therefore, the search for optimal approaches to monitoring the functional and psycho-emotional state for the timely detection of risk factors and hidden and unrecognized cases of diseases should be considered an urgent task of war.

A review of approaches to the structure of military readiness [1-3] indicates the following components: motivational, emotional and volitional, personal and functional.

The study pays the most attention to the functional component, which is seen as the ability to calculate the resources of one's forces in relation to the enemy's forces and means, knowledge of tactical combat techniques, and physical endurance.

We consider the functional state of the body to be an integral characteristic of the level of its functional reserve, which can be used for adaptation. The components of the functional state are cognitive, psychoemotional, resource and energy components.

The concept of "functional state" is often used to characterize the general state of human health. Among the components of the psychological readiness of servicemen to perform combat tasks, the functional component also has the greatest applied importance. The most successful definition of functional status for us is the level of functional reserve that can be used for adaptation in difficult conditions. All scenarios of the monitoring that we carried out are, to a large extent, a type of pre-hospital diagnosis.

In many armies of the world, the monitoring of the functional and psycho-emotional state of servicemen in combat conditions is carried out by commanders, doctors, chaplains, soldier mentors, fellow soldiers, family members, medical specialists, psychologists and their assistants in the system of combat and operational stress control [4-6]. At the same time, the methods for assessing the functional reserve of servicemen in combat conditions have remained unchanged for a long time and use subjective assessments.

The general approach to monitoring the functional capabilities of military personnel was developed during World War II and improved during the Vietnam War. According to this approach, when the functional state deteriorates, the responsibility for health correction gradually shifts from commanders to medical specialists of the unit.

According to our approach, it is advisable to monitor the combat and operational stress of servicemen in combat conditions through their moral and physiological qualities.

Such a comprehensive indicator of functional state is formed on the basis of the following indicators: heart rate variability (HRV), amplitude-time ECG, heart rhythm disturbances, and psychoemotional state.

Heart rate variability (HRV) is a sequence of time values of intervals between the R-waves of ECG complexes of sinus origin, i.e., under conditions of normal functioning, the sinoatrial node is the first and main driver (pacemaker) of the heart rate.

The index of psycho-emotional state is determined on the basis of the analysis of heart rate variability by the modified McCraty algorithm (USA) based on the model of the so-called neurovisceral integration.

In the research in various combat conditions were used so-called wearable “on-body” ECG patch devices as well as miniature ECG devices with finger electrodes.

When analyzing the data, ECG devices were implemented in the principle of multi-faceted analysis, which allows obtaining physiologically based information, which includes 4 sections: heart rate variability, amplitude-time indicators of the ECG, heart rhythm disorders, and psycho-emotional state.

In this study, a complex index of functional state was evaluated, which was formed on the basis of estimates of heart rate variability, waveforms and intervals of the electrocardiogram, as well as an index of psycho-emotional state, formed according to the modified McCraty algorithm.

The result of the study of each subject is a conclusion about the adaptation reserve and the scope and nature of the measures necessary to preserve health.This scale is divided into 4 ranges: norm, adaptation stress, unsatisfactory adaptation, and adaptation disorder. A similar division is used in NATO armies to assess mental health.

Therefore, monitoring the functional and psycho-emotional state of certain categories of commanders and specialists of important specialties of the Armed Forces of Ukraine according to the proposed methodology will allow us to objectively determine the individual operational readiness of each of them and prevent a critical excess of their physiological and functional capabilities.

The proposed methods and means can be considered the main tool for ensuring that the commander makes a decision on the ability of units to perform combat missions according to the functional state of personnel.

The objective stratification of military personnel by the indicator of adaptation reserve (resistance) to physical and mental stress ensures an effective distribution of efforts to improve these qualities.

References

[1] STANDARD OF NATO AMedP - 8.6 FORWARD MENTAL HEALTHCARE 2019, STANDARD OF NATO AMedP - 8.10 A PSYCHOLOGICAL GUIDE FOR LEADERS ACROSS THE DEPLOYMENT CYCLE 2019URL: https://www.coemed.org/files/stanags/03_AMEDP/AmedP

[2] Combat psychology: activities of the unit commander in maintaining the morale and psychological state of personnel during hostilities: educational and methodological manual / A.M. Romanyshyn, O.V. Boyko, D.V. Bogoroditsky and others. Lviv: NASV, 2015. 320p.

[3] Gichun V., Kyrychenko A., Kornatskyi V., Myasnikov G., Naida S., Osyodlo V., Steblyuk V., Shvets A. (2019). Stress-related health disorders in the conditions of armed conflict: a monograph. Dnipro: 324 p.

[4] AMed P-8.10: A Psychological Guide For Leaders Across The Deployment Cycle. Edition A, Version 1. October, 2019. URL: https://www.coemed.org/files/stanags/03_AMEDP/AmedP 8.10_EDA_V1_E_2565.pdf (dateofappeal: 05.07.2024)

[5] Combat and Operational Stress Control PCN 147 000045 80, headquarters, department of the army, FM №4-02.51 (8-51), 240 c.(date of appeal: 05.07.2024)

[6] Meredith L., Sherbourne C. Promoting psychological resilience in the of U.S. URL: http://www.rand.org/publications/permissions (date of appeal: 03.05.2024) (in USA).

AI INTERTITLE TRANSLATE TOOL:
OLD MOVIES, NOWADAYS OPPORTUNITY

Andrii Chuian

Research Department, Taras Shevchenko National University of Kyiv, Kyiv 01601, Ukraine,
email: british_idler@knu.ua

Today, machine learning tasks for computer vision problems are de facto solved. Services such as Google Lens, GPT4 Vision, Llava, and others are quite successful in searching for images and sometimes processing them. A number of them can run locally, on consumer hardware, thus covering the needs of small businesses and the rest. Resources like Github are full of ready-made solutions for analyzing and translating subtitles, photos, and images. In this stream of development, there are only minor gaps that have not been filled by individual software solutions. One of them is the translation of intertitles to old movies. The task is trivial, because the volume of texts in them is absolutely insignificant and can reach several A4 pages in standard Times New Roman 14. However, an important aspect is that the significance of this text is considerable, because by translating it (ideally, following the visual style of the movie), we actually get a new product for the viewer. Intertitle translation is something that is unlikely for a significant number of films, but it is quite interesting as a whole layer of culture that is being lost, in particular, by the Ukrainian audience. Thanks to automated translation, those Ukrainian citizens who do not speak foreign languages will be able to get acquainted with film classics such as American "The Covered Wagon" (1923), German "Metropolis" (1927) or French "The Passion of Joan of Arc" (1928). The same can be seen vice versa - translation of Ukrainian masterpieces such as films by Oleksandr Dovzhenko or movies with Vira Kholodna.

Taking into account the current possibilities and the need to create actual code for its further distribution as a commercial product, this publication describes the components of this software, along with indicative ways of implementation.

Description of the app. Requirements

Taking into account the gradual decrease in system requirements for many AI models, the use of retraining of neural network layers (like MobileNet in Google Teachable machine), the use of optimized training samples (like 128x128 images), and the low resource usage in the program described below (due to the type of task itself - very short texts), this program can have as low requirements as 6GB RAM and an Intel i3 with 3rd-generation CPU (or mobile Snapdragons 400+). Even smaller values, like 4GB RAM and an Intel i5 with 2nd generation may be enough, but the above specifications are for sure.

Given the relatively low system requirements, the application can be developed for desktop PCs, smartphones, and tablets. This is especially interesting in the context of watching movies on the go, using public domain movies (as many films from the early 20th century are freely available and can be saved without copyright issues).

Thus, the application can be distributed for major operating systems such as Android, Windows, Linux, and, if specialists are available, ported to iOS and MacOS. The following text describes a variant of the implementation in the Python programming language, but given the ways to port code (like auto-py-to-exe and so on), the same project can be implemented in such languages as Java, Swift and so on.

Graphical user interface (GUI)

The simplest off-the-shelf solution is, of course, "gradio". but for being user-friendly on mobile devices and for originality, it may be better to focus on creating a unique interface. Moreover, all its components can be easily found in templates of various libraries. Here are the following components:

- drag & drop field for file selection
- language choose dropdown (or/and search field) menu
- save button (and any other buttons, that may be needed, but not are necessary as much).

File manager for directory choosing may be created, but preferably to use the external file manager (that is already installed on the system) for this purpose.

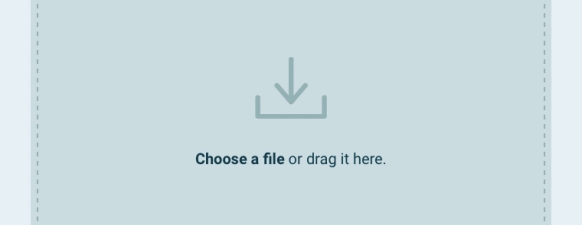

Fig. 1. Example of drag and drop file selector

Algorithm of the workflow

As noted earlier, the basic components for creating such an application have long been available in the open source community and generally meet the quality requirements even in self-hosted mode. Perhaps the bottleneck is the translation, which is currently provided better by the non-free models such as DeepL, but the text below refers to webless solutions as the basis:

Basic algorithm:

1. Scan all frames for text (*most non-optimizable process; using any python computer vision (CV) libraries*)
2. Ignore frames by some rules (f*or example, with text less than 50% of frame - shop names, license plates, etc.*)
3. Store arrays of text frames (*each unique array for each intertitle; the same CV: NumPy, Pandas, OpenCV*)
4. Translate one frame from each array (*less computing power; using Argos translate, but DeepL is preferred*)
5. Regenerate frame for each array (*using pillow library and any font, or, perfectly, with any font identifier*)
6. Replace each array with translated frame (*most computational power consuming; using ffmpeg*)

Optionally:

- Restore faces (*using GFPGAN or else*)
- Colorize video (*using Deoldify or else*)
- Enhance music quality (*using Resemble enhance or else*)

Optional part may be done to all the video (without any division) or can be optimized by the same algorithm to work with arrays of frames or audios. But it is worth mentioning that the amount of tasks could increase the amount of time, that will absolutely eliminate the advantages of the original application (the ability to launch self-hosted, even on a smartphone, offline, conditionally - on the go).

References

[1] See details here: llava-vl.github.io, platform.openai.com/docs/guides/vision, lens.google
[2] See details here: imdb.com/name/nm0235590, imdb.com/name/nm0451762
[3] See details here: imdb.com/title/tt0013951, imdb.com/title/tt0017136, imdb.com/title/tt0019254.
[4] See details here: github.com/gradio-app/gradio
[5] See details here: numpy.org, pandas.pydata.org, opencv.org
[6] See details here: argosopentech.com, github.com/DeepLcom/deepl-python, pypi.org/project/deepl_cli
[7] See details here: ffmpeg.org
[8] See details here: github.com/TencentARC/GFPGAN
[9] See details here: deoldify.ai
[10] See details here: github.com/resemble-ai/resemble-enhance

THE DEVELOPMENT OF AN INFORMATION-ANALYTICAL SYSTEM FOR MANAGING FINANCIAL CONTRIBUTIONS TO CHARITY BASED ON WEB TECHNOLOGIES

Hlobina Anastasiia

e-mail: ipzm232_gav1@student.ztu.edu.ua
Faculty of Information and Computer Technologies, Zhytomyr Polytechnic State University, Zhytomyr 10005, Ukraine, email: fikt@ztu.edu.ua

The development of an information-analytical system for managing financial contributions to charity based on web technologies is a crucial step in enhancing the efficiency and transparency of charitable organizations. Such a system automates key processes related to the collection, analysis, and management of funds directed towards charitable initiatives. In today's digital world, charitable organizations face the need not only to efficiently collect and allocate financial resources but also to ensure transparency and accountability to donors. This is essential for maintaining public trust and attracting new donors.

The goal of creating a web-based system is to provide a convenient and efficient tool for managing contributions, giving easy access to information for both donors and charity administrators. The system automates the recording of donations, generates reports on financial inflows and expenditures, and enables data analysis to improve resource efficiency. Through integration with payment systems, the platform also automates transaction processing, reducing manual effort and minimizing the risk of errors. Transparency is a key feature, allowing donors to receive real-time reports on how their contributions are being used, which significantly strengthens trust in the charitable organization.

Moreover, the system fosters better communication and collaboration between stakeholders. Donors, beneficiaries, and administrators can interact within a unified platform, reducing communication delays and ensuring timely information sharing. This creates a cohesive environment for managing projects, distributing funds, and providing reports on the progress of initiatives. The ability to track donations in real-time and update donors on fund allocation encourages sustained participation, enhancing the long-term sustainability of charitable efforts.

Additionally, the analytical capabilities of the system provide valuable insights into donation behaviors, enabling charities to optimize fundraising strategies. By analyzing data on donor preferences, seasonal patterns, and campaign effectiveness, organizations can refine their outreach methods and target potential contributors more effectively. This data-driven approach aids in better resource allocation, ensuring that funds are used efficiently to achieve the organization’s goals. The system helps direct resources where they are most needed, maximizing the impact of donations.

The implementation of such systems also contributes to the enhancement of donor engagement and satisfaction. With personalized dashboards, donors can easily monitor their individual contributions, track the progress of specific charitable campaigns they’ve supported, and receive notifications about how their funds are making a difference. This level of transparency and interaction strengthens the emotional connection between donors and the causes they support, encouraging continued and potentially larger donations in the future. The ability to receive instant feedback creates a sense of community and involvement, making donors feel more integral to the success of the charity’s initiatives.

Another important aspect of these web-based systems is their potential for integration with other digital tools and platforms. Many modern charitable organizations operate across multiple channels, using social media, email campaigns, and mobile apps to reach a wider audience. A well-designed web-oriented financial management system can integrate with these platforms, enabling seamless synchronization of fundraising efforts, marketing campaigns, and donor management. This not only helps centralize data but also improves the effectiveness of cross-channel outreach, ensuring that no potential donors are overlooked and all campaigns are fully aligned.

Furthermore, these systems play a vital role in regulatory compliance and audit processes. Charitable organizations are often subject to strict reporting requirements to ensure that funds are used appropriately and transparently. An information-analytical system simplifies the task of generating accurate financial reports and complying with both local and international regulations. The system can automatically generate detailed financial statements, track expenditures against specific budgets, and maintain an audit trail of all financial transactions. This ensures that charities are always prepared for inspections or audits, reducing the administrative burden and minimizing the risk of errors or non-compliance.

Finally, the integration of advanced security features ensures the protection of sensitive donor and financial information. Web-based financial management systems must comply with data protection laws and offer robust safeguards against potential cyber threats. Implementing encryption, secure payment gateways, multi-factor authentication, and regular security updates are essential to maintaining donor confidence and preventing fraud. Ensuring that donor data and transaction information are secure builds trust in the platform and the organization, further encouraging donors to engage with the charity without fear of data breaches or financial fraud.

In summary, the development of a web-oriented information-analytical system for managing financial contributions in charity provides numerous benefits that extend beyond simple automation. By improving transparency, enhancing donor engagement, optimizing fundraising strategies, ensuring regulatory compliance, and safeguarding sensitive data, such systems are integral to the modern operation of charitable organizations. As the digital landscape continues to evolve, charitable organizations that embrace these technologies are better positioned to grow, foster deeper connections with their donor base, and maximize the social impact of their efforts. This not only simplifies the work of charity administrators but also ensures that funds are managed responsibly and used for maximum benefit, helping organizations grow and make a greater impact in their communities.

References

[1] Boehm, B., & Turner, R. (2004). Balancing Agility and Discipline: A Guide for the Perplexed. Addison-Wesley Professional.

[2] Django Documentation. The Web framework for perfectionists with deadlines.

[3] Martin, R. C. (2008). Clean Code: A Handbook of Agile Software Craftsmanship. Prentice Hall.

[4] Owens, S. (2013). SQL Queries for Mere Mortals: A Hands-On Guide to Data Manipulation in SQL. Addison-Wesley Professional.

[5] Nielsen, J. (1993). Usability Engineering. Academic Press.

[6] Panko, R. R. (2008). Corporate Computer and Network Security. Pearson Prentice Hall.

POWER PROFILING OF FPGA EDGE COMPUTING SYSTEM AS A STAGE OF CI/CD PROCESS

Oleksandr Hryshchuk*, Sergiy Zagorodnyuk**

** Faculty of RadioPhysics, Electronics and Computer Systems Taras Shevchenko National University of Kyiv, Kyiv 01601, Ukraine, e-mail: oleksandr_hryshchuk@knu.ua*

*** Faculty of RadioPhysics, Electronics and Computer Systems Taras Shevchenko National University of Kyiv, Kyiv 01601, Ukraine, e-mail: szagorodniuk@knu.ua*

This work examines the integration of power profiling into the CI/CD pipeline for FPGA-based edge computing systems to address power optimization in resource-constrained environments. The research demonstrates a new approach using an Intel MAX 10 FPGA system with matrix multiplication on the NIOS II soft-core CPU as a sample task. The development workflow incorporates early power estimation and monitoring steps, enabling power efficiency analysis of hardware and firmware in edge computing applications.

Introduction

Edge computing devices often operate under strict power constraints due to limited battery life, remote locations, or thermal considerations, making power efficiency crucial for operational longevity and cost-effectiveness. Moreover, as edge computing applications become more computationally intensive with AI and ML workloads, optimizing power consumption becomes essential to balance performance requirements with energy limitations while maintaining device autonomy and reducing operational expenses. FPGA computing devices provide extreme configuration flexibility, which makes them a crucial component of cutting-edge computing solutions. At the same time, because of a high degree of flexibility, firmware and hardware development are vulnerable to errors [1]. Continuous integration (CI), which covers the build process validation using unit tests via test branches and power analysis, can solve the problem. Such an approach has already been used to develop several SoC devices, such as Zynq UltraScale MSSoC [2, 3]. However, existing state-of-art approaches do not emphasize energy optimization, so this question remains open.

Since most computing tasks nowadays are executed using a multithread approach, power optimization problems can be defined as finding a set of start configurations for jobs allocated to a set of available resources in the required condition [4]. The issue of energy-efficient active time scheduling is NP-complete, so to find suitable solutions in adequate time, such workarounds as heuristic methods or predefined constraints and precalculated configurations must be used. Applying power optimization gating conditions as a way of power profiling in CI flow can play a crucial role in energy-efficient software and firmware development processes.

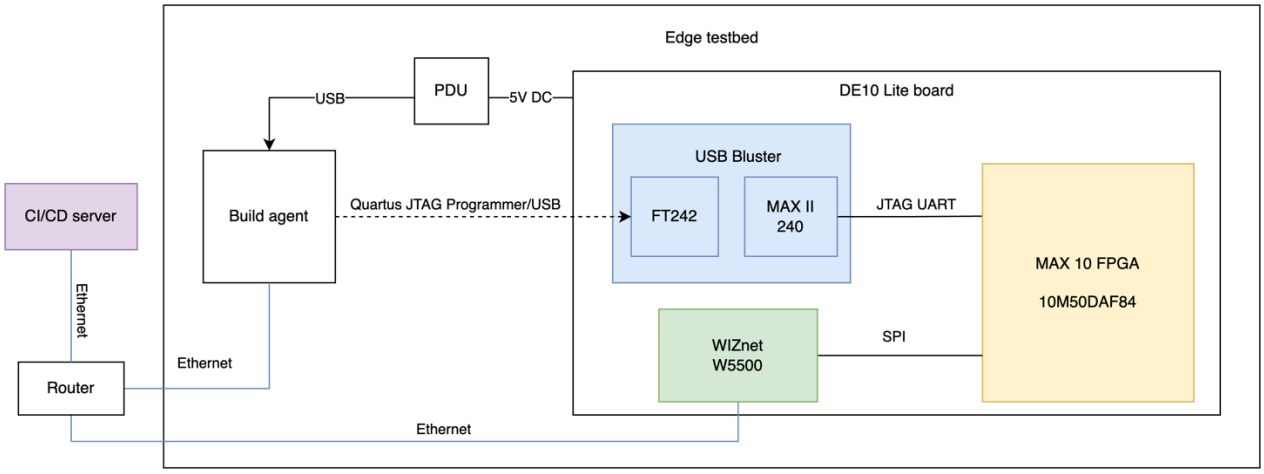

Fig. 1. Developed testbed for FPGA edge computing system

Methodology

A simple FPGA edge computing system was used to evaluate the developed CI/CD process model. It consists of a server used for monitoring, management, and configuration, an edge device (Intel MAX 10 FPGA), and network devices for communication between the server and the edge(generalized architecture shown in Figure 1). The developed system uses a simple MPP matrix multiplication application on a NIOS II soft-core CPU to create data for further power monitoring and profiling operations.

The developed system integrates into the CI pipeline depicted in Figure 2. This pipeline consists of four significant flows – Soft-core IP integration and HDL, FPGA build flow (HDL compilation and analysis), NIOS II build flow, and Edge computing flow. It's essential to note that Edge computing flow can be used as a standalone solution for power profiling research purposes (when no changes in source code are required). This pipeline has three specific points that distinguish it from known solutions – its early power estimation during FPGA HDL build and power monitoring steps in the execution flow, which are used to analyze the power proficiency of developed hardware and firmware.

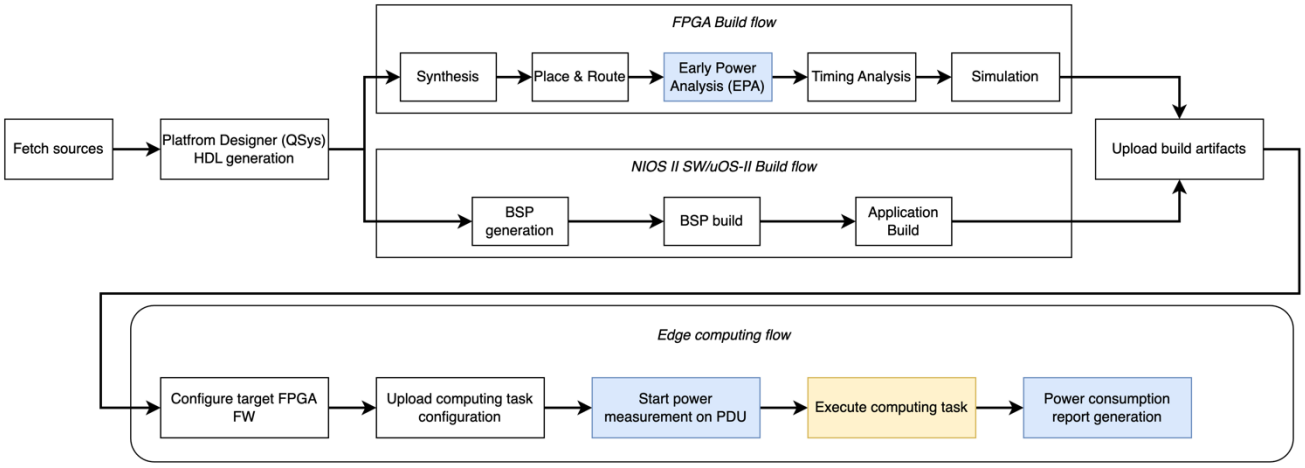

Fig. 2. Continuous integration flow for FPGA edge computing system

References

[1] R. Glein, A. S. Perloff and K. A. Ulmer, Continuous Integration of FPGA Designs for CMS, Geneva: CERN, 2019.

[2] V. Amoiridis, "An automated CI/CD framework for Zynq UltraScale+ MPSoC devices. Ένα αυτόματο πλαίσιο για συνεχή ενσωμάτωση και συνεχή ανάπτυξη/παράδοση για ολοκληρωμένα της οικογένειας Zynq UltraScale+ MPSoC", Aristotle U., Thessaloniki, 2022.

[3] A. R. Bucknall, S. Shreejith and S. A. Fahmy, "Build Automation and Runtime Abstraction for Partial Reconfiguration on Xilinx Zynq UltraScale+", International Conference on Field-Programmable Technology (ICFPT), 2020.

[4] O. V. Hryshchuk and S. P. Zagorodnyuk, "Modern methods of energy consumption optimization in FPGA-based heterogeneous HPC systems", CS&SE@SW. 2023.

SYNTHETIC MEDIA: WHAT IT IS AND HOW IT IS CREATED – AN OVERVIEW

Bohdan Karlash[1], Yuriy Boyko[2]

Faculty of RadioPhysics, Electronics and Computer Systems Taras Shevchenko National University of Kyiv, Kyiv 01601, Ukraine
1– email: bohdankarlash@knu.ua
2 – email: yuriyboyko@knu.ua

Introduction

In the recent years media, generated by AI, has risen in popularity and volume. There are now far more synthetic texts, images and videos all around the Internet, particularly in social media, than ever before. Therefore there often arises a need to distinguish this not real media from real. But, in order to do that, we first need to see, how this type of media can be created. This, in it's essence, is the focus of this work. We will discuss just what is synthetic media and what tools are used to create, or generate it.

From data to synthetic data to synthetic media

In order to define synthetic media we must first go to the roots. We must define what data and synthetic data mean. According to *Microsoft Computer Dictionary 5th edition*, data is defined as "meaning an item of information"[1], *National Institute of Standards and Technology (NIST) Computer security resource center (CSRC) Glossary* defines data in multiple ways: "information in a specific representation, usually as a sequence of symbols that have meaning", "distinct pieces of digital information that have been formatted in a specific way", "pieces of information from which "understandable information" is derived", "representation of facts, concepts, or instructions in a manner suitable for communication, interpretation, or processing by humans or by automatic means"[2], according to *IBM Dictionary of Computing, 1994,* data is "a re-interpretable representation of information in a formalized manner suitable for communication, interpretation, or processing"[3]. As we can see, data is and was generally referred to as a piece of information. There exists a relatively common term, used in computer science, called *synthetic data,* which refers to information, that is artificially generated rather than produced by real-world events, or, according to [4], it is "data, that has been artificially annotated and was produced by computer algorithms or simulations, … although artificial, statistically mimics the patterns and characteristics of real-world data". *National Institute of Standards and Technology (NIST) Computer security resource center (CSRC) Glossary* also defines *synthetic data generation* as "a process in which seed data are used to create artificial data that have some of the statistical characteristics of the seed data". As we can see, synthetic data is close to what we mean, when we talk about information, that has been generated rather than real information, created by a human, but it mostly is used in the context of statistical data, rather than media. So we need a term that would mean just that: media, that is artificially generated and is not real media. In [5] there is a term, called *synthetic media*, which is "automatically and artificially generated or manipulated photo, audio, and video content". We propose to use this definition and further extend it to all forms of media, including synthetic text. This also sometimes is called AI-generated media.

What tools are generally used to generate synthetic media: an overview

Generally, as there are different forms of media (text, audio, image and video), there are different tools, for each one. There are:

- **Text generators –** most commonly, these are chatbots and LLMs (Large language models). Chatbots usually use specific LLMs.

- **Audio generators –** typically these are either voice or music generators. As music generators aren't typically used maliciously, they will not be discussed here, but one prominent example of an AI music generator is Suno AI.

- **Image generators –** these are multipurpose usually, although there exist some models for different types of images, and generally are text-to-image generators.

- **Video generators –** these can be divided into general video generators, that create videos from text or, sometimes images from the ground up, and deepfake tools, that alter videos to create deepfakes.

In our study, multiple most common generators were considered and we found 11 chatbots, 49 LLMs (including different versions), 9 voice generators, 14 image generators and 5 video generators that all can be used for creating synthetic media. The results of the analysis are presented in the following tables. As there are too many LLMs and the table for them would be too large, we will not be listing them here.

Table 1 – Chatbots

№	Developer	Name	LLM(s) used	Availability
1	Yandex	Alice	YandexGPT	Free
2	Google	Assistant	Gemini	Free
3	Brainasoft	Braina	Braina, Claude 3, Llama 3, Mistral, Gemini, GPT-3.5 Turbo, GPT-4-Turbo	Paid, has a free tier
4	Huawei	Celia	PanGu-Σ 3.0	Free, but limited to Huawei phones
5	OpenAI	ChatGPT	GPT-4.x	Paid, has a free tier
6	Anthropic	Claude	Claude 3.5	Paid, has a free tier
7	Microsoft	Copilot	GPT-4.x	Free
8	Google	Gemini	Gemini 1.5	Free
9	Sberbank	GigaChat	NeONKA ensamble: ruGPT-3.5, Kandinsky 2.1, ruCLIP, FRED-T5	Free, but requires Russian government ID or a Telegram account
10	xAI	Grok	Grok-1.5, Grok-2	Paid and limited to US and X Premium+ subscribers
11	Amazon	Q	Amazon Titan, Amazon Bedrock	Paid

Table 2 – Voice generators

№	Developer	Name	Availability
1	ElevenLabs	ElevenLabs (Eleven English v2, Eleven Multilingual v2)	Paid, but has a free tier, that cannot clone voices
2	Conqui	YourTTS	Has a free demo
		Conqui TTS	Has a free demo
3	Wang et al. [6]	Vall-E	Has an unofficial free implementation
4	Applio	Applio	Free
5	James Betker [7]	Tortoise-TTS	Free
6	FakeYou	FakeYou	Paid, has a free tier
7	Myshell-AI	OpenVoice	Has a free demo
8	Meta	Audiobox	Has a free demo
9	Resemble.AI	Resemble.AI	Paid, has a free trial

Table 3 – Image generators

№	Developer	Name	Major Version	Availability
1	OpenAI	DALL-E	DALL-E 3	Paid
2	Google DeepMind	Imagen	Imagen 2	Free in Gemini
3	Adobe Inc.	Firefly	Firefly Image 2	Free
4			FIrefly Image 3	Free
5	Midjourney, Inc.	Midjourney	Midjourney	Paid, has a free trial
6	Stability AI	Stable Diffusion	Stable Diffusion 2.1	Has a free demo
7			Stable Diffusion XL	Paid, available via an API, has free trial
8			Stable Diffusion XL Turbo	Paid, has a free tier
9			Stable Diffusion 3.0	Paid, available via an API, has free trial
10	Boris Dayma et al. [8]	Craiyon (formerly DALLE-mini)	Craiyon v3, v4 in beta	Free
11	Mighty Computing, Inc.	Playground AI	Playground v2.5	Paid, has a free tier
12	Leonardo Interactive Pty Ltd	Leonardo AI	Leonardo XL	Paid, has a free tier
13	LimeWire	BlueWillow	BlueWillow v4	Paid, has a free tier
14			BlueWillow v5	Paid, has a free tier

Table 4 – Video generators

№	Developer	Name	Availability
1	Runway	Runway	Paid, has a free tier
2	Kuaishou	Kling AI	Paid, has a free tier
3	Luma AI	Dream Machine	Paid, has a free tier
4	HeyGen	HeyGen	Paid, has a free tier
5	Mellis, Inc.	Pika	Paid, has a free tier

As can be seen, most of these generators are paid, but also most, if not all of them, provide a free option, that anyone can use. Considering how many easily accessible tools for creating synthetic media there are, it is no wonder that it has become such a common occurrence over the Internet. And this number only keeps growing with multiple new models being developed each month.

References

[1] Microsoft Computer Dictionary 5th edition, 2002. (Retrieved from https://burmastarrecords.files.wordpress.com/2009/12/microsoft_computer_dictionary__fifth_edition1.pdf)

[2] National Institute of Standards and Technology (NIST) Computer security resource center (CSRC) Glossary. See details here: https://csrc.nist.gov/glossary/term/information

[3] IBM Dictionary of Computing, 1994. (Retrieved from https://archive.org)

[4] See details here: https://moez-62905.medium.com/synthetic-data-is-the-future-of-artificial-intelligence-6fcfd2ce1a14

[5] L. Whittaker, et al. ""All around me are synthetic faces": the mad world of AI-generated media", IT Professional, 22.5: pp. 90-99, Sep. 2020.

[6] Ch. Wang, et al. "Neural Codec Language Models are Zero-Shot Text to Speech Synthesizers", arXiv:2301.02111, Jan. 5, 2023.

[7] J. Betker "Better speech synthesis through scaling", arXiv:2305.07243, May 12, 2023.

[8] B. Dayma, et al. "Borisdayma/dalle-mini: Initial Release. v0.1-alpha", Zenodo, July 29, 2021.

INCREASING SECURITY AND RELIABILITY OF BLOCKCHAIN SYSTEMS USING MATHEMATICAL MODELING

O.M. Liubymenko[1], A.O. Popova[1], N.O. Maslova[1], O.A. Shtepa[1]

Donetsk National Technical University "Donetsk National Technical University", str. Potebni, 56, Lutsk, 43003, Ukraine, e.n.lyubimenko@gmail.com ; anna.popova.kita@donntu.edu.ua; nataliia.maslova@donntu.edu.ua ; oleksandr.shtepa@donntu.edu.ua

Blockchain technologies are decentralized databases that allow you to store a sequence of records (blocks) connected by cryptographic methods, which makes unauthorized changes impossible. In ensuring the security and reliability of blockchain systems, the main role is played by mathematical approaches that allow assessing risks and increasing resistance to attacks. The use of mathematical models can significantly improve data security and system reliability.

The application of mathematical models allows to optimize key aspects of the operation of blockchain systems, including the effectiveness of cryptographic algorithms, management of computing resources, mechanisms for achieving consensus and risk management. For this, mathematical methods from various fields are used, such as probability theory, game theory, graph theory, cryptographic protocols, etc.

One of the most important problems of blockchain systems is their limited bandwidth, which becomes critical when the number of users and transactions increases. Using the methods of graph theory and coding, it is possible to improve the data storage structure and increase the efficiency of transaction processing.

Mathematical models also make it possible to predict the behavior of blockchain network participants. For example, game theory helps to explore participants' motivations for fair or unfair interactions, allowing for the development of more robust consensus protocols. Cryptographic algorithms, the stability of which is checked by mathematical models, provide reliable protection against attacks.

Mathematical models can also help optimize the distribution of computing resources among network participants to reduce the risk of failures and increase the overall reliability of the system. They allow choosing optimal strategies for reaching consensus, minimizing resource costs.

One of the key areas of application of mathematical models is risk assessment and development of defense strategies against attacks, such as double spend attacks or attacks using quantum computing. Mathematical models allow not only to predict possible threats, but also to estimate the probability of their success.

The following model is used for this: $q_z = \begin{cases} 1 & if\ p \le q \\ (q/p)^z & if\ p > q \end{cases}$,

where p is the probability of an honest node finding the next block,

q is the probability of the attacker finding the next block,

q_z is the probability that the attacker will be able to make up the difference in z blocks.

Given the assumption that p > q, the probability decreases exponentially with the increase in the number of blocks by which the attacker lags behind. Therefore, without a successful gap from the very beginning, the attacker's chances of success are extremely small [1].

The probability of success of such an attack decreases exponentially as the number of blocks behind the overall chain increases, making such attacks extremely unlikely without a significant advantage to the attacker.

References

[1] Nakamoto S. Bitcoin: A Peer-to-Peer Electronic Cash System. - 2008.

[2] Myronets I.V., Shkrebtiy A.V. Cryptographic algorithms and features of their use in blockchain systems. Information security. - 2019. - Volume 25, No. 2. - P. 104-109.

APPLICATION OF DEEPLABV3+ NEURAL NETWORK ARCHITECTURE FOR DRIVABLE ZONE SEGMENTATION IN ROAD IMAGES

Matus Volodymyr*, Andriy Konovalov**

Taras Shevchenko National University of Kyiv
Faculty of RadioPhysics, Electronics and Computer Systems , Kyiv 01601, Ukraine
*email: * volodymyrmatus@knu.ua , ** konam@knu.ua*

This paper presents a model for semantic segmentation of driving areas on images captured by vehicle cameras. The research focuses on improving the accuracy of existing semantic segmentation models applied to the BDD100K [1] dataset using advanced convlutional neural networks (CNNs). Several models based on DeepLabV3+ neural network architecture with different backbones, including YOLOv8_m [2], EfficientNetV2_s [3] and others, are implemented and compared, achieving Intersection over Union (IoU) scores of 92.59% and 92.69%, respectively, which surpass current literature benchmarks.

Introduction

The rapid increase in global vehicle usage and the integration of innovative technologies in the automotive industry have led to a greater demand for improved driver assistance systems. The paper applies deep learning techniques to perform pixel-level semantic segmentation of driving zones from images captured by in-car cameras. Semantic segmentation is a core task in computer vision that involves labeling each pixel in an image with a class corresponding to the object semantic type, allowing for detailed scene understanding. In this research, the goal was to segment drivable areas on the road from images captured by vehicle cameras. A number of models have already been presented in the literature [4] that solve this task and achieve an IoU value of 91.5%. However, improving the accuracy of semantic segmentation of driving zones is important for developing autonomous driving and advanced driver assistance systems, as accurately identifying the regions of the road that vehicles can safely traverse is critical for navigation and safety.

Dataset

The BDD100K dataset [1], one of the largest and most diverse for autonomous driving tasks, was used to train and evaluate the models. This dataset contains 100,000 photos with corresponding labeled images, spanning a wide variety of driving conditions, including day and night scenes, urban and highway settings, and diverse weather conditions. The images are annotated for semantic segmentation, with the main focus on identifying drivable road areas. The dataset was preprocessed to optimize model performance, including resizing the images to 640x384 pixels and performing data augmentation techniques such as random rotations and reflections.

Methodology

To improve the semantic segmentation of driving areas, the study employs the DeepLabV3+ neural network architecture [5], leveraging its robust feature extraction and segmentation capabilities. Various backbone CNN architectures, including EfficientNetV2_s, YOLOv8_m and MobileNet_v3, were tested to optimize performance and computational efficiency. These backbone networks were pretrained on large-scale datasets such as ImageNet and then fine-tuned on the BDD100K dataset for the specific task of semantic segmentation.

Each model was trained using supervised learning, utilizing TensorFlow and KerasCV libraries. The dataset, similar to work [4], was divided into training, validation and test subsets with 70, 1 and 9 thousand images, respectively. The training process incorporated data augmentation techniques to improve generalization and prevent overfitting. Additionally, intersection over union (IoU) was used as the primary evaluation metric, while cross-entropy loss was minimized during training using the AdamW optimizer.

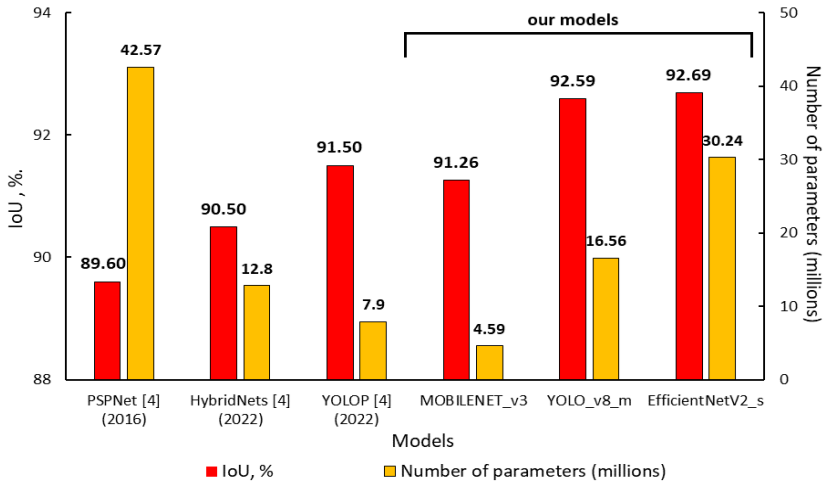

Fig. 1. IoU quality metric and the number of parameters of our models and models presented in the literature.

The models were trained with batch size of 12, and a key focus was on hyperparameter fitting, including learning rate adjustments and regularization, to maximize model accuracy, by maximizing the IoU metric on the validation subset. Additionally, several backbones were tested to maximize accuracy, while ensuring computational efficiency to make them well suited for real-time applications.

Results

The models demonstrated high performance on the test subset as shown in Fig.1, with YOLOv8_m and EfficientNetV2_s achieving the best results, while MobileNet_v3 provided a favorable balance between computational cost and segmentation accuracy. The IoU scores reached 92.59%, 92.69% and 91.26%, respectively, outperforming existing models like YOLOP (91.5%) and HybridNets (90.5%). Fig. 2 illustrates an example of the model's performance on an image from the test subset, where the drivable area is accurately segmented despite challenging conditions.

Fig. 2. An example of the input image of the test subset (left), the true mask (middle) and the predicted mask (right) with the EfficientNetV2_s model.

Conclusion

The results of this study demonstrate that DeepLabV3+ architecture with backbones like YOLOv8 and EfficientNet can not only accurately predict the driving zones for cars, but can also improve the accuracy of semantic segmentation for driving areas, outperforming existing models. Future work will focus on further optimizing model performance using other neural network architectures for semantic segmentation.

References

[1] F. Yu et al., 2018, "BDD100K: A Diverse Driving Dataset for Heterogeneous Multitask Learning," arXiv. doi: 10.48550/ARXIV.1805.04687.

[2] Ultralytics. "Ultralytics YOLO Docs." Accessed: Oct. 4, 2024. [Online]. Available: https://docs.ultralytics.com

[3] M. Tan i Q. V. Le, "EfficientNetV2: Smaller Models and Faster Training," 2021, doi: 10.48550/ARXIV.2104.00298.

[4] D. Wu et al., "YOLOP: You Only Look Once for Panoptic Driving Perception," Mach. Intell. Res., vol. 19, no. 6, pp. 550–562, Dec 2022, doi: 10.1007/s11633-022-1339-y.

[5] L.-C. Chen, G. Papandreou, I. Kokkinos, K. Murphy, i A. L. Yuille, "DeepLab: Semantic Image Segmentation with Deep Convolutional Nets, Atrous Convolution, and Fully Connected CRFs," 2016, arXiv. doi: 10.48550/ARXIV.1606.00915.

CROSS-SITE REQUEST FORGERY: MODERN PREVENTION TECHNIQUES

Studennykov V. D.

Faculty of Computer Sciences and Cybersecurity, National Aviation University, Liubomyra Huzara ave. 1, Kyiv 03058, Ukraine, email: vladstwork2@gmail.com

Cross-Site Request Forgery (CSRF) attacks occur when a malicious web site causes a user's web browser to perform an unwanted action on a trusted site. [1] In 2010 this type of attack was reported as one of the most dangerous vulnerabilities by Open Web Application Security Project [2], so every developer needs to understand how to avoid these types of attack. The aim of this article is to describe CSRF attacks and provide the list of ways to avoid them in modern web applications.

The description of an attack

In CSRF attack the attacker exploits the fact that the user's browser automatically includes authentication cookies or session tokens when interacting with the trusted site. This allows the attacker to perform unauthorized actions, such as changing account settings or transferring money, without the user's consent or knowledge. The easiest example of CSRF attack is the next: consider an example web-page http://example.com where the form is embedded (Figure 1). When the user fills the form, he submits it and data is sent to the server using GET request to http:/example.com/send_email.html, data from the form is being passed through the URL parameters that are added to the mentioned URL.

```
<form
action="http://example.com/send_email.htm"
method="GET">
Recipient's Email address:  <input
type="text" name="to">
Subject:  <input type="text" name="subject">
Message:  <textarea name="msg"></textarea>
<input type="submit" value="Send Email">
</form>
```

Figure 1: an example of form

Some attacker may create the web page where he can embed the link to http:/example.com/send_email.html with his own necessary parameters. Usually this link could be embedded into an image on the attacker`s web-page that is attended by victim [1]. In this way attacker could make another user submit some data from his name and using his session data.

The attack was described for GET HTTP method, but it could be also conducted for another requests methods. Figures 2, 3 and 4 show how generally this attack work.

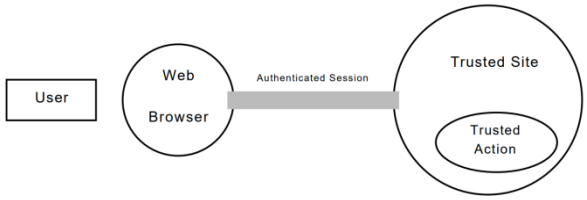

Figure 2: user`s browser establishes the session with trusted site

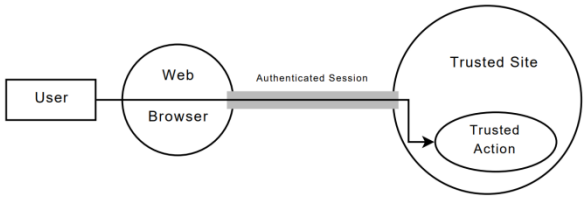

Figure 3: user can perform an action on trusted site because he is authenticated

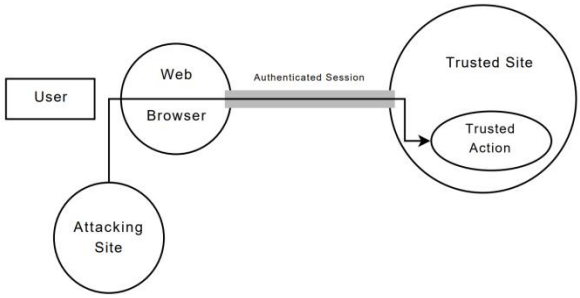

Figure 4: an attacker can use another user`s session data to accomplish an action from his name. Web app cannot understand that the action is being conducted not by the user himself

Ways of prevention

There are lots of ways to save the app from CSRF attack, among most effective – the creation of random temporal token that is stored in session data and approves that the particular user conducts an action on the web page. For obtaining and modifying data GET HTTP should not be used, instead should be used POST, PUT or DELETE methods for data changes, they are more secure. Also lots of proxies between client and server were created to prevent this type of attack. [2] The task of proxies is to check the requests and deny it when it considers them invalid or insecure.

References

[1] Sentamilselvan K. Survey on Cross Site Request Forgery (An Overview of CSRF). IEEE - International Conference on Research and Development Prospects on Engineering and Technology (ICRDPET 2013). 2013. Vol. 5.
URL: https://www.researchgate.net/publication/281583832_Survey_on_Cross_Site_Request_Forgery_An_Overview_of_CSRF.

[2] Zeller W., Felten E. W. Cross-Site Request Forgeries: Exploitation and Prevention. Department of Computer Science, Center for Information Technology Policy, Princeton University. 2018. P. 1–13.
URL: https://people.eecs.berkeley.edu/~daw/teaching/cs261-f11/reading/csrf.pdf.

RADIO ENGINEERING AND COMMUNICATIONS

ANALYSIS OF THE OUTPUT SIGNAL AND RANDOM DRIFT CHARACTERISTICS OF A HOMOGENEOUS MEMS GYROSCOPE ARRAY

R. Andriichuk, V. Boretskij

Taras Shevchenko National University of Kyiv, 64/13, Volodymyrska Street, Kyiv, Ukraine,
e-mail: r.andriichuck@gmail.com

This research aims to investigate the nature of the factors that cause errors in the output signal of an array consisting of 16 digital MEMS accelerometers and gyroscopes. The sensor array was oscillated on a test rig with a predefined angular velocity and constant frequency. Data from all sensors within the array, along with encoder readings, were analyzed to evaluate the efficiency of the gyroscope array, and the displacement of the oscillation rig's shaft was calculated over the entire experiment period.

Introduction

Utilizing an array of multiple identical and cost-effective MEMS gyroscopes is an efficient approach for minimizing measurement errors and improving the navigation accuracy of inertial sensors by leveraging redundant data [1-3]. This approach offers advantages when the behaviour of the sensors used is analyzed beforehand to detect potential biases, random zero drift, or installation errors that may occur when mounting the sensors on the vibrating body under analysis.

Experimental setup

The primary goal of the experimental setup was to develop a system capable to replicate real-world angular disturbances. Following this concept, both hardware and software components were selected and developed to simulate platform oscillation scenarios, collect gyroscope data, and perform control algorithms.

Hardware Components:

- ODrive v3.6 Brushless Motor Control Board.
- CUI AMT102 Incremental encoder.
- The array of gyroscopes consists of 16 LSM6DS3 sensors with 16-bit resolution and configured at ±250 DPS [5]. The array consists of two PCBs, each equipped with eight sensors, positioned perpendicular to the rotational axis with an equal offset of 12 mm. Data from each sensor is acquired at a frequency of 108 Hz. The array was attached to the rotational axis.
- STM32H743 is the core of the data acquisition system and driver control system of the motor speed.

Results and Discussions

A series of repeatable experiments were conducted to evaluate the suitability of the proposed configuration for comparing the accuracy of capturing the oscillatory motion of the test rig using the gyroscope array (virtual gyroscope) and an individual gyroscope selected from the same array.

Each measurement session lasted approximately 1500 seconds and consisted of three stages: a 250-second period of rest before the oscillatory motion, 1000 seconds at a frequency around 0.5 Hz, and a 250-second rest period after the oscillations.

For the initial assessment of the measurement results, calibration was performed in a stationary mode during the first 10 seconds of the experiment and integrated to evaluate the deviation from the true position value. As a result of this operation, the following behaviour of the shaft displacement estimates was observed throughout the experiment (see Fig. 1 left): during the first stage, individual gyroscopes exhibited a linear increase in the position error estimate, which can be attributed to the presence of zero offsets in each gyroscope. In contrast, the virtual gyroscope also deviated from the true value but at a slower rate, approximately 9 to 10 times less. After the oscillatory

component of the experiment, individual gyroscopes continued to show an increasing error rate. In contrast, the virtual gyroscope began to deviate from the true value even more rapidly than during the first stage of the experiment. The resulting deviation of the individual gyroscopes ranged from +1.15 to -2.2 revolutions, while the virtual gyroscope deviated by 0.4 revolutions. It was decided to perform a linear approximation over the first phase of the experiment with durations of 10s, 50s, and 250s to investigate whether this would be sufficient to eliminate significant deviations of the readings from the absolute position obtained from the encoder during the experiment. Analyzing the behaviour of the rotor position estimate change of the investigated setup in Figure 2, one can conclude that using a sufficiently long time interval for linearization can reduce the error. However, a closer examination of Figure 2, particularly the graph depicting the use of linearization on data collected over 250s, reveals a nonlinear nature of the error, suggesting a more complex nature of the zero drift in the sensor output signal.

This type of deviation likely contains low-frequency components with small amplitudes, which over time can lead to significant deviations in inertial position estimation and require further investigation including both static and dynamic testing, as demonstrated in the study [4-5].

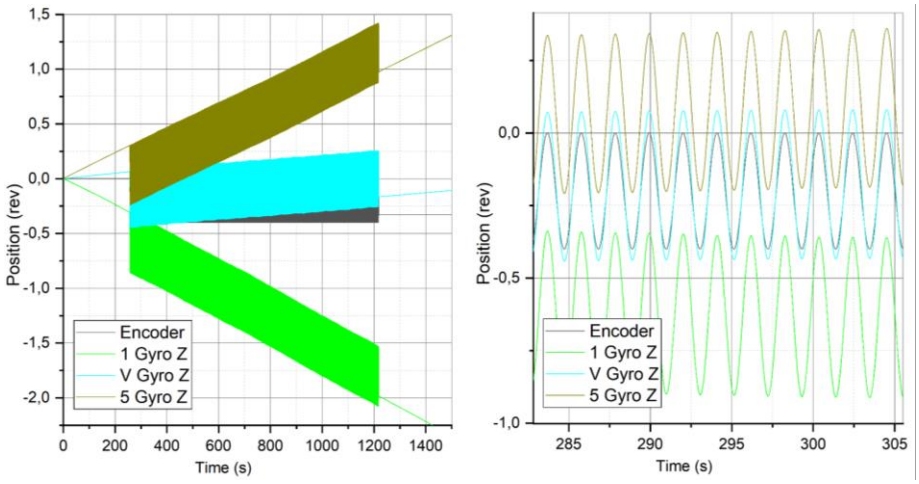

Fig. 1. The shaft displacement of the oscillation stand based on the Encoder and the results of integrating the Virtual Gyroscope (V Gyro Z) and several individual gyroscopes (1 Gyro Z, 5 Gyro Z) after one-step static calibration.

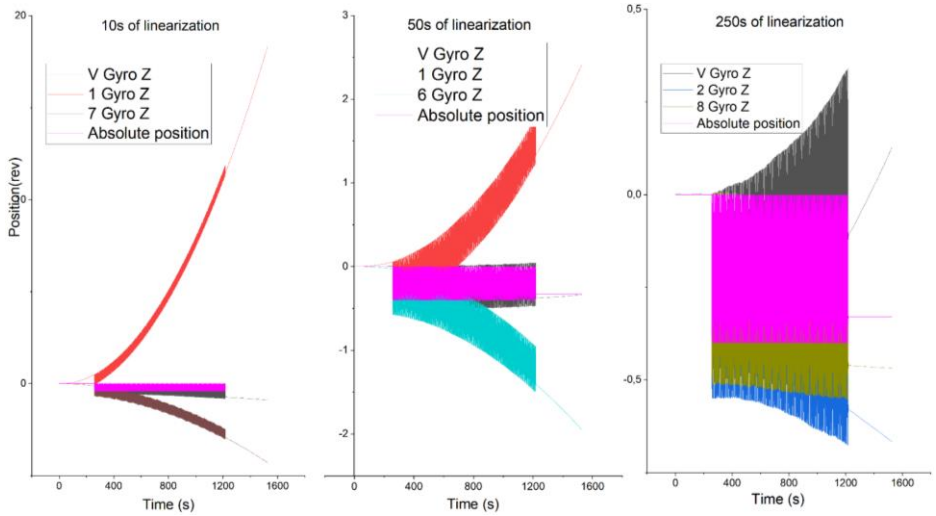

References

[1] H. Li, X. Xiao and P. Peng, "Gyroscope Array Analysis Based on EMKF Algorithm," 2023 42nd Chinese Control Conference (CCC), Tianjin, China, 2023, pp. 3279-3284, doi: 10.23919/CCC58697.2023.10240851.

[2] L. Wang, H. Tang, T. Zhang, Q. Chen, J. Shi and X. Niu, "Improving the Navigation Performance of the MEMS IMU Array by Precise Calibration," in IEEE Sensors Journal, vol. 21, no. 22, pp. 26050-26058, 15 Nov.15, 2021, doi: 10.1109/JSEN.2021.3118455.

[3] J. Wang and E. Olson, “High-Performance Inertial Measurements Using a Redundant Array of Inexpensive Gyroscopes (RAIG),” in 2015 IEEE International Conference on Multisensor Fusion and lntegration for Intelligent Systems (MFI), San Diego, CA, USA, 2015, pp.71-76.

[4] Georgy, J., Noureldin, A., Korenberg, M. J., & Bayoumi, M. M. (2010). Modeling the Stochastic Drift of a MEMS-Based Gyroscope in Gyro/Odometer/GPS Integrated Navigation. IEEE Transactions on Intelligent Transportation Systems, 11(4), 856–872.

[5] Lei Huang, Zhaochun Li, Fei Xie, Kai Feng (2018). Novel Time Series Modeling Methods for Gyro Random Noise Used in Internet of Things. IEEE Collaboration for Internet of Things, (6), 47911 - 47921.

CLASSIFICATION OF AIR QUALITY IN KYIV DURING PERIODS OF HIGH POLLUTION LEVELS

A. Antonenko, V. Boretskij, O. Zagaria

Faculty of Radio Physics, Electronics and Computer Systems, Taras Shevchenko National University of Kyiv, Kyiv 01601, Ukraine, email: andrii.antonenko@knu.ua

The study explores the application of a neural network trained under laboratory conditions for air pollutant classification. The training was conducted on samples of pollutants such as alcohol vapors, flux, leaves, and cigarette smoke. Outdoor data collected from the urban air quality monitoring station LUN Misto Air in Kyiv over a week, when high pollution levels were observed, were used to validate the results. The neural network results were compared with official pollution level notifications from the city portal.

Introduction

With the growth of urban populations and the acceleration of industrialization, air quality has become an increasingly important issue for the health of city residents. In Ukraine, the situation is further complicated by the consequences of the war, which contributes to additional air pollution due to infrastructure destruction, fires, and the use of military equipment. Pollution affects not only physical health but also the environmental state of the ecosystem. The networks of air quality monitoring stations are created to inform the public. Government monitoring systems use highly accurate and expensive equipment that measures a wide range of parameters, such as SO_2, CO, O_3, NO_2, H_2S, PM particles, radiation levels, and others. However, deploying a network with high coverage density is a costly process, making it difficult to scale. Civil networks partially address this issue, but they use less accurate equipment and typically monitor only certain parameters, such as PM2.5, PM10, humidity, and pressure. Data from government monitoring systems can be used to calibrate sensors in civic networks, which can improve the accuracy of their data and provide broader monitoring coverage overall.

An average city resident is not familiar with pollutant concentration levels or air quality readings. These indicators still do not answer the question of what the source of the pollution is, although society almost always has an interest in this. Given these factors, there is a need for new approaches to monitoring, specifically the classification of air pollutant types. In previous studies [1], the application of a neural network successfully identified two types of pollutants in a binary format, namely flux vapors and alcohol combustion products. This approach demonstrated the potential of using neural networks for pollutant classification with low-cost sensors. However, these experiments were conducted under laboratory conditions.

Experimental Setup and Methods

This study investigates the potential of using low-cost sensors and an artificial neural network, developed under laboratory conditions, for the classification of pollutants in outdoor environments. A neural network from a previous study [1] was selected for this purpose, where the initial steps were taken in classifying pollutants such as alcohol vapors, flux vapors, and combustion products of paper and cigarettes under laboratory conditions. In that experiment, five measurements were taken for each pollutant, the ignition time lasted about 15 seconds, and training was conducted using the TensorFlow library. Among all the trained models, the one with the best data correlation was chosen. Air quality data was obtained from the civic network LUN Misto Air, specifically from station 135 [2], located at 13 Myropilska Street on the 12th floor. Data on PM particles were selected for the week of September 19 to September 26, 2024, during which elevated pollution levels were observed. Since the neural network has a notification function, in the initial stages, we focused on official reports from the Kyiv City State Administration portal [3].

Results and Discussions

Figure 1 shows the response of the neural network to air quality over one week (from September 19 to September 26). The X-axis represents time, and the Y-axis represents the output of the neural network classifier analyzing the air quality: values closer to 1 indicate probable air pollution, while values closer to 0 indicate clean air. The red curve represents the real-time values obtained from the neural network. The gray bar shows official notifications from the Kyiv City State Administration portal, where the data is classified into three levels: 0 — low or very low pollution, 0.5 — moderate pollution, and 1 — high pollution when it is recommended to limit prolonged outdoor activity and avoid ventilating indoor spaces.

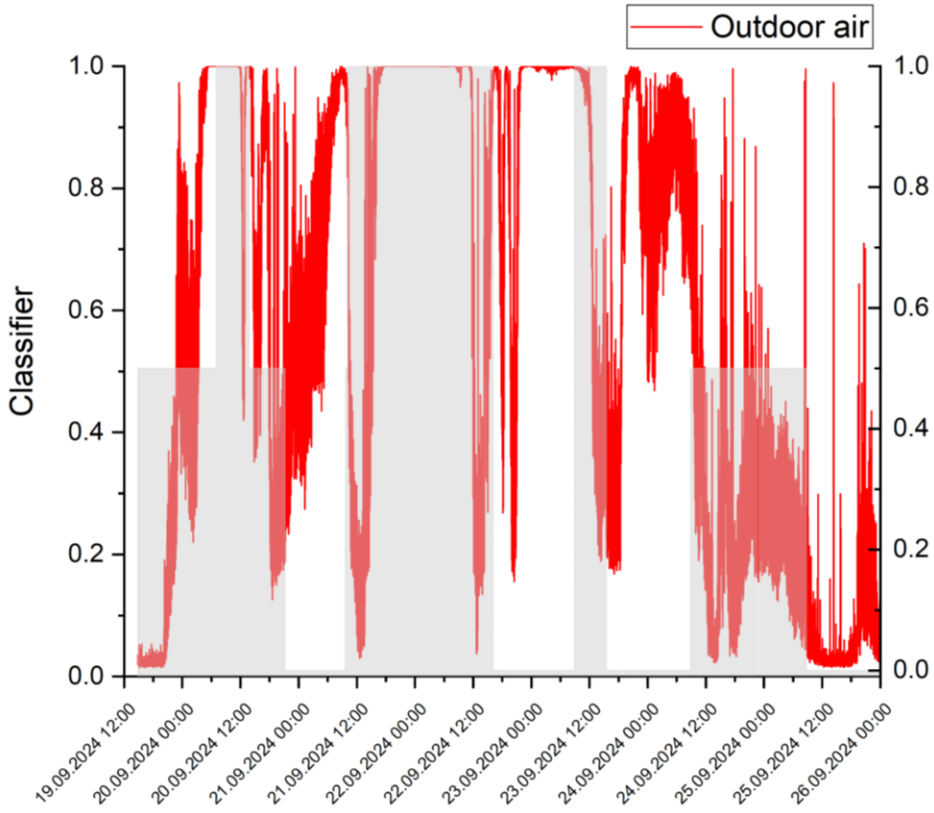

Figure 1. Neural network response.

As seen from the graph, the neural network signaled a high level of pollution at 3 a.m. on September 20, while the official notification was received only at 7 a.m. This indicates that the neural network responds to changes faster than official sources. In the second instance on September 21, it can be observed that the situation changed dynamically, and the official data no longer reflected the actual air quality. A similar situation occurred on September 23, when pollution was detected at night, but the notification was only received at 9 a.m.

References

[1] A. Antonenko, V. Boretskij, and O. Zagaria, "Classification of indoor air pollution using low-cost sensors by machine learning," EGU General Assembly 2023, Vienna, Austria, 24–28 Apr. 2023, EGU23-14856. [Online]. Available: https://doi.org/10.5194/egusphere-egu23-14856.

[2] "Рівень забруднення повітря," Lun Misto. [Online]. Available: https://misto.lun.ua/air/135.

[3] "Забруднення повітря в Києві," Kyiv City Government. [Online]. Available: https://kyivcity.gov.ua/navkolyshnie_seredovyshche_mista/zabrudnennia_povitria/.

THE IMPACT OF IONOSPHERIC DISTURBANCES ON DECAMETER RADIO WAVE TRAJECTORIES

L. F. Chernogor*, V. F. Pushin*, Y. H. Zhdanko*

**School of Radiophysics, Biomedical Electronics and Computer Systems,*
V. N. Karazin Kharkiv National University, Kharkiv 61022, Ukraine, e-mail: Leonid.F.Chernogor@gmail.com

The results of calculations of decameter radio wave trajectories for quiet and disturbed ionospheric conditions are presented. The multiparameter computer modeling was used and the adequacy of the results are demonstrated.

Introduction

Recently, interest in decameter radio waves for global communications has been sharply renewed. In addition, this range is used in over-the-horizon radar systems, decameter radio astronomy, etc. The propagation of decameter radio waves is entirely determined by the state of the ionosphere, space weather, and the presence of disturbances. Disturbances are caused by a number of high-energy sources, including geospace storms, atmospheric weather variations, volcanic eruptions, earthquakes, and a number of man-made sources.

The purpose of the report is to present the results of numerical modeling of decameter radio wave trajectories in an inhomogeneous magnetoactive ionosphere.

Methods and Techniques

The main parameter of a propagating radio wave is its trajectory. It determines all the main parameters of a radio signal: propagation time, amplitude, phase shift, Doppler shift, angles of arrival, etc. Modeling of radio wave trajectories was performed using original software that has been developed and improved by the authors. A system of ordinary differential equations of geometric optics has been used for calculations. We consider virtual radio paths of HF signals propagating in a three-dimensionally inhomogeneous magnetoactive stationary medium.

Basic Equations

The basis of the program are ray equations in the form [1, 2]:

$$d\mathbf{r}/d\tau = J\mathbf{p} - K\mathbf{Y}, \qquad d\mathbf{p}/d\tau = L\nabla X, \tag{1}$$

where $\mathbf{r}$ is the radius vector of the ray, τ is the independent variable, $\mathbf{p}$ is the wave normal vector,

$$J = -2(2(1-X-Y^2)(q+1)+(\mathbf{Yp})^2+Y^2), \quad K = 2(p^2-1)\mathbf{Yp},$$
$$L = (-(p^2-1)+(\mathbf{Yp})^2+2(1-2X)-Y^2)q+2-3X, \tag{2}$$

here $X = \omega_p^2/\omega^2$, $\omega_p^2 = e^2N/\varepsilon_0 m$ is the plasma frequency, e and m are the electron charge and mass, N is the electron number density, ε_0 is the electric constant, $\mathbf{Y} = Y\mathbf{B}/B$, $Y = \omega_B/\omega$, $\mathbf{B}$ and B are geomagnetic field induction vector and its modulus, $\omega_B = eB/m$ is the electron gyrofrequency, $q = a/(-b \pm \sqrt{b^2-ac})$, $a = 1-X$, $b = a - Y_T^2/2$, $c = a - Y^2 + XY_L^2$, Y_L and Y_T are longitudinal and transverse components of $\mathbf{Y}$ relative to the induction vector of the geomagnetic field, the «+» sign is for the *O*-wave, the «–» sign is for the *X*–wave. To solve the 2-point problem for given boundary points, equations (1) and (2) are supplemented by equations for the $\mathbf{r}_\alpha$ and $\mathbf{p}_\alpha$ derivatives. As a result, we have an extended system of ray equations.

Models of Undisturbed and Disturbed Ionosphere

To calculate trajectories, it is necessary to specify a regular distribution of the electron density $N(x, y, z)$ by height z and horizontal coordinates x and y, as well as a disturbance model. When studying disturbances, it is usually assumed that the regular ionosphere is the background against which electron density inhomogeneities are

formed. To describe the background, the IRI-2016 global electron density distribution model has been used. The model of a disturbed ionosphere takes into account the distribution of the electron density both vertically and horizontally, as well as the magnitude of the disturbance. Disturbances of various types are multiplicatively superimposed on the regular profile specified by the IRI-2016 model.

Results of Modeling

Examples of trajectory calculations for different values of the elevation angle θ, transmitter–receiver path length *x*, radio wave frequency *f*, and relative disturbance *N* equal to $\delta_N = \Delta N/N_0$ are shown in Fig. 1.

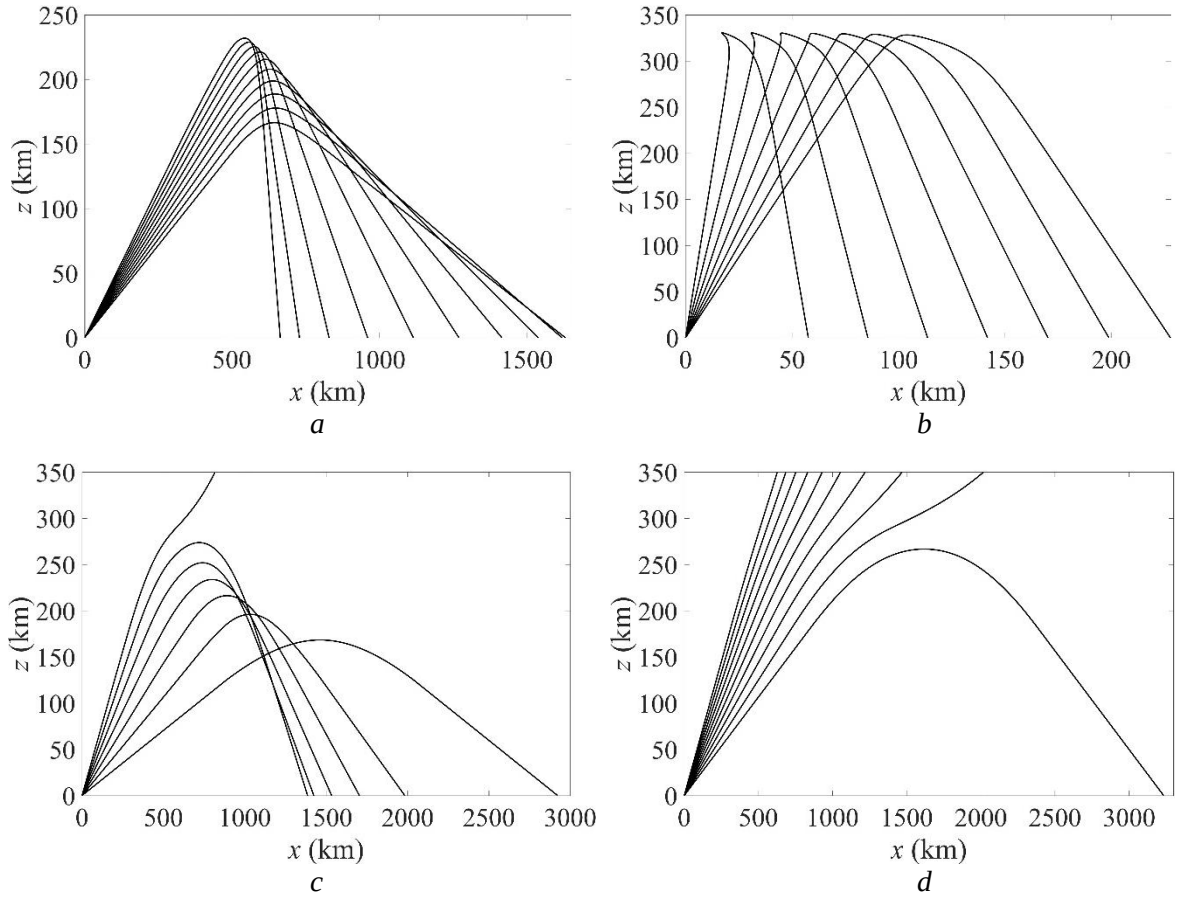

Fig. 1. Nighttime radio wave trajectories with a 2-degree step: (a) f = 3 MHz, δ_N = +30%, θ_0 = 20°; (b) f = 5 MHz, δ_N = 0%, θ_0 = 80°; (c) f = 7 MHz, δ_N = –30%, θ_0 = 20°; (d) f = 15 MHz, δ_N = 0%, θ_0 = 20°

Main Results

1. Original software for calculating decameter radio wave trajectories in a three-dimensionally inhomogeneous magnetoactive stationary medium (ionosphere) has been developed and improved.

2. The results of modeling decameter radio wave trajectories for a given set of parameters (frequency, elevation angle, disturbance magnitude, time of day) are recommended for practical application of radio wave propagation under undisturbed and disturbed conditions.

This work was supported by Ukraine state research projects #0122U001476 and #0124U000478.

References

[1] C. B. Haselgrove and J. Haselgrove, “Twisted Ray Paths in the Ionosphere,” Proceedings of the Physical Society, vol. 75, is. 3, pp. 357–363, 1960.

[2] K. Davies, *Ionospheric Radio*. London: Peter Peregrinus Ltd., 1990.

IONOSPHERIC EFFECTS OF STRONG ATMOSPHERIC PROCCESS ON HF RADIO WAVE PROPAGATION CHARACTERISTICS

L.F. Chernogor*,,***, Yiyang Luo*, K.P. Garmash*, Qiang Guo**, Yu Zheng*****

**V.N. Karazin Kharkiv National University, 4 Svobody Sq., Kharkiv 61022, Ukraine, Address, e-mail: Leonid.F.Chernogor@gmail.com; yiyangluo@163.com; Garmash@univer.kharkov.ua*
***College of Information and Communication Engineering, Harbin Engineering University, 145 Rd. Nantong, Harbin, Prov. Heilongjiang, P.R. of China, e-mail: guoqiang@hrbeu.edu.cn*
****School of Electronics and Information Engineering of Qingdao University, 308 Rd. Ningxia, Qingdao, Prov. Shandong, P.R. of China, e-mail: zhengyu@qdu.edu.cn*

This research investigates the ionospheric effects of strong atmospheric process, specifically focusing on hurricanes (typhoons), on high-frequency (HF) radio wave propagation. As telecommunications, radio navigation, radar, radio astronomy, and remote sensing systems heavily rely on the disturbances of the atmosphere-ionosphere radio channel, understanding these impacts is crucial. We explore how hurricanes generate substantial disturbances not only in the atmosphere but also within the ionosphere, leading to significant variations in electron density that often exceeding 10%. This results in traveling ionospheric disturbances and increased plasma turbulence, ultimately distorting radio wave trajectories. The study highlights the resultant alterations in key HF radio wave parameters, including signal propagation time, phase, angle of arrival, Doppler frequency, amplitude, polarization, and signal-to-noise ratio.

Introduction

Strong atmospheric processes, particularly tropical cyclones and typhoons, significantly affect ionospheric dynamics and high-frequency (HF) radio wave propagation [1]. Typhoons, characterized by intense pressure drops and high wind speeds, generate electron density (N) disturbances and atmospheric gravity waves (AGWs) that modulate N in the ionosphere. Research has shown that these cyclones induce traveling ionospheric disturbances (TIDs) and alter the ionospheric D region through electromagnetic emissions from lightning, which heat electrons and influence their density [2]. Additionally, localized electric currents within thunderstorm clouds disrupt the global electric circuit, enhancing quasi-sinusoidal electric fields that can affect the motion of high-energy electrons in the radiation belts [1, 3]. Understanding these interactions is crucial for comprehending HF radio wave propagation characteristics under extreme atmospheric conditions.

Equipment and Method

The investigation employed a passive multi-frequency multiple path software-defined radio system for oblique-incidence sounding of the ionosphere, situated at Harbin Engineering University (45.78°N, 126.68°E), PRC. This system facilitates data acquisition, signal processing, display, and automated analysis. It leverages an existing network of HF radio stations, which transmit in the 5–10 MHz frequency range [3]. Throughout the study, measurements were conducted along 12 radio-wave propagation paths, each approximately 1,000 to 2,000 km in length, as shown in Fig. 1. Data processing analyzed the universal time dependencies of Doppler spectra, main ray amplitude $A(t)$, and Doppler frequency shift $f_D(t)$ using auto-regressive spectrum analysis, achieving a Doppler resolution of 0.01 Hz and a temporal resolution of 7.5 s. Trends and fluctuations over 1 to 60 minutes were extracted using spectral techniques, including short-time Fourier transform and Morlet wavelet transform [4]. It is worth noting that during the 1000–2000 km propagation path, daytime detection primarily reflects from the E layer, yielding Doppler shifts (f_D) near 0 Hz, making them ineffective for ionospheric dynamics. Conversely, nighttime waves reflect from the F region, showing shifts of 0.1 to 0.5 Hz or greater, making these measurements more valuable. However, the dataset is limited by the discontinuity of broadcast station signals.

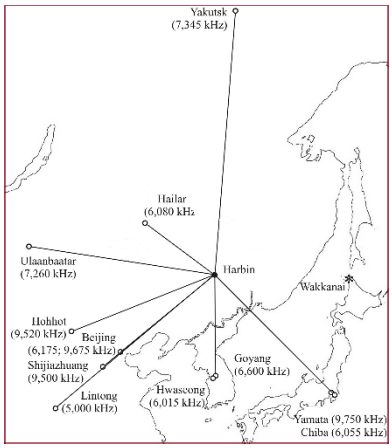

Fig. 1. Layout of Radio Wave Propagation Paths for Observing Ionospheric Dynamics.

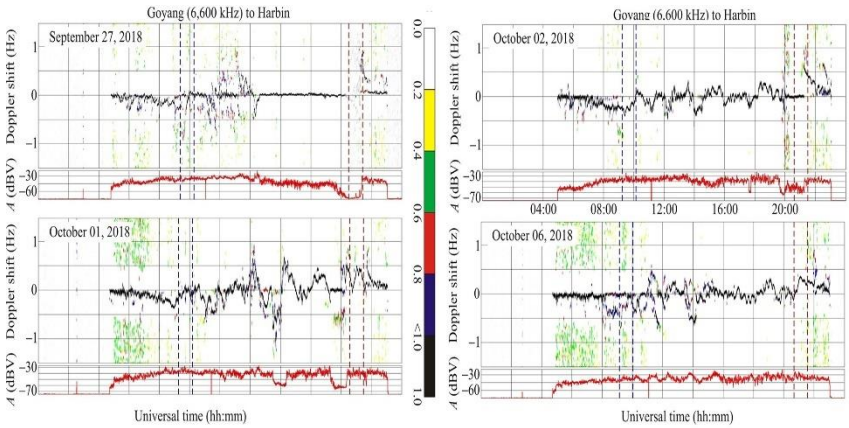

Fig. 2.Time Variation of Doppler Spectra and Signal Amplitude (A) on the Goyang-Harbin Radio Wave Propagation Path: September 27 (Reference Day), October 1, 2, and 6 (Disturbance Days), 2018.

Results

Taking Typhoon Kong-Rey's ionospheric effects as an example [3] for explanation, data analysis of the Goyang-Harbin radio wave path indicated that only 8 of the 14 radio wave propagation path in the 6–10 MHz band were effective. The Goyang transmitter operates at 6600 kHz and is located 910 km from the receiver; it is inactive from 00:00–05:00 UT and 22:20–24:00 UT. Fig. 2 presents the observation results, with September 27, 2018, chosen as the reference day for analysis. Different from the reference day, significant Doppler spectrum broadening of ±0.6 Hz was observed on October 1, 2018, with variations having a period T of 20–120 min and amplitude f_{Da} of 0.1–0.7 Hz, alongside signal amplitude variations up to 20 dBV. On October 2, the Doppler shift varied significantly at ±(0.2–0.3) Hz, with a quasi-sinusoidal T of 24 min and amplitude f_{Da} of 0.2 Hz. On October 6, it increased to ±(0.3–0.5) Hz from 11:00 to 14:00 UT, and from 15:00 to 18:00 UT, quasi-sinusoidal oscillations in the Doppler shift were observed with a period T of ~20 min and amplitude f_{Da} of ~0.1 Hz. Quasi-sinusoidal variations in signal amplitude $A(t)$ were noted with a period T of 55–80 min and amplitude of 7–8 dBV. These observed quasi-sinusoidal variations indicate atmospheric gravitational waves that modulate electron density.

References

[1] L. F. Chernogor, "A tropical cyclone or typhoon as an element of the Earth–Atmosphere–Ionosphere–Magnetosphere system: Theory, simulations, and observations," Remote Sens., vol. 15, no. 4919, 2023. [Online]. Available: https://doi.org/10.3390/rs15204919

[2] J. Bortnik, U. S. Inan, and T. F. Bell, "Temporal signatures of radiation belt electron precipitation induced by lightning-generated MR whistler waves: 1. Methodology," J. Geophys. Res., vol. 111, A02204, 2006. [Online]. Available: https://doi.org/10.1029/2005JA011182

[3] L. F. Chernogor, K. P. Garmash, Q. Guo, V. T. Rozumenko, and Y. Zheng, "Effects of the super-powerful tropospheric western Pacific phenomenon of September–October 2018 on the ionosphere over China: results from oblique sounding," Ann. Geophys., vol. 41, no. 1, pp. 173–195, 2023. [Online]. Available: https://doi.org/10.5194/angeo-41-173-2023

[4] L. F. Chernogor, "Advanced Methods of Spectral Analysis of Quasiperiodic Wave-Like Processes in the Ionosphere: Specific Features and Experimental Results," Geomag. Aeron., vol. 48, pp. 652–673, 2008. [Online]. Available: https://doi.org/10.1134/S0016793208050101

THE INCLUSION OF A QUARTZ RESONATOR IN POWERFUL AUTOGENERATORS

Dmytro Chernov*, Vladimir Krizhanovski*

**Faculty of Information Technology Vasyl Stus Donetsk National University*
Vinnytsa 21021, Ukraine, email: D.Chernov@donnu.edu.ua

To obtain the possibility of including a quartz resonator in the circuits of powerful oscillators with high efficiency, a circuit was developed to amplify the power that can pass through the quartz and match the input and output impedances of the circuit. The circuit is aimed at exciting a powerful transistor with a sinusoidal voltage, which is the best solution from the point of view of high-frequency and energy parameters of oscillators. The results of the experimental study of the scheme and its field of application are discussed.

Introduction

Autogenerators (oscillators) with high efficiency are widely used and are the object of improvement [1, 2]. There is a problem of creating powerful autogenerators with high stability. A technically acceptable solution is to use a separate highly stable generator, and then a powerful amplifier with high efficiency. But sometimes problems arise in which simpler circuits need to be made, and then the possibility of using high-Q (quartz) oscillating systems in powerful oscillators needs to be studied. Consider what power is required for the active element to work as a key in a class E oscillator. According to [3], the high-frequency current flowing in the gate circuit can be calculated from the gate charge, which is required to switch the transistor

$$I_g = \frac{Q_g}{\int_0^{t_{on}} \cos(\omega_s t)\,dt} = \frac{Q_g \omega_s}{\sin(\omega_s t_{on})} \tag{1}$$

where $\omega_s = 2\pi f_s$ is the circular frequency of the oscillator, t_{on} is the transistor turn-on time. The power dissipated in the gate circuit is equal to

$$P_g = \frac{1}{2} I_g^2 \left(R_c + R_g\right) \tag{2}$$

Here R_c is the resistance of the transistor control circuit, for the case of sinusoidal current control it is close to the active resistance of the inductor in the gate circuit, R_g it is equivalent to the series active resistance of the transistor gate. The power for switching the transistor at high frequencies increases sharply with the frequency and the increase in the input capacitance of the transistor and many times exceeds the power and current that can be transmitted through the crystal resonator (drive level).

Scheme for inclusion of a quartz resonator

The scheme built taking into account the satisfaction of these requirements is shown in Fig. 1. The device is connected between the feedback output (near the oscillator load) and the gate of a powerful transistor, in the figure, a powerful transistor is modeled by a serial RC link and the task is to obtain the required signal amplitude at the operating frequency. The voltage on the gate of the power transistor increases when it is included in a series oscillating circuit. The Q-factor of this circuit is equal to $Q(C_{in}) = 1/(2\pi R_{sum} C_{in})$, where C_{in} is the input capacitance of the transistor, and R_{sum} is the sum of the equivalent series input resistance of the transistor and the output resistance of the output stage with a common drain. An increase in the power of the key transistor leads to an increase in its input capacitance and, accordingly, to a decrease in the Q factor. Therefore, with an increased frequency and power of the oscillator, it is necessary to increase the amplification factor in the circuit, which leads to an increase in the consumption of the circuit in general.

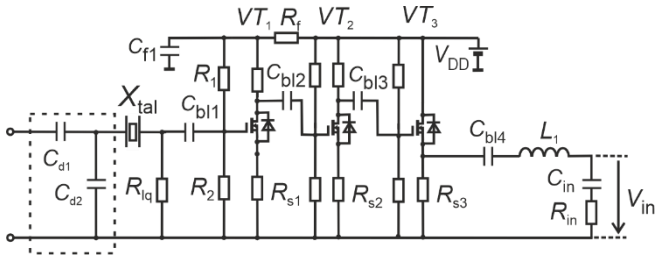

Fig. 1. Scheme for inclusion of a quartz resonator in the feedback loop of a powerful autogenerator

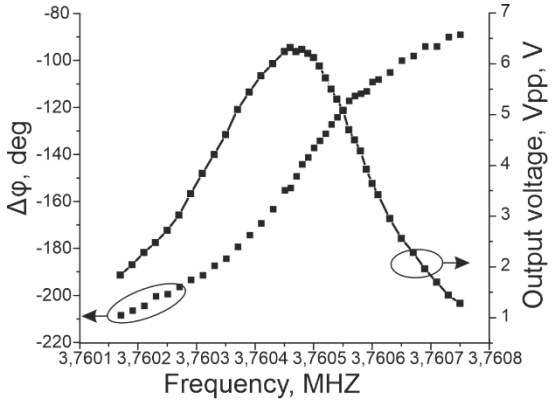

Fig. 2. Measured characteristics of the experimental layout

The purpose of this circuit is to provide the required amplitude-frequency and phase-frequency characteristics so that the Barhausen conditions for amplitude and phase are satisfied in the feedback loop. The inclusion of a quartz resonator and a large value of the derivative of the phase shift from the frequency $d\varphi/df$ will ensure the stability of the frequency of the powerful oscillator. In fig. 2 shows these dependencies for an experimental layout of a circuit with a quartz resonator at a frequency of 3.760 MHz. According to these dependencies, it was determined that the circuit in the cell is equivalent to a resonator with a Q factor of 15,000 and has a slope of the phase characteristic near the resonance of approximately 0.3 degrees/Hz. For use as part of powerful autogenerators, the phase shift on this scheme should be around ±90° (taking into account the phase shift in the resonant circuits of the amplifier [4]), in the experimental conditions the value is approximately minus 155°, but we have resonant elements at the input and output devices, which in a specific scheme may have a different value or be included in a different composition, therefore the phase shift in a specific application may be changed. The amplitude of the signal, which is achieved at a capacitance of 300 pF, is sufficient to drive a certain number of powerful field-effect transistors at a given frequency. As the frequency increases, this will be difficult to achieve due to the drop in the Q-factor of the series loop. But the idea of this device can have improved implementations.

Conclusion

A scheme for including a quartz high-pass resonator in the feedback circuit of a powerful oscillator with a high efficiency is proposed and experimentally investigated. In this scheme, the conditions for the input and output impedance, for limiting the current and power that pass through the quartz, and the conditions for obtaining the desired amplification factor in terms of voltage and current at the operating frequency are fulfilled. Experimental studies have shown that at the equivalent of the input impedance of a powerful field-effect transistor, a double voltage amplitude of up to 8 V is obtained at a supply voltage of 9 V, and preservation of the main frequency and phase properties of the quartz resonator.

References

[1] S.-A. El-Hamamsy “Design of high-efficiency RF Class-D power amplifier” IEEE Transactions on Power Electronics, Volume: 9 Issue: 3, May 1994. P. 297-308.

[2] V. G. Krizhanovski “Current state and development trends of class E oscillators: an overview” Radiotekhnika. All-Ukr. Sci. Interdep. Mag. 2023. N 212. P. 134-140.

[3] S. Pezeshkpour, M. M. Ahmadi “A Self-Tuned Class-E/F3 Power Oscillator” IEEE Trans. on Power Electronics https://doi.org/10.1109/tpel.2024.3390243

[4] J. Ebert, M. Kazimierczuk “Class E High-Efficiency Tuned Power Oscillator” IEEE Journal of Solid-State Circuits, Vol. SC-16, No. 2, April 1981, P. 62-66.

STUDY ON EXTRACTION OF MILLIMETER-WAVELENGTH RADIO EMISSION FROM A RELATIVISTIC MAGNETRON

A.B. Batrakov, S.I. Fedotov, O.M. Lebedenko, V.S. Mukhin, I.N.Onishchenko,

O.L. Rak, A.O. Shtanko, V.G.Sinitsin, M.V. Volovenko*

Institute for Plasma Electronics and New Methods of Acceleration,
National Science Center 'KIPT', Kharkiv 61000, Ukraine
**E-mail: mykola.uz@gmail.com*

Results are presented of a research into operating modes of a high-voltage (relativistic), pulsed magnetron for the 8 mm wavelength range. Technical solutions are proposed for improving the outputting system of the device - such as to increase the efficiency of power extraction from the field-particle interaction space. The authors expect, among other results, an increased operational stability of the magnetron, improved quantitative indices of the power output, and a stabilized frequency spectrum of the radiation

.Introduction

The early projects on studying millimeter waveband relativistic magnetrons (RM) were carried out with the use of the accelerator *Astra* based on a low-impedance about 8 Ohm) dual pulse forming line (DFL) [1]. The output impedance of an operating RM is equal to 100 Ohm. The lack of matching between the RM and the low-resistance DFL often resulted in multiple reflections along the propagation path for the radiation under study, as well as an increased duration of the voltage acting in the electrodynamic structure (EDS) and consequently, to rapid deterioration of the structure [1,2]. Thus, the previous results of experimentation with different RM designs - both hornless or equipped with a horn for radiation output - now can be characterized as unsatisfactory. Indeed, the output power of those early magnetrons never was in excess of 100 kW, which figure corresponded to a lower efficiency than 0.1% [2]. Therefore, the question arose of improving the method of high frequency power removal from the EDS of the magnetron..

Experimental

To that end, a new accelerator was created by the end of 2023 [3], characterized by a noticeably higher impedance of its DFL[3]. This makes it possible to better match the pulse forming line and the RM, thus increasing the durability and operational stability of the magnetron. Currently, the research is carried out on a modernized version of the installation whose schematic is shown in Fig. 1

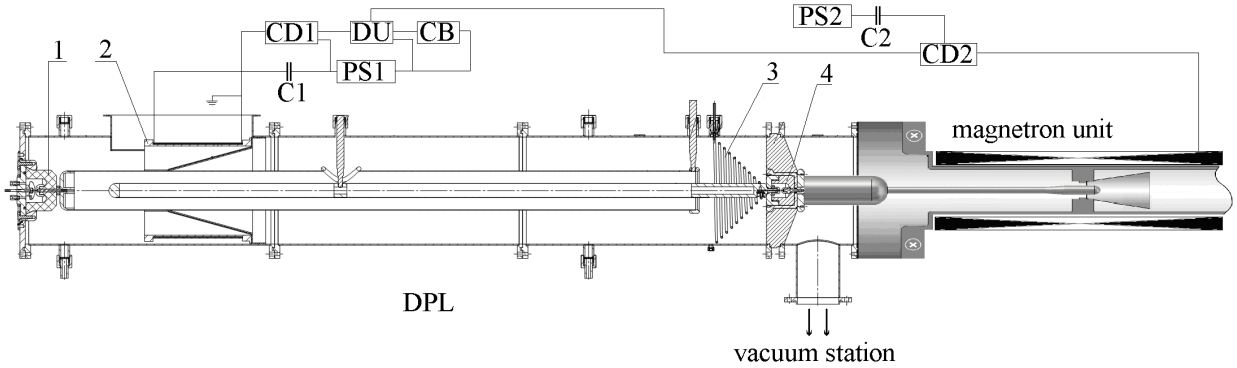

Fig. 1. Schematic of the relativistic magnetron:
positions PS1 and PS2 represent power supply circuits;
CD1and CD2 are controllable discharges to provide driving voltage to the magnetron proper.

The pulsed generation from the RM was observed in the frequency range between 33 and 39 GHz, with d.c. magnetic bias levels B_0=0.5 to 0.9 T. Over the period of 2019 through 2021 several versions of the EDS, with 30. 40 and 48 cavities were investigated. The most complete set of results was obtained for the 48-cavity structure. Experiments with the RM-48 magnetron revealed microwave generation at 36 to 41 GHz with the magnetic induction magnitudes B_0=0.35to 0.8 T and anode voltages U_0=190 to 250 kV. The oscillations excited could be identified as belonging to the π/2; π, or (2/3)π modes . The anode and the cathode diameters were, accordingly, d*a*=22 mm and dc=12-16 mm, while the cathode-anode gap varied like d*ca*=3 to 5 mm,). Yet, the net outcome of the experiments with a horn-supported axial extraction of microwave power still needs to be be characterized as unsatisfactory. Indeed, the RF power at the output never exceeded 100 kW, while the e-beam power at the entrance to the EDS was about 400 MW. This meant an efficiency below 0.1 per cent, which was in a drastic contrast with the results of many numerical experiments with centimeter-wavelength RMs (like the famous A6) which demonstrated efficiencies about 10 per cent. This is why our further studies of VHF generation and power extraction from relativistic magnetrons have become concentrated on ways to increase the amount of microwave power radiated from the anode - cathode space. Some of the recent results on microwave emission, as dependent on the magnetic induction, are shown in Fig. 2 below. As can be seen from Fig. 2***a***, the most efficient regimen is when the magnetic induction B is close to 7.6 kOe. The oscillogram for this case is shown in Fig. 2***b***, where the yellow curve represents the feed voltage, the blue one is current, and the purple-colored curve represents the level of microwave generation. .

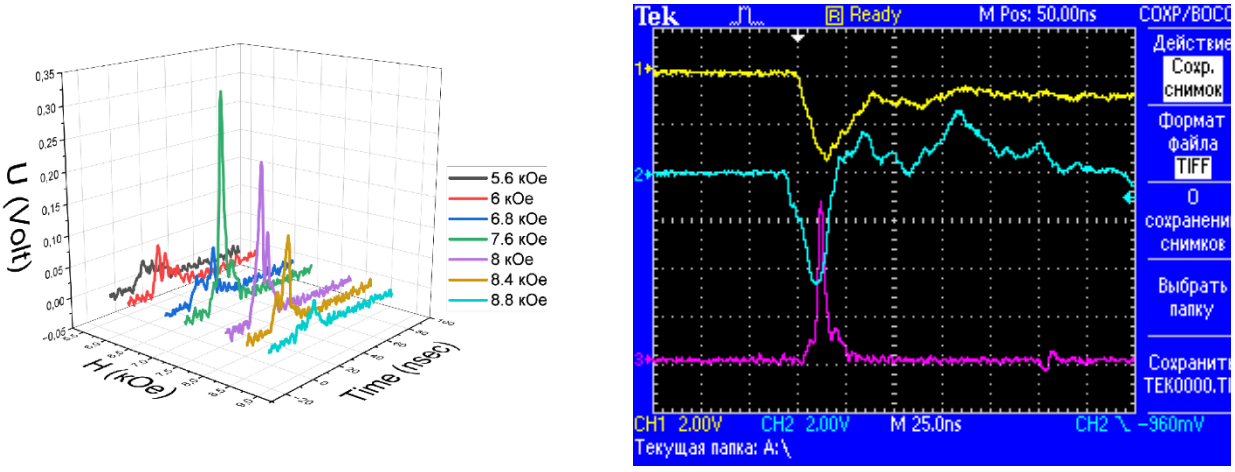

a ***b***

Fig. 2. Microwave generation in the RM-48 ***:*** *Experimental data*

Conclusions

As can be seen, the design that has been proposed offers new opportunities for enhancing the level of microwave power extraction from the magnetron, owing to a better matching of impedances of the anode-cathode space and the transmission line at the output.

References

[1] N.P. Gadetski, E.I. Kravtsova, I.I. Magda, V.D. Naumenko, S.S. Pushkaryov, S.N. Terekhin, A.S. Tischenko. Relativistic magnetron of 8 mm wave-and // Problems of Atomic Science and Technology. Series “Plasma Electronics”. 2008, № 4, p. 18-20.

[2] N.P. Gadetsky, A.N. Lebedenko, I.I. Magda, O.G. Melezhik, A.A. Shtanko, M.V. Volovenko. A relativistic magnetron-type source of nanosecond-length pulsed radiation in the 8 mm waveband // Problems of Atomic Science and Technology. Series “Plasma Electronics”. 2017, № 6, p. 40-42.

[3] N.P. Gadetski, V.G. Korenev, A.N. Lebedenko, I.I. Magda, O.G. Melezhik, V.G. Sinitsin, A.A. Shtanko, and N.V. Volovenko. Millimeter-wavelength relativistic magnetron: problems of microwave power extraction // Problems of Atomic Science and Technology, Series: Nuclear Physical Investigations, 2021, №6 (136), pp. 80-84.

FEATURES OF THE FORMALIZATION OF SITUATION MANAGEMENT CYCLES OF THE GROUND SPECIALIZED COMPLEX OF RADIO ELECTRONIC COUNTERMEASURES FOR SMALL DRONES

V. Kantsedal

Dept. of physical principles of radiolocation O.Ya.Usikov Institute for Radiophysics and Electronics of the National Academy of Sciences of Ukraine, Kharkiv 61085, Ukraine, e-mail: kantsedalvaleri@gmail.com

Obtaining the conflicting advantages of the ground-based specialized radio-electronic countermeasures complex for small drones is possible due to the improvement of the functioning of the control circuits of its automated control system (ACS) at the main stages of its functioning. The achievement of an advantage lies in the use of methodological features of the application of a system-process approach to management, formalized formulations and solutions of tasks of situational management cycles of the radio electronic suppression (RES) complex, taking into account the goals and management criteria set at the stages of operation, the selection and application of critical performance characteristics and their indicators, effective information, control and executive means of the control circuits, as well as resource constraints.

The report examines the features of the conflict interaction between a ground-based specialized RES complex and small reconnaissance-strike drones when they penetrate the rear to a depth of 10-100 km to hit important objects and guide ballistic missiles [1,2]. Based on the information description of multifunctional structures and the performance characteristics of the technical appearance of a small drones and the RES complex, the presentation of a conflict situation as counteraction to their performance characteristics, the formulation of tasks of the situational control cycle [3] with the participation of information, control and executive means of the control loops of the ACS on the its main functions - the stages of drones reconnaissance and the formation of data necessary for control, physical signal and covert information suppression of it in conditions without counteraction from the drones and in its presence, along with external sources of electronic warfare threats is considered.

The main objectives of interstage situational control of the electronic warfare system using artificial intelligence tools and restrictions on the level of resource expenditure are the maximum values of probability indicators:

1) overcoming with the information of the means of internal and external control circuits of the ACS the uncertainty of the observation conditions, due to the performance characteristics of the drone type, indicators of the energy and structural covert of the signals emitted by it, the information messages transmitted by it, with the timely allocation of complete, reliable and accurate information necessary for the operational control of technical executive means of operational stages;

2) the choice of the control means of the control circuits of the ACS in accordance with the level of intelligence data of the most effective technical means of its implementation and their modes of operation to overcome the interference immunity of the means of receiving and processing signals or the resistance of ciphers of transmitted messages in drones and radio-electronic countermeasures to drone threats, determining the optimal order of application of each of them to achieve the goal of management:

- the maximum effectiveness or efficiency of the modes of operation of the RES complex in the fight against the threats of small drones in the absence of drone countermeasures;
- the stability of the modes of operation of the RES complex - support at a given level of values of their tactical and technical characteristics in the conditions of drone countermeasures and the presence of external sources of RES of the functional tasks of the drone reconnaissance stage;

3) implementation of adopted control decisions by technical means of flexible and rapid reconfiguration of the structure of the RES complex;

4) tracking of the drone being suppressed, targeting it with technical means of suppressing the electronic complex with minimal errors and activating them;

5) control by information means of the automatic control system of the conditions for observation of drone, decision-making and evaluation of the results of the implementation of adopted control decisions as a result of the use of the designated set of electronic warfare means at the operational stage.

At the reconnaissance stage, achieving completeness, reliability, accuracy of the characteristics of a small drone and timely information description of the components and dynamic states of the current conflict situation is ensured by the performance characteristics and integration of the capabilities of radar, electronic system measurement (ESM)), electronic intelligence (ELINT) and the formation of target designation for the control means of the ACS to organize various types of suppressive effects and create conditions for increasing the effectiveness of their use. Thus, gaining a conflict advantage can be achieved through the use of:

- all-weather UWB radar with circular or sector coverage with increased radiation covert in probing modes based on the basic model of a stochastic signal form, which best takes into account the features of long-range detection of small drone as a radar object;
- in the means of ESM and ELINT more advanced methods of searching and spectral analysis of emissions, identifying and exploiting vulnerabilities and messaging in the lines of radio communication and radio navigation of drone, the implementation of a more accurate differential-range measurement method of drone coordinates, the formation of databases of information description of components and, in general, conflict situations with the structure of the information description in the interests of increasing the effectiveness of algorithms for physical signal and covert information suppression of drone based on structural and parametric data of radar, ESM and ELINT means by forming and emitting, respectively:
- combinations of barrier and imitation types of active interference aimed at vulnerable points of individual communication lines of the drone command and control radio link and navigation of the satellite radio navigation system, as well as variants of combinations of these combinations and the order of their application for targeted change the dynamic state of the electromagnetic environment (EME) created by a set of signals of the radio communication lines and radio navigation of the drone, taking into account the degree of their uncertainty;
- combinations of barrier and imitation types of active interference to suppress symbols of encrypted information messages; imitation active interference and information technology impacts (ITI) to simulate or substitute messages; ITI to disrupt information exchange protocols specifically for individual radio communication lines and drone radio navigation, as well as options for combining these combinations and the order of their application for targeted change the dynamic state of the environment (sets) of information messages and information exchange protocols (EIMP) created by a set of drone radio communication lines and radio navigation;
- types of ITI to influence decision-making algorithms in the information and control system of the drone command and control radio link as part of the drone ground control point for managing equipment for managing the dynamic states of the drone EME and EIMP in the in the interests of disrupting the operation of the drone command and control radio link and intercepting of the drone control, taking into account the level of a priori knowledge about the functioning of the information and control system.

The report also presents formulations of the goals and objectives of the cycles of intra-stage situational management [3] of the processes of functioning of the RES complex, the search for adaptive and operational solutions at its stages using a specific list of specific performance characteristics and their indicators. These particular performance characteristics reveal generalized probabilistic indicators of interstage control are a critically important systemic tool for the formalization of management processes at the stages of operation, taking into account their features, conditions of observation and decision-making.

References

[1] Unmanned aerial vehicles Supercam, https://sprotyvg7.com.ua/lesson/bpla-supercam.

[2] ZALA - 421-16E5G HD, Sprotyv G7, https://sprotyvg7.com.ua › Zala_Aero_Group_G2.

[3] V. Kantsedal. Rationale for construction of the structure of the system for cognitive control of types of signal resource surveillance radar / Book of proceedings of the 19th InternationaI Scintific Conference on Electronics and Applied Physics (APHYS 2023). 17-21 October 2023. – Kuiv, Ukraine, Taras Shevchenko National University of Kyiv Faculty of Radio Physics Electronics and Computer Systems. – 91 - 92 p.p.

COMBINED RADAR METER OF ACTUAL SPEED AND SLIPPAGE OF AGRICULTURAL VEHICLES

Maltsev V. P.

O. Ya.Usikov Institute for Radiophysics and Electronics
of the National Academy of Sciences of Ukraine, Kharkov
e-mail: valentynmaltsev@gmail.com

Currently, there is a problem of transport vehicles speed measurement, when the data on their speed are subsequently used to control technological processes in the engineering and mining industry, maneuvering on the road or performing various operations, in particular, sowing of various agricultural crops. At the same time, even a small error in determining the speed of an industrial plant or vehicle can negatively affect the quality of work as a whole, which can cause significant financial, labor and time costs. Traditional methods of speed measurement are related to the measurement of the wheels rotation period and contain in their indications errors related to wheels slip and conveyor belts, subsidence of wheels in the soil, as well as other effects occurring in the zone contact of the tire tread and the ground surface. The problem of measuring the true speed of vehicles is particularly acute in agriculture due to the unprepared surface for traffic and the significant load during traction operations by agricultural units (ploughing, cultivation, disking, etc.). Many agricultural operations (planting, weeding, cultivating, applying fertilizers, etc.) are connected with the drives of the engines of agricultural machines. When the wheels slip, situations often arise when the technological requirements for the cultivation and processing of agricultural plants are violated. Most agricultural units are equipped with contact speedometers, which measure the movement speed by the wheels rotation speed. At the same time, depending on the type and condition of the soil (plowed or unplowed field, wet or dry soil, etc.), the movement of the unit is characterized by more or less slip, which certainly affects the accuracy of measuring the speed of movement by the contact method. At the same time, the specific fuel consumption and the quality of field work (uniformity of sowing, application of fertilizers and spraying) significantly depend on the vehicle and, no less important, on the stability of this speed to maintain the vehicle optimal movement mode.

For this measurements was developed combined sensor or actual speed and wheel slip (fig.1) consisting of Doppler radar, wheel rotation sensor, based on Hall sensor, processing unit and power supply.

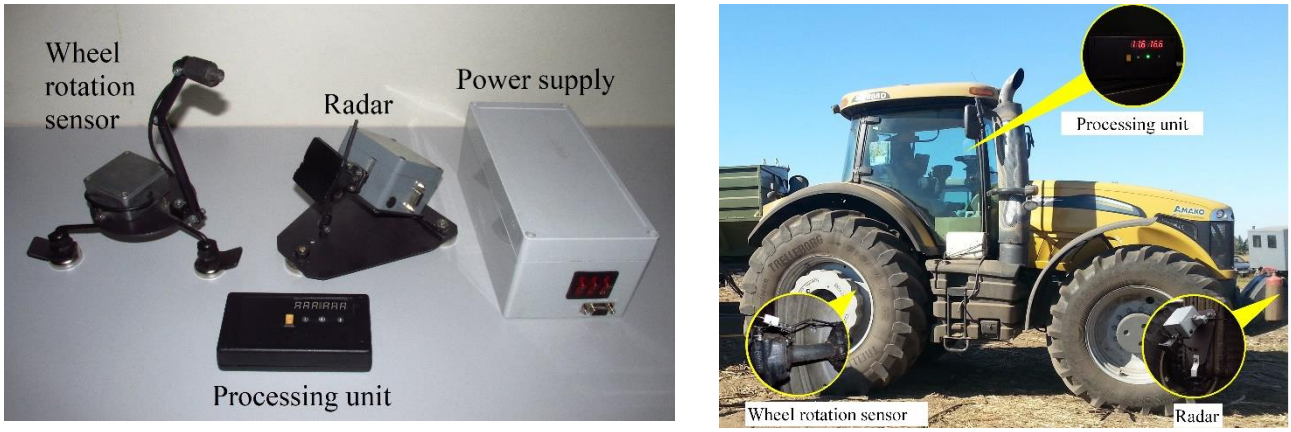

Fig. 1. General view of radiometer system

The sensor was tested in laboratory conditions on a specially designed stand (fig. 2) consisting of a base with driving and driven pulleys and a belt with artificial roughness simulating the movement of the underlying surface.

During operation, the machine pulley was covered by an absorbing panel. Measurements have shown that the measurement error does not exceed 1%.

Fig. 2. Laboratory measuring stand

The sensor was tested in natural conditions on various types of tractors and different soils. Fig. 3 shows the results of measurements when a tractor was operating with a harrow. A strong difference is visible between the actual speed and the speed calculated through the rotation of the wheel. In this case, the slip coefficient reaches 12%.

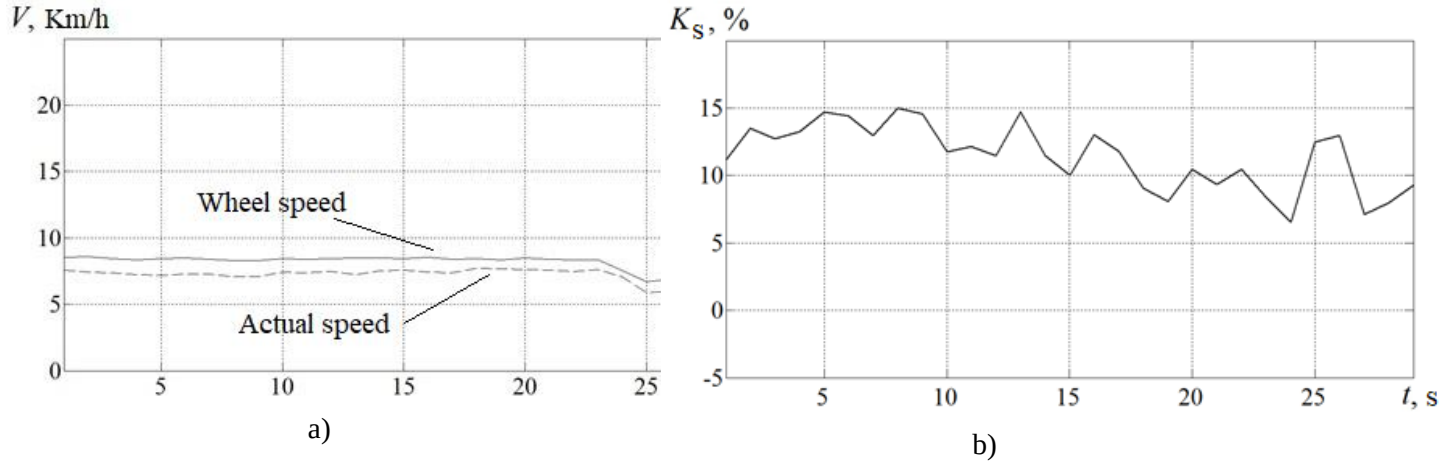

Fig. 3. Speed (a) and slip coefficient (b) when moving a tractor with a harrow

References

[1] Maloratsky L. G. Radar speed meters for tractor units// Abroad electronics - 1986.- N7.-p.84 -91.

[2] Лебедев С. А., Мальцев В. П., Хлопов Г. И., Шуляк М. Л. Комбинированный измеритель буксования и скорости сельскохозяйственных машин на основе РЛС миллиметрового диапазона и датчика Холла// Системи обробки інформації.–2015.–№5.– с. 23-28.

[3] Калинин Е. И., Мальцев В. П., Шуляк М. Л. Вплив нестаціонарності гакового навантаження на буксування рушіїв колісного трактора// Системи обробки інформації, Вид-во ХУПС.–2016.–№5.– с. 27-30.

SOFTWARE-DEFINED RADIO RECEIVING SYSTEM FOR PASSIVE HF DOPPLER RADAR FOR MULTIPLE PATH MULTI-FREQUENCY AND FREQUENCY-AND-ANGULAR PROBING TRAVELING IONOSPHERIC DISTURBANCES

K.P. Garmash*

** School of RadioPhysics, Biomedical Electronics and Computer Systems, V.N. Karazin Kharkiv National University, Kharkiv 61022, Ukraine, email: garmash@karazin.ua*

The software and breadboard of hardware system for passive multiple path multi-frequency and frequency-and-angular determining the parameters of traveling ionospheric disturbances have been developed using two USRP N210 devices. The results of the test of metrological and field measurements confirmed the high technical and quality characteristics of the layout, which allows it to be used for monitoring of traveling ionospheric disturbances.

Introduction

The study of physical processes that ensure the generation of and accompany the propagation of acoustic-gravity waves in the different layers of the earth's atmosphere is relevant for the sustainable development of a wide range of human technologies. In the ionosphere this waves are usually observed in the form of travelling ionospheric disturbances (TIDs) and can affect the propagation of electromagnetic waves. The experimental observations of TIDs in the upper atmosphere and ionosphere are mostly based on optical observations of the airglow, measurements of fluctuations in the total electron content using dual-frequency receivers of signals from global positioning system satellites, and the use of the SuperDARN system in high latitudes. Probing with reflected from the ionosphere obliquely incident high frequency radio waves is widely used. In particular, continuous Doppler sounding using broadcast radio signals [1, 2] is very common due to the relatively cheap equipment and simple methodology. Attempts to determine the parameters of the TID during oblique-incidence ionospheric sounding by a network of synchronized DPS-4D digisondes look quite promising [3, 4]. The Doppler frequency, the angle of arrival and the propagation time of probing signals over the radio paths between each pair of digisondes are measured simultaneously. Information about the TID amplitude, speed, and direction of its propagation in the ionospheric regions, where radio signals are reflected, can be obtained from these data using the frequency-and-angular sounding (FAS) tecnique [5, 6]. Unfortunately, the digisonde is a rather expensive device. The usage of software-defined radio (SDR) technology in the equipment for continuous Doppler sounding using broadcast radio signals [7, 8] is able to increase the informativeness of the technique up to the level of frequency-and-angular Doppler sounding, remaining within the low budget framework.

The purpose of the report is to discuss the designing, on the basis of SDR technology, a non-expensive prototype of a device for multi-channel Doppler sounding of TIDs using signals of broadcast radio stations with the implementation of frequency-and-angular methodology.

Description of the system breadboard

Ettus Research's USRP N210 type SDR device with a 1 Gigabit Ethernet network interface and LFRX/LFTX front-end daughter boards for operation in the frequency range from 0 Hz to 30 MHz has been chosen as the basis for constructing a breadboard of the hardware and software system for passive multiple path multi-frequency and frequency-and-angular sounding on the oblique radio paths. The internal architecture of the USRP N-series devices has a two-channel structure of the input and output circuits, and the built-in MIMO (Multi In – Multi Out) interface allows to synchronize the operation of analog-to-digital and digital-to-analog converters, as well as large integrated circuits of programmable logic, in a pair of such devices. In this way, a fully synchronized hardware four-channel SDR system is easily implemented, suitable for the organization of measurements of phase shifts of radio wave signals received by four spatially separated antenna elements. Each antenna element is a vertical short dipole 5 m long.

The host computer of the breadboard system for Doppler measurements on oblique radio paths with the implementation of the FAS technique is based on the Intel Core i7-12700K processor (total of 12 cores, total of 20 threads, max turbo frequency 5 GHz), 32 GB of DDR5 RAM and the GeForce GTX1660 graphics. Each USRP N210 device is connected to the host computer via a separate 1 Gigabit Ethernet adapter. The host operate under the 64-bit MS Windows 10 Enterprise LTSC operating system. The GNU Radio environment version 3.8.2.0 with the GNU Radio Companion utility and the Python package version 3.9.0 [9] are installed on the host. The USRP Hardware Driver (UHD) from Ettus Research, version 3.12.0.0 for 64-bit MS Windows 10 [10] is used for the low-level interaction between GNU Radio environment and USRP N210 equipment.

The test metrological measurements of phase-frequency and phase-amplitude characteristics non-identity in different channels of the breadboard system demonstrated that they are in good agreement. The differences in the average values of the pairwise phase difference in the frequency range of 3 MHz – 9 MHz and the range of input signal amplitudes of 0.1 mV – 10 mV do not exceed 1° – 4°, while the root mean square deviation varies from 0.005° to 0.6° in the indicated above frequency and amplitude ranges of the test signal.The test measurements of the amplitude-frequency characteristic of the antenna element demonstrated its uniformity no worse than ± 2 dB in the frequency band from 3 MHz to 15.5 MHz. In general, the proposed breadboard system is capable of recording Doppler variations in signals at any frequency in the range of 3 – 15.5 MHz simultaneously on six radio paths.

Conclusions

The characteristics of the developed hardware and software breadboard of passive multiple path multi-frequency and frequency-and-angular radio sounding system using SDR technology allows it to be widely used for monitoring of TIDs caused by powerful non-stationary processes in geospace.

Support was provided by Ukraine state research projects # 0122U001476 and # 0124U000478.

References

[1] M. Chilcote, J. LaBelle, F.D. Lind, A.J. Coster, E.S. Miller, I.A. Galkin, et al., “Detection of traveling ionospheric disturbances by medium-frequency Doppler sounding using AM radio transmissions”, Radio Sci., vol. 50, pp. 259-263, 2015, doi:10.1002/2014RS005617

[2] J. Fišer, J. Chum and J.-Y. Liu, “Medium-scale traveling ionospheric disturbances over Taiwan observed with HF Doppler sounding”, Earth, Planets and Space, vol. 69, 131, 2017, doi:10.1186/s40623-017-0719-y

[3] T. Verhulst, D. Altadill, J. Mielich, B. Reinisch, I. Galkin, A. Mouzakis, et al., “Vertical and oblique HF sounding with a network of synchronised ionosondes”, Adv. Space Res., vol. 60, pp. 1644-1656, 2017, doi:10.1016/j.asr.2017.06.033

[4] B. Reinisch, I. Galkin, A. Belehaki, et al., “Pilot ionosonde network for identification of traveling ionospheric disturbances”, Radio Sci., vol. 53, 2018, doi:10.1002/2017RS006263

[5] X. Huang and B.W. Reinisch, “Real time HF raytracing through a tilted ionosphere”, Radio Sci., vol. 41(5), RS5S47, 2006, doi:10.1029/2005RS003378

[6] V.G. Galushko, V.S. Beley, A.V. Koloskov, Y.M. Yampolski, V.V. Paznukhov, B.W. Reinisch, J. Foster and P. Erickson, “Frequency-and-angular HF sounding and ISR diagnostics of TIDs”, Radio Sci., vol. 38(6), 1102, 2003, doi:10.1029/2002RS002861

[7] H. Nakata, K. Nozaki, Y. Oki, K. Hosokawa, K. K. Hashimoto, T. Kikuchi, J. Sakai, I. Tomizawa and S. Saita, “Software-defined radio-based HF Doppler receiving system”. Earth, Planets and Space, vol. 73:209, 2021, doi: 10.1186/s40623-021-01547-5

[8] Q. Guo, L.F. Chernogor, K.P. Garmash, V.T. Rozumenko and Y. Zheng, “Dynamical processes in the ionosphere following the moderate earthquake in Japan on 7 July 2018”, J. Atmos. and Solar-Terr. Phys., vol. 186, pp. 88-103, 2019, doi: 10.1016/j.jastp.2019.02.003

[9] “GNURadio WindowsInstall”, https://wiki.gnuradio.org/index.php/WindowsInstall

[10] “USRP Hardware Driver and USRP Manual. Binary Installation”, Ettus Research, https://files.ettus.com/manual/page_install.html

C-BAND METEOROLOGICAL RADAR ANTENNA. DESIGN, CALCULATIONS AND THE FIRST MEASUREMENTS

V. Glamazdin, M. Natarov, O. Shubnyi, A. Mogyla

Dept. of physical principles of radiolocation O.Ya.Usikov Institute for Radiophysics and Electronics of the National Academy of Sciences of Ukraine, Kharkiv 61085, Ukraine,
e-mail: m.nataroff@gmail.com, moganat1196@gmail.com

Parabolic antenna system for meteo radar with compact feed system that separate linear polarized signals has been designed. Operation frequency band of antenna is 7-7.5 GHz. The expected level of sidelobes is less than -20 dB. The antanna has a good matching level of all feed ports. Some features of the antenna design and the feed system are presented.

Introduction

This work presents the results of antenna development for use in meteorological radar. The operating frequency band of the radar is 7-7.5 GHz. The feed system consists of a conical horn and polarizer that designed to divide the linearly polarized components of the reflected signal into main polarization and cross polarization channels. Design of the polarizer is described in [1]. The goal of the work was to design an antenna system using a ready-made parabolic reflector with a diameter of D = 1 m and a focal length of F = 540 mm. This antenna system must satisfy the standard requirement for radar antennas that the first side lobes of the radiation pattern less than -20 dB. Design features that allow to achieve these parameters are presented in this work.

The base design and operation features

The general view of the antenna system based on the reflector and the feed with polarizer is presented in the fig. 1.

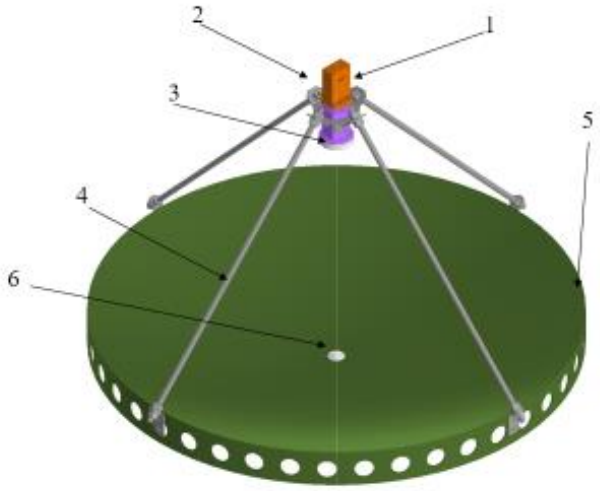

Fig. 1. The base antenna system design. 1 - main polarization; 2 - cross polarization; 3 – feed horn with teflon radom; 4 - mounting rods; 5 - parabolic reflector; 6 – metal cone.

The antenna system is designed according to the prime-focus scheme. Preliminary calculations of construction options, a) according to the two-reflector scheme (Cassegrain) and b) the prime-focus scheme, by methods of geometric optics showed that with a ratio of F/D = 0.54 and D/λ ≈ 23.5, the prime-focus antenna has a lower level of the first side lobes of the radiation pattern. This is due to the smaller blocage of the aperture created by the feed

system, which is placed at the focus of the parabolic reflector, compared to the blocage created by the sub-reflector, in any acceptable variants of the subreflector – feed horn system.

The feed system consists of the conical horn with an aperture of 60 mm and an opening angle of 90° and a compact polarizer attached to it. The conical horn is closed by the teflon radom. All dimensions of the feed system elements are mutually optimized for the best match The waveguide ports of the polarizer are made in opposite directions, above the feed system mounting rods (Fig. 1), to reduce the blocage effect from the waveguides. A compact 90° polarization rotator [2] is connected to port 1 of the main polarization. Thus, connected waveguide is oriented by a narrow wall to the antenna aperture, that minimizes the blocage effect. The waveguide connected to the cross-polarization port 2 has the same orientation. A metal cone is placed in the center of the reflector to improve matching of the feed.

The calculated and measured radiation pattern of the feed horn in the E-plane is presented in Fig. 2a. The measured diagram is somewhat narrowed in the range of amplitude levels from 0 dB to 10 dB, but in directions of angles ±50°, the amplitudes of the theoretical and experimental diagrams practically coincide. This directions are to the edge of the parabolic reflector from the focus. Therefore, it can be assumed that the real pattern of the parabolic antenna will be close to the theoretical one (Fig. 2b)

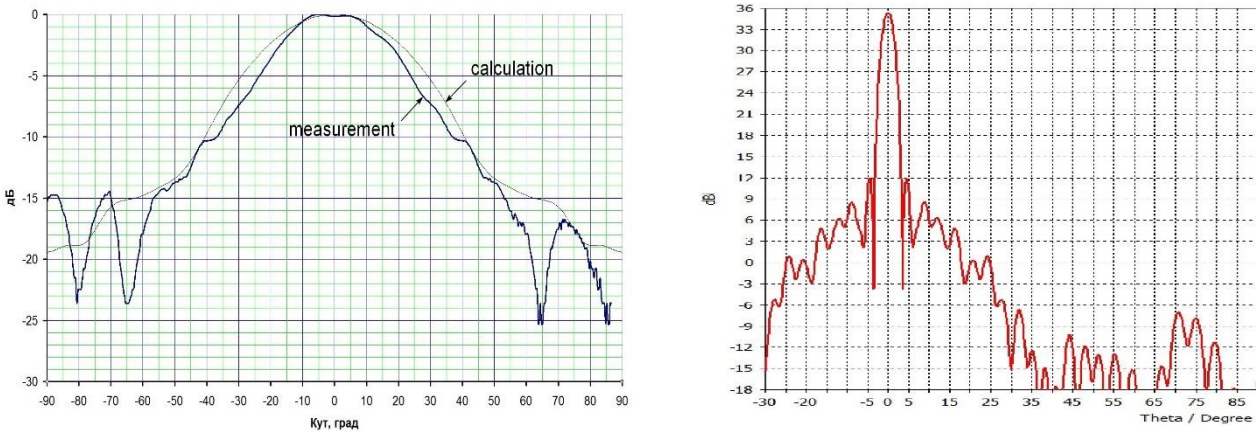

(a) (b)

Fig. 2. Radiation patterns of the feed system and the parabolic antenna.

The calculated gain of the antenna is 35.5±0.2 dB at frequencies of 7.1±0.2 GHz, the level of the first sidelobes does not exceed -23 dB, the width of the radiation pattern at the level of -3 dB is 2.9±0.1°. Calculations of the antenna characteristics were carried out using the COMSOL program.

Conclusions

The development of a parabolic antenna for use in a meteorological radar has been carried out. The antenna is built on the basis of a ready-made parabolic reflector according to the prime-focus scheme with the minimum possible blocage of the aperture due to the minimization of all sizes of the feed system. The necessary characteristics for use as part of a weather radar have been achieved.

References

[1] V. Glamazdin, M. Natarov, O. Shubnyi, A. Mogyla “The Compact Polarization Separator for Weather Radar”, Proceedings of the 19th International conference on electronics and applied physics, APHYS 2023, 18-20 October, 2023, Kyiv, Ukraine.

[2] Kirilenko A.A., Kulik D.Yu., Rud L.A. “Compact 90º twist formed by a double-corner-cut square waveguide section”, IEEE Trans. Microw. Theory Tech. – 2008. - Vol. 56, No 7. - P. 1633–1637

MEASURING THE LEVEL OF HIGH-TEMPERATURE OBJECTS BY ACOUSTIC LOCATION METHOD

A.V. Odnovol

O.Ya. Usikov Institute for Radio Physics and Electronics, National Academy of Sciences of Ukraine,
e-mail: ur3lnh@yandex.com

The work discusses the features of the functioning of location-type acoustic level meters when monitoring the level of high-temperature objects.

The aim of the work is to study the processes in a high-temperature channel of acoustic wave propagation.

Methodology of conducting experiments

Studies of the time dependencies of the amplitude of the reflected signal and the measured time interval proportional to the distance to the controlled surface were carried out in a high-temperature channel "level gauge transmitter-receiver – acoustic environment – high-temperature reflection surface", formed in an open-top cylindrical tank with a height of about 1.2 m. The choice of an open tank was determined by the maximum influence of temperature inhomogeneities in the refractive index of air, arising in a non-standard propagation channel on the amplitude of the reflected signal [1], and its height was determined by the possibility of experimental modeling of natural operating conditions.

High-temperature controlled objects were simulated using two heaters, alternately installed at the bottom of the tank. The temperature of the reflective surfaces of the heaters was about 150^0C and 800^0C. A channel with a controlled surface without a heat source was used as a reference.

To conduct the research, modified acoustic level meter transmitters and receivers [2,3] with operating frequencies of 10 kHz and 20 kHz were used. During the research, for each probing pulse, information about the amplitude of the reflected signal envelope and the time interval proportional to the distance to the reflecting surface were transmitted to the computer. The setting up of experimental studies at two operating frequencies was caused by the need to determine the optimal frequency range for monitoring the level of high-temperature objects.

To study the temporal fluctuations of the envelope amplitude, the correlogram method of spectral estimation [4,5] was used, according to which the spectral power density (SPD) of a discrete random stationary process is defined as:

$$P(f) = T \sum_{k=-L}^{L} r[k] \exp(-j2\pi fkT), -1/2T \le f \le 1/2T,$$

where f - is the frequency, T - is the sampling period, $r[k]$ - is the correlation function of the random process under study, the estimate of which can be calculated from the available finite sample of process data $x[n]$, $n = \overline{0,..N-1}$

In order to study the influence of processes occurring in a high-temperature propagation channel on the magnitude of the reflected signal amplitude for both operating frequencies, estimates of the PSD of the envelope amplitude fluctuations were found for three different cases:

- case I - no heat source;
- case II - presence of a medium power heat source (150^0C);
- case III - presence of a powerful source (800^0C).

The SPD estimates were found from data records with a length of 2000-5000 readings, which for a level meter probing pulse repetition period of 0.9 seconds corresponded to an observation time of 30-75 minutes.

Research results

Fig. 1 shows an example of the time dependence of the measured signal delay time. $t_{zad}[n]$, reflected from the controlled surface, at an operating frequency of 20 kHz for case II. The ordinate axis in this figure shows the values of the delay time of the reflected signal, proportional to the distance to the controlled surface in internal time units (i.e.u.), and the abscissa axis shows the numbers of readings. From the data in Fig. 3 it is evident that the delay time of the reflected signal (1200 i.e.u.) basically corresponds to the actual distance to the controlled surface. However, there were cases of short-term absence of the reflected signal (0). There were also situations when the measured time interval (2400 i.e.u.) corresponded to approximately double the distance to the controlled surface.

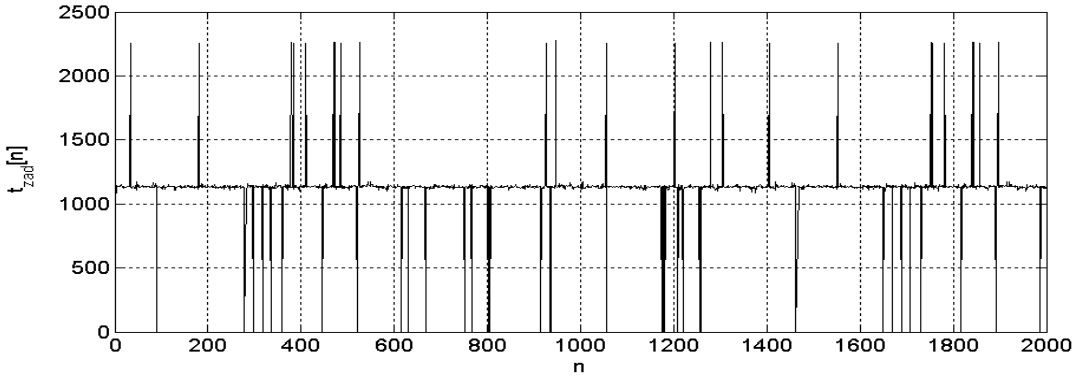

Fig. 1. Measured signal delay time

The first case (0), when the reflected signal is absent or its amplitude is below the set threshold, should be identified in the level meter processing unit as a failure of the transceiver.

The second case corresponds to a situation in the propagation channel in which the amplitude of the first reflected signal was below the established threshold, and the amplitude of the signal that passed through the channel under study twice exceeded the detection threshold of the useful signal. In this case, the processing unit must make a decision that the distance to the controlled surface is approximately twice the actual distance.

In addition, there were short-term situations in which the time delays of the reflected signal could be in the range (0.5-1.5). It should be noted that during the process of in-kind monitoring of the bitumen level at a temperature of the monitored surface of about 270^0C, similar short-term failures and jumps in level readings were observed at an operating frequency of 10 kHz.

References

[1] P. Stoica, R.M. Moses. Introduction to Spectral Analysis. New Jersey 1997, 319 p.

BIPOLAR LC-OSCILLATOR AS AMPLITUDE AND FREQUENCY MODULATOR

Bohdanov R.V.

Faculty of RadioPhysics, Electronics and Computer Systems, Taras Shevchenko National University of Kyiv, 64/13, Volodymirska Str., City of Kyiv, Ukraine, 01601,
e-mail: semsterfx2@gmail.com

Scheme of universal amplitude (AM) and frequency (FM) modulator based on the Peltz bipolar LC-oscillator [2] proposed. It contains a minimum of additional components and can be used in a laboratory workshop on radio electronics.

Scheme of the modulator

The "bipolar" LC-oscillator (Fig.1(a)) given in the article by Peltz G. [2] can work with various parallel and series oscillating LC-circuits. Transistors Q1 and Q2 with same conductivity type, when connected on such way, have a negative galvanic feedback through resistor R1 and positive feedback through an oscillating circuit L1L2C1D1. The amplitude of one of the half-waves of quasiharmonic oscillations in L1L2C1D1 circuit is limited by the drop on the base-emitter diode of the transistor Q2 and resistance R1, and the second on the base-collector diode of the transistor Q1. Thus, in this ocsillator, the amplitude remains at the level of 0.8-1.4 V [1, 2, 3]. So the noticed easiest way to obtain an amplitude modulation (AM) is changing of an supply voltage at R1 (Fig.1(a)) according to low frequency of an informational signal (V8), which became possible in lower schematic stage of a switch S1 (Fig.1(a)).

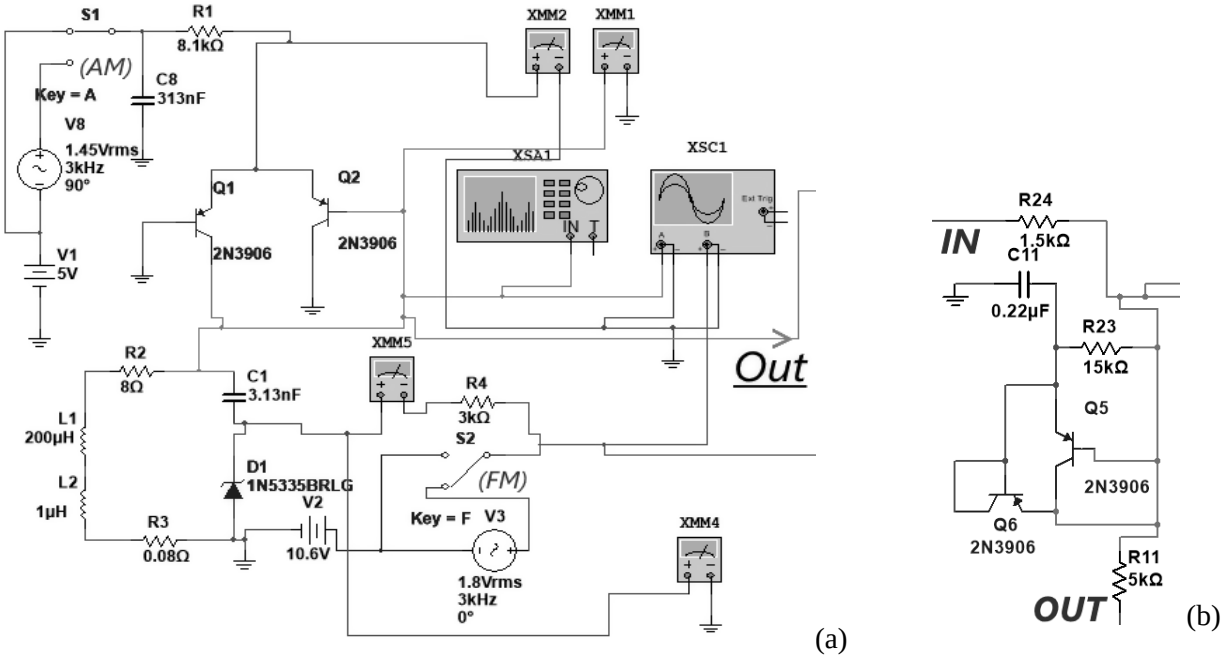

Fig. 1. Principal scheme of bipolar LC-oscillator [2] with curcuits for amplitude (AM) and frequency (FM) modulations of high frequency otput signal: (a) – switches S1 and S2 are in FM-mode; (b) – variant of parallel diodes amplitude limiter at output of additional amplifier (not shown) for removing of an parasitic AM in an FM-mode

Frequency modulation (FM) was achieved by variation of the barrier capacitance of reversely biased (closed) p-n junction of the Zener diode D1. The bias voltage contains constant voltage V2 and alternating voltage V3, connected through the switch S2 (Fig.1(a)). Also the scheme contains other optional parts like amplifier for increasing of output signal amplitude and amplitude limiter Fig.1(b), which seriously reduces of a parasitic AM (Fig.2(c(2))).

Simulation results

So, simulations in NI Multisim demonstrated that variation of bias voltage V2 can non-linearly variate output frequency (Fig. 2(a)) and output voltage of the modulator (Fig.2(b)). Output FM signals are shown at Fig.2(c), as spectrum of better of them at Fig.2(d). Output FM signal demonstrated spectra noticeable difference to AM ones at this universal modulator.

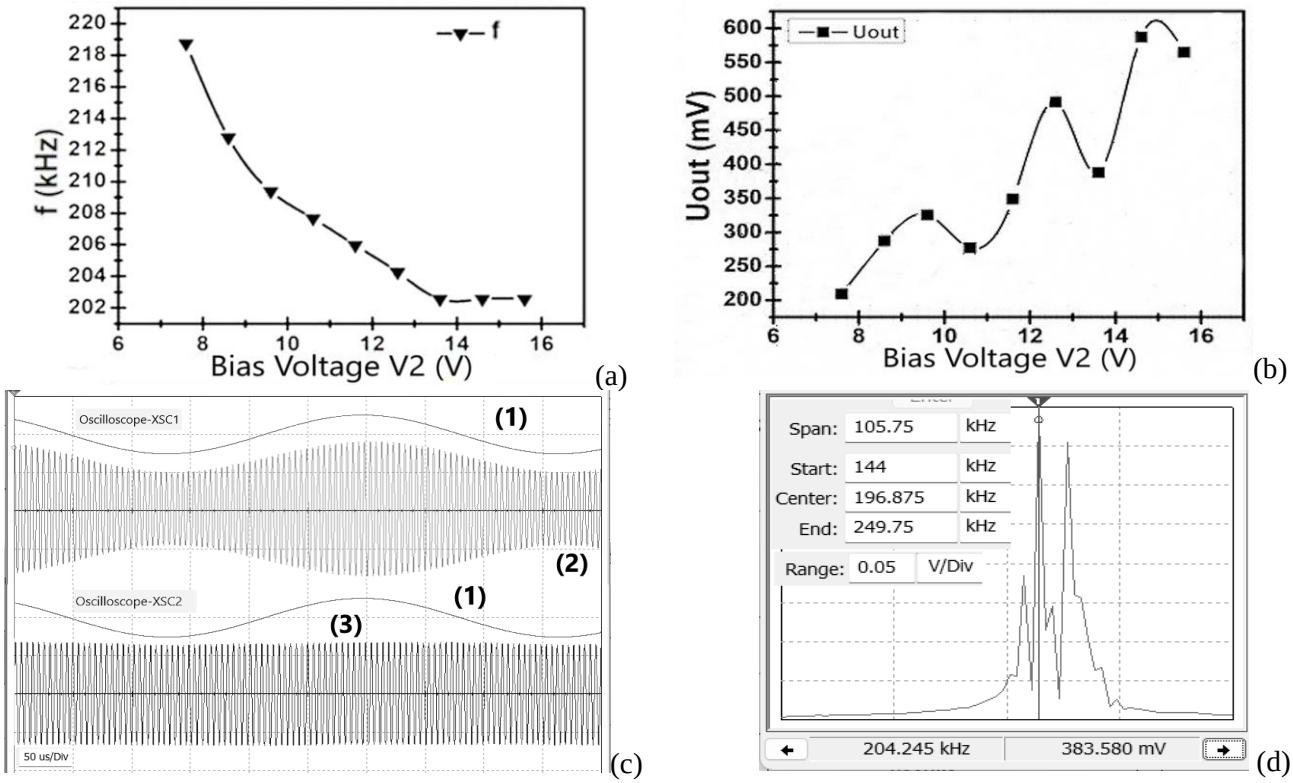

Fig. 2. Simulation results: (a) – output frequency and (b) voltage vs. diode D2 bias voltage V2; (c) – FM-mode signals ((1) input low-frequency voltage V3, (2) output FM with parasitic AM (see Fig.1(a)), (3) – clear FM after amplitude limitation (see Fig.1(b))); (d) – spectrum of output FM signal with amplitude limitation.

References

[1] Bohdanov R.V. Detection and restoration of digital information signal from amplitude shift keying (ASK) radio signal with stochastic noise-like carrier / R.V. Bohdanov. // Proceedings of the XIX international scientific conference Electronics and Applied Physics 'APHYS 2023' October 17-21, 2023, Kyiv, Ukraine, Taras Shevchenko National University of Kyiv, Faculty of RadioPhysics, Electronics and Computer Systems. – 2023. – P. 83–84.

[2] Peltz G. LC-Oszillator für (fast) beliebige L/C-Verhaltnisse / Günter Peltz. // Funkschau. – 1978. – №18. – C. 898.

[3] Rasulova I.V. Stochastic noise LC-oscillator in very low frequency (VLF) electromagnetic digital data transmission channel / Rasulova I.V., Bohdanov R.V. // Abstracts of the seventh (XXII) International Young Scientists Conference on Applied Physics, May 24-27, 2022, Kyiv, Ukraine, Faculty of Radio Physics, Electronics and Computer Systems, Taras Shevchenko National University of Kyiv. – 2022. – P. 47–48.

MULTY FREQUENCY REMOTE SENSING SURFACE OF WATER AND OIL FILMS IN CRITICALLY SMALL SIZED TANK

Uzlenkov A.* Lyubitsky A.*

**A.Usikov Institute Radio Physics and Electronics, National Academy of Science of Ukraine, 12, Academician Proskura St., Kharkiv 61085, Ukraine, e-mail: alexandruzlenkov@gmail*

Remote sensing (RS) in situ is an expensive research that does not guarantee success. Partially the problem solves computer modeling. However, models do not take into account unknown or poorly studied mechanisms. Some subtle mechanisms of in situ are masked by more powerful processes. Studies conducted in critically small tank (the dimensions are comparable with the longest waves) are useful with multi -frequency sounding made it possible to clarify some features of inter -wave interaction, scattering EMF waves, transforming the signals of signals scattered in the bonds of the film.

Wave generation in the small tank

The generation of gravity (GW), gravity-capillar and capillary wind waves (W) in a critically small tank requires specific equipment and has some features and restrictions on frequency and amplitude [1]. The most effective frequency range in the tank is 1.7-5Hz. At higher frequencies, due to interference the harmonic coefficient, SWR, and "three -dimensionality" of waves increase. A feature of the excitement generated in the laboratory complex is the absence of development. Waves spectra are decrease in accordance the approximations $1/\omega^4$ and $1/\omega^{\frac{7}{3}}$ in agreement with the gravitational-capillary part of the Kitaygorodsky-Toba spectrum [2]:

$$S_{\Gamma KB}(\omega) \cong \alpha_g \cdot u_* \cdot g \cdot \omega^{-4},$$

where $\alpha_g(u_*) = 0.02 - 0.024$ with $u_* = 60$ м/с; ω – wave circular frequency. The spectra of two scale waves (TSW) with GW at frequency 2.3Hz are shown in Fig. 1.

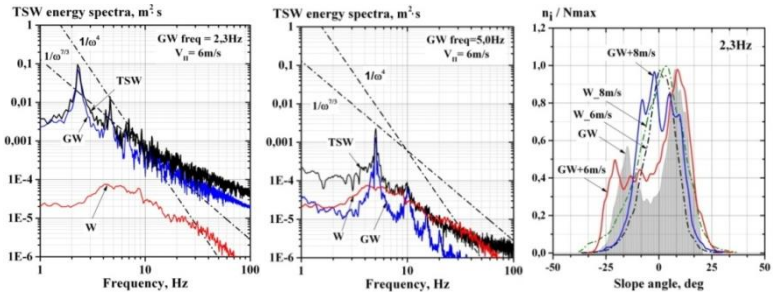

Fig. 1. TSW waves energy spectra and their components (GW, W), histograms of their slope angles

Remote sensing of pure water

Five-channels radar was used for RS (MM, CM, DM). Backscattered EMF contains Bragg and non-Bragg components forming by scatterers with different nature [3]. Therefore, processing of spectra includes smoothing, normalizing and using the method of decomposition of spectra in the system of three spectral lines in accordance with their nature [4]. The base of this system is formed by Gauss, Lorentz and Voigt (G, L, V) spectral lineshapes: $S_i(f) = K_i\hat{S}_i(f)$, $i = G,\ L,\ V$, where $\hat{S}_i$– form-factors of the spectral lines ($\hat{S}_{i_{max}} = 1$), K_i – weight coefficients [5]. The measurement results confirmed the correspondence processes in the tank and in situ in certain range of wind speed and GW amplitude. Anomalies in TSW spectra were detected with GW growth. An abnormal decrease in the maximum of spectra and displacement in the high -frequency area occurred. To explain this help method of

decomposition and the theory of the "fast" three wave nonlinear interaction of decimeter and capillary waves (see Fig. 2.) [6].

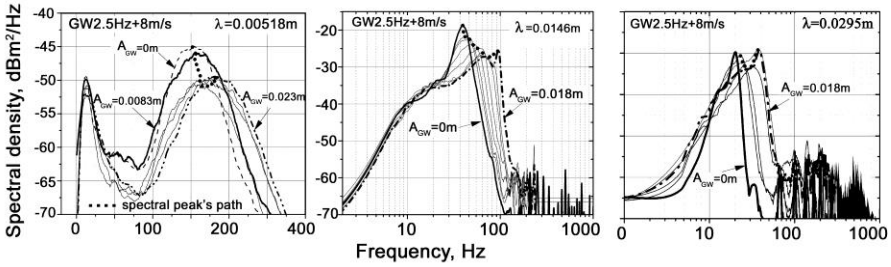

Fig. 2. Anomalous spectral signatures of TSW transformations with GW growth

Remote sensing of oil film

The laboratory tank was equipped by special system of oil film generation and stabilization. The system provides stability of the film for a certain time, then the film requires renovation. The parameters of the film are calculated by a certain method were confirmed by contact measurements. The radar contrast created by it is close to the theoretical.

Deviations of the frequency parameters of the spectra from the theoretical ones were noted. They are in the growth of central Doppler frequencies in the presence of films (see Fig. 3a.). The causes of the seeming anomalies are explained using the decomposition method: in the presence of the film, the spectrum energy is redistributed between the scatterers with different nature (see Fig. 3b.).

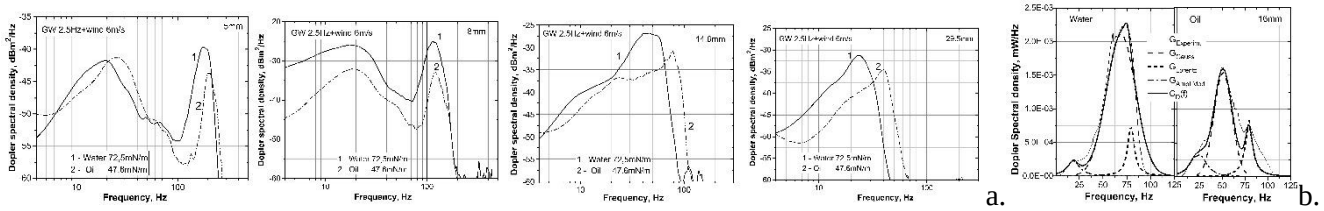

a. b.

Fig. 3. Doppler spectra of pure water and oil film (a), example of decomposition (b)

References

[1] A. V. Uzlenkov and A. A. Lyubitsky, Remote Sensing in the Wave Complex with Critically Small Sizes: Properties of the Waves under these Conditions, *J. Telecommunication and Radio Engineering*, vol. 81, no. 4, pp. 1-15, 2022.

[2] I. N. Davidan, L. I. Lopatukhin and V. A. Rozhkov, *Wind Disturbance in the Ocean*, Leningrad: Hydrometeoizdat, pp. 32-35, 1980.

[3] P. H. Y. Lee, J. D. Barter, K. L. Beach, C. L. Hindman, B. M. Lake, H. Rungaldier, Thompson, H. R. Jr., and Yee, R., Experiments on Bragg and Non-Bragg Scattering Using Single-Frequency and Chirped Radars, *J. Radio Science*, vol. 32, no. 5, pp. 1725-1744, September-October, 1997.

[4] M. B. Kanevsky, and V. Yu. Karayev, Spectrum of Radar Signal Reflected by Sea Surface, *J. Izv. Vuz. Radiophysics*, vol. 36, no. 1, pp. 3-15, 1993.

[5] V. A. Dulov, Weakly Linear Energy Transfer in the Gravitational-Capillary Interval of Surface Waves. Influence of Spectrum Form, *J. Marine Hydrophysical Journal*, no. 1, pp. 21-31, 2001.

[6] V. G. Polnikov, Nonlinear Three-Wave Interactions in the System of Gravity-Capillary Waves on Water, *J. Izv. vuz. RAS., Physics of the atmosphere and ocean*, vol. 41, no. 2, pp. 253-266, 2005.

MICROSTRIP SUPERCONDUCTING RESONATOR WITH A NONLINEAR LUMPED ELEMENT IN THE FORM OF A CONSTRICTION

O.A. Kalenyuk*,, S.I. Futimsky*,**, A.P. Shapovalov*,**,**

** G. V. Kurdyumov Institute for Metal Physics, N.A.S. of Ukraine, Kyiv, 03142, Ukraine,*
e-mail: oleksii.kaleniuk@gmail.com
*** Kyiv Academic University, Kyiv, 03142, Ukraine*

We study the nonlinear response of two niobium superconducting microstrip resonators, one of which contains a small length constriction in the center of the microstrip line to increase the microwave current density. This constriction leads to sharp dips in the amplitude-frequency characteristic. Analysis conducted using ABCD matrix-based modeling showed that the cause of the dips is the formation of temperature domains in the constriction that transition to the normal state, with these domains increasing in size as the current in the resonator increases.

Introduction

Superconducting resonators are widely used in various devices, such as kinetic inductance detectors (MKIDs) [1], rf SQUIDs, filters, single-photon detectors, and so on. The high quality factor is the main advantage of a superconducting resonator compared to resonators made from conventional metals. The resonance frequency and quality factor of a superconducting resonator depend on the concentration of superconducting pairs. The characteristics of the resonator can change under the influence of various factors, such as the amplitude of the microwave current. As a result, the amplitude-frequency characteristic of the resonator becomes nonlinear. The nonlinearity effect can present both negative aspects, such as the appearance of harmonic distortions, and positive ones, such as a shift in resonance frequency due to photon absorption (as in MKIDs). The maximum change in characteristics occurs when the superconductor transitions to a normal state. Therefore, in single-photon detectors, a current close to the critical current is applied to a narrow superconducting bridge. This study investigates the nonlinear response when the critical microwave current density is reached in the constriction of the microstrip line at the center of the resonator.

Experiment, Modeling, Result and Discussion

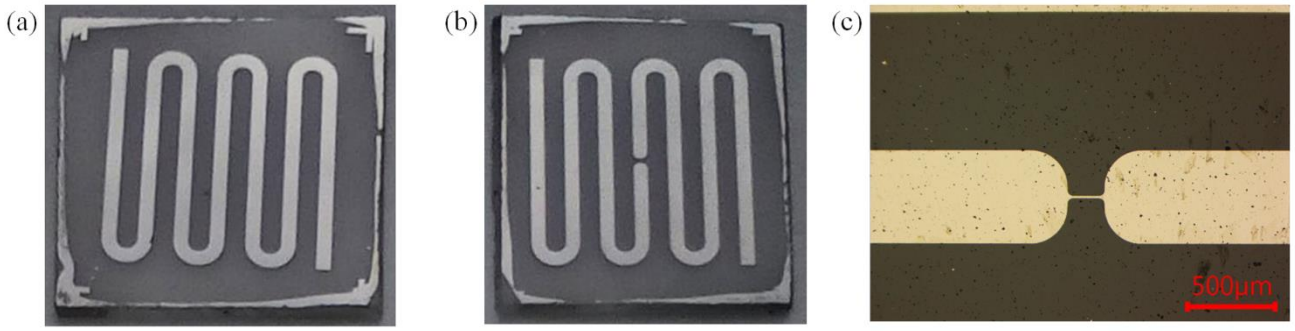

Fig. 1. Meander resonators without (a) and with strip constriction (b), enlarged image of the resonator strip constriction (c).

Thin (100 nm) niobium films were deposited onto two polycrystalline Al_2O_3 substrates, each 0.5 mm thick, using magnetron sputtering. Using standard lithography, two microstrip resonators were etched from these films, each with dimensions of 8x8 mm (Fig. 1(a) and 1(b)) and a line width of 500 μm. One of the resonators featured a constriction in the microstrip line with a length of 140 μm and a width of 12 μm (Fig. 1(c)). The resonators were connected to microwave lines via capacitive couplings. Measurements using the two-port method revealed dips in the amplitude-

frequency characteristics of the resonator with the constriction (Fig. 2 b), which are typical when a part of the resonator undergoes a sharp transition from the superconducting to the normal state, forming a resistive thermal domain. Since the constriction is 42 times narrower than the main line, the domain formation occurs precisely in the constriction. To analyze the amplitude-frequency characteristics, an ABCD [2] matrix-based model was used. A similar constriction in a microstrip transmission line has already been studied in the work [3]. Unlike in a transmission line, the domain size significantly affects the current in the resonator, which, in turn, changes the domain size. Thus, the system exists in a quasi-equilibrium state, where the domain sustains the current necessary to maintain itself. Therefore, an iterative approximation method was used to determine the microwave response of such a resonator. The essence of the method lies in gradually reducing the current until the system reaches equilibrium. The following rules were applied in the simulation: the microwave current never exceeds the critical current in the constriction; the reduction of the supercritical current occurs due to the increase in the size of the resistive domain in the constriction; and the size of the resistive domain has a finite value. Figure 2(c) shows the simulation results of the nonlinear response, which demonstrated acceptable agreement with experimental data. The critical current in the constriction was found to be 80 mA, corresponding to a critical current density of 6.7×10^{10} A/m², which is a standard value for niobium. Thus, local nonlinearity is realized in the constriction, leading to sharp dips. The resonator without the constriction exhibited a distributed nonlinear response, with a shift in the resonance frequency and a decrease in quality factor as the current in the resonator increased (Fig. 2(a)).

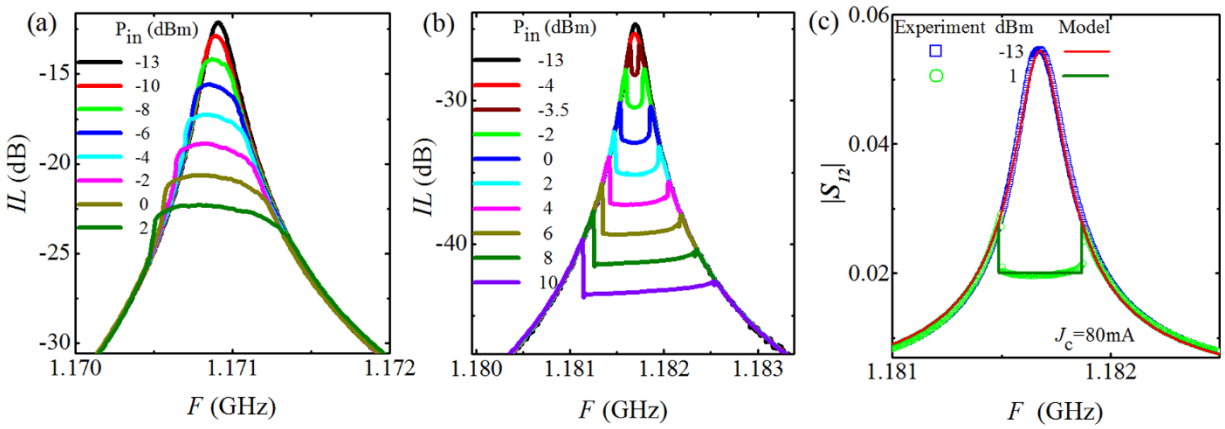

Fig. 2. Experimental amplitude-frequency characteristics at different P_{in} power levels for resonators without (a) and with (b) a constriction;calculated (solid curve) and measured (points) amplitude-frequency characteristics of the nonlinear response (c).

Acknowledgments

This research was carried out within the framework of the project 2023.04/0157 funded by the National Research Foundation of Ukraine «High-speed matrix kinetic detector of long-wave infrared radiation».

References

[1] C. Zhang, W. Xie, C. Li, J. Dai, Y. Yuan, R. Jiang, X. Wang, J. Wang, Y. Wu, L. Sun and Y. He, "Recent progress on high-temperature superconducting filters," Superconductivity, vol. 2, Jun. 2022, Art. no. 100012.

[2] J. F. White, *High Frequency Techniques: An Introduction to RF and Microwave Engineering.* Hoboken, New Jersey, USA: John Wiley & Sons, Inc., 2004.

[3] A. A. Kalenyuk, "Nonlinear microwave response of a superconducting $YBa_2Cu_3O_{7-\delta}$ microstrip transmission line with a constriction," Low Temp. Phys., vol. 35, pp. 105–111, Feb. 2009.

POLARIZATION-SPECTRAL SIGNATURES OF SIGNALS SCATTERED BY SURFACE OBJECTS IN THE CENTIMETER AND MILLIMETER WAVE RANGE

Yi-yang Luo, V.I. Lutsenko, I.V. Lutsenko, O.V. Soboliak, S.O. Masalov

O.Ya. Usikov Institute for Radiophysics and Electronics of the National Academy of Sciences of Ukraine, 12 Ac. Proskura st., Kharkiv, 61085, Ukraine, e-mail: yiyangluo@163.com; vladislavlutsenko@ukr.net; irene-lutsenko@ukr.net; sobolyak@ukr.net; s.masalov.2020@gmail.com

There are many articles devoted to the recognition of various classes of objects by radar information, which consider the features of the spatio-temporal distribution of reflecting points, frequency dependences of the backscattering indicatrices of objects and their spectral portraits. Significantly fewer works are devoted to the use of polarization scattering matrices. This article considers the possibility of using polarization-spectral features to solve detection and recognition problems.

Equipment

The experiments were conducted using millimeter-wave measuring systems in pulsed (4.3 cm, 2 cm, 8 mm and 4 mm wavelengths) and continuous (10 cm, 3 cm, 8 mm and 4 mm wavelengths) radiation modes [1]. The polarization characteristics of pulse radars were studied by switching the reception polarization from pulse to pulse using p-i-n attenuators at an 8 mm wavelength and a ferrite switch based on the Faraday effect at a 4 mm wavelength with radiation of inclined at an angle of 450 or vertical polarization. The isolation between the channels of orthogonally polarized components was at least 25 dB with direct losses on the switches of no more than 3.5 dB at an 8 mm wavelength and 5 dB at a 4 mm wavelength. For measurements with continuous monochromatic radiation the following were used: a three-frequency homodyne polarimeter with wavelengths of 10 cm, 8 mm and 4 mm; a two-frequency polarimeter with wavelengths of 3 cm and 8 mm. In addition, a polarimeter with a wavelength of 8 mm and with tone frequency modulation of the emitted signal was used. with channel decoupling of orthogonally polarized components no worse than 25 dB. Polarization selectors were developed to isolate orthogonal components of the signal [2, 3]. The study of signals reflected from surface and ground objects made it possible to formulate the classification features listed below for each class of objects.

Research results

Boats and motorboats, ships. In the reflection spectrum, the hull line predominates over other components. The operation of the propulsion system and disturbances of the water surface, manifested in the form of a breaker and a wake, lead to the appearance of additional spectral components in the reflected signal, located above and below the spectral line of the hull. There are spectral lines caused by the operation of the propulsion system, which lead to phase modulation of the scattered signal due to vibration of the hull. Shortening the operating wavelength leads to an increase in the phase modulation index of the signal, and, as a consequence, to an increase in the level of spectral components - Fig. 1. Disturbances of the water surface by the hull of the object lead to the emergence of ship waves, the scattering of which lies in frequency below the spectral line of the hull. A high level of correlation (more than 0.7) of the spectral components of the signal caused by vibration of the hull of the surface object of the ship both at different radiation frequencies and reception polarizations is characteristic.

Yachts, windsurfing. Changes in the average intensity of the reflected signal and the Doppler frequency shift are observed when changing course and shifting the sail. The current spectra also show the presence of a dominant spectral line of the hull.

Rowing boats. The periodicity and correlation of the Doppler frequency shift and scattered signal amplitude are governed by the stroke rate. In the current spectra, high-frequency "flashes" above the hull line correspond to the oars' movement during the air phase of preparation for the stroke. At high frequency resolution (< 1 Hz), the spectra exhibit linearity, with line spacing equivalent to the stroke frequency.

Transport vehicles. It should be noted that the amplitude fluctuations and the Doppler frequency shift are uncorrelated. The current spectra are characterized by the presence of lines of translational motion of the hull and components caused by vibration from the running engine.

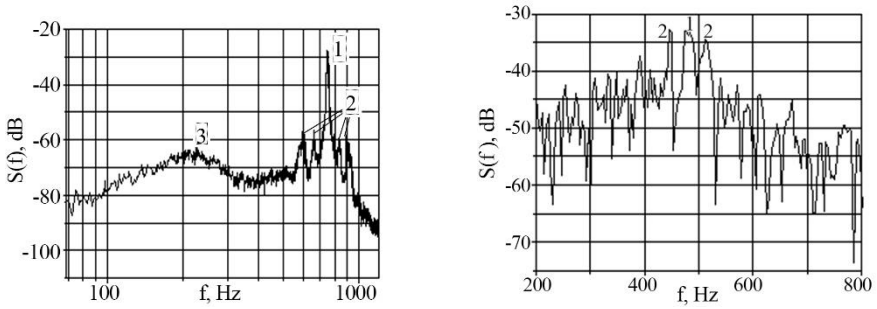

Fig. 1. The influence of hull vibrations on the spectrum of the ship's echo signal: 1-hull line; 2-spectral lines associated with vibration; 3-reflections from ship waves, a) λ = 4 cm "Kometa", b) λ = 0.4 cm hydrographic ship.

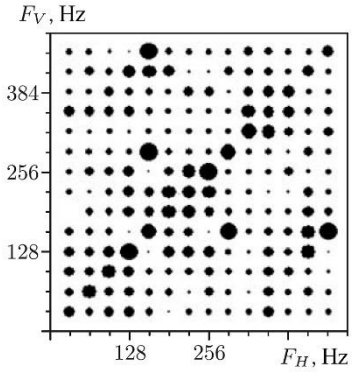

Fig.2. Matrix of correlation coefficients of orthogonal components of the Doppler spectrum of reflections from a ship.

All types of land and surface targets are characterized by a high correlation of signals reflected on different polarizations and a small width of the main spectral line of the hull (≈1–3 Hz). Intraspectral relationships of reflections from objects on orthogonal polarizations were studied, with the data presented in the form of matrices of mutual correlation coefficients of various spectral components (Fig. 1), in which the dimensions of the graphic element are proportional to the value of the correlation coefficient. It was found that for all types of vehicles, the highest correlation values (≈0.5–0.85) correspond to diagonal elements caused by hull lines and components due to vibrations (Fig. 1), as well as matrix elements that correspond to their combinations. The width of the high correlation region when shifted from the diagonal elements for signals of all considered types of objects does not exceed tens of Hertz. The high level of correlation of identical components, signals scattered by surface and land objects on orthogonal polarizations and the weak correlation of components of reflections from the sea surface and land areas covered with vegetation, allows us to conclude that their joint processing is appropriate when solving the problem of detection and selection.

References

[1] V.F. Kravchenko, V.I. Lutsenko, I.V. Lutsenko, Scattering of radio waves by the sea and the detection of objects on its background. Moscow: Fizmatlit, 2015, 448 p.

[2] I.I. Deineka, V.I. Lutsenko, M.S. Yanovsky, “Polarization separator”, USSR Author's Certificate No. 1450016 for application No. 4182804/24-09, 16 Jan. 1987.

[3] I.I. Deineka, V.I. Lutsenko, V.G. Sugak, M.S. Yanovsky, “Polarization Separator”, USSR Author's Certificate No. 17359445, 22 Jan. 1992.

CORRELATION OF SPECTRAL COMPONENTS OF INTERFERENCE TO ACTIVE-PASSIVE DECAMETER RANGE RADIO SYSTEMS FROM HF BROADCASTING STATIONS

Yi-yang Luo*, V.I. Lutsenko*, I.V. Lutsenko*, O.V. Soboliak*, Nguyen Xuan Anh**

**O.Ya. Usikov Institute for Radiophysics and Electronics of the National Academy of Sciences of Ukraine, 12 Ac. Proskura st., Kharkov, 61085, Ukraine,*
e-mail: yiyangluo@163.com; vladislavlutsenko@ukr.net; irene-lutsenko@ukr.net; sobolyak@ukr.net
***Vietnam Academy of Science and Technology, Vietnam, F8, 18 Hoang Quoc Viet Str., Cau Giay Dist., Hanoi, Vietnam, e-mail: nxuananh05@gmail.com*

Using the proposed apparatus of correlation matrices of spectral components (CMSC), the intraspectral correlation of interference to active-passive systems of the decameter range from HF broadcasting stations was experimentally studied. It was shown that high correlation is characteristic only of the same spectral components. The appearance of nonlinear distortions in the path leads to the appearance of high correlation between harmonics of the same frequencies.

Introduction

Recently, significant interest has been shown in active-passive radar systems that use radiation from existing ground-based and space-based systems for illuminating the environment. The use of HF broadcasting stations for illuminating the ionospheric wave allows detecting airborne objects at distances of thousands of kilometers from the illumination station, which increases the stealth and survivability of such systems. For decameter-range waves (10–100 m), the sizes of detected aircraft lie in the resonance region. Their RCS can reach from hundreds to thousands of square meters and cannot be reduced even when using Stealth technology, which facilitates their detection. However, up to now, data on the statistical characteristics of the illumination signals, which act as interference to reflected target signals, are extremely limited. In the synthesis of multichannel detection systems, it is of interest to study the statistical relationships between signals of different channels. For target type recognition systems, it is important to know the statistical relationships between active-passive systems are used to illuminate the environment and are interference for secondary fields scattered by the target. It is of interest to study the intra-spectral correlation relationships in the illumination signals. The goal of the work is an experimental study of the CMSC interference to active passive radars created by HF broadcasting stations.

Correlation matrices of spectral components

Let there be a signal $S(t)$ and its windowed Fourier transform on a time segment of duration T. To study the correlation links, the matrices of the correlation coefficients of the spectral components of the CMSC proposed in [1, 2] were used:

$$\rho(F_i,F_j)=\frac{\left\langle S(F_i,t)S(F_j,t)\right\rangle_t-\left\langle S(F_i,t)\right\rangle\left\langle S(F_j,t)\right\rangle_t}{\sqrt{\left(\left\langle S^2(F_i,t\right\rangle_t-\left\langle S(F_i,t)^2\right\rangle_t\right)\left(\left\langle S^2(F_j,t)\right\rangle_t-\left\langle S(F_j,t)\right\rangle_t^2\right)}},$$

where $S(F_i,t)$, $S(F_j,t)$, $\rho(F_i,F_j)$ are the spectral density at F_i and F_j frequencies at time t and the coefficient of their mutual correlation, respectively.

The study of the coefficients of mutual correlation of various spectral components allowed us to reveal the presence of a highly correlated region in the spectrum of broadcast station signals. Fig. 1 shows the matrix of correlation coefficients of spectral components $\rho(F_i,F_j)$ at frequencies F_i, F_j at various gains and receiver operating modes. It is evident that the diagonal elements have the highest correlation. When shifting from the diagonal, the correlation coefficient drops sharply. The presence of nonlinear distortions in the receiver path (Fig. 1b) leads to the appearance of harmonics in the spectrum, which in turn manifests itself in the appearance of correlation sections corresponding to these harmonics, i.e. additional correlation diagonals can be used to estimate the degree of nonlinear distortions of the signal in the path.

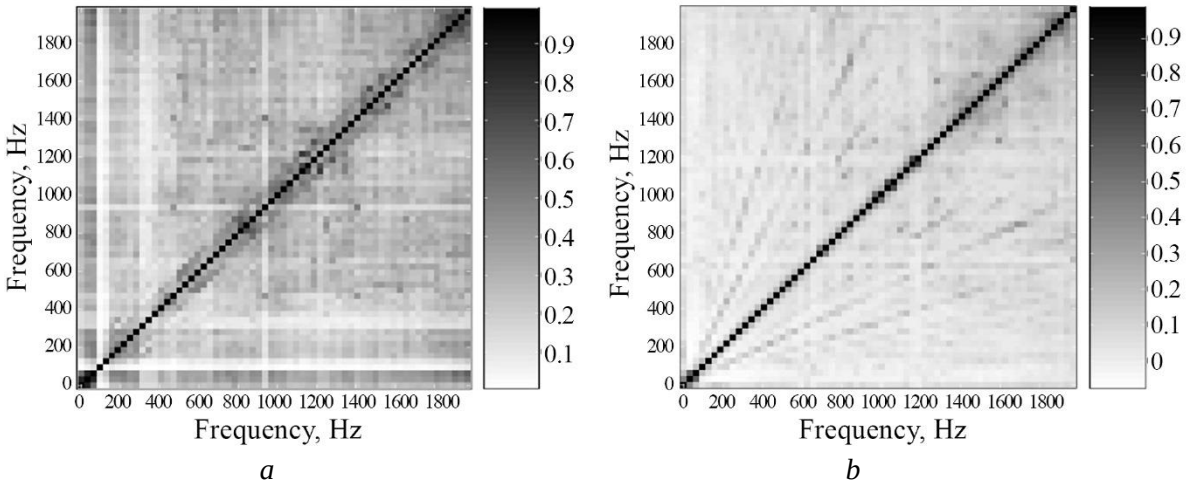

Fig. 1. Matrices of correlation coefficients of spectral components for the Kashi backlight station, China with a range of 3302 km, a power of 500 kW in telegraph (a) and telephone (b) modes.

Conclusion

1. It has been established that between the carrier and the information signal for HF and VHF broadcast stations there is a spectrum section with a spectral density level significantly lower than that of the carrier and information components of the spectrum. It extends to approximately 50...60 Hz relative to the carrier. For HF broadcast radio stations, these frequencies correspond to the Doppler frequency shifts of signals reflected from airborne objects moving at speeds of up to 2500 km/h. At frequencies of 8...60 Hz, the spectral density level is approximately 15...30 dB lower than the spectral density level of the useful signal in the band (100...4000) Hz. In relation to the total power of the useful signal, the spectral components in the band 8...60 Hz with a frequency resolution of 8 Hz are approximately 30...40 dB lower.
2. In the spectral component correlation matrices, the highest correlation is between identical spectral components, i.e. diagonal elements. The appearance of additional elements with high correlation at harmonic frequencies indicates the presence of nonlinear distortions in the path and can be used for its monitoring.
3. Filtering the signal in the Doppler frequency band 0…70 Hz allows to weaken the interference at the expense of the information speech signal by approximately 30-35 dB. In this case, the degree of non-Gaussianity of the process increases significantly by several times. This leads to an increase in the signal-to-noise ratio losses during detection, arising due to the non-Gaussianity of the interference.
4. The spectra of interference created by the emissions of broadcasting stations can be approximated by fractal dependencies with an exponent, for both the low-frequency and high-frequency sections of the spectrum $1.6<n<2.3$.

References

[1] I.V. Lutsenko, I.V. Popov, V.I. Lutsenko “Bistatic Radars with Illumination by Ionospheric Signals of High-Frequency Communication Stations”, Telecommunications and Radio Engineering. 2008, V. 67, № 4, pp. 285-292. DOI: 10.1615/TelecomRadEng.v67.i4.10

[2] Lutsenko V.I., Lutsenko I.V. & Popov I.V. “Illumination of the Air Environment Using Radiation of HF Broadcast Stations”, Radiophysics and Quantum Electronics. 2015, Vol. 58, P. 9–18. DOI: 10.1007/s11141-015-9576-3

USING DIELECTRIC COATINGS IN MILLIMETER AND SUBMILLIMETER WAVE DEVICES TO INCREASE GENERATION POWER

Yi-yang Luo [*], O.V.Kryvenko[*], V.I.Lutsenko[*], S. O. Masalov[*]

[*]*O. Ya. Usikov Institute for Radiophysics and Electronics of the National Academy of Sciences of Ukraine, 12 Ac. Proskura st., Kharkiv, 61085, Ukraine,*
email: yiyangluo@163.com; talvi@ukr.net; vladislavlutsenko@ukr.net; s.masalov.2020@gmail.com

Introduction

Backward-wave oscillator (BWO) and diffraction radiation generators (DRG) are widely used in various fields of radio physics and radio engineering [1,2]. It is known that the intensity of the electromagnetic wave, which propagates along the periodic slow-wave system (PSS), decreases exponentially with distance from its working surface. In this regard, the distributed interaction of electrons in backward-wave tubes of the Optical-BWO (O-BWO) type - carcinotrons is carried out with a high-frequency field that is non-uniform across the thickness of the ribbon electron flow. The presence of pulsations of a layer depleted in the number of charged particles in the formed tape electron flow, as well as a weak impedance of the coupling of the field of space charge waves and the wave of the first negative spatial harmonic of the electromagnetic field of the PSS of the "comb" or "counter pins" type, contributes to a significant decrease in the output power of O-BWO -carsinotrons in the terahertz frequency range. The remaining layers of charged particles interact with the electromagnetic field, the intensity of which exponentially decreases with distance from the working surface of the PSS. That is, in O-BWO -carsinotrons, the tape electron flow interacts with a high-frequency field that is non-uniform in intensity across the thickness of the electron tape. In this regard, with shortening the length of the working wave, the requirements for a significant decrease in the thickness of the electron flow tape and an increase in the density of its current increase. These requirements bring the terahertz frequency range O-BWO -carsinotrons to the technological limit of their implementation. Similar problems arise in DRG.

O-BWO and DRG of millimeter and submillimeter range

To overcome this contradiction, backward wave tubes, klinotrons, were created in the millimeter wave range. Klinotrons are backward wave tubes of the O type (O-BWO) with a ribbon electron flow, which is incident at an acute angle on the surface of a periodic slowing structure - a comb. The generation of increased oscillation power is due to the fact that the ribbon electron flow in the klinotron falls on the working surface of the periodic slowing structure - a comb at an acute angle α, which ensures effective interaction with the intense high-frequency field at the working surface of the comb of all layers of charged particles of the electron tape.

The DRG with the "klinotron" mode of electron flow input (oblique beam) provides a significantly higher output signal power in the millimeter and submillimeter wavelength ranges than the DRG with the classical input of the paraxial electron beam parallel to the surface of the slow-wave structure. This is due to the high coefficient of energy use of the ribbon electron flow. The generation of increased oscillation power is due to the fact that the ribbon electron flow in such a DRG falls on the working surface of the periodic slow-wave structure, made in the form of a comb at an acute angle φ_0. With an oblique incidence of the electron beam (EB), sequential introduction of various layers of the periodic system into the region with high values of the electromagnetic field is ensured. This allows for effective interaction with the intense high-frequency field at the working surface of the comb of all layers of charged particles of the electron tape.

The speed of electrons in the beam V_0 at accelerating voltage U_0 :

$$V_0 = \sqrt{\frac{2eU_0}{m}}, \qquad (1)$$

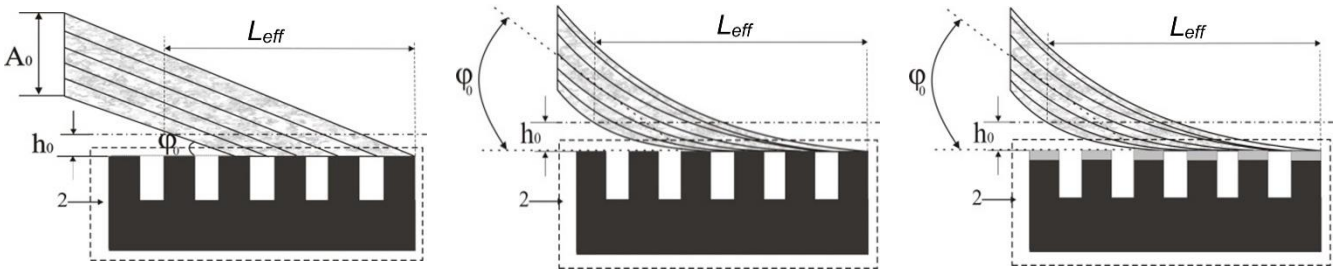

(a) (b) (c)

Fig. 1. Schematic Diagram of Electron Beam Behavior Under Different Magnetic Field and Dielectric Coating Conditions: a) In an uniform magnetic field; b) In a non-uniform magnetic field; c) In a non-uniform magnetic field with a dielectric layer applied to a periodic structure. h_0, L_{eff} – effective thickness and length of the interaction space of the electron beam with the field.

where e, m is the charge and mass of the electron e =-1.602×10^{-19} C, m = 9.11×10^{-31} kg. At characteristic voltages of clinotrons and DRG of the millimeter range of 2.5...4 kV, the speed is: $V_0 \approx$ 2,5 10^7 m/s. Since the speed of light c = 3 × 10^8 m/s, then this means that $V_0 / c \approx 10^{-1}$, which corresponds to the slowdown factors implemented by the PSS of ~10. The normal velocity with respect to the PSS when the beam φ_0 is tilted at an angle will be:

$$V_n = V_0 \sin \varphi_0 , \tag{2}$$

which at angles of inclination of the electron beam in klinotrons and DRG of several degrees is approximately 1...2% of the EB velocity. If a thin layer of dielectric is applied to the surface of the slow-wave structure [3.4], then the settling of the beam electrons on it will lead to the emergence of a braking electric field, under the influence of which the beam trajectory will be lengthened and become parabolic - Fig. 1, which will lead to an increase in the efficiency of its interaction with the field of the slow-wave structure and a more efficient transfer of beam energy to the field, and therefore an increase in the generation power and efficiency of the device. Application of a dielectric layer can give the same effect as the use of a non-uniform magnetic field, which also leads to an increase in the space of interaction of the EB with the field of the slow-wave structure. To equalize the potential, a layer of resistive material is applied to the dielectric layer and the side surface of the slow-wave structure, which also ensures the flow of electrons onto the metal substrate of the slow-wave structure.

A similar approach can be used to increase the beam-field interaction space and, accordingly, increase the power; it can also be used in a millimeter and submillimeter wave range DRG. Thus, applying dielectric and resistive thin film coatings to the PSS of klinotrons and DRGs allows, due to the settling of a part of the electron flow, to form a braking electric field and, accordingly, increase the length of the interaction region, power and efficiency of the generator.

References

[1] Levin G. Ya., Borodkin A. I., Kirichenko A. Ya. i dr. Pod red. A. Ya. Usikova. Klinotron [Clinotron]. Kiev, Naukova dumka, 1992, 200 p.

[2] Generatori difraktsionnogo izlucheniya. Pod .red. Shestopalova V.P., AN USSR, Kiev, Naukova dumka, 1991, 320p.

[3] Klinotron: Pat. 116690 Ukrainy: H01J25/34, H03B9/08. №a 2016 04980; ziavl. 04.05.2016; opubl. 25.04.2018, Biul.№8/2018, 11p.

[4] Henerator dyfraktsiinoho vyprominiuvannia: Patent Ukrainy №118040: H01J25/00, H01J23/00. № a 2016 08186; ziavl. 25.07.2016; opubl. 12.11.2018, Biul.№21/2018, 9p.

MONITORING RESPIRATORY DISEASES BY ACOUSTIC NOISE

Yi-yang Luo*, Yehor Kryvenko*, Olena Kryvenko*, Vladyslav Lutsenko*, Sergyi Masalov*

**O.Ya. Usikov Institute for Radiophysics and Electronics of the National Academy of Sciences of Ukraine, 12, Ac. Proskura st., Kharkov, 61085, Ukraine, e-mail: yiyangluo@163.com; yiyangluo@163.com; kryvenkoehor@gmail.com; talvi@ukr.net; vladislavlutsenko@ukr.net; s.masalov.2020@gmail.com*

Introduction

Lung disease is one of the leading causes of disability. Dysfunction of the respiratory system causes a change in the functional state of its organs, and is reflected in respiratory noise - signals, proper pro-cessing of which can ensure the selection of signs of these disorders, which are indicators of changes in the functional state of the respiratory system. How-ever, despite the rapid innovation and technological progress in medicine, in practice, the primary diag-nosis of lung condition is the method of listening to the sounds of breathing (lung auscultation) [1]. The use of modern information technologies in creating a system of analysis of acoustic noise [2] for the differential diagnosis of lung disease will create a modern system of medical examination and monitoring of lung diseases in the population of Ukraine.

In this regard, it is important to conduct research in this field and work in this direction is evolving with the development of computer technology, types of sensors, methods of artificial intelligence in the field of diagnosis and decision making, telemedicine [3–5]. This work is focused on solving an important scientific problem - the creation of information technology for the detection of lung diseases by acoustic noise [6- 8].

There are significant differences in the spectra of healthy 2.4 and sick 3.5 lungs, in the frequency range above 300 Hz (Fig. 1). At the same time during the disease the spectra of both the diseased and healthy lungs do not change significantly. However, in the high-frequency region of the spectrum in the middle part of the disease in the spectrum of the diseased lung in the frequency range 1 ... 2 kHz there is an emission in the spectrum associated with crepitation noise.

Therefore, to identify pathologies associated with pneumonia, it is sufficient to consider differences in the spectra of healthy and sick lungs in the frequency range up to 2 ... 3 kHz (Fig. 2). As a criterion can be used to minimize the variance of the difference between the test and reference spectra, expressed on a logarithmic scale, and to maximize the correlation coefficient of these spectra.

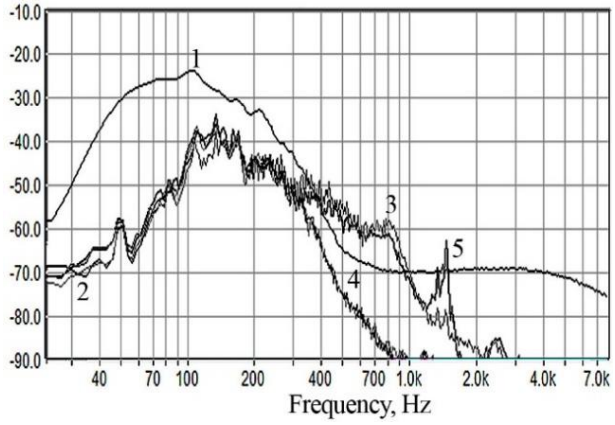

Fig. 1. Spectra: 1 – vesicular respiration; 2 – healthy lung, the onset of the disease; 3 – sick lung the beginning of the disease; 4 – a healthy lung in the middle of the disease; 5 – sick lung, the middle of the disease.

In Fig. 2 shows the noise spectra of vesicular respiration – 1, in pneumonia healthy – 2 and sick – 3 lungs, and in Tab. 1 the correlation coefficients of these spectra. The symbols: 1 – vesicular respiration; 2 – pneumonia initial phase of the disease (4 days) healthy lung; 3 – pneumonia initial phase of the disease (4 days) sick lung.

Analysis of these data Tab.1 shows that the coefficient of cross-correlation of the lung noise spectra with vesicular respiration and healthy pneumonia (0.992) is significantly higher than the noise spectrum of the lung with pneumonia (0.856; 0.865), so this parameter can be used as a criterion for detection pathologies [7, 8].

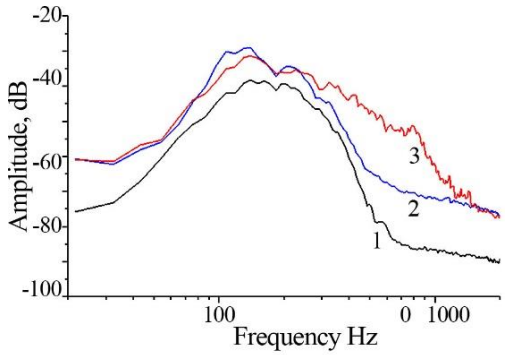

Fig. 2. Spectra of respiratory noise: 1 – vesicular respiration; 2 – healthy lung with pneumonia; 3 – sick lung with pneumonia.

Table 1 Spectrum correlation coefficient.

Type of respiration	1	2	3
1	1	0,9915	0,855-
2	0.9915	1	0,8650
3	0.8555	0.8650	1

Conclusions

The description of acoustic noises of the respiratory process can be based on the use of a model of nested semi-Markov processes. To detect pathologies, it is advisable to use the difference between the normalized levels of noise spectra on a logarithmic scale. This allows us to emphasize those spectral components that have a relatively small level and their presence is characteristic of pathologies. A comparison of the spectra of different phases of respiration for the left and right lungs is used as an additional criterion that increases the reliability of the classification. In the absence of pathology, the spectra are slightly different from each other and slightly different from the standard. Differential diagnosis of noise can be based on the use of cross-correlation functions of the spectra displayed on a logarithmic scale, as well as their time characteristics (changes in the mean and rms values).

References

[1] Korenbaum V.I. Akusticheskaja diagnostika sistemy dyhanija cheloveka na osnove ob'ektivnogo analiza dyhatel'nyh zvukov. Vestnik DVO RAN, 2004, no 5, pp. 68–79.

[2] Artemenko M.V., Kalugina N.M. Analiz akusticheskih shumov kak osnova differencial'nojj diagnostiki sostojanija legkih cheloveka, [Elektronij resurs]. Medicinskie nauki. – Rezhim dostupu: http://abstract.science-review.ru/pdf/2016/4/1794.pdf.

[3] Vovk I.V., Dahnov S.L., Krizhanovskii V.V., Olijnyk V.N. Vozmozhnosti i perspektivy diagnostiki legochnyh patologij s pomoshh'ju komp'juternoj registracii i obrabotki shumov dyhanija. Akus. Visn, 1998, 1, no 2, pp. 21–33.

[4] Vovk I.V., Grinchenko V.T., Krasnyj L.G., Makarenkov A.P. Problemy registracii i klassifikacii shumov dyhanija cheloveka. Akust. Zhurnal, 1994, vol. 40, no. 1, pp. 750 – 756.

[5] Lomaka V.V., Sin`kov Ye.O. Akusty`chni metody` diagnosty`ky` respiratornoyi sy`stemy`. Aktual`ni py`tannya s`ogodennya: zb. nauk. pracz` Mizhnarodnoyi naukovo-prakty`chnoyi konferenciyi. – Obuxiv: Drukarnya «Drukary`k», 2018, vol. 9, pp.. 22–28.

[6] Rao A., Huynh E., Royston T. J., Kornblith A. and Roy S. Acoustic Methods for Pulmonary Diagnosis. IEEE Reviews in Biomedical Engineering, 2019, vol. 12, pp. 221-239. doi: 10.1109/RBME.2018.2874353.

[7] Bespalov Y. G., Vysotska O., Porvan A., Linnyk E., Stasenko V. A., Doroshenko G. D., Amirgaliyev Y. Information system for recognition of biological objects in the RGB spectrum range. Paper presented at the Information Technology in Medical Diagnostics II - Proceedings of the International Scientific Internet Conference on Computer Graphics and Image Processing and 48th Interna-tional Scientific and Practical Conference on Appli-cation of Lasers in Medicine and Biology, 2019, pp. 101-110. doi:10.1201/9780429057618-13.

[8] Henry B., Royston T.J. Localization of ad-ventitious respiratory sounds. J Acoust Soc Am., 2018, vol. 143(3), pp. 1297. doi: 10.1121/1.5025842.

THE INFLUENCE OF VOLCANISM ON THE PARAMETERS OF THE ATMOSPHERIC RADIO COMMUNICATION CHANNEL

Chernogor L.F.*, Liashchuk O.I., Shevelev M.B.*, Tilichenko N.M.***

**V.N. Karazin Kharkiv National University,*
Kharkiv, 61022, Ukraine, Svobody Square, 4, e-mail: leonid.f.chernogor@gmail.com
*** Main center of special monitoring, Kosmichna str. 1, urban village Gorodok,*
Zhitomir region, Ukraine, 12265, e-mail: alex_liashchuk@ukr.net

Utilizing Ukrainian infrasound stations, global pressure disturbances within the atmospheric communication channel, induced by the supervolcano eruption, were identified. The main parameters of these disturbances were subsequently estimated.

Introduction

The atmosphere serves as a traditional communication channel for radio waves across various ranges, exerting the most significant influence on the propagation of meter and shorter radio waves. The efficiency of communication, radar, radio navigation, radio astronomy, and remote radio sensing systems is heavily dependent on the state of the atmospheric channel, which is influenced by numerous high-energy sources of both natural and anthropogenic origin. Volcanism is one such source [1–6]. Explosions and volcanic eruptions induce a complex array of physical effects within the Earth–atmosphere–ionosphere–magnetosphere (EAIM) system. The physical effects within the EAIM system resulting from the Tonga supervolcano explosion on January 15, 2022, were theoretically investigated. Detailed studies were conducted on geomagnetic, ionospheric, and infrasound effects. The primary characteristics of seismic waves and tsunamis were analyzed. The propagation of acoustic and atmospheric gravity waves (AGW) is utilized for global diagnostics of the atmospheric communication channel's state. This report aims to present examples of the results from the system spectral analysis of temporal fluctuations in atmospheric pressure generated by the Tonga volcano explosion.

Methods and Techniques

Infrasound was registered by the Ukrainian network of acoustic stations, one of which was the Akademik Vernadskyi (AIA, distance $r \approx 8867$ km) and Kamianets-Podilskyi (KPDI, $r = 16330$ km) stations. System spectral analysis was used for processing. It consists of three complementary short-time (SFT) and adaptive (AFT) Fourier transforms, as well as a wavelet transform (WT). The first of them has the best resolution by time, the second has better resolution by periods. The wavelet transform «equalizes» the chances of components with different periods and amplitudes.

Results of the system spectral analysis of atmospheric pressure variations

An example of the analysis results is shown in Fig. 1. From Fig. 1 it can be seen that the explosion of the volcano caused wide-band perturbations of the atmospheric pressure, and consequently the parameters of the atmospheric communication channel. Oscillations with a period from 400 to 600 s had the largest amplitude. In addition, oscillations with a period of 700 to 1000 s were observed at the more distant KPDI station. The speed of a wave with a shorter period is close to the speed of a Lamb wave (about 312 m/s). Longer periods are characteristic of AGW, the speed of which for the KDPI station was about 277 m/s. The duration of disturbances from the volcano explosion reached about 2.5 hours.

Conclusion

Disturbances in the atmospheric radio communication channel caused by the explosion of the Tonga volcano were detected. The duration of atmospheric pressure disturbances reached 2.5 hours. The speed of propagation of disturbances was about 304 and 315 m/s for acoustic waves and Lamb waves and about 277 m/s for AGW. 700–1000 c). Perturbations of the parameters were of a global nature and could significantly affect the characteristics of radio waves.

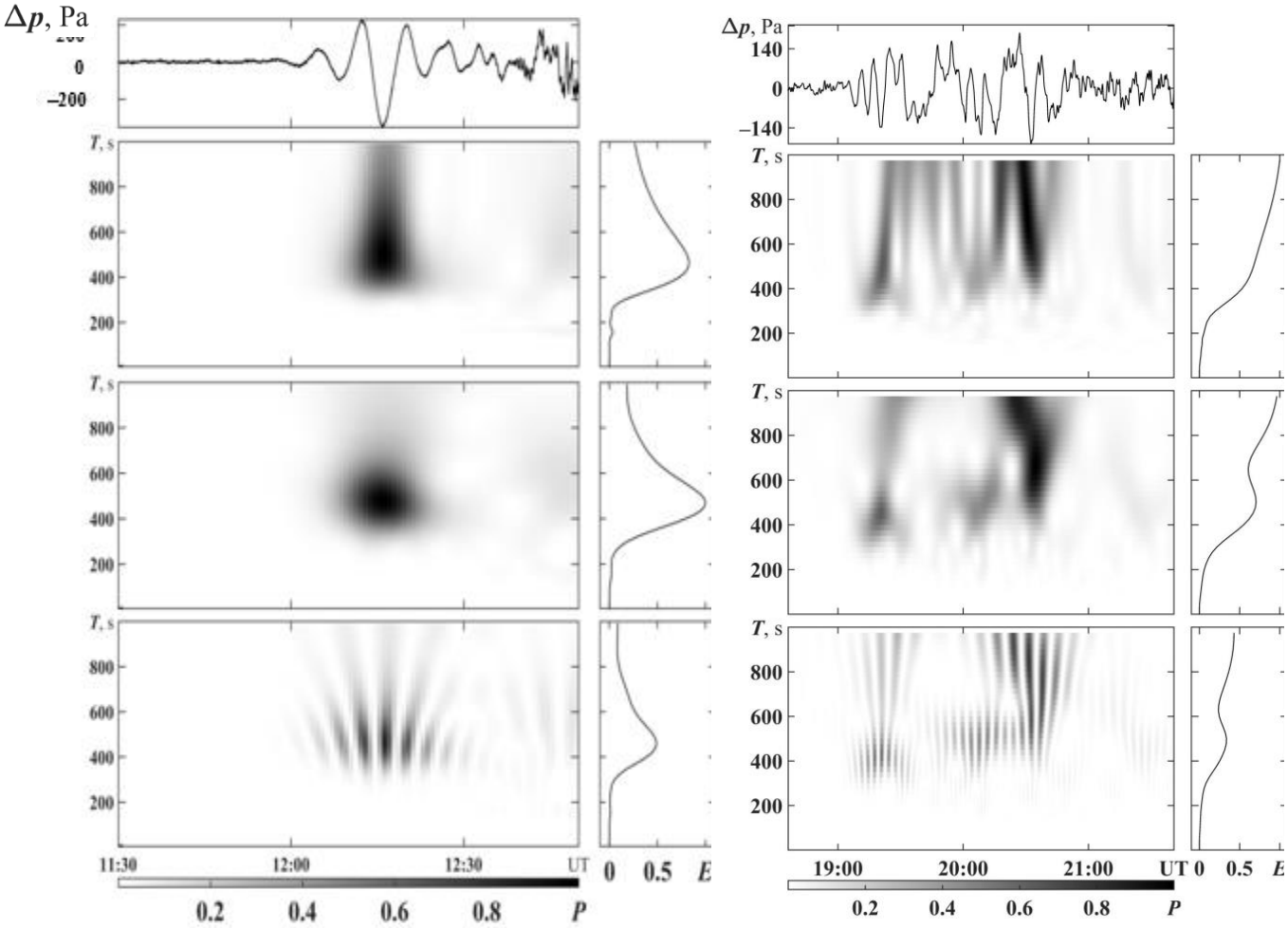

Fig. 1. Band-pass filtering and SSA results pressure fluctuations in the infrasonic wave registered at the station AIA (on the left, r ≈ 8867 km) and KPDI (on the right, r ≈ 16330 km). Panels from top to bottom: waveform, results of SFT, AFT and WT. Energy diagrams are shown on the right.

Support was provided by Ukraine state research projects # 0122U001476, # 0124U000461 and # 0124U000478.

References

[1] L. F. Chernogor, "Physical effects from the powerful Tonga volcanic eruption of January 15, 2022, in the Earth–atmosphere–ionosphere–magnetosphere system," J. Atmos. Solar-Terr. Phys. vol. 253, paper No. 106157, 2023. https://doi.org/10.1016/j.jastp.2023.106157

[2] Chernogor L. F., Holub M. Yu. Bay-Shaped Variations in the Geomagnetic Field that Accompanied the Catastrophic Explosion of the Tonga Volcano on January 15, 2022 // Kinematics and Physics of Celestial Bodies. – 2023. – Vol. 39, No. 5. – P. 247–260. https://doi.org/10.3103/S0884591323050033

[3] L. F. Chernogor, "Ionospheric total electron content variations caused by the Tonga volcano explosion on January 15, 2022," Space Sci. Tech. vol. 29, no. 3(142), pp. 67—87 [In Ukrainian].

[4] L. F. Chernogor, "Global variations in the geomagnetic field caused by the explosion of the Tonga volcano on January 15, 2022," Space Sci. Tech. vol. 29, no. 4 (143), pp. 78—105 [In Ukrainian].

[5] L. F. Chernogor, M.B. Shevelev "A statistical study of the explosive waves launched by the Tonga Super-volcano on January 15, 2022," Space Sci. Tech., vol. 30, no. 1(146), pp. 66—79, 2024. https://doi.org/10.15407/knit2024.01.066

[6] L.F. Chernogor, Y. Luo, Statistical Analysis of Seismic and Tsunami Waves Generated by the 2022 Tonga Volcano's Eruption. *A Comprehensive Study of Volcanic Phenomena*, ed.: Dr. Károly Németh.

DETERMINING THE DISTANCE TO A TARGET USING PASSIVE RADAR OVER THE SEA SURFACE

Mytsenko I.M.*, Roenko A.N.**

O.Ya. Usikov Institute for Radiophysics and Electronics, National Academy of Sciences of Ukraine
Kharkiv 61085, Ukraine, email: igor.mytsenko@gmail.com, e-mail**: alexnikrnk@gmail.com*

A method for determining the distance to a target using passive radar over the sea surface with one reference receiving point is proposed. One of the features is the use of a radiating radio beacon located at a significant distance from the coastline.

Introduction

At present, modern technologies and new "intelligent" methods of processing the information received from the target, allow detecting the slightest signs of the presence of a signal reflected from the target, including passive radar. As is known [1-3], the advantage of passive radar compared to active one is a greater detection range, stealth, lower energy consumption, lower equipment weight, etc. The disadvantages of passive radar include the impossibility of determining the range to the target and its coordinates with one reference receiving point. In passive radar there are a number of methods for determining the distance to the target and its coordinates, such as goniometric (triangulation), difference-range, goniometric-difference-range, etc. However, none of the existing methods allows determining the distance to the target with one reference point, one passive radar. The aim of the work is to develop a method for determining the distance to a target in the presence of one reference receiving point for passive radar over the sea surface and the means for implementing such a method.

A method for determining the distance to the target

The proposed method for determining the distance to a target using passive radar is based on the idea of using a surface radio beacon installed beyond the radio horizon [4-5]. The transmitting device is installed on the radio beacon beyond the radio horizon and the receiving device is installed on the shore and receives a direct signal from the radio beacon and a signal reflected from a surface object. To determine the range to the target, it is necessary to know the difference in the arrival time of the direct and reflected beams, the angle α between the directions to the radio beacon and the surface object, and the distance to the radio beacon. Then, using a special algorithm, the range to the surface object R_D is determined

$$R_D = \frac{\Delta R^2 + 2\Delta R R_0}{2(\Delta R + R_0(1-\cos\alpha))}, \quad (1)$$

where R_0 is the distance to the radio beacon, $\Delta R = \Delta T \cdot c$ is the difference in the path of the forward and return signals, and c is the speed of light (3×10^8 m/s). Fig.1 shows a simplified functional diagram of the proposed passive radar using a radio beacon, where 1 is a highly directional rotating antenna installed on the shore, 2 is a receiving device, 3 is an amplifier-repeater installed on the radio beacon, 4 is an amplifier-repeater antenna, omnidirectional in the horizontal plane and narrowed in the vertical one. After simple transformations we express R_D

$$R_D = \frac{2\Delta R R_0 - \Delta R^2}{2(\Delta R - R_0(1-\cos\alpha))} = \frac{\Delta R \cdot (2R_0 - \Delta R)}{2(\Delta R - R_0(1-\cos\alpha))}. \quad (2)$$

The determination of ΔT is made by the receiving device 1 (see Fig.1a) and, using expression (2), the processing unit determines the distance to the target R_D. In this case, it is necessary to take into account the features of using expression (2). Analysis of this formula shows that when $R_0 = const$ and the angle α changes, and the distance to the target ΔR can have both a positive and a negative value. In addition, for some values of α, let's call them $\alpha_{\lim}$, the denominator of expression (6) becomes equal to 0, and the value $R_D \approx \infty$.

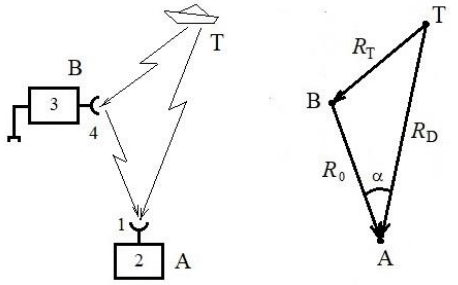

a) b)

Fig. 1. Simplified functional diagram of the proposed passive radar using a radio beacon

Critical angles α_{lim} will be observed in cases where the expression $\Delta R = R_0 \cdot (1 - \cos\infty)$ in the denominator of (2) is equal to 0. Therefore

$$\alpha_{\text{lim}} = \arccos\left(1 - \Delta R / R_0\right). \tag{3}$$

At these angles, it is impossible to determine the distance to the target without additional signal processing. The method of combating this phenomenon when using a radio beacon and passive radar is beyond the scope of this presentation and will be presented in the next work.

Conclusions

Determining the distance to a target using passive radar over the sea surface is possible using a radio beacon with an amplifier-repeater installed. When using the algorithm for calculating the distance to a target, it is necessary to take into account the critical angles of the antenna system direction, at which it is necessary to apply additional processing of the received signals.

References

[1] Dzuyba V.P., Eremka V.D., Zykov A.F., Milinevsky L.P., Mytsenko I.M., Prokopenko O.I., Roenko A.N., Roskoshny D.V. Physical principles and electronic means of monitoring the surface situation and navigation. Moskov-Kiev-Minsk-Sevastopol: Veber, 2012.

[2] Eremka V.D., Kabanov V.A., Logvinov Yu.F., Mytsenko I.M., Razscazovsky V.B. Roenko A.N. Peculiarities of radio wave propagation over the sea surface. Moskov-Kiev-Minsk-Sevastopol: Veber, 2013.

[3] Eremka V.D., Kabanov V.A., Logvinov Yu.F., Mytsenko I.M., Razscazovsky V.B. Roenko A.N. Unconventional methods and means of radar. FOP Panov A.M., Kharkov, 2015.

[4] Mytsenko I.M., Roenko A.N. On the possibility of estimating the distance to the target by passive radar methods in the case of distant tropospheric propagation of radio waves. Radiophysics & Electronics, v.(26), No.4, 2021, pp.22-27. DOI:10.15407/rej2021.04.022.

[5] Mytsenko I.M., Roenko A.N. Environmentally safe over-the-horizon radar of the meter range for the protection of territorial waters. Radiophysics & Electronics. v.(28), No.4, pp.287-295, 2023. https://doi.org/10.15407/rpra28.04.287.

THE IMPACT OF IONOSPHERIC WEATHER ON GNSS RADIO SYSTEMS

L. F. Chernogor, M. Yu. Tkachenko

V. N. Karazin Kharkiv National University, Ukraine, 61022, Kharkiv, Svobody Square, 4
e-mail: Leonid.F.Chernogor@gmail.com
e-mail: tkachenko.postgrad@gmail.com

The results of the analysis of spatiotemporal dependencies of the Total Electron Content (TEC) caused by the geospace storm on November 4-5, 2023, are presented. Significant disturbances in TEC magnitude, as well as in the parameters of TEC distribution around the globe, have been identified.

Introduction

One of the most important tasks in applied physics and radiophysics is to improve the functioning of global positioning systems, as well as radio systems whose operation is connected to processing data received from global positioning systems. The reliability and accuracy of their performance largely depend on the magnitude of TEC variations, which arise under the influence of powerful energy sources. One such source is a geospace storm, which leads to global disturbances in all subsystems of the Earth–atmosphere–ionosphere–magnetosphere system. The ionospheric response to a geospace storm significantly depends on the time of day, season of the year, and the coordinates of the observation location. Significant advances in satellite technologies have made it possible to cover almost the entire globe with measurements.

The goal of this study is to present the results of analyzing the temporal dependencies of TEC caused by the geospace storm on November 4-5, 2023. We analyzed global ionospheric maps, as well as percentage TEC increment maps for the entire globe, for the observation period starting from the background day of November 3, 2023, and ending with the recovery phase on November 6, 2023.

General information

The geospace storm of November 4-5, 2023, eventually reached a G3 level, which is classified by NOAA as a "strong" storm. Such storms can cause disruptions in the operation of various radio systems, create interference that hinders their functioning, and even affect power transmission lines. This storm also triggered rare red auroras, which were observed as far south as regions of Ukraine. The geomagnetic storm began at 18:00 UT on November 4, 2023, and continued until 08:00 UT on November 6, 2023, after which the recovery phase began. Data on the temporal dependencies of solar wind parameters, interplanetary magnetic field components, and geomagnetic activity indices are available on the [1] resource. The analysis of space weather conditions allowed for identifying the characteristics of the ionospheric storm. To detect the ionosphere's response to the geospace storm of November 4-5, 2023, global ionospheric maps provided by the Center for Orbit Determination in Europe [2] on the website of The Crustal Dynamic Data Information System [3] were used. An analysis of percentage TEC increment maps was also conducted, which can be interpreted as a distribution of the ionospheric disturbance index values.

The results of analysis and calculations

Based on the analysis of global ionospheric maps and percentage TEC increment maps, the following characteristics of TEC variations were identified. On the reference day, TEC values displayed typical monthly undisturbed values, consistent with their latitudes, time of day, and season. As seen in Fig. 1, on the first day of the geomagnetic storm, November 4, 2023, significant disturbances in TEC values were observed across all latitudes, especially in the eastern part of the Northern Hemisphere during daylight hours. On November 5, significant disturbances in TEC values were also observed globally (Fig. 2). On the day the covery phase began, the disturbances were significantly reduced in magnitude but were still noticeable until the end of the day. The impact of TEC variations on the accuracy of GNSS functionality has been assessed. Even for a G3-class storm, the influence was significant.

Summary

Temporal variations of TEC in the ionosphere were analyzed on a global scale for the quiet reference day (November 3, 2023), during the main phase of the geomagnetic storm (November 4-5, 2023), and on the day

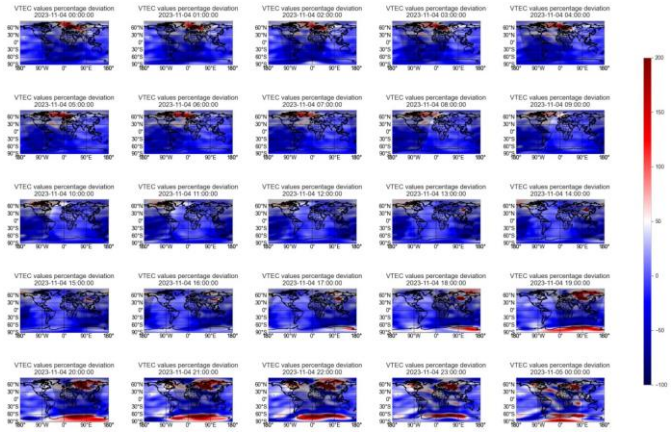

Fig. 1: Hourly percentage increment maps of TEC throughout the day on November 4, 2023.

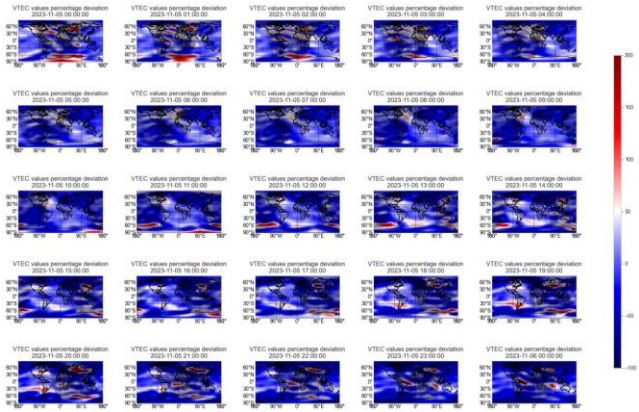

Fig. 2: Hourly percentage increment maps of TEC throughout the day on November 5, 2023.

the recovery phase began (November 6, 2023). The maximum TEC values behaved as follows: on the background day of November 3, the maximum TEC values reached 140-141 TECU. On November 4, the maximum TEC value was 132 TECU. On November 5, the maximum TEC value reached 130 TECU. However, on November 6, a significant increase in the maximum TEC value was observed, reaching 149.9 TECU. The highest TEC values were observed in equatorial latitudes. Strong disturbances were identified across all latitudes, especially in the auroral regions, with percentage TEC increments reaching up to 180% on the maps for November 4, 2023. Significant disturbances were also observed in the mid-latitude ionosphere (up to 150%), which corresponded to the red auroras observed during the main phase of the geomagnetic storm at these latitudes (up to ±30° during the daytime on November 5, 2023). Additionally, disturbances in the equatorial ionosphere were recorded on the recovery phase day, November 6, 2023, reaching 50-80%. These findings suggest significant restructuring in the current system between the magnetosphere and ionosphere during the geomagnetic storm, as well as the influence of the equatorial ionospheric anomaly. The assessments showed that the TEC variations caused by the geospace storm significantly affect the accuracy of object positioning using global positioning systems.

References

[1] NASA's OMNIWeb Database. Available at: https://omniweb.gsfc.nasa.gov

[2] Center for Orbit Determination in Europe (CODE). Available at: http://www.aiub.unibe.ch/download/CODE/

[3] Crustal Dynamics Data Information System (CDDIS). Available at: https://cddis.nasa.gov/archive/gnss/products/ionex/

DIFFRACTION RADIATION OSCYLLATOR FOR TERAHERTZ FREQUENCIES

Miroshnichenko V.S.*, Senkevych O.B.**

**O. Ya. Usikov Institute for Radiophysics and Electronics NAS of Ukraine, Kharkiv 61085,*
e-mail: v.mirosh2015@gmail.com
*** O. Ya. Usikov Institute for Radiophysics and Electronics NAS of Ukraine, Kharkiv 61085,*
e-mail: senkevych@gmail.com

The problems that arise during the developing of diffraction radiation oscillator (DRO) on the terahertz frequencies are considered. To overcome technological limitations is proposed the use in the DRO a higher spatial harmonics in reflective grating with wide slots. The width of the grating slots was optimized to increase the amplitude of higher spatial harmonics using local maxima of the resonance field near the rectangular edges of the grating.

The higher spatial harmonics in grating with wide slots

In the development of powerful DRO for terahertz (THz) frequencies there is a problem by manufacturing of periodic structures with a small period [1]. So, for the reflective grating used in the DRO, the minimum width of the slots d by using electro-erosion technology is ~ 0.05 mm, that allows developing of the DRO only up to frequencies 0.30÷0.34 THz. The traditional use of higher spatial harmonics in reflective grating with narrow slots increases only the period l of the structure and does not overcomes the technological limitations [2]. For higher frequencies (0.60÷1.00 THz), it is possible to use the higher spatial harmonics in reflective grating with wide slots, but an increase of the grating slots leads to a decrease in the amplitude of spatial harmonics and, accordingly, to an increase of the starting current I_{st} in DRO.

The modern theory of EM-diffraction [3] gives the field distribution on reflective grating, placed on the mirror of the DRO's open resonator (OR), and to calculate the spatial harmonic using the Fourier series decomposition. For gratings with the depth of slots $h = 0.25\lambda$ and the same phase velocity of spatial harmonics $v_{ph,n}$ obtained results are presented on Fig.1. There are local maxima of the field near the grating rectangular edges as a result of change the direction of induced current in the grating surface. Therefore, the amplitude of 2-nd and 3-rd spatial harmonics may be increased, when local maxima of E_y-field are shifted to the maxima of A_n –field of spatial harmonics by reducing of grating slots.

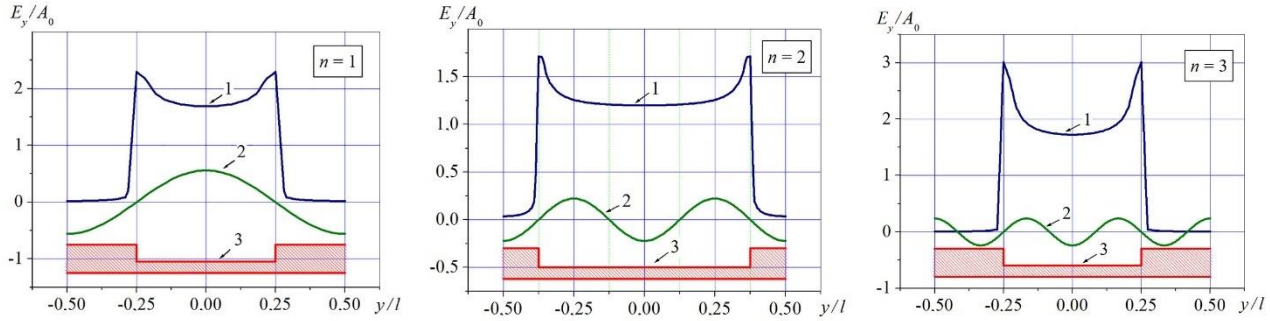

Fig.1. The distribution of resonant field (1) and spatial harmonic field (2) on grating (3): A_0 - amplitude of resonant field in OR; λ=0.88mm; $v_{ph,n} = cl/(n\lambda) = 0.136c$.

The starting current of DRO depends on $(A_n/A_0)^2$ and on Q-factor of OR [2]: $I_{st} \sim 1/(\psi Q)$; $\psi \sim (A_n/A_0)^2$ – the factor of resonant field using. The results of optimization for slots width according the maximum of $\psi \times Q$ are presented on Fig.2: resonant mode $TEM_{0\text{-}0\text{-}10}$; λ = 0.88mm; $v_{ph,n}$ = 0.136c; cross section of electron beam S_b = 0.030×4.0 mm^2. For 2-nd spatial harmonic the optimal slots width is d/l = 0.67, and for 3-rd spatial harmonic the optimal slots width is d/l = 0.45.

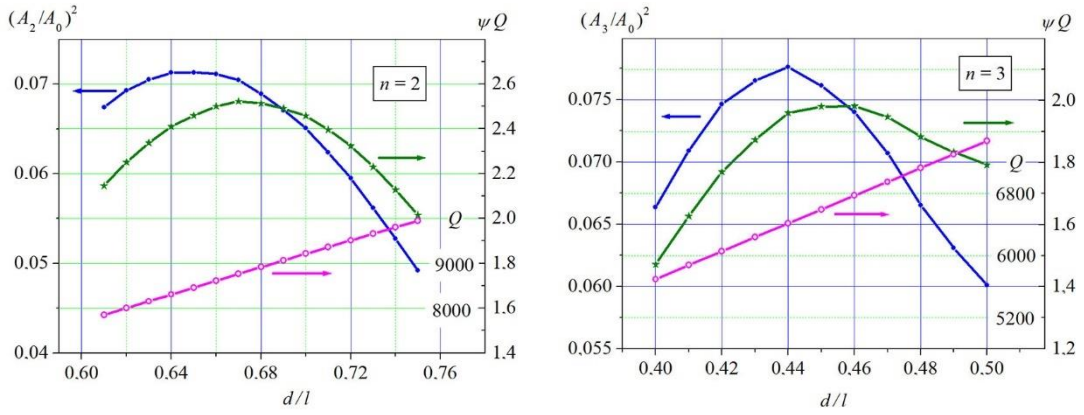

Fig.2. Optimal slots width (d/l) for 2-nd space harmonic and 3-rd space harmonic.

The starting current in DRO on THz frequencies

Let compare the starting current in DRO on $TEM_{0\text{-}0\text{-}10}$-mode with reflective grating, designed on 1-st, 2-nd ad 3-rd spatial harmonics (see Table 1). The length of beam-field interaction is D =12mm, and the acceleration voltage is $U_{ph,n}$ = 4760 V. The use of the grating with wide slots on 2-nd spatial harmonic increases I_{st} by 2.16 times, but improves the Q-factor in compare to operation of DRO on the 1-st spatial harmonic. The use of the grating with wide slots on 3-nd spatial harmonic increases I_{st} by 2.82 times. The maximum of current density (16 A/cm^2) does not exceed emission of L-cathode (J = 40÷60 A/cm^2). The use of 2-nd spatial harmonic in grating with wide slots allows to design DRO, operated on f = 1.0 THz (the slots width is d = 0.054 mm).

Table 1. The starting current in DRO by operation on 1-st, 2-nd and 3-rd spatial harmonics.

Spatial harmonic	l, mm	d, mm	h, mm	Q	I_{st}, mA	J, A/cm^2
f = 0.341 THz, S_b = 0.030×4.0 mm^2						
n = 1	0.120	0.060	0.220	3951	4.56	3.80
n = 2	0.240	0.1608	0.220	8786	9.84	8.20
n = 3	0.360	0.162	0.220	6612	12.86	10.72
f = 0.682 THz, S_b = 0.015×4.0 mm^2						
n = 1	0.060	0.030	0.110	2793	3.28	5.46
n = 2	0.120	0.0804	0.110	6212	7.24	12.07
n = 3	0.180	0.081	0.110	4675	9.65	16.09

The obtained results confirm the possibility of creating DRO up to 1.0 THz, operated on higher spatial harmonics of reflective grating with wide slots. To increase the amplitude of higher spatial harmonics the width of the slots was optimized using the local maxima of the resonance field near the rectangular edges of the grating.

References

[1] V. K. Korneenkov, V. S. Miroshnichenko and B. K. Skrynnik, "Diffraction Radiation Oscillators for CW and Pulsed Operation," Telecommunications and Radio Engineering, 51(6), pp.144-147, 1997.

[2] V. S. Miroshnichenko, V. K. Korneenkov, Y. B. Senkevich and D. V. Yudintsev, "Operation of the Diffraction Radiation Oscillator on Higher Space Harmonics of Periodic Structure," Telecommunications and Radio Engineering, 69(4), 2010.

[3] O. P. Kusaikin, P. M. Melezhik, S. B. Panin and A. Y. Poedynchuk, "Dispersion Properties of Reflecting Grating Filled with Metamaterial," Radiophysics and Radioastronomy, vol.14, No4, pp.404-413, 2011.

GLOBAL VARIATIONS OF THE GEOMAGNETIC FIELD DURING EXTREME GEOSPACE STORM ON MAY 10–11, 2024

Chernogor L.F., Shevelev M.B.

School of RadioPhysics, Biomedical Electronics and Computer Systems
V.N. Karazin Kharkiv National University, Department of Space Radio Physics, Kharkiv 61022, Ukraine
e-mail: leonid.f.chernogor@karazin.ua

An urgent task is to study the latitudinal and longitudinal (diurnal) manifestations of the unique geomagnetic storm on May 10–11, 2024. The purpose of this paper is to study the features of latitudinal and longitudinal manifestations of the outstanding geomagnetic storm on Mother's Day. It has been established that, according to a number of parameters, the magnetic storm of May 10–11, 2024 is extraordinary. The dependence of the level of variations in the geomagnetic field on May 10–11, 2024 on the time of day was analyzed. The analysis was performed for stations located in the area of the globe with both polar day and polar night. It was shown that there were both qualitative and quantitative differences in variations in the geomagnetic field level during the day and night.

Introduction

It is well known that powerful solar storms, accompanied by flares of UV and X-rays, generation of solar cosmic ray fluxes, coronal mass ejections, generation of shock waves, as well as high-speed flows of matter of solar origin, cause a complex set of processes in the interplanetary medium and on Earth [1, 2]. Geospace storms significantly affect the functioning of space-based and ground-based systems, the operation of radio navigation, radar, telecommunications, radio astronomy, radio sounding of the Earth from space and space from the Earth, as well as human well-being and health. A large number of papers are devoted to the study of the effects of storms The main attention has been paid to the strongest of them. Despite significant advances in the study of geospace storms, the problem of their further study is still relevant.

The *Kp* index increased from 2 to 9– in the second half of May 10, 2024. During May 11, it fluctuated between 8 and 9, and the total *Kp* index was 67, while on the reference days it did not exceed 10–12. On May 9 and in the first half of May 10, 2024, the *Dst* index fluctuated around 0 nT. From 16:00 to 19:00 on May 10, 2024, it increased to a maximum value of 62 nT. Further, this index, slightly fluctuating, from 19:00 on May 10 to ~01:00 on May 11, 2024 decreased from 0 nT to a minimum value of –412 nT. After 01:00 on May 11, 2024, the *Dst* index, fluctuating, gradually increased from –412 nT to –50 nT at the end of the day on May 15, 2024.

The day of May 14, 2024 was found to be the most appropriate as the reference day.

Analyses and calculations results

Analysis of temporal variations in the strength of the northward, *X*, eastward, *Y*, and vertical, *Z*, components of the geomagnetic field over the period 10–17 May 2024 has been performed. The magnetometers acquired measurements with 1-nanotesla (nT) strength resolution at one min intervals. For the high-latitude GDH station at the altitudes of the ionospheric dynamo region ($z \approx$ 100–150 km), which makes the main contribution to the geomagnetic effect, the Sun practically did not set, and a polar day was observed. The magnetic storm occurred during the daytime on both May 10 and May 11, 2024. The range of variations in the *X*-, *Y*-, and *Z*-components reached 1900, 1300, and 900 nT, respectively. The IQA station also belongs to the high latitude ones. For it, the duration of the night at the altitudes of the dynamo region did not exceed ~1 hour. The behavior of variations in the geomagnetic field components for the GDH and IQA stations is qualitatively similar. The range of the levels of the *X*-, *Y*-, and *Z*-components was 2200, 1750, and 2050 nT, respectively. For the mid-latitude OTT station, the duration of the night at the dynamo region altitudes increased to approximately 6 h. The main effects of the geomagnetic storm, as before, were observed during the daytime. The range of variations at night was 2–3 times smaller than during the daytime. During the solar terminator passage, the amplitude and frequency of fluctuations in the level of all components increased significantly. The range of the *X*-, *Y*-, and *Z*-components did not exceed 2200, 1400, and

1600 nT, respectively. For the PIL station, located in the Southern Hemisphere at the boundary of low and middle latitudes, the duration of nighttime at the dynamo region altitudes was 1 h less than daytime duration. The largest range for the *X*-component reached 580 nT in the local daytime and evening on May 10, 2024. The maximum range for the *Y*- and *Z*-components was close to 55 and 110 nT, respectively. The drop in the *X*- and *Z*-component levels was very sharp in the local evening on May 10, 2024. For the high-latitude AIA station located in the Southern Hemisphere, the duration of the night at the altitudes of the dynamo region was more than 1 hour longer than the duration of the day. Therefore, the greatest disturbances of the geomagnetic field level occurred during local nighttime. The range of variations in the *X*-, *Y*-, and *Z*-components reached 2450, 1430 and 1350 nT, respectively. For the mid-latitude PET station, the duration of the night at the dynamo region altitudes did not exceed ~4 h. The main effects of the geomagnetic storm occurred during the daytime. The range of the *X*- , *Y*-, and *Z*-component levels reached 900, 700, and 850 nT, respectively. For the mid-latitude KHB station the range of variations for the *X*-, *Y*-, and *Z*-components was about 750, 400, and 200 nT, respectively. The CYG station is also a mid-latitude station. The variations in the levels of all components were largest during the daytime and were qualitatively similar to the variations at the PET and KHB stations. The range of variations did not exceed 590, 250 and 140 nT for the *X*-, *Y*-, and *Z*-components, respectively. At the low-latitude KDU and CTA stations, the range of variations in the *X*-, *Y*-, and *Z*-components was within 400, 190, and 107 nT, respectively. The largest variations occurred at night. The CNB station is a mid-latitude station in the Southern Hemisphere. The largest variations in the level of all components occurred at night. The range of variations in the *X*-, *Y*-, and *Z*-components did not exceed 650, 550, and 300 nT, respectively. Variations in the level of all components at the MCQ station differed qualitatively and quantitatively from the variations at the stations considered above. This may be due to the geographic location of the station. The largest variations, the range of which was about 2600, 1800, and 1500 for the *X*-, *Y*-, and *Z*-components, respectively, took place at night. At the high-latitude CSY station, the duration of the night was close to 14 hours. Therefore, the largest disturbances in the level of all components occurred at night. The range of variations did not exceed 950, 1200, and 980 nT for the *X*-, *Y*-, and *Z*-components, respectively.

Analyses and calculations results

It has been established that, according to a number of parameters, the magnetic storm of May 10–11, 2024 is extraordinary. There have been no such storms since 2003. The energy of the geospace storm of May 10–11, 2024 reached 6.5 EJ, and its power reached 0.4 PW. Such a storm is classified as extreme. The energy of the magnetospheric storm of May 10–11, 2024 was about 6.5 PJ, and its maximum power was 1.2 TJ/s. The magnetic storm had similar parameters. The latitude dependence of the disturbance magnitude of the level of all geomagnetic field components has been analyzed. In the Eastern Hemisphere, a clear tendency to decrease the range of variations with decreasing latitude was observed. For the Western Hemisphere, this tendency also took place, but was expressed less clearly (due to the small number of stations). The dependence of the level of geomagnetic field variations on May 10–11, 2024 on the time of day was analyzed. The analysis was performed for stations located in the area of the globe with both polar day and polar night. It was shown that there were both qualitative and quantitative differences in the variations of the geomagnetic field level during the daytime and nighttime. A comparative analysis of magnetic storms on April 23–24, 2023 (G = 4, $D_{st\min} \approx -212$ nT) and May 10–11, 2024 (G = 5, $D_{st\min} \approx -412$ nT) with a super unique storm of the Carrington event type (G = 7, $D_{st\min} \leq -1000$ nT) was carried out. The extraordinary character of the storm on May 10–11, 2024 was established. At the same time, its parameters differed significantly (to a lesser extent) from the parameters of the super unique storm. The range of variations in the level of all components during the storm on May 10–11, 2024 increased by tens of times compared to the range on the reference days. During the storm on April 23–24, 2023, this excess usually (except for individual stations) did not exceed 5–10 times.

Support was provided by Ukraine state research projects # 0122U001476, # 0124U000461 and # 0124U000478.

References

[1] L. F. Chernogor, “Physics of geospace storms,” Space Science and Technology, vol. 27, pp. 3–77, 2021.

[2] L. F. Chernogor and I. F. Domnin, *Physics of geospace storms*. Kharkiv: V. N. Karazin Kharkiv National University Publ., 2014.

THE INFLUENCE OF LITHOSPHERE PROCESSES ON THE PARAMETERS OF THE ATMOSPHERIC AND IONOSPHERIC RADIO COMMUNICATION CHANNEL

I. G. Zakharov, L. F. Chernogor

V. N. Karazin Kharkiv National University, 4, Svoboda Sq., Kharkiv, 61022, Ukraine
e-mail: giz-zig@ukr.net

Statistically reliable seismo-atmospheric and seismo-ionospheric effects of moderate earthquakes have been revealed. For the first time, it was established that the lithosphere continuously affects the atmosphere and ionosphere and the corresponding radio channel, regardless of powerful disturbances in the lithosphere-atmosphere-ionosphere system.

Introduction

The atmospheric-ionospheric radio channel is the only one channel widely used by systems of communication, radio navigation, radar, remote radio sensing, etc. The effectiveness of functioning of these systems depends significantly on channel condition. Channel parameters are affected by a number of high-energy sources, which leads to a decrease in performance or even to termination of the functioning of radio systems of various purposes. One such source is seismicity. It leads to activation of the subsystems interaction in the lithosphere – atmosphere – ionosphere – magnetosphere system, to disturbance of the atmospheric-ionospheric radio channel parameters.

Radiophysical remote methods of research of the atmosphere and ionosphere have shown their effectiveness during the study of disturbances of various nature. Searches for atmospheric and ionospheric earthquakes precursors are relevant. Basically, they study local disturbances before strong earthquakes [1-4]. The global atmospheric and ionospheric effects of strong earthquakes have been also revealed [5, 6]. However, not every local seismically active zone is characterized by strong earthquakes. Therefore, the question arises about the lower limit of the influence of the lithosphere on the atmospheric-ionospheric radio channel parameters and about the ratio of local and global effects. Based on this, the paper examines the atmospheric and ionospheric effects of the Vrancea seismically active zone (Romania), relevant for Ukraine, which is characterized mainly by moderate earthquakes with a magnitude of $M = 4.4 – 6.2$, but sometimes earthquakes with M up to 7.6 occur. The purpose of the work is to assess the atmospheric and ionospheric effects of moderate earthquakes and the possibility of their use in seismic forecasts and forecasts of the influence on the atmospheric-ionospheric radio channel parameters.

Data and methods

The local effects of 27 earthquakes with M from 3.9 to 5.6 in the Vrancea area for the years 2012-2018 were considered using the https://earthquake.usgs.gov/earthquakes/search catalog. To estimate the global seismic effect, data for the same years on 42 earthquakes with $M \geq 7.0$ far outside the Vrancea zone were used. The day-to-day changes of the daily average temperature and pressure of the surface atmosphere from the website https://psl.noaa.gov/data/timeseries/daily/, as well as the total electron content (TEC) of the ionosphere from the website http://www. .aiub.unibe.ch/download/CODE/. Since the influence of the lithosphere on the atmosphere and ionosphere occurs against the background of the continuous influence of atmospheric and space weather, data on solar (index $F_{10.7}$) and geomagnetic (index A_p) activity from the website https://kp.gfz-potsdam.de/en/data#c222 were also used. Calculations were made by the superimposed epochs analysis.

Research results

Atmospheric and ionospheric effects, similar to those known from the literature for stronger earthquakes, have been established for moderate earthquakes in the Vrancea zone. The average amplitude of local atmospheric anomalies before earthquakes in the Vrancea zone is: pressure – 2.6 hPa, temperature – 1.8 K. Changes in the TEC due to the significant influence of space weather could not be detected, but a reliable increase in the spatial gradients of the TEC over the seismically active zone was established. The average amplitude of the effects in the Vrancea zone caused by remote earthquakes is similar to those established earlier for other seismically active regions: pressure – 2.2 hPa, temperature – 0.5 K, TEC – 4.6%. An increase in the spatial gradients of TEC over the Vrancea zone under the influence of distant earthquakes was also established, the value of which is

approximately half of the local effect (Fig. 1). The established regularities confirm the radon mechanism of lithosphere-atmosphere-ionosphere interaction known in the literature [1, 7].

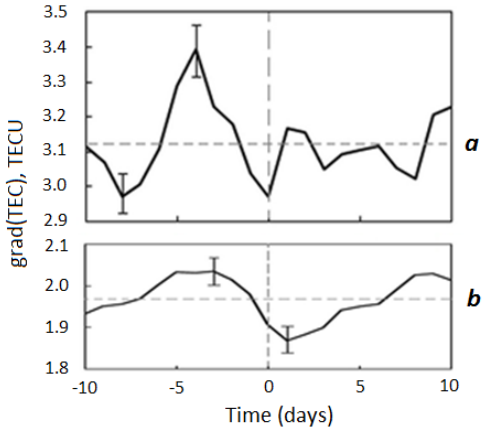

Fig. 1. Spatial gradients of the TEC over the Vrancea zone during local (a) and distant (b) earthquakes.

Conclusions

1. From the comparison of the obtained results with those published earlier, it was established that the amplitude of seismo-atmospheric and seismo-ionospheric effects is determined by the coordinates of the observation point, the background value of atmospheric pressure and has a moderate tendency to increase with the increase in the magnitude of earthquakes.

2. The existence of statistically reliable seismo-atmospheric and seismo-ionospheric effects from earthquakes with a magnitude of $M \sim 4–5$, which occur almost daily, has been proven. It is substantiated that the lithospheric-atmospheric-ionospheric interaction is implemented continuously, regardless of the presence or absence of powerful disturbances in the earth's crust and the near-Earth space.

3. The revealed regularities are explained by the radon mechanism of lithospheric-atmospheric-ionospheric interaction.

References

[1] [1] S. A. Pulinets, D. P. Ouzounov, A. V. Karelin, and D. V. Davidenko, "Physical bases of the generation of short-term earthquake precursors: A complex model of ionization-induced geophysical processes in the lithosphere–atmosphere–ionosphere–magnetosphere system", Geomagnetism and Aeronomy, vol. **55,** pp. 521–538, https://doi.org/10.1134/S0016793215040131, 2015.

[2] [2] V. A. Shuvalov, A. L. Makarov, and D. N. Lazuchenkov, "Identification of earthquakes by satellite measurements of disturbed ionospheric plasma," Space Science and Technology, vol. 22, no. 1, p. 64–78, https://doi.org/10.15407/knit2016.01.064, 2016. [In Russian].

[3] [3] K. Heki, "Ionospheric electron enhancement preceding the 2011 Tohoku-Oki earthquake", Geophys. Res. Lett., vol. **38,** L17312, DOI:10.1029/2011GL0479082011, 2011.

[4] [4] S. Pulinets, M. Tsidilina, D. Ouzounov, and D. Davidenko, "From Hector Mine M7.1 to Ridgecrest M7.1 earthquake. A look from a 20-year perspective", Atmosphere, vol. **12**, № 262, 16 p., DOI: https://doi.org/10.3390/atmos1202026, 2021.

[5] [5] I. G. Zakharov and L. F. Chernogor, "Influence of global seismic activity on processes in the atmosphere and ionosphere", Space Science and Technology, vol. 27, no. 5, p. 19–34, https://doi.org/10.15407/knit2021.04.000, 2021. [In Ukrainian].

[6] [6] I. G. Zakharov and L. F. Chernogor, "Global and local effects of seismic activity in the ionosphere", Space Science and Technology, vol. 28, no. 6, p. 12–24, https://doi.org/10.15407/knit2022.06.012, 2022. [In Ukrainian].

[7] [7] L. F. Chernogor, "Physics and Ecology of Catastrophes", Kharkiv: V. N. Karazin Kharkiv Nat. Un-ty, 556 p., 2012. [In Russian].

FEATURES OF THE GEOMAGNETIC EFFECT CAUSED BY THE SOLAR ECLIPSE ON APRIL 8, 2024 IN THE AMERICAN REGION

L. F. Chernogor *, M. Yu. Holub **

** V. N. Karazin Kharkiv National University, Ukraine, 61022, Kharkiv, Svobody Square, 4*
e-mail: Leonid.F.Chernogor@gmail.com
*** V. N. Karazin Kharkiv National University, Ukraine, 61022, Kharkiv, Svobody Square, 4*
e-mail: marya160588@gmail.com

The analysis of the temporal variations of the X, Y, and Z geomagnetic field components recorded at 9 stations of the INTERMAGNET network during the Great North American Eclipse on April 8, 2024, as well as on reference days, was carried out. Results of estimates of the geomagnetic effect are in good agreement with the observational results.

Introduction

From the above review of the literature on the geomagnetic effects of SEs, it follows that at present time geophysicists do not have a consensus on the existence of this effect. The data published in the literature are very contradictory. Some authors believe that there is no geomagnetic effect of SE. Other geophysicists, and the majority of them, claim that the effect does occur. The purpose of this paper is to describe the results of the analysis of variations in the three geomagnetic field components (*X*, *Y*, and *Z*), which were recorded by the INTERMAGNET network of magnetic stations during the SE on April 8, 2024. This eclipse, called the Great North American Eclipse, was total (the maximum magnitude was 1.0566). The SE was observed over the Pacific Ocean, Mexico, the USA and Canada.

General information on the solar eclipse

The SE of 139 Saros began on April 8, 2024 at 15:42:07 UT (hereinafter UT is Universal Time) over the Pacific Ocean and ended at 20:52:13.8 UT over the Atlantic Ocean (https://science.nasa.gov/eclipses/future-eclipses/eclipse-2024). The greatest eclipse magnitude of $M_{max} \approx 1.056$ took place in the area with coordinates 25°17.5′ N, 104°07.2′ W. The altitude of the Sun was 69.8° and the azimuth was 149.4°. The duration of the total SE was 04 min 28.1 s. The width of the umbral shadow region was 197.5 km. External and Internal contact of umbra are as follows: U_1 = 16:38:44.4 UT, U_2 = 16:41:01.7 UT, U_3 = 19:53:13.9 UT, U_4 = 19:55:29.1 UT. The total SE was observed in 6 Mexican states, 15 US states and in 6 Canadian provinces.

Means and Methods

Temporal variations of the *X*-, *Y*-, and *Z*-components (corresponding to the North–South, West–East and vertical directions) of the geomagnetic field for a number of American and Canadian magnetic stations were analyzed. These stations belonging to the INTERMAGNET network (https://www.intermagnet.org). The data for April 5–11, 2024, was analyzed. The SE took place on April 8, 2024. The remaining days were used as reference days. The amplitude resolution of the source data is 0.1 nT, and the time resolution is 1 min. The processing algorithm was as follows. First of all, the direct component estimated for the given day was subtracted. This component was different at different stations. The dependences obtained $X(t)$, $Y(t)$, and $Z(t)$ were subjected to the moving average process over a time interval of 60 min, and the $\overline{X}(t)$, $\overline{Y}(t)$, and $\overline{Z}(t)$ dependences of trends over time were constructed. The non-sinusoidal SE effect was determined from these dependencies. In addition, to identify a possible quasi-sinusoidal effect, the differences between $X(t)$ and $\overline{X}(t)$, $Y(t)$ and $\overline{Y}(t)$, as well as $Z(t)$ and were constructed.

The search for SE effects in the geomagnetic field should be preceded by a thorough analysis of the space weather state (https://omniweb.gsfc.nasa.gov/form/dx1.html). The values of the K_p-index did not exceed 3.3, and in the second half of April 8, 2024, they varied from 0.3 to 1. The D_{st}-index values fluctuated within the range from 0 nT to –30 nT. Hence, the space weather state was undisturbed and favorable for searching for geomagnetic field variations associated with the SE.

The results of analysis and calculations

The main parameters of the aperiodic disturbance of the geomagnetic field components level for all stations are given in Table.

Table. Main parameters of non-sinusoidal disturbances in the level of geomagnetic field components that accompanied the SE (parameters of other types of variations are indicated in parentheses).

Station	A_{max}, %	ΔX_{max}, nT	ΔT, min	ΔY_{max}, nT	ΔT, min	ΔZ_{max}, nT	ΔT, min
STJ*	96	–8	130	–7 (7)	140 (160)	–8	160
OTT	96	–9 (3)	160 (160)	–8 (8)	120 (130)	–9	200
SBL*	84	–7	140	–1 (1)	120 (140)	–6	180
FRD	80	–3	130	–1 (1.5)	170 (110)	–8	170
TUC	68	–12 (10)	210 (175)	–8	200	–4 (4)	180 (180)
BOU	62	–8 (8)	210 (155)	–6	180	–4 (3)	240 (170)
BRD	48.5	–8 (5)	150 (160)	–6 (–4)	135 (165)	–6	145
FRN	40	–4 (9)	120 (175)	–4	175	–4	180
NEW	27	–4	120	–5 (–2)	105 (165)	–3	160

*SE took place 1–3 hours before sunset on the Earth's surface.

The geomagnetic effect of an SE is caused by a decrease in the electron density N in the dynamo region of the atmosphere (heights $z \approx 90$–150 km). In this case, the specific conductivity of the ionospheric plasma decreases and the system of ionospheric currents is disrupted. For comparison with the observational results, we numerically estimated the magnitude of changes in the level of the geomagnetic field components using theoretical relations from [1, 2].

Summary

The SE was most often accompanied by a decrease in the level of all geomagnetic field components. At a number of stations, in addition to the decrease in level, there was its increase in other time intervals. The magnitude of disturbances in the level of all geomagnetic field components was usually comparable and did not exceed approximately 10 nT. The duration of the disturbances of all components was close and usually ranged from 120 to 200 min, with the duration of the SE being about 130–135 min. The delay or advance time of the geomagnetic effect depended on the geometry of the Moon's shadow. The SE was accompanied by a suppression of the oscillation that existed before the eclipse with a period of about 60 min and an amplitude of 1–3 nT. With an increase in the SE magnitude, a tendency towards an increase in the geomagnetic effect was observed. It has been confirmed that the magnitude of the geomagnetic effect of the SE depends not only on the eclipse magnitude, but also on the location of the magnetic station, the geometry of the Moon's shadow, the state of the ionosphere and the system of ionospheric currents. The results of estimates of the geomagnetic effect are in agreement with the observational results.

Work by L. F. Chernogor and M. Yu. Holub was supported by Ukraine state research projects #0124U000478 and #0122U001476.

References

[1] L. F. Chernogor, Physical effects of solar eclipses in atmosphere and geospace. Kharkiv: V. N. Karazin Kharkiv National University Publ., 480 p., 2013. (in Russian).

[2] L. F. Chernogor and N. Blaunstein, Radiophysical and Geomagnetic Effects of Rocket Burn and Launch in the Near-the-Earth Environment. Boca Raton, London, New York: CRC Press. Taylor & Francis Group, 542 p., 2018. https://doi.org/10.1201/b15614.

EFFECT OF A SOLAR ECLIPSE ON GNSS RADIO SIGNALS

L. F. Chernogor, Y. B. Mylovanov, V. L. Dorokhov, A. M. Tsymbal

School of Radiophysics, Biomedical Electronics and Computer Systems,
V. N. Karazin Kharkiv National University, Kharkiv 61022, Ukraine, e-mail: Leonid.F.Chernogor@gmail.com

The results of the analysis of time dependencies of the total electron content (TEC) caused by the solar eclipse (SE) on 20 April 2023 in the subpolar and equatorial ionosphere are presented. The dependence of the magnitude of the depletion and relative decrease of the TEC caused by the SE on latitude and time of day is revealed.

Introduction

One of the main tasks of applied physics and radioscience is further improvement of functioning of radio navigation, telecommunication, radar, radio astronomy and remote radio sounding systems. Reliability and accuracy of their functioning essentially depends on the value of TEC variations arising under the action of a number of powerful sources of energy release. One of them is a solar eclipse, which leads to global perturbations of the Earth–atmosphere–ionosphere–magnetosphere system. The response of the ionosphere to an SE depends significantly on the magnitude of the eclipse, the time of day, the season of the year and the coordinates of the observation site. Significant development of satellite technologies made it possible to cover large regions with measurements.

The purpose of this report is to present the results of the analysis of TEC time dependencies caused by the hybrid (total/annular) SE on 20 April 2023 in the equatorial and subpolar ionosphere. We analysed 172 TEC time dependencies that covered a significant region with the eclipse.

General Information

The solar eclipse on 20 April 2023 of the 129th Saros was a hybrid eclipse [https://www.eclipsewise.com/solar/SEprime/2001-2100/SE2023Apr20Hprime.html].

The SE began at 01:34:23 UT at 40°17.3' S and 075°59.5' E near the Kerguelen archipelago (France) located in the southern Indian Ocean and ended at 06:59:20 UT at 11°16.8' N and 167°13.6' E near the Tuvalu archipelago in the western Pacific Ocean. The maximum magnitude of 1.013 of the eclipse was observed at 04:16:45 UT on Timor Island of the Lesser Sunda Islands. The maximum duration of totality was 1 min 16 s. The SE travelled more than half of its path near the equatorial ionospheric anomaly.

Data on time dependencies of solar wind parameters, interplanetary magnetic field components and geomagnetic activity indices are given at [https://omniweb.gsfc.nasa.gov]. The state of space weather was favorable for the study of the SE effects on 20 April 2023.

To identify the ionospheric response to hybrid SE on 20 April 2023, the Global Navigation Satellite System (GNSS) signal records were processed. The signals from 18 satellites with numbers G01, G03, G04, G06–G09, G14, G16, G17–G19, G21, G22, G26, G27, G30, G31 were processed. In addition to the analysis of temporal dependencies, statistical analysis of absolute and relative TEC values for the entire data set was also performed.

Results of the Observation Data Analysis

The observation results are presented by temporal dependencies of TEC at the measurement points relative to the observation station. The designations in the figures are as follows: the eclipse magnitude M, the obscuration A, and the relative illuminance E of the measurement point under the absence and presence of the SE. At the sunlit point of the Earth the relative illuminance is assumed to be equal to unity. The numbers in the figures indicate the time dependence of TEC on the reference days 18 and 22 April 2023. The dotted curve represents the calculated expected values of TEC under the assumption of no obscuration. The temporal dependence of the expected TEC values is limited along the overflight by the positive magnitude M of the eclipse increased by the assumed average

ionospheric relaxation time, taken to be 40 min. The vertical and horizontal line segments reflect the choice of the TEC depletion maximum value and the time relative to the maximum of the eclipse magnitude *M*.

The most interesting results of the analysis are presented in Fig. 1 and Fig. 2, which clearly show that the SE was accompanied by a significant decrease in TEC. The magnitude of the TEC depletion depended on the magnitude of the SE, time of day, and geographic coordinates of the observation station.

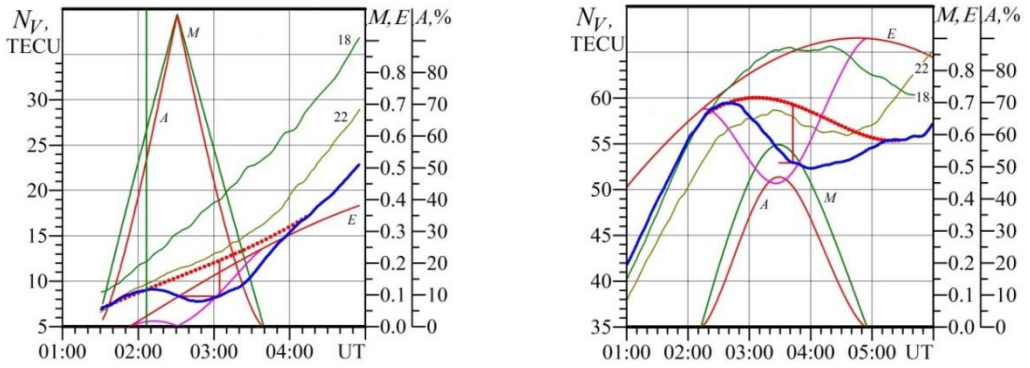

a *b*

Fig. 1. Temporal dependencies of TEC for (a) G04 satellite relative to the KRGG station and (b) G09 satellite relative to the XMIS station

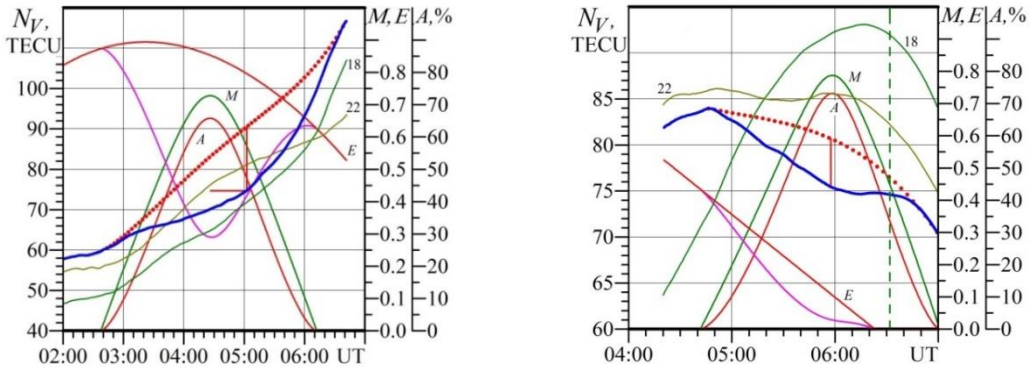

a *b*

Fig. 2. Temporal dependencies of TEC for (a) G03 satellite relative to the DARW station and (b) G04 satellite relative to the KIRI station

The impact of TEC variations on GNSS performance accuracy is evaluated.

Main Results

On a global scale, the temporal variations of TEC in the ionosphere on the reference days and on the SE day were analysed. For this purpose, the results of measurements at 31 stations and signals from 18 satellites were used. It was established for the first time that the relaxation time of the ionosphere after the end of the eclipse depends on the total TEC level. In the TEC range from 10 TECU to 50 TECU the relaxation time was 30–15 min. As the TEC increases from 50 TECU to 90 TECU, the time decreases to units of minutes. The 10% increase in the solar shading area results in a decrease in TEC of about 0.6 TECU. During the eclipse, the maximum decrease in TEC was about 10–15 TECU. Estimates have shown that TEC variations caused by the SE have a significant impact on the accuracy of GNSS positioning. Correct accounting of these variations is required.

The work was partially supported within the framework of state budgetary research projects assigned by the Ministry of Education and Science of Ukraine (state registration numbers 0122U001476 and 0124U000478).

VARIATIONS OF IONOSPHERIC WEATHER DURING GEOSPACE STORM ON MAY 10–11, 2024

L. F. Chernogor, V. O. Bessarabova

School of Radiophysics, Biomedical Electronics and Computer Systems,
V. N. Karazin Kharkiv National University, Kharkiv 61022, Ukraine e-mail: Leonid.F.Chernogor@gmail.com

The main features of the global manifestation of a unique geospace storm on May 10–13, 2024 in the F-region of the ionosphere are studied. The largest negative disturbances were observed on May 11, 2024, during the recovery phase of the geomagnetic storm. At most stations, the storm was strong or very strong during the daytime. At night, the manifestations of strong, very strong and extremely strong storms were mainly observed. The storm of May 13, 2024 was less intense compared to the storm of May 11, 2024.

Introduction

Variations in ionospheric weather have a significant impact on the vital activity of our civilization, on the functioning of telecommunications, radio navigation, radar, radio astronomy, remote sensing of the earth from space and space from the earth. Ionospheric storms are extreme manifestations of ionospheric weather, which are an integral part of space weather. During the 25th cycle of solar activity, the most significant was the storm of May 10-11, 2024 (Mother's Day storm) [1, 2]. Significant progress has been made in the study of ionospheric storms and ionospheric weather. It has been established that there are no two identical ionospheric storms, each of them has its own unique features [3, 4]. All of this makes it important to study each new ionospheric storm, and even· more so a unique event. The ionospheric storm of May 10-11, 2024, should be considered unique.

The state of space weather

On May 8, 2024, the active region of the Sun, NOAA 13664, generated X1.0 and X1.02 flares and several M-class flares, as well as coronal mass ejections (CMEs) directed towards our planet. The next day, the same area generated flares of class X2.25 and X1.12. The flares were accompanied by CMEs. On May 10, 2024, a class X3.98 flare occurred. On May 11 and 14, solar flares of class X5.8 and X8.7 were recorded, respectively. It should be added that the X8.7 flare was the most powerful in the 25th solar activity cycle. CMEs reached the Earth on May 10 and 11, 2024, causing a geospace storm. On May 10, 2024, there was also an outbreak of solar cosmic ray activity with energies greater than 10 MeV. 9 and in the first half of May 10, 2024, the *Dst*-index fluctuated around 0 nT. From 16:00 to 19:00 on May 10, 2024, it increased to a maximum value of 62 nT. There was a sudden onset of a magnetic storm. Further, this index, fluctuating slightly, from 19:00 on May 10 to ~01:00 on May 11, 2024, decreased from 0 nT to a minimum value of -412 nT. This indicated the onset of the main phase of the magnetic storm. After 01:00 on May 11, 2024, the Dst-index, fluctuating, gradually increased from -412 nT to -50 nT at the end of the day on May 15, 2024. The duration of the magnetic storm was about four days. It consisted of two storms. For the first storm Kp_{max} = 9, which observed on May 10, 2024, and for the second storm Kp_{max} = 6. The second storm occurred on the night of May 12-13, 2024. During the storm of May 10-11, 2024, the aurorae were observed not only in high and middle latitudes, but also in low geographic latitudes (close to 22.7° and --17.0°). They correspond to the geomagnetic latitudes of 30.7° and -24.2°.

Data and tools

The data on the critical frequency f_oF2 of the F region obtained with the help of the international global ionosonde network GIRO [https://giro.uml.edu/index.html] were used as the initial data. The F region is the best indicator of ionospheric storms. In the western hemisphere, data from ionosondes located in both the northern and southern parts of the globe were used. For the eastern hemisphere, no operating ionosonde was found in the southern latitudes. The values of f_oF2 were recorded at 15-minute intervals. During the most intense negative ionospheric storm on May 11, 2024, the data at f_oF2 were incomplete or absent (blackout phenomenon). Since the

temporal variations fluctuated in time, a moving average was used over a time interval of 90 minutes with a 15-minute shift. The day of May 9, 2024 was chosen as the reference day.

Analysis results

In general, the effects of the ionospheric storm in the eastern and western hemispheres were similar. Signs of a negative ionospheric storm prevailed. At night, the effects were noticeably greater than during the day. The duration of the blackout decreased as we moved south. However, there were differences. In the eastern hemisphere, only negative ionospheric storms were observed, while at some stations in the western hemisphere, there were manifestations of a weak to moderate positive storm. The most significant difference was in the behavior of foF2 and N during the main phase of the magnetic storm. In the eastern hemisphere, the frequency of foF2 sharply decreased from 7-10 MHz to 2-3 MHz, i.e., the storm was super strong. In the western hemisphere, at stations located at lower latitudes (EG931, AU930, CAJ2M and BBJ3R), on the contrary, during the main phase of the magnetic storm, this frequency increased from 10 MHz to 15 - 17 MHz. Such values are characteristic of a positive ionospheric storm varying from moderate to strong [3, 4]. The described differences are explained by different local times of onset of the main phase of the magnetic storm. While in the eastern hemisphere this phase took place from evening to the first half of the night on May 10, 2024, in the western hemisphere the main phase occurred from approximately 11:00 to 19:00 local time on May 10, 2024, i.e. in the middle of the day and evening. The parameters of the ionospheric storms recorded at CAJ2N station differ significantly from those at other stations. This is caused by the influence of the equatorial ionization anomaly, the crest of which moved in both hemispheres from the equator. Thus, the ionospheric storm from May 10 to 13, 2024, had a number of features. It differed from other storms not only in its significant intensity, sometimes reaching the level of very strong and even extremely strong, but also in the generation of positive-negative-positive storms. The negative storms were more intense and long-lasting. The conducted research confirmed the expediency of a detailed study of each new ionospheric storm with its unique features.

Conclusions

The main features of the global manifestation of a unique geospace storm on May 10–13, 2024 in the F-region of the ionosphere are studied. The largest negative disturbances were observed on May 11, 2024, during the recovery phase of the geomagnetic storm. At most stations, the storm was strong or very strong during the daytime. At night, the manifestations of strong, very strong and extremely strong storms were mainly observed. The storm of May 13, 2024 was less intense compared to the storm of May 11, 2024. During the daytime, it was classified as weak to medium, and at night it was mostly classified as strong and even as very strong. At times, negative and positive ionospheric storms replaced each other. Positive ionospheric storms were weaker. The duration of the blackout tended to decrease with decreasing geogrephical latitude of the station.

The example of the unique storm of May 10-11, 2024, confirmed the expediency of a detailied study of each new ionospheric storm and the state of ionospheric weather.

References

[1] L. Spogli, T. Alberti, P. Bagiacchi, L. Cafarella, C. Cesaroni, G. Cianchini, I. Coco, D. Di Mauro, R. Ghidoni, F. Giannattasio, A. Ippolito, C. Marcocci, M. Pezzopane, E. Pica, A. Pignalberi, L. Perrone, V. Romano, D. Sabbagh, C. Scotto, S. Spadoni, R. Tozzi, M. Viola, “The effects of the May 2024 Mother’s Day superstorm over the Mediterranean sector: from data to public communication”, 2024. https://doi.org/10.4401/ag-9117.

[2] R. Singh, D. E. Scipion, K. Kuyeng, P. J. C. Patilongo, C. De La Jara, J. P. Velasquez, R. Flores, E. Ivan, “Ionospheric Disturbances observed over the Peruvian sector during the Mother's Day Storm (G5-level) on May 10-12, 2024”, 2024. https://doi.org/10.22541/essoar.172108210.04033367/v1,

[3] L. F. Chernogor, I. F. Domnin, “Physics of geospace storms”, Kharkiv: V. N. Karazin Kharkiv National University Publ., 2014.

[4] L. F.Chernogor, “Physics of geospace storms”, Space Science and Technology, 27, 3–77, 2021a. https://doi.org/10.15407/knit2021.01.003.

GLOBAL VARIATIONS OF THE GEOMAGNETIC EFFECT DURING THE OCTOBER 14, 2023 ANNULAR SOLAR ECLIPSE IN THE AMERICAS

L. F. Chernogor, M. Yu. Holub, V. T. Rozumenko

School of Radiophysics, Biomedical Electronics and Computer Systems,
V. N. Karazin Kharkiv National University, Kharkiv 61022, Ukraine e-mail: Leonid.F.Chernogor@gmail.com

The analysis was made possible due to the data on temporal variations in the X, Y, and Z components of the geomagnetic field collected at thirteen INTERMAGNET network magnetometer stations. The solar eclipse acted to cause non-sinusoidal and quasi-sinusoidal perturbations of 180–240 min duration in all geomagnetic field components on a global scale. The estimates made on the assumption that the magnetic effect is due to the ionospheric current disruptions show good agreement with the observations.

Introduction

A solar eclipse (SE) is a convenient solar-terrestrial phenomenon of opportunity for studying coupling in the solar-terrestrial system comprised of the Sun, interplanetary medium, magnetosphere, ionosphere, atmosphere, and solid earth. In the course of a SE, a number of parameters become disturbed in all subsystems and geophysical fields, and in particular, in the geomagnetic field. The objectives of this paper are the investigation of temporal variations in the northward, *X*, eastward, *Y*, and downward, *Z*, components of the geomagnetic field recorded during the October 14, 2023 annular SE and over magnetically quiet days, used as a reference period, at thirteen INTERMAGNET magnetometer stations in the Americas.

The basic information on the October 14, 2023 annular SE of Saros 134 may be found at https://eclipse.gsfc.nasa.gov/SEdecade/SEdecade2021.html. The SE began at 15:03:47 UTC and ended at 20:55:15 UTC. The eclipse magnitude $M_{max} \approx 0.9520$ occurred at the instant of greatest eclipse 17:59:29 UTC at the point (11°22' N, 0.83°06.1' W). Other parameters of interest are the solar altitude of 67.9°, the azimuth of 208.0°, the annularity duration of 5 min 17.2 s, and the 187.4-km width of path of annularity, which started at the point (41.6° N, 150° W) in the northeastern Pacific, crossed the U.S.A., Central America, South America, and ended at the point (5.6°S, 30°W) in the Atlantic Ocean. The main features of the October 14, 2023 SE include its annularity, its occurrence from dawn to dusk, its magnitude variation from 0.30 to 0.86, and the longest ever-observed path across the mainland of the Americas, covering latitudes from ~65°N to 12°S.

The eclipse magnitude M_{max} at a total of thirteen magnetometer stations varied from 0.30 to 0.86. All stations are located in the Americas, their longitude varies from ~66°W to ~160°W and latitude changes from ~12°S to 65°N. The effects of the solar eclipse were analyzed during morning, sunlit, and evening hours. The raw data have 0.1-nT amplitude resolution and 1-min time resolution. First, DC components, different for different stations, are subtracted from the raw data, and the dependences $X(t)$, $Y(t)$, and $Z(t)$ are formed. Then, the 60-min running averages are used to form temporal variations in the trends $\overline{X}(t)$, $\overline{Y}(t)$, and $\overline{Z}(t)$. In addition, the differences between $X(t)$ and $\overline{X}(t)$, $Y(t)$ and $\overline{Y}(t)$, $Z(t)$ and $\overline{Z}(t)$ are calculated. The dependences $\overline{X}(t)$, $\overline{Y}(t)$, $\overline{Z}(t)$ are used for finding the non-sinusoidal SE effect, and the differences are used for revealing possible quasi-sinusoidal perturbations in the geomagnetic field. To determine the response of the geomagnetic field to the SE, the closer analysis of the state of space weather needs to be done. Use has been made of both the data retrieved from https://omniweb.gsfc.nasa.gov/form/dx1.html and the results of original calculations. During magnetically quiet times, the planetary K_p index did not exceed 1–2; however, it attained 3.7 on October 13, 2023 and was briefly rising to 3 on October 14, 2023. The minimum of 30 nT in the equatorial hourly D_{st}-index was observed at the end of the day on October 12, 2023. The next day, this index increased to almost 0 nT. Thus, it can be assumed that the geomagnetic field was weakly disturbed on October 14, 2023, which allowed the geomagnetic effect of the SE to be detected. The magnetically quiet days October 11 and 16, 2023 were chosen to be quiet time reference period.

Data Analysis

The non-sinusoidal perturbations in the *X*-component of the geomagnetic field, which are associated with the SE, exhibit quite a complicated dependence on eclipse obscuration A_{max}. A decrease in geomagnetic field strength is determined not only by relative amplitudes δN_{min} but also by electron density N_0 and the eastward velocity component, v_y. At the same time, N_0 and v_y are dependent on latitude and the time of day. The largest perturbations in $\Delta\overline{X}$, which were observed to occur at the Boulder, Huancayo, Victoria, and Newport stations, attained 15–20 nT. For both the Boulder and Victoria stations, A_{max} = 81%, which resulted in $\delta_N \approx -(0.41–0.56)$ for $N_0 \approx 4.6 \times 10^{11}$ m^{-3} and $N_0 \approx 3.6 \times 10^{11}$ m^{-3}, respectively. A considerable value of the magnetic effect of the solar eclipse is explained by a large enough value of both A_{max} and *E* region dynamo N_0. Approximately the same may be noted with regard to the Newport station. The Huancayo station is located within the equatorial anomaly where the N_0 at the *E* region dynamo heights attained 8×10^{11} m^{-3} during the daytime that resulted in a decrease of 20 nT in the *X*-component strength when A_{max} = 55%. The SE effect was considerable, with the absolute value of $\overline{X}(t)$ attaining ~10–13 nT, at the Tucson, Fresno, and Bay St. Louis stations because the A_{max} varied within (82–72)% and N_0 under quiet conditions sometimes reached $(2.3 – 3) \times 10^{11}$ m^{-3}. For the Shumagin station, A_{max} = 81%, i.e., the Sun's surface area occulted by the Moon was the same as that at the Boulder station, but the solar eclipse effect was only –2 nT, whereas at the Boulder station it was –20 nT, an order of magnitude greater. This difference is explained by the time of the SE at the Shumagin station, just after sunrise, when $N_0 \approx 0.46 \times 10^{11}$ m^{-3}. The perturbation at the Sitka station was insignificant, $\Delta\overline{X} \approx -3$ nT; the main reason for this was the time of the observation, after sunrise, when $N_0 \approx 10^{11}$ m^{-3}, in addition, A_{max} = 64%. The obscuration A_{max} was equal to 47% for the College and Brandon stations; however, the v_y, at the Brandon station was by a factor of about 4 smaller than at the College station, but the electron density, N_0, under quiet conditions, on the contrary, was by a factor of 3.9 greater, which sustained virtually an unchangeable level of the geomagnetic effect. For the San Juan station, A_{max} = 44%, which is not very different from A_{max} = 46.5% at the Brandon station, but the trend in the *X* component, $\Delta\overline{X}$, is by a factor of approximately 4 smaller. This is explained by the time of the observation, during sunset at the San Juan station, when $N_0 \approx 1.1 \times 10^{11}$ m^{-3}. The effect was insignificant (–2 nT) at the Ottawa station, although $N_0 \approx 2.7 \times 10^{11}$ m^{-3} there, which is explained by a small value of A_{max} = 19%. The quasi-sinusoidal perturbations amplitude usually did not exceed 5–6 nT. Only at the Huancayo and College stations, the amplitude sometimes attained 15 nT. Both these stations are located in the regions with the more powerful current systems. The quasi-sinusoidal perturbations appeared with time delays of 30 to 150 min relative to the SE onsets, durations of 180–240 min, and with periods of 10–80 min.

Conclusions

The SE acted to produce a decrease of up to 10–20 nT in the strength of all geomagnetic field components. The *X*-component experienced the greatest disturbance, while the *Z*-component was disturbed the least. The duration of the perturbation was observed to be ~120–240 min, while the onset of the decrease in the strength was delayed by 80–100 min relative to the SE first contact. Quasi-sinusoidal variations of up to 5 – 15 nT and period within 10–80 min were recorded. The time delay of the appearance of quasi-sinusoidal perturbations varied from 30 to 150 min, and they persisted for 180–240 min. A tendency was shown for the magnitude of the non-sinusoidal and quasi-sinusoidal perturbations to increase as the SE magnitude increased. The magnitude of the geomagnetic effect of the SE is significantly dependent on the geographic coordinates of the magnetometer station, local time, the state of the ionosphere and ionospheric current system. The electron density depletion was estimated to be ~ 0.10 to ~ 0.40–0.60 when the eclipse obscuration A_{max} varied from 19% to 82%. The movement of the lunar shadow was accompanied by the generation and propagation of atmospheric gravity waves with ~10–80-min periods and electron density perturbations with amplitudes of the order of 0.01–0.03. The estimates show good agreement with the observations.

Support for L. F. Chernogor, M. Yu. Holub, and V. T. Rozumenko was provided by Ukraine state research projects # 0122U001476 and # 0124U000478.

CONTENTS OF THE CONFERENCE